AGGREGATION-INDUCED EMISSION

APPLICATIONS IN BIOSENSING, BIOIMAGING AND BIOMEDICINE VOLUME II

Edited by Xinggui Gu and Ben Zhong Tang

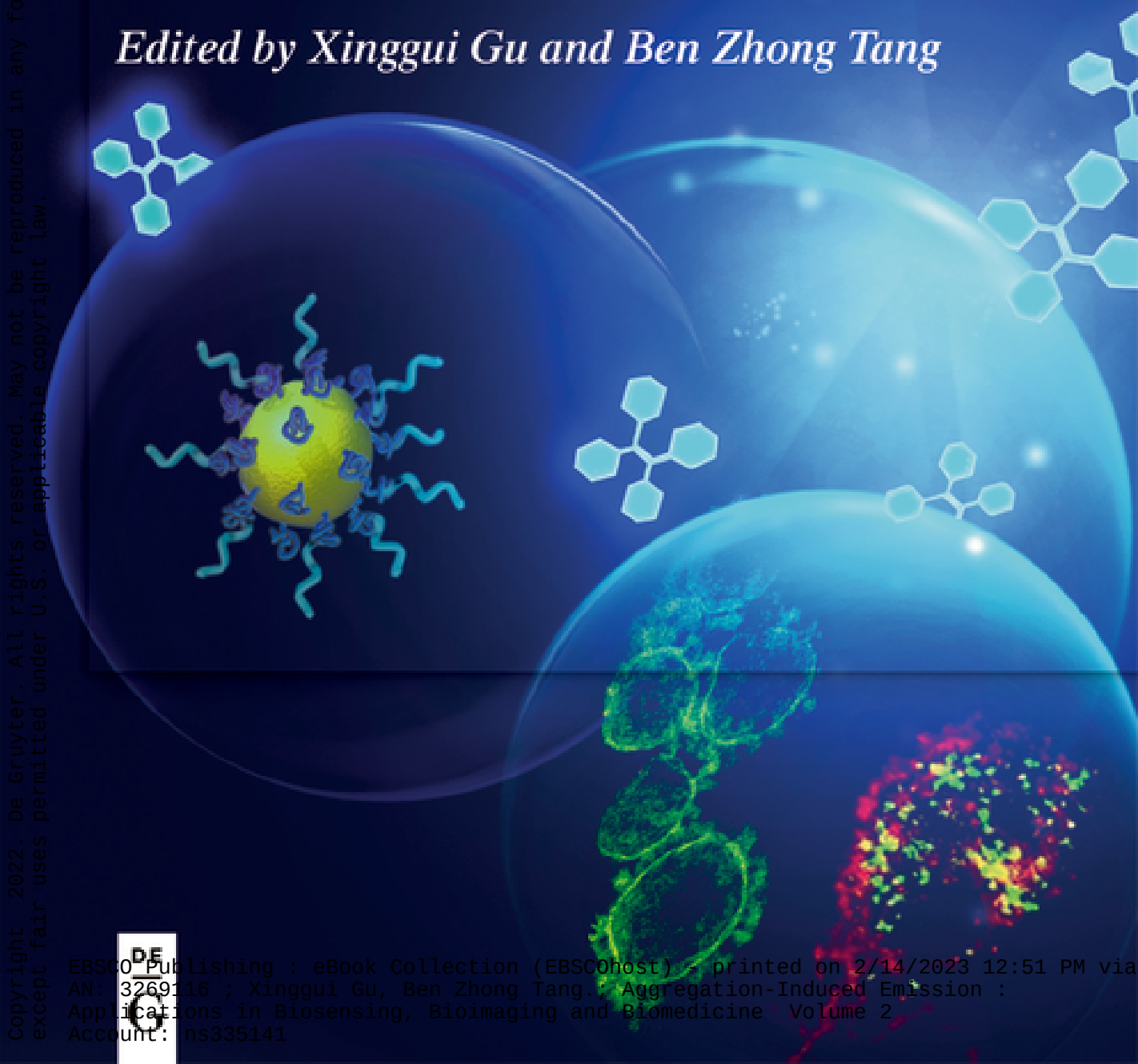

Xinggui Gu, Ben Zhong Tang (Eds.)

Aggregation-Induced Emission

Also of interest

Aggregation-Induced Emission.
Applications in Biosensing, Bioimaging and Biomedicine – Volume 1
Xinggui Gu, Ben Zhong Tang (Eds.), 2022
ISBN 978-3-11-067210-7, e-ISBN 978-3-11-067222-0

Biosensors.
Fundamentals and Applications
Chandra Mouli Pandey und Bansi Dhar Malhotra, 2019
ISBN 978-3-11-063780-9, e-ISBN 978-3-11-064108-0

Metal Ions in Bio-Imaging Techniques
Astrid Sigel, Eva Freisinger, Roland K.O. Sigel (Eds.), 2021
ISBN 978-3-11-068556-5, e-ISBN 978-3-11-068570-1

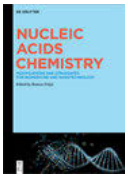

Nucleic Acids Chemistry.
Modifications and Conjugates for Biomedicine and Nanotechnology
Ramon Eritja, 2021
ISBN 978-3-11-063579-9, e-ISBN 978-3-11-063953-7

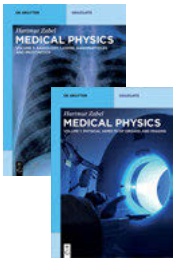

Medical Physics
Hartmut Zabel, 2017
Volume 1: Physical Aspects of Organs and Imaging
ISBN 978-3-11-037281-6, e-ISBN 978-3-11-037283-0
Volume 2: Radiology, Lasers, Nanoparticles and Prosthetics
ISBN 978-3-11-055310-9, e-ISBN 978-3-11-055311-6

Aggregation-Induced Emission

Applications in Biosensing, Bioimaging and Biomedicine – Volume 2

Edited by
Xinggui Gu and Ben Zhong Tang

DE GRUYTER

Editors
Prof. Xinggui Gu
Beijing Advanced Innovation Center for Soft
Matter Science and Engineering,
Beijing University of Chemical Technology,
100029, Beijing,
People's Republic of China
guxinggui@mail.buct.edu.cn

Prof. Ben Zhong Tang
Shenzhen Institute of Aggregate Science and Technology,
School of Science and Engineering,
The Chinese University of Hong Kong (Shenzhen),
Shenzhen 518172,
People's Republic of China
tangbenz@cuhk.edu.cn

ISBN 978-3-11-067298-5
e-ISBN (PDF) 978-3-11-067307-4
e-ISBN (EPUB) 978-3-11-067313-5

Library of Congress Control Number: 2021951719

Bibliographic information published by the Deutsche Nationalbibliothek
The Deutsche Nationalbibliothek lists this publication in the Deutsche Nationalbibliografie; detailed bibliographic data are available on the Internet at http://dnb.dnb.de.

Typesetting: Integra Software Services Pvt. Ltd.
Printing and binding: CPI books GmbH, Leck

www.degruyter.com

Contents

Contributing authors

Pengfei Zhang
Institute of Biomedicine and Biotechnology
Shenzhen Institutes of Advanced Technology
Chinese Academy of Sciences
Shenzhen 518055
People's Republic of China
pf.zhang@siat.ac.cn

Xiuli Xu
Institute of Biomedicine and Biotechnology
Shenzhen Institutes of Advanced Technology
Chinese Academy of Sciences
Shenzhen 518055
People's Republic of China

Xiaoxi Ma
Institute of Biomedicine and Biotechnology
Shenzhen Institutes of Advanced Technology
Chinese Academy of Sciences
Shenzhen 518055
People's Republic of China

Hanlin Ou
State Key Laboratory of Medicinal
Chemical Biology
Key Laboratory of Bioactive Materials
Ministry of Education, and College
of Life Sciences
Nankai University, Tianjin 300071
People's Republic of China

Zhiyuan Gao
State Key Laboratory of Medicinal
Chemical Biology
Key Laboratory of Bioactive Materials
Ministry of Education, and College
of Life Sciences
Nankai University, Tianjin 300071
People's Republic of China

Dan Ding
State Key Laboratory of Medicinal Chemical
Biology
Key Laboratory of Bioactive Materials
Ministry of Education, and College
of Life Sciences
Nankai University, Tianjin 300071
People's Republic of China
dingd@nankai.edu.cn

Nuernisha Alifu
State Key Laboratory of Pathogenesis
Prevention and Treatment of High Incidence
Diseases in Central Asia
School of Medical Engineering
and Technology
Xinjiang Medical University
Urumqi 830054
People's Republic of China
State Key Laboratory of Modern Optical
Instrumentations
Centre for Optical and Electromagnetic
Research, College of Optical Science
and Engineering
International Research Center
for Advanced Photonics
Zhejiang University
Hangzhou 310058
People's Republic of China

https://doi.org/10.1515/9783110673074-203

Jun Qian
State Key Laboratory of Modern Optical Instrumentations
Centre for Optical and Electromagnetic Research, College of Optical Science and Engineering
International Research Center for Advanced Photonics
Zhejiang University
Hangzhou 310058
People's Republic of China
qianjun@zju.edu.cn

Yupeng Shi
Ming Wai Lau Centre for Reparative Medicine
Karolinska Institutet
Hong Kong, People's Republic of China

Chuen Kam
Ming Wai Lau Centre for Reparative Medicine
Karolinska Institutet
Hong Kong, People's Republic of China

Engui Zhao
School of Science
Harbin Institute of Technology, Shenzhen
HIT Campus of University Town
Shenzhen 518055
People's Republic of China

Sijie Chen
Ming Wai Lau Centre for Reparative Medicine
Karolinska Institutet
Hong Kong, People's Republic of China
sijie.chen@ki.se

Yi-Feng Wang
CAS Key Laboratory for Biomedical Effects of Nanomaterials and Nanosafety
CAS Center for Excellence in Nanoscience
National Center for Nanoscience and Technology of China
No. 11, First North Road
Zhongguancun
Beijing, 100190
People's Republic of China
University of Chinese Academy of Sciences
Beijing 100049
People's Republic of China

Yufei Wang
CAS Key Laboratory for Biomedical Effects of Nanomaterials and Nanosafety
CAS Center for Excellence in Nanoscience
National Center for Nanoscience and Technology of China
No. 11, First North Road
Zhongguancun
Beijing, 100190
People's Republic of China
University of Chinese Academy of Sciences
Beijing 100049
People's Republic of China

Shengliang Li
CAS Key Laboratory for Biomedical Effects of Nanomaterials and Nanosafety
CAS Center for Excellence in Nanoscience
National Center for Nanoscience and Technology of China
No. 11, First North Road
Zhongguancun
Beijing, 100190
People's Republic of China
College of Pharmaceutical Sciences,
Soochow University
Suzhou 215123
People's Republic of China

Jinchao Zhang
Key Laboratory of Medicinal Chemistry and Molecular Diagnosis of the Ministry of Education
College of Chemistry and Environmental Science
Hebei University
Baoding 071002
People's Republic of China

Yuanyuan Zhang
Wake Forest Institute for Regenerative Medicine
Wake Forest University School of Medicine
Winston-Salem,
North Carolina
USA

Peter Timashev
Laboratory of Clinical Smart Nanotechnologies
Institute for Regenerative Medicine
Sechenov University
Moscow
Russia

Aiping Zheng
Institute of Pharmacology and Toxicology of Academy of Military Medical Sciences
27 Taiping Road Haidian District
Beijing 100850
People's Republic of China

Xing-Jie Liang
CAS Key Laboratory for Biomedical Effects of Nanomaterials and Nanosafety
CAS Center for Excellence in Nanoscience
National Center for Nanoscience and Technology of China
No. 11, First North Road
Zhongguancun
Beijing, 100190
People's Republic of China
University of Chinese Academy of Sciences
Beijing 100049
People's Republic of China

Guan Wang
Beijing Advanced Innovation Center for Soft Matter Science and Engineering
College of Materials Science and Engineering
Beijing University of Chemical Technology
Beijing 100029
People's Republic of China

Xinggui Gu
Beijing Advanced Innovation Center for Soft Matter Science and Engineering
College of Materials Science and Engineering
Beijing University of Chemical Technology
Beijing 100029
People's Republic of China
guxinggui@mail.buct.edu.cn

Ben Zhong Tang
Shenzhen Institute of Aggregate Science and Technology
School of Science and Engineering
The Chinese University of Hong Kong (Shenzhen), Guangdong 518172
People's Republic of China
tangbenz@cuhk.edu.cn

Shunjie Liu
Key Laboratory of Polymer Ecomaterials
Changchun Institute of Applied Chemistry
Chinese Academy of Sciences
Changchun 130022
School of Applied Chemistry and Engineering
University of Science and Technology of China
Hefei 230026
People's Republic of China
sjliu@ciac.ac.cn

Lirong Wang
State Key Laboratory of Luminescent Materials and Devices,
Guangdong Provincial Key Laboratory of Luminescence from Molecular Aggregates
Center for Aggregation-Induced Emission,
South China University of Technology,
Guangzhou 510640,
People's Republic of China

Xinzhe Yang
State Key Laboratory of Luminescent Materials and Devices,
Guangdong Provincial Key Laboratory of Luminescence from Molecular Aggregates
Center for Aggregation-Induced Emission,
South China University of Technology,
Guangzhou 510640,
People's Republic of China

Anjun Qin
State Key Laboratory of Luminescent Materials and Devices,
Guangdong Provincial Key Laboratory of Luminescence from Molecular Aggregates
Center for Aggregation-Induced Emission,
South China University of Technology,
Guangzhou 510640,
People's Republic of China

Shengnan Liu
Key Laboratory of Nanobiosensing and Nanobioanalysis at Universities of Jilin Province
Department of Chemistry
Northeast Normal University
5268 Renmin Street, Changchun
Jilin Province 130024
People's Republic of China

Yu Pei
Key Laboratory of Nanobiosensing and Nanobioanalysis at Universities of Jilin Province
Department of Chemistry
Northeast Normal University
5268 Renmin Street, Changchun
Jilin Province 130024
People's Republic of China

Dongxia Zhu
Key Laboratory of Nanobiosensing and Nanobioanalysis at Universities of Jilin Province
Department of Chemistry
Northeast Normal University
5268 Renmin Street, Changchun
Jilin Province 130024
People's Republic of China
zhudx047@nenu.edu.cn

Dan Wu
Key Lab of Organic Optoelectronics & Molecular Engineering
Department of Chemistry
Tsinghua University
Beijing 100084
People's Republic of China
College of Materials Science and Engineering
Zhejiang University of Technology
Hangzhou 310014
People's Republic of China

Zhixuan Zhou
Max Planck Institute for Polymer Research
Mainz 55128
Germany
zhixuan.zhou@mpip-mainz.mpg.de

Xuzhou Yan
School of Chemistry and Chemical Engineering
Frontiers Science Center for Transformative Molecules
Shanghai Jiao Tong University
Shanghai 200240
People's Republic of China

Guocan Yu
Key Lab of Organic Optoelectronics & Molecular Engineering
Department of Chemistry
Tsinghua University
Beijing 100084
People's Republic of China
guocanyu@mail.tsinghua.edu.cn

Pengfei Zhang, Xiuli Xu, Xiaoxi Ma

Chapter 12
NIR aggregate-biohybrid systems for biomedical applications

12.1 Introduction of NIR aggregate

Fluorescence imaging techniques have become an indispensable imaging modality in fundamental biological research and preclinical and clinical applications. Compared to other imaging technologies, fluorescence imaging techniques possess unique features such as high spatiotemporal resolution, high sensitivity, fast acquisition speed, low toxicity, and relatively low cost. However, biological tissues/organs usually possess endogenous high autofluorescence in the visible region (400–700 nm), which leads to strong interference for conventional fluorescence imaging, resulting in reduced sensitivity and imaging contrast [1]. Infrared radiation is an electromagnetic radiation whose wavelength is longer than the longest wavelength of red color in visible light but shorter than that of microwave. The infrared region spans from roughly 300 GHz (1 mm) to 400 THz (750 nm) and can be divided into three parts: near-infrared (NIR), mid-infrared, and far-infrared. The NIR region typically falls in the spectrum from 120 to 400 THz (2,500–750 nm) (Figure 12.1). NIR materials are defined as the substances that interact with NIR light, such as absorption and reflection, and emit NIR light under external stimulation such as photoexcitation, electric field, and chemical reaction. NIR materials can roughly be divided into two groups: inorganic materials including metal oxides and semiconductor nanocrystals; and organic materials including metal complexes, ionic dyes, extended p-conjugated chromophores, and donor–acceptor (D–A) charge transfer (CT) chromophore [2]. However, these materials are typically restrained within inorganic compounds such as metal-containing inorganic complexes, particularly rare earth luminophores where the emissions usually come from the f–f or d–f electron transitions, or quantum dots, whose size-dependent

Acknowledgements: The authors gratefully acknowledge the financial support provided by National Key R&D Programs (2021YFA0910000), Guangdong Province International Scientific and Technological Cooperation Projects (2020A0505100047), and the Shenzhen basic research (key project) (JCYJ20210324120011030).

Pengfei Zhang, Institute of Biomedicine and Biotechnology, Shenzhen Institutes of Advanced Technology, Chinese Academy of Sciences, Shenzhen 518055, P.R. China,
e-mail: pf.zhang@siat.ac.cn
Xiuli Xu, Xiaoxi Ma, Institute of Biomedicine and Biotechnology, Shenzhen Institutes of Advanced Technology, Chinese Academy of Sciences, Shenzhen 518055, P.R. China

https://doi.org/10.1515/9783110673074-013

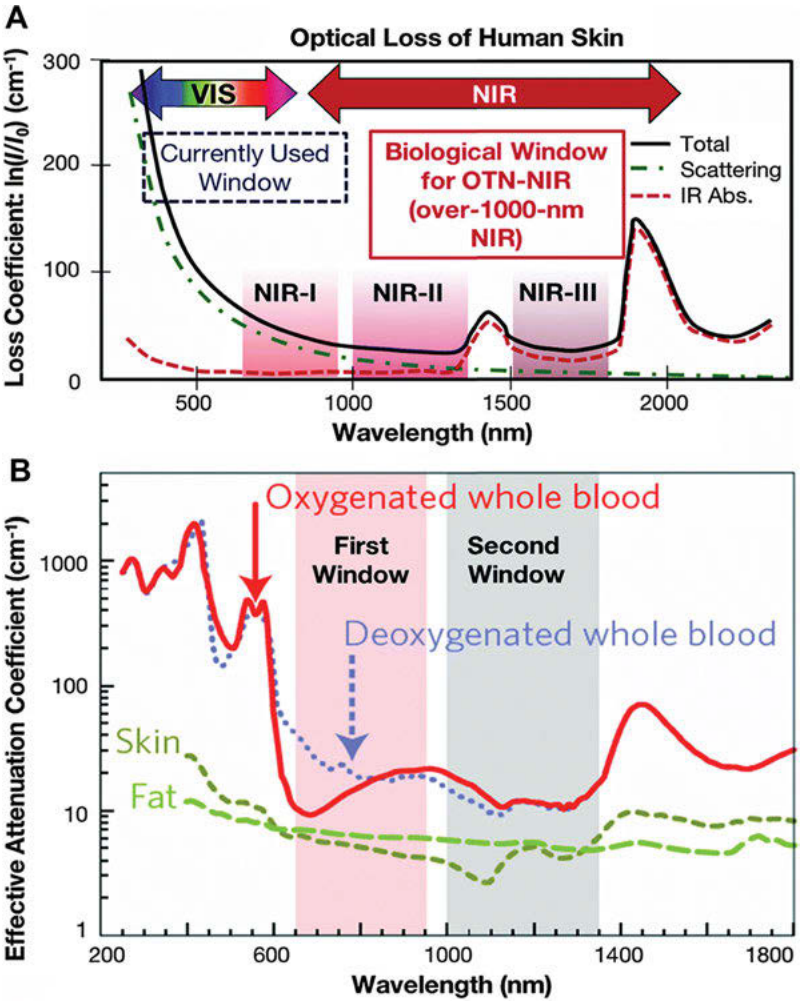

Figure 12.1: (A) Human skin absorption spectra in NIR-I, NIR-II, and NIR-III regions [5]. Copyright © 2013, The Royal Society of Chemistry. (B) Absorption and scattering spectra from oxygenated blood, deoxygenated blood, skin, and fatty tissue [6]. Copyright © 1969, Nature Publishing Group; Copyright © 2016, The Royal Society of Chemistry.

multiple luminescence emissions originate from the d–d electron transitions. Unfortunately, the emission wavelengths of rare earth luminophores are very difficult to manipulate due to the shielding effect from exterior orbitals and the fixed energy levels of the rare earth ions while quantum dots suffer from both high toxicity of the heavy metals and environmentally sensitive emissions in the NIR region, which have prevented them from even wider applications. On the contrary, organic luminophores are more desired due to their competitive advantages such as arbitrarily tunable molecular

structures and chemical compositions, easy for functionalization and scalable synthesis, and promising potentials to satisfy biomedical-related and especially flexible electronics-oriented expectations [3]. Moreover, compared with the inorganic NIR emitters, organic NIR emitters have attracted widespread attention due to their own advantages, including relatively smaller molecular weight, easier functionalization, and shorter retention time in organisms [4]. The organic agents with large p domains, elongated p conjugations, or ordered packing in aggregates have been developed to redshift the absorption and emission windows. Efforts to mitigate thermal deactivation processes, p–p stacking interactions, and solvent-disruption effects have also been made to improve the fluorescence brightness. The molecular design strategy and the underlying mechanism for regulating the balance between fluorescence (radiative pathway), photothermal effect (nonradiative pathway), and photodynamic effect (intersystem crossing (ISC) pathway) in these narrow band gap materials remain obscure.

With the development of scientific research on dye aggregation, the construction of dye self-assembly provides new ideas for controlling photophysical properties and in vivo delivery of dyes. Tian et al. reported a series of 2-/2,6-aryl-substituted boron-dipyrromethene dyes with wide-range and multifluorescence emissions across red and NIR in their aggregation states. Experimental data of X-ray diffraction, UV-vis absorption, and room temperature fluorescence spectra have proved the multiple excitations and easy-adjustable emission features in aggregated boron-dipyrromethene dyes. Temperature-dependent and time-resolved fluorescence studies have indicated a successive energy transfer from high to step-wisely lower located energy levels that correspond to different excitation states of aggregates. Consistent quantum chemical calculation results have proposed possible aggregation modes of boron-dipyrromethene dyes to further support the above-described scenario. Thus, this study greatly enriches the fundamental recognition of conventional boron-dipyrromethene dyes by illustrating the relationships between multiple emission behaviors and the aggregation states of boron-dipyrromethene molecules (Figure 12.2) [3].

J-aggregates discovery of pseudoisocyanine in 1937 launched the new chapter in aggregate science. J-aggregation is an efficient strategy for the development of fluorescent imaging agents in the second NIR window. However, the design of the second NIR fluorescent J-aggregates is challenging due to the lack of suitable J-aggregation dyes. The structures and properties of functional materials are inherently linked. Generally, structure decides the material property and the property can in part reflect the structural variation. Li et al. reported meso-[2.2]paracyclophanyl-3,5-bis-*N*,*N*-dimethylaminostyrl BODIPY (PCP-BDP2) as an example of BODIPY dye with J-aggregation induced the second NIR fluorescence. PCP-BDP2 shows an emission maximum at 1,010 nm in the J-aggregation state. Mechanism studies reveal that the steric and conjugation effect of the PCP group on the BODIPY play key roles in the J-aggregation behavior and photophysical properties tuning. Notably, PCP-BDP2 J-aggregates can be utilized for lymph node imaging and fluorescence-guided surgery in the nude mouse, which demonstrates their potential clinical

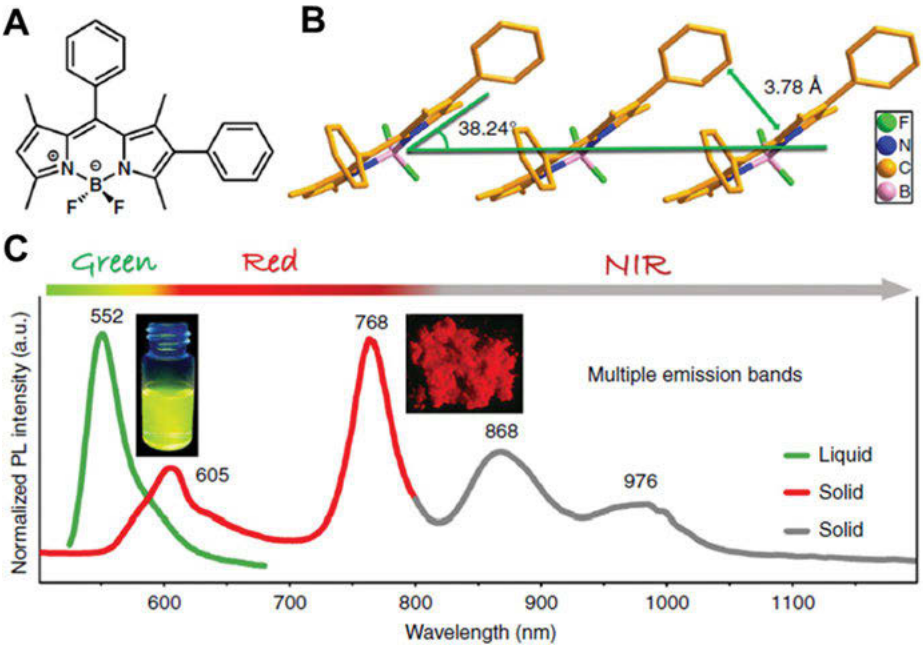

Figure 12.2: Structural details and fluorescent properties of BDP1. (A) Molecular structure of BDP1. (B) Molecular packing diagrams of BDP1 at room temperature extracted from single-crystal XRD data. (C) Normalized photoluminescence (PL) spectra of BDP1 in solution (green curve) and microcrystalline powder state (red and gray curves) [3] Copyright © 2018, The Author(s).

application. This study demonstrates BODIPY dye as an alternate J-aggregation platform for developing the second NIR imaging agents (Figure 12.3) [7].

Sun et al. reported a novel biocompatible NIR-II J-aggregates labeled mesoporous implant for imaging-guided osteosynthesis with minimal invasion. The uniform mesoporous silica-layer-coated titanium plate was fabricated through a bi-phase stratification reaction system. Meanwhile, the NIR-II cyanine dyes of FD-1080 were loaded into mesoporous channels by physical adsorption. Because of the confinement of the mesopores, the uniform J-aggregates of FD-1080 dyes with the maximum absorption and emission wavelengths beyond 1,300 nm could be formed by adjusting the polarity of the solvent. Meanwhile, the biocompatible NIR-II J-aggregates labeled mesoporous implant has exhibited deep tissue penetration depth and high resolution for bioimaging. More importantly, the NIR-II fluorescence of implantable plates could guide the osteosynthesis with minimal surgical wound and operational duration (Figure 12.4) [4].

The establishment of Ben Zhong Tang's aggregation-induced emission (AIE) theory also provides a new direction for the design and application of aggregated dyes [8]. Since the concept was coined in 2001, AIE has changed people's way of thinking about chromophore aggregation and brought forth a revolution both conceptually

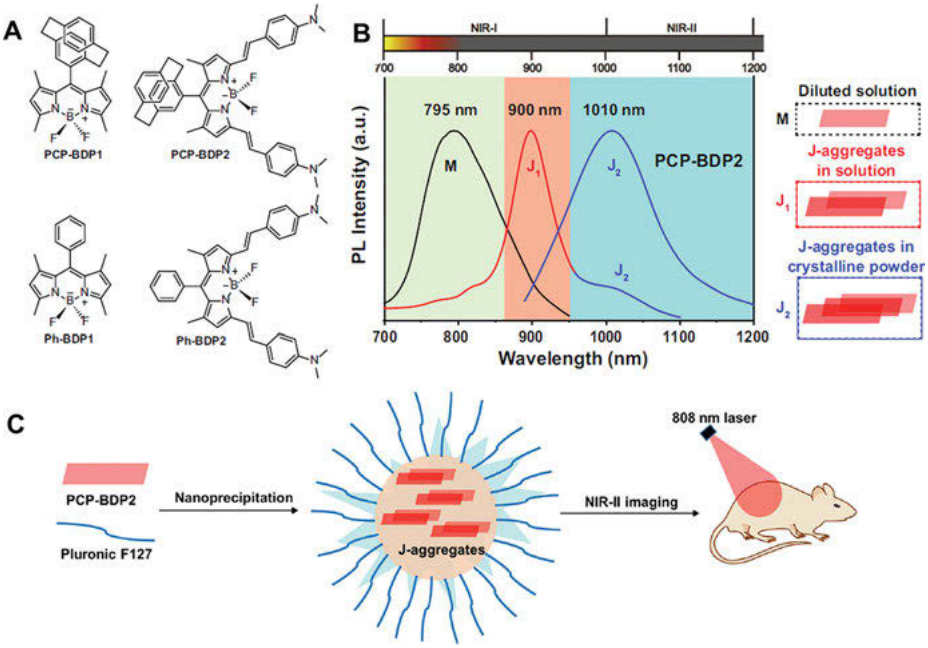

Figure 12.3: Molecular structures and working principle. (A) Chemical structures of PCP-BDP1, PCP-BDP2, Ph-BDP1 and Ph-BDP2. (B) Fluorescence spectra of PCPBDP2 in diluted dichloromethane solution (10 μM) (black line, "M" refers to monomer), THF–water binary solvents (10 μM, 1:9, v/v) (red line, J1-band) and the crystalline powder (blue line, J2-band). The parallelogram in red represents the single molecular PCP-BDP2. (C) Schematic illustration of the construction of the PCP-BDP2 nanoparticles for NIR-II imaging. Source data underlying (B) are provided as a source data file [7].

and technically. AIE-related research is booming now, which has permeated a large number of research disciplines with a widespread influence [9]. Shao et al. have synthesized a series of red/NIR quinoline-malononitrile (QM)-based AIEgens with different π-bridges, that is, thiophene and 3,4-ethylene-dioxythiophene (EDOT). The thiophene-containing molecule (QM-2) forms rod-like structures, while the aggregate of EDOT-based AIEgen (QM-5) is predominated with sphere nanoparticles (NPs). This phenomenon is originated from the different packing ability of the two kinds of AIEgens. QM-2 has a twisted conformation with large torsional angles and no obvious π–π stacking interaction is observed, while QM-5 bearing EDOT unit exhibits totally different intermolecular interaction [10]. To further improve the imaging quality of the NIR fluorescence imaging technique, Qi et al. reported an NIR AIEgen (TQ (thiadiazolo[3,4-g]quinoxaline)–BPN (*N*,*N*-diphenylnaphthalen-1-amine)), the D–A approach was employed to build the organic molecule, in which BPN and TQ were used as the donor and acceptor units, respectively. The encapsulated TQ–BPN dots could emit light in a broad range of 700–1,200 nm with a high QY of 13.9%, and the

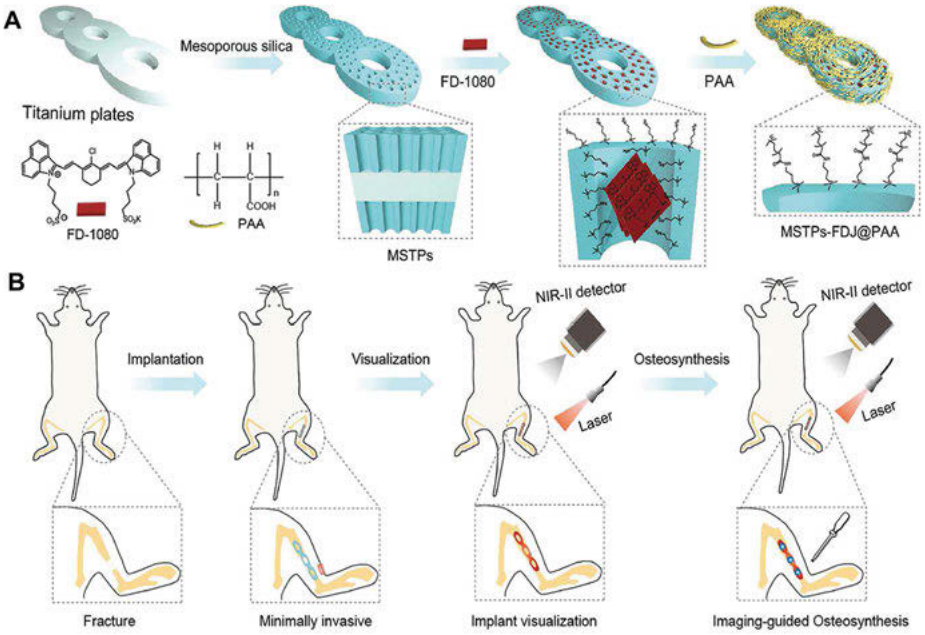

Figure 12.4: (A) Schematic illustration of the preparation of NIR-II J-aggregates labeled mesoporous silica layer-coated titanium plates (MSTPs-FDJ@PAA). (B) The NIR-II imaging-guided osteosynthesis based on the MSTPs-FDJ@PAA [4]. Copyright © 2021, Wiley-VCH GmbH.

QY in short-wave infrared (SWIR) region (>900 nm) also reached 2.8%, which was better than some typically used SWIR emitters, e.g., CNTs (≈0.4%) [11]. The first example of AIEgen-based NIR-II fluorescence and photoacoustic imaging was reported by Sheng et al. They designed a new D–A-tailored NIR-II emissive AIE molecule called TB1. The formulated TB1 dots show a very high fluorescence QY of 6.2% with a large absorptivity of 10.2 L g^{-1} cm^{-1} at 740 nm and emission maximum at 975 nm. The molecular structure of AIEgen TB1 was precisely designed with a large extinction coefficient and fluorescence emission in NIR-II region centered at around 1,000 nm. To obtain fluorescence and photothermy in one go, co-encapsulation is a simple but straightforward method. 2,3-Bis(4-(phenyl(4-(1,2,2-triphenylvinyl)phenyl)amino)phenyl) fumaronitrile (TPETPAFN), an AIEgen and a semiconducting polymer (SP), was co-encapsulated into organic dots for bright red fluorescence and photothermy, respectively. TNSP NPs emit a bright red fluorescence with a peak at 655 nm and a quantum yield (QY) of 16.5% upon excitation at 510 nm [12]. Gao et al. reported that BPBBT is a D–A–D-structured fluorogen with both twisted intramolecular CT (TICT) and AIE characteristics [13]. The emission QY of BPBBT in solvent decreased as the solvent polarity increased: hexane (8.72%) > toluene (5.56%) > chloroform (0.90%) > tetrahydrofuran (THF, 0.72%) > dimethylformamide (0.42%).

An intermediate state was tailored by preparation of albumin-bound BPBBT NPs to obtain reasonable fluorescence and photothermal efficiency at the same time. Li et al. recently designed an AIEgen (2TT-oC26G) with emission in the NIR-IIb region by combining the effects of both AIE and TICT. Strong electron-withdrawing unit benzobisthiadiazole serving as an electron acceptor and triphenylamine (TPA) unit working as both a donor and a molecular rotor was selected to denote the TICT property. By adding multiple molecular rotors that enabled the twisted AIEgen to be intramolecularly mobile in its aggregated state, the resulting 2TT-oC26G showed redshifted emission (λ = 1,600 nm) with high QY values (11.5% and 0.12% in NIR-II and NIR-IIb, respectively), thus making its application in whole-body in vivo imaging possible (Figure 12.5) [14]. Recently, Li et al. reported a self-assembly approach to prepare AIE dots with good consistency and uniform NP sizes (~35 nm). In their approach, amine-functionalized polyethylene glycol (PEG) chains were conjugated to alkyne-containing

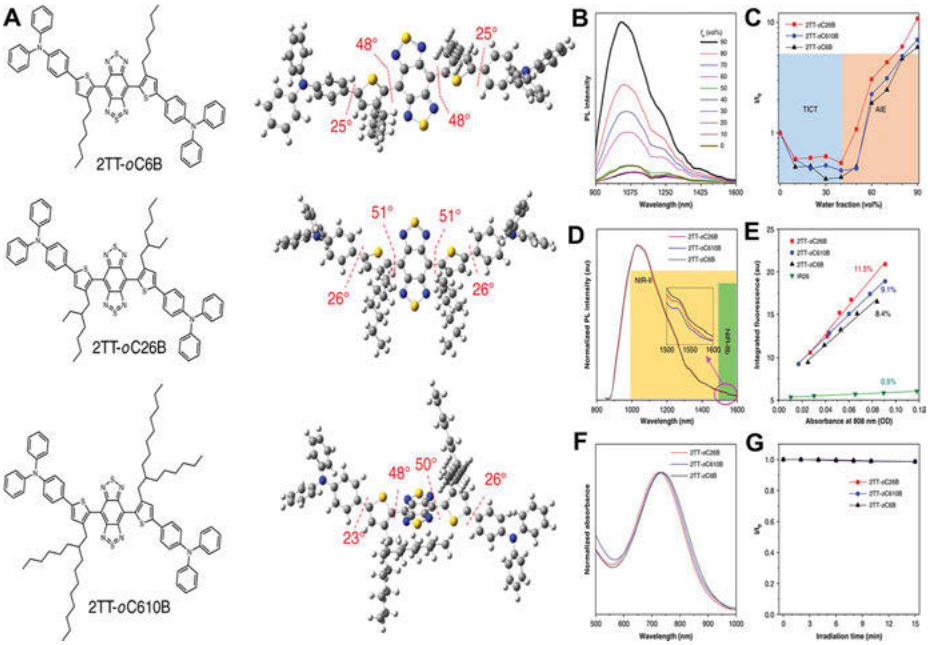

Figure 12.5: (A) Chemical structures and optimized ground state (S_0) geometries of the molecules. (B) PL spectra of 2TT-oC26B in THF/water mixtures with different water fractions (f_w). (C) Variation in PL intensity (I/I_0) of the three molecules with f_w, where I and I_0 were the maximal PL intensity. (D) PL spectra of the nanoparticles. Inset: zoom-in emission spectra in the range of 1,500–1,600 nm. (E) The plots for the integrated fluorescence spectra of the three compound nanoparticles (1,000–1,600 nm) and IR-26 (1,050–1,500 nm, QY = 0.5% in dichloroethane) at five different concentrations. (F) Absorption spectra of nanoparticles. (G) The plot of absorption intensity (A/A_0) under continuous irradiation (110 mW cm^{-2}), where A and A_0 were the maximal absorption intensities before and after laser irradiation, respectively [14]. Copyright © 2020, The Author(s).

AIEgens by an amine–alkyne click reaction to obtain an amphiphilic polymer which self-assembled into AIE dots in aqueous solution. The resulting AIE dots exhibited NIR-II emission at λ =1,050 nm with a QY of 10.3% in water [15]. In 2017, Cai et al. discovered that most propeller-based AIEgens displayed significantly weaker fluorescence as aggregates than in their crystalline forms. Following this concept, they next designed a propeller-containing AIEgen (BTPETTQ) with a D-A-D configuration. As a consequence of the strong intramolecular CT (ICT) along its backbone, BTPETTQ exhibited strong NIR absorption and displayed strong PA signals. After encapsulation of BTETTQ within a phospholipid–polymer matrix endowed the resulting NPs (~39 nm) with good water solubility and biocompatibility [16].

According to the Jablonski diagram, organic optical agents at the S_1 excited state can also undergo a nonradiative ISC process to the highly sensitive T_1 state, followed by which, these triplet excitons are further utilized to realize phosphorescence or photosensitization capabilities for persistent luminescence imaging and photodynamic therapy (PDT), respectively. Phosphorescence occurs when optical agents undergo a radiative decay from T_1 to S_0 with photon emission. As compared to fluorescence, phosphorescence possesses unique features of far longer lifetime and larger Stokes shifts. In particular, organic optical agents with room temperature phosphorescence (RTP) and long lifetime (4,100 ms) hold great potential in bioimaging applications since they eliminate the interference from tissue autofluorescence, hence providing excellent SBR and imaging sensitivity. When the triplet excited energy is transferred to the surrounding molecules such as oxygen to generate reactive oxygen species (ROS), it is able to cause cell damage and apoptosis, and such PDT modality represents one of the indispensable components of phototheranostic systems [1]. Liu et al. further applied polymerization-enhanced photosensitization to a two-photon excited PDT (2PE-PDT) area. As compared to conventional one-photon excited PDT, 2PE-PDT provides deeper tissue penetration depth and better spatial control of photosensitizer (PS) activation in three dimensions as excitation of PSs only occurs at the focal point of the two-photon absorption process. In this study, they further adjusted the linkage position on the TPE motif, which yielded CP-based PSs, i.e., PTPEDC-1 and PTPEDC-2. As compared to PTPEDC-1, PTPEDC-2 showed smaller torsional angles and longer conjugation length, which made PTPEDC-2 NPs (DSPE-PEG2000 as the encapsulation matrix) more favorable for a larger 2 PA cross section in aqueous solution (7.36×10^5 GM for PTPEDC-2 NPs, 3.56×10^5 GM for PTPEDC-1 NPs, and 1.13×10^5 GM for TPEDC NPs). Moreover, the denser energy levels of PTPEDC-2 produced more efficient ISC processes and a higher $_1O^2$ generation ability as compared to PTEPDC-1 under both one-photon and two-photon excitations. The improved 2 PA cross section and higher $_1O^2$ generation ability therefore worked together to make PTPEDC-2 NPs a promising 2PE-PDT agent for precise ablation of cancer cells. With a zebrafish liver tumor model, intravenous microinjection of TPEDC-2 NPs led to their effective accumulation in liver tumors and 20% reduced tumor volume post 2PE-PDT. Collectively, polymerization of small molecules to their counterpart SPs/CPs

could improve absorbance and promote ISC processes, which represented a promising approach to design efficient PSs for promoted PDT (Figure 12.6) [17].

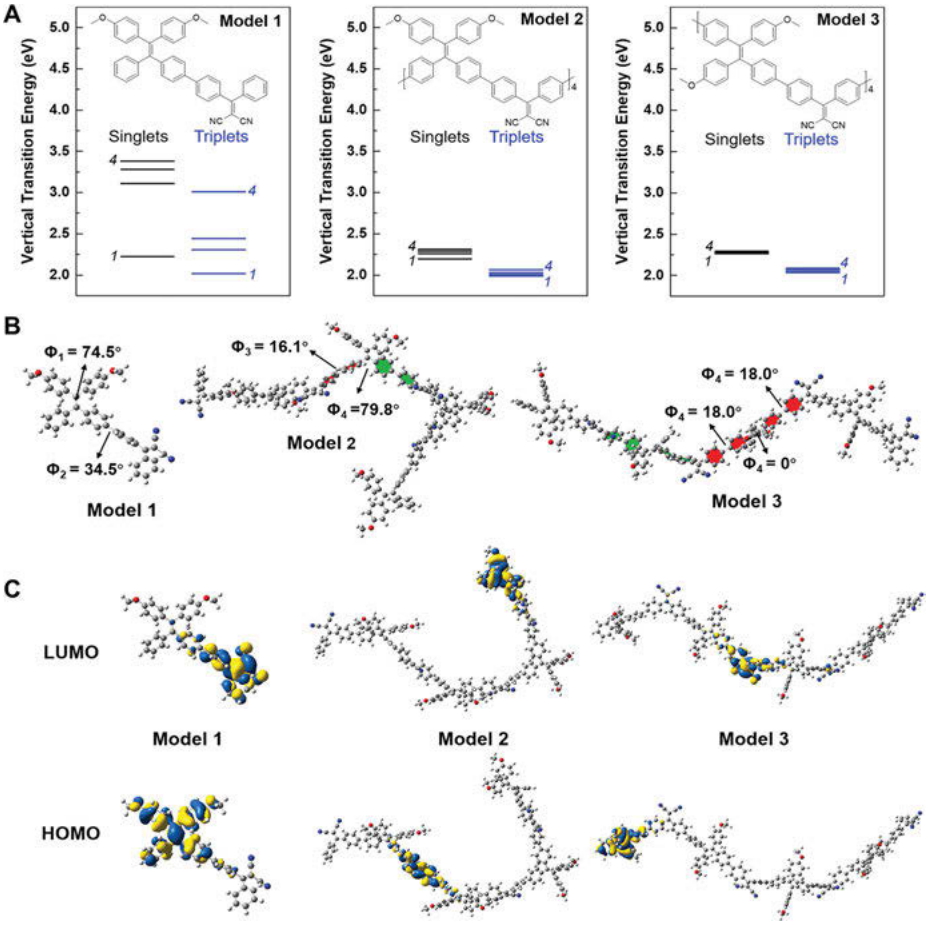

Figure 12.6: (A) Chemical structures and singlet and triplet energy levels of three model compounds. (B) Optimized structures of the three model compounds. Green and red colors highlight the conjugated benzene rings within the same plane. (C) DFT-calculated HOMO and LUMO wave functions of the geometry-optimized structures (Gaussian 09/B3LYP/6-31 G(d)) of the three model compounds [17]. Copyright © 2019, American Chemical Society.

The development of type-I PS that show hypoxia-tolerant PDT efficiency provides a straightforward way to address the tumor issue. However, type-I PDT materials have rarely been discovered. Herein, Li et al. reported a π-conjugated molecule with A–D–A configuration, COi6-4Cl. The H_2O-dispersible NP of COi6-4Cl can be activated by an 880 nm laser, and displays hypoxia-tolerant type I/II combined PDT capability, and more notably, a high NIR-II fluorescence with a QY over 5%.

Moreover, COi6-4Cl shows a negligible photothermal conversion effect. The nonradiative decay of COi6-4Cl is suppressed in the dispersed and aggregated states due to the restricted molecular vibrations and distinct intermolecular steric hindrance induced by its four bulky side chains. These features make COi6-4Cl a distinguished single-NIR-wavelength-activated phototheranostic material, which performs well in NIR-II fluorescence-guided PDT treatment and shows an enhanced in vivo antitumor efficiency over the clinically approved Chlorin e6, by the equal stresses on hypoxia-tolerant antitumor therapy and deep-penetration imaging. Therefore, the great potential of COi6-4Cl in precise PDT cancer therapy against hypoxia challenges is demonstrated (Figure 12.7) [18].

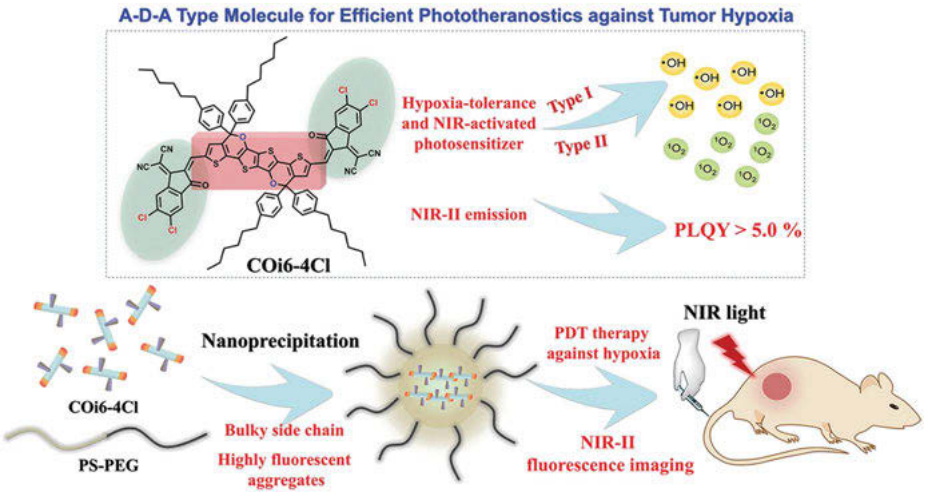

Figure 12.7: Schematic illustration of the NIR-II-emissive photosensitizer (COi6-4Cl) for hypoxia-tolerant photodynamic theranostics [18]. Copyright © 2020, Wiley-VCH GmbH.

Recently, Wan et al. developed the first type I AIE PS for NIR imaging-guided cancer PDT. Four AIEgens were synthesized with increased electron-donating ability (TBZPy < MTBZPy < TNZPy < MTNZPy) due to stronger electron donating ability of methoxy-substituted TPA and naphtho[2,3-c][1,2,5]thiadiazole (NZ) compared to TPA and benzo-2,1,3-thiadiozole (BZ). BZ-based AIEgens exhibited highly efficient $_1O^2$ generation, while NZ-based AIEgens primarily generated free radical ROS (Figure 12.8) [19]. Wu et al. developed a prodrug, DCM-S-CPT (camptothecin), with an excellent tumor-inhibiting ability based on dicyanomethylene-4 H-pyran derivatives as the NIR-emissive AIEgens and CPT as the cancer drug. Owing to its D –π –A structure, DCM-S-CPT exhibits a typical ICT broad absorption band at 455 nm with fairly weak emission at 665 nm in DMSO/PBS buffer solution (50/50, v/v, pH = 7.4, 10 mM). On the other hand, DCM-NH_2 has a strong NIR fluorescence at 665 nm in the same condition with the absorption band at 492 nm [20].

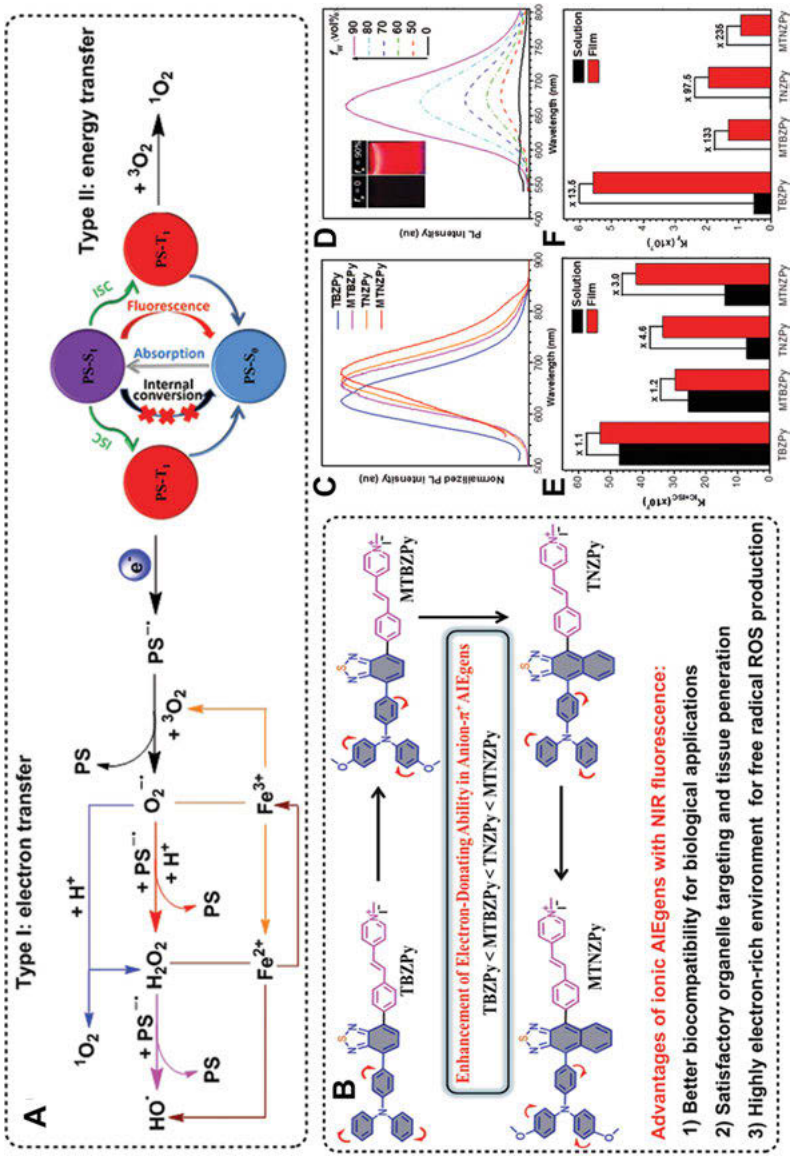

Figure 12.8: (A) ROS generation mechanism: Type II energy transfer to form singlet oxygen, and type I electron transfer to form free radical ROS and hydrogen peroxide. (B) Chemical structures of TBZPy, MTBZPy, TNZPy and MTNZPy. (C) PL emission spectra of four BZ/NZ-based fluorophores in THF. (D) PL spectra of TNZPy in a mixture of DMSO/water with different fw values (inset: photographs of TNZPy in DMSO and DMSO/water (v/v =1:90) under irradiation from a UV lamp). (E) Nonradiative transition speeds (KIC + ISC) of the four fluorophores in DMSO solution and a film. (F) Radiative transition speeds (Kr) of the four fluorophores in DMSO solution and a film [emitters] = 10 μm [19]. Copyright © 2020, Wiley-VCH GmbH.

Zhao et al. introduced a class of NIR-absorbing organic molecules with intramolecular motion induced photothermic inside NPs, which enables most absorbed light energy to dissipate as heat. Such a property makes the nanoaggregate a superior photoacoustic imaging agent and allows them for high-contrast photoacoustic imaging of tumors in live mice. This study not only provides a strategy for developing advanced photothermal/photoacoustic imaging nanoagents but also enables molecular motion in a nanoplatform to find a way for practical application (Figure 12.9) 21].

In a single-component aggregate, the property studies mainly focus on the intrinsic structure of the compound under investigation and any external stimuli present. There are generally no synergistic effects based on intermolecular interactions [22]. The CT complex (CTC) is a kind of material that involves significant charge transfer from an electron donor (D) to an acceptor (A), resulting in electron delocalization between the two molecules. CTCs with improved photophysical/physicochemical properties over their constituting components have been employed in organic optoelectronic devices. By manipulating the energy gaps of CTCs, their potentials have been demonstrated for light-harvesting and amplifying, and bioimaging applications. The energy gaps of CTCs originating from the highest occupied molecular orbital (HOMO) level of the donor and the lowest unoccupied molecular orbital (LUMO) level of the acceptor allows easy tuning of the absorption properties of CTCs via their constituting components. Considering the prominent characteristics of organic CTCs, it is reasonable to conceive that tunable nano-CTC with NIR-II absorption could be a practical strategy of photothermal therapy (PTT). Herein, Tian et al. prepared three CTC NPs (CT NPs) by combining commercially available donors and acceptors. Interestingly, they demonstrate for the first time CT NPs with absorption peaks in the NIR-II region by combining perylene (PER, donor) and tetracyanoquinodimethane (TCNQ, acceptor). The CT NPs showed excellent photothermal performance with an absorption peak at 1,040 nm at the NIR-II therapy window, so it was applied for antibacterial therapy by using NIR-II laser (1,064 nm). As the first demonstration, the present nanosized PER-TCNQ NP system shows a promising bacterial inhibition efficiency of 99% with photothermal conversion efficiency of 42% under 1,064 nm irradiation. The present work reveals that by employing different donor and acceptor small molecules, the optical absorption of CTCs can be extensively tuned to enable efficient photothermal conversion extending to the NIR-II region. Hence, CTC is considered as a promising class of photothermal agent (PTA) materials for light-harvesting deserving more attention (Figure 12.10) [23]. In organic cocrystal, donors (D) and acceptors (A) self-assemble with a crystalline structure through noncovalent interactions. The electron delocalization from the donor to the acceptor in CT cocrystals contributes more to the appealing physicochemical properties as well as the band engineering for the orbital hybridization. Through effective control of the CT nature, such as the degree of CT, ground state and excited state dynamics, charge generation, separation, and recombination processes, it is possible to achieve rational designed functional

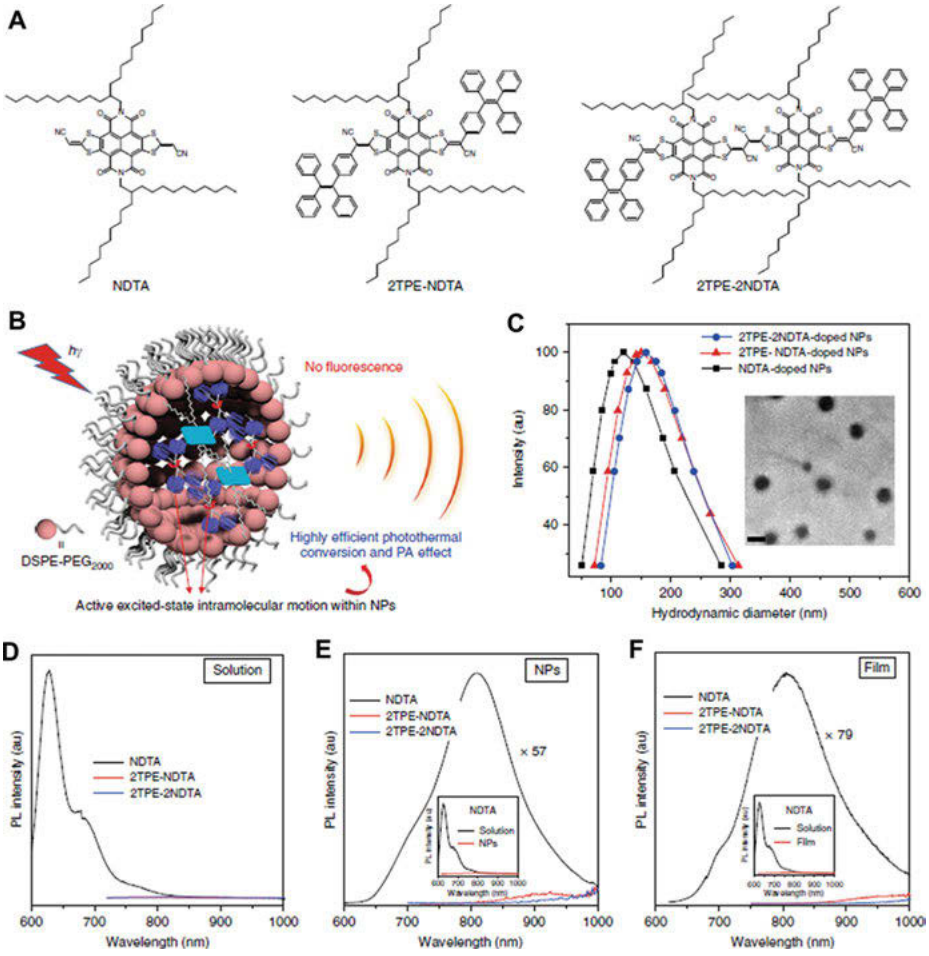

Figure 12.9: Preparation and characterization of compounds and NPs. (A) Molecular structures of NDTA, 2TPE-NDTA, and 2TPE-2NDTA. (B) Schematic of 2TPENDTA-doped NP, showing active excited-state intramolecular motion within NPs. (C) Dynamic light scattering profiles of the NPs indicated. Inset: transmission electron microscopy image of 2TPE-2NDTA-doped NPs. Scale bar, 200 nm. (D–F) The photoluminescence (PL) spectra of NDTA (black), 2TPENDTA (red), and 2TPE-2NDTA (blue) in THF solution (D), the doped NPs (E) in water and thin films (F). Inset: the contrast of the PL intensity of the as-prepared NPs in water and in a THF solution of NDTA (E), and the contrast of the PL intensity of thin film and THF solution of NDTA (F) [21]. Copyright © 2019, The Author(s).

cocrystals. Ou et al. prepared versatile CT complex NPs (TMB-F4TCNQ and TMB-TCNQ) via supramolecular assembly and nanoprecipitation by using multicyanosubstituted and strong electron-withdrawing acceptors (TCNQ and F4TCNQ). Because of the larger energy gap beween donor and acceptor, TMB-F4TCNQ presents higher CT degree (72%) than that of TMB-TCNQ (48%) in nanoaggregates.

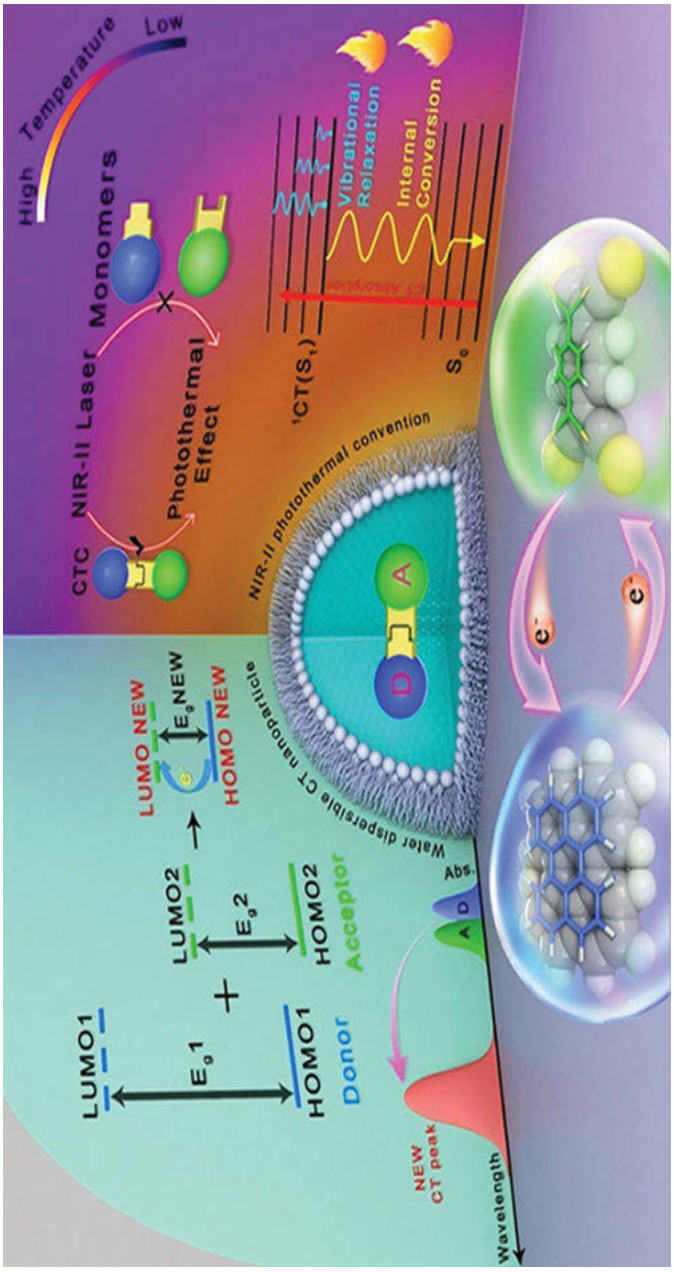

Figure 12.10: Diagram showing photothermal effect in charge transfer cocrystal nanoparticle [23]. Copyright © 2021, Wiley-VCH GmbH.

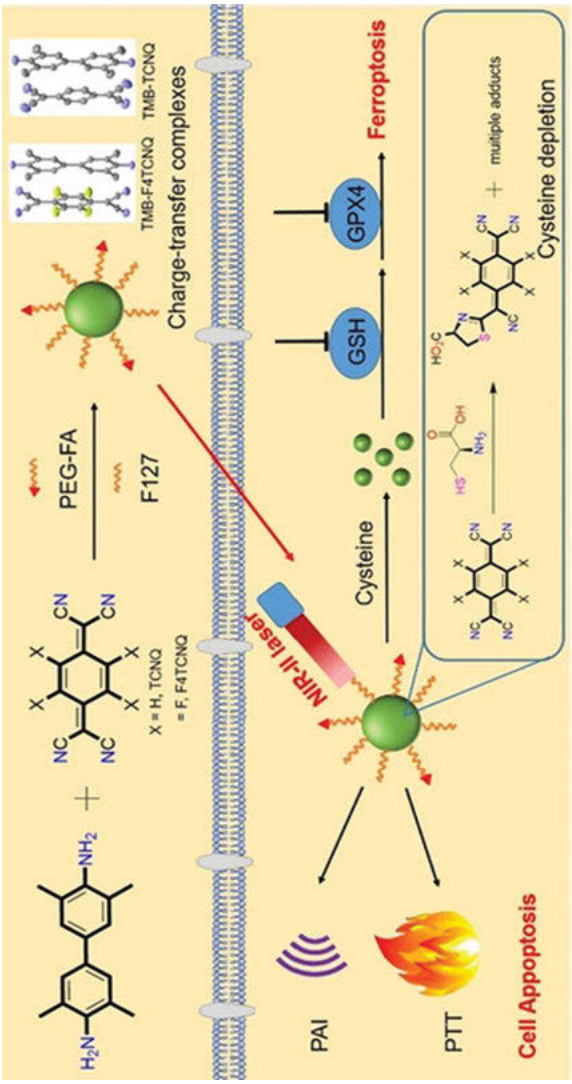

Figure 12.11: The preparation of tumor-targeting charge transfer complex nanoparticles and illustration of ferroptosis and NIR-II-triggered phototherapeutics [24]. Copyright © 2021, Wiley-VCH GmbH.

Therefore, TMB-F4TCNQ exhibits stronger NIR-II absorption ability with a mass extinction coefficient of 15.4 Lg^{-1} cm^{-1} at 1,300 nm and excellent photothermal effect. Impressively, the specific cysteine response can make the TMBF4TCNQ effectively inhibit the intracellular biosynthesis of GSH, leading to redox dsyhomeostasis and ROS-mediated ferroptosis. TMB-F4TCNQ can serve as a contrast agent for NIR-II photoacoustic imaging to guide precise and efficient PTT in vivo (Figure 12.11) [24].

12.2 Nucleic acid-based NIR aggregate-biohybrid for biomedical applications

As the foundation of life, nucleic acids (NAs) are biomacromolecules that encode genetic information for living organisms. Specific sequences translate certain genetic traits, protein expression, and, ultimately, cellular function. Yet, NAs not only store genetic information but they can be very useful for the recognition of biological compounds. As solid-phase NA synthesis techniques are now well developed, their unique molecular structure and conformation make NAs interesting molecules in the field of materials science. Due to specific Watson–Crick base pair interactions, NAs can work as building blocks or linkers to construct and regulate different molecular aggregates. Therefore, NA-based aggregate-biohybrids feature precise molecular recognition and sequence programmability, versatility, as well as marked biocompatibility, providing promising candidates for biomedical applications.

Spherical NAs (SNAs) are built from multiple strands of DNA, all dangling from a common center like the woolen threads of a pom-pom. Arranging DNA in this way drastically changes its physical and chemical properties. Unlike isolated double helices, the spheres can penetrate the membranes of cells, cross the skin and blood–brain barrier (BBB), and avoid attack by the human immune system. Tian et al. developed a kind of organic SNA whose hydrophobic core can accommodate NIR-II emitting fluorescent dyes. The resultant NIR-II emitting organic SNA can effectively cross BBB and target brain tumors, thereby enhancing the diagnostic imaging of brain tumors (Figure 12.12A). In order to prevent the early leakage of organic dyes in in vivo applications, polystyrene with high hydrophobicity was selected as the hydrophobic block to synthesize DNA block copolymer, PS-b-DNA. As shown in Figure 12.12B, PS-b-DNA was successfully synthesized by a solid-phase "Click" reaction. After cleaved from beads, PS-b-DNA directly assembled into spherical micelles with the size of ≈20 nm in aqueous solution, which was determined by transmission electron microscopy and dynamic light scattering. The densely packed DNAs on the surface of PS-b-DNA SNA showed hybridization ability comparable to free DNA. As for biostability, the in vivo half-life of micellar DNA was determined to be ≈65 min, which was much larger than that of free DNA (≈19 min), because dense DNA arrangements hinder the accessibility

of nucleases. Compared with the counterpart PS-b-PEG, PS-b-DNA SNA showed ≈3-fold enhanced cell penetration ability, measured by flow cytometry (FCM). Specific aptamers were introduced into the PS-b-DNA SNA with 10% of the total surface DNAs to obtain PS-b-DNA/Apt. The cell penetration ability of PS-b-DNA/Apt was determined to be 1.5-fold stronger than that of PS-b-DNA SNA. Scavenger receptor (SR) was proved to be a key receptor for PS-b-DNA SNA penetrating cells through competitive inhibitor experiments. What is more, SR-mediated transcytosis is a promising strategy for crossing BBB. Therefore, the ability of PS-b-SNA to cross BBB was evaluated, and the results indicated that PS-b-DNA showed 4.5-fold higher traversing efficiency than that of PS-b-PEG (Figure 12.12C). The NIR-II emitting organic dye (FE) was encapsulated into the PS-b-DNA polymer matrix by using nanoprecipitation method to obtain FE@PS-b-DNA. SNA with 25% FE showed highest brightness and a fluorescence QY of 9.6%. FE@PS-b-PEG and FE@PS-b-DNA/Apt were also prepared under the same conditions. Subsequently, in vivo brain tumor imaging was performed. At 24 h administration of different samples, FE@PS-b-DNA and FE@PS-b-DNA/Apt showed strong fluorescence signal at brain tumor sites compared with FE@PS-b-PEG. After imaging experiment, the isolated brains were collected. The enhanced accumulation of FE@PS-b-DNA was observed due to the ability of PS-b-DNA in BBB crossing; the targeted aptamer further enhanced the tumor penetrating ability of FE@PS-b-DNA/Apt. Therefore, compared with FE@PS-b-DNA, FE@ PS-b-DNA/Apt showed a 3.8-fold signal enhancement (Figure 12.12D). Finally, the biocompatibility of FE@ PS-b-DNA has also been demonstrated, showing excellent biosafety. These results indicate that as a versatile polymer matrix, PS-b-DNA can facilitate functional organic dyes to cross BBB for the diagnosis and imaging of brain diseases [25].

Liu et al. developed noncationic gene carrier and achieving efficient endo/lysosome escape of functional NAs in cytosol are two major challenges faced by the field of gene delivery. Herein, they demonstrate a concept of self-escape SNA to achieve light-controlled noncationic gene delivery with sufficient endo/lysosome escape capacity. In this system, Bcl-2 antisense oligonucleotides (OSAs) were conjugated onto the surface of AIE PS NPs to form core–shell SNA. Once the SNA were taken up by tumor cells, upon light irradiation, the accumulative $^1O_2$ produced by AIE PSs could rupture the lysosome structure to promote OSA escape. Prominent in vitro and in vivo results validated that the AIE-based core–shell SNA could remarkably downregulate the antiapoptosis protein (Bcl-2) and induce tumor cell apoptosis without any transfection reagent. The design of the Bcl-2 SNA starts with the AIE PS. To realize AIE PSs with far red /NIR emission and effective $^1O_2$ production under white light irradiation, a D (donor)–A' (auxiliary acceptor)–π (π spacer)–A (real acceptor) structure was applied to design. A PS with a terminal acetylene group was synthesized, which allows for subsequent PEG conjugation to yield an amphiphilic polymer containing a terminal -N3 group. In aqueous media, the amphiphilic polymer

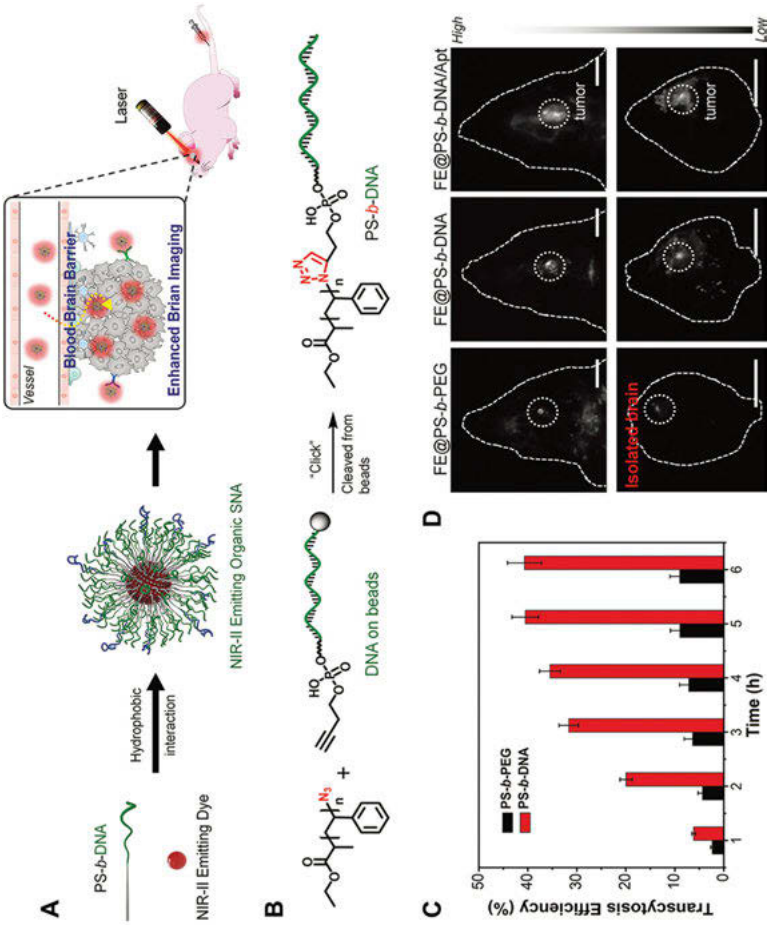

Figure 12.12: (A) Scheme of the preparation of NIR-II emitting organic SNAs and their application in brain tumor imaging. (B) Scheme of PS-*b*-DNA synthesized by solid-phase "click" reaction. (C) Transcytosis efficiency for different samples over time. (D) NIR-II fluorescence imaging of the mouse heads and isolated brains by using different NIR-II emitting materials under irradiation at 808 nm. All panels are reproduced with permission [25]. Copyright © 2020, WILEY-VCH Verlag GmbH & Co. KGaA, Weinheim.

forms NPs with -N3 exposed for further conjugation with an antisense OSA targeting Bcl-2 mRNA, named as Bcl-2 antisense OSA, to form the core–shell SNA. To realize smart release of Bcl-2 OSA, biodegradable ester bond was introduced between OSA and AIE PS (Figure 12.13) [26].

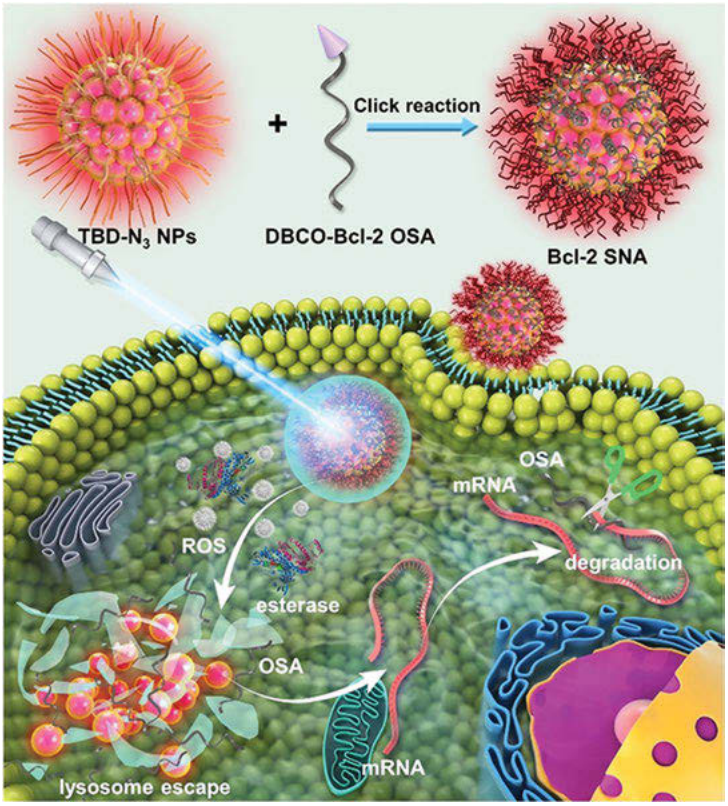

Figure 12.13: Preparation of AIE PS-based Bcl-2 SNA. Schematic representation of Bcl-2 SNA being taken up by tumor cells. The accumulative $^1O_2$ in the lysosome could rupture its structure, promote Bcl-2 OSA escape from the lysosome, eventually degrade Bcl-2 mRNA and improve PDT effect [26].

Recently, DNA nanotechnology, especially DNA origami technology, has been useful in the bottom-up fabrication of well-defined nanostructures ranging from tens of nanometers to sub-micrometers. Ding et al. demonstrate that DNA origami can work as a multifunctional platform integrating a chemotherapeutic drug (doxorubicin, DOX), gold nanorods and a tumor-specific aptamer MUC-1, to realize the effective circumvention of drug resistance. DOX was loaded efficiently onto DNA origami through base pair intercalation and surface-modified gold nanorods (AuNRs) were assembled onto the DNA origami through DNA hybridization. Due to the active targeting effect of the assembled aptamers, the multifunctional nanostructures achieved increased cellular internalization of DOX and AuNRs. Upon NIR laser irradiation, the P-glycoprotein (multidrug resistance pump) expression of multidrug resistant MCF-7 (MCF-7/ADR) cells was down-regulated, achieving the synergistically

chemotherapeutic (DOX) and photothermal (AuNRs) effects (Figure 12.14). In summary, they developed a synergistic cancer therapeutic platform based on self-assembled DNA nanostructures and demonstrated the circumvention of drug resistance. DOX, AuNRs, and MUC-1 aptamer sequences were incorporated in DNA origami templates, realizing tumor-targeting chemothermal therapeutic functions in mucin protein overexpressed MCF-7/ADR cells. In their system, the doses of the DOX payload could be fine-tuned by the DNA origami concentration and the loading conditions. Both intracellular two-photon laser and single-photon laser imaging results proved that the MUC-1 aptamer-modified DNA origami carrier enhanced the internalization of AuNRs and DOX. Due to the hyperthermia effect caused by the laser irradiation of AuNRs, the molecular pump overexpressed on the MCF-7/ADR cells and P-glycoprotein was inhibited. The downregulation of P-gp results in circumvention of the DOX resistance by MODA. In this work, we demonstrate that the DNA origami is a designable platform for the integration of multiple functional elements, such as targeting aptamer sequences, chemotherapeutic drugs, imaging probes and photothermal gold particles. Moreover,

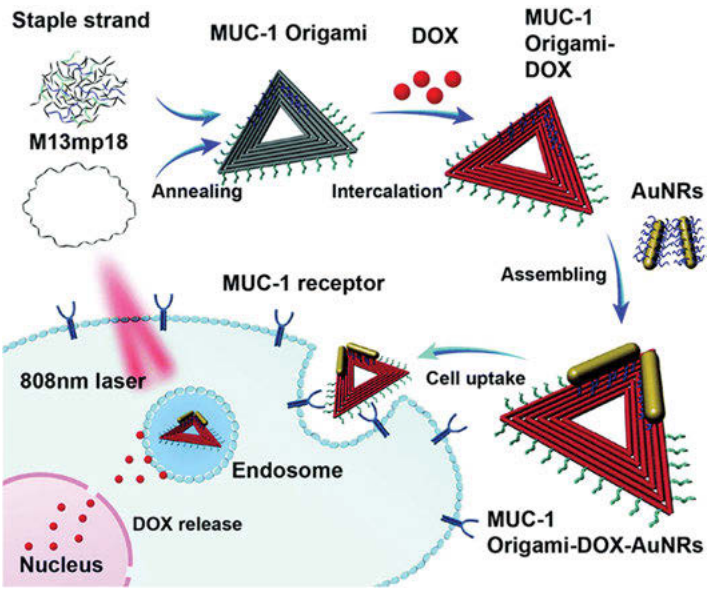

Figure 12.14: Schematic illustration of the multifunctional carrier. A long scaffold single DNA strand M13mp18 (gray) is folded into the triangular-shaped DNA origami structures through hybridization with rationally designed staple strands (gray), MUC-1 aptamer strands (green), and capture strands (blue). Doxorubicin (DOX) molecules are loaded into the origami nanostructure through intercalation with the DNA base pairs. Functionalized by the corresponding complementary thiolated ssDNA strands, gold nanorods (AuNRs, 50 nm × 10 nm) were assembled at the predesigned locations on the origami template. The multifunctional DNA nanostructures (MUC-1 aptamer–DNA origami–DOX–AuNRs complex, MODA) were administered to the MCF-7/ADR cells, and the photothermal effects were investigated [27]. Copyright © 2017, The Royal Society of Chemistry.

based on the addressability and programmability of the DNA origami, additional functional groups, such as antibodies and therapeutic peptides, can be accurately assembled. Rationally designed DNA nanostructures show tremendous potential as drug carriers and promising candidates for the treatment of cancer. Among these succinct nanostructures, DNA tetrahedron (DNA-T), a classical three-dimensional framework with the strategy of DNA origami, provides a promising platform to construct prominent drug delivery systems [27]. Zhu et al. employ DNA-T as the carrier for the intracellular delivery of palmatine hydrochloride (PaH), which is a natural PS with AIE characteristics. By taking advantages of DNA-T binding, the cellular uptake of PaH significantly increases and the PaH transportation efficiency to the nucleus is accelerated by light-driving. The combination of DNA-T and PaH not only enhances the fluorescence intensity but also promotes the photodynamic effects, which are beneficial to cancer diagnosis and treatment. This study thus provides a novel pathway for the theranostics using natural AIE luminogens [28].

NA aptamers are single-stranded DNA or RNA with a length ranging from 10 to 100 nucleotides (nt), which are produced from a process termed "systematic evolution of ligands by exponential enrichment." Recently, micellar aggregates composed of a single-stranded DNA corona and a hydrophobic polymer core have emerged as new types of functional micelles. These micelles have been synthesized and applied for the delivery of antisense DNA, 2a as a 3D scaffold for organic reactions, and 2f as a combinatorial tool for cancer nanotechnology. Zhang et al. demonstrated a facile one-step assay to construct aptamer-anchored micelle-like aggregate-biohybrids with NIR fluorescence properties. The aptamer-anchored aggregate-biohybrids were fabricated through mixing of the aptamer-cholesterol, lipids, PEG-lipids, and AIEgens under sonication. The hydrophobic lipid parts tend to embed themselves in integrations of hydrophobic AIEgens, and the hydrophilic PEG segments tend toward the aqueous media to provide the AIE dots with promising water solubility. The aptamer-anchored aggregate-biohybrids can target cancer cells with specific recognition, favorable photostability, and superior biocompatibility as a result of strong AIE emission and the cell-targeting ability of aptamers (Figure 12.15) [29].

12.3 Organism-based NIR aggregate-biohybrid for biomedical applications

An organism is an individual form of life that is capable of growing and reproducing and has one or more cells. Organism organelles are intracellular, membrane-bound compartments that function to separate distinct biochemical pathways and concentrate the enzyme activity within cells. Organelles are, with rare exceptions,

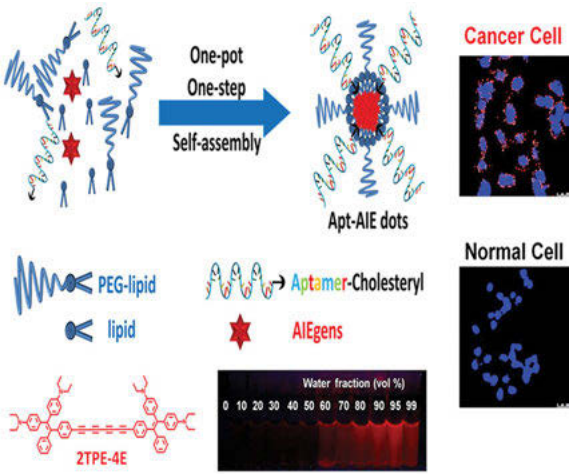

Figure 12.15: Schematic illustration of aptamer-anchored micelle-like aggregate-biohybrids preparation by one-pot self-assembly method [29]. Copyright © 2017 American Chemical Society.

uniquely eukaryotic, and their evolution is likely to have influenced the development of multicellular organisms. Chloroplasts (cp) in the mesophyll of intact plants localize to the cell cortex. This positioning maximizes gas exchange and light interception and is primarily enforced by the outward turgor of the vacuole [30]. The isolated cp is the basic light-driven metabolic factory of higher plant cells. However, there is an incomplete match between the solar radiation spectrum and absorption profile of cp. It is hard for the photosynthetic pigments to fully utilize the sunlight energy. Herein, Bai et al. synthesized cp-based aggregate–biohybrid. Under mild conditions, the synthesized TPE–PPO and TPA–TPO were artificially manipulated on the live cp by a metal-free "Click" reaction. Furthermore, the AIEgens could harvest and convert harmful ultraviolet radiation and photosynthetically inefficient radiation into photosynthetically active radiation for cp absorption. As a result, the AIEgen-cp exhibited a better capability of water splitting and electron separation, and produced more adenosine triphosphate (ATP). For the constructed photosynthesis system, the AIEgens contributed to the specific AIE characteristics and avoided the common aggregation-caused quenching effect. In addition, the bioconjugation strategy contributed to the directed manipulation toward photosynthetic units, beyond the random modification or mixture route. This work reports the first conjugation and light conversion tactics based on AIEgens for augmenting photosynthetic efficiency. This proof of concept shows that the excellent AIE materials have enormous potential to develop modern bioenergy in future. The material chemists have a great stage for reforming the cp, optimizing the photosynthetic system, and transforming Nature (Figure 12.16) [31].

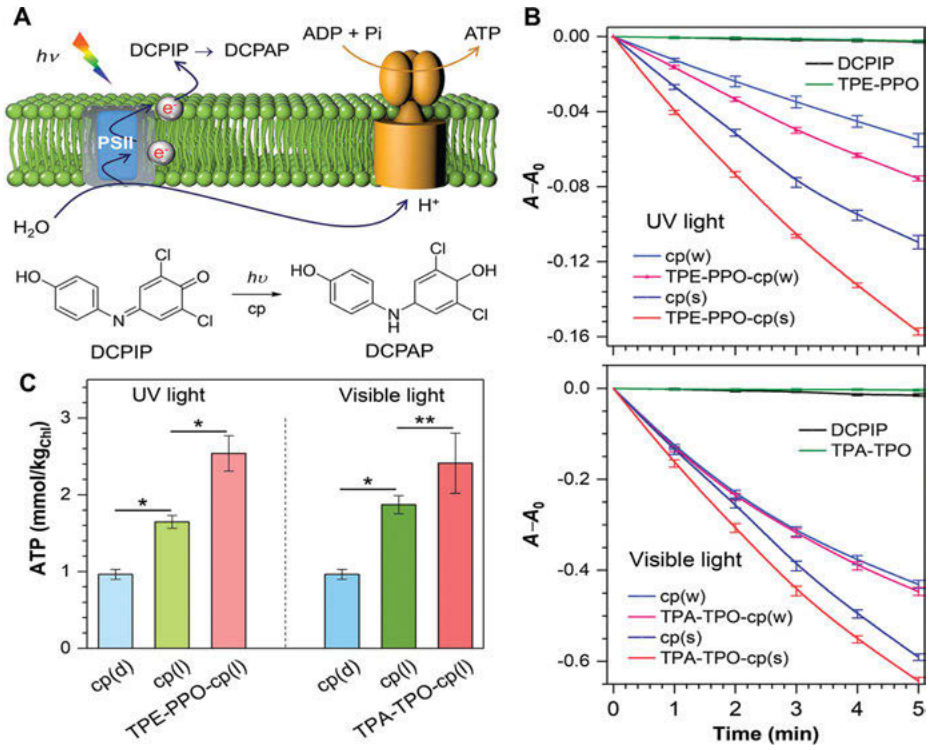

Figure 12.16: (A) Simplified illustration of photoinduced electron generation (PEG) in the photosynthesis process of cp; reaction schedule for evaluating PEG efficiency by 2, 6-dichlorophenolindophenol (DCPIP). (B) Time dependence of absorbance of DCPIP at 600 nm in aqueous suspensions of pristine and AIEgen-cp under irradiation of (top panel) UV light of 0.5 (weak, w) and 1 mW cm^{-2} (strong, s) and (bottom panel) visible light of 1 (weak, w) and 2 mW cm^{-2} (strong, s), *P < 0.001 and **P < 0.05. (C) Production of adenosine triphosphate (ATP) in pristine and AIEgen-cp in the dark (D) and under light irradiation (l) [31].

Mitochondria (Mito) are powerful and dynamic organelles, which play a fundamental role in growth, differentiation, survival, and apoptosis beyond sustaining the energetics of the cell. Aging, tissue damage, and diseases challenge the cell and its Mito, thereby affecting their integrity, function, and homeostasis. In cancer cells, the Mito is not only severely reduced in number but also extremely abnormal in structure and function. Owing to the malfunction of Mito, the metabolism of cancer cells would be altered by using the aerobic glycolytic pathway for ATP synthesis. Additionally, the mitochondrial dysfunction of cancer cells could also result in hypoxia-like pathway activation for tumorigenesis, reduced apoptosis, and treatment resistance. Fortunately, Mito transplantation by delivering exogenous functional Mito into damaged organ/tissue/cells has been demonstrated to be a revolutionary treatment for a variety of

diseases or injuries. It has been found that Mito transplantation could inhibit the proliferation of cancer cells by suppressing oncogenic pathways and glycolytic metabolism. Therefore, Liu et al. fabricated Mito-based aggregate-biohybrid by labeling isolated bioactive Mito with synthetic AIEgen-lipid molecules, which possess the natural component of a phospholipid, through hydrophobic interaction between the conjugates and mitochondrial membrane. After internalization into cancer cells, the Mito-AIEgen-lipid established a more normal and efficient metabolic pathway for ATP synthesis though reversing aerobic glycolysis into the oxidative phosphorylation. In addition, it could reactivate the apoptotic pathway by downregulating the expression of antiapoptotic protein and upregulating the apoptosis-inducing factors. Due to the biological regulation of Mito, the PDT effect of Mito-AIEgen-lipid under light irradiation was significantly enhanced when compared with free AIEgen-lipid. Therefore, the integration between artificially modified organelles and PSs offers a new strategy for efficient cancer therapy (Figure 12.17) [32].

Live bacteria have drawn widespread interest as carriers to deliver genes and proteins into eukaryotic cells for the treatment of various cancer types, owing to their good biocompatibility and active targeting ability, including (i) their unique ability to preferentially colonize tumors in an active motility by an aerotaxis or chemotaxis pathway; (ii) their intrinsic genetic system, which allows live bacteria to be genetically engineered to deliver tumoricidal agents such as genes or proteins; (iii) because they are a natural protein-making factory, bacteria vectors are cost-effective compared with most artificial synthetic carriers. However, how to realize effective gene and protein release remains an issue, and whether the bacteria could efficiently deliver therapeutic agents has not been successfully realized. Wu et al. reported a new bacteria-based aggregate-biohybrid system composed of AIE photosensitizer nanoaggregate (AIE PS NP) TDNPP-coated *Escherichia coli* (*E. coli*), which serve as a PS delivery vector for effective imaging and ablation of tumor cells (Figure 12.18). The TDNPP coating layer on the surface of *E. coli* could facilitate bacteria to invade cancer cells and efficiently release protein through the production of ROS upon light irradiation. Furthermore, multifunctional TDNPPs delivered by bacteria have also achieved enhanced cancer cell imaging and effective light-mediated cancer killing in vitro as compared to the same PS NPs without the bacteria carrier. Their study thus presents an alternative strategy to optimize bacteria-mediated cancer therapy and intracellular protein delivery [33].

Liu et al. developed bacteria-based aggregate-biohybrid based on attenuated *Salmonella* via metabolic engineering using an AIE photosensitizer, MeTTPy-D-Ala (AIE PS MA), to realize light-controlled gene release for breast cancer therapy (Figure 12.19). The labeling of MA does not inhibit *Salmonella* reproduction so that the administered MA-engineered *Salmonella* carrying vascular endothelial growth factor receptor 2 (VEGFR2) plasmids can be localized in the tumor tissues and continue to colonize and express exogenous genes. Following an appropriate treatment schedule, the constructed plasmid could be released with a controlled manner into the cytoplasm

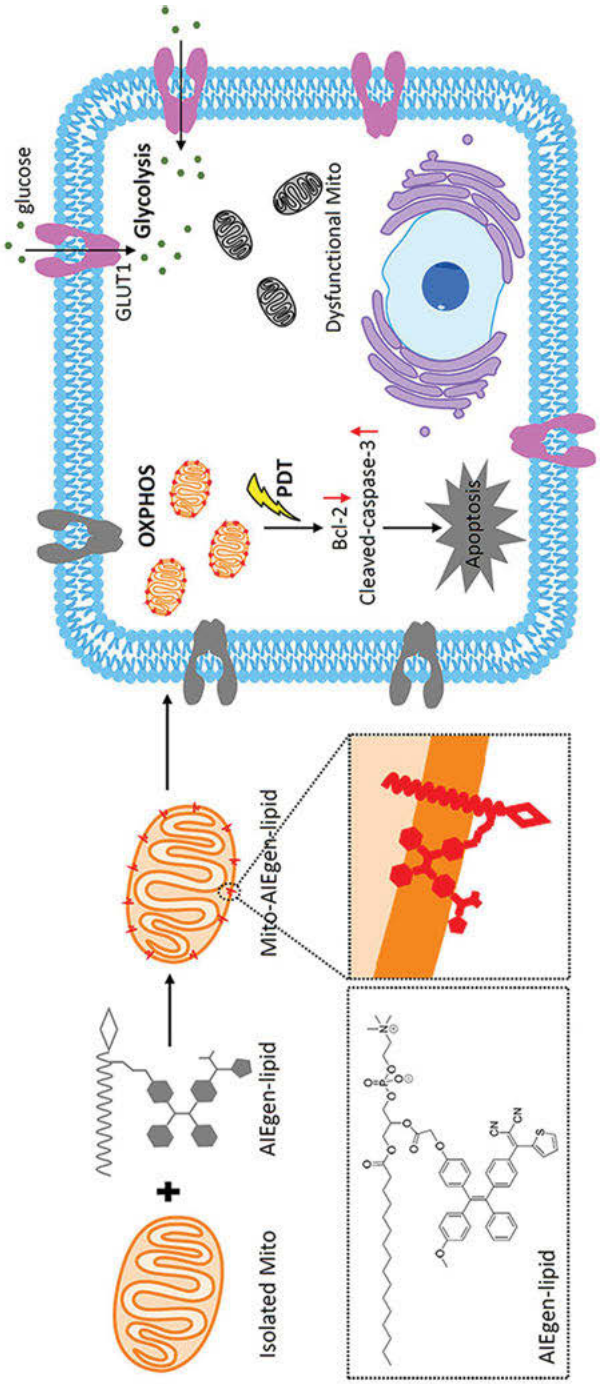

Figure 12.17: Scheme of AIEgen-lipid-modified mitochondria (Mito-AIEgen-lipid) synergistically rescuing the energy metabolism (oxidative phosphorylation: OXPHOS) and re-establishing the intracellular apoptotic pathway of cancer cells through attenuating glycolysis and downregulating the Bcl-2 protein and upregulating the cleaved-caspase-3 protein. Besides, the AIEgen-lipid-based photodynamic therapy (PDT) could further activate the apoptotic pathway for a more efficient anticancer effect. GLUT1: glucose transporter 1 [32]. Copyright © 2020, American Chemical Society.

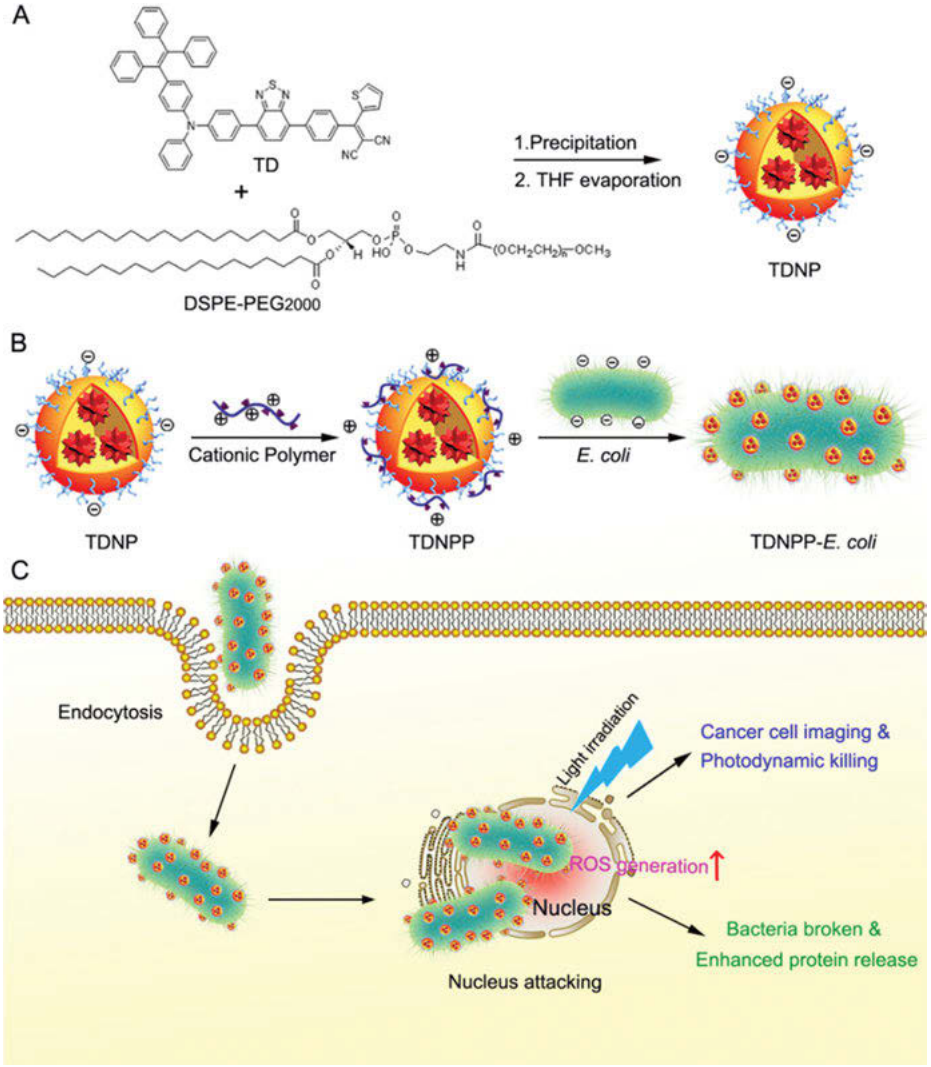

Figure 12.18: (A) The structure of TD and illustration of nanoparticle formation. (B) Process of TDNPP-coated live *E. coli*. (C) Intracellular trafficking of nanoparticle-coated live *E. coli* and PS delivery [33]. Copyright © 2019, American Chemical Society.

of the host cells under light irradiation. The designed expression of VEGFR2 proteins could then block the immunological tolerance to VEGFR2 and induce a T-cell-mediated autoimmune antiangiogenic response. Through a series of in vitro and in vivo experiments, prominent tumor suppression performance was validated with the engineered living therapeutic system, demonstrating its great potential in precise tumor treatment [34].

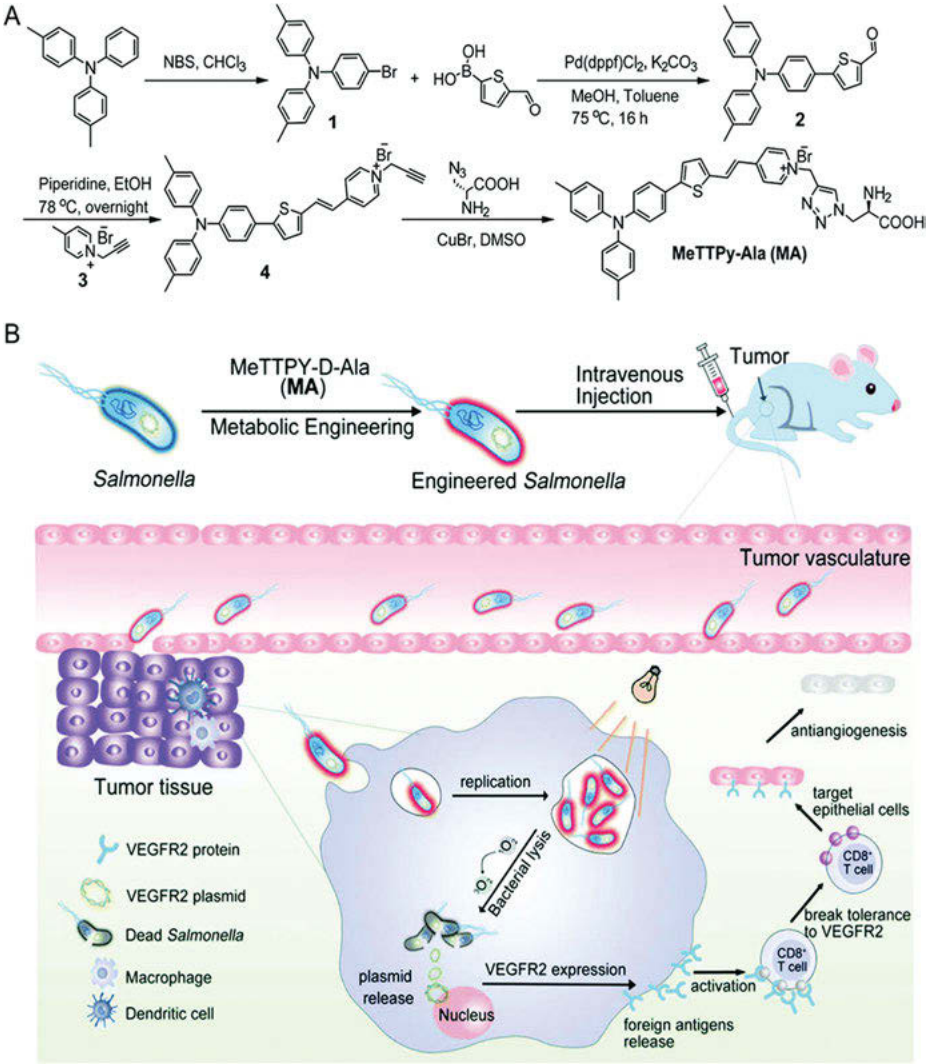

Figure 12.19: Schematic illustration of (A) the synthetic route to target compound MA and (B) *Salmonella* encoding the VEGFR2 plasmid engineered with MA and its antiangiogenesis therapy of breast cancer in vivo [34]. Copyright © 2021, The Royal Society of Chemistry.

Bacteriophage, or phage for short, is a virus that infects bacteria. Like other types of viruses, bacteriophages vary a lot in their shape and genetic material. He et al. reported bacteriophage-based aggregate-biohybrid by integrating AIEgens with bacteriophage to form a new class of antimicrobial bioconjugates (TVP–PAP) for the imaging and killing of a certain species of bacterium. The generated TVP–PAP perfectly preserved the properties of both AIEgen and phage, with intrinsic AIE fluorescence serving

the function of real-time monitoring of phage–bacterium interaction and particular specificity in bacterial targeting. What is more, the synergistic antibacterial effect with efficiency that significantly surpassing both individuals in the bioconjugates was achieved by integrating the PDI activity of AIEgen and the infection ability of phage itself [35].

Immune cells have attracted substantial attention because they can act as "living" carriers to travel through blood flow and accumulate in sites of inflammation or injury. As the most abundant immune cells, neutrophils possess an innate ability to penetrate the BBB and specifically infiltrate into the inflammatory sites. In addition, they can carry drugs and migrate along the chemotactic gradients toward the inflamed target, while still maintaining physiological activities. On the basis of this consideration, Liu et al. developed NEs-based aggregate-biohybrid. They utilized NEs as live carriers to deliver NIR-II AIE dots for accurate diagnosis of brain inflammation (Figure 12.20). Herein, it is shown that NEs carrying 2TT-oC6B NPs can penetrate the BBB and visualize the deeply located inflammation through an intact scalp and skull.

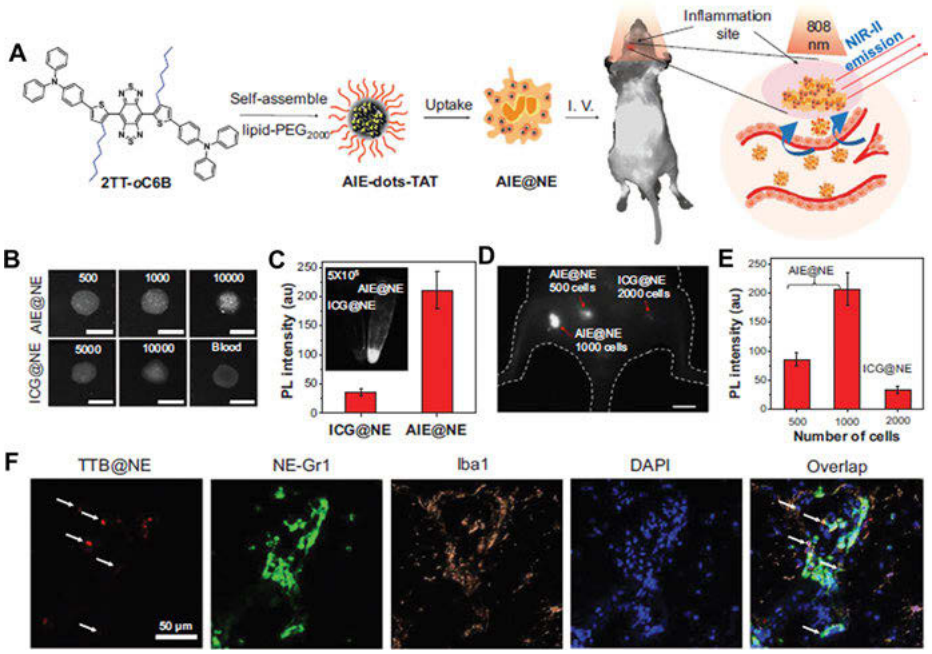

Figure 12.20: (A) Schematic of the NE-mediated NIR-II AIE dots for brain inflammation imaging. (B) NIR-II fluorescence images with different cell number (1,000 nm LP, 50 ms). (C) The average fluorescence signals at cell number of 5 × 105. (D) Subcutaneous fluorescence images with different cell number. (E) The average fluorescence signals of the data from (D). (F) The confocal images of inflammation slice. Representative images of TTB@NE, NE-Gr1, Iba1, DAPI and overlap. Scale bar = 5 mm for (B, D) [36]. Copyright © 2019, WILEY-VCH Verlag GmbH & Co. KGaA, Weinheim.

Notably, the bright 2TT-oC6B contributes to a significantly enhanced signal-to-background ratio of 30.6 in the brain inflammation site [36].

Recent work has shown that the primary role of the lipid-based NPs is to enhance cellular uptake into cancer cells rather than increasing the accumulation in the tumur [37]. Liu et al. reported neutrophil-based aggregate-biohybrid. They synthesized an AIEgen conjugated with lysophosphatidylcholine to label live neutrophils in an ultrafast (30 s) and wash-free manner with bright turn-on fluorescence. The insertion of TL into the lipid bilayer of the cell membrane could lead to restriction of intramolecular rotation. This contributed to the enhanced NIR fluorescence for TL, along with the reduced microenvironment polarity in cell membrane. This fast-labeling method does not affect the inherent neutrophil properties and physiological activities, including cell viability and chemotaxis ability. In addition, neutrophils labeled with TL using the simple, fast yet biocompatible labeling method have been successfully used to monitor neutrophil behaviors, such as the process of chemotaxis and migrating function toward sites of inflammation. The TL labeling strategy offers new opportunities to monitor the fate of neutrophils by fluorescence imaging both in vitro and in vivo, which may provide insights for new strategy design of living neutrophil-based nanotherapeutic studies (Figure 12.21) [38].

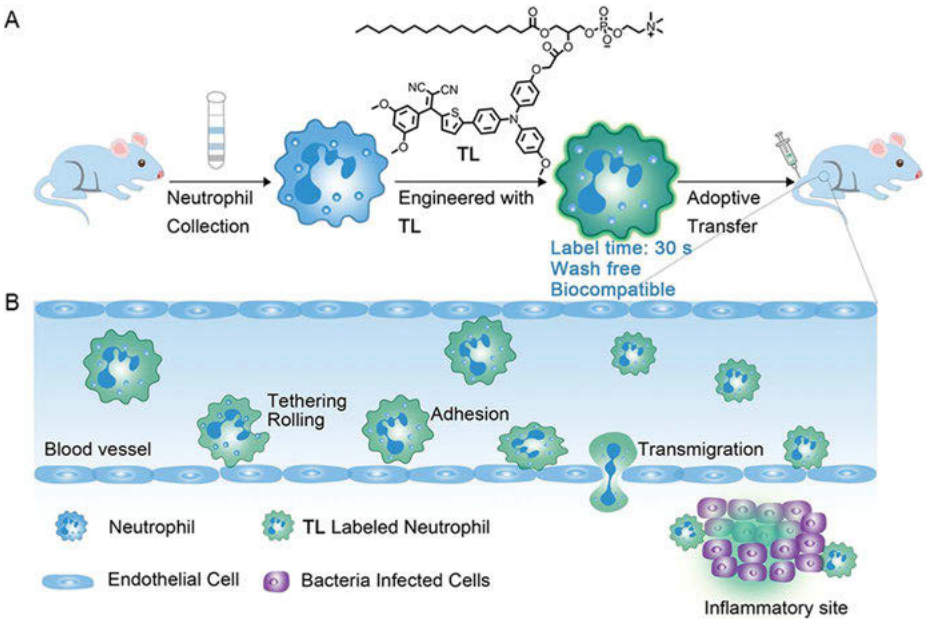

Figure 12.21: Illustration of the fabrication and inflammation imaging of TL-labeled neutrophils. (A) The preparation of TL-labeled neutrophils. (B) Inflammation-active TL-labeled neutrophils used for monitoring neutrophil behaviors such as migrating function toward inflammation sites and fluorescence imaging of inflammatory disorder [38]. Copyright © 2020, Wiley-VCH GmbH.

By virtue of coating NPs with cell membranes from diverse cell sources, active proteins on cell membranes can impart a variety of desired functionalities or supplementary therapeutic effects to NPs, providing ways for enhanced cancer immunotherapy. Recent advances of cell membrane camouflaged NPs applied to the improved immunotherapy are discussed on the basis of different sources of cell membranes and corresponding working mechanisms. These biomimetic NPs can potentially deliver therapeutic agents to the designated sites and actively engage in particular stages of the cancer immunity cycle, eliciting antitumor immunity with less off-target toxicities [39]. Deng et al. developed the natural killer cell membrane-based aggregate-biohybrid (NK@AIEdots) by coating NK cell membrane on the AIE-active polymeric endoskeleton, PBPTV, a highly bright NIR-II AIE-active conjugated polymer (Figure 12.22). Owing to the AIE and soft-matter characteristics of PBPTV, as-prepared NK@AIEdots maintained the superior NIR-II brightness (QY ~7.9% in water) and good biocompatibility. In addition, they could serve as tight junctions (TJs) modulator to trigger an intracellular signaling cascade, causing TJ disruption and actin cytoskeleton reorganization to form intercellular "green channel" to help themselves crossing BBB silently. Furthermore, they could initiatively accumulate to glioblastoma cells in the complex brain matrix for high-contrast and through-skull tumor imaging. The

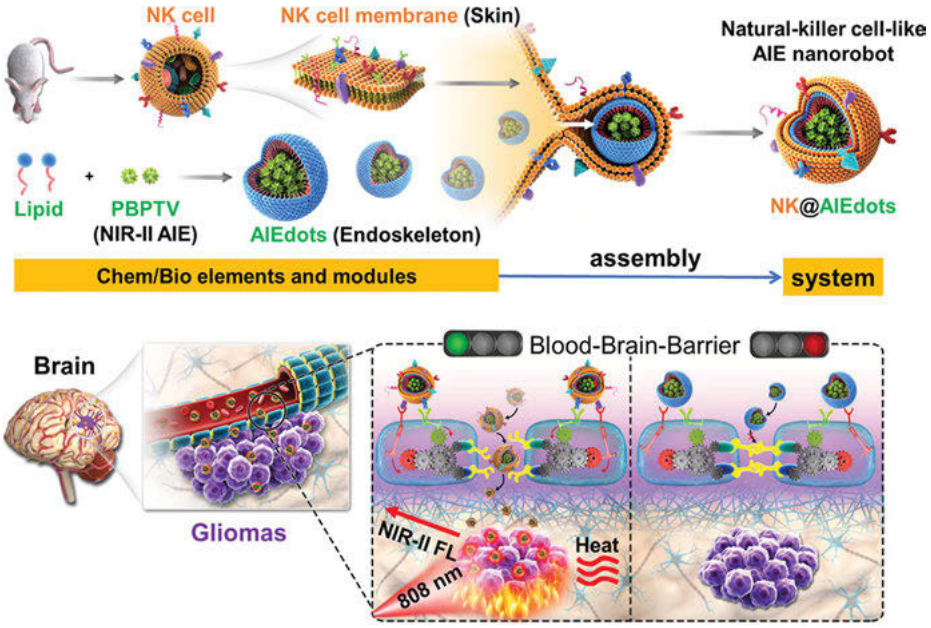

Figure 12.22: Schematic illustration showing the preparation and assembly process of NK cell that mimics AIE nanoparticles (NK@AIEdots) and the "smart" tight junctions (TJs) that modulated blood–brain barrier (BBB) penetration of NK@AIEdots for brain tumor-targeted light-up and inhibition [40]. Copyright © 2020, American Chemical Society.

tumor growth was also greatly inhibited by these NK@AIEdots under the NIR light illumination. As far as we know, the QY of PBPTV is the highest among the existing NIR-II luminescent conjugated polymers. Moreover, the NK-cell biomimetic nanorobots showed great potential for BBB-crossing active delivery [40].

Xu et al. developed dendritic cell (DC) membrane-based aggregate-biohybrid PSs with antigen-presenting and hitchhiking abilities (DC@AIEdots) by coating DC membranes on the nanoaggregates of the AIE PSs. Notably, the inner AIE PSs could selectively accumulate in lipid droplets of tumor cells, and the outer cell membrane could facilitate the hitchhiking of DC@AIEdots onto the endogenous T cells and enhance the tumor delivery efficiency by about 1.6 times. Furthermore, DC@AIEdots could stimulate the in vivo proliferation and activation of T cells and trigger the immune system. This study not only indicates the potential applications of therapeutic agents targeting lipid droplets for immunotherapy but also provides a new hitchhike approach for drug delivery. Lastly, our study presents a photoactive and artificial antigen-presenting platform for effective T-cell stimulation and cancer photodynamic immunotherapy (Figure 12.23) [41].

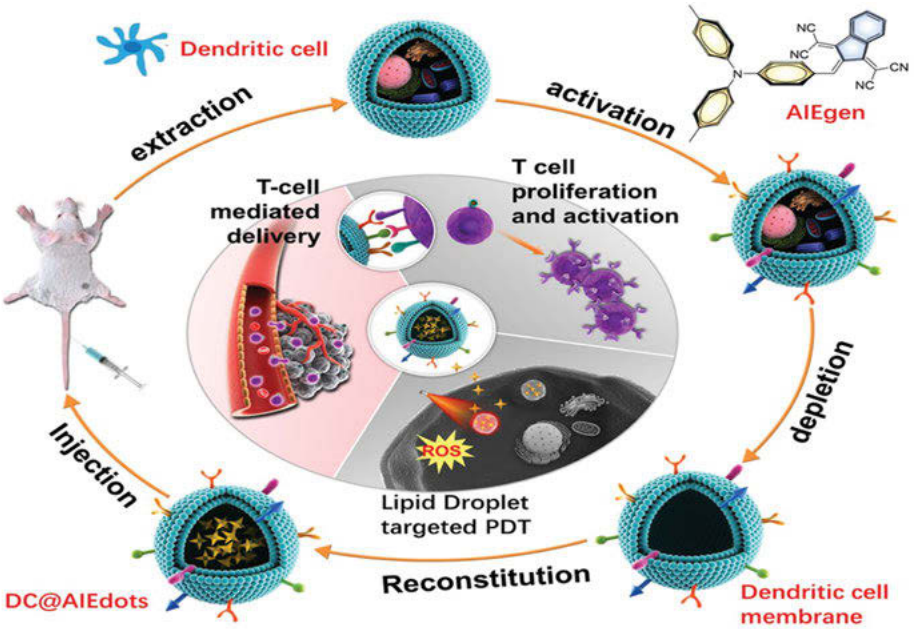

Figure 12.23: The schematic illustration represents preparation and assembly of AIE photosensitizers with dendritic cell membrane coating (DC@AIEdots) and in vivo photodynamic immunotherapy. The inner AIE photosensitizers selectively accumulated in tumor cells, and the outer cell membrane facilitated DC@AIEdots to hitchhike on endogenous T cells to enhance the tumor delivery efficiency, and stimulate in vivo T-cell proliferation and activation to activate the immune system [41]. Copyright © 2021, Wiley-VCH GmbH.

Conclusion

In this chapter, we introduced the recent progress of NIR materials designed based on aggregate structures. As a promising and emerging strategy for NIR material development, moving beyond single molecules and well-defined complexes, aggregates serve as a particularly useful form of materials that often display modified or wholly new properties compared to their molecular components. Many exclusive structures and NIR properties have only been discovered in the aggregate state but not in molecular species. Thus, it is foreseeable that there is a plenty room for developing NIR materials by manipulating the molecular aggregate (i.e., irregular clusters of many molecules) instead of complex synthesis. We also introduced different hybrids of naturally biological component and artificially synthetic materials at aggregate level by starting from different biological elements at different scales (e.g., DNA fragments, bacteria, cells, and entire organs). By leveraging the performance of living cells and tissues and directly interfacing them with artificial components, it should be possible to exploit the inherent metabolic efficiency of biological functions within artificial materials and to provide novel solutions to the problems of biocompatibility. Recent work has shown that this is, in principle, possible and that some biohybrid systems are working as expected and are producing a therapeutic impact in animal models of human diseases. However, there is still a long way to go until aggregate biohybrid systems will be a clinical reality.

References

[1] Feng G, Zhang GQ, Ding D, Design of superior phototheranostic agents guided by Jablonski diagrams, Chem Soc Rev, 2020, 49(22), 8179–8234.
[2] Qian G, Wang ZY, Near-infrared organic compounds and emerging applications, Chem Asian J, 2010, 5(5), 1006–1029.
[3] Tian D, Qi F, Ma H, Wang X, Pan Y, Chen R, Shen Z, Liu Z, Huang L, Huang W, Domino-like multi-emissions across red and near infrared from solid-state 2-/2,6-aryl substituted BODIPY dyes, Nat Commun, 2018, 9(1), 2688.
[4] Sun C, Sun X, Pei P, He H, Ming J, Liu X, Liu M, Zhang Y, Xia Y, Zhao D, Li X, Xie Y, Zhang F, NIR-II J-Aggregates labelled mesoporous implant for imaging-guided osteosynthesis with minimal invasion, Adv Funct Mater, 2021, 31(23), 2100656.
[5] Hemmer E, Venkatachalam N, Hyodo H, Hattori A, Ebina Y, Kishimoto H, Soga K, Upconverting and NIR emitting rare earth based nanostructures for NIR-bioimaging, Nanoscale, 2013, 5(23), 11339–11361.
[6] Smith AM, Mancini MC, Nie S, Bioimaging: Second window for in vivo imaging, Nat Nanotechnol, 2009, 4(11), 710–711.
[7] Li K, Duan X, Jiang Z, Ding D, Chen Y, Zhang GQ, Liu Z, J-aggregates of meso-[2.2] paracyclophanyl-BODIPY dye for NIR-II imaging, Nat Commun, 2021, 12(1), 2376.
[8] Ji C, Lai L, Li P, Wu Z, Cheng W, Yin M, Organic dye assemblies with aggregation-induced photophysical changes and their bio-applications, Aggregate, 2021, e39.

[9] Mei J, Leung NL, Kwok RT, Lam JW, Tang BZ, Aggregation-Induced emission: Together we shine, united we soar!, Chem Rev, 2015, 115(21), 11718–11940.
[10] Shao A, Xie Y, Zhu S, Guo Z, Zhu S, Guo J, Shi P, James TD, Tian H, Zhu WH, Far-Red and Near-IR AIE-Active Fluorescent Organic Nanoprobes with Enhanced Tumor-Targeting Efficacy: Shape-Specific Effects, Angew Chem, Int Ed Engl, 2015, 54(25), 7275–7280.
[11] Qi J, Sun C, Zebibula A, Zhang H, Kwok RTK, Zhao X, Xi W, Lam JWY, Qian J, Tang BZ, Real-time and high-resolution bioimaging with bright aggregation-induced emission dots in short-wave infrared region, Adv Mater, 2018, 30(12), e1706856.
[12] Sheng Z, Guo B, Hu D, Xu S, Wu W, Liew WH, Yao K, Jiang J, Liu C, Zheng H, Liu B, Bright aggregation-induced-emission dots for targeted synergetic NIR-II fluorescence and NIR-I photoacoustic imaging of orthotopic brain tumors, Adv Mater, 2018, e1800766.
[13] Gao S, Wei G, Zhang S, Zheng B, Lu W, Albumin tailoring fluorescence and photothermal conversion effect of near-infrared-II fluorophore with aggregation-induced emission characteristics, Nat Commun, 2019, 10(1), 2206.
[14] Li Y, Cai Z, Liu S, Zhang H, Wong STH, Lam JWY, Kwok RTK, Qian J, Tang BZ, Design of AIEgens for near-infrared IIb imaging through structural modulation at molecular and morphological levels, Nat Commun, 2020, 11(1), 1255.
[15] Li Y, Hu D, Sheng Z, Min T, Zha M, Ni JS, Zheng H, Li K, Self-assembled AIEgen nanoparticles for multiscale NIR-II vascular imaging, Biomaterials, 2021, 264, 120365.
[16] Cai X, Liu J, Liew WH, Duan Y, Geng J, Thakor N, Yao K, Liao L-D, Liu B, Organic molecules with propeller structures for efficient photoacoustic imaging and photothermal ablation of cancer cells, Mater Chem Front, 2017, 1(8), 1556–1562.
[17] Wang S, Wu W, Manghnani P, Xu S, Wang Y, Goh CC, Ng LG, Liu B, Polymerization-enhanced two-photon photosensitization for precise photodynamic therapy, ACS Nano, 2019, 13(3), 3095–3105.
[18] Li L, Shao C, Liu T, Chao Z, Chen H, Xiao F, He H, Wei Z, Zhu Y, Wang H, Zhang X, Wen Y, Yang B, He F, Tian L, An NIR-II-Emissive photosensitizer for hypoxia-tolerant photodynamic theranostics, Adv Mater, 2020, 32(45), e2003471.
[19] Wan Q, Zhang R, Zhuang Z, Li Y, Huang Y, Wang Z, Zhang W, Hou J, Tang BZ, Molecular Engineering to Boost AIE-Active Free Radical Photogenerators and Enable High-Performance Photodynamic Therapy under Hypoxia, Adv Funct Mater, 2020, 30(39), 2002057.
[20] Wu X, Sun X, Guo Z, Tang J, Shen Y, James TD, Tian H, Zhu W, In vivo and in situ tracking cancer chemotherapy by highly photostable NIR fluorescent theranostic prodrug, J Am Chem Soc, 2014, 136(9), 3579–3588.
[21] Zhao Z, Chen C, Wu W, Wang F, Du L, Zhang X, Xiong Y, He X, Cai Y, Kwok RTK, Lam JWY, Gao X, Sun P, Phillips DL, Ding D, Tang BZ, Highly efficient photothermal nanoagent achieved by harvesting energy via excited-state intramolecular motion within nanoparticles, Nat Commun, 2019, 10(1), 768.
[22] Zhang H, Zhao Z, Turley AT, Wang L, McGonigal PR, Tu Y, Li Y, Wang Z, Kwok RTK, Lam JWY, Tang BZ, Aggregate Science: From Structures to Properties, Adv Mater, 2020, 32(36), e2001457.
[23] Tian S, Bai H, Li S, Xiao Y, Cui X, Li X, Tan J, Huang Z, Shen D, Liu W, Wang P, Tang BZ, Lee CS, Water-Soluble organic nanoparticles with programmable intermolecular charge transfer for NIR-II photothermal anti-bacterial therapy, Angew Chem, Int Ed Engl, 2021, 60(21), 11758–11762.
[24] Ou C, Na W, Ge W, Huang H, Gao F, Zhong L, Zhao Y, Dong X, Biodegradable charge-transfer complexes for glutathione depletion induced ferroptosis and NIR-II photoacoustic imaging guided cancer photothermal therapy, Angew Chem, Int Ed Engl, 2021, 60(15), 8157–8163.

[25] Xiao F, Chen Z, Wei Z, Tian L, Hydrophobic interaction: A promising driving force for the biomedical applications of nucleic acids, Adv Sci, 2020, 7(16), 2001048.
[26] Shi L, Wu W, Duan Y, Xu L, Xu Y, Hou L, Meng X, Zhu X, Liu B, Light-Induced self-escape of spherical nucleic acid from endo/lysosome for efficient non-cationic gene delivery, Angew Chem, Int Ed Engl, 2020, 59(43), 19168–19174.
[27] Song L, Jiang Q, Liu J, Li N, Liu Q, Dai L, Gao Y, Liu W, Liu D, Ding B, DNA origami/gold nanorod hybrid nanostructures for the circumvention of drug resistance, Nanoscale, 2017, 9(23), 7750–7754.
[28] Zhu W, Ma K, Yan Z-C, Wu Q, Wang D, Tang BZ, A DNA tetrahedron-loaded natural photosensitizer with aggregation-induced emission characteristics for boosting fluorescence imaging-guided photodynamic therapy, Mater Chem Front, 2021.
[29] Zhang P, Zhao Z, Li C, Su H, Wu Y, Kwok RTK, Lam JWY, Gong P, Cai L, Tang BZ, Aptamer-Decorated Self-Assembled Aggregation-induced emission organic dots for cancer cell targeting and imaging, Anal Chem, 2018, 90(2), 1063–1067.
[30] Sheahan MB, Rose RJ, McCurdy DW, Mechanisms of organelle inheritance in dividing plant cells, J Integr Plant Biol, 2007, 49(8), 1208–1218.
[31] Bai H, Liu H, Chen X, Hu R, Li M, He W, Du J, Liu Z, Qin A, Lam JWY, Kwok RTK, Tang BZ, Augmenting photosynthesis through facile AIEgen-chloroplast conjugation and efficient solar energy utilization, Mater Horizons, 2021, 8(5), 1433–1438.
[32] Liu J, Liu X, Wu M, Qi G, Liu B, Engineering Living Mitochondria with AIE Photosensitizer for Synergistic Cancer Cell Ablation, Nano Lett, 2020, 20(10), 7438–7445.
[33] Wu M, Wu W, Duan Y, Li X, Qi G, Liu B, Photosensitizer-bacteria biohybrids promote photodynamic cancer cell ablation and intracellular protein delivery, Chem Mater, 2019, 31(18), 7212–7220.
[34] Liu X, Wu M, Wang M, Duan Y, Phan C, Qi G, Tang G, Liu B, Metabolically engineered bacteria as light-controlled living therapeutics for anti-angiogenesis tumor therapy, Mater Horizons, 2021, 8(5), 1454–1460.
[35] Sun Z, Deng G, Peng X, Xu X, Liu L, Xu Z, Ma Y, Zhang P, Gong P, Cai L, NIR-active nanoterminator with mature dendritic cell activities for immunopriming mild photothermal cancer therapy, (Preprint) chemrxiv:12546698.v2, submitted, Jun, 2020.
[36] Liu S, Chen C, Li Y, Zhang H, Liu J, Wang R, Wong STH, Lam JWY, Ding D, Tang BZ, Constitutional isomerization enables bright NIR-II AIEgen for brain-inflammation imaging, Adv Funct Mater, 2019, 30(7), 1908125.
[37] Davis ME, Chen ZG, Shin DM, Nanoparticle therapeutics: An emerging treatment modality for cancer, Nat Rev Drug Discov, 2008, 7(9), 771–782.
[38] Liu X, Wu M, Wang M, Duan Y, Phan CU, Chen H, Tang G, Liu B, AIEgen-Lipid conjugate for rapid labeling of neutrophils and monitoring of their behavior, Angew Chem, Int Ed Engl, 2021, 60(6), 3175–3181.
[39] Zeng Z, Pu K, Improving cancer immunotherapy by cell membrane-camouflaged nanoparticles, Adv Funct Mater, 2020, 30(43), 2004397.
[40] Deng G, Peng X, Sun Z, Zheng W, Yu J, Du L, Chen H, Gong P, Zhang P, Cai L, Tang BZ, Natural-Killer-Cell-Inspired Nanorobots with Aggregation-Induced Emission Characteristics for Near-Infrared-II Fluorescence-Guided Glioma Theranostics, ACS Nano, 2020, 14(9), 11452–11462.
[41] Xu X, Deng G, Sun Z, Luo Y, Liu J, Yu X, Zhao Y, Gong P, Liu G, Zhang P, Pan F, Cai L, Tang BZ, A biomimetic aggregation-induced emission photosensitizer with antigen-presenting and hitchhiking function for lipid droplet targeted photodynamic immunotherapy, Adv Mater, 2021, 33, 2102322.

Hanlin Ou, Zhiyuan Gao, Dan Ding

Chapter 13
Fluorescent and afterglow luminescent AIE dots for biomedical applications

13.1 Introduction

Optical imaging has aroused increasing attention in the biomedical field, owing to the advantages of well safety, high time-domain resolution, excellent sensitivity, and real-time imaging [1–5]. Among various optical imaging methods, fluorescence imaging is the longest developed and most mature imaging technology. Currently, large amounts of fluorescent dyes, including noble metal materials, inorganic materials, and organic materials, have been developed for fluorescence imaging [6–10]. Among them, organic fluorescent dyes have attracted more attention from researchers due to their good biocompatibility, flexible processability, and other advantages [2, 11–13], However, most of these traditional organic fluorescent dyes are hydrophobic in nature and tend to aggregate by π–π stacking in aqueous environments [14]. The enhanced nonradiation dissipation favored by the serious π–π stacking interactions releases the laser energy absorbed by fluorescent molecules, resulting in the severely reduced luminescence efficiency of traditional organic fluorescent dyes [14, 15]. This phenomenon of aggregation-caused quenching (ACQ) effect severely limits the application of conventional fluorescent molecules in aqueous biological environments [16]. Fortunately, the discovery of aggregation-induced emission (AIE) materials provides a good solution to overcome this bottleneck [17–19]. The motion of propellers in AIE materials is strongly restricted in the aggregated state, leading to the significantly enhanced fluorescence emission of AIE materials according to the Jablonski diagram [20–22].

In the past two decades, a large number of AIE fluorescent materials have been developed for biomedical applications [23–28]. However, although great efforts have made to improve the brightness of fluorescent materials, the signal-to-noise (S/N) ratio of fluorescence imaging in vivo is still severely limited by the tissue autofluorescence of the organism itself [4, 29, 30]. In order to improve the S/N ratio of optical imaging, afterglow imaging, which harvests photons continuously emitted

Hanlin Ou, Zhiyuan Gao, State Key Laboratory of Medicinal Chemical Biology, Key Laboratory of Bioactive Materials, Ministry of Education, and College of Life Sciences, Nankai University, Tianjin 300071, China, Tel: +86-22-23501229, Fax: +86-22-23498775
Dan Ding, State Key Laboratory of Medicinal Chemical Biology, Key Laboratory of Bioactive Materials, Ministry of Education, and College of Life Sciences, Nankai University, Tianjin 300071, China, Tel: +86-22-23501229, Fax: +86-22-23498775, e-mail: dingd@nankai.edu.cn

https://doi.org/10.1515/9783110673074-014

from luminescent materials after termination of the applied laser excitation, has been developed in recent years [31–34]. Compared with traditional fluorescence imaging techniques, afterglow imaging requires no real-time laser excitation and completely avoids the interference of tissue autofluorescence and thus has higher sensitivity and S/N ratio, which is extremely advantageous for early detection of diseases in vivo [35, 36]. However, most of the afterglow materials developed so far are inorganic substances composed of rare earth/heavy metal ions such as europium, praseodymium, and chromium, whose potential biotoxicity and difficult structural modification greatly limit their application in biomedical fields [37–40]. Compared with inorganic afterglow materials, organic afterglow materials with good biocompatibility are more suitable for biomedical applications [35]. Nevertheless, only a few organic afterglow probes have been reported to be applied in the biomedical field [41–43]. Moreover, the afterglow signal intensity of these probes in vivo still needs to be further improved due to their intrinsic ACQ properties [44]. It has been shown that combining afterglow properties with AIE characteristics is beneficial to enhance the afterglow emission and thus improve the S/N ratio for disease diagnosis [44, 45].

To date, although a large amount of book chapters/reviews have summarized the biomedical applications of fluorescent or afterglow materials, however, book chapters/reviews focusing on fluorescent and afterglow luminescent AIE dots for biomedical applications are still rare [46–50]. In this chapter, we summarize the recent advances in the biomedical applications of fluorescent and afterglow luminescent AIE dots. Firstly, we expound the applications of fluorescent luminescent AIE dots in drug-release monitoring, bacteria discrimination, fluorescent image-guided cancer surgery, lymph node imaging, and vascular imaging. Next, we introduce the biomedical applications of emerging afterglow luminescent AIE dots in the imaging of tumors and lymph nodes, image-guided cancer surgery, and image-guided cancer surgery. Finally, a brief summary and outlook on the biomedical applications of fluorescent and afterglow luminescent AIE dots is presented.

13.2 Fluorescent luminescent AIE dots for biomedical applications

Fluorescence is the light emitted by a substance after it absorbs light energy. In the fluorescence emission process, upon light irradiation, the electrons of the fluorescent molecules jump from the ground state to the excited singlet state, after which they return to the ground state to emit photons. Due to the high sensitivity of fluorescence imaging, fluorescent luminescent AIE dots are widely used in drug-release monitoring, bacteria discrimination, fluorescent image-guided cancer surgery, lymph node imaging, and vascular imaging and other fields [51–58].

13.2.1 Monitoring of drug release

Small chemotherapeutic drugs play a key role in the clinical therapy of tumors. Due to the inherently hydrophobic structure, the blood circulation time of most molecule chemotherapeutic drugs is short. To prolong their circulation time, the hydrophobic small-molecule chemotherapeutic drugs are usually prepared into nanodrugs, by being encapsulated into the hydrophobic core of amphiphilic polymers [59, 60]. The surface (or core) of these nanodrugs is usually modified (or loaded) with fluorescent materials to trace the destination of these chemotherapeutic drugs [61]. However, this approach is unable to trace whether these chemotherapeutic drugs are released from the carriers.

Recently, Yi et al. reported a self-guiding polymeric prodrug micelle, TB@PMPT, realizing the monitoring of paclitaxel (PTX) release from the micelles [57]. As shown in Figure 13.1, by conjugating PTX and AIE photosensitizer PyTPE (yellow fluorescence dye) on the side chain, the reduction-sensitive polymeric prodrug PEG (polyethylene glycol)-b-PMPMC-gPTX-g-PyTPE (PMPT) was constructed. The final TB@PMPT micelles were prepared by encapsulating another AIE photosensitizer TPA-BDTP (TB, red fluorescence dye) into the hydrophobic cavity of PMPT micelles. Before injection, the TB@PMPT micelles can emit two kinds of fluorescence. After reaching the tumor sites, small amounts of reactive oxygen species (ROS) generated by PyTPE and TB after the first light exposure-induced lipid peroxidation and increase the permeability of cell membranes, thus improving the ability of cells to take up TB@PMPT micelles. Soon afterward, the disulfide bond in PMPT was broken in response to glutathione overexpressed in tumor cells, releasing PTX. Meanwhile, the hydrophilicity of the residual polymer conjugated with PyTPE was enhanced, leading to decreased fluorescence of PyTPE. Since the fluorescence of TB remained unchanged, the ratio of the fluorescence of TB to PyTPE can be used to monitor the release of PTX and indicate the timing for second laser irradiation to achieve photodynamic therapy (PDT).

13.2.2 Bacteria discrimination

Although bacteria are widespread in the human body and mostly harmless, some bacteria could still cause serious diseases. Antibiotics are an effective tool used clinically to kill bacteria [62]. However, due to the abuse of antibiotics in recent years, superbugs with antibiotic resistance have emerged. Proper selection and control of the use of antibiotics is beneficial to reduce the emergence of antibiotic-resistant bacteria. Bacteria are classified into Gram-positive and Gram-negative bacteria based on the composition of their cell walls. Gram-positive and Gram-negative bacteria have different pathogenic mechanisms, with Gram-positive bacteria producing exotoxins and Gram-negative bacteria producing endotoxins. Distinguishing the type of infecting bacteria facilitates the

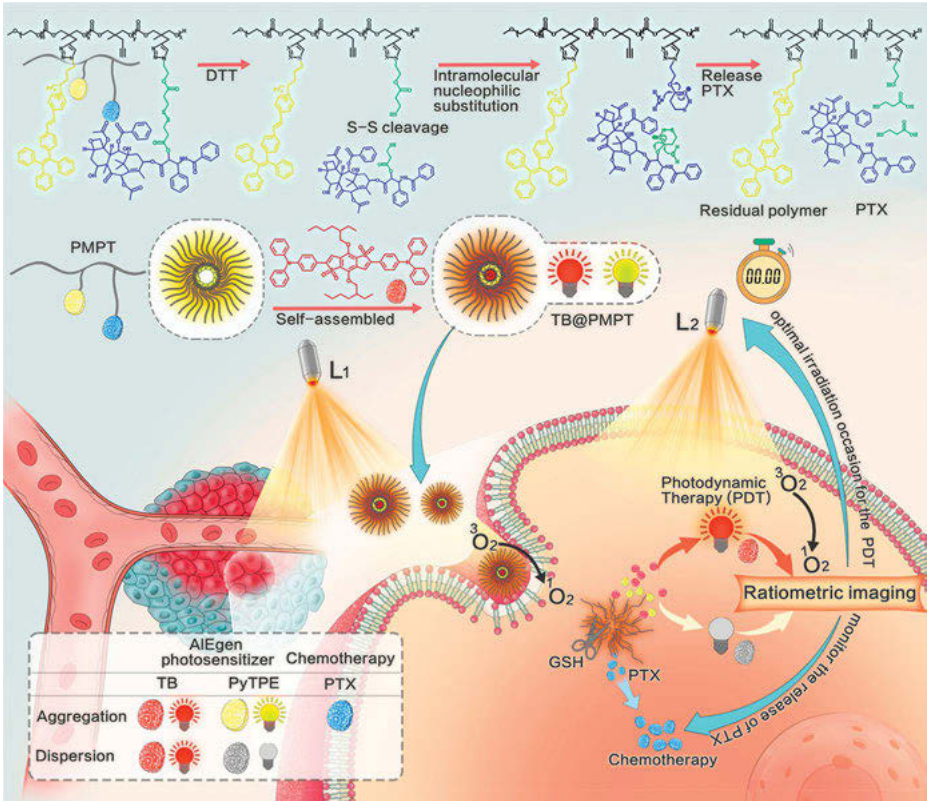

Figure 13.1: Mechanistic diagram of the monitoring of PTX release from TB@PMPT. Adapted with permission from ref. [57]. Copyright 2021, American Chemical Society.

targeted selection of antibacterial drugs for treatment. Gram staining is the traditional method to identify Gram-positive and Gram-negative bacteria, but its operation is tedious and complicated and requires operators to have high operating skills.

Recently, Bao et al. reported a peptide-based AIE bioprobe, AIE-DCM-2 polymyxin B, allowing for rapid detection of Gram-negative bacteria [54]. AIE-DCM-2 polymyxin B is composed with a core of an AIE dye AIE-DCM and two heads of polymyxin B peptides (Figure 13.2A). Owing to the high specific binding affinity of polymyxin B toward lipopolysaccharides (LPS), which is the major components on the cell wall of Gram-negative bacteria, AIE-DCM-2 polymyxin B can specifically bind to the surface of Gram-negative bacteria [63]. In addition, the introduction of polymyxin B increases the hydrophilicity of AIE-DCM, resulting in a weak fluorescence of AIE-DCM-2 polymyxin B in aqueous solution (Figure 13.2B). In contrast, for AIE-DCM-2 polymyxin B bound to the surfaces of Gram-negative bacteria, an intense fluorescence is emitted due to the restricted intramolecular motion of AIE-DCM, allowing for rapid and specific detection of Gram-negative bacteria (Figure 13.2C, D).

Moreover, AIE-DCM-2 polymyxin B is able to generate ROS under laser irradiation and could also be used for photodynamic sterilization.

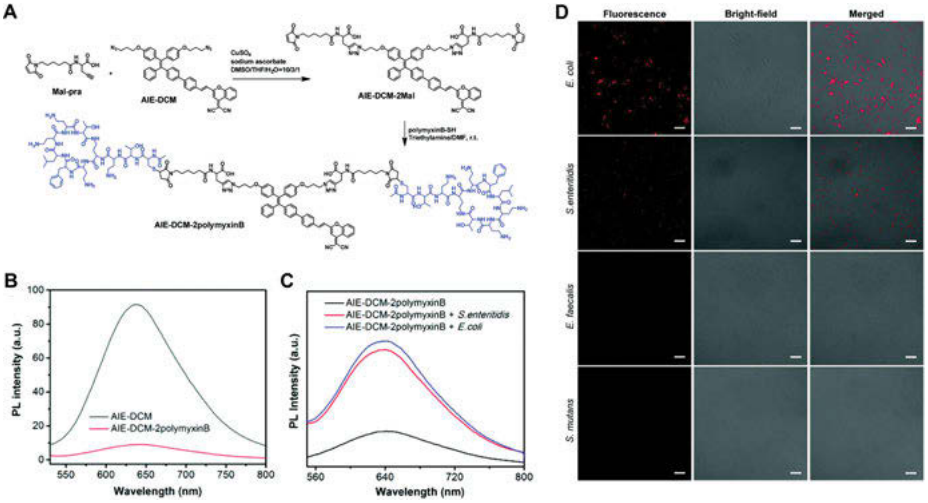

Figure 13.2: (A) Synthetic route of AIE-DCM-2 polymyxin B. (B) Emission spectra of AIE-DCM and AIE-DCM-2 polymyxin B in aqueous solution. (C) Emission spectra of AIE-DCM-2 polymyxin B with and without bacteria. (D) Confocal images of AIE-DCM-2 polymyxin B after incubation with different kinds of bacteria. Adapted with permission from ref. [54]. Copyright 2021, The Royal Society of Chemistry.

The specific identification of Gram-positive bacteria is also very important. Recently, Hu et al. reported an AIE probe, 2-(((diphenylmethylene)hydrazono)methyl) naphthalene (M1-DPAN), to be able to rapidly distinguish Gram-positive bacteria from Gram-negative bacteria and fungus [58]. Owing to the high binding affinity toward lipoteichoic acid (LTA), which is the major components on the cell wall of Gram-positive bacteria, M1-DPAN can efficiently bind to the surface of Gram-positive bacteria (Figure 13.3A). Subsequently, the DPAN moieties in M1-DPAN insert into the outer layers of Gram-positive bacteria due to the strong hydrophobic interactions between DPAN and cross-linked peptidoglycan, the major components of the outer layers of Gram-positive bacteria. On account of the restricted intramolecular motion, M1-DPAN emits strong fluorescence upon laser irradiation (Figure 13.3B). For the Gram-negative bacteria, except for the low binding affinity of M1-DPAN toward LPS, the small amount of M1-DPAN that adheres to the surface of Gram-negative bacteria is also difficult to insert into the interior of the bacteria due to the inhibition by phospholipid layer, the major components of the outer layers of Gram-negative bacteria (Figure 13.3C). While for fungus, although a small number of M1-DPAN adhering to the surface of the fungus can insert into the interior of the fungus, the alkalinity of morpholine moiety in M1-DPAN is not suitable for binding with the outer layer structure of fungus, resulting in the easy removal of the inserted part (Figure 13.3D). This

work provides a novel strategy to achieve specific discrimination of Gram-positive bacteria without antibody or protein modification.

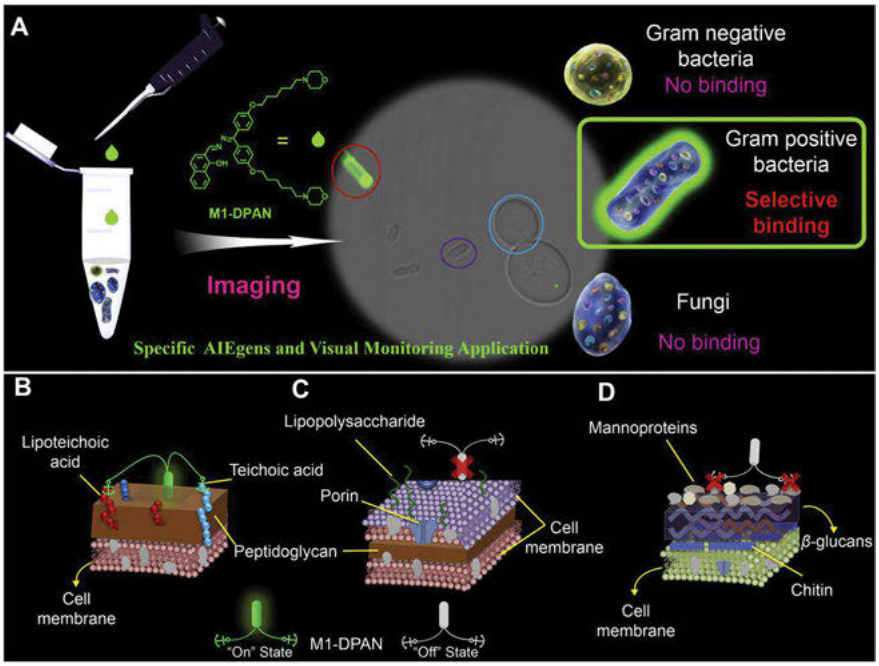

Figure 13.3: (A) Schematic diagram of the process of G specific discrimination by M1-DPAN. (B–D) Schematic diagram of the binding between M1-DPAN and the outer cell walls after coincubation with the Gram-positive bacteria (B), Gram-negative bacteria (C), or fungus (D). Adapted with permission from ref. [58]. Copyright 2018, Elsevier.

13.2.3 Fluorescent image-guided cancer surgery

Although new methods such as chemotherapy, radiotherapy, and immunotherapy have been developed for tumor treatment, surgical resection is still an important method to treat tumors in the clinic. However, at present, doctors mainly rely on their experience in naked eye observation and palpation to find tumors for resection, which may cause tiny tumors to be missed and result in tumor recurrence. Therefore, it is clinically important to develop new methods for guiding surgeons to accurately identify and resect tiny tumors.

Recently, Gu et al. reported corannulene-incorporated AIE nanodots with highly suppressed nonradiative decay for bright fluorescent image-guided cancer surgery [51]. By encapsulating TPP-TPA, an AIEgen with "rotor-rich" skeleton and an inherent charge, into the hydrophobic core of corannulene-decorated PEG, a corannulene-

incorporated AIE nanodot, Cor-AIE dot, was constructed (Figure 13.4A). Owing to the large intraparticle rigid microenvironments endowed by the large dipole moment, superhydrophobicity, and hyper-rigidity of corannulene, the nonradiative decay of TPP-TPA embedded inside the corannulene was highly suppressed, leading to the greatly enhanced fluorescence emission and ROS generation compared to TPP-TPA encapsulated by DSPE-PEG_{2000}. Thanks to the excellent enhanced permeability and retention (EPR) effect and bright fluorescence emission of Cor-AIE dots, the tiny tumors in the peritoneal carcinomatosis-bearing mouse model were clearly presented by the fluorescence of Cor-AIE dots, demonstrated by the overlap of the autofluorescence signal from luciferase-expressed 4T1 cancer cells and the fluorescence signal from Cor-AIE dots (Figure 13.4B, C). As shown in Figure 13.4D–F, a small amount of tiny tumors still remained after a fluorescence image-blind tumor resection, while under the guidance of the fluorescence of Cor-AIE dots, a complete removal of the tiny tumors was achieved. In addition, owing to the excellent ROS generation capability, Cor-AIE dots also performed well in PDT of tumors that were not appropriate for surgical excision.

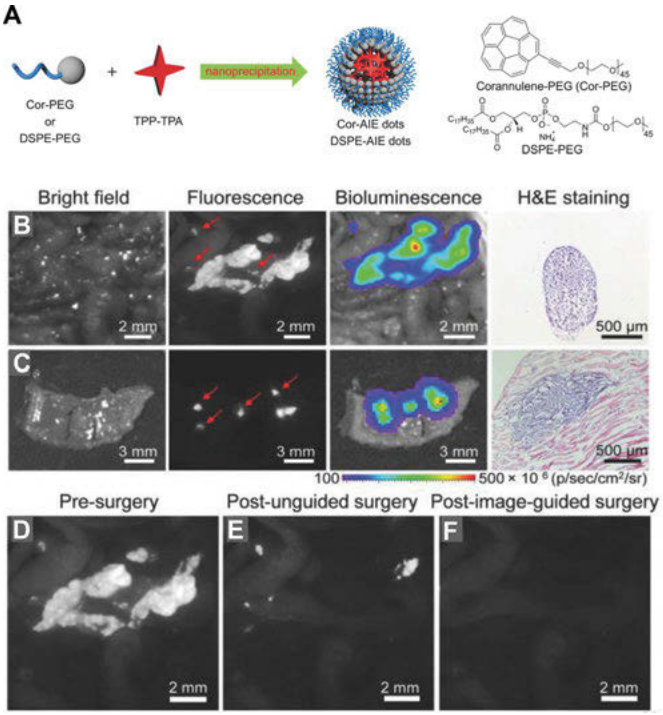

Figure 13.4: (A) The preparation of Cor-AIE dots and DSPE-AIE dots. (B, C) Bright field, NIR fluorescence, bioluminescence, and HE staining images of the tumor nodules on the surface of the intraperitoneal intestines (B) and the peritoneum (C). (D–F) NIR fluorescence imaging of the peritoneal cavity before surgical tumor removal (D), after unguided surgery (E), and after the second guided surgery (F). Adapted with permission from ref. [51]. Copyright 2018, Wiley-VCH.

13.2.4 Lymph node imaging

The sentinel lymph nodes are the first lymph nodes through which the primary tumor metastasizes to other sites. Lymph node imaging helps clinicians to quickly locate the sentinel lymph nodes and determine whether the tumor has metastasized through biopsy results after resection, thus guiding whether to perform further lymph node dissection. Blue dye staining is the traditional method for detecting sentinel lymph nodes, however, due to the poor tissue penetration ability of the fluorescence of blue dyes such as methylene blue, a commonly used blue dye, naked eye observation is clinically used to look for lymph nodes marked with blue dyes, which is ineffective and requires high skills of doctors.

In order to overcome the disadvantage of poor tissue penetration of blue dyes, Luo et al. developed a deep-red fluorescent dye, BTA-TPA, for highly bright imaging of lymph nodes in vivo [53]. By integrating the hybridized local and charge-transfer state and separated dimers into one aggregate, BTA-TPA achieved a high bright and deep-red/near-infrared (NIR) emission, with a photoluminescent quantum yield (QY) of 54.8% for the fluorescence peak at 690 nm. Owing to the bright deep-red/NIR fluorescence, BTA-TPA nanoparticles (NPs) were able to clearly image tumor cells in vitro and lymph nodes in vivo.

However, NIR-I (700–900 nm) fluorescent dyes are difficult to image tiny lymphatic vessels due to the high background fluorescence of living organism in NIR-I window [29]. Benefitting from the strong tissue penetration and low background fluorescence, NIR-II (1,000–1,700 nm) fluorescent dyes are well suited for imaging lymphatic vessels [64, 65]. Recently, Liu et al. reported NIR-II fluorescent dye with planar and twisted molecular structure for clear imaging of the lymphatic network [52]. By integrating the planar structure of the ACQ molecule and the twisted structure of the AIE molecule in one unit, pNIR-4 achieves the unification of a high absorption coefficient and a high fluorescence QY (Figure 13.5A). As shown in Figure 13.5B, owing to the bright fluorescent emission of pNIR-4 NPs in NIR-IIa region (1,300 – 1,400 nm), the lymph nodes and lymphatic vessels of mice were clearly imaged after subcutaneous injection of pNIR-4 NPs into the footpads of nude mice (Figure 13.5C). Moreover, guiding by the NIR-IIa fluorescence of pNIR-4 NPs, the lymph nodes were also successfully excised (Figure 13.5D).

13.2.5 Vascular imaging

Vascular imaging is an imaging of blood vessels, which performed after injecting a contrast agent into the blood vessels. The visualization of the vascular system is of great significance to the diagnosis and treatment of cardiovascular diseases [66, 67]. It can intuitively and accurately reflect the location and extent of vascular lesion, helping doctors find the disease in time and control the progress of the disease. For

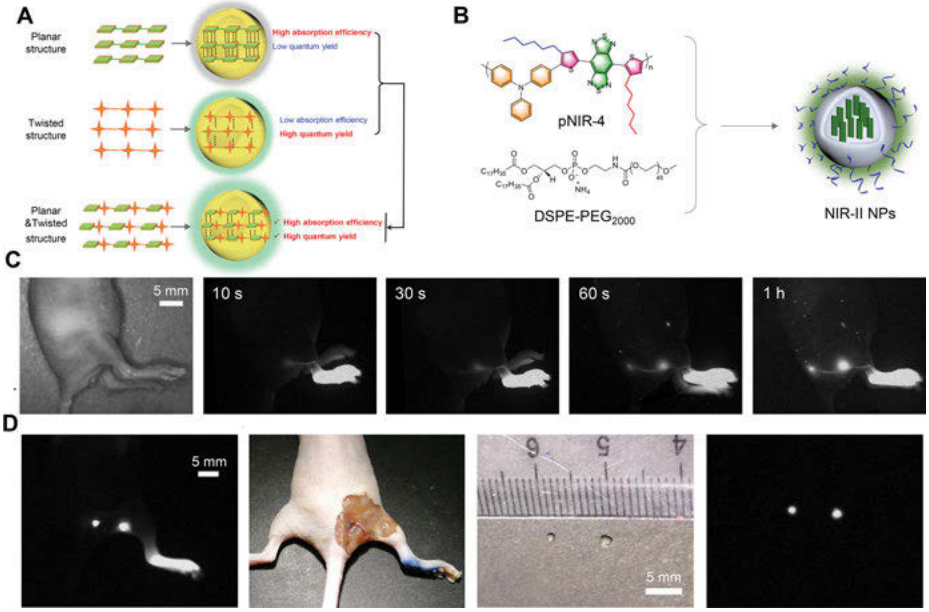

Figure 13.5: (A) Schematic illustration of the molecular design principle of highly bright SPNs. (B) The preparation of NIR-II NPs. (C) Bright field and fluorescence images of the lymphatic network of mice by subcutaneous injection of pNIR-4 NPs at different times. (D) NIR-IIa fluorescence guided surgery of lymph nodes after intradermally injection of pNIR4 NPs. Adapted with permission from ref. [52] Copyright 2020, American Chemical Society.

example, diagnosis of ischemic diseases, real-time monitoring of changes in the width of the carotid artery to evaluate the efficacy of antihypertensive drugs. At present, there are several traditional vascular imaging methods commonly used in clinical practice, such as Magnetic resonance imaging, X-ray computed tomography and ultrasound imaging. These imaging modes had a chronic lack of micron resolution. Fluorescence imaging has the advantages of high sensitivity and sharp spatial resolution, but it is limited by low tissue penetration depth. The NIR-II fluorescence imaging is a new imaging technology that has developed rapidly in recent years. It has the advantages of high penetration depth and high S/N ratio. Therefore, many efforts of NIR-II fluorophores for fluorescence imaging have already been made. Among them, AIE dots have been widely reported due to their excellent optical properties and good stability and biocompatibility.

The most common strategy for preparing water-soluble AIEgens with good biocompatibility is to coat hydrophobic AIE molecules in NPs composed of amphiphilic polymers. Although this method is simple and easy to implement, it is difficult to achieve uniformity of size and load rate. Therefore, it is still a challenge to develop a preparation strategy for AIEgens that can achieve uniform size and stable

loading rate. Based on this, Li et al. developed an amphiphilic AIEgens (TTB-PEG) composed of a hydrophobic core and a hydrophilic PEG chain, and realized its application in vascular imaging for large animal models [56]. Assisted by self-assembly, a nanoprobe called SA-TTB NPs that was stably dispersed in water could be obtained (Figure 13.6A). The probe not only had a maximum emission peak of more than 1,000 nm and a highly efficient optical fluorescence QYs of more than 10%, but also has uniform and stable physical properties of diameter. When the skin was stretched to the right, the researchers clearly observed that the position of the superficial blood vessels had changed, while the position of the external iliac veins in the deep tissues remained unchanged (Figure 13.6D). Then the researchers used conventional ultrasound imaging to measure and observe the depth of the external iliac vein (Figure 13.6E). In summary, the NIR-II fluorescence imaging results show that the in vivo resolution could reach ~38 μm and the penetration depth is ~1 cm (Figure 13.6B, C). Therefore, the efficient self-assembly strategy designed by the researchers could effectively construct high-performance AIE dots, which had guiding significance for the design and development of NIR-II self-assembled AIEgens and its application in vascular imaging.

There is a close evolutionary relationship between nonhuman primates and humans. In order to push AIE dots into clinical translational research, imaging of nonhuman primates is an essential step. Qian's group used high-brightness NIR-II fluorescent AIE dots to achieve large-depth cranial (thinned skull) cerebrovascular imaging on nonhuman primates for the first time, and accurately measured the blood flow velocity in the cerebrovascular system [55]. They first encapsulated the hydrophobic AIE molecules into hydrophilic AIE dots (Figure 13.7A), and then injected the AIE dots intravenously. With the bright emission and good biocompatibility of AIE dots, fluorescent dots floating in the blood can be captured under NIR-II fluorescence microscopy. Next, the researchers selected six blood vessels of the same depth, and recorded the displacement of the fluorescent spots every 40 ms (Figure 13.7B). The same blood vessel was recorded three times repeatedly, and finally the average flow velocity of the selected six blood vessels was calculated (Figure 13.7C). In addition, according to the flow direction, it is judged that these six blood vessels are all venous blood vessels because veins collect blood from the branches. More importantly, the AIE dots could be used to observe the blood vessels in the brains of nonhuman primates at a depth of 700 μm (Figure 13.7D), and the in vivo resolution could reach ~5.2 μm (Figure 13.7E). In summary, this study used the NIR-II fluorescent AIE dots to clearly observe the deep veins of the brain and measure the blood flow, which is of great significance for accelerating the clinical transformation process of the AIE dots in the second NIR region.

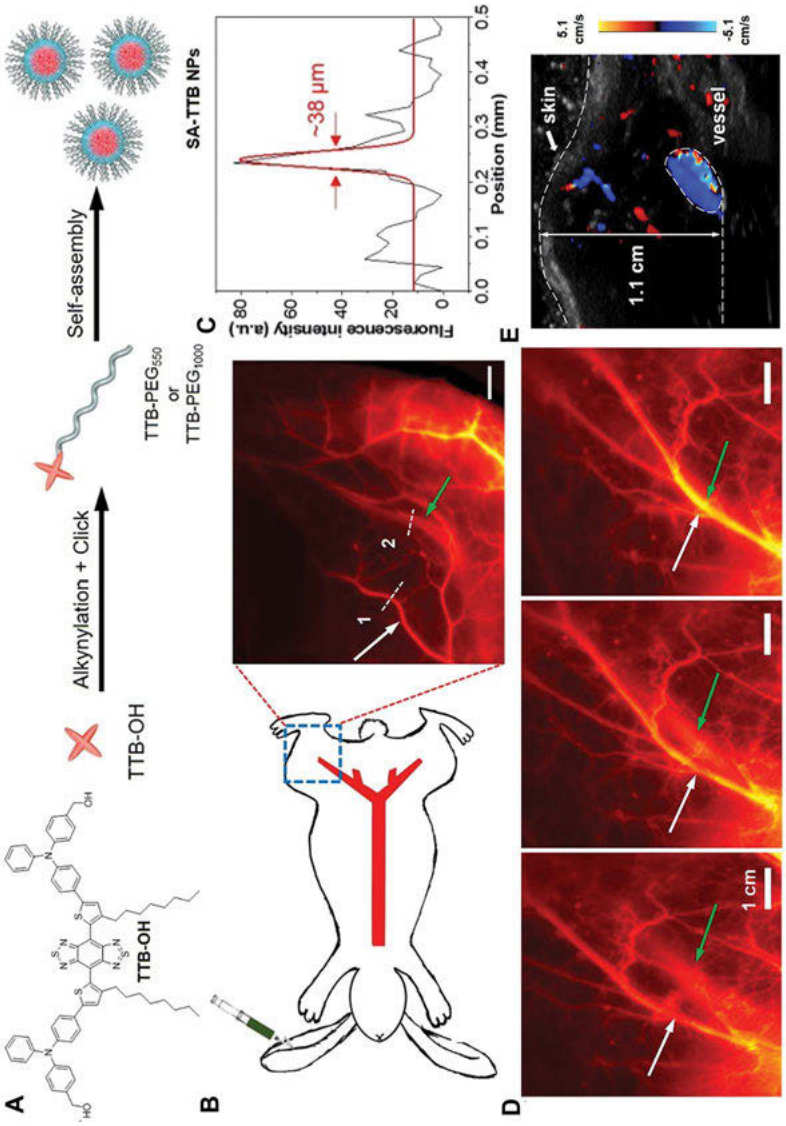

Figure 13.6: (A) The structural formulas of TTB-OH and the PEGylation of TTB-OH through click reaction, followed by self-assembly to obtain SA-TTB NPs. (B) Schematic illustration of NIR-II fluorescence imaging of rabbit hindlimb vasculature postintravenous injection of SA-TTB NPs. The white arrow and the green arrow point to the superficial vein and the external iliac vein, respectively. (C) Cross-sectional fluorescence intensity profile along the blood vessel corresponding to the dotted line. (D) Changes of relative position between the external iliac vein in deep tissue and superficial veins while stretching the skin. (E) The depth of the external iliac vein of rabbit hind limbs was measured by ultrasound imaging to be 1.1 cm. Adapted with permission from ref. [56]. Copyright 2021, Elsevier.

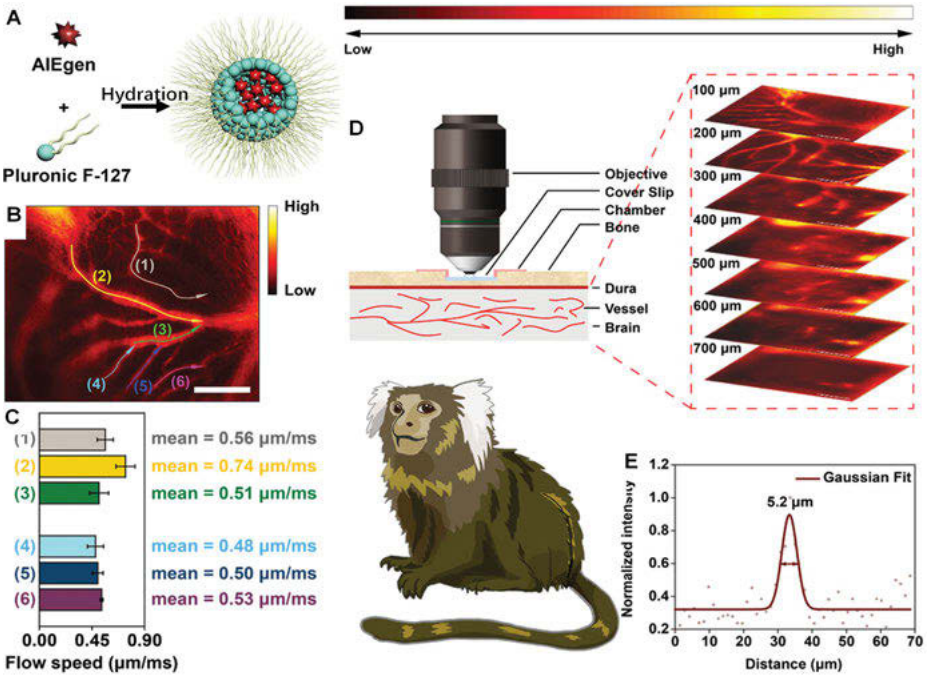

Figure 13.7: (A) The preparation of NIR-II AIEgen NPs from AIEgen and F-127. (B) NIR-II fluorescence imaging of six blood vessels of the detected blood flow velocity of the cerebrovascular system. (C) The mean blood flow rates in the vessel (1–6) in (B). (D) Schematic illustration of microscopy imaging and its results at different depths. (E) The cross-sectional NIR-II fluorescent intensity profile of the cerebral blood vessel. Adapted with permission from ref. [55]. Copyright 2021, Wiley-VCH.

13.3 Afterglow luminescent AIE dots for biomedical applications

Afterglow luminescence refers to a process that allows continuous luminescence after the excitation light source is removed, which substantially reduces the interference of autofluorescence from the organism because it can emit light independently of the external light source. Therefore, afterglow imaging has the advantages of higher sensitivity and S/N ratio compared to fluorescence imaging, which made afterglow imaging widely concerned in the field of biomedical imaging. Afterglow imaging consists of phosphorescence imaging and chemiluminescence imaging. While phosphorescence imaging relies on the return of electrons from the triplet state to the ground state to emit photons, chemiluminescence imaging relies on the energy generated by chemical reactions for chemical excitation to emit light. In the

following, we will introduce the biomedical applications of afterglow luminescent AIE dots by phosphorescence imaging and chemiluminescence imaging, respectively.

13.3.1 Phosphorescent imaging of tumors and lymph nodes

Unlike fluorescence emission, the electrons in the excited singlet state during phosphorescence emission further pass on to the excited triplet state through intersystem crossing and then return to the ground state. Due to the long duration of this process and the dissipation of much energy before radiative decay, the phosphorescence lifetime is generally long (>100 ms) and exhibits redshifted phosphorescence emission [68]. As a result, the phosphorescence often exhibits photophysical properties such as longer lifetime and greater Stokes shift compared to the material's own fluorescence. Organic room-temperature phosphorescence (RTP) materials have great potential for applications in the field of bioimaging, especially in vivo imaging, since their long phosphorescence lifetime can effectively bypass the autologous tissue fluorescence interference generated by real-time laser excitation to obtain high-quality images with high sensitivity and high S/N ratio. So far, the development of advanced organic RTP materials revolves around extending the lifetime of phosphorescent emission and increasing the QY of phosphorescence.

Recently, Gao et al. reported an organic RTP material with long lifetime and AIE characteristic for phosphorescence imaging of lymph nodes and orthotopic lung tumors [69]. By regulating the molecular aggregation states through simple alkyl group modifications, the luminescence performance of the compounds in 4-(9H-carbazol-9-yl) benzaldehyde (CBA) family was successfully improved, with CBA-CH_3 crystals reaching a lifetime of 868 ms and a phosphorescence QY of 6.22% (Figure 13.8A). The long phosphorescence lifetime and high phosphorescence QY of CBA-CH_3 crystals are very beneficial for imaging application (Figure 13.8B). In order to apply CBA-CH_3 in vivo, CBA-CH_3 was encapsulated inside the hydrophobic core of PEG-*b*-PPG-*b*-PEG (F127) to form water-soluble nanodots after co-crystallization and grinding (Figure 13.8C). The capacity of CBA-CH_3 nanodots to be applied to sentinel lymph node imaging was first evaluated (Figure 13.8D). Owing to the high phosphorescent brightness of CBA-CH_3 nanodots and the absence of autologous tissue fluorescence interference in phosphorescent imaging, a highly sensitive sentinel lymph node phosphorescent imaging with a high S/N ratio of 110 was achieved after 365 nm laser irradiation at 30 min postinjection of CBA-CH_3 nanodots. This S/N ratio is much higher than that of sentinel lymph node fluorescence imaging. Encouraged by the excellent performance of CBA-CH_3 nanodots in sentinel lymph node imaging, the application of CBA-CH_3 nanodots in orthotopic lung tumor detection was further evaluated. As shown in Figure 13.8E, at 6 h postinjection of CBA-CH_3 nanodots into pulmonary metastatic carcinoma-bearing mice, strong phosphorescence signals were detected in lung tumors, resulting in a high S/N ratio of 65 in lung tumor imaging.

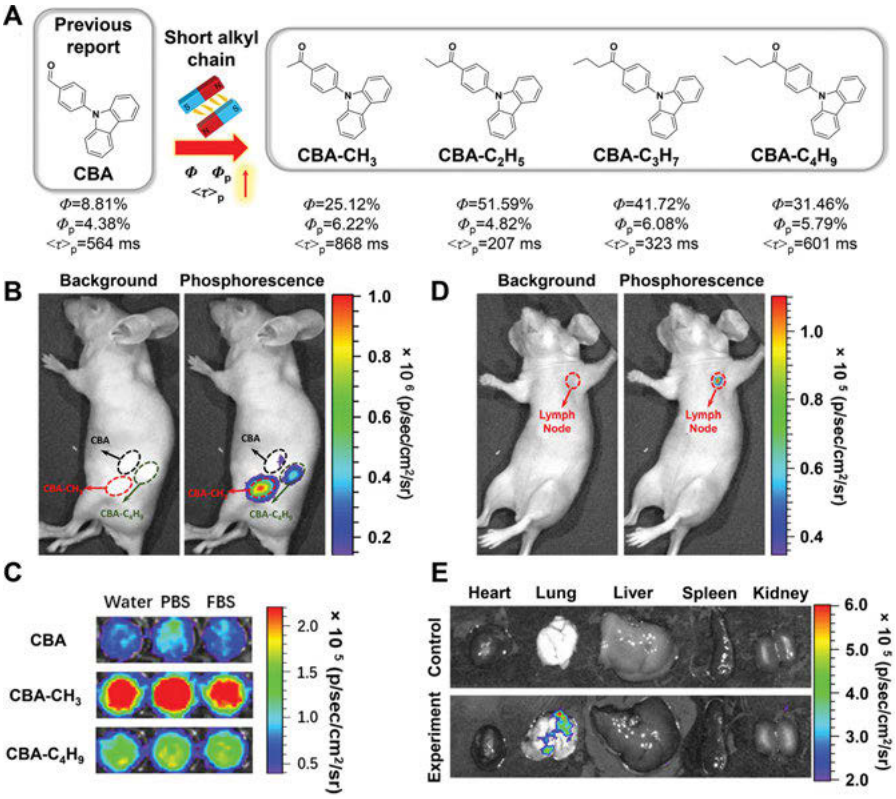

Figure 13.8: (A) Chemical structures and optical parameters of CBAs. (B) Phosphorescent images of mice before and after subcutaneous injection of CBA, CBA-CH_3, and CBA-C_4H_9 nanodots. (C) Phosphorescent images of CBA, CBA-CH_3, and CBA-C_4H_9 nanodots in different kinds of aqueous solution. (D) Phosphorescent images of the sentinel lymph node in mice before and after subcutaneous injection of CBA-CH_3 nanodots. (E) Phosphorescent images of major organs 6 h after the injection of saline solution or CBA-CH_3 nanodots into pulmonary metastatic carcinoma-bearing mice. Adapted with permission from ref. [69]. Copyright 2021, Wiley-VCH.

13.3.2 Chemiluminescence-guided cancer therapy

Although phosphorescence imaging has a high S/N ratio, its application in biomedical field is still limited due to its short afterglow time. Chemiluminescence has a longer luminescence time compared to phosphorescence. The basic principle of chemiluminescence is that certain organic compounds (such as reaction substrates, intermediates, and fluorophores) are activated by oxidation to form an oxidized high-energy intermediate state, which is in an unstable state and will decompose to produce energy or transfer its energy to nearby fluorophores, and then return to the ground state along with the radiation decay pathway. Thanks to its long

luminescence time, chemiluminescence has more applications in the biomedical field than phosphorescence.

PDT is a new type of cancer treatment. The photosensitizer in PDT is excited by external light and transfers energy to the surrounding oxygen to generate highly active singlet oxygen. Singlet oxygen can oxidize with the nearby biological macromolecules, produce cytotoxicity, and kill tumor cells. Similar to being excited by external light, photosensitizers can also produce singlet oxygen ($^1O_2$) when excited by chemical energy to kill tumor cells. Therefore, Liu's group synthesized a chemiluminescent NP (C-TBD) with AIE properties through a reasonable molecular structure design [41]. This NP is composed of four parts: AIE photosensitizer (TBD), chemiluminescent molecule (CPPO), F127 polymer, and soybean oil (Figure 13.9A). It can not only overcome the shortcomings of quenching caused by the aggregation of dyes in chemiluminescent NPs but also undergo chemical energy (H_2O_2) excitation that can effectively generate singlet oxygen and NIR fluorescence. C-TBD NPs can be enriched in tumor tissues through the EPR effect, and the level of H_2O_2 in the tumor microenvironment is higher, so that NPs can be specifically activated (Figure 13.9B). In order to verify these ideas, the researchers injected C-TBD NPs into the tail vein of mice with peritoneal tumors. The results show that the chemiluminescence imaging of C-TBD NPs breaks through the limitation of traditional fluorescence imaging tissue penetration depth, and accurately visualizes tiny tumors in the abdominal cavity through intravital imaging (Figure 13.9C). Next, the researchers also selected a clinical anti-tumor drug β-phenylethyl isothiocyanate (FEITC) for the treatment of tumors, which can increase the concentration of H_2O_2 in the tumor microenvironment without affecting the normal tissue function (Figure 13.9D). The combination of FEITC and C-TBD NPs can further increase the intensity of the signal of the tumor (Figure 13.9E, F). At the same time, after the combined treatment process, the researchers also observed a significant reduction in tumor volume (Figure 13.9G). In summary, these AIE-based chemiluminescent nanodots can provide a powerful and effective tool for accurate tumor positioning and antitumor treatment in the future, and it also provides novel ideas for the design of disease diagnostic materials.

13.3.3 Chemiluminescence-guided cancer surgery

Although a large number of NIR fluorescent probes, including Indocyanine Green (ICG) approved by the FDA, have been widely used to help surgeons remove tumors faster and more accurately, however, in the process of fluorescence-guided surgical navigation, the background signal is often high due to the interference of tissue fluorescence, which is not conducive to the surgeon's accurate distinction between tumor and normal tissue. Afterglow imaging has huge advantages, especially the low tissue background signal, which makes it a more ideal imaging method for guided tumor resection during surgery. However, most of the research on afterglow luminescent

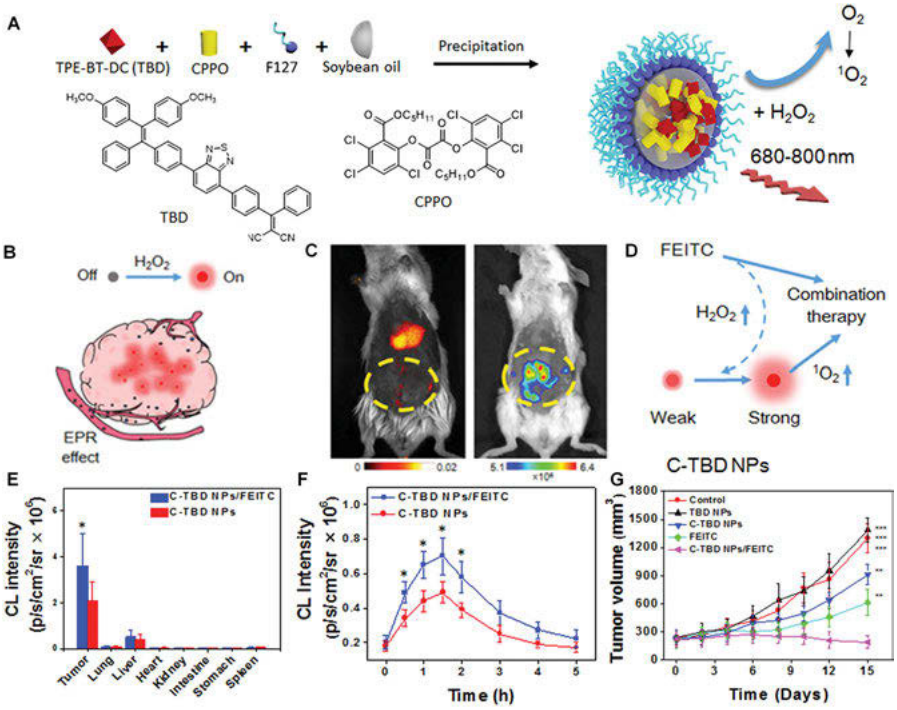

Figure 13.9: (A) The schematic diagram of C-TBD NPs. (B) Schematic diagram of imaging with C-TBD NPs activated by H_2O_2 at the tumor site. (C) After intravenous injection of C-TBD NPs, mice were subjected to in vivo fluorescence (left) and chemiluminescence (right) imaging of abdominal metastatic breast tumors. (D) Schematic illustration of a hypothetical mechanism of C-TBD NPs and FEITC combination therapy. (E) Chemiluminescence signal intensity of different tissues with or without FEITC treatment of mouse tumors. (F) Chemiluminescence signal intensity of mouse tumors treated with or without FEITC at different time points. (G) Changes in tumor volume over time in different therapy groups. Adapted with permission from ref. [41]. Copyright 2017, Elsevier.

materials has focused on inorganic materials. Therefore, there is an urgent need to develop pure organic afterglow luminescent materials with better biocompatibility and luminescence time comparable to or even surpassing inorganic materials.

To solve this problem, Ding's group first developed the NIR afterglow AIE dots with ultralong afterglow emission time, and used it for imaging-guided cancer surgery [45]. The researchers' specific approach is to give the chemiluminescence probe AIE characteristics so as to achieve NIR emission. It is worth mentioning that AIE fluorescent molecules can not only emit NIR light but also generate singlet oxygen. The chemical energy released by the decomposition of afterglow luminogen oxidized by singlet oxygen is transferred back to the AIE luminogen (Figure 13.10A). Multiple cycles of energy between afterglow luminogen and AIE luminogen can extend the light-emitting time to 10 days. Then, the researchers discovered that the

afterglow signal of afterglow AIE dots is quickly quenched in important normal tissues, which provides ultrahigh tumor-to-normal tissue signal ratio, which is more suitable for accurate image-guided cancer surgery (Figure 13.10B). Finally, the comparison of the surgical resection of abdominal tumors with and without imaging guidance proves that afterglow imaging can help doctors achieve precise tumor resection in mice (Figure 13.10C).

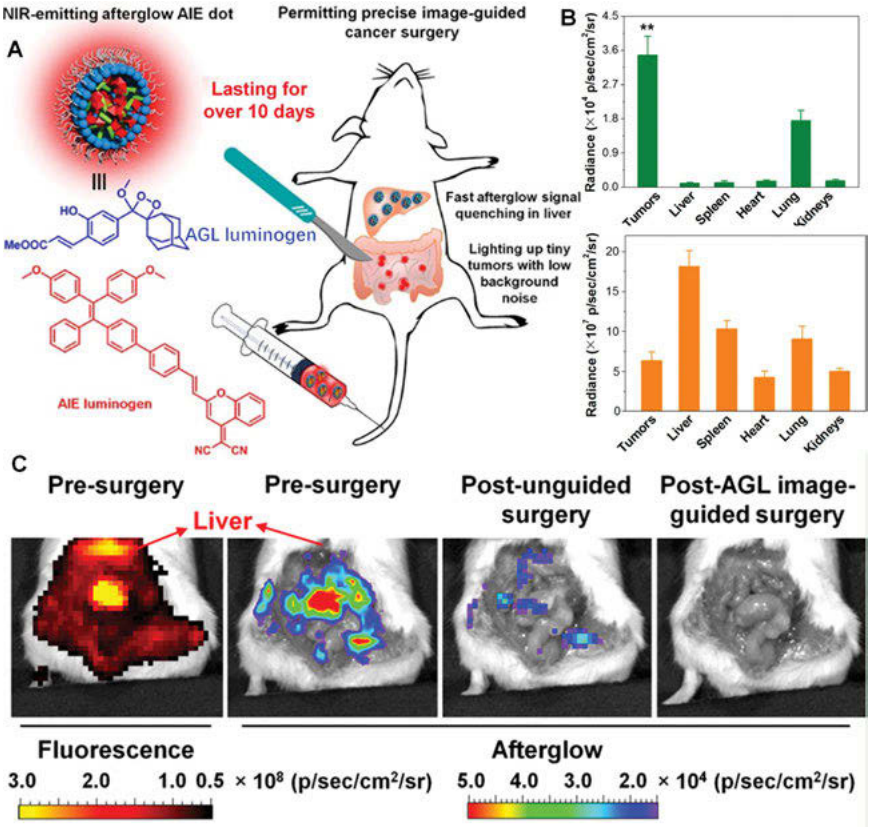

Figure 13.10: (A) Schematic illustration of the AGL AIE dots with ultrahigh signal ratio for promoted cancer surgery. (B) Afterglow and fluorescent signal intensity of different tissues. (C) NIR fluorescence and afterglow imaging of the abdominal cavity before tumor resection and afterglow images of the mice after unguided surgery and after the second surgery guided. Adapted with permission from ref. [45]. Copyright 2018, American Chemical Society.

13.4 Conclusions and perspectives

Owing to the strong luminescence of AIE materials under aggregation conditions and the high sensitivity of fluorescence/afterglow imaging, fluorescent and afterglow luminescent AIE dots give excellent performance in biomedical applications. Depending on the type of imaging, this chapter successively summarizes the recent advances in the biomedical applications of fluorescent and afterglow luminescent AIE dots, respectively. Specifically, among the biomedical applications of fluorescent luminescent AIE dots, their applications in fields such as drug-release monitoring, bacteria discrimination, fluorescent image-guided cancer surgery, lymph node imaging, and vascular imaging are highlighted. The afterglow AIE dots can be further subdivided into phosphorescent luminescent AIE dots and chemiluminescent AIE dots. For phosphorescent AIE dots, their properties and applications in imaging of tumors and lymph nodes are discussed in detail. While for chemiluminescent AIE dots, the focus is on their application in areas such as H_2O_2 detection, chemiluminescence-guided cancer therapy, and chemiluminescence-guided cancer surgery. Although great achievements have been made in the development of advanced fluorescent and afterglow luminescent AIE dots for biomedical applications, many challenges still exist. For instance, the tissue penetration capacity of currently developed fluorescent/afterglow materials is still limited, and there is an urgent need to develop fluorescent/afterglow materials with longer wavelength emission for deep tissue imaging. In addition, the short lifetime of organic RTP materials severely restricts their wider application in biomedical field, and new strategies are urgently required to prolong the phosphorescence lifetime of organic RTP materials. Moreover, there are few types of chemiluminescent AIE dots. More chemiluminescent AIE dots need to be developed to expand their application in biomedical field. In view of the increasing attention attracted by fluorescent and afterglow luminescent AIE dots, the abovementioned issues are expected to be overcome in the near future, and advanced fluorescent and afterglow luminescent AIE dots will have better performance and more applications in the biomedical field.

References

[1] Zhang S, Guo W, Wei J, Li C, Liang X-J, Yin M, Terrylenediimide-based intrinsic theranostic nanomedicines with high photothermal conversion efficiency for photoacoustic imaging-guided cancer therapy, ACS Nano, 2017, 11(4), 3797–3805.

[2] Zheng XC, Mao H, Huo D, Wu W, Liu BR, Jiang XQ, Successively activatable ultrasensitive probe for imaging tumour acidity and hypoxia, Nat Biomed Eng, 2017, 1(4), 0057.

[3] Cai Q, Fei Y, Hu L, Huang Z, Li L-L, Wang H, Chemotaxis-instructed intracellular Staphylococcus aureus infection detection by a targeting and self-assembly signal-enhanced photoacoustic probe, Nano Lett, 2018, 18(10), 6229–6236.

[4] Li J, Pu K, Development of organic semiconducting materials for deep-tissue optical imaging, phototherapy and photoactivation, Chem Soc Rev, 2019, 48(1), 38–71.
[5] Xiao H, Zhang W, Li P, Zhang W, Wang X, Tang B, Versatile Fluorescent Probes for Imaging the Superoxide Anion in Living Cells and, In Vivo Angew Chem Int Ed, 2020, 59(11), 4216–4230.
[6] Medintz IL, Uyeda HT, Goldman ER, Mattoussi H, Quantum dot bioconjugates for imaging, labelling and sensing, Nat Mater, 2005, 4(6), 435–446.
[7] Yuan L, Lin W, Zheng K, He L, Huang W, Far-red to near infrared analyte-responsive fluorescent probes based on organic fluorophore platforms for fluorescence imaging, Chem Soc Rev, 2013, 42(2), 622–661.
[8] Jiang K, Sun S, Zhang L, Lu Y, Wu A, Cai C, Lin H, Red G, and Blue Luminescence by Carbon Dots: Full-Color Emission Tuning and Multicolor Cellular Imaging, Angew Chem Int Edit, 2015, 54(18), 5360–5363.
[9] Wolfbeis OS, An overview of nanoparticles commonly used in fluorescent bioimaging, Chem Soc Rev, 2015, 44(14), 4743–4768.
[10] Fan Y, Zhang F, A new generation of NIR-II probes: lanthanide-based nanocrystals for bioimaging and biosensing, Adv Opt Mater, 2019, 7(7), 1801417.
[11] Gu K, Xu Y, Li H, Guo Z, Zhu S, Zhu S, Shi P, James TD, Tian H, Zhu W-H, Real-time tracking and in vivo visualization of β-galactosidase activity in colorectal tumor with a ratiometric near-infrared fluorescent probe, J Am Chem Soc, 2016, 138(16), 5334–5340.
[12] Liu J, Chen C, Ji S, Liu Q, Ding D, Zhao D, Liu B, Long wavelength excitable near-infrared fluorescent nanoparticles with aggregation-induced emission characteristics for image-guided tumor resection, Chem Sci, 2017, 8(4), 2782–2789.
[13] Xiaofeng F, Xuanze C, Rongqin L, Zhihe L, Haobin C, Zezhou S, Bo J, Yifei L, Xiao-An ZS, Dan D, Yujie S, Changfeng W, Multicolor photo-crosslinkable AIEgens toward compact nanodots for subcellular imaging and STED nanoscopy, Small, 2017, 13(41), 1702128.
[14] Gao H, Zhang X, Chen C, Li K, Ding D, Unity makes strength: how aggregation-induced emission luminogens advance the biomedical field, Adv Biosyst, 2018, 2(9): 1800074.
[15] Chen C, Ou H, Liu R, Ding D, Regulating the photophysical property of organic/polymer optical agents for promoted cancer phototheranostics, Adv Mater, 2020, 32(3), 1806331.
[16] Ding D, Li K, Liu B, Tang BZ, Bioprobes based on AIE fluorogens, Acc Chem Res, 2013, 46(11), 2441–2453.
[17] Luo J, Xie Z, Lam JWY, Cheng L, Chen H, Qiu C, Kwok HS, Zhan X, Liu Y, Zhu D, Tang BZ, Aggregation-induced emission of 1-methyl-1,2,3,4,5-pentaphenylsilole, Chem Commun, 2001, 18, 1740–1741.
[18] Hong Y, Lam JWY, Tang BZ, Aggregation-induced emission, Chem Soc Rev, 2011, 40(11), 5361–5388.
[19] Hu R, Leung NLC, Tang BZ, AIE macromolecules: Syntheses, structures and functionalities, Chem Soc Rev, 2014, 43(13), 4494–4562.
[20] Kwok RTK, Leung CWT, Lam JWY, Tang BZ, Biosensing by luminogens with aggregation-induced emission characteristics, Chem Soc Rev, 2015, 44(13), 4228–4238.
[21] Mei J, Leung NLC, Kwok RTK, Lam JWY, Tang BZ, Aggregation-Induced Emission: Together We Shine, United We Soar!, Chem Rev, 2015, 115(21), 11718–11940.
[22] Feng G, Zhang G-Q, Ding D, Design of superior phototheranostic agents guided by Jablonski diagrams, Chem Soc Rev, 2020, 49(22), 8179–8234.
[23] Ding D, Mao D, Li K, Wang X, Qin W, Liu R, Chiam DS, Tomczak N, Yang Z, Tang BZ, Kong D, Liu B, Precise and Long-Term Tracking of Adipose-Derived Stem Cells and Their Regenerative Capacity via Superb Bright and Stable Organic Nanodots, ACS Nano, 2014, 8(12), 12620–12631.

[24] Song Z, Mao D, Sung SHP, Kwok RTK, Lam JWY, Kong D, Ding D, Tang BZ, Activatable fluorescent nanoprobe with aggregation-induced emission characteristics for selective in vivo imaging of elevated peroxynitrite generation, Adv Mater, 2016, 28(33), 7249–7256.
[25] Li D, Qin W, Xu B, Qian J, Tang BZ, AIE nanoparticles with high stimulated emission depletion efficiency and photobleaching resistance for long-term super-resolution bioimaging, Adv Mater, 2017, 29(43), 1703643.
[26] Qi J, Chen C, Zhang X, Hu X, Ji S, Kwok RTK, Lam JWY, Ding D, Tang BZ, Light-driven transformable optical agent with adaptive functions for boosting cancer surgery outcomes, Nat Commun, 2018, 9(1), 1848.
[27] Kang M, Zhou C, Wu S, Yu B, Zhang Z, Song N, Lee MMS, Xu W, Xu F-J, Wang D, Wang L, Tang BZ, Evaluation of Structure–Function Relationships of Aggregation-Induced Emission Luminogens for Simultaneous Dual Applications of Specific Discrimination and Efficient Photodynamic Killing of Gram-Positive Bacteria, J Am Chem Soc, 2019, 141(42), 16781–16789.
[28] Liu S, Li Y, Zhang J, Zhang H, Wang Y, Chuah C, Tang Y, Lam JWY, Kwok RTK, Ou H, Ding D, Tang BZ, A two-in-one Janus NIR-II AIEgen with balanced absorption and emission for image-guided precision surgery, Mater. Today Bio, 2021, 10, 100087.
[29] Smith AM, Mancini MC, Nie SM, Bioimaging: Second window for in vivo imaging, Nat Nanotechnol, 2009, 4(11), 710–711.
[30] Jiang Y, Pu K, Multimodal biophotonics of semiconducting polymer nanoparticles, Acc Chem Res, 2018, 51(8), 1840–1849.
[31] Dodeigne C, Thunus L, Lejeune R, Chemiluminescence as a diagnostic tool. A review, Talanta, 2000, 51(3), 415–439.
[32] Hananya N, Eldar Boock A, Bauer CR, Satchi-Fainaro R, Shabat D, Remarkable enhancement of chemiluminescent signal by dioxetane-fluorophore conjugates: turn-on chemiluminescence probes with color modulation for sensing and imaging, J Am Chem Soc, 2016, 138(40), 13438–13446.
[33] Huang JG, Li JC, Lyu Y, Miao QQ, Pu K, Molecular optical imaging probes for early diagnosis of drug-induced acute kidney injury, Nat Mater, 2019, 18(10), 1133–1143.
[34] Wang Y, Gao H, Yang J, Fang M, Ding D, Tang BZ, Li Z, High Performance of Simple Organic Phosphorescence Host–Guest Materials and their Application in Time-Resolved Bioimaging, Adv Mater, 2021, 33(18), 2007811.
[35] Miao Q, Xie C, Zhen X, Lyu Y, Duan H, Liu X, Jokerst JV, Pu K, Molecular afterglow imaging with bright, biodegradable polymer nanoparticles, Nat Biotechnol, 2017, 35(11), 1102–1110.
[36] Huang J, Jiang Y, Li J, Huang J, Pu K, Molecular Chemiluminescent Probes with a Very Long Near-Infrared Emission Wavelength for in Vivo Imaging, Angew Chem Int Ed, 2021, 60(8), 3999–4003.
[37] Maldiney T, Lecointre A, Viana B, Bessiere A, Bessodes M, Gourier D, Richard C, Scherman D, Controlling electron trap depth to enhance optical properties of persistent luminescence nanoparticles for in vivo imaging, J Am Chem Soc, 2011, 133(30), 11810–11815.
[38] Maldiney T, Bessiere A, Seguin J, Teston E, Sharma SK, Viana B, Bos AJJ, Dorenbos P, Bessodes M, Gourier D, Scherman D, Richard C, The in vivo activation of persistent nanophosphors for optical imaging of vascularization, tumours and grafted cells, Nat Mater, 2014, 13(4), 418–426.
[39] Li Z, Zhang Y, Wu X, Huang L, Li D, Fan W, Han G, Direct Aqueous-Phase Synthesis of Sub-10 nm “Luminous Pearls” with Enhanced in Vivo Renewable Near-Infrared Persistent Luminescence, J Am Chem Soc, 2015, 137(16), 5304–5307.
[40] Lecuyer T, Teston E, Ramirez-Garcia G, Maldiney T, Viana B, Seguin J, Mignet N, Scherman D, Richard C, Chemically engineered persistent luminescence nanoprobes for bioimaging, Theranostics, 2016, 6(13), 2488–2524.

[41] Mao D, Wu WB, Ji SL, Chen C, Hu F, Kong DL, Ding D, Liu B, Chemiluminescence-guided cancer therapy using a chemiexcited photosensitizer, Chem-Us, 2017, 3(6), 991–1007.
[42] Xie C, Zhen X, Miao Q, Lyu Y, Pu K, Self-assembled semiconducting polymer nanoparticles for ultrasensitive near-infrared afterglow imaging of metastatic tumors, Adv Mater, 2018, 30(21), 1801331.
[43] Lu L, Li B, Ding S, Fan Y, Wang S, Sun C, Zhao M, Zhao C-X, Zhang F, NIR-II bioluminescence for in vivo high contrast imaging and in situ ATP-mediated metastases tracing, Nat Commun, 2020, 11(1), 4192.
[44] Zhang Y, Yan C, Wang C, Guo Z, Liu X, Zhu W-H, A sequential dual-lock strategy for photoactivatable chemiluminescent probes enabling bright duplex optical imaging, Angew Chem Int Ed, 2020, 59(23), 9059–9066.
[45] Ni X, Zhang X, Duan X, Zheng HL, Xue XS, Ding D, Near-infrared afterglow luminescent aggregation-induced emission dots with ultrahigh tumor-to-liver signal ratio for promoted image-guided cancer surgery, Nano Lett, 2018, 19(1): 318-330.
[46] Warrier S, Kharkar PS, Fluorescent probes for biomedical applications (2009-2014), Pharmaceut Patent Analyst, 2014, 3(5), 543–560.
[47] Peng H-S, Chiu DT, Soft fluorescent nanomaterials for biological and biomedical imaging, Chem Soc Rev, 2015, 44(14), 4699–4722.
[48] Zhang K, Gao Y-J, Yang -P-P, Qi G-B, Zhang J-P, Wang L, Wang H, Self-assembled fluorescent organic nanomaterials for biomedical imaging, Adv Healthcare Mater, 2018, 7(20), 1800344.
[49] Huang J, Pu K, Activatable molecular probes for second near-infrared fluorescence, chemiluminescence, and photoacoustic imaging, Angew Chem Int Ed, 2020, 59(29), 11717–11731.
[50] Yang M, Huang J, Fan J, Du J, Pu K, Peng X, Chemiluminescence for bioimaging and therapeutics: Recent advances and challenges, Chem Soc Rev, 2020, 49(19), 6800–6815.
[51] Gu X, Zhang X, Ma H, Jia S, Zhang P, Zhao Y, Liu Q, Wang J, Zheng X, Lam JWY, Ding D, Tang BZ, Corannulene-incorporated AIE nanodots with highly suppressed nonradiative decay for boosted cancer phototheranostics in vivo, Adv Mater, 2018, 30(26), 1801065.
[52] Liu S, Ou H, Li Y, Zhang H, Liu J, Lu X, Kwok RTK, Lam JWY, Ding D, Tang BZ, Planar and twisted molecular structure leads to the high brightness of semiconducting polymer nanoparticles for NIR-IIa fluorescence imaging, J Am Chem Soc, 2020, 142(35), 15146–15156.
[53] Luo Q, Li L, Ma H, Lv C, Jiang X, Gu X, An Z, Zou B, Zhang C, Zhang Y, Deep-red fluorescence from isolated dimers: A highly bright excimer and imaging in vivo, Chemical Science, 2020, 11(23), 6020–6025.
[54] Bao P, Li C, Ou H, Ji S, Chen Y, Gao J, Yue X, Shen J, Ding D, A peptide-based aggregation-induced emission bioprobe for selective detection and photodynamic killing of Gram-negative bacteria, Biomaterials Science, 2021, 9(2), 437–442.
[55] Feng Z, Bai S, Qi J, Sun C, Zhang Y, Yu X, Ni H, Wu D, Fan X, Xue D, Liu S, Chen M, Gong J, Wei P, He M, Lam JWY, Li X, Tang BZ, Gao L, Qian J, Biologically excretable aggregation-induced emission dots for visualizing through the marmosets intravitally: horizons in future clinical nanomedicine, Adv Mater, 2021, 33(17), 2008123.
[56] Li Y, Hu D, Sheng Z, Min T, Zha M, Ni J-S, Zheng H, Li K, Self-assembled AIEgen nanoparticles for multiscale NIR-II vascular imaging, Biomaterials, 2021, 264, 120365.
[57] Yi X, Hu -J-J, Dai J, Lou X, Zhao Z, Xia F, Tang BZ, Self-Guiding Polymeric Prodrug Micelles with Two Aggregation-Induced Emission Photosensitizers for Enhanced Chemo-Photodynamic Therapy, ACS Nano, 2021, 15(2), 3026–3037.
[58] Hu R, Zhou F, Zhou T, Shen J, Wang Z, Zhao Z, Qin A, Tang BZ, Specific discrimination of gram-positive bacteria and direct visualization of its infection towards mammalian cells by a DPAN-based AIEgen, Biomaterials, 2018, 187, 47–54.

[59] Golombek SK, May J-N, Theek B, Appold L, Drude N, Kiessling F, Lammers T, Tumor targeting via EPR: Strategies to enhance patient responses, Adv Drug Deliv Rev, 2018, 130, 17–38.
[60] Vargason AM, Anselmo AC, Mitragotri S, The evolution of commercial drug delivery technologies, Nat Biomed Eng, 2021, 5, 951–967.
[61] Cheng T, Ma R, Zhang Y, Ding Y, Liu J, Ou H, An Y, Liu J, Shi L, A surface-adaptive nanocarrier to prolong circulation time and enhance cellular uptake, Chem Commun (Camb), 2015, 51(81), 14985–14988.
[62] Gilbert JA, Blaser MJ, Caporaso JG, Jansson JK, Lynch SV, Knight R, Current understanding of the human microbiome, Nat Med, 2018, 24(4), 392–400.
[63] Tsubery H, Ofek I, Cohen S, Fridkin M, Structure–function studies of polymyxin B nonapeptide: implications to sensitization of gram-negative bacteria, J Med Chem, 2000, 43(16), 3085–3092.
[64] Li C, Zhang Y, Wang M, Zhang Y, Chen G, Li L, Wu D, Wang Q, In vivo real-time visualization of tissue blood flow and angiogenesis using Ag2S quantum dots in the NIR-II window, Biomaterials, 2014, 35(1), 393–400.
[65] Antaris AL, Chen H, Cheng K, Sun Y, Hong G, Qu C, Diao S, Deng Z, Hu X, Zhang B, Zhang X, Yaghi OK, Alamparambil ZR, Hong X, Cheng Z, Dai H, A small-molecule dye for NIR-II imaging, Nat Mater, 2016, 15(2), 235–242.
[66] Hong G, Lee JC, Robinson JT, Raaz U, Xie L, Huang NF, Cooke JP, Dai H, Multifunctional in vivo vascular imaging using near-infrared II fluorescence, Nat Med, 2012, 18(12), 1841–1846.
[67] Hong GS, Antaris AL, Dai HJ, Near-infrared fluorophores for biomedical imaging, Nat Biomed Eng, 2017, 1(1), 1–22.
[68] Itoh T, Fluorescence and phosphorescence from higher excited states of organic molecules, Chem Rev, 2012, 112(8), 4541–4568.
[69] Gao H, Gao Z, Jiao D, Zhang J, Li X, Tang Q, Shi Y, Ding D, Boosting room temperature phosphorescence performance by alkyl modification for intravital orthotopic lung tumor imaging, Small, 2021, 17(22), 2005449.

Nuernisha Alifu, Jun Qian

Chapter 14
High-order nonlinear optical in vivo microscopy based on AIEgens

14.1 Introduction

As a most widely used technique, fluorescence imaging plays a significant role in biomedical research and clinical applications [1–3]. Fluorescence imaging possesses advantages of high spatial resolution, nonradiative properties, rich information, and fast response [4, 5]. Fluorescence imaging is also a powerful tool for detection ability of the morphological details in biological species from living cells to animals [6, 7]. To achieve high-quality fluorescence imaging, it is important to label biological samples (organs, cells, or tissues) with the endogenous fluorescence (autofluorescence) or suitable exogenous fluorescence probes [8]. Although the endogenous fluorophores have been utilized widely, many biological samples and processes still cannot be imaged or probed due to a lack of endogenous fluorophores. Therefore, there is a great demand for well-designed organic exogenous contrast agents.

Organic nanoprobes such as organic dyes and organic-dye-doped nanoparticles (NPs) with excellent biocompatibility and simple synthesis processes are favorable for fluorescence bioimaging [9, 10]. However, a majority of conventional organic dyes usually suffer from an aggregation-caused quenching (ACQ) effect. During the ACQ process, the fluorescence of organic dyes would quench in aggregate state or

Acknowledgements: This work was supported by National Natural Science Foundation of China (61975172, 82001874, 82060326, and 61735016), Fundamental Research Funds for the Central Universities (2020-KYY-511108-0007), Zhejiang Provincial Natural Science Foundation of China (LR17F050001), Fundamental Research Funds for the Central Universities and State Key Laboratory of Pathogenesis, Prevention and Treatment of High Incidence Diseases in Central Asia Fund (No. SKL-HIDCA-2019-3), Natural Science Foundation of Xinjiang Uygur Autonomous Region (2020D01C151).

Nuernisha Alifu, State Key Laboratory of Modern Optical Instrumentations, Centre for Optical and Electromagnetic Research, College of Optical Science and Engineering, International Research Center for Advanced Photonics, Zhejiang University, Hangzhou 310058, China; State Key Laboratory of Pathogenesis, Prevention and Treatment of High Incidence Diseases in Central Asia, School of Medical Engineering and Technology, Xinjiang Medical University, Urumqi 830054, China

Jun Qian, State Key Laboratory of Modern Optical Instrumentations, Centre for Optical and Electromagnetic Research, College of Optical Science and Engineering, International Research Center for Advanced Photonics, Zhejiang University, Hangzhou 310058, China, e-mail: qianjun@zju.edu.cn

https://doi.org/10.1515/9783110673074-015

at high concentration due to π–π stacking [11, 12]. In 2001, Tang's group firstly proposed the concept of aggregation-induced emission (AIE) effect, that is, 1-methyl -1,2,3,4,5-pentaphenylsilole molecules were nonemissive when dissolved in benign solvent but highly luminescent in the aggregation states [13, 14]. With the development of nanotechnology, more and more AIEluminogens (AIEgens) such as tetraphenylethene (TPE), tetraphenylsilole, and distyrylanthracene derivatives have been developed [15–17]. The fluorescence of these AIEgens covers from blue to red to near-infrared (NIR) spectral region [18]. The AIEgens become a prominent candidate with excellent fluorescence emission under restriction of intramolecular motions (RIM) condition [19, 20]. Especially, the AIEgen-doped NPs embody high-fluorescence brightness and photostability, which is essential for high-quality fluorescence bioimaging [21, 22]. Nevertheless, most of the AIEgens are always excited by one- and two-photon absorption with limited imaging quality [23, 24]. High-order nonlinear optical effects such as three-photon fluorescence (3PF) and third-harmonic generation (THG), which occurs within a spatially confined volume at the focal plane, compared with the traditional one- and two-photon fluorescence, can achieve higher resolution and deeper tissue penetration [25–27].

Under 3PF and THG excitation, a single AIEgen absorbs three photons simultaneously and emits one-photon. In 3PF process, the AIE molecules transfer to a real excited state, while in THG process the molecules transfer to the virtual state. 3PF is conducted under a short-pulse femtosecond (fs) near-infrared II (NIR-II, 900–1700 nm) excitation laser with reduced photon scattering, deeper tissue penetration, and attenuated autofluorescence [28, 29]. In contrast, fs laser of any wavelength can excite THG signals, and the emission wavelength is 1/3 of the excitation wavelength [30, 31]. Besides, 3PF is a third-order nonlinear optical process, and THG is a fifth-order nonlinear optical process [32, 33]. Despite these differences, the fluorescence intensity of both 3PF and THG is proportional to the cube of the excitation power density [34, 35]. Hence, 3PF and THG exhibit high signal-to-background ratio (SBR), good optical sectioning capability without a confocal pinhole, and low auto-fluorescence [36, 37]. Moreover, less tissue damage would happen in the out-of-focus region. Compared with other imaging modalities, such as optical Doppler and laser speckle imaging, NIR-II fs laser excitation of high-order nonlinear fluorescence (HONF) microscopic imaging could provide more clear vision of the target area [38, 39].

In view of the great progress in this field, it is necessary to summarize the latest research results of AIEgens in HONF microscopic bioimaging. Herein, in vivo applications of AIEgens based on the HONF microscopic bioimaging were introduced briefly. Significant progress achieved by our and other groups in the past few years is summarized. Based on the previous research foundations and conclusions, some challenges and opportunities for the applications of AIEgens in biomedical diagnosis and treatment are proposed.

14.2 AIEgens for in vivo THG fluorescence imaging

Zheng et al. designed a type of nanocrystal by attaching electron-donating diphenylamine and electron-withdrawing dicyanomethylenebenzopyran unit at the 2,7-positions of the electron-rich carbazole ring [40]. As shown in Figure 14.1a, the density functional theory (DFT) calculation of DCCN nanocrystal was performed. The electron clouds of the highest occupied molecular orbital (HOMO) were mainly located on the diphenylamino and carbazole units, whereas the orbitals of lowest unoccupied molecular orbital (LUMO) were primarily localized on the acceptor moiety with the band gap of 2.38 eV (Figure 14.1b). This DFT result illustrated an intramolecular charge transfer (ICT) characteristic of DCCN. Then the AIE and optical property of DCCN were characterized. The absorption peak of DCCN in acetone was

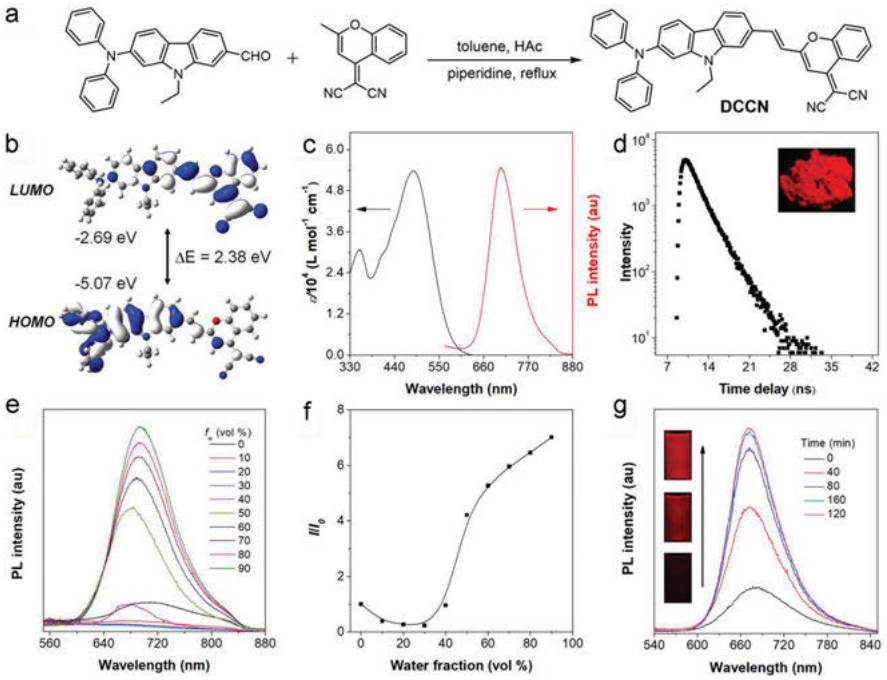

Figure 14.1: (a) Chemical structure and (b) HOMO and LUMO of DCCN (c) Absorption spectrum of DCCN in acetone (black) and photoluminescence (PL) spectrum of DCCN in the solid state (red). (d) Fluorescence decay curve of DCCN in the solid state. Inset: fluorescence photograph of powder of DCCN taken under UV irradiation. (e) PL spectra of DCCN in acetone/water mixtures with different water fractions: [DCCN] = 10×10^{-6} M. (f) Plot of relative PL intensity (I/I_0) versus the composition of the acetone/water mixtures of DCCN. (g) Time-resolved PL spectra of DCCN in acetone/water mixture (10×10^{-6} M) with 50% water fraction. Inset: fluorescence photographs of the suspensions taken under UV irradiation. Excitation wavelength: 480 nm. Adapted with permission from [40]. Copyright (2019) John Wiley & Sons Group.

487 nm. In addition, the polarity of the solvent on the absorption and PL (photoluminescence) intensity of DCCN was studied. DCCN exhibited a bright NIR emission centered at 704 nm in the solid state with fluorescence quantum yield of 12% (Figure 14.1c) and lifetime of 2.44 ns (Figure 14.1d). The AIE characteristic of DCCN was further evaluated in acetone/water mixtures with different water fractions (f_w) as shown in Figure 14.1e and 14.1f. DCCN exhibited a weak PL in pure acetone solution, and the PL intensity would decrease with increasing f_w from 0% to 30% for the enhancement of twisted ICT (TICT) effect. When f_w increased from 40% to 90%, the PL intensity strengthened again and even 7-fold higher than that in pure acetone. As $f_w = 90\%$, the absorption/PL was getting its maximum ($\lambda_{abs} = 509$ nm and $\lambda_{PL} = 694$ nm). This result suggested the apparent AIE characteristic of DCCN. The formation of the nanoaggregates leads to the enhancement of PL. However, the PL of a freshly prepared DCCN suspension at $f_w = 50\%$ changed as time in room temperature, as shown in Figure 14.1g. The PL intensity and peak changed with time, and up to 2 h, the PL would enhance a 4.5-fold and PL peak would have blueshifted from 681 to 671 nm. These results were consistent with the characteristics of crystallization-induced emission (CIE) behavior of AIE molecules [41].

Zheng et al. then evaluated the morphology of DCCN in 50% aqueous solution at different time points by the scanning electron microscopic (SEM) image as shown in Figure 14.2a-j. At first in 50% aqueous solution, the spherical morphology began to be transformed into fibers in 2 min. As time went by, the morphology of nanoaggregates was transformed from fibers to thin microrods and eventually formed microblock morphology after 5 h. The result was the same when increasing the f_w of the suspension. The crystalline characteristics of the nanocrystals were further verified by X-ray diffraction (Figure 14.2k). Then Zheng et al. studied the molecular conformation and molecular packing of DCCN in the crystalline state. They obtained the single crystal of DCCN via evaporating its ethanol/CH_2Cl_2 mixture which is suitable for X-ray crystallography with planar and conjugated structure of good π-electron delocalization (Figure 14.2l-n). Thus, strong push–pull character and extended π-conjugation of the fluorophore endow it NIR emission. Further, each dimeric molecule experienced the two same intermolecular π–π interactions (3.39 Å) between the carbazole and the 2-(4H-chromen-4-ylidene) malononitrile units with two adjacent molecules, which means that the distances of the intermolecular π–π interactions were shorter than the typical values (3.5 Å).

To improve the colloidal stability and biocompatibility of DCCN nanocrystals in physiological conditions, Zheng et al. encapsulated the nanocrystals ($f_w = 80\%$ aqueous solution) with F127 (Pluronic F127) matrix, to form crystalline dots (CDs) with the size of 143 nm as shown in Figure 14.2o [41]. The morphology and crystalline feature of CDs were well characterized by SEM and the selected area electron diffraction pattern (SAED). For better comparison, amorphous dots (ADs) were also prepared by encapsulating DCCN in F127 matrix via a nanoprecipitation. As illustrated in

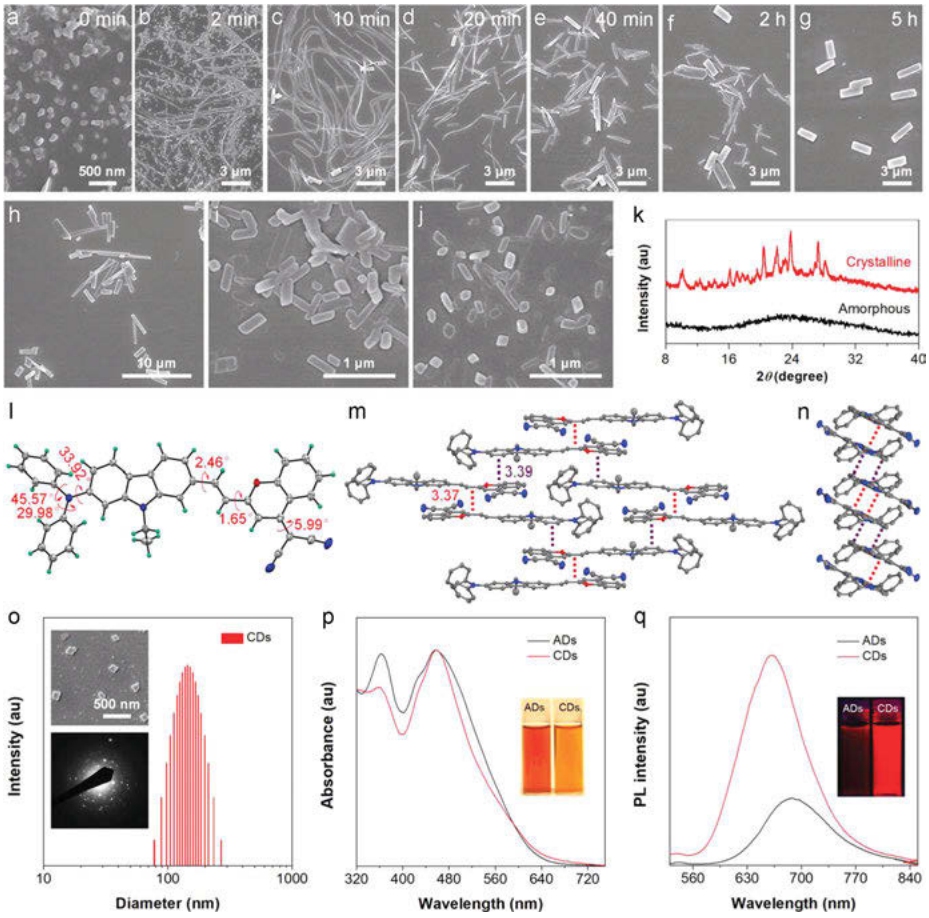

Figure 14.2: (a–g) SEM images of DCCN in an acetone/water mixture with water fraction (f_w) of 50% taken at different storage times: (a) 0 min, (b) 2 min, (c) 10 min, (d) 20 min, (e) 40 min, (f) 2 h, and (g) 5 h. (h–j) SEM images of DCCN NPs formed in acetone/water mixtures with water fractions of (h) 60%, (i) 70%, and (j) 80%. (k) XRD patterns of DCCN nanoaggregates before and after crystallization in an acetone/water mixture with f_w = 80%. (l–n) Single crystal structure of DCCN (l) and molecular π–π stacking structures along the long molecule axis (m) and the short molecule axis (n). (o) Hydrodynamic mean particle size distribution of crystalline dots (CDs) by dynamic light scattering along with their SEM image and SAED pattern. (p) Absorption and (q) PL spectra of DCCN in amorphous dots (ADs) and CDs in water. Excitation wavelength: 480 nm. The insets of (p) and (q) showed the fluorescence photographs of the suspensions taken under daylight and UV irradiation, respectively. Adapted with permission from [40]. Copyright (2019) John Wiley & Sons Group.

Figure 14.2p, the absorption spectrum of CDs displayed slight difference from that of ADs, both showing an absorption maximum at ≈ 458 nm. Significantly, the PL of CDs was stronger than that of ADs by more than 320% accompanied with a blueshift in the emission maximum by 28 nm. These results demonstrated the boosted emission

property of CDs over ADs taking advantage of their regular and close molecular packing.

The THG and 3PF scanning microscopic system is shown in Figure 14.3. A commercial 1560-nm fs laser (FLCPA-01 C, Calmar Laser, 1 MHz, 400 fs) was utilized as excitation source (average power: 90 mW) and induced into an upright scanning microscope (BX61 + FV1200, Olympus). Then the excitation beam passed through a series of optical elements, such as a mirror, two computer-driven galvanometers, scan lens, tube lens, a dichroic mirror (980 nm short pass), and then focused onto the sample by a scan lens (LSM03, 5 ×, 0.26 NA, WD = 25.1 mm, focus size = 9.2 μm, Thorlabs, large-field imaging: imaging size = 2.5 mm × 2.5 mm) or a 25 × objective (XLPLN25XWMP2, 1.05 NA, WD = 2 mm, focus size = 2.6 μm, Olympus). The THG and 3PF signals excited by the 1550 nm fs laser were epicollected via the same objective, then pass through the abovementioned dichroic mirror and filter (THG signals for 495–540 nm band pass filter and 3PF signals for 570 nm long pass filter), and finally, that emission signals are collected by a photomultiplier tube (PMT) for computer processing.

The strong push–pull dipolar character and the extended π-conjugation endowed CDs nonlinear optical property of 2PF, 3PF, and THG (Figure 14.4a) [42]. The 2PF, 3PF, and THG of the CDs were analyzed on a lab-built nonlinear optical measurement system. The 2PF occurred when the two photons of 1,040 nm were simultaneously absorbed by the CDs molecule and pumped to the excited state with the relation of a photon (Figure 14.4a). Under 1,040 nm fs laser excitation, the fluorescence intensity of CDs has a good linear relationship with the square of incident power density, and the 2PF spectrum of CDs was recorded in Figure 14.4b [43]. Furthermore, below 1,550 nm fs laser excitation, the 3PF and THG signals of CDs were also recorded. As shown in Figure 14.4c, the 3PF of CDs was centered at 680 nm and THG at 517 nm. Different from the 2PF process, during the 3PF process the CDs molecule simultaneously absorbed three photons and transferred to the excited state, with the same radiative decay pathway of 1PF and 2PF processes, which suggested the similar PL spectra of 1PF, 2PF, and 3PF. The power dependence relationship of CDs under a 1,550 nm fs laser excitation was also studied, and the 3PF intensity of CDs exhibited linear proportion to the cubic of the excitation intensity, demonstrating that 3PF was the main nonlinear optical process [44]. Followed by a 3PF signal, strong THG signal peaked at ≈ 520 nm under the same excitation of a 1,560 nm fs laser occurred. Cubic of the excitation power density had linear relationship with THG signals, which demonstrated third-order optical nonlinearity of THG [45]. 2PF, 3PF, and THG of the capillaries containing ADs and CDs were further imaged under the aforementioned imaging system (Figure 14.3) with 1,040 nm (for 2PF) and 1,560 nm (for 3PF and THG) fs laser excitation. As shown in Figure 14.4d, the DCCN solution exhibited very weak 2PF and 3PF signals. CDs showed enhanced 2PF, 3PF, and THG signals than ADs due to the stronger RIM effect in CDs.

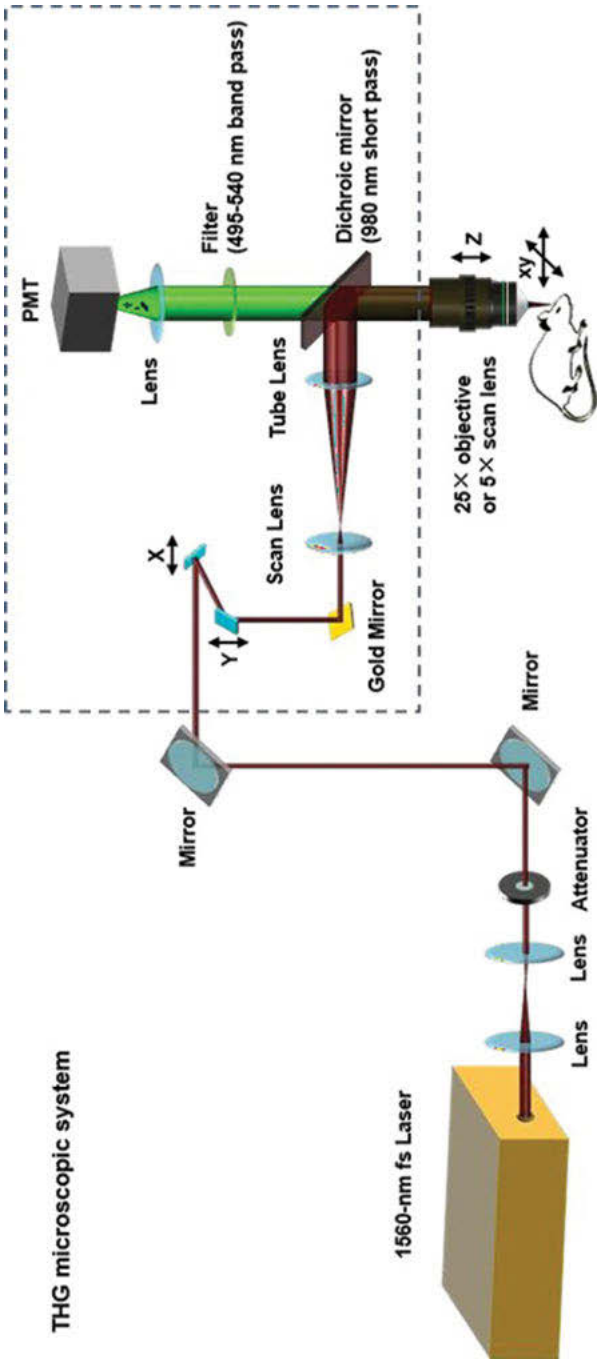

Figure 14.3: Schematic of the THG and 3PF scanning microscopy. Adapted with permission from [40]. Copyright (2019) John Wiley & Sons Group.

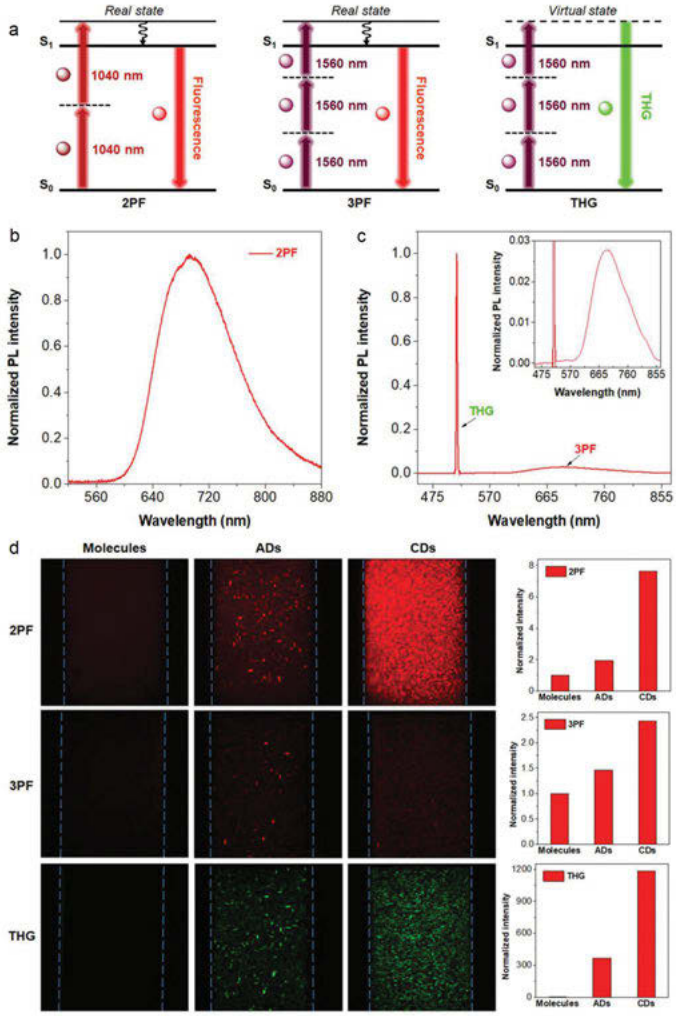

Figure 14.4: (a) Schematic illustration of 2PF, 3PF, and THG processes. (b) 2PF spectrum of CDs in water. (c) 3PF and THG spectra of CDs in water. Inset was the intensified spectrum at a wavelength range of 450–870 nm. (d) 2PF, 3PF, and THG images of acetone solution, ADs, and CDs in capillary glass tube. Adapted with permission from [40]. Copyright (2019) John Wiley & Sons Group.

Then, Zheng et al. used CDs for in vivo cerebral multiphoton microscopic fluorescence imaging of mouse brain. About 250 μm of imaging depth was obtained under the 3PF microscopic fluorescence imaging for the weakness of 3PF signals from CDs. Then they conducted THG and 2PF microscopic fluorescence imaging, as shown in Figure 14.5. Same area (500 μm × 500 μm) at the same imaging depth (200 μm) of mouse brain was observed postinjection of CDs under the same imaging

condition. There was no apparent difference between the fluorescence signal and background, with increasing imaging depth. However, in the deep-tissue region, the axial resolution of THG images was much better than 2PF images.

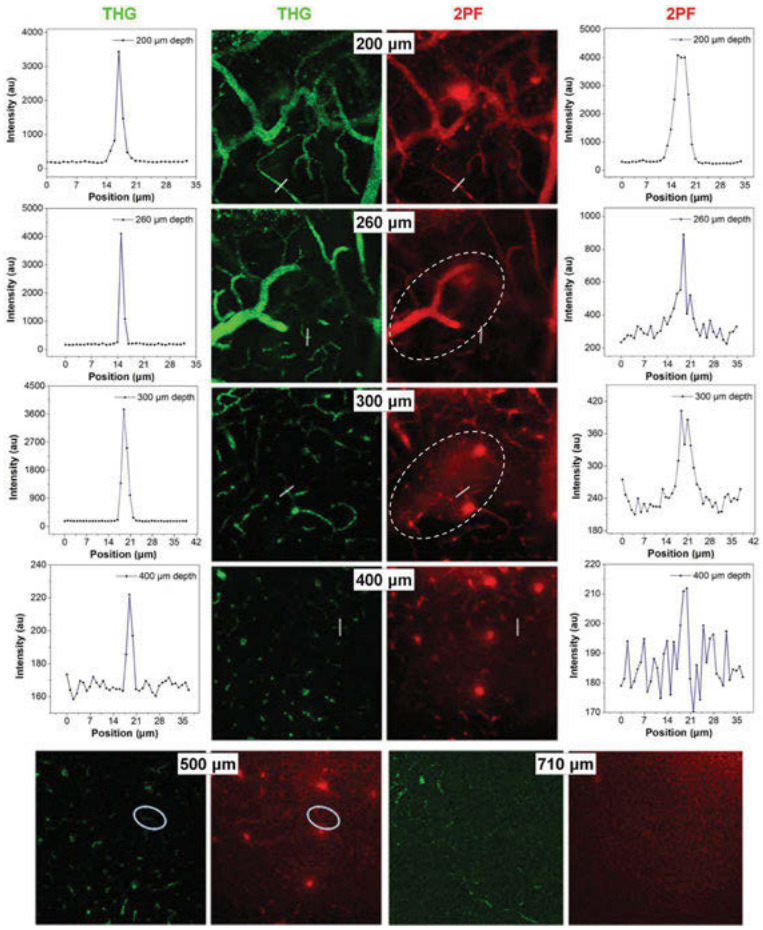

Figure 14.5: In vivo THG microscopic images of CDs-stained cortical vasculature at different depths as indicated. Full width at half-maximum (FWHM) of a blood vessel at depths of 400 μm and 800 μm as indicated with the white line in images. 3D reconstruction of the vasculature from top to 800 μm depth. The scale bars indicate 100 and 150 μm, respectively. The average power of the 1,560 nm fs excitation laser before objective was 90 mW. Adapted with permission from [40]. Copyright (2019) John Wiley & Sons Group.

Furthermore, Zheng et al. selected an area with abundant small blood vessels for in vivo THG microscopic imaging postinjection of CDs (Figure 14.6a–j). As shown in Figure 14.6a–g, clear blood vessels could be detected with high spatial resolution even at deep focal planes. The full width at half-maximum (FWHM) results illustrated the

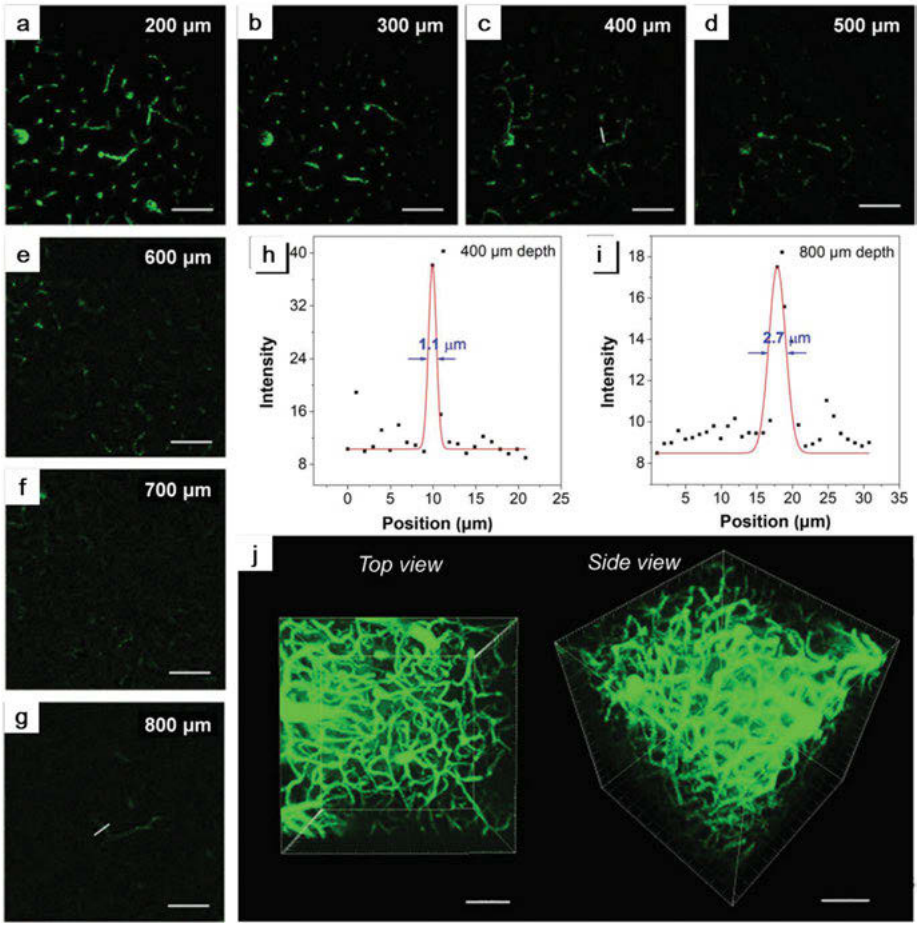

Figure 14.6: (a–g) In vivo THG microscopic imaging of CD-stained cortical vasculature at different depths as indicated. (h, i) FWHM of a blood vessel at depths of 400 μm (h) and 800 μm (i) as indicated with the white line in (c) and (g) images. (j) 3D of the vasculature from top to 800 μm depth. The scale bars in (a–g) and (j) indicate 100 and 150 μm, respectively. The average power of the 1,560 nm fs excitation laser before objective was 90 mW. Adapted with permission from [40]. Copyright (2019) John Wiley & Sons Group.

better imaging quality (Figure 14.6h and 14.6i). Although, 2PF and THG were both the third-order nonlinear optical processes, the intensity of THG is proportional to the cube of the excitation light intensity, and intensity of 2PF is proportional to the square of the excitation light intensity. Therefore, the intensity of THG decays faster with an increase in the defocusing distance. Thus, the THG microscopy could reach the imaging depth of 800 μm (Figure 14.6g) with FWHM ≈ 2.7 μm (Figure 14.6i) for small blood vessels. This result was one of the largest penetration depths and best spatial resolutions of

in vivo THG imaging. Superiority of the high-order nonlinear optical effects for high-quality fluorescence bioimaging was further illustrated.

In another work, DCCN nanocrystals were further utilized for in vivo brain vascular THG microscopic imaging through visible-NIR-II compatible skull optical clearing agents (VNSOCA)-induced transparent skull window by Li et al. [46]. The current USOCA consisted of two aqueous solutions which were solution 1 (S1) and solution 2 (S2) [47]. The optical clearing skull window is established by the treatment of S1 and S2, respectively.

Next, water absorption had been measured with peak at 1,490 nm in which only less than 10% of light can transmit, as shown in Figure 14.7. Under 1,560 nm excitation, the transmittance of water was less than 40%. Therefore, both S1 and S2 of USOCA suffer from strong absorption at NIR-II region, which was not good for further imaging. By comparison, deuterium oxide (D_2O) exhibited high transparency from visible to NIR-II spectral region (Figure 14.7a). Thus, D_2O was utilized to evaluate optical clearing efficiency. As shown in Figure 14.7b and c, the transmittance of S2 under 1550 nm laser excitation was more than 70%, which was larger than that of S1. Further, THG imaging was conducted by the THG microscopic imaging system (Figure 14.3) with imaging medium of S1 and S2. As shown in Figure 14.7d and e, due to higher transmittance of VNSOCA under 1560-nm excitation light, the THG signals show 5.2 and 3.6 times increase in the case of S1 and S2, respectively.

Li et al. firstly utilized a 5× scan (NA = 0.26) lens to obtain large-field THG vasculature images. As shown in Figure 14.8, without clearance treatment, only a few brain blood vessels could be observed with weak signals for the scattering of turbid skull. After treatment of VNSOCA, rich blood vessels could be detected clearly with high contrast. Further, a 25× objective was utilized to replace the 5× objective for its higher NA (1.05 vs 0.26) and smaller focus size (2.3 μm vs 9.2 μm at 1,560 nm) which could observe the invisible small vasculature. Thus, the combination of THG microscopy and VNSOCA extremely enhances the image quality and sensitivity.

Then, deep-tissue THG imaging was conducted. As shown in Figure 14.9, at the shallow imaging depth (at 50 μm), there was no obvious difference before and after skull optical clearing procedure (Figure 14.9a,e, and i). However, when the imaging depth increased (Figure 14.9b–h and 14.9j–l), the THG signal intensity became stronger in the skull optical clearing window. Finally, when the imaging depth was up to 200 μm, the blood vessels could be hardly recognized through the turbid skull, while angiography could be easily observed through the skull optical clearing window. The brain vessels could still be distinguished at the imaging depth of 650 μm (Figure 14.9m) and 3D reconstruction of deep-tissue vasculature could be achieved vividly with high spatial resolution (Figure 14.9n–p).

Then, Li et al. chose a small vessel and irradiated it by 1,560-nm fs laser for 10 s, after which the DCCN nanocrystals quickly diffused into the surrounding tissue, as shown in Figure 14.10a. Further, they selected a larger blood vessel and scanned

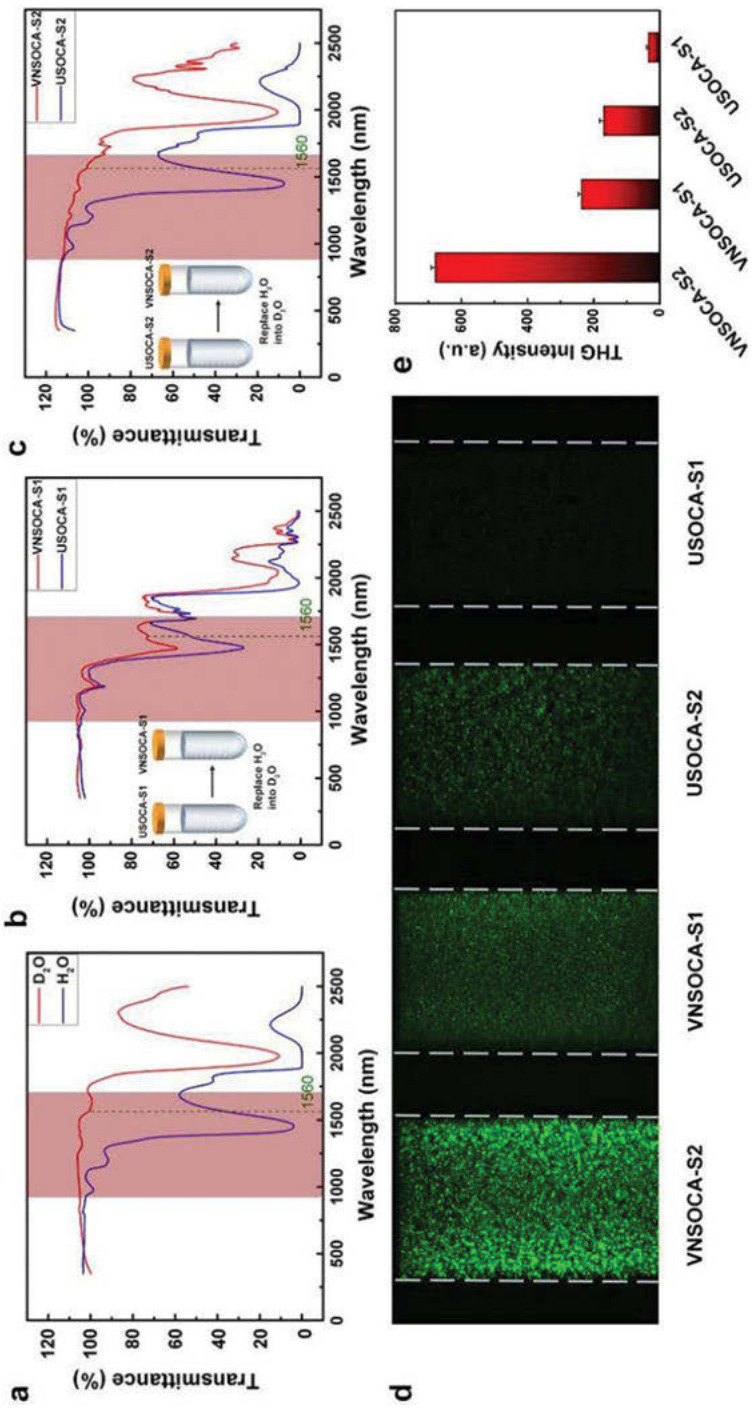

Figure 14.7: (a) Transmission spectra of D_2O (red line) and H_2O (blue line). (b) Transmission spectra of S1 of VNSOCA (red line) and USOCA (blue line). (c) Transmission spectra of S2 of VNSOCA (red line) and USOCA (blue line). (d) THG images of glass capillaries filled with DCCN nanocrystal dispersion with 25× objective immersed in S1 and S2 of VNSOCA and USOCA, respectively. The dashed lines represent the edges of the capillaries. (e) The THG intensities of DCCN nanocrystal dispersion filled in capillaries with the objective immersed in S1 and S2 of VNSOCA and USOCA, respectively. Adapted with permission from [47]. Copyright (2020) John Wiley & Sons Group.

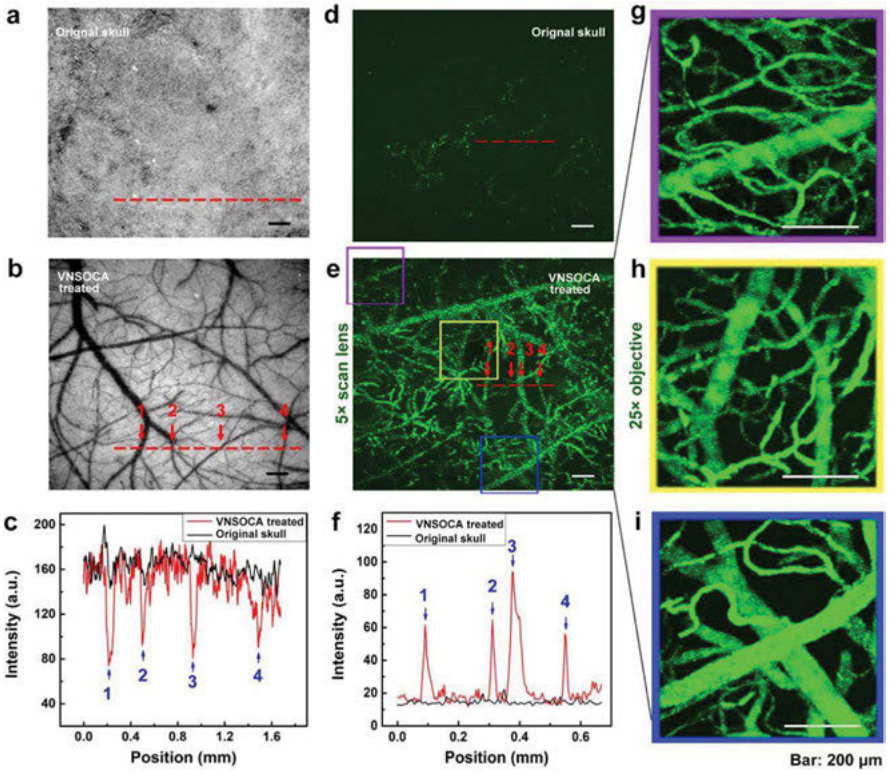

Figure 14.8: (a, b) Typical white-field images of cortical blood vessels before and after VNSOCA treatment. (c) Intensity profiles along the red dashed lines across the vasculature in (a) black and (b) red. The arrows indicate vessels that could not be observed before VSOCA treatment. (d, e) Typical large-field THG images collected with a 5× scan lens before and after skull clearing. (f) Intensity profiles along the red dashed lines across the vasculature in (d) black and (e) red. The arrows indicate vessels that could not be observed before VSOCA treatment. (g–i) THG microscopic images of various areas in (e), using a 25× objective. The frame color was used to represent the congruent relationship. Adapted with permission from [47]. Copyright (2020) John Wiley & Sons Group.

with the 1,550 nm fs laser for 15 s (Figure 14.10b). During the process, the fracture of the vessel wall was clearly observed and up to 10 min, the broken blood vessel was blocked as well as the DCCN nanocrystals remained in the surrounding tissue. These results suggested that precise NIR-II light manipulation could be performed through the established skull optical clearing window.

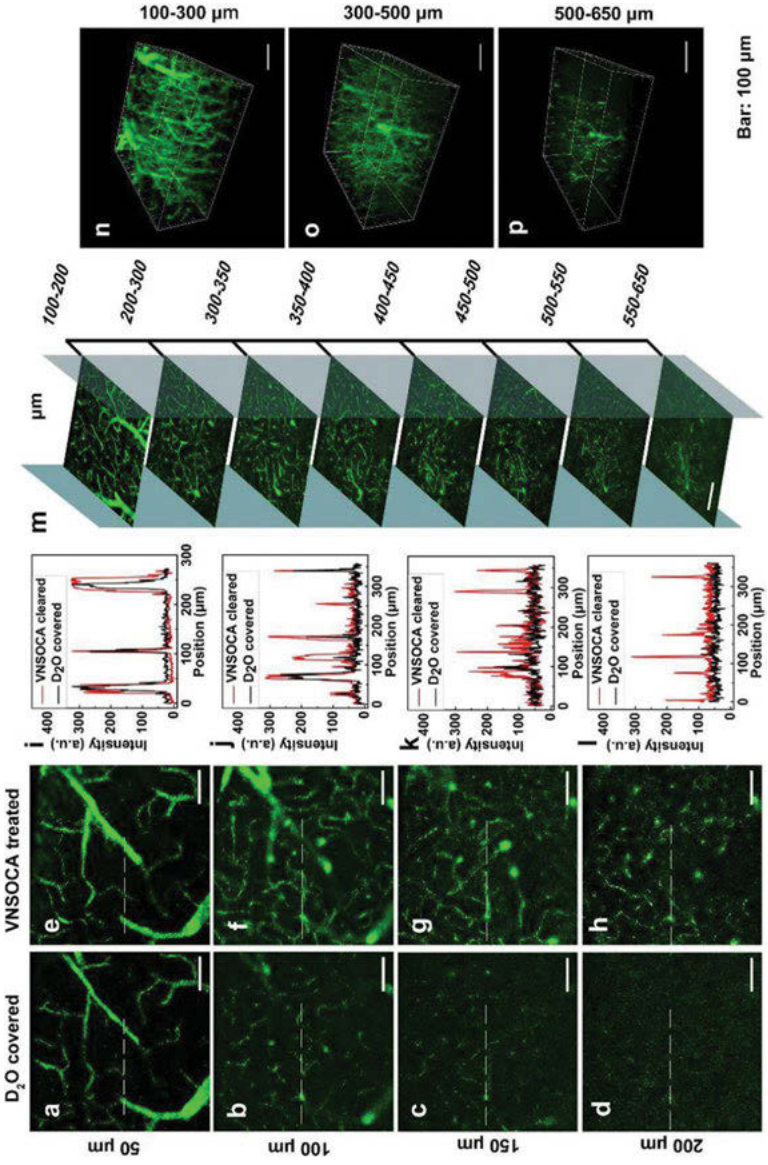

Figure 14.9: (a–d) THG scanning microscopy at different depths using the 25× objective without skull clearing. (e–h) THG scanning microscopy at different depths using the 25× objective with skull clearing. (i–l) Intensity profiles along the white dashed lines across the vasculature in (a–h), respectively. (m) THG imaging of cortical vasculature at particular imaging depths. (n–p) Three-dimensional reconstruction of vasculature in certain volumes. The dwell time in the depth less than 300 μm was 10 μs/pixel; the dwell time in the depth from 300 to 500 μm was 20 μs/pixel; the dwell time in the depth deeper that 500 μm was 40 μs/pixel. Adapted with permission from [47]. Copyright (2020) John Wiley & Sons Group.

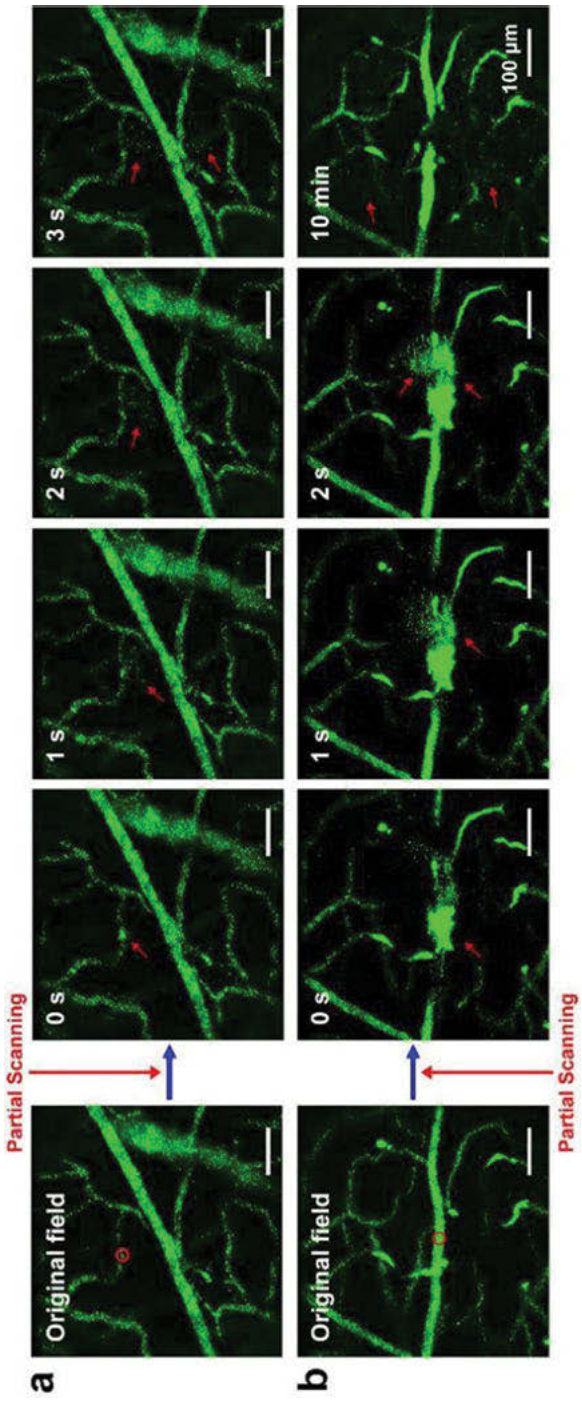

Figure 14.10: Dynamically observing cerebral hemorrhage using THG scanning images. The cerebral hemorrhage was made by partially scanning the region showed by the red circles for (a) 10 s and (b) 15 s. Adapted with permission from [47]. Copyright (2020) John Wiley & Sons Group.

14.3 In vivo 3PFM imaging for cranial window

Zong et al. synthesized four kinds of perylenetetracarboxylic diimide (PDI) derivatives with different isolation groups by Suzuki coupling reaction, as shown in Figure 14.11 [48]. SPhPDI utilized the isolation group of phenyl moiety which is the smallest one in this system. Then, the twisted structures of isolation groups were built by the linkage of different aromatic rings to meta-position of the involved phenyl unit, and the substituted aromatics varied from one phenyl (DPhPDI) to one carbazolyl (SCzPDI), then to two carbazolyl (DCzPDI) moieties. Thus, the sizes of isolation groups in spatial configuration became larger and larger gradually, which was helpful to inhibit the π–π stacking in the aggregated state.

The isolation groups influence the fluorescent properties of these PDI derivatives in the aggregated state. This ACQ-to-AIE conversion was mainly due to the tunable molecular packing modes and intermolecular interactions in the aggregated state by the variation of isolation groups [49, 50].

Basically, the isolation groups with twisted configurations and big sizes could enlarge the distances between π-plane efficiently, resulting in the bright deep-red emission of DCzPDI as NPs (Figure 14.12). However, the fluorescence intensity of DCzPDI in solution is not always enhanced in the formation of NPs by the addition of methanol. It decreased slightly as f_m in the region of 10–30%, which may be related to the varied polarities of solvent systems. Thus, with the aim to investigate the effect of solvents with different polarities on their emission properties, the fluorescence spectra of these PDI derivatives in cyclohexane, toluene, tetrahydrofuran (THF), and dichloromethane were conducted as shown in Figure 14.13. Interestingly, SCzPDI and DCzPDI with AIE property showed the intensive fluorescence quenching effect with the increased polarities of solvents; however, it was not so obvious in the ACQ ones with the similar conditions. These different behaviors meant that the ICT in two kinds of PDI derivatives changed with the incorporation of varied isolation groups, which could be proved by theoretical calculation.

Zong et al. designed and synthesized the isolation groups with twisted configurations, and big sizes could enlarge the distances between π-plane efficiently, which would endow DCzPDI with the bright deep-red emission (λ_{max} = 638 nm) and high fluorescence QY = 12.3%. The biocompatibility and fluorescence intensity of DCzPDI were improved by encapsulation of F-127 to form DCzPDI-NPs as shown in Figure 14.14a. These DCzPDI-NPs exhibited good photostability under continuous laser excitation (450 nm, 100 mW). After 3 h of exposure, the fluorescence intensity of DCzPDI-NPs remained 79%. The morphology of DCzPDI-NPs was characterized by TEM (transmission electron microscope), and the average hydrodynamic diameter for DCzPDI-NPs was measured to be about 100 nm by

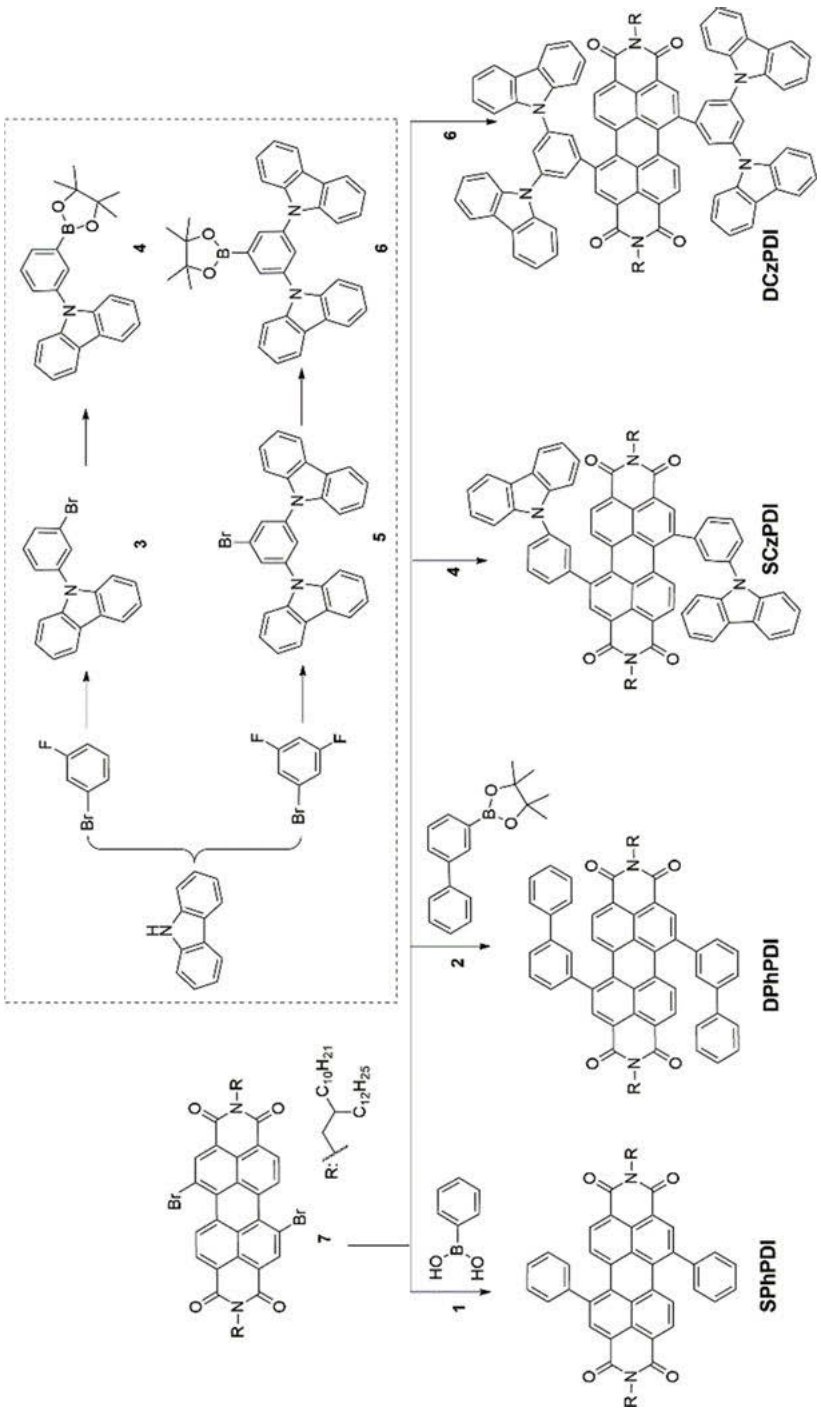

Figure 14.11: Synthetic routes of four PDI derivatives. Adapted with permission from [48]. Copyright (2018) American Chemical Society.

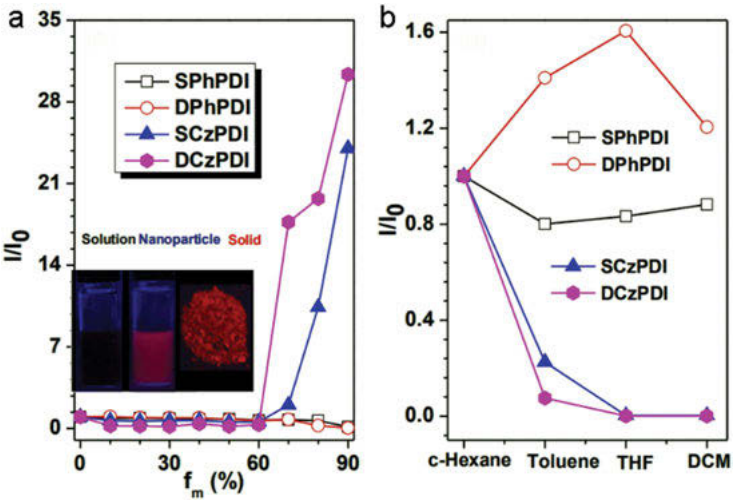

Figure 14.12: (a) The changes of fluorescence intensities of PDI derivatives in dichloromethane solution with the addition of different fractions of methanol (f_w). Inset: the photos of DCzPDI in different conditions under UV lamp. (b) The changes of fluorescence intensity of PDI derivatives in different solvents. Adapted with permission from [48]. Copyright (2018) American Chemical Society.

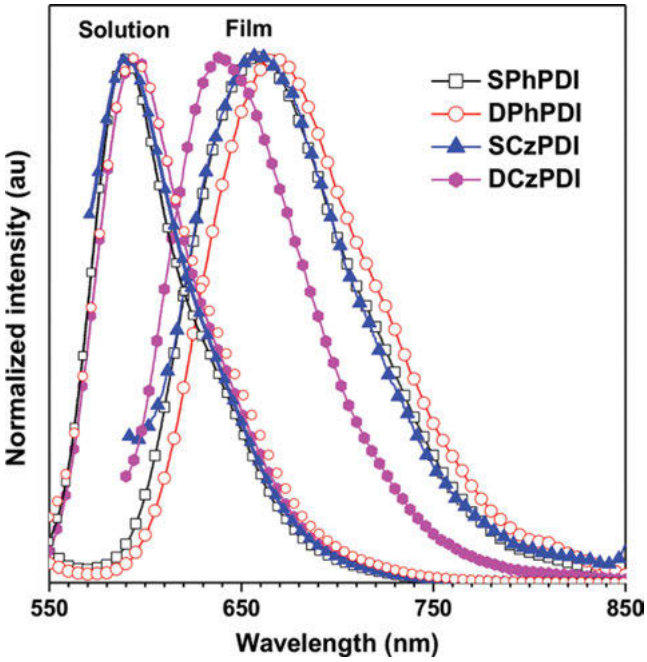

Figure 14.13: Fluorescence spectra of PDI derivatives in solutions and thin films. Adapted with permission from [48]. Copyright (2018) American Chemical Society.

dynamic light scattering (DLS). A bright deep-red emission ($\lambda_{max} = 658$ nm) with the QY = 2.37% was observed from the single photon fluorescence spectrum of DCzPDI-NPs in water.

The 3PF property of the DCzPDI-NPs under 1,550 nm fs laser excitation was studied on a lab-built 3PF measuring system. The 3PF peak was at deep red wavelength region (650 nm) and its tail extending into NIR range. Figure 14.14b shows the linear relationship between the logarithm of 3PF intensity of DCzPDI-NPs, and the logarithm of the excitation power was demonstrated, which illustrated that 3PF was the main nonlinear optical process. Then the 3 PA cross section of DCzPDI-NPs was measured to be 6.80×10^{-80} $cm^6 \cdot s^2$ by nonlinear transmissivity method. Accordingly, under the excitation of a 1,550 nm fs laser, DCzPDI-NPs were utilized for in vivo 3PFM imaging of cerebral vessels of mice.

As shown in Figure 14.15, DCzPDI-NPs exhibited a bright 3PF signal in brain blood vessels, and 3PFM images of brain blood vessels at various vertical depths could be obtained. Since some coarser vessels existed in the imaging depth from 0 to 100 μm, the structures of capillaries can be observed in the depth of 150–450 μm. Moreover, the corresponding 3D image of the DCzPDI-NPs in the blood provided a general and clear spatial picture about major blood vasculature networks and tiny capillaries in detail. Furthermore, FWHM of 3PFM images were measured and it was high enough to clearly observe the tiny blood vessel with diameter of 1.26 μm at the depth of 150 μm, and 2.39 μm at the depth of 435 μm (Figure 14.16). Thus, DCzPDINPs can be served as a deep-red 3PF probe successfully to realize the real-time monitoring of the dynamic blood flow process in vivo with high spatial resolution.

In another work, rat was utilized as an animal model [51]. Rat brain is larger than the mice brain, and it needs powerful imaging tools to implement better penetration against the scattering of the thicker brain tissue. Zhang et al. utilized a kind of deep-red emissive AIEluminogen named 5,6-bis(40-(diphenylamino)-[1,10-biphenyl]-4-yl) pyrazine-2,3-dicarbonitrile (DCDPP-2TPA) and encapsulated DCDPP-2TPA with F-127 to form DCDPP-2TPA NPs. The chemical structure of DCDPP-2TPA and the encapsulation process of DCDPP-2TPA NPs were shown in Figure 14.17.

The morphology of DCDPP-2TPA NPs was characterized by TEM as shown in Figure 14.18a. The absorption and FL spectra were also characterized, and the peak wavelength were $\lambda_{abs} = 440$ nm and $\lambda_{FL} = 650$ nm as shown in Figure 14.18b. The size of the DCDPP-2TPA NPs was also characterized by DLS, and the diameter was measured to be 40 nm which was ideal for the in vivo circulation as shown in Figure 14.18c.

Zhang et al. further studied the nonlinear optical property of DCDPP-2TPA NPs. The 3PF spectrum of DCDPP-2TPA NPs in aqueous dispersion was recorded under 1,550 nm fs laser excitation with a peak of ~650 nm and extended into NIR region as shown in Figure 14.19a. The deep-red and NIR 3PF emission of DCDPP-2TPA NPs

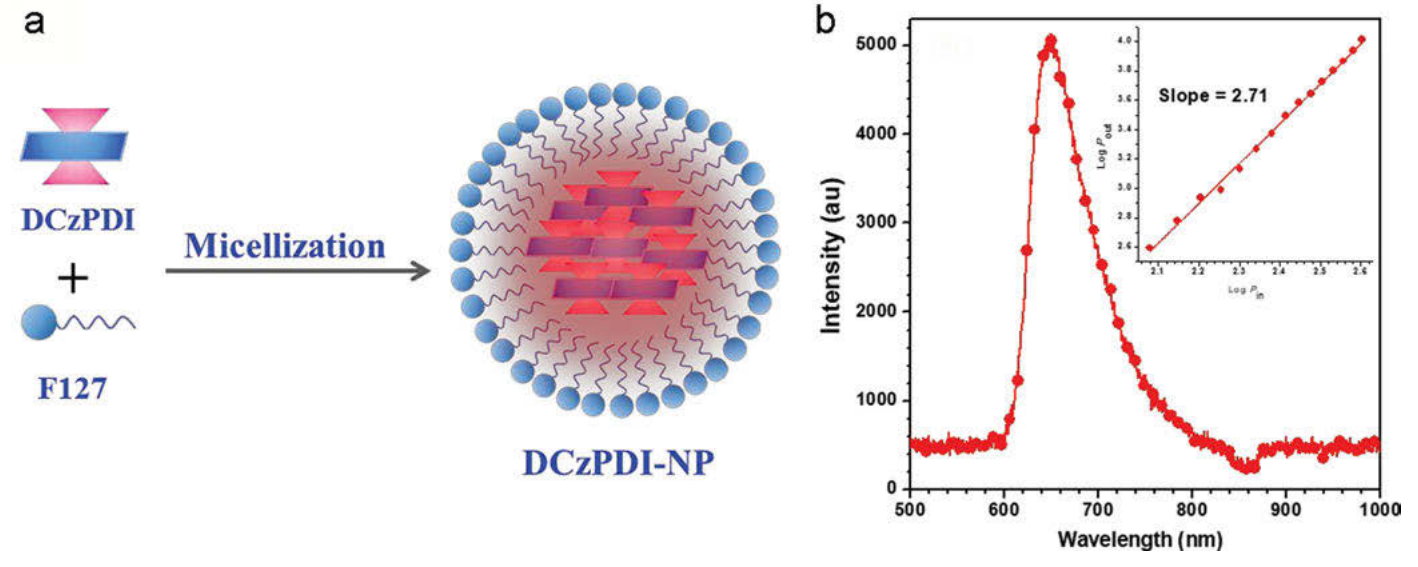

Figure 14.14: (a) A schematic illustration of the process of DCzPDI-NPs encapsulated with F127 polymer matrix; (b) Nonlinear optical property of DCzPDI-NPs in aqueous dispersion, under the 1,550 nm fs laser excitation, inset: power dependence relationship of the fluorescence from DCzPDI-NPs under the 1,550 nm fs laser excitation. Adapted with permission from [48]. Copyright (2018) American Chemical Society.

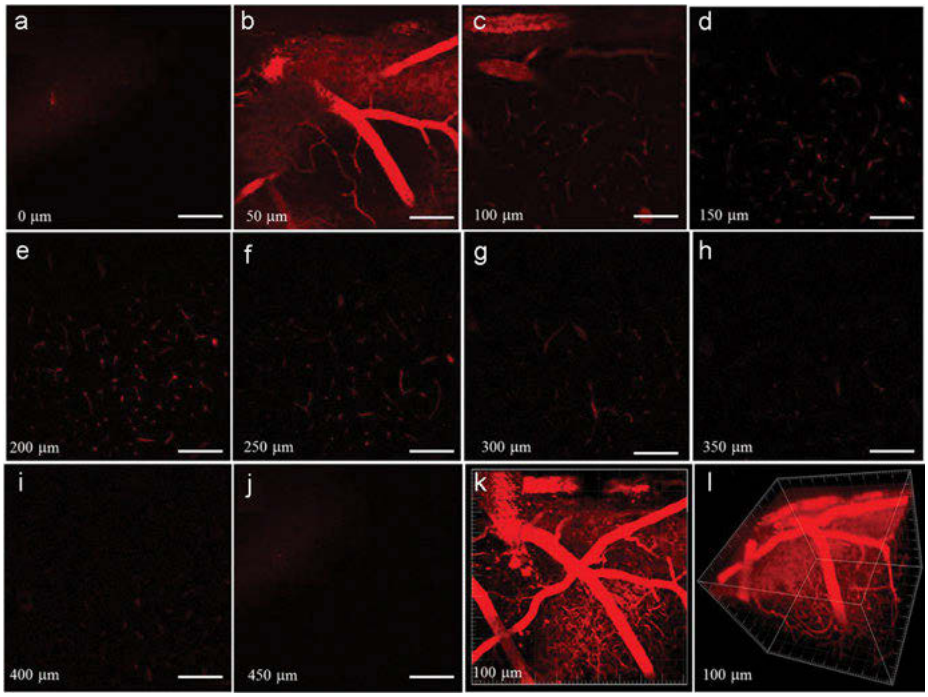

Figure 14.15: 3PFM imaging of brain blood vessels of a mouse treated with DCzPDI-NPs. Individual images taken at depths of (a) 0 μm, (b) 50 μm, (c) 100 μm, (d) 150 μm, (e) 200 μm, (f) 250 μm, (g) 300 μm, (h) 350 μm, (i) 400 μm, and (j) 450 μm, (k) a stacked three-photon fluorescence image from a depth of 0 to 450 μm, (l) A reconstructed 3D image showing the distribution of the DCzPDI-NPs in blood vessels of the mouse. The scale bar: 100 μm. Adapted with permission from [48]. Copyright (2018) American Chemical Society.

were beneficial for deep-tissue bioimaging for the reduced tissue absorption and scattering in biotissues. By analyzing the linear power dependence between the 3PF intensity from DCDPP-2TPA NPs and the power density of excitation laser, the 3PF was demonstrated the main nonlinear optical process under 1,550 nm fs laser excitation, as shown in Figure 14.19.

Zhang et al. further applied DCDPP-2TPA NPs for in vivo 3PFM imaging of the brain vasculature in rat. Functional imaging such as blood flow velocity is of great importance for the brain vascular research. Furthermore, Zhang et al. measured the brain blood flow velocity noninvasively by the 3PFM imaging experiment. The DCDPP-2TPA NPs moved with the blood flow but not attached into blood cells; thus, in the 3PFM images the blood cells imaged as shadow. Then they calculated the blood velocity by drawing a line scan parallel to the blood vessel which was demonstrated to be 5.6 mm/s as shown in Figure 14.20.

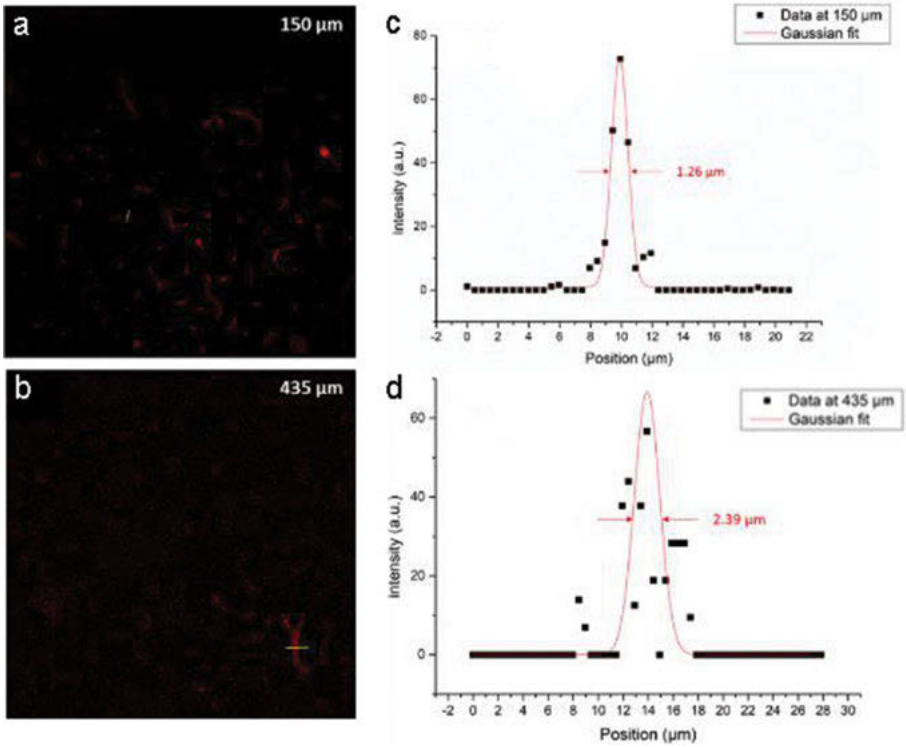

Figure 14.16: 3PFM imaging of brain blood vessels of a mouse treated with DCzPDI-NPs at 150 μm (a) and 435 μm (b), FWHM of a blood vessel at the depth of 150 μm (c) and 435 μm (d) as indicated with the dotted white line in the corresponding image. Adapted with permission from [48]. Copyright (2018) American Chemical Society.

For the large 3PA cross section, high QY and good biocompatibility, the DCDPP-2TPA NPs were utilized as 3PF nanoprobes for in vivo 3PFM imaging of the vasculature in rat brain. As shown in Figure 14.21, bright 3PF signals from DCDPP-2TPA NPs were observed from rat brain vessels under 1,550 nm fs laser excitation. Deep 3PFM images of the blood vessels at different vertical depths were obtained, and the structure of cerebral vessels could still be recognized at 600 μm imaging depth with high spatial resolution. As shown in Figure 14.22, the FWHM of the 3PFM images were calculated to be 2.57 and 4.60 μm at the depth of 100 and 600 μm. The DCDPP-2TPA NP-assisted 3PFM imaging still has much potential in deep-tissue bioimaging.

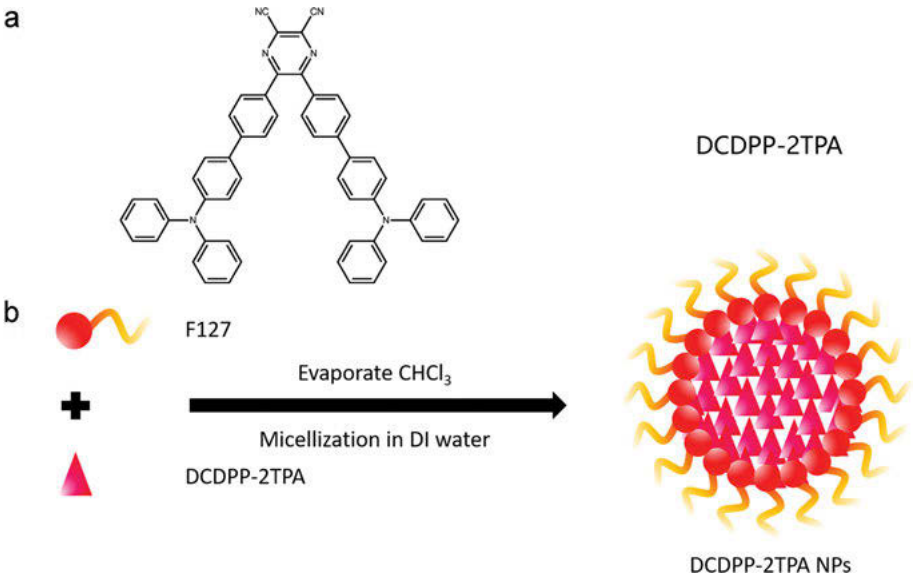

Figure 14.17: (a) Chemical structure of DCDPP-2TPA. (b) Synthesis scheme of DCDPP-2TPA NPs. Adapted with permission from [51]. Copyright (2019) World Scientific.

14.4 In vivo 3PFM imaging for through skull imaging

Qin et al. designed and synthesized a new kind of non-TPE-based AIE luminogens named BTF according to the simple synthetic pathways [52]. As shown in Figure 14.23a, the BTF chemical structure contained strong electron-donating triphenylamine (TPA) carrying *tert*-butyl (*t*-Bu) groups and electron-accepting fumaronitrile moiety. The donor–acceptor (D-A) structure of BTF endowed BTF with the FR/NIR emission and distinct multiphoton absorption. Moreover, BTF contains more freely rotatable phenyl rings and *t*-Bu groups to favor the consumption of excited-state energy in the solution state through active intramolecular motions which was helpful to facilitate the AIE process. Furthermore, the twisted TPA moieties and the bulky *t*-Bu groups of BTF hampered the formation of strong π–π stacking interactions. Thus, BTF exhibited long wavelength emission and high quantum efficiency.

The absorption and PL spectra of BTF were characterized, with peaks of λ_{abs} = 498 nm and λ_{PL} = 649 nm, respectively. The AIE effect and solvent polarity on the PL of BTF in THF/water mixtures with different water fractions (f_w) were measured as shown in Figure 14.23b and c. When f_w < 50%, the emission of BTF was weakened and redshifted to 650 nm for the typical TICT effect. In polar environment, these molecules undergo rapid intramolecular electron transfer from the donor to the acceptor moiety, and intramolecular D-A conformation changes from a coplanar structure to a

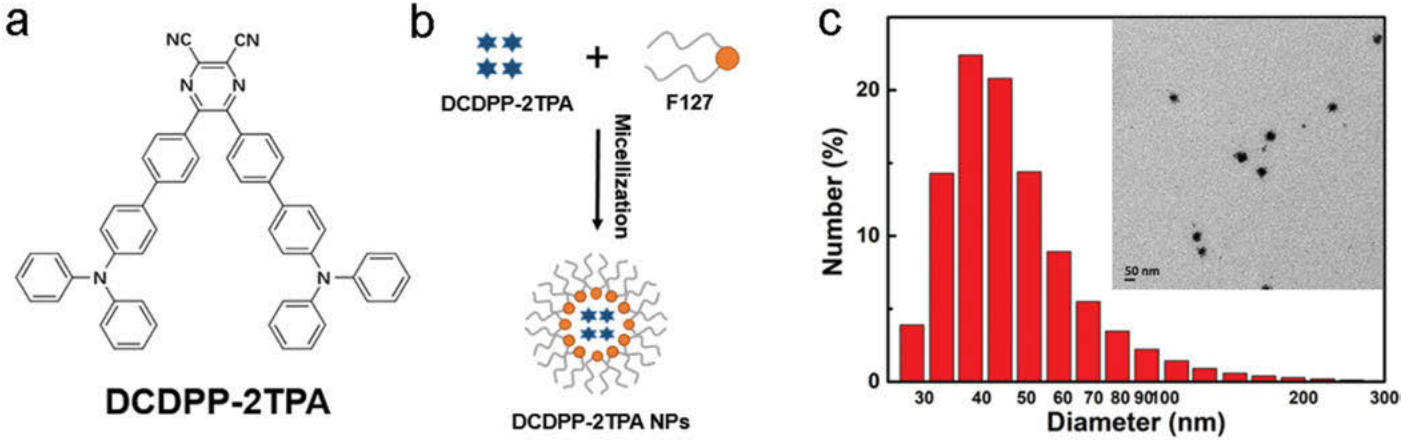

Figure 14.18: (a) TEM image of DCDPP-2TPA NPs. Scale bar: 100 nm. (b) Extinction spectrum (blue) and fluorescence spectrum (red) of DCDPP-2TPA NPs in aqueous dispersion; 0.05 mg/mL of DCDPP-2TPA. Excitation wavelength = 450 nm. (c) Dynamic light scattering data of DCDPP-2TPA NPs. Adapted with permission from [51]. Copyright (2019) World Scientific.

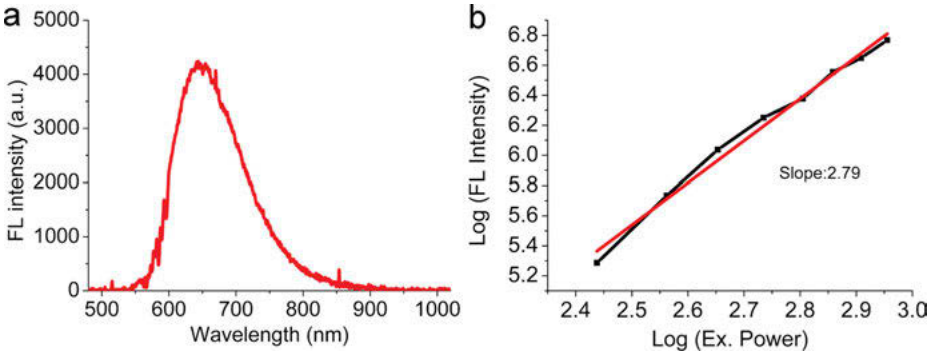

Figure 14.19: (a) Nonlinear response of DCDPP-2TPA NPs solution under 1,550 nm fs laser excitation. (b) Power dependence relationship of 3PF signal from DCDPP-2TPA NPs. Adapted with permission from [51]. Copyright (2019) World Scientific.

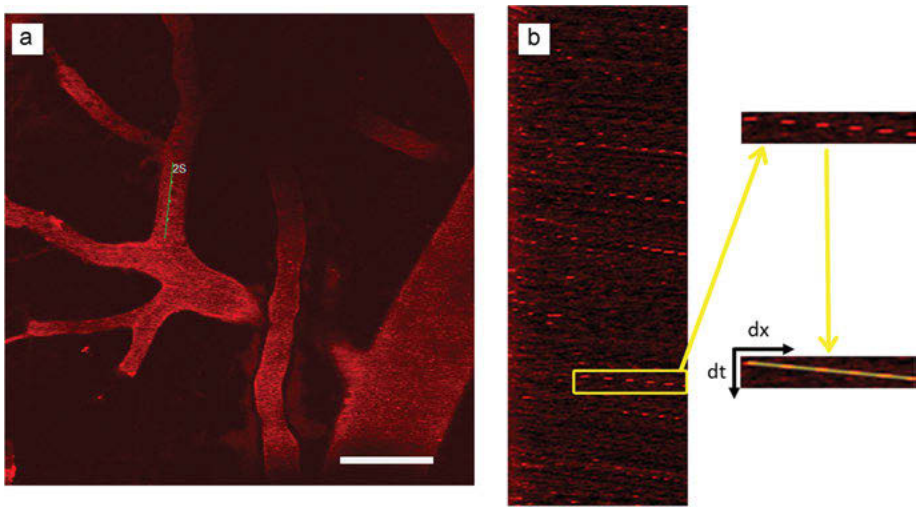

Figure 14.20: Measurement of the blood flow velocity in the rat brain. (a) An area for the line scan during 3PFM imaging, and the scan line (2S) was parallel to the blood vessel. Scale bar: 100 μm. (b) The enlarged image of a line scan image, d*x*/d*t* of one selected 3PF signal was computed to be 5.6 mm/s. Adapted with permission from [51]. Copyright (2019) World Scientific.

twisted conformation. And when $f_w > 50\%$, BTF molecules start to form nanoaggregates due to their hydrophobic effect which would enhance the AIE effect. Up to $f_w = 90\%$, the maximum PL intensity is attained, which is 5-fold higher than that in pure THF solution as shown in Figure 14.23d, which illustrated the AIE-active property of a BTF molecule. The fluorescence quantum efficiency (Φ_F) of BTF in pure THF solution was measured to be 2.7%, and enhanced to 42.6% in the solid state.

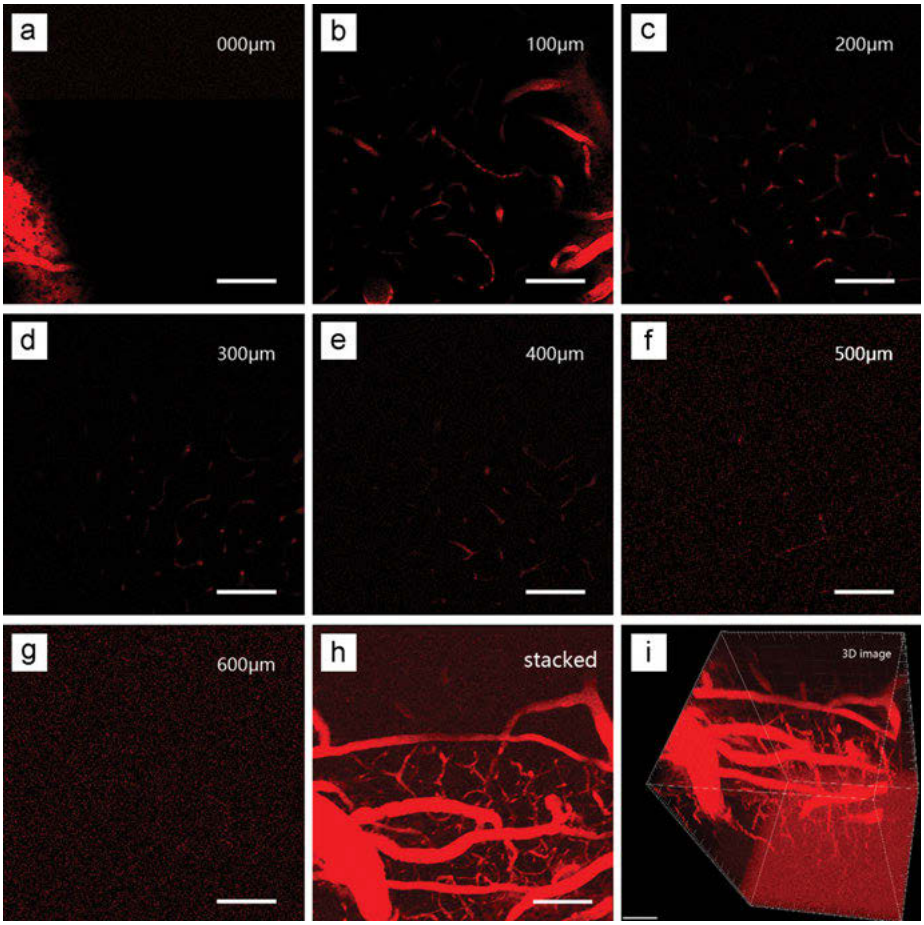

Figure 14.21: In vivo 3PFM imaging of brain vasculature of a rat injected with DCDPP-2TPA NPs. Each image taken at different depths from 0 to 600 μm (a–g). (h) A stacked three-photon fluorescence image from a depth of 0 to 600 μm. (i) A reconstructed 3D image showing the blood vessels of rat brain stained by DCDPP-2TPA NPs. Scale bar: 100 μm. Adapted with permission from [51]. Copyright (2019) World Scientific.

To improve the biocompatibility and dispersibility in aqueous media, BTF molecules were further encapsulated by F-127 to form BTF dots as shown in Figure 14.24a. The average size of BTF dots in aqueous solution was measured via DLS with a hydrodynamic diameter of 128 nm. The absorption (λ_{abs} = 500 nm) and PL (λ_{PL} = 645 nm) property of BTF dots were characterized and Φ_F was demonstrated to be 36.1%. Under 1,550 nm fs laser excitation, three photons of 1,550 nm were absorbed simultaneously by BTF molecule and emit one photon. The bright 3PF of the BTF dots was observed at 645 nm accompanied with a sharp signal from THG at 517 nm as shown in Figure 14.24b and c. Then the proportional relationship of 3PF intensity from BTF dots to the cubic power of

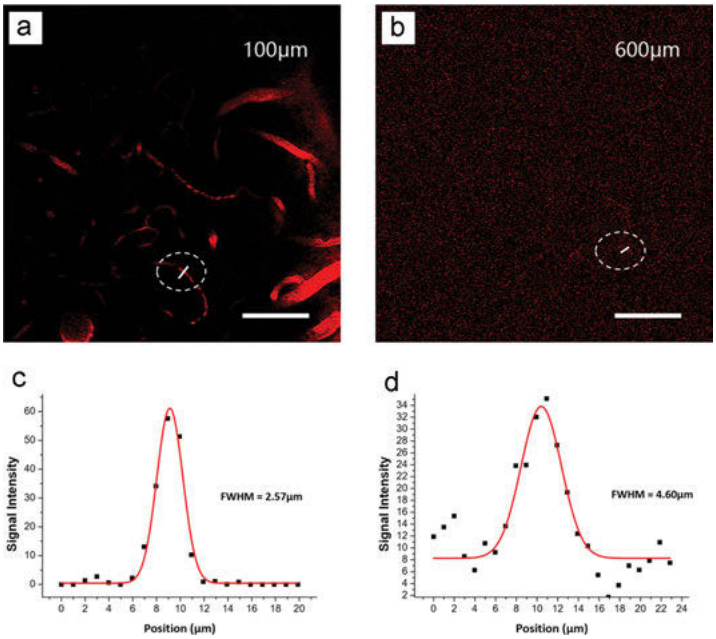

Figure 14.22: 3PF signals in cerebral vasculature of rats at different vertical depths. (a) and (b) 3PFM images of the vasculature at 100 μm (a) and 600 μm (b) to analyze FWHMs. (c) and (d) FWHMs of 3PF signal of images at 100 μm (c) and 600 μm (d). Scale bar: 100 μm. Adapted with permission from [51]. Copyright (2019) World Scientific.

the excitation intensity at 1,550 nm was measured as shown in Figure 14.24d, which demonstrated 3PF was the main nonlinear optical process. The 3PA of the BTF dots was further measured to be 2.56×10^{-79} $cm^6 \cdot s^2$. Then the photostability of the BTF dots was studied by monitoring the PL change upon continuous laser irradiation at 1,550 nm, and after 40 min the PL of BTF dots remain 90% of their initial 3PF intensity which was good for long-term bioimaging applications (Figure 14.24e).

For the good 3PF and biocompatibility of the BTF dots, Qin et al. further investigated the real-time 3PF microscopic imaging of mouse cerebrovascular through skull. As shown in Figure 14.25a–c, the 3PF and THG signals were well matched, and the combination of 3PF and THG imaging modes enhanced the reliability of deep-tissue imaging. Figure 14.25d–f showed the 3D high-resolution reconstruction vasculature images of the mouse brain at various penetration depths from 0 μm to 900 μm. The FWHM and SBRs of the 3PF images at different imaging depths were attributed to the high-order nonlinear optical effect and the strong 3PF signal of the BTF dots as well as good penetration capability of the NIR-II excitation light.

Qin et al. took full advantage of 3PF imaging, and utilized the fluorescent BTF dots for practical applications in visualization of brain blood vessels of mouse with intact skull in vivo. As shown in Figure 14.26a–c, high-resolution 3D reconstruction

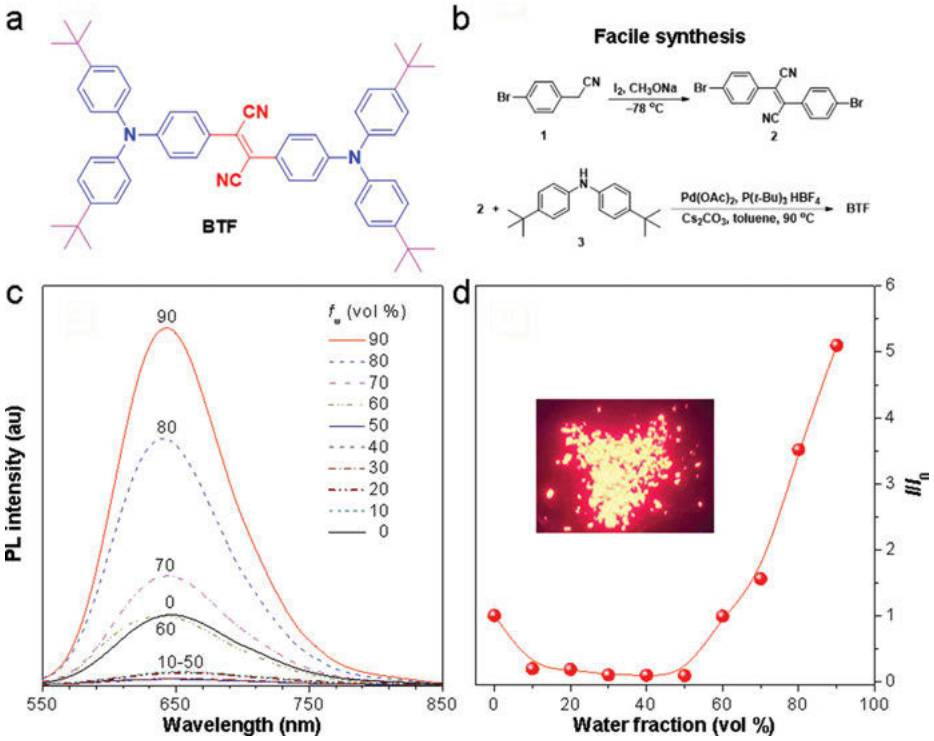

Figure 14.23: (a) Chemical structure and (b) synthetic pathway of BTF molecules. (c) PL spectra of BTF in THF/water mixtures with different water fractions (f_w). (d) Plot of the relative PL intensity (I/I_0) versus the composition of the THF/water mixtures of BTF. I_0 = emission intensity in pure THF. Solution concentration = 10 μM; Excitation wavelength = 500 nm. Inset: fluorescent photograph of BTF powders taken under 365 nm UV irradiation. Adapted with permission from [52]. Copyright (2020) John Wiley & Sons Group.

images of the mouse brain vessels were obtained. The FWHM of the indicated tiny capillary is calculated to be 0.95 μm at 200 μm depth, 1.59 μm at 300 μm depth, and 2.08 μm at 400 μm depth as shown in Figure 14.26d–f. Then the average blood flow velocity (dx/dt) of the indicated capillary was calculated to be ~3. 8 mm/s with a volume blood flow of 1.45×10^{-2} μL/min.

Effective detection of cerebral thrombosis plays a key role in brain science. Qin et al. further utilized the BTF dots to monitor the cerebral stroke process of mouse with the intact skull. Firstly, 3PF imaging of mouse brain with intact skull was conducted using BTF dots and general information on a large field of vasculature structure was obtained via 5× objective. After the BTF dots were cleared from the mouse, a microsurgery was performed which was to induce occlusion in the origin of the middle cerebral artery (MCA). Then occlusion of MCA in mouse brain was occurred and BTF dots were intravenously injected into the mouse. As shown in Figure 26g–I, the process of

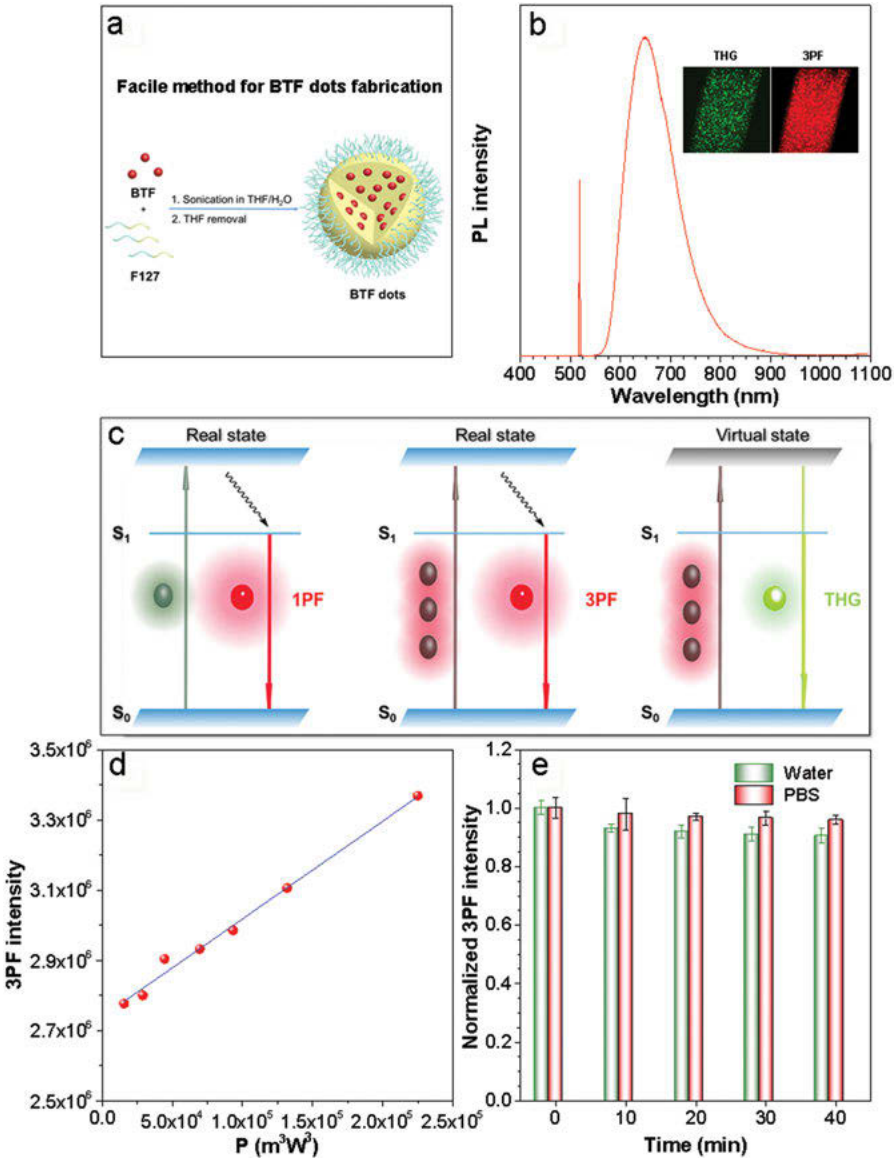

Figure 14.24: (a) Illustration of the formulation process of BTF dots using F127 as the polymer matrix. (b) Schematic illustration of 1PF, 3PF, and THG processes. (c) Nonlinear optical property of BTF in aqueous dispersion measured under 1,550 nm fs laser excitation. Inset: THG and 3PF images of BTF aqueous dispersion in capillary glass tube. (d) Power dependence relationship of the fluorescence intensity of the BTF dots under 1,550 nm fs laser excitation. (e) 3PF intensity of the BTF dots at different time points under continuous laser irradiation at 1,550 nm. Adapted with permission from [52]. Copyright (2020) John Wiley & Sons Group.

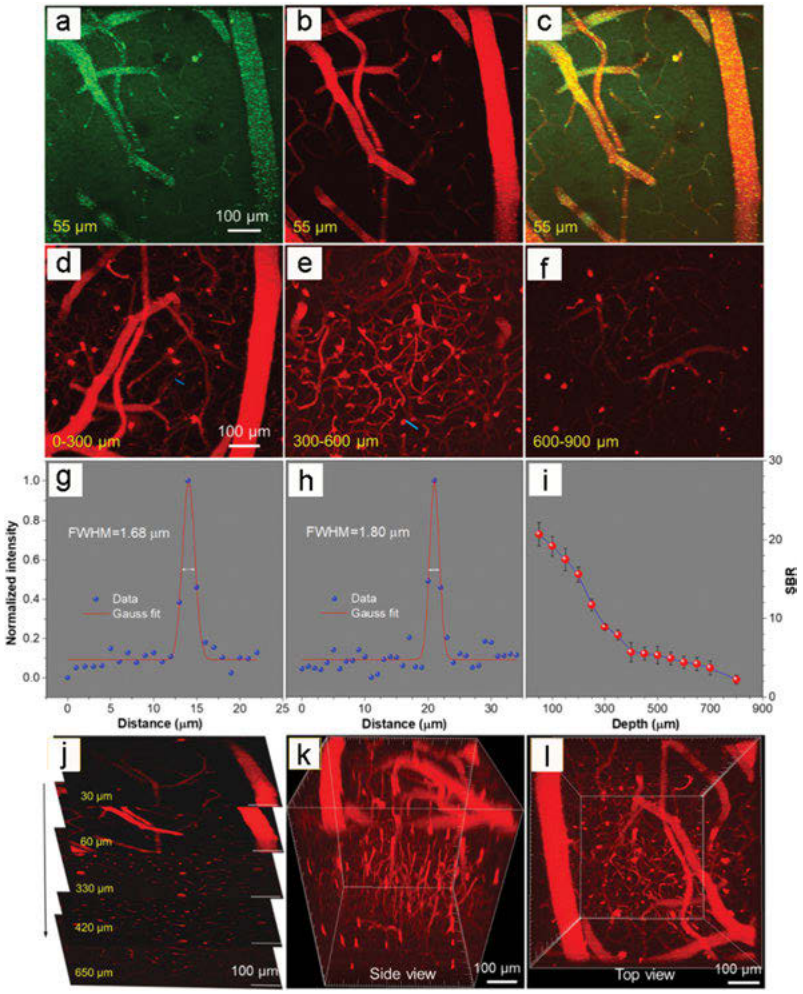

Figure 14.25: (a) THG, (b) 3PF, and (c) overlay images of the mouse brain vessels at penetration depth of 55 μm. Scale bar: 100 μm. (d–f) In vivo 3D high-resolution images of the mouse brain vessels at penetration depth from 0 to 900 μm. (g–h) A cross-sectional intensity profile measured along the blue line in (d) and (e). (i) Attenuation curve of the fluorescence signal. (j) Fluorescence images of the brain vessels at various penetration depths. Scale bar: 100 μm. (k) The side and (l) top views of the constructed 3D images of the blood vessels of the mouse brain at penetration depth from 0 to 900 μm. Scale bar: 100 μm. Excitation wavelength: 1,550 nm. Adapted with permission from [52]. Copyright (2020) John Wiley & Sons Group.

cerebral thrombosis was clearly observed by 3PF microscopic imaging with a high SBR value of 92.1, while the mouse without microsurgery was used as control under the same 3PF microscopic imaging condition. No obvious cerebral thrombosis process could be observed.

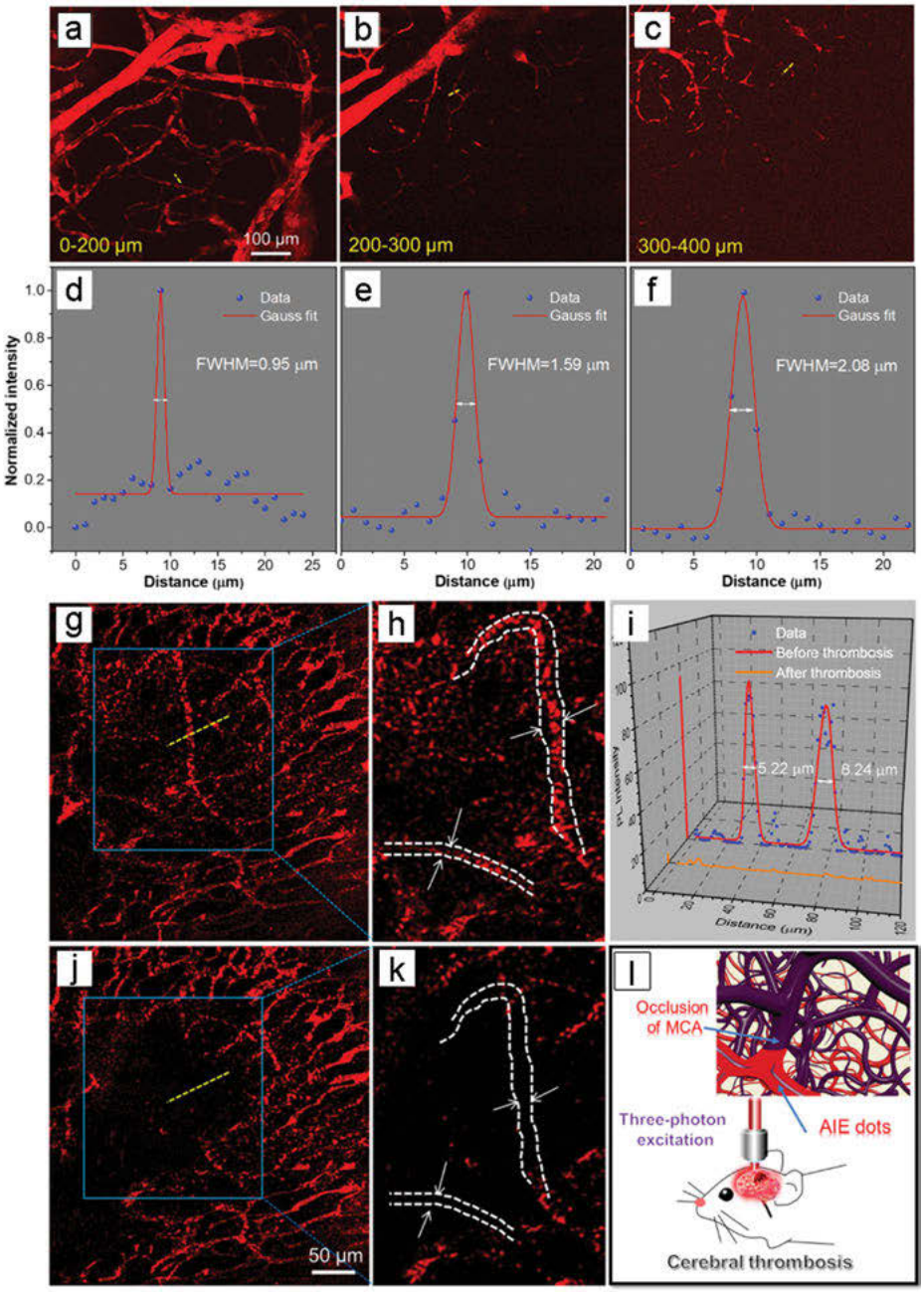

Figure 14.26: (a–c) In vivo 3D high-resolution images of the mouse brain vessels with intact skull at penetration depth from 0 to 400 μm. Scale bar: 100 μm. (d–f) A cross-sectional intensity profile measured along the yellow line in (a), (b), and (c). 3PF images of brain blood vessels of a mouse

14.5 In vivo three-photon fluorescence lifetime microscopic imaging

Weak fluorescence signals can be effectively detected by the fluorescence lifetime imaging microscopy (FLIM) which was based on the single photon counting (TCSPC) technique [53, 54]. Therefore, it was very beneficial to combine the 3PFM imaging with the FLIM. Ni et al. reported a red-emissive AIEgen DCDPP-2TPA and utilized the AIEgen as fluorescent probes for in vivo 3PF lifetime microscopic imaging [55]. Figure 14.27a showed the chemical structure of DCDPP-2TPA, and the DCDPP-2TPA was further encapsulated by F-127 as shown in Figure 14.27b. The morphology and size distribution of DCDPP-2TPA NPs were characterized via TEM image and DLS method as shown in Figure 14.27b. The average size of DCDPP-2TPA NPs was ~40 nm, which means that DCDPP-2TPA NPs were suitable for in vivo blood circulation.

As shown in Figure 14.28a, the extinction spectrum and the transmission spectrum (the inset) of DCDPP-2TPA NPs in water (0.03 mg/mL) were recorded. The spectra indicated that the DCDPP-2TPA NPs at 1,550 nm have very low one-photon absorption. According to our previous study, the 3PA cross section of DCDPP-2TPA molecule was 2.95×10^{-79} $cm^6 \cdot s^2$ at 1,550 nm. Figure 14.28b shows the 1PF and 3PF spectra of DCDPP-2TPA NPs in water (1 mg/mL) excited under 450 nm CW laser and 1550 nm fs laser, respectively. The 1PF and 3PF spectra were almost the same with the fluorescence peak at 645 nm.

The 3PF lifetime microscopic imaging system was shown in Figure 14.29. The 1,550 nm fs laser was adopted and divided into two perpendicular directions by a polarization beam splitter (PBS), and one of which was utilized to excite the 3PF and another was used to trigger the time synchronization of TCSPC system. The stronger laser beam was introduced into a scanning microscope (FV1200&BX61, Olympus) and was reflected by an 800 nm short-pass dichroic mirror (DC) to excite AIEgen NPs focusing by *Z*-axis of the 25× water-immersed objective (XLPLN25XWMP2, Olympus). Then the 3PF signals were collected by the same objective and DC, finally, were captured by a PMT (HPM-100-50, Becker&Hickl GmbH). The weaker laser beam was utilized as synchronization signals via a photodetector in the TCSPC system (Becker&Hickl GmbH, SPC-150). Then the 3PF lifetime imaging was conducted based on the system shown in Figure 14.29.

Figure 14.26 (continued)
with intact skull (g and h) before and (i and j) after brain thrombosis. Scale bar: 50 μm. (k) A cross-sectional intensity profile measured along the yellow line in (g) and (i). (l) Schematic illustration of the visualization of brain thrombosis process with intact skull based on the AIE dots through 3PF microscopic imaging technique. Excitation wavelength: 1,550 nm. Adapted with permission from [52]. Copyright (2020) John Wiley & Sons Group.

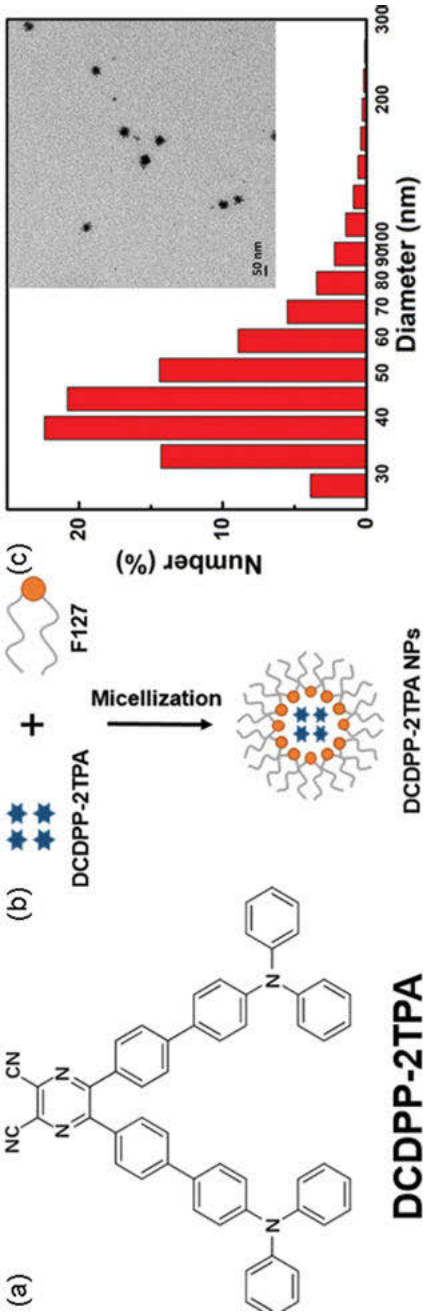

Figure 14.27: (a) Chemical structure of DCDPP-2TPA. (b) Preparation scheme of DCDPP-2TPA NPs. (c) DLS result of DCDPP-2TPA NPs in aqueous dispersion (inset: a typical TEM image of DCDPP-2TPA NPs. Scale bar: 50 nm). Adapted with permission from [55]. Copyright (2020) World Scientific.

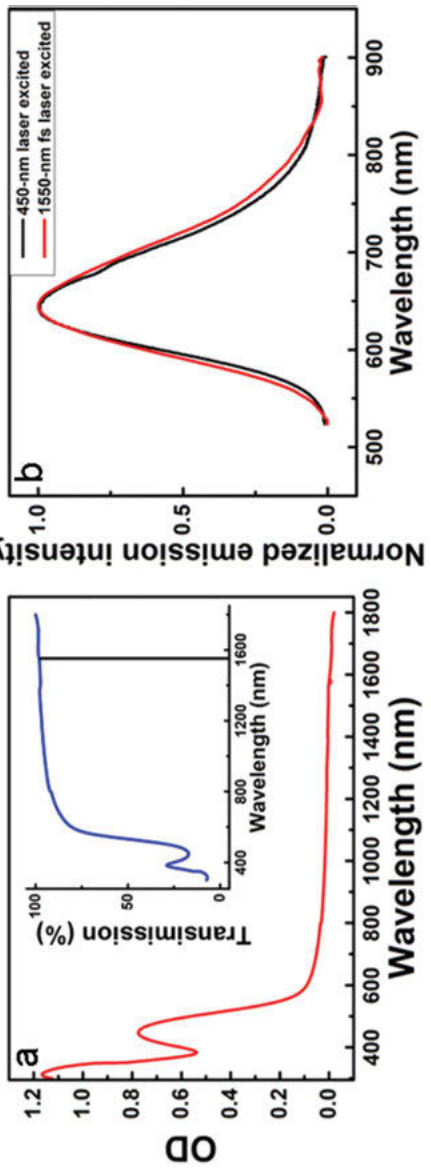

Figure 14.28: (a) Extinction spectrum of DCDPP-2TPA NPs in water (1 mg/mL). OD, optical density (inset: the transmission spectrum of DCDPP-2TPA NPs in water (1 mg/mL)). (b) One-photon and three-photon fluorescence spectra of DCDPP-2TPA NPs in water (1 mg/mL). Adapted with permission from [55]. Copyright (2020) World Scientific.

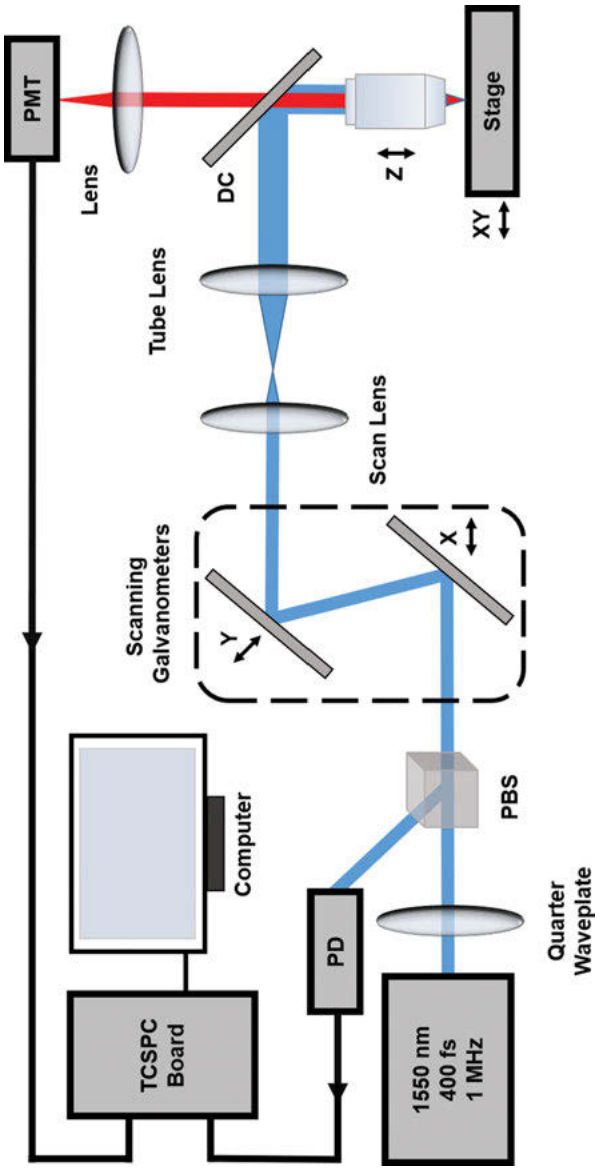

Figure 14.29: Schematic illustration of 3PF lifetime microscopic imaging system. Adapted with permission from [55]. Copyright (2020) World Scientific.

Then, the 3PF lifetimes of DCDPP-2TPA molecule in THF, chloroform, and toluene were measured. As shown in Figure 14.30, the 3PF lifetime of DCDPP-2TPA molecule in THF were 570 ps, 960 ps in chloroform and 3,366 ps in toluene. The 3PF lifetime of DCDPP-2TPA NPs in water were further measured, which was 5,215 ps for the aggregation state of DCDPP-2TPA molecules in NPs.

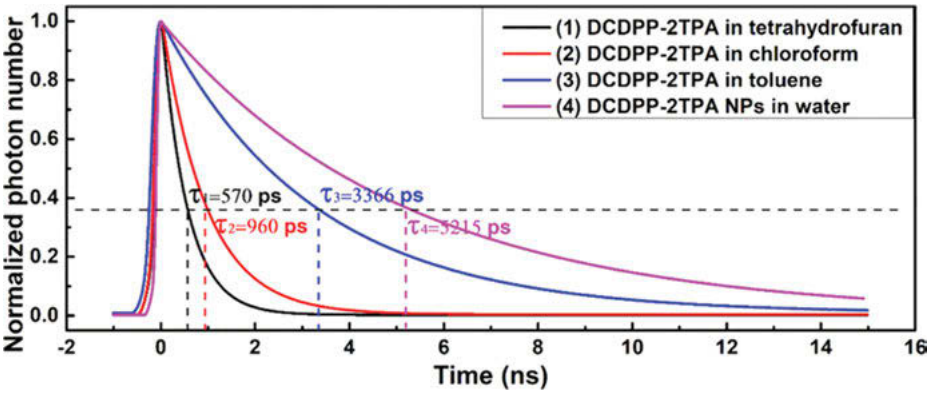

Figure 14.30: Time-resolved decay probes of 3PF of DCDPP-2TPA in tetrahydrofuran (black line), chloroform (red line), toluene (blue line), and DCDPP-2TPA NPs in water (pink line). The lifetimes of each solution were measured to be 570, 960, 3,366, and 5,215 ps. Adapted with permission from [55]. Copyright (2020) World Scientific.

3PF intensity image (in grayscale) and 3PF lifetime image (quadrate color map) of DCDPP-2TPA NPs in water (contained in a glass capillary tube) were both recorded as shown in Figure 14.31a. The distribution of 3PF lifetime within the color map region (Figure 14.31a) was shown in Figure 14.31b, and the central lifetime was measured to be 5.2 ns.

Ni et al. further performed in vivo 3PFLIM, and utilized the DCDPP-2TPA NPs as 3PF nanoprobes for brain vessels of mice (Figure 14.32). A mouse with craniotomy was intravenously injected with DCDPP-2TPA NPs (1 mg/mL, PBS× 1, 200 μL). Then the mouse was imaged under 1,550 nm fs laser excitation. The 3PF lifetime images of brain vessels at different vertical depths were obtained and recorded at a step of 20 μm. Brain blood vessels having 600 μm penetration depth were achieved with a high spatial resolution of 3D reconstruction as shown in Figure 14.33. 3PFLIM images of brain vasculatures at different depths were recorded, and some specific images (0, 200, 400, 600 μm) were shown in Figure 14.33a–d. The 3PF lifetimes of some spots of the blood vessels in these images were further analyzed. At the imaging depth of 0 μm the 3PF lifetime was 4,086 ps, at the imaging depth of 200 μm the 3PF lifetime was 4,656 ps, at 400 μm it was 4,646 ps, and at 600 μm it was 6,470 ps. Thus, the 3PF lifetime stability of DCDPP-2TPA NPs in the mouse brain vessels was illustrated. Therefore, DCDPP-2TPA NPs have great potential in in vivo

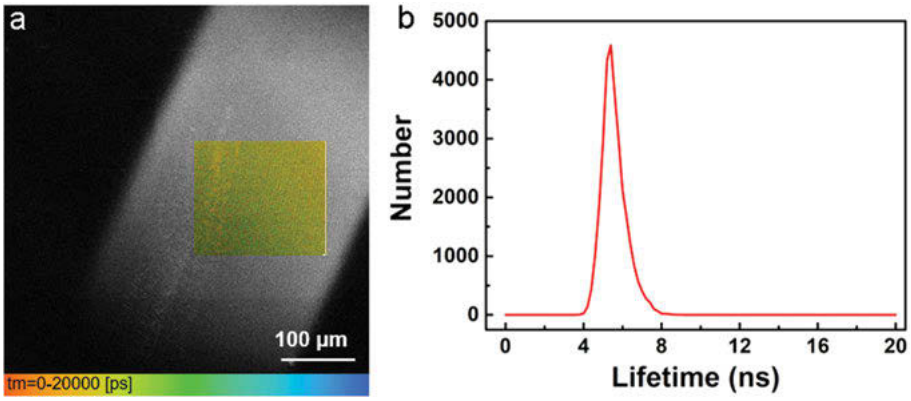

Figure 14.31: (a) 3PF intensity image (in grayscale) and 3PF lifetime image (quadrate color map) of DCDPP-2TPA NPs in water contained in a glass capillary tube (scale bar: 100 μm). (b) Distribution of lifetime within the region of color map in (a). Adapted with permission from [55]. Copyright (2020) World Scientific.

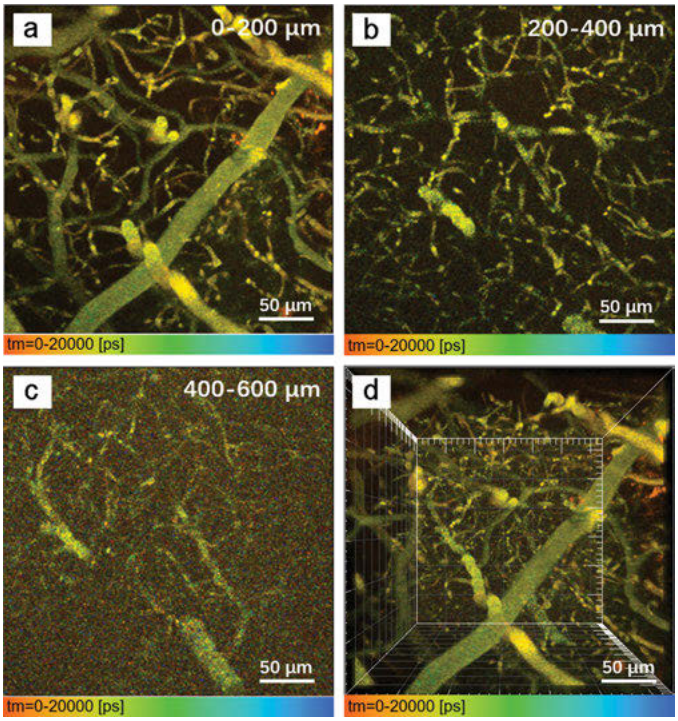

Figure 14.32: In vivo 3PFLIM stacked images (every 200 μm) of mouse with craniotomy brain vasculature at various vertical depths: (a) 0–200 μm, (b) 200–400 μm, and (c) 400–600 μm. (d) Three-dimensional reconstruction of the blood vessels in brain with 600 μm depth (scale bar: 50 μm). Adapted with permission from [55]. Copyright (2020) World Scientific.

3PFLIM. Further, the spatial resolution of 3PF lifetime images was analyzed by FWHM. As shown in Figure 14.33, at the imaging depth of 600 μm, tiny capillary vessels of 1.9 μm could still be recognized clearly.

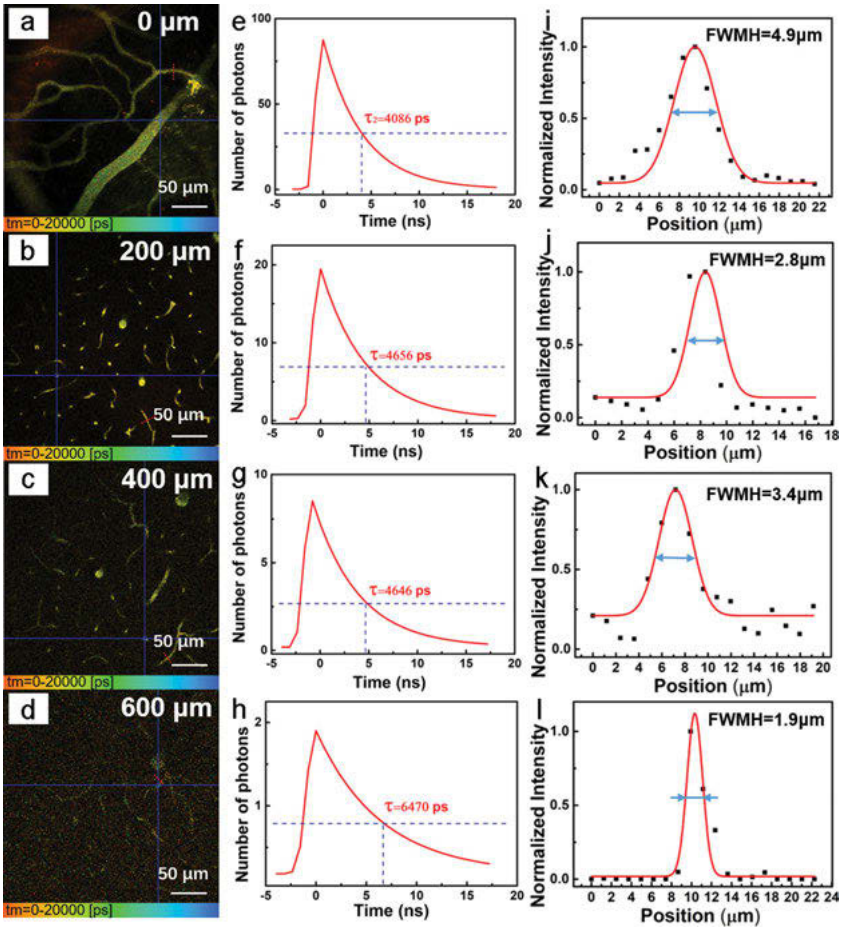

Figure 14.33: (a), (d), (g), (j) In vivo 3PFLIM images of brain vasculature of mouse with craniotomy at various vertical depths: 0, 200, 400, and 600 μm (scale bar: 50 μm). (b), (e), (h), (k) Time-resolved decay of the intersection of blue lines (drawn in (a), (d), (g), (j)) at various vertical depths. (c), (f), (i), (l) The cross-sectional intensity profiles across the capillary vessels marked with red-dashed lines in (a), (d), (g), and (j). Adapted with permission from [55]. Copyright (2020) World Scientific.

14.6 Summary and perspectives

In this chapter, recent advances on AIEgens-assisted in vivo THG and 3PF microscopic bioimaging are summarized. The abundant biological applications based on 3PF and THG high-order nonlinear optical effect are revealed in this chapter. A variety of new AIEgens with good nonlinear optical properties have been developed and encapsulated into multifunctional AIE nanoprobes. The as-synthesized AIE nanoprobes presented great application potentials in high-order nonlinear optical bioimaging. However, their further applications that are still at an early stage with many important issues need to be addressed.

To achieve high-quality deep-tissue fluorescence imaging, it is necessary to overcome the influence of scattering. According to Mie theory, the scattering of light in biological tissue decreases with the increase of wavelength. Light in the NIR-II spectral window is ideal for its low scattering coefficient. Thus, utilizing the fs NIR-II excitation laser could improve imaging efficiency to a high degree. Meanwhile, optical, chemical, and biological properties of AIEgens are still needed to be improved. AIEgens with excellent optical property, such as long lifetime, large 3 PA cross section, high QY, and deep red/NIR emission are favored. Besides, photochemically stable, biocompatible, and nontoxic AIEgen-based nanoprobes are still expected. Furthermore, 3PF and THG microscopic imaging systems need to be optimized according to the optical properties of AIEgens. The laser pulse, output power, repetition rate, duty cycle and other factors, and the appropriate excitation wavelength should be considered comprehensively during the whole experiment. The optical elements used in the optical path, such as lens, mirror, and dichroic mirror, need to be further antireflective to obtain better transmission and reflection in NIR-II window to get enhanced excitation/emission efficiency.

References

[1] Merian J, Gravier J, Navarro F, Texier I, Fluorescent nanoprobes dedicated to *in vivo* imaging: From preclinical validations to clinical translation, Molecules, 2012, 17, 5564–5591.
[2] Yuan L, Lin W, Zheng K, He L, Huang W, Far-red to near infrared analyte-responsive fluorescent probes based on organic fluorophore platforms for fluorescence imaging, Chem Soc Rev, 2013, 42, 622–661.
[3] Prasad PN, Introduction to Biophotonics, Hoboken NJ, Wiley-Interscience, 2003.
[4] Ye D, Shuhendler AJ, Cui L, Tong L, Tee SS, Tikhomirov G, Felsher DW, Rao J, Bioorthogonal cyclization-mediated in situ self-assembly of small-molecule probes for imaging caspase activity in vivo, Nat Chem, 2014, 6, 519–526.
[5] Chen XY, Nanoplatform-based Molecular Imaging, Wiley, Hoboken NJ, 2011.
[6] Birks JB, Photophysics of Aromatic Molecules, London, New York, Wiley-Interscience, 1970.

[7] Luo JD, Xie ZL, Lam JWY, Cheng L, Chen HY, Qiu CF, Kwok HS, Zhan XW, Liu YQ, Zhu DB, Aggregation-induced emission of 1-methyl-1,2,3,4,5-pentaphenylsilole, Chem Commun, 2001, 18, 1740–1741.
[8] Shi H, Liu J, Geng J, Tang BZ, Liu B, Specific detection of integrin alpha(v) beta (3) by light-up bioprobe with aggregation-induced emission characteristics, J Am Chem Soc, 2012, 134, 9569–9572.
[9] Mei J, Leung NLC, Kwok RTK, Lam JWY, Tang BZ, Aggregation-induced emission: Together we shine, united we soar, Chem Rev, 2015, 115, 11718–11940.
[10] Liu J, Chen C, Ji SL, Liu Q, Ding D, Zhao D, Liu B, Long wavelength excitable near-infrared fluorescent NPs with aggregation-induced emission characteristics for image-guided tumor resection, Chem Sci, 2017, 8, 2782–2789.
[11] Leung NLC, Xie N, Yuan W, Liu Y, Wu Q, Peng Q, Miao Q, Lam JWY, Tang BZ, Restriction of intramolecular motions: The general mechanism behind aggregation-induced emission, Chem Eur J, 2014, 20, 15349–15353.
[12] Yuan WZ, Lu P, Chen S, Changing the behavior of chromophores from aggregation caused quenching to aggregation-induced emission: Development of highly efficient light emitters in the solid state, Adv Mater, 2010, 22, 2159–2163.
[13] Mei J, Hong Y, Lam JWY, Qin A, Tang Y, Tang BZ, Aggregation-induced emission: The whole is more brilliant than the parts, Adv Mater, 2014, 26, 5429–5479.
[14] Hong Y, Lam JW, Tang BZ, Aggregation-induced emission, Chem Soc Rev, 2011, 40, 5361–5388.
[15] Zhao Z, Lam JW, Tang BZ, Tetraphenylethene: A versatile AIE building block for the construction of efficient luminescent materials for organic light-emitting diodes, J Mater Chem, 2012, 22, 23726–23740.
[16] Chen J, Law CC, Lam JW, Synthesis, light emission, nanoaggregation, and restricted intramolecular rotation of 1, 1-substituted 2, 3, 4, 5-tetraphenylsiloles, Chem Mater, 2003, 15, 1535–1546.
[17] He J, Xu B, Chen F, Aggregation-induced emission in the crystals of 9, 10-distyrylanthracene derivatives: The essential role of restricted intramolecular torsion, J Phys Chem C, 2009, 113, 9892–9899.
[18] Ding F, Zhan Y, Lu X, Sun Y, Recent advances in near-infrared II fluorophores for multifunctional biomedical imaging, Chem Sci, 2018, 9, 4370–4380.
[19] Qian J, Tang BZ, AIE luminogens for bioimaging and theranostics: From organelles to animals, Chem, 2017, 3, 56–91.
[20] Yao L, Zhang S, Wang R, Li W, Shen F, Yang B, Ma Y, Highly efficient near-infrared organic light-emitting diode based on a butterfly-shaped donor-acceptor chromophore with strong solid-state fluorescence and a large proportion of radiative excitons, Angew Chem Int Ed, 2014, 53, 2119–2123.
[21] Li DY, Zhang HQ, Streich LL, Wang YL, Lu P, Wang L, Prevedel R, Qian J, AIE-nanoparticle assisted ultra-deep three-photon microscopy in the *in vivo* mouse brain under 1300-nm excitation, Mater Chem Front, 2021, 5, 3201–3208.
[22] Hao YX, Xu SP, Xu SP, Qian J, Tang BZ, Bioapplications manipulated by AIE gens with nonlinear optical effect, Chem Res Chinese U, 2020, 37, 25–37.
[23] Rice WL, Kaplan DL, Georgakoudi I, Two-photon microscopy for non-invasive, quantitative monitoring of stem cell differentiation, PLOS One, 2010, 5, e10075.
[24] Kim HM, Cho BR, Two-photon probes for intracellular free metal ions, acidic vesicles, and lipid rafts in live tissues, Acc Chem Res, 2009, 42, 863–872.
[25] Zipfel WR, Williams RM, Webb WW, Nonlinear magic: Multiphoton microscopy in the biosciences, Nat Biotechnol, 2003, 21, 1369–1377.

[26] Chow DM, Sinefeld D, Kolkman KE, Ouzounov DG, Akbari N, Tatarsky R, Bass A, Xu C, Fetcho JR, Deep three-photon imaging of the brain in intact adult zebrafish, Nat Methods, 2020, 17, 605–608.
[27] Gu B, Wu W, Xu G, Feng G, Yin F, Chong PHJ, Liu B, Precise two-photon photodynamic therapy using an efficient photosensitizer with aggregation-induced emission characteristics, Adv Mater, 2017, 29, 1701076.
[28] Wang Y, Zhang H, Alifu N, Qian J, AIE nanoprobes for multi-photon *in vivo* bioimaging, Fujiki M, Liu, B, Tang, BZ, ed, Aggregation-induced Emission: Materials and Applications, Vol. 2, Chapter 10 ACS symposium series, vol 1227 Washington, DC, ACS Publications, 2016, 245–270.
[29] Horton NG, Wang K, Kobat D, *In vivo* three-photon microscopy of subcortical structures within an intact mouse brain, Nat Photon, 2013, 7, 205–209.
[30] Qian J, Zhu Z, Qin A, Qin W, Chu L, Cai F, He S, High-order non-linear optical effects in organic luminogens with aggregation-induced emission, Adv Mater, 2015, 27, 2332–2339.
[31] Li Z, Zhang H, Li Y, Gong Y, Li D, Wang J, Li Z, Tunable aggregation-induced emission NPs by varying isolation groups in perylene Diimide derivatives and application in three-photon fluorescence bioimaging, ACS Nano, 2018, 12, 9532–9540.
[32] Wang Y, Chen M, Alifu N, Li S, Qin W, Qin A, Qian J, Aggregation-induced emission luminogen with deep-red emission for through-skull three-photon fluorescence imaging of mouse, ACS Nano, 2017, 11, 10452.
[33] Mandal AK, Sreejith S, He T, Maji SK, Wang XJ, Ong SL, Zhao Y, Three-photon-excited luminescence from unsymmetrical cyanostilbene aggregates: Morphology tuning and targeted bioimaging, ACS Nano, 2015, 9, 4796.
[34] Zhu Z, Qian J, Zhao X, Qin W, Hu R, Zhang H, Li D, Xu Z, Tang BZ, He S, Stable and size-tunable aggregation-induced emission NPs encapsulated with nanographene oxide and applications in three-photon fluorescence bioimaging, ACS Nano, 2015, 10, 588.
[35] Muller S, Wilson B, 3D microscopy of transparent objects using third-harmonic generation, J Microsc, 1998, 191, 266–274.
[36] Wang D, Qian J, AIE Luminogens for Three-Photon Fluorescence Bioimaging, Principles and Applications of Aggregation-induced Emission, Tang Y, Tang, BZ, ed, Cham, Springer International Publishing, 2019, 425.
[37] Wang S, Liu J, Feng G, Ng LG, Liu B, NIR-II excitable conjugated polymer dots with bright NIR-I emission for deep *in vivo* two-photon brain imaging through intact skull, Adv Funct Mater, 2019, 29, 1808365.
[38] Kim KY, Jin H, Park J, Jung SH, Lee JH, Park H, Kim SK, Bae J, Jung JH, Mitochondria-targeting self-assembled NPs derived from triphenylphosphonium-conjugated cyanostilbene enable site-specific imaging and anticancer drug delivery, Nano Res, 2018, 11, 1082–1098.
[39] Qi J, Sun C, Li D, Zhang H, Yu W, Zebibula A, Tang BZ, Aggregation-induced emission luminogen with near-infrared-II excitation and near-infrared-I emission for ultradeep intravital two-photon microscopy, ACS Nano, 2018, 12, 7936–7945.
[40] Zheng Z, Li D, Liu Z, Peng H, Sung HHY, Kwok RTK, Tang BZ, Aggregation-induced nonlinear optical effects of AIE gen nanocrystals for ultradeep *in vivo* bioimaging, Adv Mater, 2019, 31, 1904799.
[41] Fateminia SMA, Wang Z, Goh CC, Manghnani PN, Wu W, Mao D, Liu B, Nanocrystallization: A unique approach to yield bright organic nanocrystals for biological applications, Adv Mater, 2017, 29, 1604100.
[42] Wang YL, Han X, Xi W, Bright AIE NPs with F127 encapsulation for deep-tissue three-photon intravital brain angiography, Adv Healthc Mater, 2017, 6, 1700685.

[43] He GS, Tan LS, Zheng Q, Prasad PN, Multiphoton absorbing materials: Molecular designs, characterizations, and applications, Chem Rev, 2008, 108, 1245.
[44] Leach J, Jack B, Romero J, Jha AK, Yao AM, Franke-Arnold S, Padgett MJ, Quantum correlations in optical angle-orbital angular momentum variables, Science, 2010, 329, 662–665.
[45] Cui L, Tokarz D, Cisek R, Ng KK, Wang F, Chen J, Zheng G, Organized aggregation of porphyrins in lipid bilayers for third harmonic generation microscopy, Angew Chem Int Edit, 2015, 54, 13928.
[46] Li DY, Zheng Z, Yu TT, Tang BZ, Fei P, Qian J, Zhu D, Visible-near infrared-II skull optical clearing window for *in vivo* cortical vasculature imaging and targeted manipulation, J Biophotonics, 2020, 13, 1–27.
[47] Zhang C, Feng W, Vodovozova E, Tretiakova D, Boldyrevd I, Li Y, Zhu D, Photodynamic opening of the blood-brain barrier to high weight molecules and liposomes through an optical clearing skull window, Biomed Opt Express, 2018, 8, 2696–2708.
[48] Zong L, Zhang H, Li Y, Gong Y, Li D, Wang J, Li Z, Tunable aggregation-induced emission NPs by varying isolation groups in perylene dimide derivatives and application in three-photon fluorescence bioimaging, ACS Nano, 2018, 12, 9532–9540.
[49] Yang J, Li L, Yu Y, Ren ZC, Peng Q, Ye SH, Li QQ, Li Z, Blue pyrene-based AIE gens: Inhibited intermolecular-stacking through the introduction of substituents with controllable intramolecular conjugation, and high external quantum efficiencies up to 3.46% in non-doped OLEDs, Mater Chem Front, 2017, 1, 91–99.
[50] Li HY, Yang LY, Tang RL, Hou YQ, Yang YZ, Wang H, Han HW, Qin JG, Li QQ, Li Z, Organic dyes incorporating N-functionalized pyrrole as conjugated bridge for dye-sensitized solar cells: Convenient synthesis, additional withdrawing group on the π-bridge and the suppressed aggregation, Dyes Pigm, 2013, 79, 863–870.
[51] Zhang H, Xie W, Chen M, Zhu L, Feng Z, Wang Y, Qian J, Aggregation-induced emission NPs for *in vivo* three-photon fluorescence microscopic rat brain angiography, J Innov Opt Heal Sci, 2019, 12, 1950012.
[52] Qin W, Alifu N, Lam JWY, Cui Y, Su H, Liang G, Tang BZ, Facile synthesis of efficient luminogens with AIE features for three-photon fluorescence imaging of the brain through the intact skull, Adv Mater, 2020, 32, 2000364.
[53] Levchenko SM, Pliss A, Qu J, Fluorescence lifetime imaging of fluorescent proteins as an effective quantitative tool for noninvasive study of intracellular processes, J Innov Opt Health Sci, 2018, 11, 1730009.
[54] Qiu J, Wang L, Gao BZ, Qu J, Shao Y, Scanless multitarget-matching multiphoton excitation fluorescence microscopy, J Innov Optical Health Sci, 2018, 11, 1750013.
[55] Ni H, Xu Z, Li D, Chen M, Tang BZ, Qian J, Aggregation-induced emission luminogen for *in vivo* three-photon fluorescence lifetime microscopic imaging, J Innov Opt Heal Sci, 2019, 12, 1940005.

Yupeng Shi, Chuen Kam, Engui Zhao, Sijie Chen

Chapter 15
Advanced optical imaging and multimodality imaging based on AIEgens

15.1 Introduction

Optical imaging is an important research approach in biological sciences to observe the intricate subcellular/tissue structures and understand various physiological functions [1]. Optical or electron microscopes are used to acquire digital images of biological specimens, thus enabling analysis of various physiological processes from the resulting images [2, 3]. With the rapid development of optical imaging technique in recent years, especially the introduction of digital imaging devices and computer image analysis, researchers are able to observe the dynamic events in living cells that can never be seen before [4–6]. Fluorescence imaging technology is therefore a complementary and indispensable tool in biological and biomedical research nowadays to reveal the dynamics in physiological processes [7–9]. In comparison with other imaging techniques, fluorescence microscopy offers great flexibility such as noninvasiveness to biological system and allows for time-lapse imaging in living cells. After labeling targets of interest with fluorescent probes, researchers can acquire information such as their localizations, relative concentrations, or subcellular structures by fluorescence imaging [10]. With these data, cellular events can be traced, which are valuable information for researchers to understand the entire biological processes.

Conventional widefield fluorescence microscopes are convenient, easy-to-operate, and have two-dimensional resolution. It is widely used in almost all biological research laboratories. However, with the rapid advancing progress in biological research, this kind of imaging system lags behind the needs for current scientific and clinical research [11, 12]. As we all know, high signal-to-noise ratio (SNR) is an important parameter to evaluate the image quality in fluorescence imaging. Theoretically, prolonging the exposure time or increasing the excitation power can improve the SNR. However, shortening the exposure time or decreasing the excitation power is taken into consideration in live-cell imaging to increase frame rate or to

Yupeng Shi, Chuen Kam, Ming Wai Lau Centre for Reparative Medicine, Karolinska Institutet, Hong Kong
Engui Zhao, School of Science, Harbin Institute of Technology, Shenzhen, HIT Campus of University Town, Shenzhen, 518055, China
Sijie Chen, Ming Wai Lau Centre for Reparative Medicine, Karolinska Institutet, Hong Kong, e-mail: sijie.chen@ki.se

https://doi.org/10.1515/9783110673074-016

avoid photobleaching and phototoxicity. This inevitably lowers the SNR [12, 13]. At the same time, interference of weak energy coincidence and strong background fluorescence reduce tissue penetration, which hinders high-resolution and deep-tissue bioimaging in live animals [14]. Therefore, developing advanced optical imaging and multifunctional imaging has become important development directions to reveal details of subcellular structures, accurately track physiological changes, and obtain multiple physiological parameters.

As an indispensable component in fluorescence imaging, the fluorophore plays a core role and its photophysical properties are crucial for the performance of these advanced optical imaging systems. Brightness, photostability, and environmental sensitivity are some of the key parameters determining the spatial and temporal resolution of images acquired from the imaging system [15, 16]. Taking these factors into consideration, conventional fluorescent dyes suitable for advanced optical imaging are highly limited as many of them are photosensitive and have the problem of aggregation-caused quenching (ACQ) [17]. Many ACQ dyes are prone to form aggregates in aqueous or hydrophilic biological environments because of their hydrophobicity, leading to severe self-quenching. Therefore, ACQ dyes are usually used at low concentrations. On the one hand, this reduces the sensitivity of the fluorescent probes. On the other hand, this also makes the fluorescent molecules easily photobleached by high-energy excitation. In addition, the ACQ effect also unfavors preparation of nanoparticles (NPs) doped with organic dyes, because increasing the loading rate or aggregation degree of the dyes in each NP cannot effectively improve the brightness of the NPs [18–20].

In recent years, aggregation-induced emission (AIE) luminogens (AIEgens) have emerged as a new family of luminescent material with atypical photophysical properties. In contrast to ACQ fluorophores, molecularly dispersed AIEgens in solutions are nonemissive or weakly emissive, but their aggregates exhibit strong fluorescence. The mechanistic study of AIE phenomenon suggests that restriction of intramolecular rotation (RIR) of the AIEgen promotes the radiative decay pathway for molecule in the excited state [21]. Meanwhile, the nonplanar conformations of AIEgens also unfavor π–π stacking and therefore inhibit fluorescence quenching. These two features account for the strong emission of aggregated AIEgens, which make them bright and photostable fluorescent probes with high SNRs [22]. By using conventional fluorescence or confocal microscopy, AIE probes have excellent performance in organelle labeling, pathogen identification, cell cycle monitoring, and photodynamic therapy [23–25]. In this chapter, we will present the recent research progress of AIEgen-based fluorescent materials in advanced imaging, including super-resolution imaging, fluorescence-lifetime imaging (FLIM), fluorescence anisotropy imaging (FAIM), multiphoton imaging, and multimodality imaging.

15.2 Advanced imaging using AIEgens

15.2.1 Super-resolution imaging

The optical resolution of an imaging system is described as the minimum distance between two distinguishable points. Due to the Abbe diffraction limit, the lateral resolution of an all-optical microscope is approximately 200 nm. However, the development of super-resolution microscopy increases the lateral optical resolution beyond the diffraction limit from a few hundred nanometers to sub-100 nm. This breakthrough allows researchers to observe the ultrastructure of organelles and dynamics of biomolecules in living cells at a nanometer scale, and thus it was acknowledged by the Nobel Prize in Chemistry 2014. The current applications of AIEgens to high-resolution imaging mainly focus on stimulated emission depletion (STED) microscopy and stochastic optical reconstruction microscopy (STORM).

15.2.1.1 Stimulated emission depletion (STED)

In 1994, German physicist Stefan W. Hell developed STED microscopy, which is now the mature and widely used technique in high-resolution imaging [26]. Its working principle is to selectively deplete the fluorescence in neighboring regions of the focal position and thus minimizing the effective fluorescence to subdiffraction regions. Two laser beams, an excitation beam and a STED beam, are paired during STED imaging (Figure 15.1a). The electrons of a fluorophore are excited by the excitation laser to an excited state, while the fluorophores surrounding the focal region are selectively de-excited (Figure 15.1b) [27]. During imaging, increasing the STED beam intensity can suppress more fluorescence in the excitation point, thereby increasing the spatial resolution of STED microscopy. However, the high-intensity STED beam may also cause many practical problems to biological specimens like photobleaching and photodamage. Therefore, STED imaging usually requires fluorescent probes with excellent photostability. Besides, fluorophores with large Stokes shift not only simplify the imaging process but also minimize the re-excitation of the probe by the STED beam. Nonetheless, conventional fluorophores with large Stokes shifts often lack photostability. The development of various photostable AIEgens with strong fluorescence emissions and large Stokes shifts therefore fills the existing gap of fluorophores in high-quality STED imaging (Figure 15.2) [28–34].

The potential application of AIEgens in STED imaging was first explored by Qian and his colleagues in 2015 [28]. They compared the photostability and emission depletion efficiencies of hexaphenylsilole (HPS, a typical AIEgen) and Coumarin 102, an organic fluorophore commonly used in STED imaging. It is shown that the HPS film is much more resistant to photobleaching than Coumarin 102. Moreover, HPS-doped NPs also exhibit higher emission depletion efficiency when compared

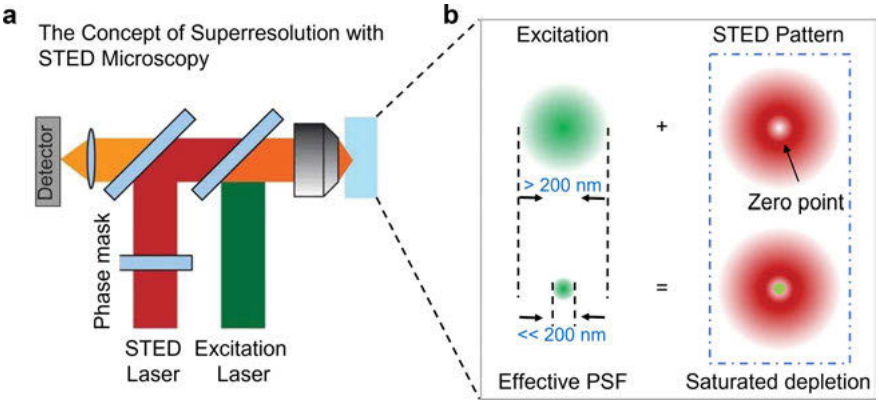

Figure 15.1: The principle of STED microscopy. (a) STED microscopy is paired with an excitation laser (green) and a STED laser (red). (b) The phase-modulated STED beam forms a focal doughnut to de-excite the fluorescence surrounding the focal position. Hence, superimposition of two laser beams leaves an effective fluorescence spot in subdiffraction regions (<200 nm in diameter) which allows nanoscale imaging. Reproduced from ref. [27] with permission from Annual Reviews.

with Coumarin 102 in solution. Comparable results are achieved only when Coumarin 102 is at a concentration seven-fold higher than that of HPS. All these advantages illustrate that AIEgens can potentially increase the spatial resolution in STED imaging.

Later, scientists demonstrate the practical applications of AIEgen-based STED imaging in live-cell organelle imaging using AIE-active small organic probes [29]. A very recent example is using AIE probes for STED imaging of lysosomes and mitochondria. In this study led by Fu et al., two high-brightness red-emitting AIE probes, **PIZ-CN** and **PID-CN**, are synthesized, which specifically label lysosomes and mitochondria, respectively, without complicated bioconjugation (Figure 15.3a) [30]. They display strong fluorescence emissions, good photostability, large Stokes shifts, and high depletion efficiency. Moreover, the measured saturation intensities of **PIZ-CN** and **PID-CN** are as low as 1.2 and 4.7 mW cm^{-2}, respectively. These results indicate that they can achieve high optical resolution with a low-power STED laser. While regular confocal microscopy is unable to resolve the ultrastructure of lysosomes and mitochondria, STED microscopy with **PIZ-CN** and **PID-CN** can easily reveal the sphere-shaped lysosomes (Figure 15.3b) and tubular mitochondria (Figure 15.3c) with high spatial resolution (69.0 and 70.9 nm, respectively). The increased optical resolution provides better observation of the organelle-related physiological processes in living cells, such as lysosomal dynamics (Figure 15.3d) and mitochondrial fusion and fission (Figure 15.3e). **PIZ-CN** and **PID-CN** are expected to serve as a superior lysosomal probe and a mitochondrial probe, respectively, in STED imaging.

Researchers have also explored the applications of AIE NPs in long-term superresolution imaging. Li et al. encapsulate a typical AIEgen (2,3-bis(4-(phenyl(4-(1,2,2-

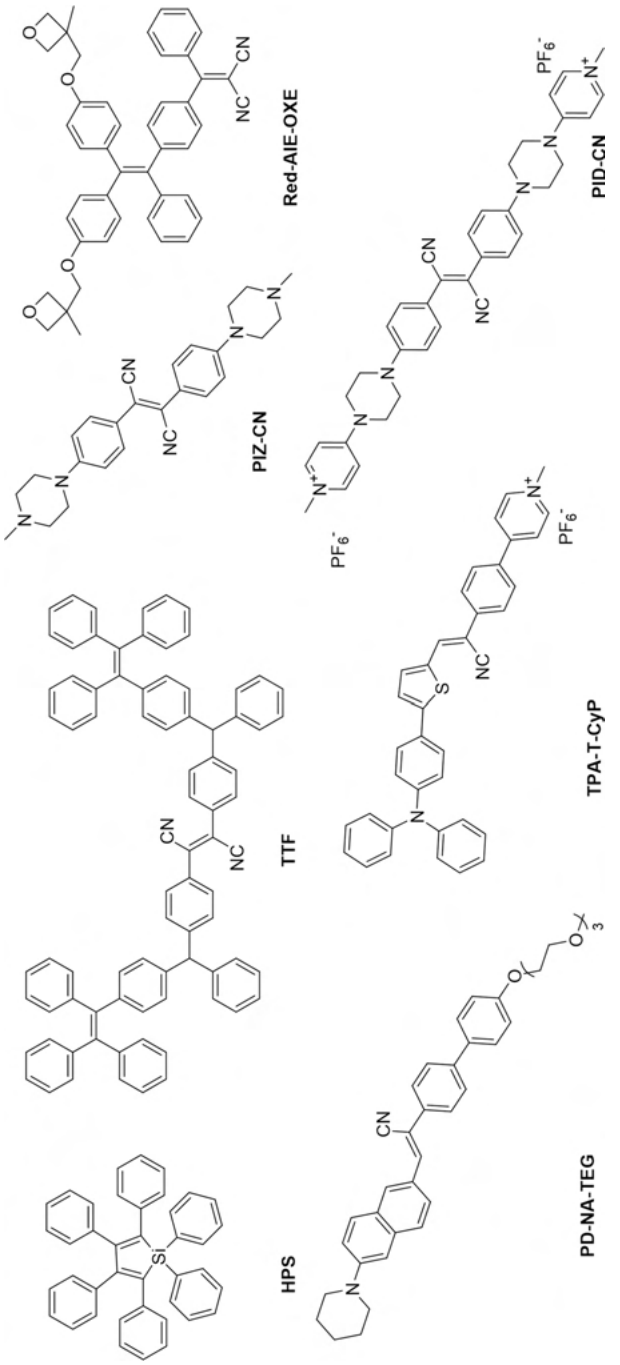

Figure 15.2: Examples of AIEgens for STED imaging.

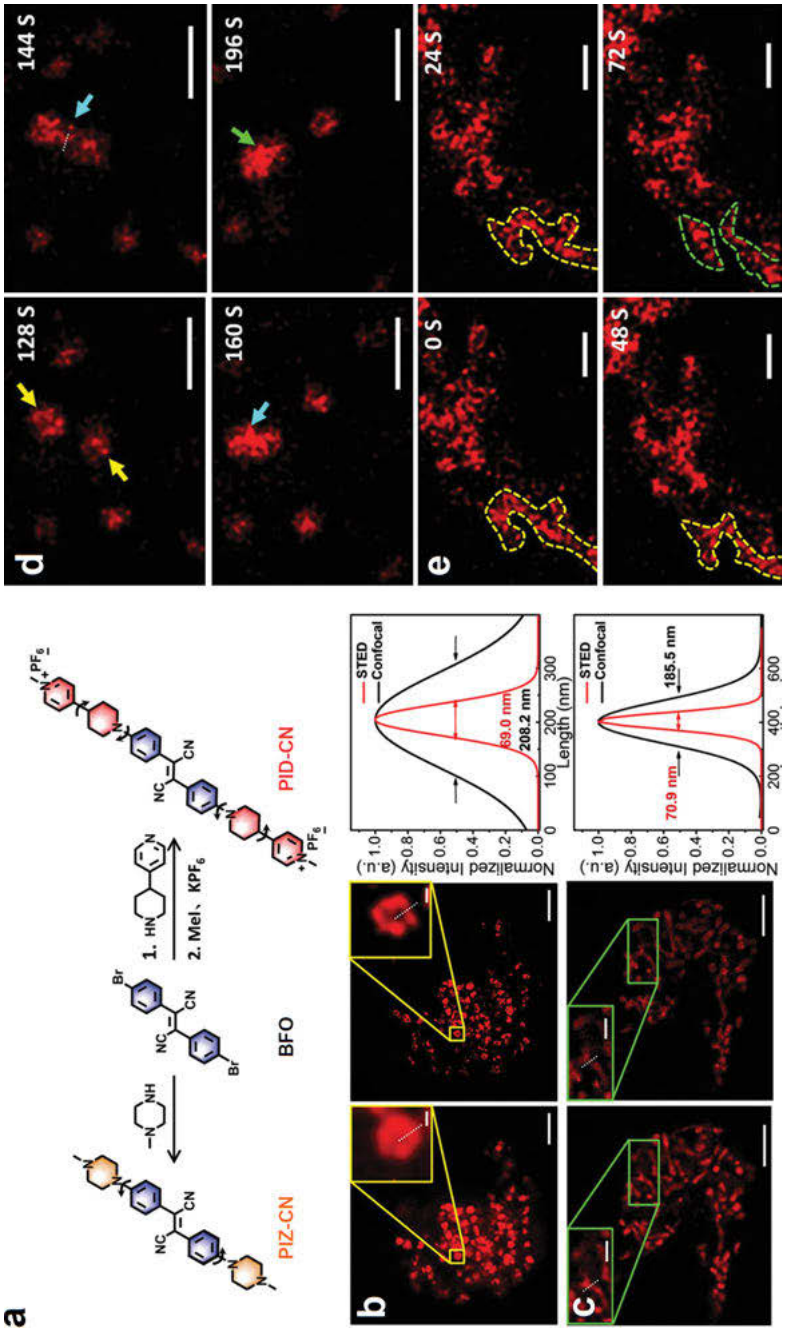

Figure 15.3: Lysosomal imaging and mitochondrial imaging using PIZ-CN and PID-CN by STED nanoscopy. (a) Structures and synthetic routes of PIZ-CN and PID-CN. (b, c) Confocal (left) and STED (right) images of lysosomes stained by PIZ-CN (b) and mitochondria stained by PID-CN (c),

triphenylvinyl)phenyl)amino)phenyl) fumaronitrile, TTF) into colloidal mesoporous silica to form fluorescent NPs with an average particle size of 24.3 nm (Figure 15.4a) [31]. The synthesized **TTF**@ SiO_2 NPs bear several significant features that can improve their optical properties. When excited by a 594-nm laser beam paired with a 775-nm STED beam at the laser power of 250 mW, **TTF**@ SiO_2 NPs possess remarkably high STED efficiency of >60%. In addition, they are highly photostable under long-term (280 s) and high-average-power excitation (312.5 mW) by the STED beam. Notably, the large Stokes shift of ~150 nm helps minimize the fluorescence background and observe single **TTF**@ SiO_2 NP. All these properties make **TTF**@ SiO_2 NPs advantageous for long-term super-resolution STED imaging. It is also shown that higher lateral resolution is obtained with a STED nanoscope when compared to a laser confocal microscope (31.2 vs 267.2 nm, respectively; Figure 15.4b). As a result, fluorescent **TTF**@ SiO_2 NPs appear to be clearer, and five NPs in close proximity can be easily distinguished. Besides, long-term ultrahigh-resolution imaging of HeLa cells shows that the fluorescence intensity of **TTF**@ SiO_2 NPs is only reduced by 30% in 30-min (1,925 s) imaging (Figure 15.4c), indicating that the NPs have excellent resistance to photobleaching.

Other than encapsulated fluorescent probes, the size of AIE-NPs also determines the quality and efficiency of subcellular labeling. Fang et al. report a new strategy to fabricate compact and ultrastable AIE nanodots through the photo-cross linking of oxetane-substituted AIEgens (**AIE–OXE**) [32]. The **AIE–OXE** nanodot with an average particle size of 15 nm exhibits ultra-stability and strong fluorescence attributed to the covalent frameworks formed inside the nanodots, which restrict the intramolecular motion. After functionalization with targeting groups, such as streptavidin, these **AIE–OXE** nanodots can recognize the biotinylated secondary antibody, which selectively binds to the primary antibody targeting to proteins of interest. By using this strategy, **AIE–OXE** nanodots are employed in microtubule imaging by STED nanoscopy. These **AIE–OXE** nanodots enjoy good photostability and are free of significant dye leakage. In the STED imaging using **AIE–OXE** nanodots, the spatial resolution can be increased to 95 nm, and the detailed structures of microtubule bundles can be observed. This streptavidin–biotin labeling approach thus enables the AIEgen-based nanodots to specifically label different subcellular structures for super-resolution imaging.

Several AIEgens tend to bind proteins and emit strong fluorescence; therefore, they have been designed to detect protein fibrillation, such as amyloid beta (Aβ) deposition. Imaging Aβ deposition in brain tissues using super-resolution technique is desirable in order to observe the fine structure of Aβ plaques with nanoscale resolution.

Figure 15.3 (continued)
respectively, in living cells. Bars for panels b and c and their insets: 3 μm and 200 nm, respectively. Corresponding fluorescence intensity profiles along the white dashed lines indicated in panel b (PIZ-CN-stained lysosomes; top) and panel c (PID-CN-stained mitochondria; bottom) are shown. (d, e) STED imaging of lysosomal dynamics (d) or dynamic change of mitochondrial morphology (e) in living cells. Bars: 1 μm. Copyright 2021 Wiley. Used with permission from ref. [30].

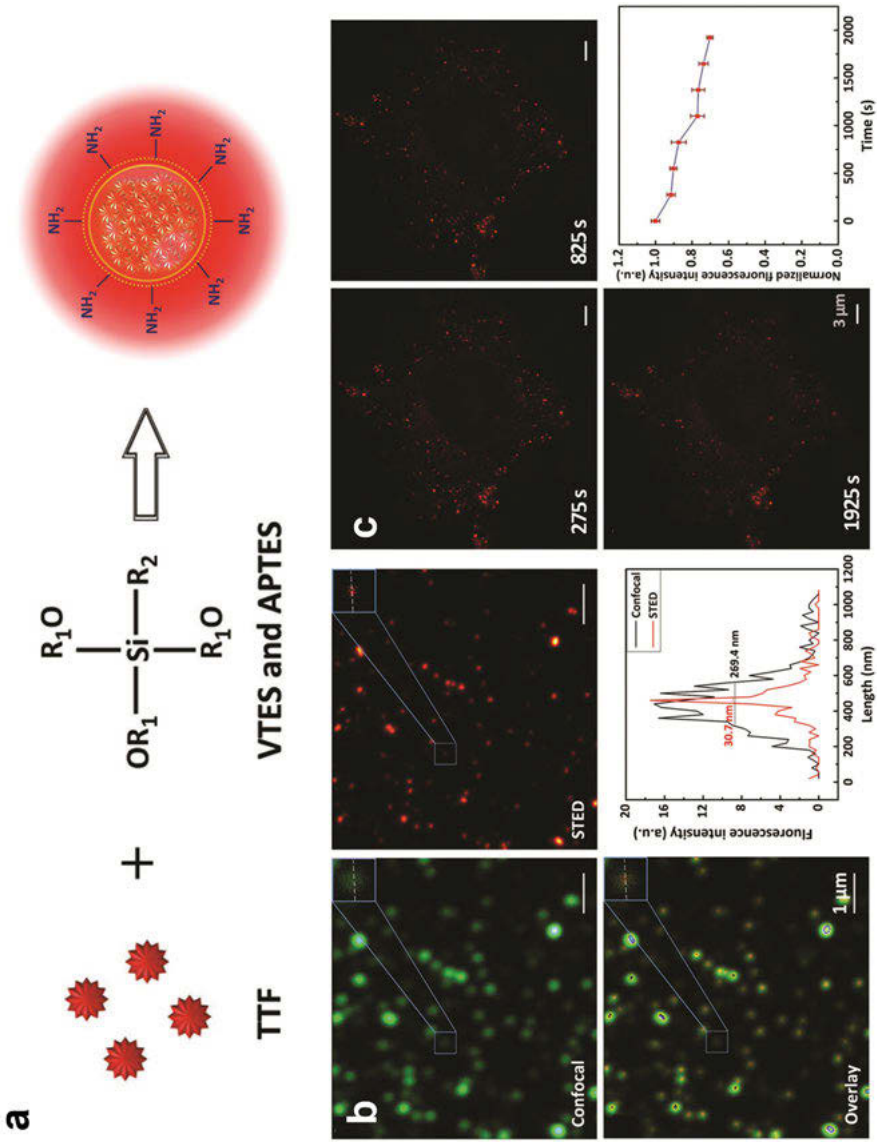

Figure 15.4: TTF@ SiO_2 NPs for STED imaging. (a) Illustration of fabrication of TTF@ SiO_2 NPs. (b) Comparison of confocal imaging and STED imaging of TTF@ SiO_2 NPs. Fluorescence intensity profiles of the NPs along the dashed lines show full-width at half-maximum of 269.4 and 30.7 nm for confocal microscopy and STED microscopy, respectively. (c) STED imaging of TTF@ SiO_2 NPs in HeLa cells taken at different time points in the period of 1,925 s. TTF@SiO_2 NPs retain ~70% of normalized fluorescence intensity in the end of imaging. Copyright 2017 Wiley. Used with permission from ref. [31].

A series of AIE-active fluorescent probes (**DM-BZ**, **PD-BZ**, **PD-NA**, and **PD-NA-TEG**) are synthesized and used for super-resolution imaging of Aβ fibrils in the brain slices of amyloid precursor protein transgenic Tg mice (Tg6799) [33]. As the AIE properties of these probes are based on Aβ-binding, it is shown that these AIEgens are excellent fluorescent probes to label Aβ plaques in the mouse brain slices. Further to regular fluorescence imaging of Aβ plaques, both **PD-NA** and **PD-NA-TEG** are shown to be compatible to super-resolution imaging (Figure 15.5a–c). In the super-resolution images, Aβ plaques show many radiant nanofibrils and **PD-NA-TEG** has a mean photon number of more than 3,000 (Figure 15.5d), providing the detailed structure of Aβ fibrillation with spatial resolution of ~30 nm (Figure 15.5e,f). Therefore, these data help understand the mechanism of amyloid plaque growth and develop new approaches for diagnosis of Alzheimer's disease.

Considering that a variety of AIEgens are widely applied to organelle labeling, intracellular tracking of biomolecules, and cancer cell imaging, it is anticipated that AIEgen-based STED nanoscopy is likely to attract the interest of scientists working in biological or biomedical areas, in which high spatiotemporal resolution is highly desirable.

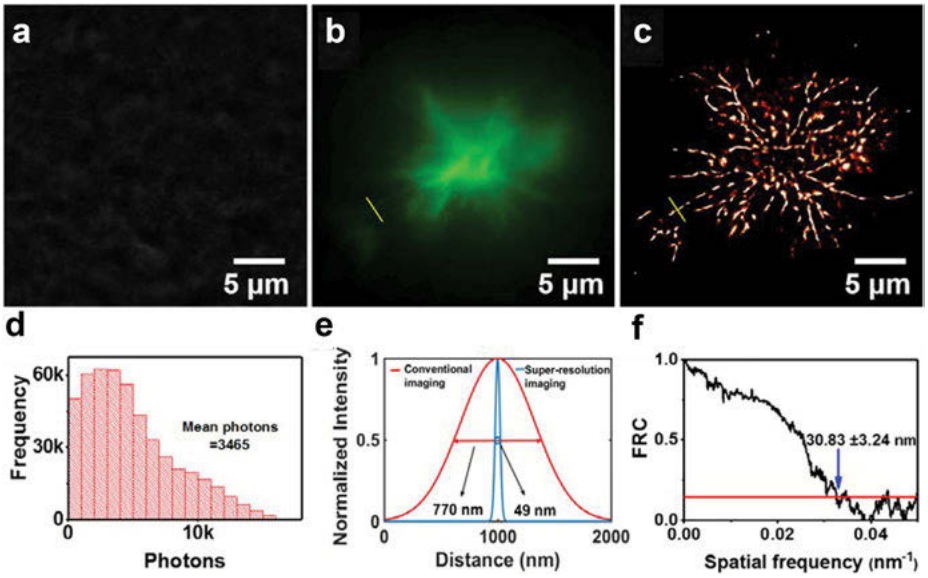

Figure 15.5: STED imaging of Aβ plaques in mouse brain slices by PD-NA-TEG. (a–c) Brightfield, confocal, and STED imaging of Aβ deposits in brain slices from a Tg6799 mouse using PD-NA-TEG. (d) The photon count distribution of PD-NA-TEG. (e) Cross-sectional profiles of PD-NA-TEG under conventional fluorescence or super-resolution imaging. (f) Fourier ring correlation (FRC) determines the image resolution to be ~30.83 nm. Reproduced from ref. [33] with permission from the Royal Society of Chemistry.

15.2.1.2 Stochastic optical reconstruction microscopy (STORM)

STORM is another type of super-resolution optical microscopy. By stochastically switching single molecules between the fluorescent state and the dark state, only a random subpopulation of fluorophores in the fluorescent state will be imaged in every single frame. Therefore, a small fraction of "switched-on" fluorophores in each frame is physically separated from each other beyond the diffraction-limited region and are optically resolvable. By capturing thousands of frames and determining the center position of single fluorophores using algorithm, a final super-resolution image can be reconstructed (Figure 15.6a) [27]. The imaging quality of STORM depends largely on the photophysical properties of the probe used. These photoswitchable fluorophores should have a high quantum yield and a high SNR to allow high-precision localization. Furthermore, a low duty cycle ensures the "switched-on" fluorophores are not densely localized in each frame. Since the advent of STORM in 2006, more and more fluorophores have been used in this imaging approach and the development of fluorophores with higher performance is still in high demand. In recent years, several AIEgens have been successfully applied in STORM imaging (Figure 15.6b) [35–39].

In 2013, Li et al. report the synthesis of a photoswitchable AIEgen, **DTE–TPE** (Figure 15.6b), by conjugating tetraphenylethylene (TPE) and dithienylethene (DTE) [35]. The structure of **DTE–TPE** can be photoswitched from the closed state (**DTE–TPE**-C) to the open state (**DTE–TPE**-O) by UV irradiation and *vice versa* by visible light (>440 nm). They are nonfluorescent in the solution. While **DTE–TPE**-C emits greenish blue fluorescence in the aggregated state, **DTE–TPE**-O remains nonfluorescence. As a result, **DTE–TPE** NPs can be photoswitched "off" by UV irradiation or photoswitched "on" by visible light. Taking advantages of the photoswitching properties of **DTE–TPE**, the **DTE–TPE**-doped film has high spatial resolution of 81 nm under STORM imaging. This demonstrates the feasibility of using AIEgens as a photoswitching probe in STORM imaging.

Gu et al. screen a new class of photoactivatable TPE derivatives for STORM imaging of mitochondria in living cells [36]. Upon photoactivation, *o*-**TPE-ON+** molecules undergo photocyclodehydrogenation and are transformed to *c*-**TPE-ON+** which is a strong emitter (Figure 15.7a). Under continuous illumination at 561 nm, *o*-**TPE-ON+** exhibits photoswitching property. Analysis of the intensity trajectory of each individual *o*-**TPE-ON+** molecule shows that the mean photon count per switching is 411 and the fluorescence on-time is 26 ms. Its photophysical properties of high photon counts and a low duty cycle favor better resolution in STORM imaging. Due to the presence of quaternary ammonium salt, *o*-**TPE-ON+** is mitochondria-specific in cells. While mitochondria are blurred under epifluorescence, their ultrastructure is revealed using STORM performed in a total internal reflection fluorescence mode (Figure 15.7b). The transverse profile of a mitochondrion has a full-width at half-maximum (FWHM) of 104.5 nm in the super-resolution image versus 697.1 nm in the epifluorescence image

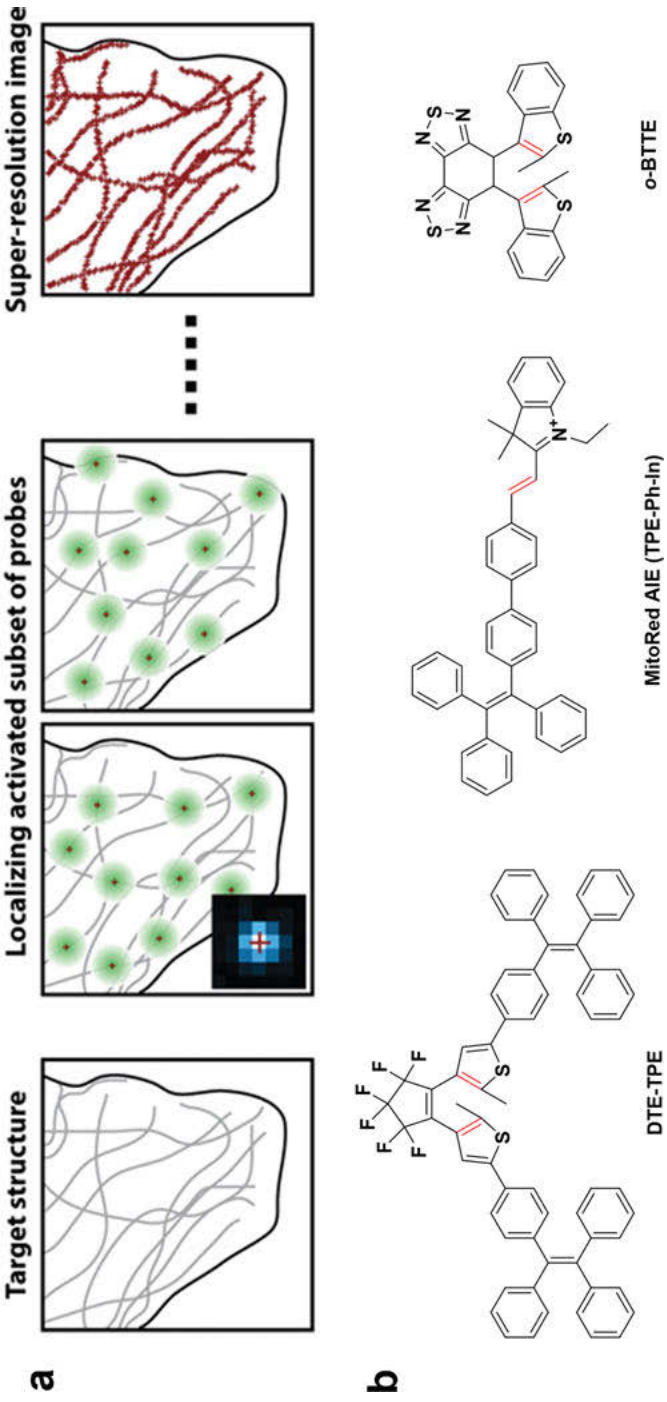

Figure 15.6: STORM imaging with AIEgens. (a) Schematic illustrations of the principle of STORM. Reproduced from ref. [27] with permission from Annual Reviews. (b) Examples of AIEgens used in STORM imaging.

(Figure 15.7c). The photoactivation of *o*-**TPE-ON**+ does not require the addition of additives during STORM imaging, which makes it compatible with long-term live-cell imaging. In the time-lapse imaging of mitochondria, detailed mitochondrial structures can be visualized with high resolution, and their fission and fusion dynamics can be recorded by using *o*-**TPE-ON**+ (Figure 15.7d).

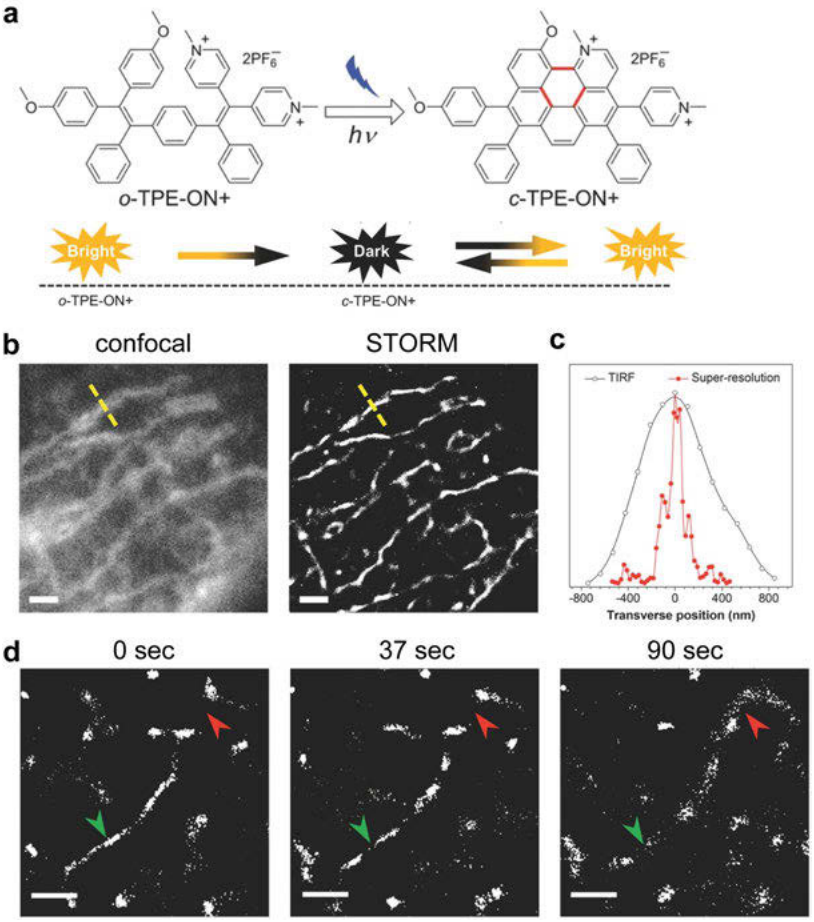

Figure 15.7: *O*-TPE-ON+ in STORM imaging of mitochondria. (a) The photocyclodehydrogenation process of transforming *o*-TPE-ON+ to *c*-TPE-ON+ under UV irradiation. (b) The diffraction-limited total internal reflection fluorescence image (left) and the STORM image (right) of mitochondria labeled with *o*-TPE-ON+ in HeLa cells. Bars: 2 μm. (c) Fluorescence intensity profiles along the yellow dashed lines across the single mitochondrion indicated in panel b. (d) STORM imaging of mitochondria labeled with *o*-TPE-ON+ in living HeLa cells shows mitochondrial dynamics of fission (green arrowheads) and fusion (red arrowheads). Bars: 500 nm. Copyright 2016 Wiley. Used with permission from ref. [36].

Lo et al. report another AIEgen for direct STORM (dSTORM) imaging of mitochondria in living cells for the observation of mitochondrial dynamics and membrane fluidity [37]. MitoRed AIE (previously known as **TPE-Ph-In**, Figure 15.6b) is a mitochondrion-specific fluorescent probe (Figure 15.8a), which undergoes spontaneous blinking. The fluorescence on-time of a single-molecule MitoRed AIE is 480 ms at a power density of 2 kW cm^{-2} and decreases significantly to 120 ms, when the power density is increased to 11 kW cm^{-2}. Meanwhile, its mean photon counts remain unchanged at ~800 at different laser power levels. When compared to MitoTracker Deep Red (MTDR), a commercial fluorescent probe for dSTORM imaging of mitochondria, MitoRed AIE demonstrates comparable mean photon counts and fraction of single molecules that can be localized but three times higher in the SNR (Figure 15.8b). The high photon count rate and the high SNR of MitoRed AIE enable its localization precision in the axial direction. By using dSTORM in three-dimensional imaging of mitochondria, the diameter of mitochondria is 100 nm in the horizontal plane and 123 nm in the axial direction. Furthermore, mitochondrial dynamics can be tracked for more than 8 min (500 s) without significant photo-induced mitochondrial fragmentation (Figure 15.8c), which enables the study of mitochondria in living cells with a high spatiotemporal resolution.

Recently, Yang et al. have demonstrated a dual AIE behavior based on sterically hindered photochromism by bridging diaromatic hydrocarbons with benzobis(thiadiazole) [38]. The superimposed effect is mainly caused by RIR, restricted intramolecular vibration, and intermolecular accumulation, which promotes the AIEgens (*o*-**BTTE** (Figure 15.6b), *o*-**ABTE**, and *ap*-**BBTE**), to have excellent AIE effects and high fluorescence quantum yield. Under the alternate change of ultraviolet (UV) and visible light, they exhibit excellent photoconversion and fatigue resistance, making them extraordinary super-resolution imaging probes. Compared with conventional fluorescence imaging, STORM imaging of *ap*-**BBTE**-doped nanostructures presents a significantly enhanced spatial resolution of ~32 nm, which is far beyond the optical diffraction limit. Notably, the FWHM in the super-resolution imaging is 12-fold higher than that in regular fluorescence imaging at 387 nm.

15.2.2 Fluorescence-lifetime imaging

FLIM is an advanced imaging technique based on measuring the fluorescence lifetime of a fluorophore. By providing the fluorescence lifetime information at microscopic spatial resolution, FLIM allows researchers to detect and visualize targets of interest in biological specimens. Besides, dynamic events can be recorded at nanoseconds resolution by FLIM. In contrast to regular fluorescence microscopy, by which the fluorescence intensity is detected for image acquisition, FLIM measures the decay rate of a fluorophore, which depends on the molecular microenvironment, such as molecular interactions or ion concentrations. Because fluorescence

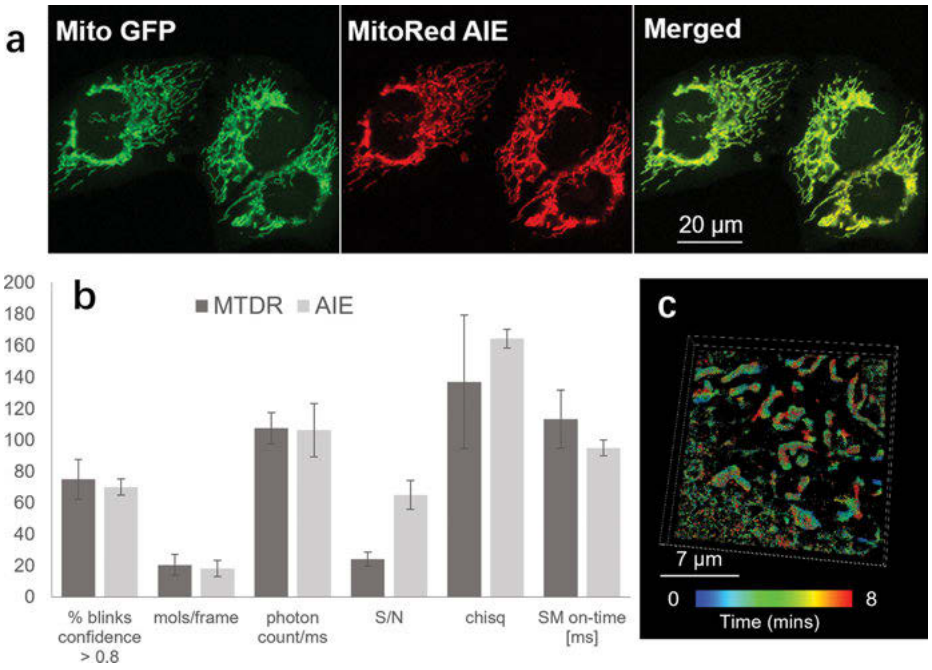

Figure 15.8: MitoRed AIE (TPE-Ph-In) in dSTORM imaging of mitochondria. (a) MitoRed AIE colocalizes with mitochondrial marker Mito-GFP in HeLa cells. Bar: 20 μm. (b) Photophysical properties of MitoRed AIE and MitoTracker Deep Red (MTDR). While both of them have comparable single-molecule blinking, MitoRed AIE has a SNR threefold higher than MTDR. (c) Three-dimensional live-cell STORM imaging of mitochondria labeled with MitoRed AIE over 8 min. Reproduced from ref. [37] under a CC-BY 4.0 International license.

lifetime is an inherent property of fluorescent materials and is closely related to the microenvironment where the luminescent materials are located, it is generally not influenced by variables, such as the fluorophore concentrations, excitation intensity, or photobleaching. As a result, FLIM is more robust than fluorescence intensity-based methods and can be used to assess physiological parameters in biological systems, such as intracellular pH, subcellular ion concentrations, oxygen contents, molecular interactions, and viscosity.

Intracellular viscosity is an important parameter for evaluating cell functions. Chen et al. employ a cell-permeable AIEgen (**TPE-Cy**, Figure 15.9) as a fluorescent probe to map the intracellular viscosity distribution in living cells [40]. Different from the conventional molecular rotors, **TPE-Cy** contains more rotatable units, which make it more sensitive to microenvironmental viscosity changes. Subsequently, a time-resolved spectral imaging system is used to perform FLIM in living cells stained with **TPE-Cy**. Under the two-photon excitation at 600 nm, the fluorescence lifetime of **TPE-Cy** in cells is widely distributed in a range from 300 to

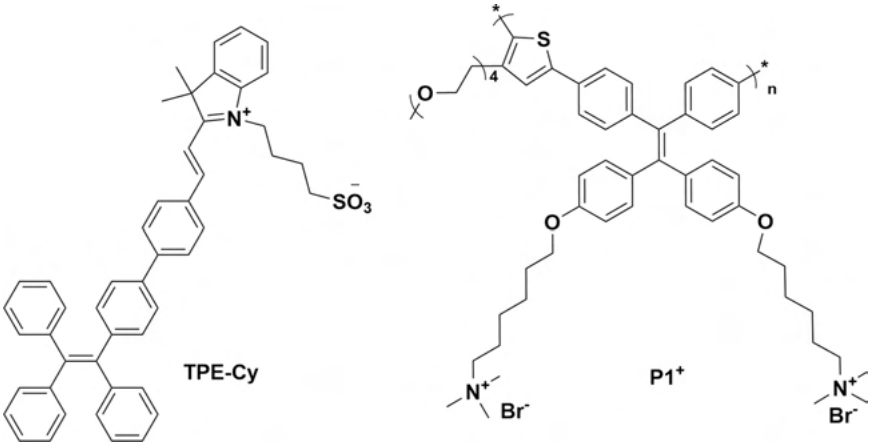

Figure 15.9: Examples of AIEgens used in FLIM.

1,500 ps. In particular, the fluorescence lifetime of **TPE-Cy** in lipid droplets (500 ps) is significantly shorter than other stained subcellular structures, such as mitochondria (1 ns). The broad distribution of **TPE-Cy** fluorescence lifetime, therefore, is useful in distinguishing different subcellular structures and reflecting changes in the intracellular microenvironment. This example demonstrates the detection of intracellular viscosity using an imaging approach.

Wang et al. crosslink a neutral TPE derivative **P1** with polyelectrolytes to prepare a water-soluble polymer $\mathbf{P1}^+$ (Figure 15.9) with AIE properties [41]. The polymer electrolyte $\mathbf{P1}^+$ has good biocompatibility and emits green fluorescence in the aggregated state. It is subsequently used to label mouse neuroblastoma neuro-2a cells for FLIM. It is found that $\mathbf{P1}^+$ molecules at high concentrations tend to be endocytosed into the cytoplasm of cells with a longer fluorescence lifetime, while those at low concentrations preferentially label the cell membrane with a shorter fluorescence lifetime. By monitoring the molecular motion of $\mathbf{P1}^+$ in the cell, it is possible to map the cellular viscosity.

Considering that AIEgens are usually viscosity sensitive, Gao et al. design a simple and effective AIE nanostructure for intracellular temperature sensing [42]. The rod-shaped nanoprobe is composed of 1,2-distearoyl-*sn*-glycero-3-phosphoethanolamine-N-[biotinyl(polyethylene glycol)-2000] (DSPE-PEG(2000)-biotin), butter, and an AIEgen of HPS (Figure 15.10a). Its working principle is as follows: At low temperatures, HPS molecules are confined in the solid butter matrix to emit strong green fluorescence. As the temperature increases, the butter gradually softens and eventually melts. This reduces the viscosity of the system and facilitates the intramolecular motion of HPS molecules, which allows nonradiative exciton decay, and results in decreased emission intensity. The thermal sensitivity of the nanoprobe is then investigated by monitoring the changes of fluorescence lifetime with temperature. As the

temperature increases, the fluorescence lifetime of HPS/butter/DSPE-PEG(2000)-biotin nanorods shows an accelerated decay trend. The fluorescence lifetime of the nanoprobe in cells is ~1.45 ns at 24.1 °C, but quickly decreases to 0.83 ns at 38.1 °C (Figure 15.10b). These results demonstrate that time-resolved fluorescence imaging is an advantageous tool for research in cell biology, especially that it does not suffer from the interference of fluorescent probe concentrations, emission intensity, and background fluorescence.

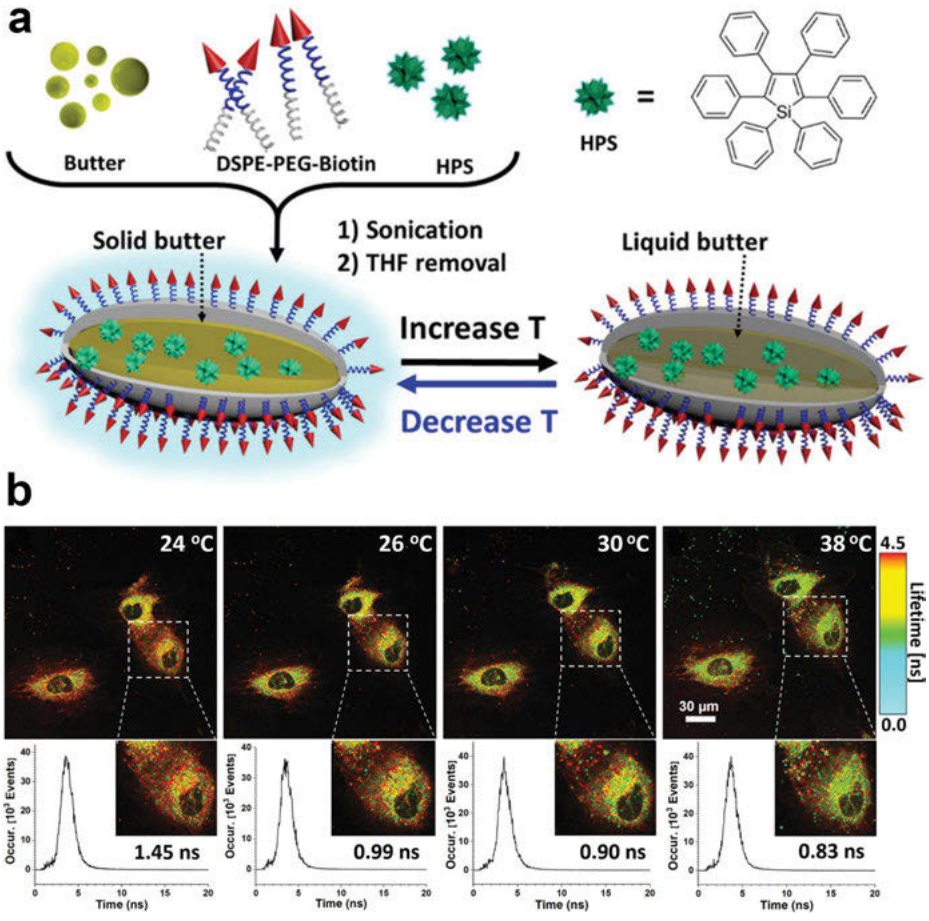

Figure 15.10: The nanorod of HPS/butter/DSPE-PEG(2000)-biotin in subcellular temperature sensing by FLIM. (a) Schematic illustration of the fabrication for the HPS/butter/DSPE-PEG(2000)-biotin nanorod and its temperature sensing. (b) The HPS/butter/DSPE-PEG(2000)-biotin nanorod in living endothelial cells is incubated at indicated temperature and is acquired by FLIM. Fluorescence lifetime of nanorods in cells is represented in pseudocolored images, and the corresponding fluorescence decay curves are shown. Reproduced from ref. [42] with permission from the Royal Society of Chemistry.

15.2.3 Fluorescence anisotropy imaging

FAIM is another imaging tool for studying physiological activities in living cells by detecting the fluorescence intensity differences of the polarized light in parallel and perpendicular planes with respect to the excitation light. In the homogeneous state, all fluorophores are randomly orientated; therefore, they exhibit the same emission intensity in all orientations. However, these fluorophores will be rotated or oriented once they are attached to large biomolecules. Their fluorescence emissions will be polarized, causing an increase in fluorescence anisotropy signals. By recording the changes in these anisotropy signals, the local environment, where the random motion of fluorophores is constrained, can be mapped.

By using this technique, Soleimaninejad et al. study the changes of protein network and the plasma membrane in cells with an AIEgen named **TPE-Py-NCS** under osmotic pressure [43]. **TPE-Py-NCS** has an amino-reactive isocyanine group (Figure 15.11a). Once entering the cell, it conjugates to the intracellular protein network. In the FAIM images, pseudo-red and pseudo-blue colors indicate subcellular regions with large fluorescence anisotropy and small fluorescence anisotropy, respectively (Figure 15.11b). By treating the cells with sorbitol to increase the osmolarity, the ratio of red-to-blue color in FAIM images increases, implying that the effect of macromolecular crowding increases the fluorescence anisotropy. Compared with the control group, the largest cell population treated with 450 mM of sorbitol has the fluorescence anisotropy increased from 0.29 to 0.35 (Figure 15.11c). In the real-time monitoring, cells treated with 450 mM sorbitol show gradual shift of the fluorescence anisotropy in 90 min (Figure 15.11d,e). In the FLIM experiment, the peak of fluorescence lifetime distribution remains at ~1.65 ns, while a minor peak at ~1.5 ns emerges when increasing osmolarity. These data suggest that the intracellular viscosity does not change abruptly upon osmotic stress as the major peak at 1.65 ns remains unchanged, while an increase in the excluded volume results in loose association of the fluorophore subpopulation with protein networks. This study demonstrates the successful exploration of AIEgens in FAIM and illustrates the feasibility of using the anisotropic signals from AIEgens to sense the biophysical microenvironment.

15.2.4 Multiphoton imaging

Single-photon excitation of AIE bioprobes is widely applied to a variety of biological fluorescence imaging. Nonetheless, the short excitation wavelength of single-photon fluorescence imaging is often accompanied with the limited tissue penetration depth and the potential photodamage to living biological specimens. Compared with single-photon imaging, multiphoton imaging has low background autofluorescence, limited photodamage, and deep tissue penetration, which is very conducive to

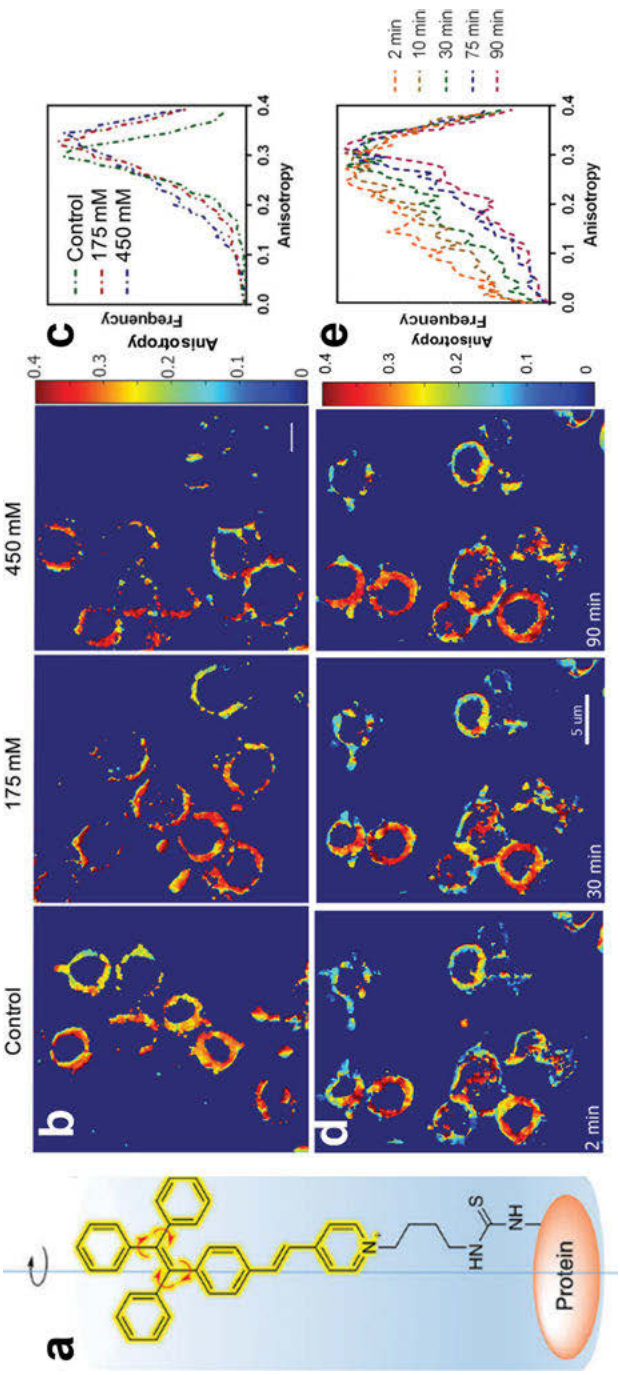

Figure 15.11: Protein imaging by TPE-Py-NCS using FAIM and FLIM. (a) Strategy of labeling proteins by amine-reactive TPE-Py-NCS and monitoring the microenvironmental change in cells by FAIM and FLIM. (b, d) FAIM of neuro-2a cells treated with 0, 175, or 450 mM of sorbitol for 30 min (b) or treated with 450 mM sorbitol for 2–90 min in the real-time monitoring (d). (c, e) The anisotropy distribution in FAIM of TPE-Py-NCS under different sorbitol concentrations (c) or at different time points under osmotic pressure (e). Reproduced from ref. [43] with permission from the Royal Society of Chemistry.

deep-tissue imaging applications. Therefore, AIEgens with large two-photon absorption cross sections and high quantum yields are designed for multiphoton imaging. At present, the main design strategy of AIEgens for multiphoton imaging is to introduce donors and acceptors into the framework of conjugated fluorophores to enhance the nonlinear optical properties of multiphoton absorption. Up to now, several new AIE probes are developed for two-photon or three-photon imaging (Figure 15.12) [44–55].

Recently, Qin et al. have prepared a red-emitting D-π-A-π-D AIEgen (**TTS**) in which arylamino units are the donor, and the benzothiadiazole core is the acceptor (Figure 15.13a) [44]. This typical fluorescent dye exhibits strong emission at 636 nm, and its solid-state fluorescence quantum yield is as high as 34.1%. By using a simple nanoprecipitation method, **TTS** nanodots decorated with DSPE-PEG are prepared, which have high water solubility and light stabilization performance for biological applications. It is worth noting that the **TTS** nanodot exhibits a large two-photon absorption cross section of 310 GM at an excitation wavelength of 900 nm, which is much higher than the conventional fluorescent protein and BODIPY dyes. Due to multiple scattering and absorption of light in the tissue, the penetration depth of single-photon imaging in the liver sections is limited to approximately 100 μm, and not beyond 120 μm. In the two-photon excitation wavelength at 900 nm, deep-tissue penetration (>200 μm) can be achieved (Figure 15.13b). In addition, **TTS** nanodots can be applied to *in vivo* two-photon fluorescence imaging of the blood vessels in mouse ears (Figure 15.13c), imaging of which is not feasible by single-photon excitation, and for the first time the capillary diameter at a depth of 110 μm in the mouse ears is quantitatively measured to be 4 μm **(**Figure 15.13d**)**. Hence, the three-dimensional reconstructed images can provide detailed information of the deep-tissue capillary networks.

On the other hand, Niu et al. design and synthesize a family of AIEgens named **NAP** for two-photon lipid droplet imaging [45]. The naphthalene-core-based **NAP** AIEgens have high fluorescence quantum yields in the solid state (up to 30%), large Stokes shifts (>110 nm), high two-photon absorption cross sections (45–100 GM at 860 nm), as well as high biocompatibility. Lipid droplets can be specifically stained by **NAP** AIEgens at a low concentration of 50 nM in 15 min. With these satisfactory results, they are used in two-photon fluorescence imaging of lipid droplets in living cells. It is demonstrated that lipid droplets at a depth of ~70 μm in living mouse liver tissues *ex vivo* can be selectively visualized.

Subsequently, Niu et al. develop other kinds of cyanostilbene-based near-infrared (NIR) AIEgens named **CS-Py$^+$SO$_3^-$** and **CS-Py$^+$** for mitochondrial imaging in living HeLa cells and living rat skeletal muscle tissues [46]. These positively charged AIEgens are able to label mitochondria specifically for *ex vivo* two-photon fluorescence imaging in rat skeletal muscle tissues at a depth of 100 μm. The impressive performances of these organelle-specific AIEgens in two-photon deep-tissue imaging

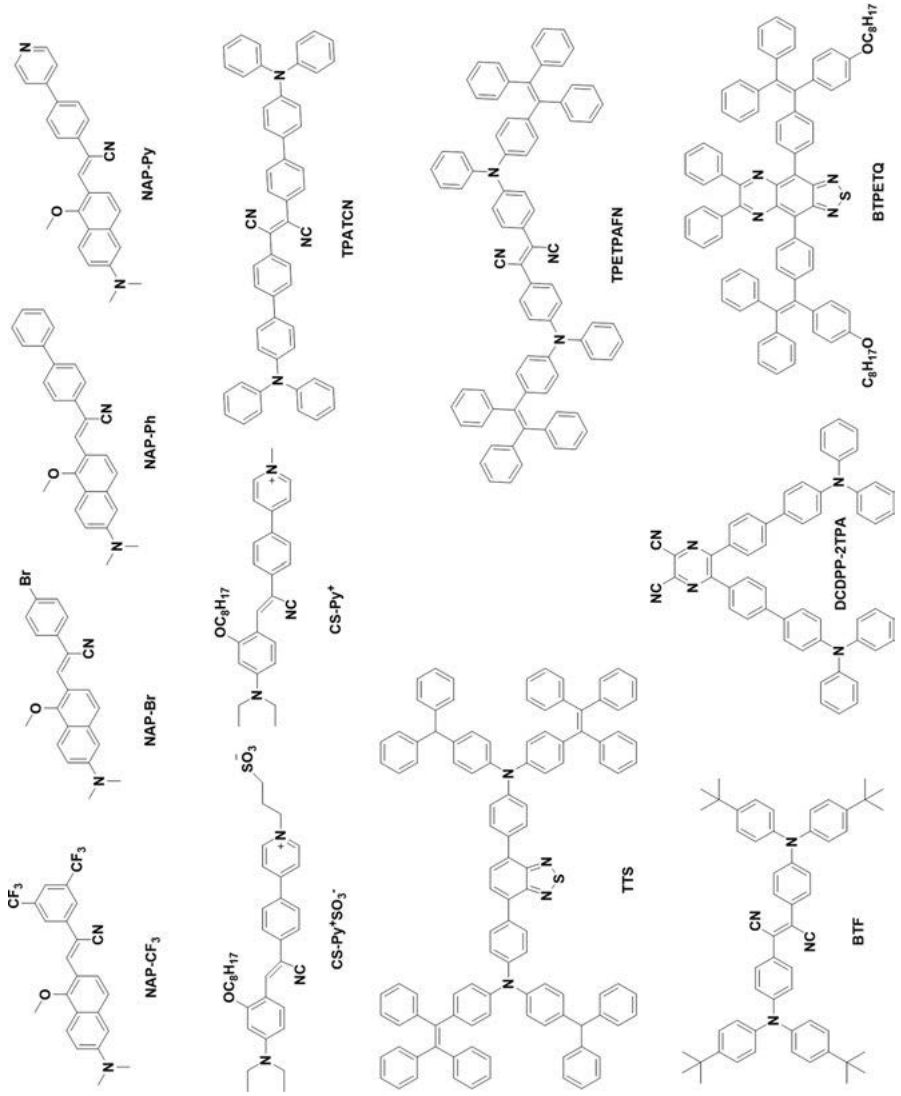

Figure 15.12: Examples of AIEgens used in multiphoton imaging.

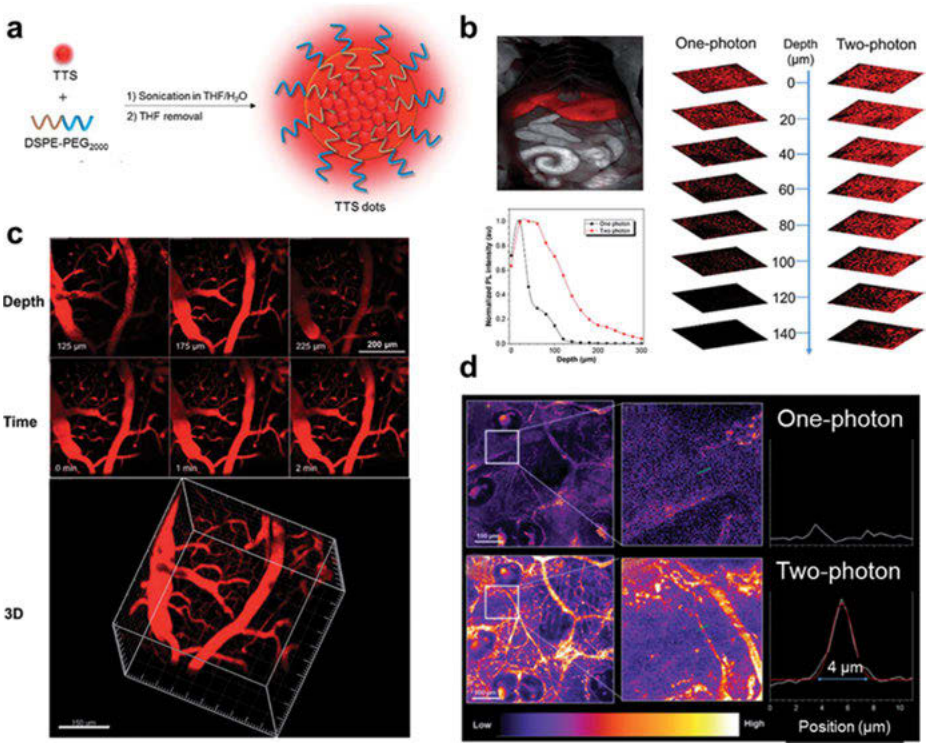

Figure 15.13: Deep-tissue imaging of blood vessels in mouse ears by TTS nanodots. (a) Schematic illustration of TTS nanodot fabrication. (b) The image of a dissected mouse under single-photon excitation (top left). Normalized photoluminescence intensity of TTS nanodots in different penetration depths under single-photon or two-photon imaging (bottom left). *Ex vivo* single-photon and two-photon confocal fluorescence images of the mouse liver injected with TTS nanodots (right). (c) Two-photon imaging of the blood vessels in a mouse brain injected with TTS nanodots at different penetration depths or monitoring time points. The reconstructed 3D image shows the blood vasculature in the mouse brain. (d) Single-photon (top), two-photon (bottom), and their corresponding zoomed images of blood vessels in mouse ears. Quantitative measurement of cross-sectional intensity profiles from two-photon imaging shows the diameter of capillary to be ~4 μm. Reproduced from ref. [44] with permission from the Royal Society of Chemistry.

illustrate their potential in visualization and monitoring of diseases associated with organelle dysfunctions, such as fatty liver disease and mitochondrial myopathies.

For clinical research and treatment of vascular-related diseases and cancers, deep-tissue fluorescence imaging of vascular morphology and intravascular dynamics in the brain and tumors is highly desirable. The use of NIR-II excitation (1,000–1,700 nm) in fluorescence imaging has deep penetrating power, high SNR, and reduced photodamage to biological tissues. Wang et al. design a high-brightness probe (**BTPETQ**) with long-wavelength absorption for *in vivo* two-photon fluorescence imaging of mouse brains and tumors (Figure 15.14a) [47]. **BTPETQ** dots are

prepared by the nanoprecipitation method and have an average particle size of 42 nm. The nanoprobe is excitable by the laser of NIR-II at 1,200 nm, showing high-brightness fluorescence emission with central wavelength at 700 nm and a high quantum yield of ~19%. In tumor vasculature imaging through the mouse ear skin, NIR-II excitation at 1,200 nm shows a deeper penetration depth than the NIR-I excitation (920 nm) for the **BTPETQ**-labeled vessels (Figure 15.14b,c). **BTPETQ** dots also show two-photon fluorescence with a high SNR in leaky tumor vasculature, which is distinguished from normal blood vessels. By using NIR-II excitation, **BTPETQ** dots in tumors at the depth of 200–300 μm show a higher signal-to-background ratio when compared with NIR-I excitation (Figure 15.14d,e). This study illustrates the potential application of effective NIR-II fluorophores for deep-tissue and high-contrast tumor imaging *in vivo*.

When compared with two-photon microscopy, three-photon microscopy has improved penetration depth with a remarkable SNR in deep-tissue imaging. To demonstrate the applicability of AIEgens in three-photon imaging, Wang et al. fabricate an AIE NP using AIEgen **DCDPP-2TPA** with a strong deep-red emission [48]. The **DCDPP-2TPA** NP can be excited by a femtosecond laser of 1,550 nm, and brain vasculature at a penetration depth of 785 μm can be imaged in the skull-opened mouse by *in vivo* three-photon imaging. Encouraged by this performance, they further demonstrate that the capillary with a diameter of 2.4 μm can be imaged by using **DCDPP-2TPA** NPs at the penetration depth of 300 μm even in the mouse with intact skull. This indicates the potential broad applications of AIEgens in non-invasive *in vivo* imaging.

Liu et al. find that a red AIEgen, named 2,3-bis(4′-(diphenylamino)-[1,1′-biphenyl]-4-yl) fumaronitrile (**TPATCN**), possesses three-photon fluorescence signals with a deep-red emission under the excitation at 1,550 nm [49]. By co-encapsulating **TPATCN** and an NIR dye NIR775, the **TPATCN–**NIR775 NP has an ultra-high imaging depth of 730 μm in the fluorescence imaging of vessels in the mouse brain. The subsequent vivid three-dimensional reconstructed images clearly show the tiny blood vessels, which are very helpful for the research of cerebrovascular diseases.

Recently, another type of non-TPE-based AIEgen has been facilely synthesized for three-photon imaging (Figure 15.12) [50]. The bright far-red/NIR AIEgen named **BTF** has a high quantum efficiency of 42.6% in the solid state. The fabricated **BTF** nanodot (Figure 15.15a) has a large three-photon absorption cross-section for *in vivo* imaging of brain vessels by NIR-II laser excitation (Figure 15.15b,c). In mice with intact skull, cerebral stroke can be traced noninvasively by three-photon imaging (Figure 15d,e). This is of great significance for the study of the complex cerebral vasculature using three-photon fluorescence microscopy to understand the pathogenesis of encephalopathy.

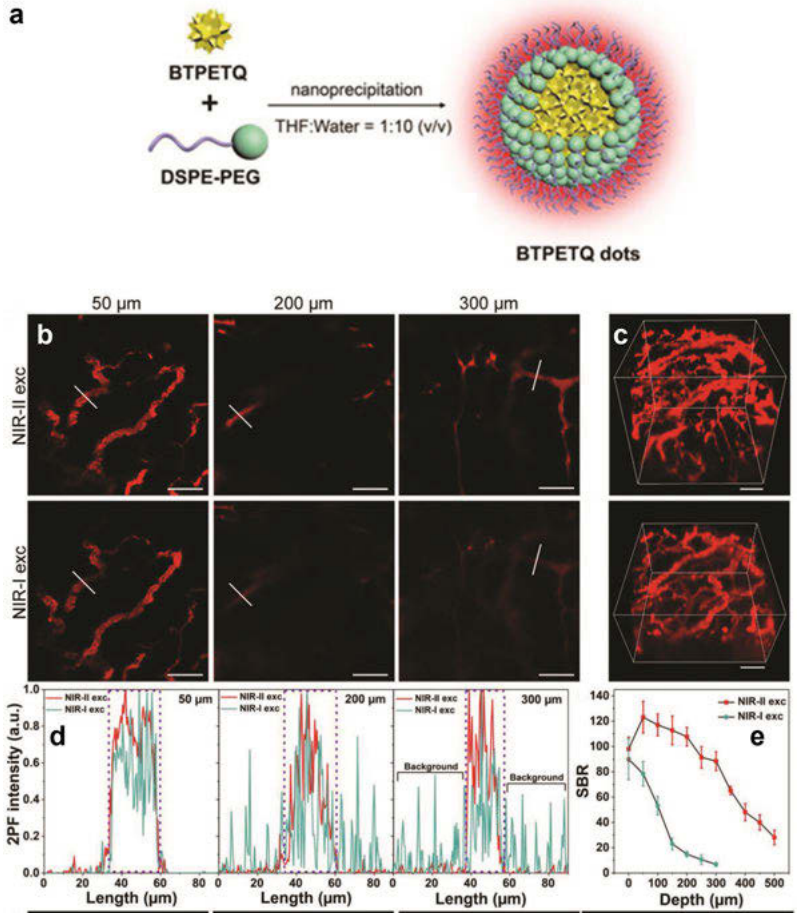

Figure 15.14: Tumor vasculature imaging in mice by BTPETQ under two-photon imaging. (a) A schematic illustration of BTPETQ dot fabrication. (b) Two-photon fluorescence images at different imaging depths and their reconstructed three-dimensional image of tumor blood vessels labeled with BTPETQ dots under NIR-II (1,200 nm) excitation. Bars: 100 μm. (c) Two-photon fluorescence images and their reconstructed three-dimensional images of the same tumor vasculature networks under NIR-II (1,200 nm) or NIR-I (920 nm) excitation. Bars: 100 μm. (d) The normalized fluorescence intensity profiles along the white lines indicated in panel b with NIR-I or NIR-II excitation. (e) NIR-II excitation shows a higher signal-to-background ratio (SBR) when compared with NIR-I excitation in the depth of 200–300 μm. Copyright 2019 Wiley. Used with permission from ref. [47].

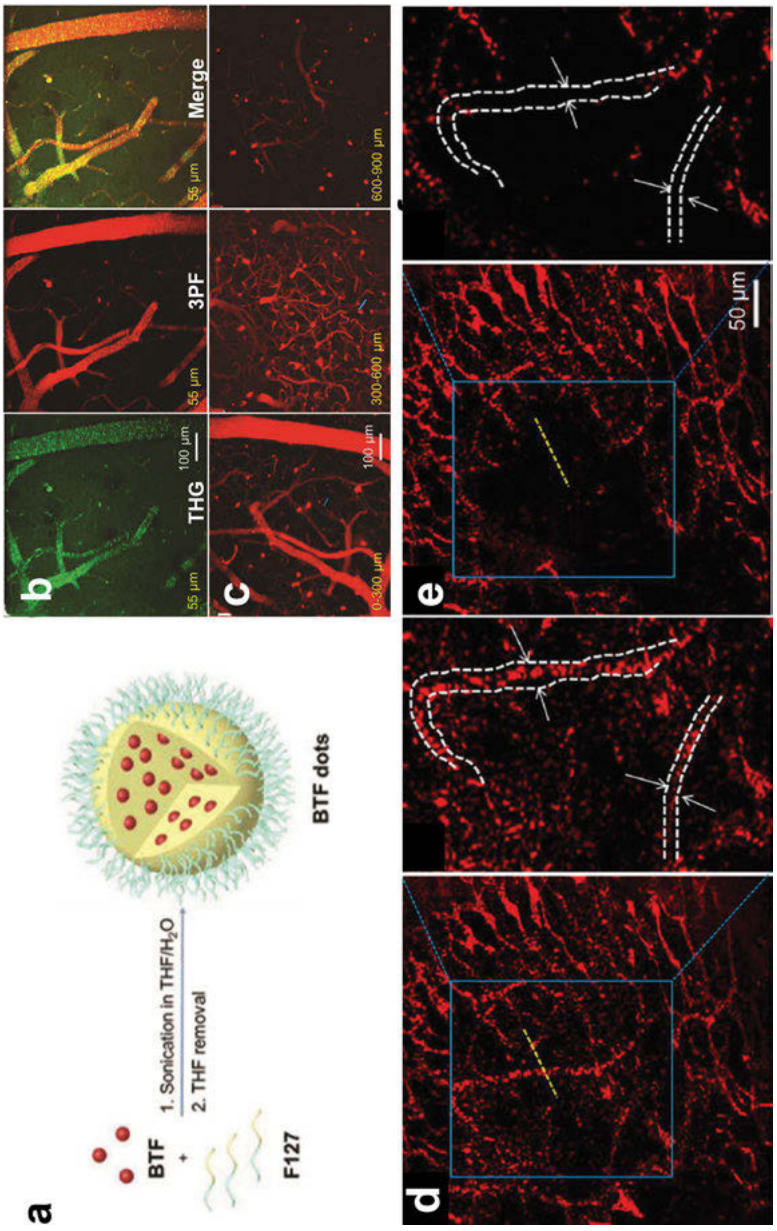

Figure 15.15: *In vivo* brain vascular imaging by BTF dots under three-photon imaging. (a) Schematic illustration of BTF dot fabrication. (b) Third-harmonic generation (THG), three-photon fluorescence (3PF), and merged image of the mouse brain vessels at penetration depth of 55 μm. (c) *In vivo* three-photon imaging of brain vessels at penetration depths from 0 to 900 μm. (d–e) Three-photon fluorescence images of blood vessels in the brain of a mouse with the intact skull before (d) and after (e) brain thrombosis. Copyright 2020 Wiley. Used with permission from ref. [50].

15.3 Multimodality imaging

Multimodality imaging refers to integration of two or more imaging modes and takes full advantage of each individual mode to overcome its inherent limitations. Despite fluorescence imaging has excellent imaging sensitivity reaching the single-molecule level, restricted tissue penetration depth limits its applications in *in vivo* deep-tissue imaging. In contrast, the commonly used medical imaging techniques, such as computed tomography (CT), magnetic resonance imaging (MRI), and photoacoustic imaging (PAI), have high tissue penetration depths but low sensitivity. As a result, multimodality imaging combining fluorescence and other imaging approaches is expected to achieve deep-tissue penetration, high spatial resolution, and excellent sensitivity. The superior optical properties of the AIEgens make them very suitable for constructing multimodal fluorescent probes. Currently, a variety of multimodality imaging techniques, such as fluorescence CT, fluorescence MRI, fluorescence positron emission tomography (PET), fluorescence PAI, and fluorescence Raman, based on AIE bioprobes have been developed and used in *in vivo* imaging.

15.3.1 Fluorescence computed tomography

X-ray CT is one of the widely used imaging techniques in clinical practice with high spatial resolution and ideal penetration depth. Nonetheless, the CT scan has the drawback of low sensitivity. Therefore, multimodality imaging combining fluorescence and CT can complement each other to offer high sensitivity and high penetration depth. As an intensively studied CT contrast agent, the gold NP has a high X-ray absorption coefficient. The bimodal contrast agent constructed by combining gold NPs with fluorescence imaging is expected to offset the low sensitivity of CT. Nonetheless, careful design is required to avoid the quenching effect of gold NPs to fluorescent probes. Zhang et al. prepare a dual-functional nanoprobe named M-**NPAPF**-Au by co-loading red AIEgen **NPAPF** and hydrophobic gold NPs into DPE-PEG(2000) micelles for bimodal fluorescence-CT imaging [56]. The prepared NPs with an average diameter of ~65 nm have an emission peak at ~640 nm and a large Stokes shift of ~120 nm. Surprisingly, **NPAPF** inside the NPs effectively overcomes the strong fluorescence quenching induced by the gold NPs and retains a high quantum yield of 8%. The data show that the probe has excellent biocompatibility, long blood circulation time, and excellent tumor targetability. Moreover, *in vivo* studies demonstrate that the nanoprobes show excellent tumor-targeting capability, superior fluorescence emission, and high-quality CT imaging. All these data illustrate that M-**NPAPF**-Au is a bimodal fluorescence-CT nanoprobe that has potential applications in noninvasive tumor imaging.

Using different design concepts, He et al. successfully design a novel type of silver@AIEgen core–shell NPs (AACSNs) to achieve multimodal fluorescence imaging,

dynamic force microscopy (DFM) imaging, and CT [57]. The AACSN is fabricated by a redox reaction between phenolic hydroxyl in the redox-active AIEgen **TPE-M2OH** and silver ions (Figure 15.16a). The formation of silver NPs will induce the AIEgens to aggregate around the NPs at the same time, thus forming a core–shell hybrid nanostructure. Noteworthy, the shell thickness of AACSNs can be tuned by changing the concentration of **TPE-M2OH** to make it larger than the Förster energy transfer distance to retain fluorescence and plasmon modes. More importantly, AACSNs have excellent photostability and biocompatibility, which enable live-cell imaging by bimodal fluorescence and DFM imaging (Figure 15.16b). *In vivo* imaging shows that AACSNs are enriched in the tumors 2 h after the intratumoral injection of AACSNs into tumor-bearing nude mice (Figure 15.16c). The CT signal in tumors is increased by as much as 183 HU at 5 h after injection and is gradually cleared in 10 h. The utilities of superior photophysical properties of AIEgens in DFM and the deep penetration depth in CT expand the applicability of bimodal fluorescence-CT imaging in future diagnosis.

15.3.2 Fluorescence magnetic resonance imaging

As a noninvasive imaging technique, MRI has attracted widespread attention over the past three decades because of its high spatiotemporal resolution, excellent penetration depth in soft tissues, as well as no radiation exposure. However, the sensitivity of MRI is unsatisfactory. Therefore, imaging probes used in MRI, fluorescence imaging, and other functional modules are attempted to integrate into single nanomaterial matrix for multimodality imaging. Conventional MRI contrast agents are chelates based on paramagnetic metal ions with unpaired electrons (Gd^{3+}, Mn^{4+}, Fe^{3+}, etc.), which can reduce the T_1 and T_2 relaxation times of the neighboring proton spins. The commonly used synthesis strategies for fluorescence-magnetic resonance probes are simply co-encapsulating Gd chelates and AIEgens with DSPE-PEG, amphiphilic polymer, or mesoporous silica by nanoprecipitation, self-assembly, or chemical cross-linking [58–60]. A variety of dual-functional nanoprobes are reported to image tumors and blood vessels, and to evaluate the antibacterial efficacy.

Chen et al. fabricate a dual-mode contrast agent by conjugating two hydrophilic moieties of gadolinium-diethylenetriaminepentaacetic acid to a hydrophobic TPE fluorophore through a click reaction (Figure 15.17a) [61]. Interestingly, amphiphilic **TPE-2Gd** molecules spontaneously aggregate in water and PBS solution at concentrations above 70 and 50 μM, respectively, to form nanoaggregates or micelles, which exhibit strong fluorescence. **TPE-2Gd** nanoaggregates can be endocytosed, showing negligible cytotoxicity and excellent photostability in cell imaging (Figure 15.17b). Meanwhile, the longitudinal relaxation of **TPE-2Gd** in water is determined to be 3.36 $mM^{-1}\ s^{-1}$ which is comparable to the commercial agent Magnevist ($R_1 = 3.70\ mM^{-1}\ s^{-1}$). **TPE-2Gd** nanoaggregates show a long circulation lifetime in rats of 1 h and specifically accumulate in the liver even 150 min after the injection.

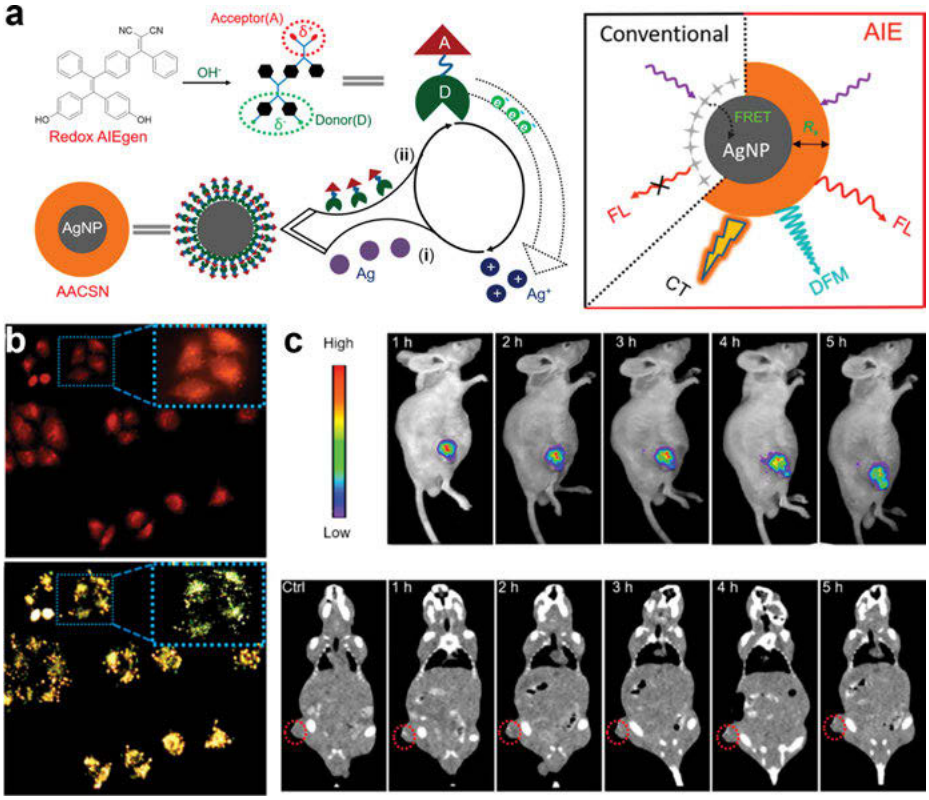

Figure 15.16: Fluorescence CT of tumors in mice using AACSNs. (a) Chemical structure of TPE-M2OH and a schematic illustration of AACSN fabrication. (b) Fluorescence (top) and dark-field microscopy (bottom) images of AACSN probes in HeLa cells. (c) Fluorescence (top) and CT (bottom) imaging of nude mice with tumors 1–5 h after intravenous injection of AACSN nanoagents. Reprinted with permission from ref. [57]. Copyright 2018 American Chemical Society.

Because of the disintegration into small molecules, **TPE-2Gd** NPs can be excreted via renal filtration (Figure 15.17c). This study demonstrates that **TPE-2Gd** is a potential MRI contrast agent specific to the liver.

Monitoring apoptosis is important for evaluating cancer therapy and screening preclinical anticancer drugs. During apoptosis, caspase-3/7 is activated and therefore their enzymatic activities are commonly used as apoptotic biomarkers. Li et al. design and synthesize a bimodal fluorescence-magnetic resonance probe which is responsive to caspase-3/7 activities (Figure 15.18a) [62]. Caspase probe 1 (CP1), which is composed of an MR contrast agent Gd-DOTA chelate, AIEgen TPE, and a caspase-3/7 substrate DEVD peptide, is soluble in aqueous solutions. In the presence of active caspase-3/7, the hydrophilic DEVD is enzymatically cleaved, which causes the remaining Gd-TPE more hydrophobic and spontaneously aggregates,

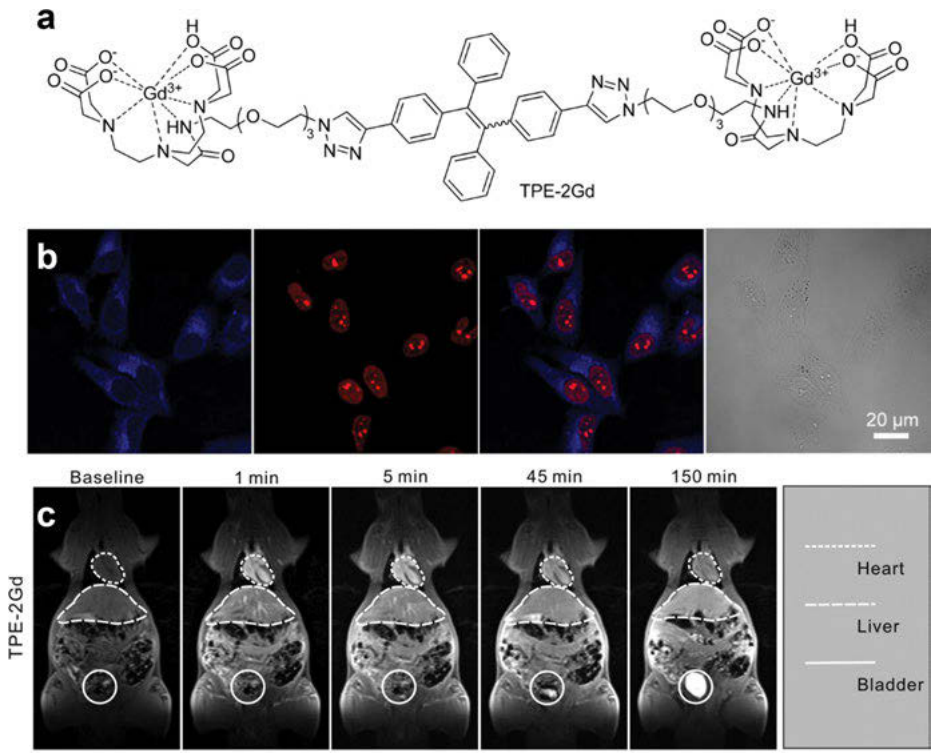

Figure 15.17: Fluorescence magnetic resonance imaging in mice using TPE-2Gd. (a) Structure of TPE-2Gd. (b) Fluorescence imaging of HeLa cells stained with TPE-2Gd (blue) and propidium iodide (red), merge of these two panels, and the brightfield image. (c) Coronal MRI of a rat before and 1–150 min after intravenous injection of TPE-2Gd. TPE-2Gd can be excreted in the urine as demonstrated by concentrating in the bladder. Reprinted with permission from ref. [61]. Copyright 2014 American Chemical Society.

leading to the enhancement of fluorescence and MR signals. This dual fluorescence-magnetic resonance "turn-on" strategy is successfully applied to monitoring the apoptotic cell (Figure 15.18b). Remarkably, the T_2-weighted MRI of this responsive probe can be used to evaluate caspase-3/7 activities *in vitro* (Figure 15.18c). This provides a promising approach for further developing multifunctional imaging agents against different targets.

In contrast to Gd agents, superparamagnetic Fe_3O_4 (SPIO) NPs have the advantages of good biocompatibility, high magnetic properties, and ease of surface modification, which are widely applied in various medical applications of MRI [63–65]. Meng et al. design an efficient fluorescent-magnetic multifunctional probe by co-encapsulating AIEgen **TB** and SPIO with polystyrene–PEG [63]. The fabricated TSP NPs exhibit red-emitting AIE properties with a maximum emission at 655 nm and a high fluorescence quantum yield of 14.6%, which help enhance the sensitivity and the SNR in

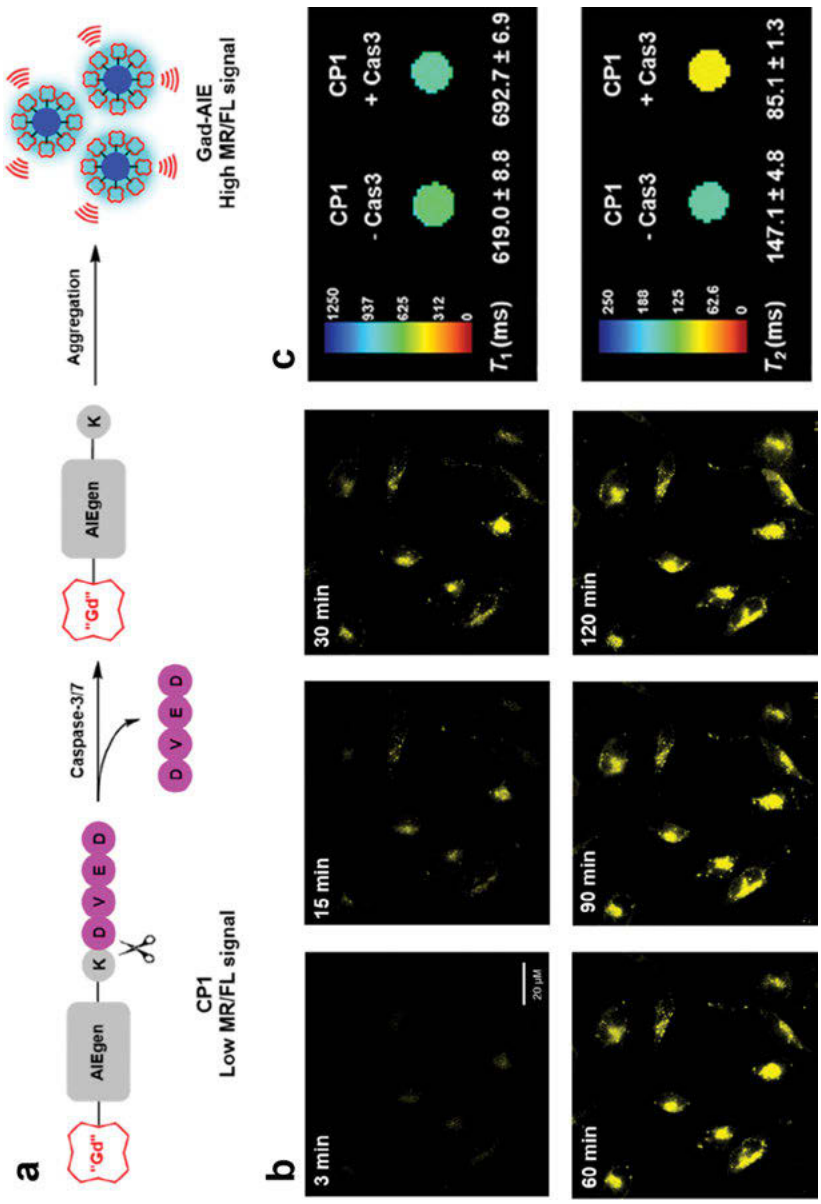

Figure 15.18: Caspase-3/7 activity-dependent fluorescence MRI using CP1. (a) Schematic illustration of CP1 turned on by the enzymatic activity of caspase-3/7. (b) Time-lapse fluorescence imaging of HeLa cells incubated with CP1 and treated with the apoptotic agent staurosporine for 3–120 min. (c) T_1-weighted (top) and T_2-weighted (bottom) MRI of CP1 and CP1-control (ctrl) solutions, respectively, incubated with or without caspase-3 overnight. T_2-weighted MRI of CP1 is sensitive enough to detect caspase-3 activity. Reprinted with permission from ref. [62]. Copyright 2012 American Chemical Society.

fluorescence imaging. TSP NPs have great superparamagnetism and relaxation properties, which can be used for MRI and magnetic particle imaging (MPI). Because of the high biocompatibility and photostability, TSP NPs are suitable for long-term fluorescence imaging. *In vivo* fluorescence imaging shows that the growth of subcutaneous tumors can be monitored by TSP NPs in real-time for more than 24 days. The multimodal probe composed of fluorescence imaging, MRI, and MPI has remarkable tissue penetration depth and high spatiotemporal resolution which can monitor liver tumors *in situ*.

15.3.3 Fluorescence positron emission tomography

PET is an advanced imaging technique in clinical nuclear medicine. It uses short-lived radionuclides to label glucose, proteins, nucleic acids, fatty acids, etc., followed by injection into the body to reflect their metabolic activities and to achieve the purpose of diagnosis. PET imaging is noninvasive, highly sensitive, and specific. It is commonly used in surveillance for liver metastases or after liver transplant, as well as in the cancer diagnosis and therapy. However, its spatial resolution is very poor with only less than 1 cm for medical scanners. Hence, the high sensitivity and spatial resolution of fluorescence imaging can make up for the shortcomings of PET.

Bimodal fluorescence-PET agents can locate the lesion according to PET imaging and allow for surgical removal of the lesion under the guidance of fluorescence imaging. Liu et al. design a PET probe named [$^{nat/68}$Ga] **5** based on AIE and can be uptaken by hepatic macrophages [66]. By modifying derivatives of TPE, it is possible to complex $^{nat}Ga^{3+}$ or $^{68}Ga^{3+}$, thereby integrating the chelating agent, AIEgens, and gallium ions into a single unit (Figure 15.19a). [^{nat}Ga] **5** has AIE properties and forms micelles in the nanometer scale, when its concentration is higher than the critical micelle concentration of 1 μM (Figure 15.19b). To explore the mechanism of [$^{nat/68}$Ga] **5** in liver imaging, liver-resident macrophages Kupffer cells and hepatic HepG2 cells in culture are incubated with [^{nat}Ga] **5** for 10, 30, and 120 min, respectively. Surprisingly, [^{nat}Ga] **5** fluoresces in the Kupffer cell membrane at 10 min but not in HepG2 cells even after 120 min. Further radiation experiments reveal that Kupffer cells have a significantly higher uptake of [$^{nat/68}$Ga] **5** than HepG2 cells. These data suggest that functional liver imaging is mainly attributed to uptake of [^{nat}Ga] **5** by Kupffer cells. After intravenous injection of [$^{nat/68}$Ga] **5** into rats, *in vivo* fluorescence imaging and autoradiography illustrate that [$^{nat/68}$Ga] **5** mainly accumulates in the liver (Figure 15.19c), and *in vivo* PET imaging exhibits a high liver-to-muscle ratio, which suggests that the liver has a slow washout rate (Figure 15.19d). Therefore, [$^{nat/68}$Ga] **5** can potentially serve as a liver-specific contrast agent for clinical PET imaging.

Aromatase is an enzyme that synthesizes estrogens and is a target to treat breast cancer. Wu et al. design a bifunctional complexing agent for targeting the

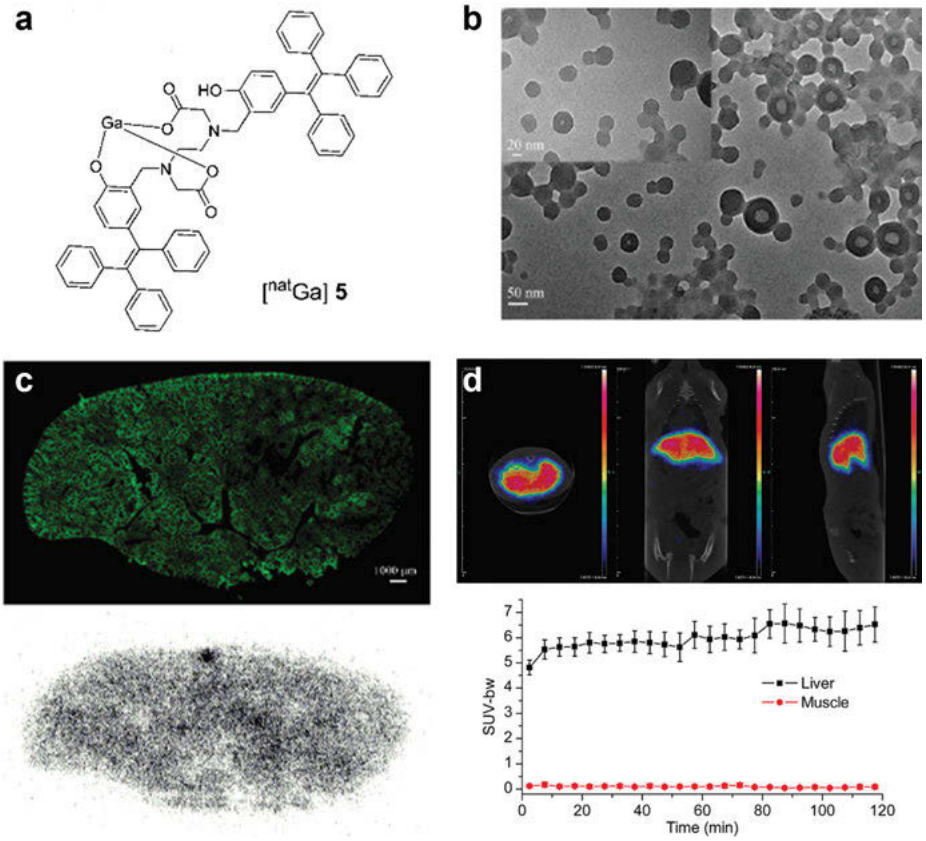

Figure 15.19: Fluorescence PET of the liver using [^{nat}Ga] 5. (a) Structure of [^{nat}Ga] 5. (b) Transmission electron micrographs of [^{nat}Ga] 5 in DMSO. (c) Fluorescence imaging (top) and *in vitro* autoradiography (bottom) of liver sections from mice injected with [^{68}Ga] 5. (d) Representative PET images of rats (transverse, coronal, and sagittal views, respectively) after intravenous injection of [^{68}Ga] 5 (top). The standardized uptake value based on body weight (SUV-bw) shows uptake and slow washout rate of [^{68}Ga] 5 in the liver throughout 2 h scan time (bottom). Reproduced from ref. [66] with permission from the Centre National de la Recherche Scientifique (CNRS) and the Royal Society of Chemistry.

aromatase [67]. In the study, TPE is modified to link triazole derivatives and complexed with $^{nat}Ga^{3+}/^{68}Ga^{3+}$. The resulting [^{nat}Ga/^{68}Ga] **2** is almost nonemissive in PBS buffer solution but becomes fluorescent in the presence of aromatase with a detection limit of 0.15 μg mL^{-1}. Compared with estrogen-receptor-negative MDA-MB-231 cells, MCF-7 cells that express estrogen receptors have a higher cellular uptake of [^{nat}Ga] **2**. Therefore, aromatase distribution in tumors can be mapped and the expression levels of estrogen receptors can be evaluated by using [^{68}Ga] **2** in PET imaging. It

is anticipated that these examples give direction to develop new PET probes with AIE properties for bimodal fluorescence PET imaging.

15.3.4 Fluorescence Raman imaging

Raman microscopy is characterized with high-speed and high-precision scanning for noninvasively evaluating and imaging the chemical composition in cells. Different from fluorescence microscopy, Raman imaging is label-free and provides a wealth of chemical information in molecular vibrations, which becomes more commonly used to characterize biological materials. Based on the complementary advantages of fluorescence microscopy and stimulated Raman scattering (SRS) microscopy, integration of these two imaging platforms can provide more accurate detection of biomolecules in high-speed *in vivo* imaging. This enables quantitative measurement of *in-vivo* biodistribution for drug or probe development.

Li et al. report a fluorescence-SRS probe named AIE-SRS-Mito for imaging mitochondria in living cells (Figure 15.20a) [68]. The probe has AIE properties and an enhanced Raman peak of alkyne at 2,223 cm^{-1}. Subsequently, selective mitochondrial targeting of AIE-SRS-Mito is investigated by a home-built fluorescence-SRS microscope. In the dual-modality imaging, the detection limit of the probe in SRS imaging is 8.5 μM. Because of the linear correlation between the probe concentrations and the SRS signals, the intracellular distribution of the probe is shown to be locally concentrated in the mitochondrial matrix with >2.0 mM, which is 100-fold of the incubation concentration (Figure 15.20b). This work encourages the use of SRS microscopy to quantitatively characterize fluorescent probes or other nonfluorescent molecules in living biological systems and to develop bimodal fluorescence-SRS probes for specific biological targets.

15.3.5 Fluorescence photoacoustic imaging

PAI is an emerging nonionizing tool for biomedical imaging. Images are acquired by collecting the ultrasound signals generated by pulsed laser irradiation on biological tissues. Fluorescence PAI integrates the superiority of sensitivity and spatial resolution in deep-tissue imaging (from millimeters to centimeters) in ultrasound tissue imaging. PAI effectively avoids the influence of light scattering and can achieve a depth of 50 mm in *in vivo* tissue imaging, which can counteract the drawbacks of fluorescence imaging [69–72].

Recently, a novel NIR-II fluorophore with AIE properties, named **TB1**, is designed for *in situ* brain tumor imaging (Figure 15.21a) [69]. The nanodots are fabricated by encapsulating **TB1** molecules in polymer matrices, which show a high quantum yield of 6.2% and large absorptivity of 10.2 L g^{-1} cm^{-1} at 740 nm with a

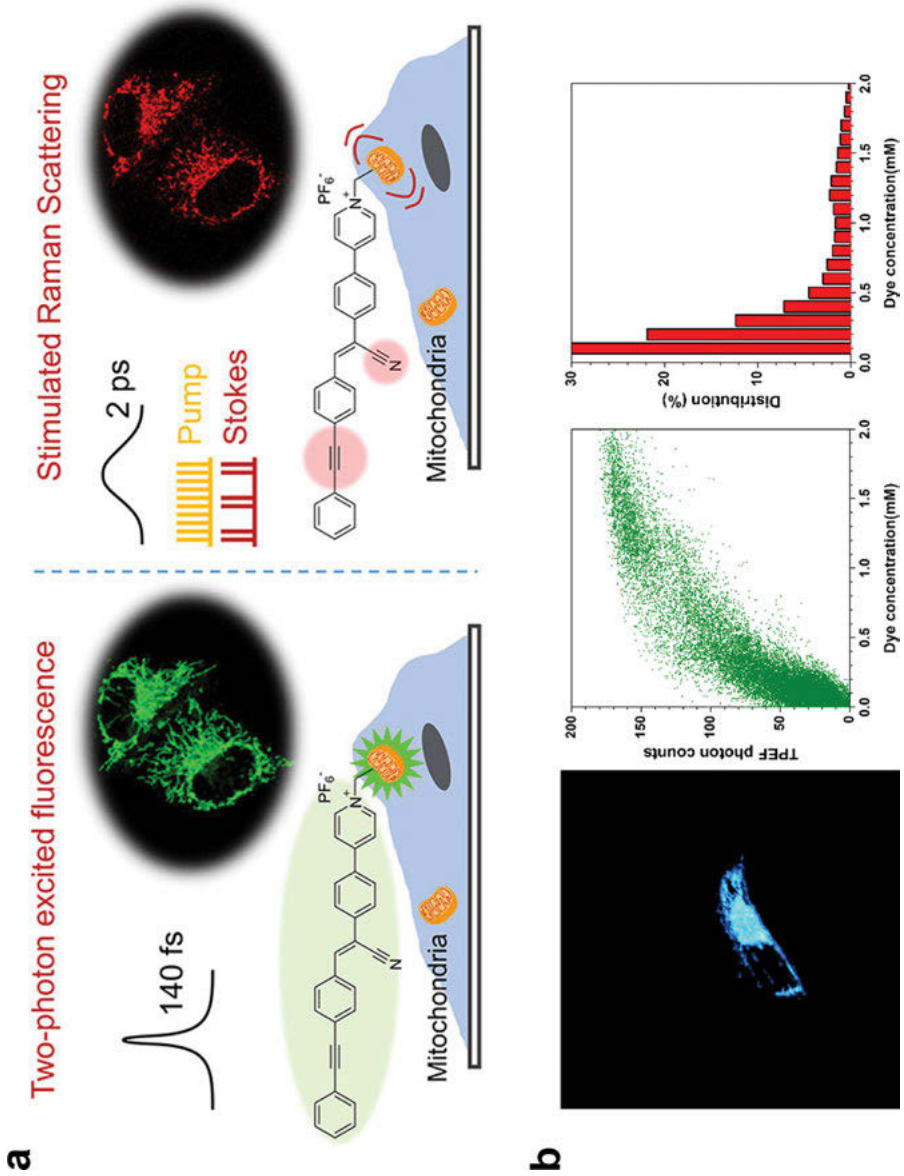

Figure 15.20: Fluorescence Raman imaging of mitochondria using AIE-SRS-Mito. (a) Schematic illustration of mitochondrial imaging in living cells by two-photon excitation (left) and SRS imaging (right). (b) The two-photon excited fluorescence image of HeLa cells stained with 20 μM AIE-SRS-Mito for 60 min. A plot of photon counts versus dye concentration and histogram of dye concentration shows that local dye concentrations of >2 mM are present in over 1% of the subcellular region. Reprinted with permission from ref. [68]. Copyright 2017 American Chemical Society.

maximum emission close to 1,000 nm. Surface modification of **TB1**-based nanodots with tumor-specific c-RGD peptides further yields **TB1**-RGD dots (Figure 15.21b). This provides tumor selectivity and specificity with a high SNR of 4.4 and lateral resolution of 38 μm. **TB1**-RGD dots are compatible with deep-tissue NIR-I PAI because of their large NIR absorptivity. Furthermore, accurate tumor depth can be determined through the intact scalp and skull (Figure 15.21c). This study demonstrates the successful brain tumor diagnosis by NIR-II AIE nanodots in dual modality of NIR-II fluorescence and NIR-I PAI.

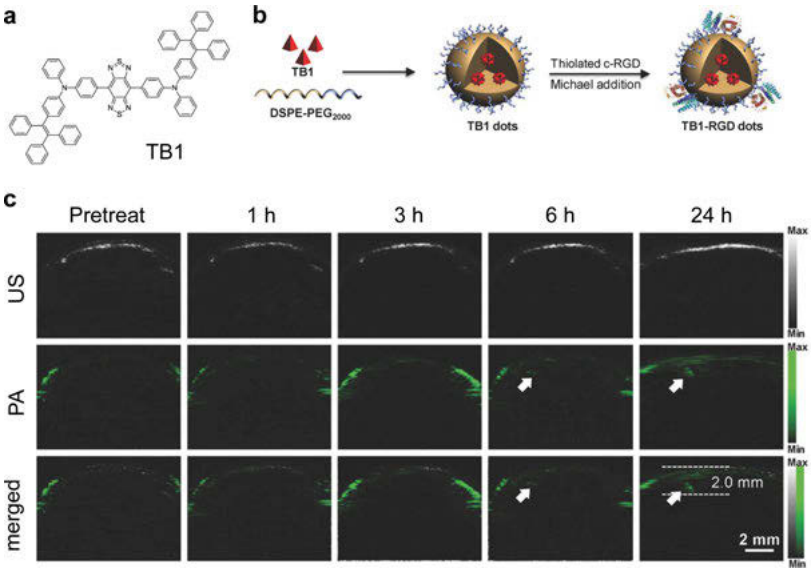

Figure 15.21: Fluorescence PAI of brain tumors using TB1. (a) Structure of TB1. (b) Schematic illustration of encapsulating TB1 in an NP followed by decoration with c-RGD peptides to form TB1-RGD dots. (c) Noninvasive ultrasonic (US) and PAI of orthotopic mouse brain tumors through the intact scalp and skull before and 1–24 h after intravenous injection of TB1-RGD dots. Copyright 2018 Wiley. Used with permission from ref. [69].

Subsequently, Qi et al. develop and apply an organic NIR contrast nanoagent, named **OTPA-TQ3**, for integrated triple-modal fluorescence-photoacoustic-Raman imaging in cancer surgery [70]. The NIR phenylalkyne-phenyl-substituted AIEgen is encapsulated by DSPE-PEG(2000), and the nanoprobes are prepared by the nanoprecipitation method. The **OTPA-TQ3**-based nanoprobe exhibits NIR-I absorption and emission, which are beneficial for PAI, and shows a strong Raman signal at 2,215 cm^{-1} in the cell-silent region. About 24 h after intravenous injection of the nanoprobes, NIR fluorescence and PA signals reach maximum levels in mouse tumors. In the first surgical resection of tumors (S1) performed at 24 h postinjection of **OTPA-TQ3**-based nanoprobes, the residual tumors left behind can be detected by dual-modal fluorescence-

Raman imaging. Subsequently, the second surgical resection (S2) is performed with the assistance of dual-modal fluorescence-Raman imaging to further remove the residual tumors. In addition, the hematoxylin and eosin (H&E) stain histologically confirms the complete tumor resection. This comprehensive NIR contrast nanoagent shows great potential clinical applications in cancer imaging and surgical navigation.

15.4 Perspective

The AIEgen is advantageous in bioimaging using conventional optical microscopy because of its intrinsic properties. In this chapter, examples of AIEgen applications in different aspects of advanced optical imaging are reviewed. The successful applications of these AIE probes in super-resolution imaging, FLIM, FAIM, multiphoton imaging, and multimodality imaging are expected to lead to new exciting discoveries. With a joint effort by researchers with different backgrounds, the development of new AIE probes in advanced optical imaging will impact various fields from chemistry, biology, to biomedical sciences. There are several future research directions in these aspects:

1 Development of high-quality AIE NPs for biolabeling and bioimaging
Due to the outstanding photostability and brightness, AIE NPs are excellent candidates for STED imaging and *in vivo* imaging. However, most AIE NPs developed thus far are in hundreds of nanometers or sub-100 nm of scales. Particles with such bulky dimensions may physically interfere with the biological system or the conjugated biomolecules. Besides, the practical spatial resolution in super-resolution imaging is partially determined and limited by the dimensions of the probes. Therefore, developing AIE NPs at a sub-10 nm scale or even smaller with high brightness is necessary to further improve the optical resolution.

2 Exploration of high-performance multiphoton AIE bioprobes and their applications
The AIE bioprobes with large multiphoton absorption cross sections are beneficial to enhance the SNR and decrease the potential photodamage to the living biological specimens. Therefore, multiphoton AIE bioprobes with high penetrability in biological systems have great potential to be applied to studies using animals as model organisms. Development of AIE probes with better performance, such as better multiphoton absorption and higher brightness, will be still highly desired. Current applications of AIE probes in *in vivo* imaging, including *in vivo* multiphoton imaging, are mainly focused on tumor imaging or blood vessel imaging. It is also expected that AIE probes targeting different biological structures will be developed and utilized in tissue imaging and *in vivo* imaging.

3 Optimization of AIE probes for AIE-based multimodality imaging

AIEgen-based multimodal probes or nanoreagents can be prepared by cross-linking, adsorption, and assembly of AIEgens with other imaging agents. By integrating fluorescence into other advanced imaging platforms, it is expected to achieve deep tissue penetration and high sensitivity in a single imaging experiment. Although some multimodal imaging using current AIE bioprobes has been demonstrated, NIR AIEgens with high quantum yield have not been widely used for such applications. In addition, this can be combined with other imaging methods, such as MRI, ultrasound imaging, and PET, to increase its versatility. Hence, optimizing multimodal AIE bioprobes may broaden the applicability of multimodality imaging for *in vivo* bioimaging or diagnosis.

References

[1] Jiao SM, Zhou CY, Shi YS, Zou WB, Li X, Review on optical image hiding and watermarking techniques, Opt Laser Technol, 109, 2019, 370–380.
[2] Gaietta G, Deerinck TJ, Adams SR, Bouwer J, Tour O, Laird DW, Sosinsky GE, Tsien RY, Ellisman MH, Multicolor and electron microscopic imaging of connexin trafficking, Science, 296(5567), 2002, 503–507.
[3] Hell SW, Far-field optical nanoscopy, Science, 316(5828), 2007, 1153–1158.
[4] Huang D, Swanson EA, Lin CP, Schuman JS, Stinson WG, Chang W, Hee MR, Flotte T, Gregory K, Puliafito CA, Optical coherence tomography, Science, New York, N.Y. 254(5035), 1991, 1178–1181.
[5] Ntziachristos V, Going deeper than microscopy: The optical imaging frontier in biology, Nat Methods, 7(8), 2010, 603–614.
[6] Matoba O, Xiangyu Q, Peng X, Nitta K, Awatsuji Y, A hybrid digital holographic microscope, 2015 14th Workshop on Information Optics (WIO) (2015) 3 pp.-3 pp.
[7] Graves EE, Weissleder R, Ntziachristos V, Fluorescence molecular imaging of small animal tumor models, Curr Mol Med, 4(4), 2004, 419–430.
[8] Medintz IL, Uyeda HT, Goldman ER, Mattoussi H, Quantum dot bioconjugates for imaging, labelling and sensing, Nat Mater, 4(6), 2005, 435–446.
[9] Betzig E, Patterson GH, Sougrat R, Lindwasser OW, Olenych S, Bonifacino JS, Davidson MW, Lippincott-Schwartz J, Hess HF, Imaging intracellular fluorescent proteins at nanometer resolution, Science, 313(5793), 2006, 1642–1645.
[10] Michalet X, Pinaud FF, Bentolila LA, Tsay JM, Doose S, Li JJ, Sundaresan G, Wu AM, Gambhir SS, Weiss S, Quantum dots for live cells, in vivo imaging, and diagnostics, Science, 307(5709), 2005, 538–544.
[11] Verveer PJ, Gemkow MJ, Jovin TM, A comparison of image restoration approaches applied to three-dimensional confocal and wide-field fluorescence microscopy, J Microsc, 193(1), 1999, 50–61.
[12] Hoebe RA, Van Noorden CJF, Manders EMM, Noise effects and filtering in controlled light exposure microscopy, J Microsc, 240(3), 2010, 197–206.
[13] Hoebe RA, Van Oven CH, Gadella TWJ, Dhonukshe PB, Van Noorden CJF, Manders EMM, Controlled light-exposure microscopy reduces photobleaching and phototoxicity in fluorescence live-cell imaging, Nat Biotechnol, 25(2), 2007, 249–253.

[14] Min G, Xiaosong G, Kisteman A, Ming Gu X, Comparison of penetration depth between two-photon excitation and single-photon excitation in imaging through turbid tissue media, Appl Phys Lett (USA), 77(10), 2000, 1551–1553.
[15] Boens N, Leen V, Dehaen W, Fluorescent indicators based on BODIPY, Chem Soc Rev, 41(3), 2012, 1130–1172.
[16] Zheng QS, Juette MF, Jockusch S, Wasserman MR, Zhou Z, Altman RB, Blanchard SC, Ultra-stable organic fluorophores for single-molecule research, Chem Soc Rev, 43(4), 2014, 1044–1056.
[17] Qi JP, Hu XW, Dong XC, Lu Y, Lu HP, Zhao WL, Wu W, Towards more accurate bioimaging of drug nanocarriers: Turning aggregation-caused quenching into a useful tool, Adv Drug Deliv Rev, 143, 2019, 206–225.
[18] Aparin IO, Melnychuk N, Klymchenko AS, Ionic aggregation-induced emission: bulky hydrophobic counterions light up dyes in polymeric nanoparticles, Adv Opt Mater, 8(14), 2020, 2000027.
[19] Li WL, Wang J, Tebyetekerwa M, Ding YX, Qiu ZY, Yan C, Liu F, Zhang JD, Retained fluorescence of aggregation-caused quenched rhodamine grafted in the hierarchical mesopores of silica MCM-41 at solid-state, Adv Powd Technol, 30(10), 2019, 2218–2224.
[20] Yamaguchi M, Ito S, Hirose A, Tanaka K, Chujo Y, Control of aggregation-induced emission versus fluorescence aggregation-caused quenching by bond existence at a single site in boron pyridinoiminate complexes, Mater Chem Front, 1(8), 2017, 1573–1579.
[21] Yin HQ, Wang XY, Yin XB, Rotation restricted emission and antenna effect in single metal-organic frameworks, J Am Chem Soc, 141(38), 2019, 15166–15173.
[22] Alam P, He W, Leung NLC, Ma C, Kwok RTK, Lam JWY, Sung HHY, Williams ID, Wong KS, Tang BZ, Red AIE-Active Fluorescent Probes with Tunable Organelle-Specific Targeting, Adv Funct Mater, 30(10), 2020, 1909268.
[23] Feng GX, Tay CY, Chui QX, Liu RR, Tomczak N, Liu J, Tang BZ, Leong DT, Liu B, Ultrabright organic dots with aggregation-induced emission characteristics for cell tracking, Biomaterials, 35(30), 2014, 8669–8677.
[24] Gui C, Zhao EG, Kwok RTK, Leung ACS, Lam JWY, Jiang MJ, Deng HQ, Cai YJ, Zhang WJ, Su HF, Tang BZ, AIE-active theranostic system: Selective staining and killing of cancer cells, Chem Sci, 8(3), 2017, 1822–1830.
[25] Bai HT, He W, Chau JHC, Zheng Z, Kwok RTK, Lam JWY, Tang BZ, AIEgens for microbial detection and antimicrobial therapy, Biomaterials, 268, 2021, 1909268.
[26] Hell SW, Wichmann J, Breaking the diffraction resolution limit by stimulated emission: Stimulated-emission-depletion fluorescence microscopy, Opt Lett, 19(11), 1994, 780–782.
[27] Huang B, Bates M, Zhuang X, Super-resolution fluorescence microscopy, Annu Rev Biochem, 78, 2009, 993–1016.
[28] Yu J, Sun X, Cai F, Zhu Z, Qin A, Qian J, Tang B, He S, Low photobleaching and high emission depletion efficiency: The potential of AIE luminogen as fluorescent probe for STED microscopy, Opt Lett, 40(10), 2015, 2313–2316.
[29] Li D, Ni X, Zhang X, Liu L, Qu J, Ding D, Qian J, Aggregation-induced emission luminogen-assisted stimulated emission depletion nanoscopy for super-resolution mitochondrial visualization in live cells, Nano Res, 11(11), 2018, 6023–6033.
[30] Lv Z, Man Z, Cui H, Xu Z, Cao H, Li S, Liao Q, He Q, Zheng L, Fu H, Red AIE luminogens with tunable organelle specific anchoring for live cell dynamic super resolution imaging, Adv Funct Mater, 31(10), 2021, 2009329.
[31] Li D, Qin W, Xu B, Qian J, Tang BZ, AIE Nanoparticles with High Stimulated Emission Depletion Efficiency and Photobleaching Resistance for Long-Term Super-Resolution Bioimaging, Adv, Mater, 29(43), 2017, 1703643.

[32] Fang X, Chen X, Li R, Liu Z, Chen H, Sun Z, Ju B, Liu Y, Zhang SX-A, Ding D, Sun Y, Wu C, Multicolor photo-crosslinkable AIEgens toward compact nanodots for subcellular imaging and STED nanoscopy, Small, 13(41), 2017, 1702128.
[33] Wang Y-L, Fan C, Xin B, Zhang J-P, Luo T, Chen Z-Q, Zhou Q-Y, Yu Q, Li X-N, Huang Z-L, Li C, Zhu M-Q, Tang BZ, AIE-based super-resolution imaging probes for β-amyloid plaques in mouse brains, Mater Chem Front, 2(8), 2018, 1554–1562.
[34] Dang D, Zhang H, Xu Y, Xu R, Wang Z, Kwok RTK, Lam JWY, Zhang L, Meng L, Tang BZ, Super-resolution visualization of self-assembling helical fibers using aggregation-induced emission luminogens in stimulated emission depletion nanoscopy, ACS Nano, 13(10), 2019, 11863–11873.
[35] Li C, Gong WL, Hu Z, Aldred MP, Zhang GF, Chen T, Huang ZL, Zhu MQ, Photoswitchable aggregation-induced emission of a dithienylethene-tetraphenylethene conjugate for optical memory and super-resolution imaging, RSC Adv, 3(23), 2013, 8967–8972.
[36] Gu X, Zhao E, Zhao T, Kang M, Gui C, Lam JW, Du S, Loy MM, Tang BZ, A Mitochondrion-specific photoactivatable fluorescence turn-on AIE-based bioprobe for localization super-resolution microscope, Adv Mater, 28(25), 2016, 5064–5071.
[37] Lo CY, Chen S, Creed SJ, Kang M, Zhao N, Tang BZ, Elgass KD, Novel super-resolution capable mitochondrial probe MitoRed AIE, enables assessment of real-time molecular mitochondrial dynamics, Sci Rep, 6, 2016, 30855.
[38] Yang H, Li M, Li C, Luo Q, Zhu MQ, Tian H, Zhu WH, Unraveling dual aggregation-induced emission behavior in steric-hindrance photochromic system for super resolution imaging, Angew Chem Int Ed Engl, 59(22), 2020, 8560–8570.
[39] Li C, Xiong K, Chen Y, Fan C, Wang YL, Ye H, Zhu MQ, Visible-light-driven photoswitching of aggregated-induced emission-active diarylethenes for super-resolution imaging, ACS Appl Mater Interfaces, 12(24), 2020, 27651–27662.
[40] Chen S, Hong Y, Zeng Y, Sun Q, Liu Y, Zhao E, Bai G, Qu J, Hao J, Tang BZ, Mapping live cell viscosity with an aggregation-induced emission fluorogen by means of two-photon fluorescence lifetime imaging, Chemistry, 21(11), 2015, 4315–4320.
[41] Wang Y, Yao H, Zhou J, Hong Y, Chen B, Zhang B, Smith TA, Wong WWH, Zhao Z, A water-soluble, AIE-active polyelectrolyte for conventional and fluorescence lifetime imaging of mouse neuroblastoma neuro-2A cells, J Polym Sci A Polym Chem, 56(6), 2018, 672–680.
[42] Gao H, Kam C, Chou TY, Wu M-Y, Zhao X, Chen S, A simple yet effective AIE-based fluorescent nano-thermometer for temperature mapping in living cells using fluorescence lifetime imaging microscopy, Nanoscale Horiz, 5(3), 2020, 488–494.
[43] Soleimaninejad H, Chen MZ, Lou X, Smith TA, Hong Y, Measuring macromolecular crowding in cells through fluorescence anisotropy imaging with an AIE fluorogen, Chem Commun (Camb), 53(19), 2017, 2874–2877.
[44] Qin W, Zhang P, Li H, Lam JWY, Cai Y, Kwok RTK, Qian J, Zheng W, Tang BZ, Ultrabright red AIEgens for two-photon vascular imaging with high resolution and deep penetration, Chem Sci, 9(10), 2018, 2705–2710.
[45] Niu G, Zhang R, Kwong JPC, Lam JWY, Chen C, Wang J, Chen Y, Feng X, Kwok RTK, Sung HHY, Williams ID, Elsegood MRJ, Qu J, Ma C, Wong KS, Yu X, Tang BZ, Specific two-photon imaging of live cellular and deep-tissue lipid droplets by lipophilic AIEgens at ultralow concentration, Chem Mater, 30(14), 2018, 4778–4787.
[46] Niu G, Zhang R, Gu Y, Wang J, Ma C, Kwok RTK, Lam JWY, Sung HH, Williams ID, Wong KS, Yu X, Tang BZ, Highly photostable two-photon NIR AIEgens with tunable organelle specificity and deep tissue penetration, Biomaterials, 208, 2019, 72–82.
[47] Wang S, Liu J, Goh CC, Ng LG, Liu B, NIR-II-excited intravital two-photon microscopy distinguishes deep cerebral and tumor vasculatures with an ultrabright NIR-I AIE luminogen, Adv Mater, 31(44), 2019, e1904447.

[48] Wang Y, Chen M, Alifu N, Li S, Qin W, Qin A, Tang BZ, Qian J, Aggregation-induced emission luminogen with deep-red emission for through-skull three-photon fluorescence imaging of mouse, Acs Nano, 11(10), 2017, 10452–10461.
[49] Liu W, Wang Y, Han X, Lu P, Zhu L, Sun C, Qian J, He S, Fluorescence resonance energy transfer (FRET) based nanoparticles composed of AIE luminogens and NIR dyes with enhanced three-photon near-infrared emission for in vivo brain angiography, Nanoscale, 10(21), 2018, 10025–10032.
[50] Qin W, Alifu N, Lam JWY, Cui Y, Su H, Liang G, Qian J, Tang BZ, Facile synthesis of efficient luminogens with AIE features for three-photon fluorescence imaging of the brain through the intact skull, Adv Mater, 32(23), 2020, e2000364.
[51] Qi J, Sun C, Li D, Zhang H, Yu W, Zebibula A, Lam JWY, Xi W, Zhu L, Cai F, Wei P, Zhu C, Kwok RTK, Streich LL, Prevedel R, Qian J, Tang BZ, Aggregation-induced emission luminogen with near-infrared-II excitation and near-infrared-I emission for ultradeep intravital two-photon microscopy, ACS Nano, 12(8), 2018, 7936–7945.
[52] Geng J, Li K, Ding D, Zhang X, Qin W, Liu J, Tang BZ, Liu B, Lipid-PEG-folate encapsulated nanoparticles with aggregation induced emission characteristics: Cellular uptake mechanism and two-photon fluorescence imaging, Small, 8(23), 2012, 3655–3663.
[53] Geng J, Goh CC, Qin W, Liu R, Tomczak N, Ng LG, Tang BZ, Liu B, Silica shelled and block copolymer encapsulated red-emissive AIE nanoparticles with 50% quantum yield for two-photon excited vascular imaging, Chem Commun (Camb), 51(69), 2015, 13416–13419.
[54] Wang Y, Han X, Xi W, Li J, Roe AW, Lu P, Qian J, Bright AIE nanoparticles with f127 encapsulation for deep-tissue three-photon intravital brain angiography, Adv Healthc Mater, 6(21), 2017, 1700685.
[55] Zhu Z, Qian J, Zhao X, Qin W, Hu R, Zhang H, Li D, Xu Z, Tang BZ, He S, Stable and size-tunable aggregation-induced emission nanoparticles encapsulated with nanographene oxide and applications in three-photon fluorescence bioimaging, ACS Nano, 10(1), 2016, 588–597.
[56] Zhang J, Li C, Zhang X, Huo S, Jin S, An FF, Wang X, Xue X, Okeke CI, Duan G, Guo F, Zhang X, Hao J, Wang PC, Zhang J, Liang XJ, In vivo tumor-targeted dual-modal fluorescence/CT imaging using a nanoprobe co-loaded with an aggregation-induced emission dye and gold nanoparticles, Biomaterials, 42, 2015, 103–111.
[57] He X, Zhao Z, Xiong LH, Gao PF, Peng C, Li RS, Xiong Y, Li Z, Sung HH, Williams ID, Kwok RTK, Lam JWY, Huang CZ, Ma N, Tang BZ, Redox-active AIEgen-derived plasmonic and fluorescent core@shell nanoparticles for multimodality bioimaging, J Am Chem Soc, 140(22), 2018, 6904–6911.
[58] Feng G, Li JLY, Claser C, Balachander A, Tan Y, Goh CC, Kwok IWH, Renia L, Tang BZ, Ng LG, Liu B, Dual modal ultra-bright nanodots with aggregation-induced emission and gadolinium-chelation for vascular integrity and leakage detection, Biomaterials, 152, 2018, 77–85.
[59] Li Y, Yu H, Qian Y, Hu J, Liu S, Amphiphilic star copolymer-based bimodal fluorogenic/magnetic resonance probes for concomitant bacteria detection and inhibition, Adv Mater, 26 (39), 2014, 6734–6741.
[60] He Z, Jiang R, Long W, Huang H, Liu M, Feng Y, Zhou N, Ouyang H, Zhang X, Wei Y, Red aggregation-induced emission luminogen and Gd(3+) codoped mesoporous silica nanoparticles as dual-mode probes for fluorescent and magnetic resonance imaging, J Colloid Interface Sci, 567, 2020, 136–144.
[61] Chen Y, Li M, Hong Y, Lam JW, Zheng Q, Tang BZ, Dual-modal MRI contrast agent with aggregation-induced emission characteristic for liver specific imaging with long circulation lifetime, ACS Appl Mater Interfaces, 6(13), 2014, 10783–10791.
[62] Li H, Parigi G, Luchinat C, Meade TJ, Bimodal fluorescence-magnetic resonance contrast agent for apoptosis imaging, J Am Chem Soc, 141(15), 2019, 6224–6233.

[63] Meng L, Ma X, Jiang S, Ji G, Han W, Xu B, Tian J, Tian W, High-efficiency fluorescent and magnetic multimodal probe for long-term monitoring and deep penetration imaging of tumors, J Mater Chem B, 7(35), 2019, 5345–5351.
[64] Yang H, He Y, Wang Y, Yang R, Wang N, Zhang LM, Gao M, Jiang X, Theranostic nanoparticles with aggregation-induced emission and MRI contrast enhancement characteristics as a dual-modal imaging platform for image-guided tumor photodynamic therapy, Int J Nanomedicine, 15, 2020, 3023–3038.
[65] Wang L, Huang M, Tang H, Cao D, Zhao Y, Fabrication and application of dual-modality polymer nanoparticles based on an aggregation-induced emission-active fluorescent molecule and magnetic Fe(3)O(4), Polymers (Basel), 11(2), 2019, 220.
[66] Liu S, Huang Y, Liu Y, Wu R, Yang Z, Sun Y, Xiao H, Cheng X, Wu Z, Aggregation-induced emission based PET probe for liver function imaging, New J Chem, 43(41), 2019, 16305–16313.
[67] Wu R, Liu S, Liu Y, Sun Y, Xiao H, Huang Y, Yang Z, Wu Z, PET probe with aggregation induced emission characteristics for the specific turn-on of aromatase, Talanta, 208, 2020, 120412.
[68] Li X, Jiang M, Lam JWY, Tang BZ, Qu JY, Mitochondrial imaging with combined fluorescence and stimulated Raman scattering microscopy using a probe of the aggregation-induced emission characteristic, J Am Chem Soc, 139(47), 2017, 17022–17030.
[69] Sheng Z, Guo B, Hu D, Xu S, Wu W, Liew WH, Yao K, Jiang J, Liu C, Zheng H, Liu B, Bright aggregation-induced-emission dots for targeted synergetic NIR-II Fluorescence and NIR-I photoacoustic imaging of orthotopic brain tumors, Adv Mater, 2018, 1800766.
[70] Qi J, Li J, Liu R, Li Q, Zhang H, Lam JWY, Kwok RTK, Liu D, Ding D, Tang BZ, Boosting fluorescence-photoacoustic-Raman properties in one fluorophore for precise cancer surgery, Chem, 5(10), 2019, 2657–2677.
[71] He X, Peng C, Qiang S, Xiong LH, Zhao Z, Wang Z, Kwok RTK, Lam JWY, Ma N, Tang BZ, Less is more: silver-AIE core@shell nanoparticles for multimodality cancer imaging and synergistic therapy, Biomaterials, 238, 2020, 119834.
[72] Li K, Liu B, Polymer-encapsulated organic nanoparticles for fluorescence and photoacoustic imaging, Chem Soc Rev, 43(18), 2014, 6570–6597.

Yi-Feng Wang, Yufei Wang, Shengliang Li, Jinchao Zhang,
Yuanyuan Zhang, Peter Timashev, Aiping Zheng, Xing-Jie Liang

Chapter 16
AIEgens-based delivery systems: application in the treatment of different diseases

16.1 Introduction

Despite great improvements at the medical level with the rapid development of modern technology, the problem of disease treatment persists. The burden is particularly high for the treatment of diseases, including cancers, diabetes, heart disease, stroke, and infectious diseases [1]. Benefiting from the unique physical and chemical properties at nanoscale, nanoparticle-based drug delivery systems (NDDSs) have been extensively developed for application in the treatment of diseases [2–4].

Acknowledgements: This work was supported by the National Natural Science Foundation of China (NSFC) key projects (grant no. 31630027 and 32030060), NSFC international collaboration key project (grant no. 51861135103) and NSFC-German Research Foundation (DFG) project (grant no. 31761133013). The authors also appreciate the support by "the Beijing-Tianjin-Hebei Basic Research Cooperation Project" (19JCZDJC64100), "Ten Thousand Elite Plan" (grant no. Y9E21Z11) and CAS international collaboration plan (grant no. E0632911ZX) as well as the National Key Research & Development Program of China (grant no. 2018YFE0117800).

Yi-Feng Wang, Yufei Wang, CAS Key Laboratory for Biomedical Effects of Nanomaterials and Nanosafety, CAS Center for Excellence in Nanoscience, National Center for Nanoscience and Technology of China, No. 11, First North Road, Zhongguancun, Beijing, 100190, P.R. China; University of Chinese Academy of Sciences, Beijing 100049, P.R. China
Shengliang Li, CAS Key Laboratory for Biomedical Effects of Nanomaterials and Nanosafety, CAS Center for Excellence in Nanoscience, National Center for Nanoscience and Technology of China, No. 11, First North Road, Zhongguancun, Beijing, 100190, P.R. China; College of Pharmaceutical Sciences, Soochow University, Suzhou 215123, P.R. China
Jinchao Zhang, Key Laboratory of Medicinal Chemistry and Molecular Diagnosis of the Ministry of Education, College of Chemistry & Environmental Science, Hebei University, Baoding 071002, P.R. China
Yuanyuan Zhang, Wake Forest Institute for Regenerative Medicine, Wake Forest University School of Medicine, Winston-Salem, NC, USA
Peter Timashev, Laboratory of Clinical Smart Nanotechnologies, Institute for Regenerative Medicine, Sechenov University, Moscow, Russia
Aiping Zheng, Institute of Pharmacology and Toxicology of Academy of Military Medical Sciences, 27 Taiping Road Haidian District, Beijing 100850, P.R. China
Xing-Jie Liang, University of Chinese Academy of Sciences, Beijing 100049, P.R. China; CAS Key Laboratory for Biomedical Effects of Nanomaterials and Nanosafety, CAS Center for Excellence in Nanoscience, National Center for Nanoscience and Technology of China, No. 11, First North Road, Zhongguancun, Beijing 100190, P.R. China, liangxj@nanoctr.cn, Tel: +86-010-82545569

https://doi.org/10.1515/9783110673074-017

To better understand the treatment process of NDDSs and diagnose the status of the disease, the integration of tracking and diagnostic function into the NDDSs has attracted tremendous research [2, 5, 6].

With advantages of easy operation, rapidness, excellent sensitivity, and specificity, fluorescent drug delivery systems provide a great means to track the process of translocation and drug release from NDDSs [7–10]. So far, lots of fluorescent NDDSs have been designed and applied in biological systems, e.g., organic dye-loaded NPs, quantum dots, rare-earth NPs, and metal nanostructures. However, the inevitable defects, e.g., aggregation-caused quenching (ACQ) effect, unsatisfactory signal-to-noise ratio, and poor photostability have limited the application [11, 12]. Among these defects, the ACQ effect is a serious deficiency for the wide application of traditional fluorescence materials. Upon concentration or aggregation of fluorescent molecules with the ACQ effect inside the nanostructures, the fluorescence intensity is reduced or even quenched; thus, the traditional fluorescent molecule is not a very suitable candidate to some degree for tracking the behavior of NDDSs [13, 14]. So, it is urgently necessary to find one kind of novel fluorescent molecule that the fluorescence is stable or enhanced when loaded into the core of nanostructures.

Fortunately, one kind of novel fluorescence material with aggregation-induced emission (AIE) effect was discovered by Tang's group in 2001 [15]. In a good solvent, the AIE molecules are in a nonaggregated state and no fluorescence emission occurs. However, the fluorescence intensity is enhanced when in a poor solvent that because of the aggregation of AIE molecules restricts the intramolecular rotations [16–18]. Benefiting from the mechanism, if the AIE molecules are loaded into the nanostructure, the rotation of AIE molecules would also be restricted by the rigid structure. This hypothesis has been widely proved by the development of stable fluorescent nanostructures and AIE molecules, which provided an alternative way to tackle the ACQ challenge [19, 20]. By now, a great deal of AIEgens-based delivery systems have been extensively designed and used for the treatment and diagnosis of different diseases [21–23].

In this chapter, we summarized the recent development of AIEgens-based delivery systems. Because the AIE-related field is very active, a lot of reviews or chapters have been reported to summarize the development and application of AIE molecules in different fields, especially in biological imaging and theranostic application [16, 17, 24–40]. Here, we focus on the application of AIEgens-based delivery systems on the treatment of different diseases, including cancer, infectious diseases, and stem cell-based therapy. A short outlook of AIEgens-based delivery systems is also discussed in the final part. In this chapter, we hope that it will promote the development and clinical application of AIEgens-based delivery systems in other more diseases.

16.2 Section 1: application in the treatment of cancer

Cancer has gradually become an intractable challenge to global public health. As for traditional treatment, surgical removal is considered the priority for patients. Moreover, chemotherapy and radiotherapy have been widely studied and applied to reduce cancer metastasis and recurrence [41]. In addition, recent advances in cancer immunotherapy have highlighted the potency of immunotherapies in cancer treatment [42].

In recent decades, nanotechnology has been extensively exploited to benefit cancer treatments [43]. Due to benign biocompatibility, targeted delivery, and stimuli-responsive drug release, NDDSs may bring out improvements of therapeutic effects with reduced side reactions [44, 45]. As the first protein-based NDDSs were approved by the United States Food and Drug Administration in 2005, the albumin-coated paclitaxel nanopharmaceuticals, Abraxane, has achieved great progress in the clinical treatment of malignant cancer. Taken advantage of AIEgens, researchers have developed AIEgens-based light-controllable NDDSs for cancer treatments. Also, due to superb photosensitivity and photostability, AIEgens can be used as imaging tools in tumor surgical resection, promoting high-accuracy imaging guidance for preoperative and intraoperative manipulation. In addition, recent advances also highlight the potential of AIEgens-based monitoring of NDDSs in vitro and in vivo, providing dynamic biological details about nano-bio interaction.

16.2.1 AIEgens-guided synergistic cancer therapy

As one of the traditional cancer treatments, radiotherapy has been widely used for clinical cancer patients for over a century. However, high-dose X-ray irradiation may lead to high toxicity on healthy organs and tissues. To reduce side reactions, researchers have developed AIEgens-based radiosensitizers for image-guided radiotherapy. As shown in Figure 16.1A, Chen et al. recently combined Au clusters to form photosensitizer (PS)-conjugated nanocomplex for radiosensitization [46]. Once irradiated by the low-dose X-ray (1 Gy), the AIEgens group could rapidly produce hydroxyl radicals and singlet oxygen, leading to lipid oxidation on the cell membrane and resensitization of tumor cells to X-ray irradiation. Through in vivo evaluation of anticancer effects, the AIEgens-based nanocomplexes showed increased DNA damage in U87MG tumors. The researchers further demonstrated that the X-ray-induced rapid reactive oxygen species (ROS) generation from AIEgens-based nanocomplexes promoted enhanced therapeutic effects on radioresistant solid tumors. From these results, AIEgens-based radiotherapy shows great potential to overcome cancer resistance.

Due to the high photosensitivity and potential phototoxicity of AIEgens, various AIEgens-based PSs have been developed for photothermal therapy (PTT) and photodynamic therapy (PDT) [47]. Recently, the research team of Tang reported an all-round nanoprecipitation for multimodal PDT–PTT synergistic treatment for breast cancer (Figure 16.1B) [48]. They first synthesized a simple AIEgen with 1,3-bis(dicyanomethylidene)indane moiety and triphenylamine (TPA), termed as TSSI. The TPA unit is regarded as the strong electronic donor into the conjugated structured chromophores as well as the intramolecular rotor. The reduced π–π stacking in propeller-like twisted moieties could also inhibit the fluorescent quenching in aggregates. Thus, the AIEgen units enable to provide a combination of PTT, PDT, photoacoustic imaging (PAI), and fluorescent imaging. When forming lipid NPs with lipid mixtures, TSSI NPs exhibited spherical morphology with the diameter of 40 nm. Importantly, TSSI NPs also showed long and strong absorption in the near-infrared (NIR) region so that they can manage deep penetration into organs and tissues. The researchers also demonstrated that after internalization into the cytoplasm, TSSI NPs preferentially accumulated into lysosomes. Upon NIR irradiation, TSSI NPs triggered the rapid production of intracellular heat and ROS, leading to significant phototoxicity toward 4T1 cells. In tumor-bearing mice, these light-controllable TSSI NPs also showed prominent antitumor effects and undetectable systemic toxicity. In addition, the fluorescence-PAI-PTI trimodal imaging of TSSI NPs could bring out real-time and long-term in vivo tracking. Conclusively, AIEgens-based TSSI NPs can act as an all-round versatile for multimodal imaging-guided synergistic anticancer therapy.

Apart from light-induced oncological therapy, AIEgens have been widely exploited in anticancer gene delivery [24, 49]. As traditional gene carriers, cationic polymers are beneficial because nucleic acids can be highly compressed via electrostatic interaction [50]. Also, those positively charged polymers can manage to endolysosomal escape through the proton sponge effect, promoting the cytosolic release of loaded nucleic acids. However, owing to severe adverse effects, cationic polymers meet great difficulty in clinical application [51]. Due to the high photocontrollability, AIEgens are expected to achieve light-driven gene delivery in living systems. As shown in Figure 16.1C, the research team of Liu reported an AIEgens-loaded noncationic NPs for efficient delivery of spherical nucleic acids [52]. They fabricated the core units of NPs with AIEgens-based amphiphilic TBD-PEG-N_3 moieties and then modified Bcl-2 antisense oligonucleotides to eventually form the core–shell NPs. After light irradiation, the AIEgens-based core could be activated to produce abundant ROS to disrupt the endolysosome membrane, promoting the intracellular delivery of loaded cargos. Through intracellular fluorescent colocalization, the researchers demonstrated the light-triggered endolysosome escape of the AIEgens-based noncationic NPs and the cytosolic release of Bcl-2 antisense oligonucleotides. Also, they verified that the AIEgens-based NPs showed a preferential accumulation in tumor sites, which efficiently reduced the systemic

toxicity. Therefore, AIEgens can be effectively used as light-controllable nanocarriers for anticancer gene delivery.

Despite PDT, PTT, radiotherapy and gene therapy, other AIEgens-based synergetic oncological interventions have been gradually developed [53, 54]. With the development of the Precision Medicine Project, researchers are capable of designing versatile and smart AIEgens-based synergetic anticancer treatments to meet various clinical demands.

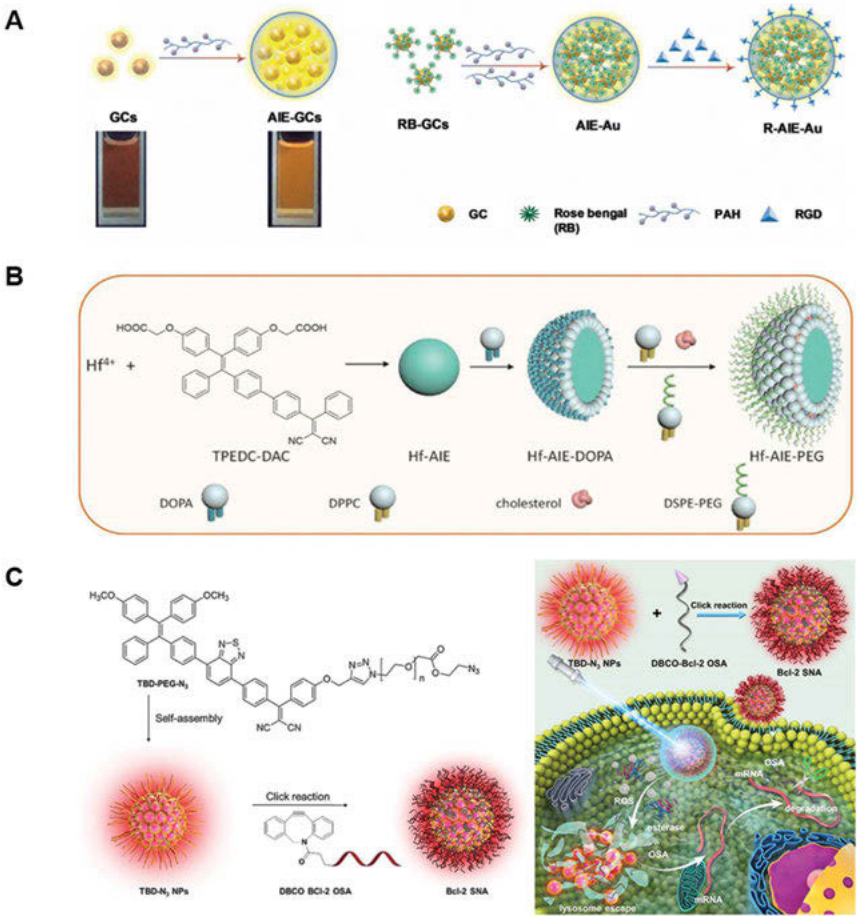

Figure 16.1: (A) AIEgens-loaded Au clusters to enhance cancer sensitivity in radiotherapy. (B) AIEgens-based lipid NPs for "all-in-one" PTT and PDT. (C) AIEgens-enhanced endolysosomal escape in gene therapy. Reproduced with permission from refs. [46, 48, 52].

16.2.2 AIEgens-assisted cancer surgical resection

Surgical resection was considered as the preferred clinical treatment for solid tumors. However, the unclear preoperative location of tumors hindered the surgical efficiency. Also, the inaccurate evaluation of resection completeness is likely to lead to the residue of cancer cells, and eventually causes postoperative recurrence in patients. Therefore, to improve the therapeutic effects of cancer surgical resections, it is in great demand to develop imaging guidance to determine tumor margins in the living bodies. Benefiting from the photostability of AIEgens, researchers focus on the fabrication of AIEgens-assisted nanosystems for the real-time guidance of tumor surgical resection [55, 56].

As for typical contrast agents, because of the complexity of the living bodies and the heterogeneity of tumors, it is difficult to achieve a high signal ratio between tumor lesions and healthy tissues. The research team of Liu reported an AIEgens-based NIR-activated nanoprobe for fluorescence-guided tumor resection, which possesses high-performance imaging with a high tumor-to-normal tissue signal ratio [57]. The AIEgens backbones were derived from α-DTPEBBTD-Cx and β-DTPEBBTD-Cx units. With the modification of DSPE-PEG2000, the researchers then prepared the AIEgens-based nanoprobes. Using 4T1 breast cancer cells and L02 liver cells, they demonstrated high-quality fluorescent imaging and benign biocompatibility at the cellular level. Through 4T1 tumor-bearing mouse models, they also observed the overlap between fluorescent signals from AIEgens-based nanoprobes and the bioluminescent signals from luciferase-expressed tumors, suggesting the high accuracy of AIEgens-guided tumor-to-normal tissue fluorescent imaging.

Similarly, Wu et al. developed an AIEgens-based enzyme-responsive nanoprobe for orthotopic hepatic tumor excision by multispectral optoacoustic tomography (MOST) and fluorescent imaging [58]. The diphenylxanthene moiety and the diethylaminodifluorodioxaborininochromenone unit were acted as the electron donor and the electron acceptor, respectively. An aromatic nitro group was also constructed near the donor to provide the recognitative ability for nitroreductase which is highly expressed on the surface of hepatic tumor cells. That is, the BH-NO2@BSA (bovine serum albumin) nanoprobe can be activated in the presence of nitroreductase. More importantly, due to the diphenylxanthene moiety, the nanoprobe can perform AIE features after the NIR-I/-II irradiation. Also, with the presence of BSA as the carrier, the nanoprobe exhibited good biocompatibility. Then, with the orthotopic hepatic tumor model, the researchers evaluated the imaging ability of BH-NO2@BSA nanoprobes. From the fluorescent results, both the NIR-I and NIR-II fluorescent signals could be observed in tumor sites. In addition, tumor margins through the NIR-II fluorescent imaging displayed more clearly than those through the NIR-I fluorescent imaging, which may result from the decreased light scattering and lower autofluorescence during NIR-II imaging. Furthermore, the 3D MOST results showed clearly depicted outlines of two distinct tumor lesions. These

findings demonstrated the potential of AIEgens-based nanosystems for imaging-assisted tumor surgical excision.

Overall, benefiting from superb photosensitivity and photostability, AIEgens can be used as assistant imaging agents in tumor surgical resection. Particularly, for deep-penetrated tumors such as gastrointestinal tumors and ovarian tumors, this AIEgens-assisted imaging promotes high-accuracy manipulation of the surgical lesions.

16.2.3 AIEgens used as anticancer therapeutic agents

Apart from the above-mentioned application of AIEgens as imaging assistance, it has been reported that AIEgens can be directly used as anticancer agents in PDT and other synergetic therapy. As for PDT, the anticancer intervention relying on the photodamage induced by irradiation, it is of great importance to develop high-efficacy PSs to achieve enhanced oncological cytotoxicity and reduced side effects. The group of Wang reported an AIEgens-based liposome for the anticancer treatment [59]. The AIEgens-based unit consisted of bis(pyrene) and MC4, two novel AIE fluorophores. When assembled with lipid mixtures, the liposomes exhibited spherical nanostructures with diameters of 160–200 nm and AIE-PSs lose their photosensitivity. However, after the liposome arrived at tumor tissues via the enhanced permeability and retention effect, the AIE-PSs were released and then self-assembled, thus the photosensitivity can be recovered and cause cytotoxicity (Figure 16.2A). Through the in vitro and in vivo studies, the researchers evaluated the light-induced ROS generation from AIEgens-based liposomes, and also confirmed the superb anticancer effects in the MCF-7 tumor-bearing mouse model (Figure 16.2B). Furthermore, the phototoxicity of AIEgens-based liposomes to normal tissues was researched with ear tissues of mice. As shown in Figure 16.2C, the ear of mice injected with the nanoaggregates of bis(pyrene) was seriously burned in the irradiated location. However, there were no changes when mice were injected with nothing as a control (Figure 16.2D) or AIEgens-based liposomes (Figure 16.2E) and then irradiated with two-photon laser, respectively. The results demonstrated that the phototoxicity of AIEgens-based liposomes to normal tissues is negligible compared with the nanoaggregates of bis(pyrene). Therefore, AIEgens can be applied in versatile PDT-based NDDSs.

In recent years, cancer immunology has been regarded as another anticancer antidote in clinics, which relies on the activation of innate and humoral immune responses to eradicate tumors [60]. Based on AIEgens and upconversion NPs, Liu et al. developed an NIR-activated nanoimmunostimulant, AUNPs, to enhance anticancer immune responses [61]. They chose TPEBTPy, the AIEgens molecule, as the PS to induce the rapid generation of ROS and trigger immunogenic cell death in solid tumors. Also, the AIEgens-coupled nanoimmunostimulant was able to capture tumor-associated antigens through electrostatic interaction. Thus, the antigen-

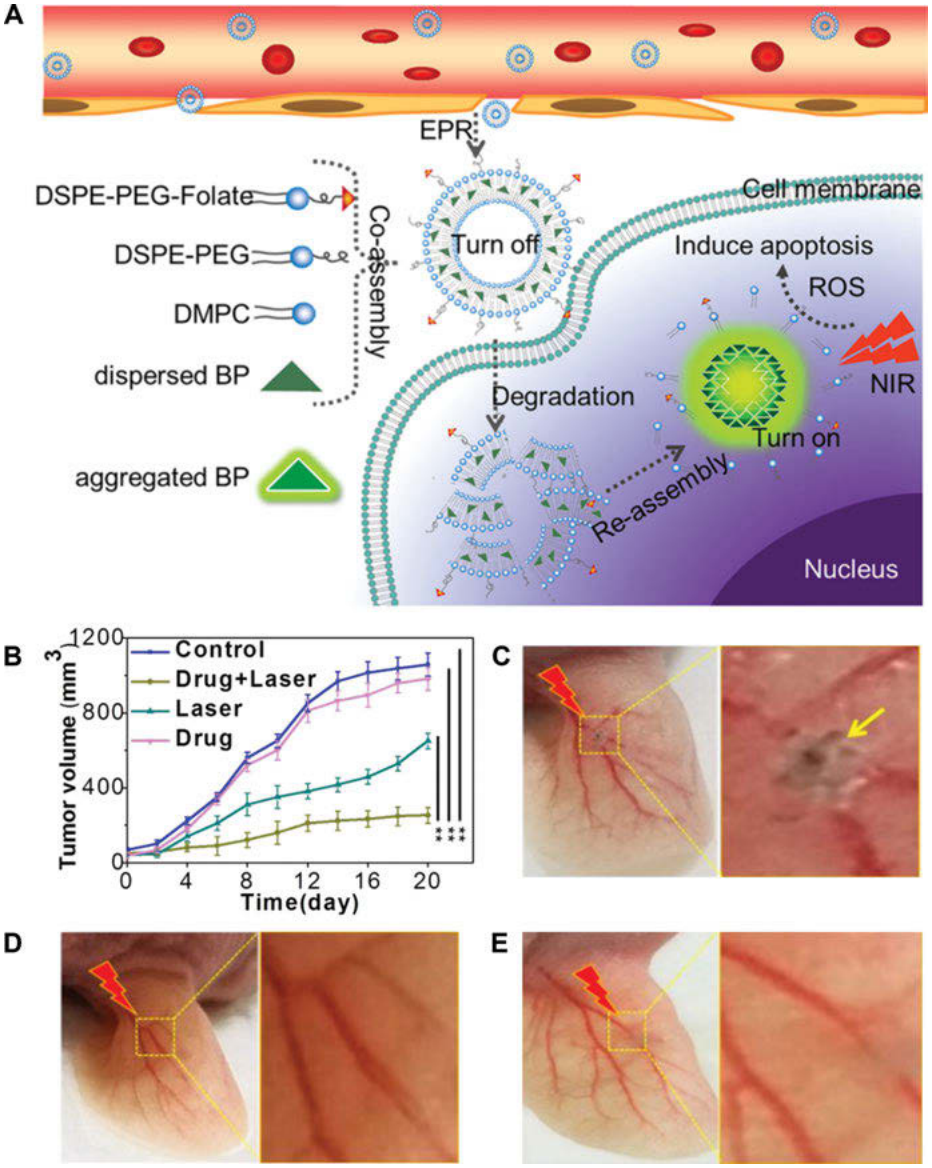

Figure 16.2: (A) Illustration of AIE-PS@liposomes in antitumor photodynamic therapy. (B) The corresponding tumor volumes after treatment in different groups. Representative photographs of the ear of mice injected with (C) nanoaggregates of bis(pyrene), (D) nothing as a control, and (E) AIEgens-based liposomes and irradiated with two-photon laser. Reproduced with permission from ref. [59].

loaded nanoimmunostimulant could further be endocytosed by antigen-presenting cells, promoting the enhanced T-cell stimulation. The researchers demonstrated the potent antitumor immune responses of the AIEgens-based nanoimmunostimulant

in the B16F10 tumor-bearing mouse model. Additionally, they also confirmed the effective long-term immune memory with the synergetic treatment of αPD-1 immune checkpoint blockade therapy, suggesting the potential of AIEgens-based light-activated immunotherapy in cancer treatment.

In conclusion, AIEgens could be directly used as pharmaceutical agents in NDDSs. Further efforts are still needed in the investigation of the druggability, pharmacodynamics, and pharmacokinetics of AIEgens. With a better understanding of their biological properties, researchers are likely to develop more exquisite NDDSs.

16.2.4 Monitoring the biological behavior of the delivery system

Due to high photostability, superior photosensitivity, and good biosafety, AIEgens are likely to achieve dynamic and real-time monitoring in the living systems, which could facilitate the pharmacokinetic and pharmacodynamic investigation of NDDSs [23, 62].

To track the intracellular behaviors of NDDSs, our group prepared AIEgens-based doxorubicin (DOX)-loaded nanosystems, named TD NPs [63]. When internalized into cells, TD NPs were wrapped into lysosomes, where the acid microenvironment induced the disassembly of TD NPs. Thus, the TPE carriers from TD NPs were observed in the cytosol, suggesting the cytosolic retention of nanocarriers. However, the red fluorescent signals from DOX were colocalized with cell nuclei, implying the successful nuclear translocation of DOX (Figure 16.3A). Therefore, through the analysis of the spatial-temporal fluorescent signals, it is possible to monitor the interaction between NDDSs and subcellular networks.

Liang et al. reported an AIEgens-based nanofiber as a self-indicating agent to monitor intracellular delivery of target genes [64]. They developed the TPE-based carriers to load Cy5-labeled plasmid DNA, and eventually prepared pDNA@TR4 nanofibers (Figure 16.3B). After incubation with HeLa cells for 24 h, the nanofibers showed much colocalization with lysosomes, suggesting their endocytosis into cytosol. Then, the researchers observed red fluorescent signals that were dispersed among the cytoplasm, indicating the disassembly of pDNA@TR4 nanofibers and the release of pDNA from lysosomes into the cytosol (Figure 16.3C). Benefiting from the real-time visualization on their intracellular trajectory, researchers are more likely to fabricate elaborate vectors for high-efficacy intracellular delivery and transfection.

As mentioned above, the flexible fabrication of AIEgens into NDDSs could achieve real-time and long-term monitoring of nanocarriers in living systems. Therefore, with a deeper understanding of nano-bio interaction, researchers could accelerate the rational design of NDDSs for clinical diagnosis and therapy.

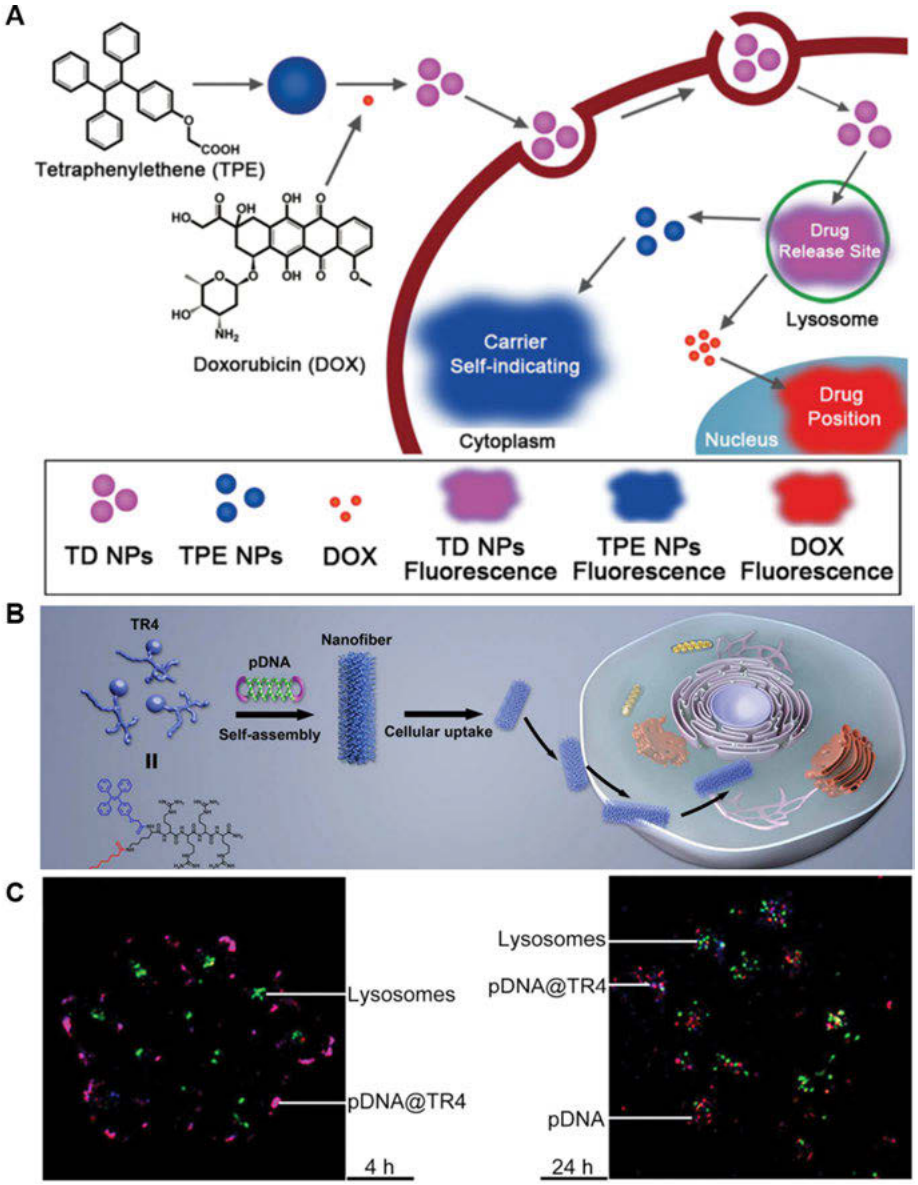

Figure 16.3: (A) Schematic illustration of spatiotemporal drug release. After internalization into cells, TD NPs were wrapped into the lysosomes. The detachment of TD NPs resulted in the lysosomal escape of TPE and DOX. After that, TPE nanocarriers were retained in cytosol, whereas DOX was further translocated into the nucleus as an anticancer agent. (B) Schematic illustration of the intracellular tracking of AIE nanofibers for traceable gene delivery. (C) Spatial distributions of pDNA@TR4 nanofibers for 4 and 24 h. Reproduced with permission from refs. [63, 64].

16.3 Section 2: application in the treatment of infectious diseases

Infectious diseases are demons that have a serious threat to human life and health [65]. Pathogen mainly includes bacterium, virus, fungus, protozoa, and prion. Statistically, more than 1,400 species of the pathogen have been discovered [66]. An epidemic of infectious diseases has a huge terrible influence on human health. For example, coronavirus disease-2019 (COVID-19), what we are fighting against caused by the severe acute respiratory syndrome coronavirus 2 (SARS-CoV-2), is exploding around the world. Until June 2021, more than 170 million people have been infected and more than 3.7 million died because of COVID-19. The treatment and eradication of infectious disease are still a big challenge. Antibiotics are widely used for the killing of bacterial infection and antiviral compounds for the killing of a virus. However, with the overuse of antibiotics, pathogen gets resistant to the therapeutic reagent, and the multidrug-resistant (MDR) pathogenic infection that has spread in the world is a huge burden on public health [67]. Thus, the effort from academic and medical communities is urgent necessity to overcome these difficulties. With the rapid development of the AIE field, scientists have developed AIEgens-based systems for imaging and killing of pathogens, including Gram-positive/negative bacteria and MDR bacteria [25, 26, 28, 32, 68–70].

16.3.1 AIEgens-based delivery systems for the killing of Gram-positive bacteria

Bacterium is one of the major pathogens for infectious diseases. Bacteria are classified into Gram-positive and -negative bacteria based on the difference between the cell wall structure and the chemical components. Gram-positive bacteria have a thick peptidoglycan layer with acidic residues in outer walls, but Gram-negative bacteria have a phospholipid bilayer outside and the thinner peptidoglycan layer embedded in the phospholipid bilayer [71]. Due to the structural difference, the sensitivity of antibiotics to different bacteria is different. Thus, the reasonable selection of antibiotics for the killing of different bacteria is important, which is one way to avoid the abuse of antibiotics. In the past few years, a series of AIEgens-based delivery systems have been developed for the specific killing of Gram-positive, or Gram-negative bacteria or both.

For the treatment of Gram-positive bacteria, the peptidoglycan on the cell wall has been widely used as the therapeutic target. Among antibiotics, vancomycin (Van) is a great compound for the killing of Gram-positive bacteria with a specific binding affinity to peptidoglycan. Liu and colleagues reported a novel AIEgens-based probe for selective recognition and photodynamic killing of Gram-positive

bacteria [72]. After conjugating Van with AIEgens, the fluorescence intensity of the new product AIE-2Van is very weak in an aqueous solution (Figure 16.4A). However, when the AIE-2Van binds specifically to Gram-positive *B. subtilis*, they can be visualized directly with the naked eye. The AIE-2Van can cause irreversible damage to the cell wall due to the generation of toxic ROS with light irradiation (Figure 16.4B). Importantly, the AIE-2Van can only selectively bind to Gram-positive bacteria but not to Gram-negative bacteria.

Considering the rich lipoteichoic acid on the cell wall of Gram-positive bacteria, Zhao et al. have designed and synthesized two AIEgens (MTMM and PTMM) with alkalinity pendants for the specific killing of Gram-positive bacteria (Figure 16.4C) [73]. Specifically, the yellow fluorescence was observed for *S. aureus* after treating with two AIEgens, but no fluorescence signal was detected for Gram-negative bacteria *E. coli*. The antibacterial activity of two AIEgens was evaluated by a colony plate-counting method. As expected, no matter with or without light irradiation after the *E. coli* treated with AIEgens, the colony-forming unit (CFU) has no obvious reduction. However, after *S. aureus* was treated with MTMM and PTMM and then irradiated by light, the CFU reduction rates were 52% and 77%, respectively, indicating that MTMM and PTMM could selectively bind to Gram-positive bacteria and kill them after light irradiation (Figure 16.4D). The immune response system plays a key role in the elimination of pathogens, and the treatment of macrophage-engulfed bacteria is an important task as they can cause severe infectious diseases. Tang and colleagues developed a new AIEgens TTVP for the elimination of macrophage-engulfed bacteria [74]. Benefiting from the AIE characteristic and electrostatic interaction, the TTVP can monitor and report the internalization process and the initiation of the digestion process of Gram-positive bacteria *B. subtilis* by macrophage Raw264.7 cells. Importantly, with the strong generation ability of ROS, TTVP can selectively target the intracellular Gram-positive bacteria *B. subtilis* and ablate them but Gram-negative bacteria. Meanwhile, the AIEgens TTVP was also used for the ultrafast discrimination of Gram-positive bacteria and showed a great antibacterial effect in vitro and in vivo [75].

16.3.2 AIEgens-based delivery systems for the killing of Gram-negative bacteria

Generally, for the imaging and treatment of negatively charged Gram-negative bacteria, the positively charged AIEgens were designed and interacted with Gram-negative bacteria based on the electrostatic interaction [76, 77]. For instance, Tang and colleagues found that the antibacterial efficiency for Gram-negative bacteria could be improved by increasing the positive charges of AIEgens, but the efficiency for Gram-positive bacteria was negligible [78]. To improve the targeting ability of the AIEgens to the Gram-negative bacteria, Ding et al. reported a peptide-based AIE

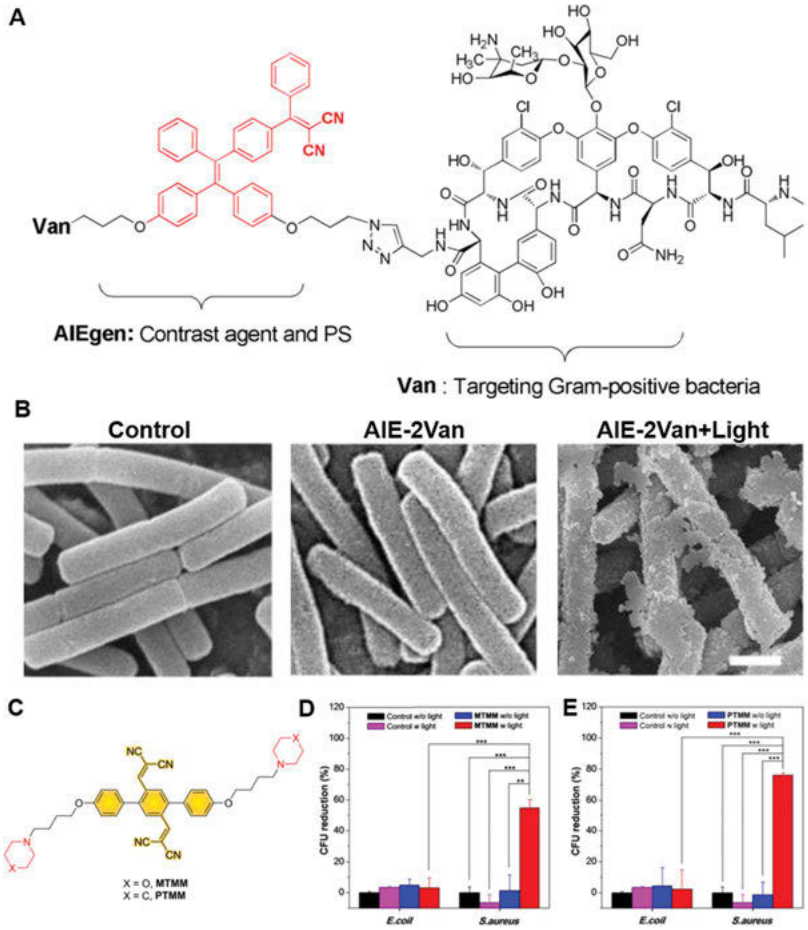

Figure 16.4: (A) Chemical structure of AIE-2Van. (B) Scanning electron microscopic images of *B. subtilis*. Control: no treatment; AIE-2Van: treated with AIE-2Van under dark; AIE-2Van+ light: treated with AIE-2Van and then light irradiation. The scale bar is 1 μm. (C) Chemical structure of MTMM and PTMM. (D) Colony-forming unit reduction of *E. coli* and *S. aureus* with or without MTMM and white light irradiation. (E) Colony-forming unit reduction of *E. coli* and *S. aureus* with or without PTMM and white light irradiation. Reproduced with permission from refs. [72, 73].

bioprobe [79]. Lipopolysaccharide (LPS) is a major component of the cell wall of Gram-negative bacteria and polymyxin B has a strong binding affinity with LPS. Thus, the researchers designed a new AIEgens probe, named AIE-DCM-2 polymyxin B, by conjugating an AIE molecule AIE-DCM with 2 of polymyxin B (Figure 16.5A). Using two Gram-positive bacteria *E. faecalis* and *S. mutans* as well as Gram-negative bacteria *E. coli* and *S. enteritidis* as models, the results indicated that AIE-DCM-2 polymyxin B could selectively target to the Gram-negative bacteria in an aqueous solution with significant enhancement of fluorescence intensity. When the bacteria were incubated

with AIE-DCM-2 polymyxin B and then treated with or without light irradiation, as shown in Figure 16.5B and C, the AIE-DCM-2 polymyxin B showed some antibacterial activity even in the absence of light irradiation, resulting from that polymyxin B could affect the cytoplasmic membrane. In the presence of light irradiation, most of the Gram-negative bacteria *E. coli* and *S. enteritidis* were killed (bacterial lethality to *E. coli* is over 95%), but there was no obvious toxicity to Gram-positive bacteria. In summary, compared with the Gram-positive bacteria, the treatment of Gram-negative bacteria is more difficult as the outer membrane acts as a permeability barrier to many antibacterial agents. Thus, developing AIEgens-based delivery systems with high selectivity and penetration ability is one of major research directions.

16.3.3 AIEgens-based delivery systems for the killing of multidrug-resistant bacteria

MDR during bacterial infection is a tricky global medical issue. At present, antibiotic therapy is still the main means to treat a bacterial infection, However, the excessive use of antibiotics nowadays, especially prophylactic antibiotic therapy, has caused serious antimicrobial resistance [80]. Therefore, it is urgent to develop alternative strategies for better tackling MDR bacterial infection.

Among the emerging alternative strategies, PDT has attracted the most attention. It utilizes PSs, molecular oxygen, and light irradiation to generate ROS, which causes oxidative damages and induces bacterial death [81, 82]. With the advantages of limited antibiotic resistance, minimal invasiveness, low toxicity, and side effects, PDT is a powerful weapon against bacterial resistance [83]. However, the traditional PSs in the aggregated state or high concentration suffer from the ACQ effect, which will weaken their antibacterial efficacy [32, 84, 85]. To address this issue, AIEgens-based PSs light up a new direction of PDT. AIEgens have several distinct advantages over conventional PSs: (1) the AIEgens can colocalize within the bacteria to elevate local drug concentration and enhanced antibacterial efficacy; (2) the AIEgens in the aggregated state can generate abundant ROS for the efficient killing of bacteria. At present, several AIEgens-based PSs have been successfully developed, and these studies suggest that AIEgens are promising candidates for killing MDR bacteria [86–88].

According to the basic mechanism of PDT, decreasing the energy gap ΔE_{ST} between the excited singlet (S_1) state and the excited triplet (T_1) state, promoting intersystem crossing (ISC) from S_1 state to T_1 state, and closing the distance between PSs and targeting sites are effective means to improve the generation efficiency of ROS [32, 82]. However, photosensitization for most traditional PSs is reduced in the aggregated state because nonradiative decay consumes the T_1 state [81]. Fortunately, with low nonradiative decay, AIEgens-based PSs can guarantee ROS generation in

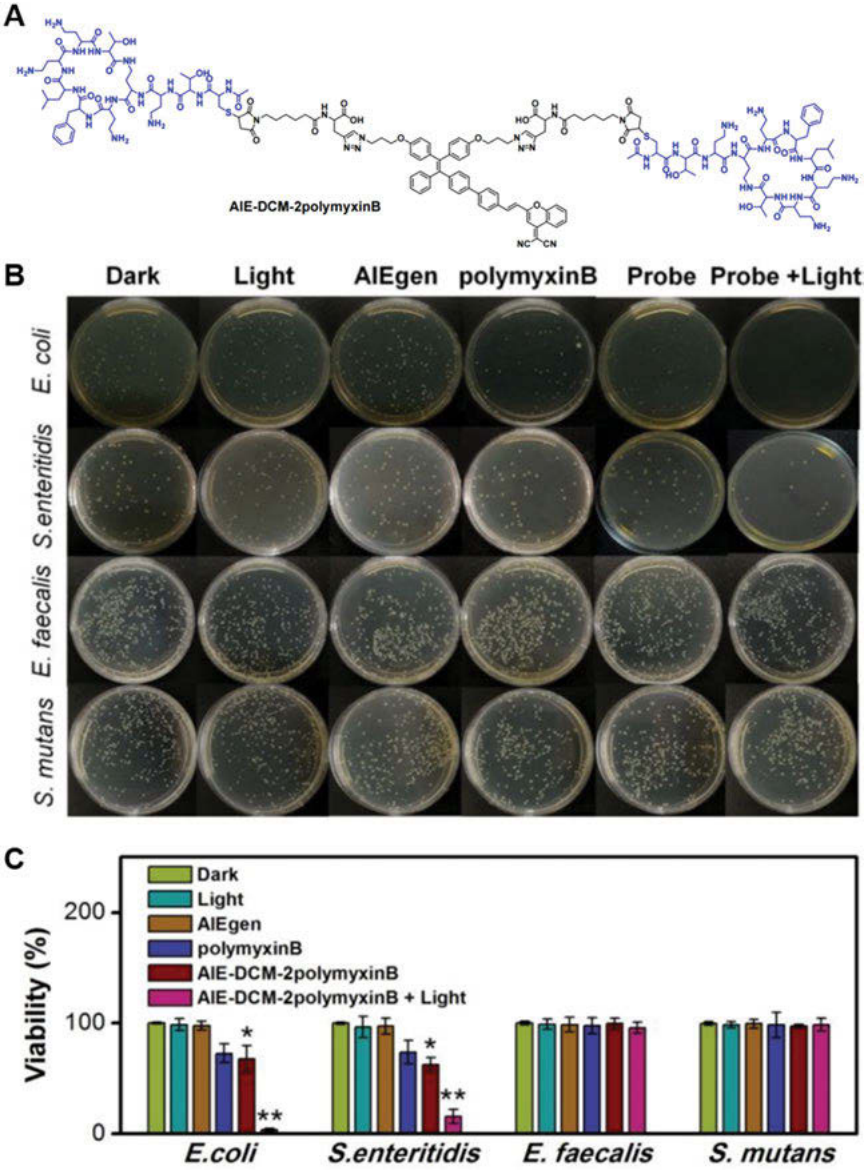

Figure 16.5: (A) Chemical structure of AIE-DCM-2 polymyxin B. (B) Photographs of colony formation of various bacteria under different experimental conditions. (C) Quantitative bacterial activities of various bacteria under different experimental conditions. Dark: keep in the dark and without treatment; light: only light irradiation; AIEgens: keep in the dark after treating with AIE-DCM; polymyxin B: keep in the dark after treating with polymyxin B; probe: keep in the dark after treating with AIE-DCM-2 polymyxin B; probe + light: light irradiation after treating with AIE-DCM-2 polymyxin B. Reproduced with permission from ref. [79].

high efficiency. AIEgens-based PSs will inject new blood into PDT treatment of MDR bacteria-associated infection.

The distance between the PSs and the bacteria is close enough to increase the oxidative damage of ROS to membrane structure and improve the antibacterial activity. Recently, Lee and colleagues reported a new membrane-anchoring AIEgens molecular named TBD-anchor [89]. Due to effective $^1O_2$ generation and bacterial membrane-anchoring abilities, TBD-anchor showed an excellent inhibition efficiency on MDR bacteria. As shown in Figure 16.6A, with the help of both hydrophobic and electrostatic interactions, the TBD-anchor could insert into the surface of bacterial membranes. The anchoring feature is conducive to elevate the oxidative damage of ROS to bacteria. The results showed that TBD-anchor could have a great bactericidal effect (over 99%) on MDR bacteria, including Gram-positive and -negative bacteria. Thus, AIEgens with PDT feature is a good sterilization assistant for eliminating MDR microbes.

Breaking the limitation of the molecular structure design of typical AIEgens-based PSs and exploring novel ideas of molecular design to improve the ISC efficiency and ΔE_{ST} have always been the hot point in this field. Due to the rigid backbones of planar luminophores, the molecular orbitals between the highest occupied molecular orbital and lowest unoccupied molecular orbital has the favor to overlap. This preference of planar luminophores can lead to a high quantum yield in solution but quench in solid or aggregated state. To overcome the hurdle, Li and colleagues developed a series of novel fluorosubstituent planar AIEgens, DMA-AB-F. As shown in Figure 16.6B, these planar AIEgens have stronger intermolecular H-bonding interaction to restrict the molecular motions, which enhance the solid-state luminescence of planar luminophores and AIE performance dramatically [84]. Furthermore, planar AIEgens are verified to facilitate ISC and produce abundant ROS in the aggregated state, which can lead to the efficient elimination of MDR bacteria. As expected, the results of the scanning electron microscopic images indicated that the cell wall lysis happened in both *E. coli* and methicillin-resistant *Staphylococcus aureus* after being treated with DMA-AB-F and light irradiation, but the morphology and cell wall had no change in other groups (Figure 16.6C). Using a standard third-degree burn infection mouse model, the results also showed that the DMA-AB-F could effectively inhibit infection in vivo and recover the wounds (Figure 16.6D and E). This study provides a unique design principle for the development of planar AIEgens-based PSs.

In conclusion, the elimination of MDR bacteria must be a protracted war without gunpowder. Owing to the unique AIE mechanism and the excellent photophysical property of AIEgens, the aggregation-induced generation of ROS effect is contributed to the wipeout of MDR bacteria. This is a great manner to prevent antibiotic tolerance from the source. Thus, the exquisite AIEgens display great potentialities for the killing of MDR bacteria and benefit public health.

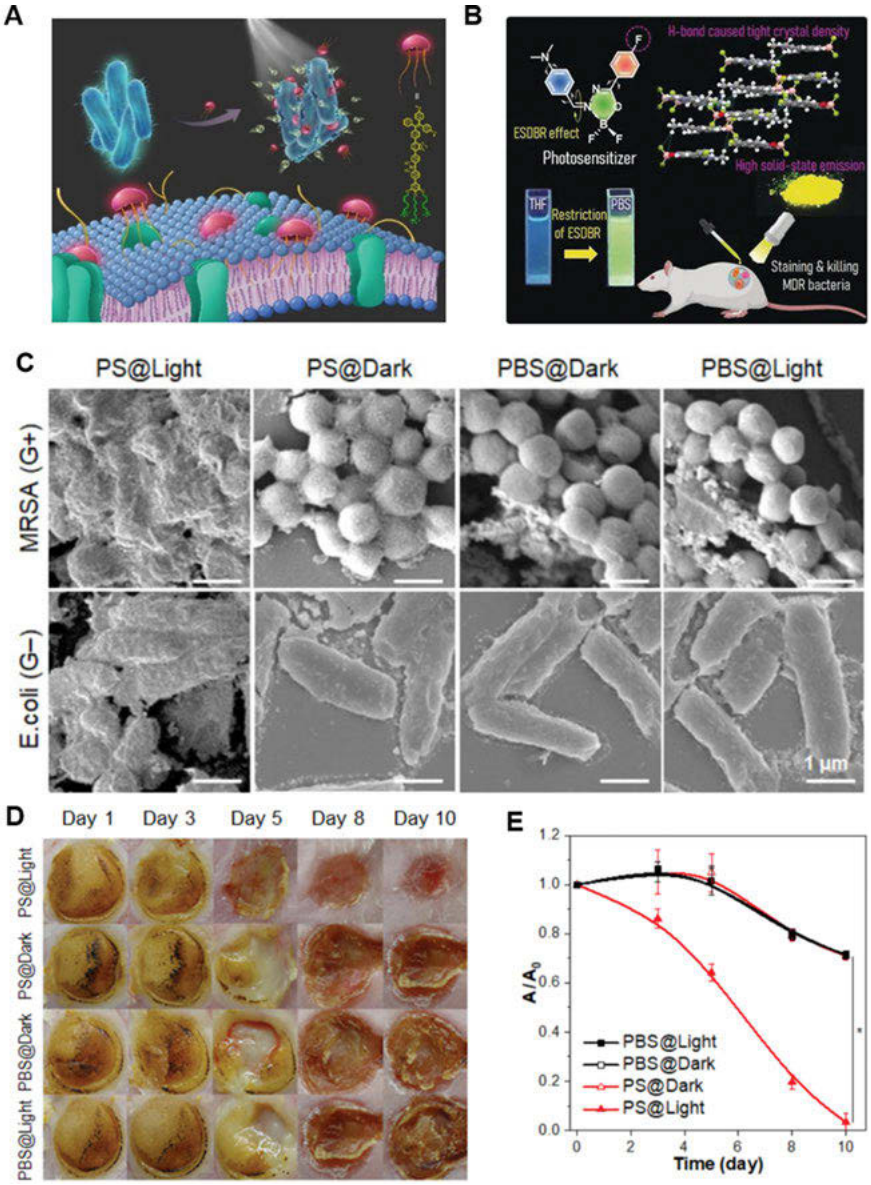

Figure 16.6: (A) Membrane-anchoring AIEgens-based photosensitizer for combating multidrug-resistant bacteria. (B) Planar AIEgens with improved ROS generation for tackling multidrug-resistant bacteria. (C) Scanning electron microscope images of *E. coli* and methicillin-resistant *Staphylococcus aureus* treated under different conditions. The scale bar is 1 μm. (D) Representative photographs of therapeutic effect of burned wounds infected by *E. coli* after treated under different conditions. (E) Relative changes of wound area after 10 days of treatment. PS@Light: PS+ light irradiation; PS@Dark: PS only; PBS@Dark: PBS only; PBS@Light: PBS+ light irradiation. Reproduced with permission from refs. [84, 89].

16.3.4 AIEgens-based delivery systems for the killing of other pathogens

Apart from bacteria, fungi play a crucial role in the eukaryotic ecosystem. Researchers have developed several AIEgens-based delivery systems for the detection and killing of fungi. For instance, Kathiravan et al. synthesized a phenol-based AIEgens (named KB-1) for efficient fungi killing [90]. Once KB-1 interacts with the membrane wall of fungi, the hydroxyl group of activated KB-1 would induce the "turn-on" state of AIE fluorescence, leading to the real-time monitoring of fungi. More importantly, the interaction of KB-1 and fungi promotes the enhanced fungi membrane permeability, which finally causes efficient fungi killing. Using *C. albicans* as a model fungus, the researchers confirmed the potent antifungal capability of KB-1. Similarly, Maurya et al. also developed supramolecular AIEgens with Cu^{2+} moiety [91]. Due to the metal activity of Cu^{2+}, the supramolecular AIEgens display efficient inhibitory action on *Bipolaris oryzae* and *Rhizoctonia solani*. Given the antimicrobial potential of AIEgens, more elaborate AIEgens-based delivery systems are expected to be applied in clinical use.

Influenza viruses are RNA viruses causing influenza among humans and animals. The research team of You reported a TPE-based DNA nanosystem for influenza virus detection [92]. Through covalent conjugation, TPE moiety was introduced with amino-modified DNA. In the presence of an intracellular reductive environment, the disulfide group was rapidly reduced so that the TPE moiety can be released into the cytosol. Due to its high hydrophobicity, TPE moiety would form aggregates with enhanced fluorescent signals. Therefore, the TPE-based DNA nanosystem can be used for intracellular biosensing and bioimaging of the influenza virus. In addition, with the pandemic outbreak of COVID-19, there arises the urgent need to develop rapid, convenient, and accurate detection and therapeutic assays for SARS-CoV-2. To realize sensitive detection, researchers have prepared various AIEgens for high-performance fluorescent viral detection. The research team of Li developed AIEgens-based polystyrene NPs for the early detection of SARS-CoV-2 [93]. BPBT, acting as the AIEgens unit with NIR emission, was loaded onto the 300 nm polystyrene NPs to form AIE810 NP. Through detection with clinical serum samples, AIE810NP-labeled SARS-CoV-2 antigen displayed high sensitivity for both IgM and IgG, suggesting the superior potential for point-of-care clinical diagnosis. Conclusively, due to the high performance of AIEgens, as well as their potential antimicrobial actions, researchers are making efforts on the development of innovative AIEgens-based delivery systems for microbe detection and killing.

16.4 Section 3: application in other diseases

With the unique mechanism of AIEgens, apart from the wide application in the treatment of cancer and infectious diseases, AIEgens have also been developed and used for the treatment of other diseases. The basic characteristic of AIEgens is that AIE molecules are intensely emissive in aggregate form. Combining with the specific characteristic of diseases, different strategies can be designed for diagnosing and treating diseases. The application of AIEgens-based delivery systems in other diseases has great research potential and we believe a lot of interesting research works will be reported. Here, we select some existing cases to discuss and show how they can be used in the future.

16.4.1 AIEgens-based delivery systems for amyloid diseases treatment

Amyloid diseases are a large group of misfolding diseases, including Alzheimer's, Parkinson's, and Huntington's diseases, rheumatoid arthritis, type II diabetes, cardiac arrhythmias, atherosclerosis, and polyneuropathy [94, 95]. The amyloidal fibrils, which have been regarded as the hallmarks of amyloid diseases, are the toxic aggregation of the insoluble and misfolding protein. The accumulation of amyloidal fibrils in tissues can lead to biological dysfunctions, such as induced cognitive decline and impaired brain function [96]. The aggregation of amyloid peptides and proteins play an important role, leading to amyloid diseases [97]. Thus, the early detection and effective inhibition of the aggregation of amyloid peptides and proteins is an irreplaceable way to reduce the number of pathogenic diseases. So far, fluorescent imaging has emerged as a powerful tool to identify and monitor the formation process of amyloidal fibrils [98]. Thanks to the mechanism of AIE that the fluorescent intensity obvious enhanced when the AIE molecules aggregated, some AIEgens-based probes have been designed for detecting and monitoring of aggregation of amyloid peptides and proteins [99–102]. However, the treatment of amyloid diseases is still a big challenge in the current world.

With the outstanding feature of AIE, the theranostic AIEgens have been developed for the inhibition of the aggregation of amyloidal fibrils. The first impressive case was reported by Tang and colleagues in 2012. Using insulin as a model protein, the researchers claimed that AIEgens, sodium 1,2-bis[4-(3-sulfonatopropoxyl)phenyl]-1,2-diphenylethene (BSPOTPE), could probe the form of insulin in buffer, and work as a bioprobe for quantitative analysis and kinetics study of amyloidal fibril formation [103]. Upon incubating with native insulin, the fluorescence of BSPOTPE is very weak. However, the fluorescence intensity of BSPOTPE is very strong when it is incubated with insulin fibrils. Importantly, the nucleation process of fibril formation can be inhibited by mixing the BSPOTPE and native insulin (Figure 16.7A).

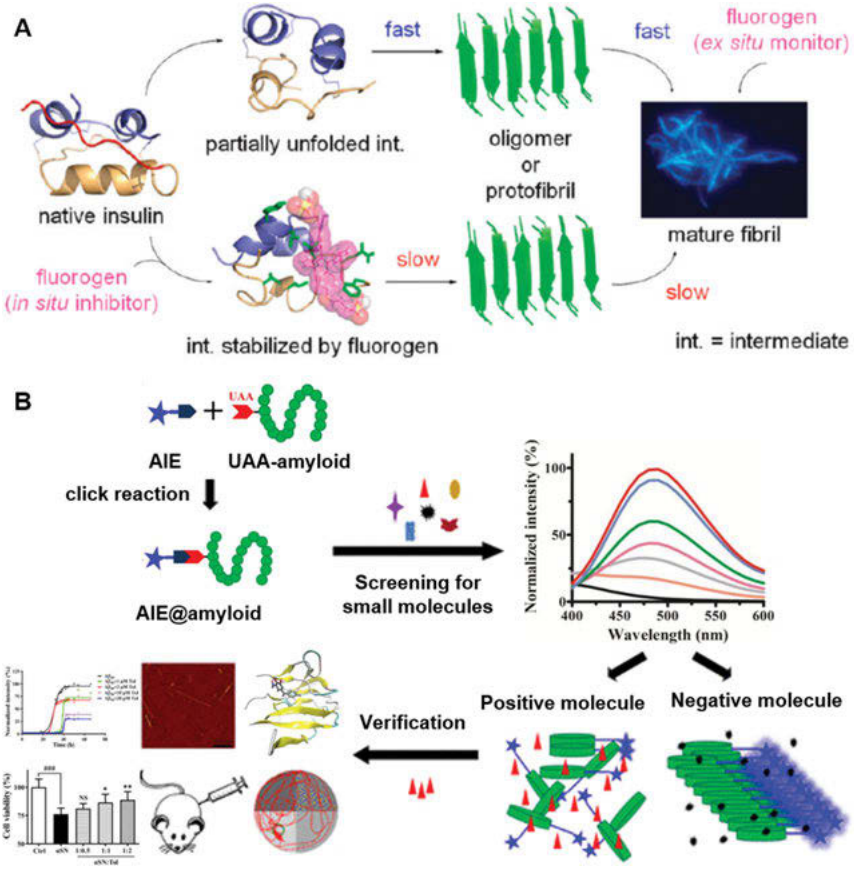

Figure 16.7: (A) Mechanistic diagrams for monitoring and inhibition of amyloidal fibril formation by BSPOTPE. (B) The workflow for screening and verification of potential amyloid inhibitors by EPB@pAzF-amyloids probe. The AIE-based probe will exhibit strong fluorescence intensity in the absence of amyloid inhibitors (negative molecule), but exhibit weak fluorescence intensity in the presence of amyloid inhibitors (positive molecule). Reproduced with permission from refs. [103, 104].

The inhibitory potency is also dependent on the dose of BSPOTPE. Thus, this work is a great and first example to prove the potential that AIEgens can be used for the treatment of amyloid disease. In addition, AIEgens were also used as a screening platform for the screen of amyloid inhibitors to help the treatment of amyloid diseases. Jia et al. developed an AIE-based antiamyloid drug platform by site-specific conjugating AIE molecule EPB with two amyloid proteins, amyloid-β protein and α-40 synuclein (Figure 16.7B) [104]. In the presence of an effective amyloid inhibitor, the aggregation of AIE-amyloid probes is inhibited and thus no fluorescence can be detected. If the candidate is not an effective inhibitor, an obvious fluorescent signal can be detected due to the aggregation of AIE-amyloid probes. Finally, a small molecule tolcapone

was screened from the Drugbank database as an effective amyloid inhibitor. In summary, when AIE meets the protein aggregates, the AIEgens can act as a powerful candidate to treat disease rooted in protein aggregation.

16.4.2 AIEgens-based delivery systems boost stem cell-based therapy

Stem cells are undifferentiated cells. Under certain stimulus conditions, they can be differentiated into specific cell types of organisms and have the self-renewal ability [105]. In our body, stem cells work as an internal repair system and they are controlled by different signals, including external (such as physical contact and chemical factor) and internal signals. Taken advantage of regeneration, stem cell-based therapy is being widely investigated and has become an advanced scientific topic. Stem cell-based therapy has been used in different diseases, including neurodegenerative diseases, cardiovascular diseases, orthopedic diseases, and inflammatory diseases [106–108]. However, for the best beneficial outcome, the potential risk related to stem cell-based therapy in vivo should be considered and resolved, such as differentiation into undesirable cell type, short survival, disturbed differentiation capacities, and immune response [109]. To resolve these potential risks, the development of an effective method to monitor the transportation behavior, differentiation process and status is highly urgent. Without a doubt, fluorescence imaging is the most appropriate choice with high brightness and stability and low toxicity.

Thanks to the contributions of researchers from the AIE field, some efforts have been made with the AIEgens-based delivery systems to boost the development of stem cell-based therapy. One of the benefits of AIEgens is that they can label stem cells for a long time, so it is very helpful to track the activity of stem cells after transplantation. For example, Liu and colleagues developed AIE dots for noninvasive in vivo long-term tracking of adipose-derived stem cells (ADSCs) in an ischemia hindlimb disease model [110]. First, the AIE molecules, TPETPAFN, were encapsulated by DSPE-PEG2000-maleimide through nanoprecipitation method, and the loading content was up to 39.8%, which offers enough brightness of AIE dots (Figure 16.8A). To increase the intracellular amount of AIE dots, the surface was further modified with cell-penetrating peptide TAT. Importantly, the fluorescence emission of AIE dots in the FR/NIR region and the Stokes shift is around 160 nm, which ensured that the AIE dots were suitable for in vivo tracking application. The safety evaluation results indicated that the AIE dots had low cytotoxicity and high biocompatibility to ADSCs in vitro and were safe for in vivo application. After incubation with ADSCs, the AIE dots exhibited long-term retention and had negligible interference on pluripotency and secretome of ADSCs, which was important to ensure the therapeutic outcome of stem cell-based therapy in vivo and avoid the potential risk as we mentioned above. More importantly, after the ischemic hindlimb

was intramuscularly injected with AIE dots-labeled stem cells, the fluorescence could be observed even after 42 days, indicating that AIE dots could track and report the fate of ADSCs in vivo for the long term (Figure 16.8B). For the treatment of ischemic diseases, the vascularization with subcutaneous blood flows could be easily observed after being treated with AIE dots-labeled stem cells for 30 days. However, the foot and even the limb were lost in the control groups due to severe ischemia (Figure 16.8C). Taken the advantage of AIE dots, they also found that ADSCs could treat ischemic diseases in two different ways. On the one hand, the ADSCs can secrete angiogenic factor to promote angiogenesis. On the other hand, ADSCs can participate in neovascularization via differentiating into necessary cells. Together, this work is a great example to illustrate the potential of AIEgens-based delivery systems in the tracking of stem cells and their regenerative capacity. Using the same AIE molecule TPETPAFN, Zeng and colleagues also reported that the AIEgens-labeled human embryonic stem cells were still detectable after 1 month of transplantation [111].

Stroke is ranked as the second most common single cause of death. It always occurs in elderly people, and more than half of patients fail to recover to normal, and long-term health care is needed [112]. Among them, stem cell-based therapy has become a promising therapeutic approach for stroke treatment [113]. However, the visualization of the injected stem cells in the ischemia region is highly desirable for ensuring a higher successful therapeutic effect. In 2016, Liu and colleagues reported a similar AIE-based system as the above case for tracking the therapy process of bone marrow stromal cells (BMSCs) [114]. In this work, they designed and synthesized a new AIE molecule, TPEEP, with bright red emission and low phototoxicity. In vitro studies showed that the targeted AIE NPs could be highly taken up by BMSCs, and the intracellular fluorescence was stable for more than 10 days. Using a rat photothrombotic ischemia model, the AIEgens-labeled BMSCs were transfused, and the density and location of BMSCs were evaluated at the lesion site after 7 days. With the advantage of AIE visualization, the fluorescence intensity was highly bright in the lesion site, but no fluorescence was observed in healthy brain sectioned slices, which indicated that the BMSCs successfully migrated to the ischemic region. Besides, as one kind of potential alternatives to stem cell-based therapy, extracellular vesicles secreted from different cells are increasingly being utilized as therapeutic agents [115, 116]. For instance, AIEgens-labeled extracellular vesicles released by mesenchymal stem cells were used for liver regeneration and improving the mitochondrial function in renal ischemia-reperfusion injury [117, 118].

Comparing with the fact that AIEgens are used to treat diseases directly, AIEgens for stem cell-based therapy act as a guard to monitor, evaluate, and control the therapeutic process. Moreover, unlike the small-molecule therapy that directly targets the diseased cells, stem cell-based therapy is a tedious process, and the differentiation process in vivo must be precisely controlled. Thus, in terms of the potential risks of stem cell-based therapy, the integration of AIEgens into the stem cell-based therapy system is a great development of regenerative medicine.

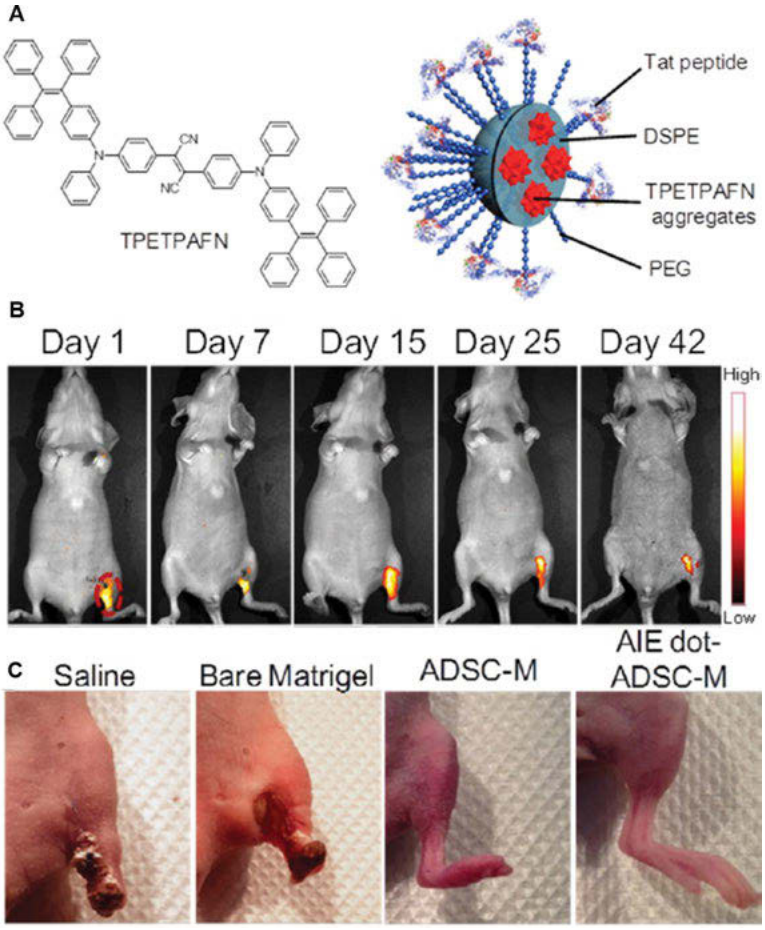

Figure 16.8: (A) Chemical structure of TPETPAFN and schematic illustration of the AIE dots. (B) In vivo fluorescence monitoring of the ischemic hind limb-bearing mouse at different time points after injected with AIE dots-labeled adipose-derived stem cells. (C) Representative photographs of the therapeutics impact of the ischemic hind limb-bearing mice for 30 days. Reproduced with permission from ref. [110].

16.5 Summary

With the high photostability, superior photosensitivity, good biosafety, and tunable structures, AIEgens-based delivery systems have been extensively designed and used for the treatment and diagnosis of different diseases. In this chapter, we mainly summarized the application of AIEgens-based delivery systems on the treatment of cancer, infectious diseases, amyloid diseases, and so forth. In most cases,

the AIE molecules were loaded or assembled into NPs, fabricated as AIEgens-based delivery systems. More importantly, it is noteworthy that the application of AIEgens-based delivery systems promotes the design and development of nanomedicine in different respects. The main reason can be concluded as that AIEgens make the NDDSs traceable and multifunctional. Of course, AIEgens, with various bioactive effects, also show a drug-like property for the treatment of diseases.

For better development of AIEgens-based delivery systems in the clinical application, we proposed that the further effort can be focused on the following respects: (1) Developing the new AIEgens-based delivery systems with multiphoton excitation and longer wavelength emission for deep-tissue monitoring; (2) understanding the absorption, distribution, metabolism, and toxicity of AIEgens-based delivery systems; (3) more in vivo and preclinical trials should be conducted to promote the clinical transformation of AIEgens-based delivery systems; (4) taking the advantages of AIE property and the physiological property of diseases, more active and multifunctional AIEgens-based delivery systems should be designed and tested in more disease models. Finally, we hope that this chapter will bring new enlightenment and promote the application of AIE-based delivery systems for the treatment of diseases.

References

[1] Chin JH, Vora N, The global burden of neurologic diseases, Neurology, 2014, 83(4), 349–351.
[2] Torchilin VP, Multifunctional, stimuli-sensitive nanoparticulate systems for drug delivery, Nat Rev Drug Discov, 2014, 13(11), 813–827.
[3] Adiseshaiah PP, Crist RM, Hook SS, McNeil SE, Nanomedicine strategies to overcome the pathophysiological barriers of pancreatic cancer, Nat Rev Clin Oncol, 2016, 13(12), 750–765.
[4] Wang Y-F, Liu L, Xue X, Liang X-J, Nanoparticle-based drug delivery systems: What can they really do in vivo?, F1000research, 2017, 6, 681.
[5] Kelkar SS, Reineke TM, Theranostics: Combining imaging and therapy, Bioconjugate Chem, 2011, 22(10), 1879–1903.
[6] Ryu JH, Lee S, Son S, et al., Theranostic nanoparticles for future personalized medicine, J Control Release, 2014, 190, 477–484.
[7] Rao J, Dragulescu-Andrasi A, Yao H, Fluorescence imaging in vivo: Recent advances, Curr Opin Biotech, 2007, 18(1), 17–25.
[8] Kang B, Afifi MM, Austin LA, El-Sayed MA, Exploiting the nanoparticle plasmon effect: Observing drug delivery dynamics in single cells via Raman/fluorescence imaging spectroscopy, Acs Nano, 2013, 7(8), 7420–7427.
[9] Guan X, Xie Z, Jing X, Fluorescent nanoparticles for drug delivery and theranostic, Nanomed Nanotechnol Biol Med, 2016, 12(2), 506.
[10] Li S, Hu K, Cao W, et al., pH-responsive biocompatible fluorescent polymer nanoparticles based on phenylboronic acid for intracellular imaging and drug delivery, Nanoscale, 2014, 6(22), 13701–13709.
[11] Ma X, Chi W, Han X, et al., Aggregation-induced emission or aggregation-caused quenching? Impact of covalent bridge between tetraphenylethene and naphthalimide, Chin Chem Lett, 2021, 32(5), 1790–1794.

[12] Yuan H, Zhao W, Wu W, How can aggregation-caused quenching based bioimaging of drug nanocarriers be improved? Ther Deliv, 2020, 11(1), 809–812.
[13] Kang T, Um K, Park J, et al., Minimizing the fluorescence quenching caused by uncontrolled aggregation of CdSe/CdS core/shell quantum dots for biosensor applications, Sens Actuators B Chem, 2016, 222, 871–878.
[14] Chi Z, Zhang X, Xu B, et al., Recent advances in organic mechanofluorochromic materials, Chem Soc Rev, 2012, 41(10), 3878–3896.
[15] Luo J, Xie Z, Lam JWY, et al., Aggregation-induced emission of 1-methyl-1,2,3,4,5-pentaphenylsilole, Chem Commun, 2001, (18), 1740–1741.
[16] Hong Y, Lam JWY, Tang BZ, Aggregation-induced emission, Chem Soc Rev, 2011, 40(11), 5361–5388.
[17] Zhao Z, He B, Tang BZ, Aggregation-induced emission of siloles, Chem Sci, 2015, 6(10), 5347–5365.
[18] Peng Q, Shuai Z, Molecular mechanism of aggregation-induced emission, Aggregate, 2021, 2(5), e91.
[19] Zhang J, Li C, Zhang X, et al., In vivo tumor-targeted dual-modal fluorescence/CT imaging using a nanoprobe co-loaded with an aggregation-induced emission dye and gold nanoparticles, Biomaterials, 2015, 42, 103–111.
[20] Wang Y-F, Che J, Zheng Y-C, et al., Multi-stable fluorescent silica nanoparticles obtained from in situ doping with aggregation-induced emission molecules, J Mater Chem B, 2015, 3(45), 8775–8781.
[21] Dong Y, Liu B, Yuan Y, AIEgen based drug delivery systems for cancer therapy, J Control Release, 2018, 290, 129–137.
[22] Yuan Y, Xu S, Zhang C-J LB, Liu B., Light-responsive AIE nanoparticles with cytosolic drug release to overcome drug resistance in cancer cells, Polym Chem-UK, 2016, 7(21), 3530–3539.
[23] Yuan Y, Liu B, Visualization of drug delivery processes using AIEgens, Chem Sci, 2017, 8(4), 2537–2546.
[24] Qian J, Tang BZ, AIE luminogens for bioimaging and theranostics: From organelles to animals, Chem, 2017, 3(1), 56–91.
[25] Chen X, Huang L, Jia Y, et al., AIE-based theranostic probe for sequential imaging and killing of bacteria and cancer cells, Adv Opt Mater, 2020, 8(14), 1902191.
[26] He X, Xiong L-H, Zhao Z, et al., AIE-based theranostic systems for detection and killing of pathogens, Theranostics, 2019, 9(11), 3223–3248.
[27] Feng G, Liu B, Multifunctional AIEgens for future theranostics, Small, 2016, 12(47), 6528–6535.
[28] Feng X, Tong B, Shi J, Zhao C, Cai Z, Dong Y, Recent progress of aggregation-induced emission luminogens (AIEgens) for bacterial detection and theranostics, Mater Chem Front, 2020, 5(3), 1164–1184.
[29] Gu X, Kwok RTK, Lam JWY, Tang BZ, AIEgens for biological process monitoring and disease theranostics, Biomaterials, 2017, 146, 115–135.
[30] Du X, Wang J, Qin A, Tang B, Application of AIE-active probes in fluorescence sensing, Chin Sci Bull, 2020, 65(15), 1428–1447.
[31] Kwok RTK, Leung CWT, Lam JWY, Tang BZ, Biosensing by luminogens with aggregation-induced emission characteristics, Chem Soc Rev, 2014, 44(13), 4228–4238.
[32] Bai H, He W, Chau JHC, et al., AIEgens for microbial detection and antimicrobial therapy, Biomaterials, 2020, 268, 120598.
[33] Liu H, Xiong L, Kwok RTK, He X, Lam JWY, Tang BZ, AIE bioconjugates for biomedical applications, Adv Opt Mater, 2020, 8(14), 2000162.

[34] Mei J, Hong Y, Lam JWY, Qin A, Tang Y, Tang BZ, Aggregation-induced emission: The whole is more brilliant than the parts, Adv Mater Weinheim, 2014, 26(31), 5429–5479.
[35] Zhao Z, Zhang H, Lam JWY, Tang BZ, Aggregation-induced emission: New vistas at the aggregate level, Angewandte Chemie Int Ed, 2020, 59(25), 9888–9907.
[36] Qi J, Chen C, Ding D, Tang BZ, Aggregation-induced emission luminogens: Union is strength, gathering illuminates healthcare, Adv Healthc Mater, 2018, 7(20), 1800477.
[37] Kang M, Zhang Z, Song N, et al., Aggregation-enhanced theranostics: AIE sparkles in biomedical field, Aggregate, 2020, 1(1), 80–106.
[38] Mei J, Leung NLC, Kwok RTK, Lam JWY, Tang BZ, Aggregation-induced emission: Together we shine, united we soar!, Chem Rev, 2015, 115(21), 11718–11940.
[39] Chen Y, Lam JWY, Kwok RTK, Liu B, Tang BZ, Aggregation-induced emission: Fundamental understanding and future developments, Mater Horiz, 2018, 6(3), 428–433.
[40] Zhu C, Kwok RTK, Lam JWY, Tang BZ, Aggregation-induced emission: A trailblazing journey to the field of biomedicine, Acs Appl Bio Mater, 2018, 1(6), 1768–1786.
[41] Herskovic A, Martz K, Al-Sarraf M, et al., Combined chemotherapy and radiotherapy compared with radiotherapy alone in patients with cancer of the esophagus, New Engl J Med, 1992, 326(24), 1593–1598.
[42] Mellman I, Coukos G, Dranoff G, Cancer immunotherapy comes of age, Nature, 2011, 480(7378), 480–489.
[43] Ioannidis JPA, Kim BYS, Trounson A, How to design preclinical studies in nanomedicine and cell therapy to maximize the prospects of clinical translation, Nat Biomed Eng, 2018, 2(11), 797–809.
[44] Jiang W, Wang Y, Wargo JA, Lang FF, Kim BYS, Considerations for designing preclinical cancer immune nanomedicine studies, Nat Nanotechnol, 2021, 16(1), 6–15.
[45] van der Meel R, Sulheim E, Shi Y, Kiessling F, Mulder WJM, Lammers T, Smart cancer nanomedicine, Nat Nanotechnol, 2019, 14(11), 1007–1017.
[46] Sun W, Luo L, Feng Y, et al., Aggregation–induced emission gold clustoluminogens for enhanced low-dose X-ray-induced photodynamic therapy, Angewandte Chemie Int Ed, 2020, 59(25), 9914–9921.
[47] Gao M, Tang BZ, AIE-based cancer theranostics, Coord Chem Rev, 2020, 402, 213076.
[48] Liu J, Hu F, Wu M, et al., Bioorthogonal coordination polymer nanoparticles with aggregation-induced emission for deep tumor-penetrating radio- and radiodynamic therapy, Adv Mater Weinheim, 2021, 33(9), 2007888.
[49] Cheng Y, Sun C, Liu R, et al., A multifunctional peptide-conjugated AIEgen for efficient and sequential targeted gene delivery into the nucleus, Angewandte Chemie Int Ed, 2019, 58(15), 5049–5053.
[50] Chen G, Abdeen AA, Wang Y, et al., A biodegradable nanocapsule delivers a Cas9 ribonucleoprotein complex for in vivo genome editing, Nat Nanotechnol, 2019, 14(10), 974–980.
[51] Bruggen CV, Hexum JK, Tan Z, Dalal RJ, Reineke TM, Nonviral gene delivery with cationic glycopolymers, Acc Chem Res, 2019, 52(5), 1347–1358.
[52] Shi L, Wu W, Duan Y, et al., Light-induced self-escape of spherical nucleic acid from endo/lysosome for efficient non-cationic gene delivery, Angewandte Chemie Int Ed, 2020, 59(43), 19168–19174.
[53] Song N, Zhang Z, Liu P, et al., Nanomaterials with supramolecular assembly based on AIE luminogens for theranostic applications, Adv Mater, 2020, 32(49), 2004208.
[54] Yi X, Hu -J-J, Dai J, et al., Self-guiding polymeric prodrug micelles with two aggregation-induced emission photosensitizers for enhanced chemo-photodynamic therapy, Acs Nano, 2021, 15(2), 3026–3037.

[55] Li H, Yao Q, Xu F, et al., An activatable AIEgen probe for high-fidelity monitoring of overexpressed tumor enzyme activity and its application to surgical tumor excision, Angew Chem-Ger Edit, 2020, 132(25), 10272–10281.
[56] Qi J, Duan X, Liu W, et al., Dragonfly-shaped near-infrared AIEgen with optimal fluorescence brightness for precise image-guided cancer surgery, Biomaterials, 2020, 248, 120036.
[57] Liu J, Chen C, Ji S, et al., Long wavelength excitable near-infrared fluorescent nanoparticles with aggregation-induced emission characteristics for image-guided tumor resection, Chem Sci, 2017, 8(4), 2782–2789.
[58] Zeng Z, Ouyang J, Sun L, Zeng C, Zeng F, Wu S, Activatable nanocomposite probe for preoperative location and intraoperative navigation for orthotopic hepatic tumor resection via MSOT and aggregation-induced Near-IR-I/II fluorescence imaging, Anal Chem, 2020, 92(13), 9257–9264.
[59] Yang Y, Wang L, Cao H, et al., Photodynamic therapy with liposomes encapsulating photosensitizers with aggregation-induced emission, Nano Lett, 2019, 19(3), 1821–1826.
[60] Ngwa W, Irabor OC, Schoenfeld JD, Hesser J, Demaria S, Formenti SC, Using immunotherapy to boost the abscopal effect, Nat Rev Cancer, 2018, 18(5), 313–322.
[61] Mao D, Hu F, Yi Z, et al., AIEgen-coupled upconversion nanoparticles eradicate solid tumors through dual-mode ROS activation, Sci Adv, 2020, 6(26), eabb2712.
[62] Xue X, Xu J, Wang PC, Liang X-J, Subcellular behaviour evaluation of nanopharmaceuticals with aggregation-induced emission molecules, J Mater Chem C, 2016, 4(14), 2719–2730.
[63] Xue X, Zhao Y, Dai L, et al., Spatiotemporal drug release visualized through a drug delivery system with tunable aggregation-induced emission, Adv Mater, 2014, 26(5), 712–717.
[64] Zhang C, Zhang T, Jin S, et al., Virus-inspired self-assembled nanofibers with aggregation-induced emission for highly efficient and visible gene delivery, Acs Appl Mater Inter, 2017, 9(5), 4425–4432.
[65] Zhao Z, Li Y, Zhou L, et al., Prevention and treatment of COVID-19 using Traditional Chinese Medicine: A review, Phytomedicine, 2020, 85, 153308.
[66] Hay SI, Battle KE, Pigott DM, et al., Global mapping of infectious disease, Philos Trans Roy Soc B Biol Sci, 2013, 368(1614), 20120250.
[67] Kaufmann SHE, Dorhoi A, Hotchkiss RS, Bartenschlager R, Host-directed therapies for bacterial and viral infections, Nat Rev Drug Discov, 2018, 17(1), 35–56.
[68] Li D, Chen J, Hong M, et al., Cationic glycopolymers with aggregation-induced emission for the killing, imaging, and detection of bacteria, Biomacromolecules, 2021, 22(5), 2224–2232.
[69] Zhang Y, Zhao X, Li Y, et al., A fluorescent photosensitizer with far red/near-infrared aggregation-induced emission for imaging and photodynamic killing of bacteria, Dyes Pigm, 2019, 165, 53–57.
[70] Kang M, Kwok RTK, Wang J, et al., A multifunctional luminogen with aggregation-induced emission characteristics for selective imaging and photodynamic killing of both cancer cells and Gram-positive bacteria, J Mater Chem B, 2018, 6(23), 3894–3903.
[71] Hu R, Zhou F, Zhou T, et al., Specific discrimination of gram-positive bacteria and direct visualization of its infection towards mammalian cells by a DPAN-based AIEgen, Biomaterials, 2018, 187, 47–54.
[72] Feng G, Yuan Y, Fang H, et al., A light-up probe with aggregation-induced emission characteristics (AIE) for selective imaging, naked-eye detection and photodynamic killing of Gram-positive bacteria, Chem Commun, 2015, 51(62), 12490–12493.
[73] Zhuang J, Yang H, Li Y, Wang B, Li N, Zhao N, Efficient photosensitizers with aggregation-induced emission characteristics for lysosome- and Gram-positive bacteria-targeted photodynamic therapy, Chem Commun, 2020, 56(17), 2630–2633.

[74] Lee MMS, Yan D, Chau JHC, et al., Highly efficient phototheranostics of macrophage-engulfed Gram-positive bacteria using a NIR luminogen with aggregation-induced emission characteristics, Biomaterials, 2020, 261, 120340.
[75] Lee MMS, Xu W, Zheng L, et al., Ultrafast discrimination of Gram-positive bacteria and highly efficient photodynamic antibacterial therapy using near-infrared photosensitizer with aggregation-induced emission characteristics, Biomaterials, 2020, 230, 119582.
[76] Li Q, Li Y, Min T, et al., Time-dependent photodynamic therapy for multiple targets: A highly efficient AIE-active photosensitizer for selective bacterial elimination and cancer cell ablation, Angewandte Chemie Int Ed, 2020, 59(24), 9470–9477.
[77] Ma H, Ma Y, Lei L, et al., Light-enhanced bacterial killing and less toxic cell imaging: Multicationic aggregation-induced emission matters, ACS Sustain Chem Eng, 2018, 6(11), 15064–15071.
[78] Shi X, Sung SHP, Chau JHC, et al., Killing G(+) or G(–) bacteria? The important role of molecular charge in AIE-active photosensitizers, Small Methods, 2020, 4(7), 2000046.
[79] Bao P, Li C, Ou H, et al., A peptide-based aggregation-induced emission bioprobe for selective detection and photodynamic killing of Gram-negative bacteria, Biomater Sci-UK, 2020, 9(2), 437–442.
[80] Li Y, Liu F, Zhang J, et al., Efficient killing of multidrug-resistant internalized bacteria by AIEgens in vivo, Adv Sci, 2021, 8(9), 2001750.
[81] Prasad P, Gupta A, Sasmal PK, Aggregation-induced emission active metal complexes: A promising strategy to tackle bacterial infections, Chem Commun, 2020, 57(2), 174–186.
[82] Hu F, Xu S, Liu B, Photosensitizers with aggregation-induced emission: Materials and biomedical applications, Adv Mater, 2018, 30(45), 1801350.
[83] Zou Q, Wang J-L, Wu M-Y, et al., A highly efficient aggregation-induced emission photosensitizer for photodynamic combat of multidrug-resistant bacteria, Chem Res Chinese U, 2021, 37(1), 150–156.
[84] Ni J, Min T, Li Y, et al., Planar AIEgens with enhanced solid-state luminescence and ROS generation for multidrug-resistant bacteria treatment, Angewandte Chemie Int Ed, 2020, 59(25), 10179–10185.
[85] Liu S, Feng G, Tang BZ, Liu B, Recent advances of AIE light-up probes for photodynamic therapy, Chem Sci, 2021, 12(19), 6488–6506.
[86] Li Y, Zhao Z, Zhang J, et al., A bifunctional aggregation-induced emission luminogen for monitoring and killing of multidrug-resistant bacteria, Adv Funct Mater, 2018, 28(42), 1804632.
[87] Qi G, Hu F, Chong KC, et al., Bacterium-templated polymer for self-selective ablation of multidrug-resistant bacteria, Adv Funct Mater, 2020, 30(31), 2001338.
[88] Li Y, Liu F, Zhang J, et al., Targeting multidrug-resistant bacteria: Efficient killing of multidrug-resistant internalized bacteria by AIEgens in vivo, Adv Sci, 2021, 8(9), 2170051.
[89] Chen H, Li S, Wu M, et al., Membrane-anchoring photosensitizer with aggregation-induced emission characteristics for combating multidrug-resistant bacteria, Angewandte Chemie Int Ed, 2020, 59(2), 632–636.
[90] Kathiravan A, Sundaravel K, Jaccob M, et al., Pyrene Schiff base: Photophysics, aggregation induced emission, and antimicrobial properties, J Phys Chem B, 2014, 118(47), 13573–13581.
[91] Maurya N, Singh AK, Indirect approach for CN– detection via Cu2+ induced turn-off sensor: Using novel AIE fluorophore with logic gate and antimicrobial application, Dyes Pigm, 2017, 147, 484–490.
[92] Hu Y, Cao X, Guo Y, et al., An aggregation-induced emission fluorogen/DNA probe carrying an endosome escaping pass for tracking reduced thiol compounds in cells, Anal Bioanal Chem, 2020, 412(28), 7811–7817.

[93] Chen R, Ren C, Liu M, et al., Early detection of SARS-CoV-2 seroconversion in humans with aggregation-induced near-infrared emission nanoparticle-labeled lateral flow immunoassay, Acs Nano, 2021, 15(5), 8996–9004.
[94] Eisenberg D, Jucker M, The amyloid state of proteins in human diseases, Cell, 2012, 148(6), 1188–1203.
[95] Sacchettini JC, Kelly JW, Therapeutic strategies for human amyloid diseases, Nat Rev Drug Discov, 2002, 1(4), 267–275.
[96] Ke PC, Sani M-A, Ding F, et al., Implications of peptide assemblies in amyloid diseases, Chem Soc Rev, 2017, 46(21), 6492–6531.
[97] Dao P, Ye F, Liu Y, et al., Development of phenothiazine-based theranostic compounds that act both as inhibitors of β-amyloid aggregation and as imaging probes for amyloid plaques in Alzheimer's disease, Acs Chem Neurosci, 2017, 8(4), 798–806.
[98] Staderini M, Martín MA, Bolognesi ML, Menéndez JC, Imaging of β-amyloid plaques by near infrared fluorescent tracers: A new frontier for chemical neuroscience, Chem Soc Rev, 2015, 44(7), 1807–1819.
[99] Fu W, Yan C, Guo Z, et al., Rational design of near-infrared aggregation-induced-emission-active probes: In situ mapping of amyloid-β plaques with ultrasensitivity and high-fidelity, J Am Chem Soc, 2019, 141(7), 3171–3177.
[100] Tang S, Ye S, Zhang X, When aggregation-induced emission meets protein aggregates, Natl Sci Rev, 2021, 8(6), nwab013.
[101] Shen D, Jin W, Bai Y, et al., Rational design of crystallization induced emission probes to detect amorphous protein aggregation in live cells, Angewandte Chemie Int Ed, 2021, 60(29), 16067–16076.
[102] Pradhan N, Jana D, Ghorai BK, Jana NR, Detection and monitoring of amyloid fibrillation using a fluorescence "switch-on" probe, Acs Appl Mater Inter, 2015, 7(46), 25813–25820.
[103] Hong Y, Meng L, Chen S, et al., Monitoring and inhibition of insulin fibrillation by a small organic fluorogen with aggregation-induced emission characteristics, J Am Chem Soc, 2012, 134(3), 1680–1689.
[104] Jia L, Wang W, Yan Y, et al., General aggregation-induced emission probes for amyloid inhibitors with dual inhibition capacity against amyloid β-protein and α-synuclein, Acs Appl Mater Inter, 2020, 12(28), 31182–31194.
[105] Zakrzewski W, Dobrzyński M, Szymonowicz M, Rybak Z, Stem cells: Past, present, and future, Stem Cell Res Ther, 2019, 10(1), 68.
[106] Regmi S, Pathak S, Kim JO, Yong CS, Jeong J-H, Mesenchymal stem cell therapy for the treatment of inflammatory diseases: Challenges, opportunities, and future perspectives, Eur J Cell Biol, 2019, 98(5–8), 151041.
[107] Bagno L, Hatzistergos KE, Balkan W, Hare JM, Mesenchymal stem cell-based therapy for cardiovascular disease: Progress and challenges, Mol Ther, 2018, 26(7), 1610–1623.
[108] Arber C, Lovejoy C, Wray S, Stem cell models of Alzheimer's disease: Progress and challenges, Alzheimers Res Ther, 2017, 9(1), 42.
[109] Lukomska B, Stanaszek L, Zuba-Surma E, Legosz P, Sarzynska S, Drela K, Challenges and controversies in human mesenchymal stem cell therapy, Stem Cells Int, 2019, 2019, 1–10.
[110] Ding D, Mao D, Li K, et al., Precise and long-term tracking of adipose-derived stem cells and their regenerative capacity via superb bright and stable organic nanodots, Acs Nano, 2014, 8(12), 12620–12631.
[111] Jang SE, Qiu L, Cai X, et al., Aggregation-induced emission (AIE) nanoparticles labeled human embryonic stem cells (hESCs)-derived neurons for transplantation, Biomaterials, 2021, 271, 120747.

[112] Chen R-L, Balami JS, Esiri MM, Chen L-K, Buchan AM, Ischemic stroke in the elderly: An overview of evidence, Nat Rev Neurol, 2010, 6(5), 256–265.
[113] Hess DC, Borlongan CV, Cell-based therapy in ischemic stroke, Expert Rev Neurother, 2014, 8(8), 1193–1201.
[114] Cai X, Zhang C, Lim FTW, et al., Organic nanoparticles with aggregation-induced emission for bone marrow stromal cell tracking in a rat PTI model, Small, 2016, 12(47), 6576–6585.
[115] Wiklander OPB, Brennan MÁ, Lötvall J, Breakefield XO, Andaloussi SE, Advances in therapeutic applications of extracellular vesicles, Sci Transl Med, 2019, 11(492), eaav8521.
[116] Andaloussi SE, Mäger I, Breakefield XO, Wood MJA, Extracellular vesicles: Biology and emerging therapeutic opportunities, Nat Rev Drug Discov, 2013, 12(5), 347–357.
[117] Cao H, Cheng Y, Gao H, et al., In vivo tracking of mesenchymal stem cell-derived extracellular vesicles improving mitochondrial function in renal ischemia–reperfusion injury, Acs Nano, 2020, 14(4), 4014–4026.
[118] Cao H, Yue Z, Gao H, et al., In vivo real-time imaging of extracellular vesicles in liver regeneration via aggregation-induced emission luminogens, Acs Nano, 2019, 13(3), 3522–3533.

Guan Wang, Xinggui Gu, Ben Zhong Tang

Chapter 17
AIEgen-based photosensitizers for photodynamic therapy

17.1 Introduction

Since the Dane of Finsen attempted to treat lupus vulgaris, a tubercular condition of the skin, by directly irradiating using the heat-filtered light from a carbon arc lamp, phototherapy has evolved and demonstrates great significance in biomedicine [1]. Owing to its noninvasive characteristic, the discipline of phototherapy has well developed and can be divided into two categories, *indirect* and *direct* phototherapy, according to the use of photosensitizer (PS). Indirect phototherapy of photodynamic therapy (PDT) utilizing PS has become an attractive therapeutic technique for eliminating cancer cells by generating reactive oxygen species (ROS), including $^1O_2$, $\cdot OH$, $O_2^{\cdot -}$, and H_2O_2 under light irradiation [2]. The selective cytotoxicity of PDT toward cancer cells could be achieved by manipulating the light irradiation area that minimizes side effects on healthy tissues or organs [3]. Taking advantage of the PSs high efficacy for generating ROS, PDT has been widely used in medicine research and clinical treatment. Now, PDT is being tested in the clinic for applications in oncology to treat cancers of the head and neck, brain, lung, pancreas, intraperitoneal cavity, breast, prostate, and skin [4].

Elements of light and PSs comprise the general PDT. Given the practical application of PDT, PS plays an important role in PDT processes, which should be seriously selected by taking various comprehensive factors into account, such as synthetic method, cytotoxic, vis-/near infrared absorbance, ROS productivity, targeting, and so on. At present, various PSs have been developed, including metal [5], metal–organic frameworks [6], polymer materials [7–10], and organic molecules. Among them, PSs based on organic molecules have drawn great attention, resulting from the sample synthesis processes and tunable absorbance.

In the past, many organic molecules have been developed as PSs as shown in Figure 17.1. Hematoporphyrin derivative, together with its derivatives of photofrin,

Guan Wang, Beijing Advanced Innovation Center for Soft Matter Science and Engineering, College of Materials Science and Engineering, Beijing University of Chemical Technology, Beijing, 100029, China
Xinggui Gu, Beijing Advanced Innovation Center for Soft Matter Science and Engineering, College of Materials Science and Engineering, Beijing University of Chemical Technology, Beijing, 100029, China, e-mail: guxinggui@mail.buct.edu.cn
Ben Zhong Tang, Shenzhen Institute of Aggregate Science and Technology, School of Science and Engineering, The Chinese University of Hong Kong (Shenzhen), Shenzhen, 518172, China

https://doi.org/10.1515/9783110673074-018

photosan, photogem, and photocarcinorin, comprised the first-generation PSs [1]. Although some of them have been approved as clinic drugs for cancer treatment, they were in serious shortages. For example, their inherent multi-composite feature leads to bad reproduction of their composition; the relatively short wavelength absorption (< 630 nm) results in the poor light penetration of tumor; the long residence time in body causes cutaneous photosensitivity, which keeps the patients away from the sunshine; and their low molar absorption coefficient makes high concentration and intense light irradiation necessary [11–13]. These deficiencies of the first-generation PSs motivated the development of second-generation of PSs, with higher chemical purity, higher yield of singlet oxygen generation, and deeper tissue penetration, demonstrating its potential in PDT, which include tetrapyrrolic compounds, such as benzoporphyrin, chlorin and porphycene [2, 14–16], However, hydrophobicity and lack of targeting limit its further use in biomedicine applications. In order to overcome the hurdles faced due to the second-generation PSs, PSs synthesized with enhanced affinity of PSs to tumor tissue, for instance, mitochondria targeting, were developed, and these well-designed PSs lead to the application of third generation PSs [17]. These have become the primary PSs for biomedicine at present.

Besides targeting the cancer tissue, it is equally important to seek ideal PS to produce ROS effectively. Although the mechanism to produce ROS from PS is not clear, it is generally considered that ROS originates from the triplet state of the excited PSs. Strategies to reduce the energy gap ($\Delta E_{S\text{-}T}$) between S_1 and T_n, and boost the transformation from S_1 to T_n are employed to enhance the generation of ROS [14]. Among these strategies, temperate aggregation of PSs might be the most feasible method to reduce $\Delta E_{S\text{-}T}$, by promoting the intersystem crossing (ISC) [18]. For example, Yin et al. employed self-assembly of pentamethine indocyanine (ICy5) dye derivative to construct the nanoparticles for enhanced $^1O_2$ generation, from which $\Delta E_{S\text{-}T}$ significantly reduced from 1.2583 to 0.9074 eV, with increased aggregation degree of ICy and a 10-fold enhanced generation of $^1O_2$ was achieved [19]. Li et al. synthesized a series of coumarin-based cationic fluorophores (Cou-n, $n = 1–4$), with varied alkyl, and demonstrated that, owing to the strong hydrophobicity, longer alkyl chains benefited the tighter molecular aggregation of fluorophores in aqueous solution, which remarkably boosted the ROS production of the aggregates [20]. The aggregation-enhanced photodynamic effect was also detected in the PSs of phthalocyanine [21, 22] and porphyrin [23].

However, the traditional PSs suffered from the notorious aggregation-caused quenching (ACQ) effect as they are condensed or aggregated, which made it difficult to balance the ACQ and aggregation-enhanced photodynamic effect. Serval strategies were developed to control PS aggregation, including chemical modification of PSs [24] and encapsulating PSs into polymer matrix [25]. However, these strategies rely on complicated chemical synthesis processes or low concentration of PSs in the PDT matrix. Fortunately, the concept of aggregation-induced emission (AIE) was put forward by Tang in 2001 [26–29], and PSs based on AIE-active luminogens (AIEgens)

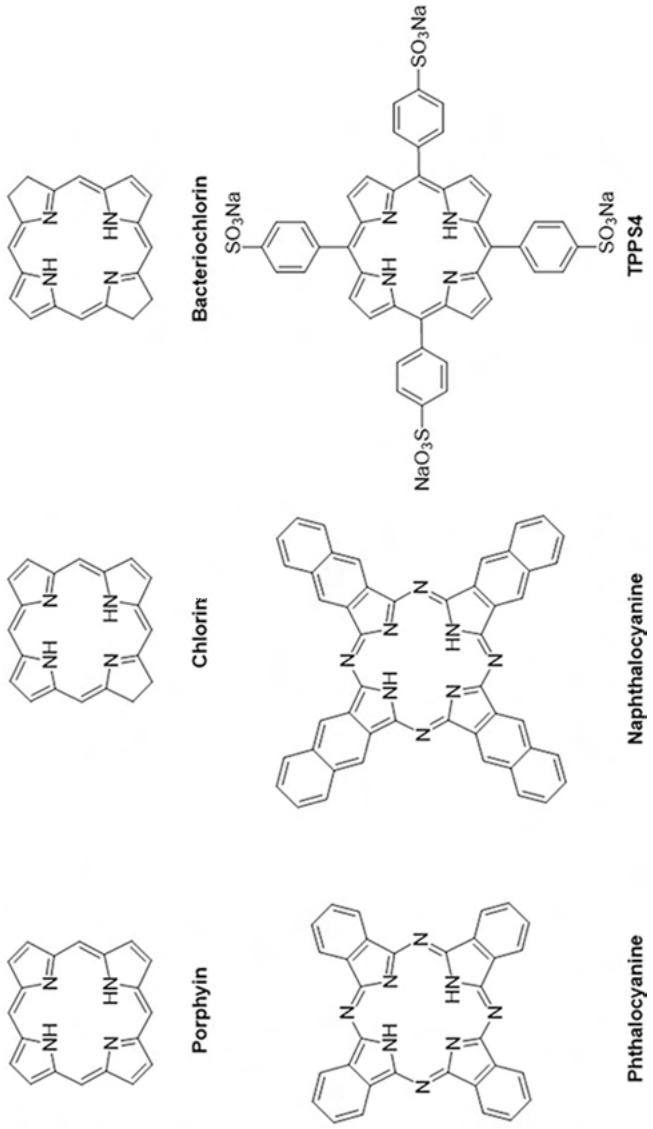

Figure 17.1: Chemical structure of the partial traditional PS used for PDT treatments. Modified with permission from the reference of [55]. Copyright 2018, Wiley-VCH.

have been substantially developed [30, 31], which cleared the way for the use of PSs in PDT treatment, without scruples of the ACQ effect. Taking advantages of AIEgen-based PSs, application potential of PSs has gradually emerged and makes it a promising approach for eliminating cancer tissues or bacterial infection in clinical treatment.

17.2 Mechanism of ROS generation

Mechanism of ROS generation of AIEgen-based PSs involves three primary components: PSs, light, and oxygen. According to the Jablonski diagram and the principles of photochemistry, as the AIEgen-based PSs absorb a photon and lead to the formation of an "excited state," the electron is excited to higher-energy orbitals (S_1, S_2 . . .) from the singlet ground state (S_0), as illustrated in Figure 17.2. The subsequent photophysical or photochemical processes would proceed from S_0 of the excited electron according to Kasha's rule [32]. Excited electron returns to S_0 by releasing energy *via* nonradiative (NR) decays through internal conversion or radiative decays as fluorescence (FL). NR and FL are not the desired pathways for the PDT application but can serve as a tool for tumor detection and imaging. However, the excited electron of S_1 could also transfer to the neighboring triplet (such as the excited triplet state (T_1)),

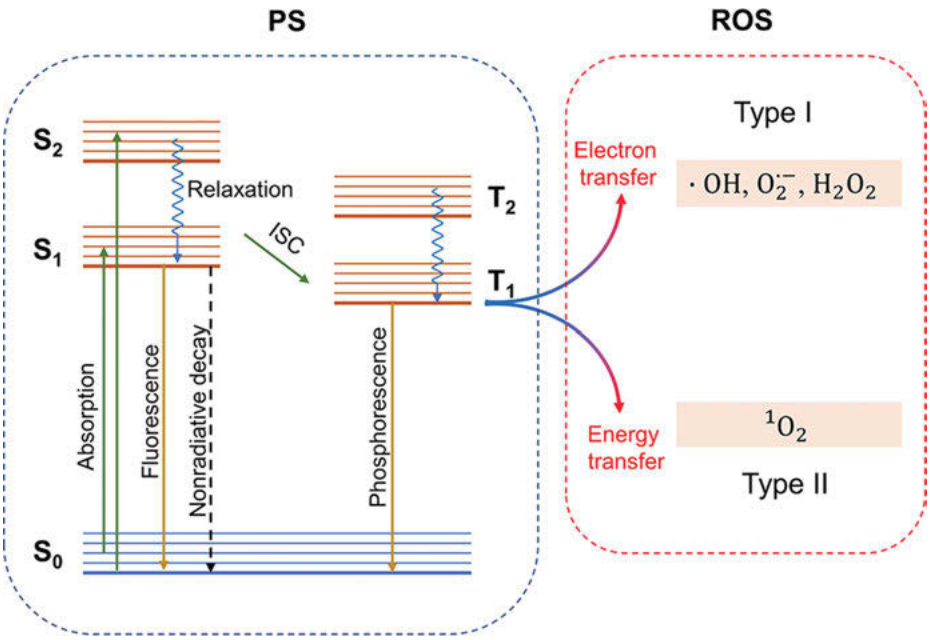

Figure 17.2: Mechanism of ROS generation illustrated by the Jablonski energy level diagram.

as their energy difference ($\Delta E_{S\text{-}T}$) is small enough, through the ISC processes. Owing to the quantum mechanically forbidden state of the excited electron from T_1 to S_0, the excited T_1 generally exhibits a longer lifetime than that of S_1, which benefits from the energy transfer (Type II) or electron transfer (Type I) of the excited PS to oxygen or other substances, forming the toxic ROS.

17.2.1 Type-I mechanism of PS

After the PSs absorb light and transition to the excited state, they always exhibit larger oxidation/reduction potential than their ground state counterparts [33], which facilitates the electron/energy transfer to the surrounding substrates for producing ROS. Hydroxyl radical is the most aggressive ROS generated from PSs, which is originated from the cascade reactions of superoxide anions or the one-step oxidation of water [34]. Type I mechanism is originated from the superoxide anions, which is generated from the oxygen by capturing one electron from the reduced substrate or directly from the exited PS. Depending on the environment, superoxide anions could act as strong reducing agents, which could further react with the oxidic PS to form the perhydroxyl radical ($HO_2^{\cdot}$). $HO_2^{\cdot}$ exhibits a more potent oxidant than superoxide anion, which could react with superoxide anion to form the H_2O_2, and H_2O_2 could be further reacted with superoxide anion or $HO_2^{\cdot}$, resulting in the formation of highly reactive hydroxyl radicals [33]. The processes of generating ROS from Type I mechanism are dependent on the target-substrate concentration and the microenvironment. Additionally, the PDT efficiency can be amplified by the interaction of PSs with proteins, DNA, or lipids.

Owing to the hypoxic microenvironment of tumor, PSs that generated Type I ROS exhibit great potential for eliminating cancer cells with low oxygen concentration. However, few studies have been reported to produce Type I ROS for AIEgen-based PSs. Tang et al [34]. employed a phosphindole oxide (PIO) core as an electron-acceptor and triphenylamine (TPA), and pyridine (Py) as an electron donor, to construct AIEgen-based PSs with donor-acceptor pairs, and the isomeric AIEgens of α-TPA-PIO and β-TPA-PIO were synthesized. Both the isomeric PSs generated Type I ROS in their study. However, β-TPA-PIO exhibited a stronger $\cdot OH$ than α-TPA-PIO. From the results, it can be concluded that the increased spin–orbit coupling (SOC) was responsible for the enhancement of Type I ROS, by comparing the two isomeric AIEgen-based PSs and the high electron affinity of PIO endowed PIO-based molecule with the ability to attract and stabilize an external electron. By providing an electron-rich aggregated microenvironment to PSs, Tang et al [35]. developed a strategy to enhance Type I ROS by utilizing anion-π^+ AIEgens to enhance intramolecular charge transfer (ICT) and suppress nonradiative internal conversion, which demonstrated the concept of "more ICT leads to more free radical ROS generation," as proposed by them. At the same time, Qi et al. proposed their strategy to

produce free radical ROS utilizing the interaction of electron-donating from anion-π^+ AIEgens to enhance ICT for producing Type I ROS [36].

17.2.2 Type II mechanism of PS

There is a close competitive relationship between Type I and Type II processes. Most AIEgen-based PSs would preferentially produce singlet oxygen *via* the Type II pathway because the Type II process is faster [37]. In typical processes, for generating singlet oxygen, PS is excited to the exited state from the ground state by absorbing the photons, and further transfers the energy to the surrounded oxygens (94 kJ/mol above ground state). Owing to the fast transformation from oxygen to singlet oxygen, Type II ROS has been the most important process for PDT, and extensively-used in biomedicine. However, the productivity of singlet oxygen is intensely related to concentration of oxygen, tissue dielectric constant, pH of the microenvironment, and photosensitizer's structure [14]. The lifetimes of singlet oxygen range from 10 to 100 μs, which restricts its active volume to within 10 nm in diameter and limits its efficiency in PDT [13].

17.3 PS design

As mentioned above, ROS is generally generated from the PS as it absorbs light and is excited from S_0 to S_1. Consequently, ISC can occur, with the electron transferred to T_n, resulting in cascade reactions to produce ROS. The common approaches to develop PSs were limited by modifying traditional cores, which include tetrapyrrole, naphthalene, benzophenone, phenothiazinium, and so on [38–41]. These strategies to design PS primarily focused on the absorption of PS, cytotoxicity, water solubility, and so on, regardless of the ISC and triplet yield. However, the properties of PS are limited and a guideline to develop more desired PSs is needed.

Aiming to guide the design of PSs, some basic principles to synthesize PSs are developed according to the mechanism of ROS generation, where the pivotal point to design an effective PS is enhancing the ISC processes from S_1 to T_n. The ways to achieve this can be assigned to the following strategies.

17.3.1 Reducing Singlet–Triplet Energy Gap

Promotion of the ISC processes offers the opportunity to improve the yield of the triplet-excited state, which would facilitate ROS generation, and the fundamental

study of ISC gives the following equation, utilizing the ISC from S_1 to T_1 as the example.

$$k_{ISC} \propto \frac{\langle T_1|H_{SO}|S_1\rangle^2}{\Delta E_{S-T}}$$

Where, k_{ISC} is the rate constant of ISC, H_{SO} is the Hamiltonian for the SOC, and $\Delta E_{S\text{-}T}$ is the energy gap between the S_1 and T_1. This equation shows the affinity between the ISC rate and $\Delta E_{S\text{-}T}$, and the smaller the $\Delta E_{S\text{-}T}$ would always lead to a higher ISC rate. Reducing $\Delta E_{S\text{-}T}$ should favor ICT to benefit ROS generation.

Liu and her collaborator [42] synthesized a series of tetraphenylethylene (TPE) - based PSs, according to the formula, with different molecular engineering strategies, and initially proposed the strategies for designing PSs by reducing $\Delta E_{S\text{-}T}$ through introducing donor-acceptor interactions and a π bridge into the PSs (Figure 17.3a). Based on the typical AIEgens of TPE, three AIEgens, namely, TPDC, TPPDC, and PPDC, were synthesized, and the AIE characteristics of the four molecules were verified. It is noteworthy that TPE is an AIEgen without photosensitivity. The modified TPE with the donor and acceptor TPDC was obtained and ROS of $^1O_2$ was detected, as TPDC was irradiated under light. Productivity of $^1O_2$ was determined by 9,10-Anthracenediylbis (methylene) dimalonic acid (ABDA), a famous indicator $^1O_2$, and the quantum yield of $^1O_2$ (ϕ_{PS}) was calculated by the following formula, with Rose Bengal (RB) employed as the standard photosensitizer.

$$\emptyset_{PS} = \emptyset_{RB}\frac{K_{PS}A_{RB}}{A_{PS}K_{RB}}$$

Where, ϕ_{RB} is the $^1O_2$ quantum yield of RB, which is 0.75 in water; K_{PS}/K_{RB} represents the decomposition rate constant of PS and RB, respectively. A_{PS}/A_{RB} is the integral area of PS and RB in UV-*via* absorption spectra of light that ranges from 400 to 800 nm.

Therefore, ϕ_{PS} of TPDC was calculated as 0.28, indicating that modification of AIEgens with donor-acceptor structure would alter their properties for ROS generation. Altering the species of donor and acceptors, ϕ_{PS} could be further increased. $\Delta E_{S\text{-}T}$ was calculated by time-dependent density functional theory (TD-DFT), which showed that the introduction of donor and acceptor to AIEgens of TPE would consequently decrease the $\Delta E_{S\text{-}T}$, leading to an increase of ROS generation. ROS productivity of AIEgens can be tuned by manipulating $\Delta E_{S\text{-}T}$ and reducing $\Delta E_{S\text{-}T}$ for enhancing ROS production has been the indicative guideline for PS molecular design [43, 44]. Furthermore, increasing the distance between donor and acceptor is another strategy to separate the highest occupied molecular orbital (HOMO) and the lowest unoccupied molecular orbital (LUMO) of AIEgens, which can be realized by adding a phenyl ring as an additional π-conjugation spacer in AIEgens. This yields AIEgen-based PS

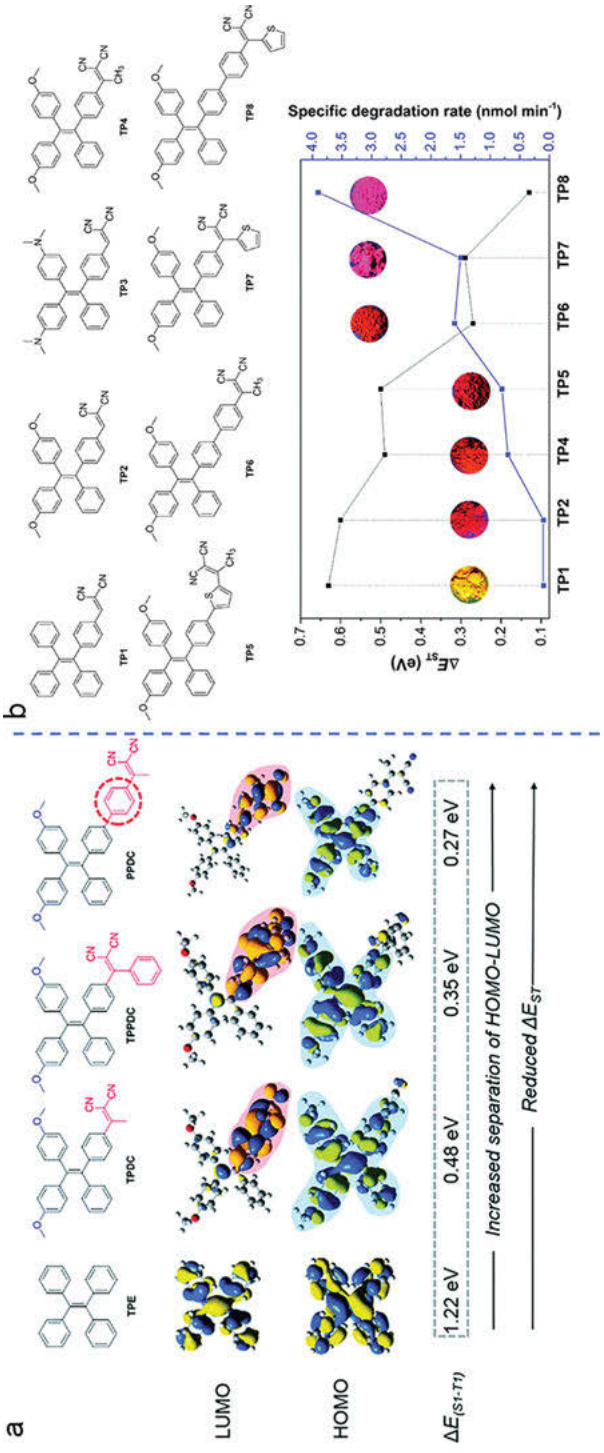

Figure 17.3: (a) Strategies to reduce $\Delta E_{S\text{-}T}$ through molecular design. Reprinted with permission from the reference of [42]. Published by The Royal Society of Chemistry. (b) Chemical structure of AIEgen-based PSs of TP1-8. Modified with permission from the reference of [45]. Published by The Royal Society of Chemistry.

of PPDC, with a much lower $\Delta E_{S\text{-}T}$ value of 0.27 eV and a 3.2-fold improvement in $^1O_2$ generation efficiency.

Hence, introducing strong electron-donor and electron-acceptor pair(s) with π spacers to AIEgens can effectively manipulate the HOMO-LUMO distribution and provide an alternative strategy to design AIEgen-based PS. Liu et al [45]. developed the strategy for precise molecular design to produce ROS according to the principle of manipulating the HOMO-LUMO distribution and by reducing the $\Delta E_{S\text{-}T}$ of AIEgen-based PSs, as given in Figure 17.3b. By modifying alkoxyl and dicyanovinyl groups of the TPE unit, $\Delta E_{S\text{-}T}$ of TP1 and TP2 exhibited a significant decrease (0.64 eV and 0.67 eV) compared with that of TPE, resulting in an ROS generation efficiency of 0.1 nmol min^{-1}, with the decomposition of ABDA under white light (400–700 nm, 250 mW cm^{-2}) irradiation, which implied that incorporating electron-donating and -withdrawing moieties on different sides of TPE molecular skeleton would facilitate the decrease of $\Delta E_{S\text{-}T}$. By adding a methyl group to TP2, the steric hindrance of introduced methyl group lead to an increase in the dihedral angle between phenyls in TPE and the acceptor unit (plane of dicyanovinyl) in TP4, which aggravated the separation of HOMO and LUMO of TP4 and a lower $\Delta E_{S\text{-}T}$ (0.11 eV) relative to TP2 was achieved for TP4. Specially, when a thiophene ring is employed to replace the methyl group (TP7), $\Delta E_{S\text{-}T}$ showed a further decrease from 0.49 for TP4 to 0.29 eV for TP7, where the LUMO electron cloud was more focused on the acceptor moiety of TP7 by DFT calculations. Aggravated separation of HOMO and LUMO should be responsible for this decrease, which indicated that increase in the HOMO–LUMO distance would favor the reduction of $\Delta E_{S\text{-}T}$. In addition, the employment of the π-bridge between the donor and acceptor groups to increase intramolecular spatial distance would be another option. Herein, TP5, TP6, and TP8 were designed and synthesized and $\Delta E_{S\text{-}T}$ of 0.5, 0.27, and 0.13 eV were obtained, respectively. From Liu's studies, strategies for reducing $\Delta E_{S\text{-}T}$ and enhancing the separation of HOMO and LUMO to realize ROS generation of AIEgen-based PSs have been demonstrated, which have become general guidelines for designing new PSs.

Following this basic principle, more AIEgen-based PSs were successfully synthesized. By extending the distance of donor and accepter in the molecules, Yang and coauthors [46] synthesized the donor-π-acceptor-donor structured AIEgen-based PSs (SMe2CN, Cz2CN, TPA2CN). The intrinsic AIE characteristics of the PSs were verified. Owing to the extended distance of the donor and acceptor, HOMO and LUMO were well separated and $\Delta E_{S\text{-}T}$ was calculated to be 0.459, 0.425, and 0.245 eV, respectively. Liu and coauthors [47] employed the stronger donor and acceptor to construct the tunable donor-donor-π-acceptor structure with twisted intramolecular charge transfer (TICT) characteristics. Through calculations, it was found that the electron cloud density of the HOMO orbital was primarily distributed on the triphenylamine group and the pyridine ring, whereas electron cloud density of LUMO orbital was mainly distributed on various electron-withdrawing groups, which revealed that smaller energy band gap could be obtained when a stronger

electron-withdrawing group was introduced into the AIEgens. Cheng et al. [48] designed an AIE compound consisting of a pyridinium moiety (acting as acceptor), a carbon-carbon double bond (π-bridge), a thiophene fragment (donor and π-bridge), and a triphenylamine fragment (donor), enhancing donor-acceptor interaction to ensure long-wavelength fluorescence emission and high ROS quantum yield. More AIEgen-based PSs were obtained through this strategy [47, 49, 50].

Besides, increasing the push–pull effect of the donor-acceptor-structured PSs and/or effectively extending the π conjugation of the PSs not only reduce the $\Delta E_{S\text{-}T}$ of the PS but also broaden their absorption and emission spectra in the red/near infrared (NIR) region or multi-photon absorption, which benefited the applications in PDT [51, 52]. Utilizing strong donor-acceptor pairs and extending the π-conjugation, Tang et al. [53] synthesized the donor-π-acceptor-structured AIEgen-based PSs. By combining strong electron donor-acceptor interaction and an extended π-conjugation with good electron delocalization in the structure, the PS exhibited a great potential of red emission and a good production of ROS. Tang et al. [54] developed a family of new red/near-infrared AIEgens by utilizing the BDTO as an electron acceptor, and taking triphenylamine and carbazole as electron donors. Through these strategies, effective PS, equipped with NIR emission, large two-photon absorption cross sections, and excellent ROS production ability in the aggregate state, was achieved.

17.3.2 Attaching heavy atom to molecular skeleton

Heavy atom effect is the special phenomenon based on the spin-orbit coupling (SOC) in quantum physics, where the SOC originated from the interaction between electron's spin magnetic moment and the magnetic field derived from the motion of nucleus [55, 56]. It is well known that heavy atom effect facilitates the SOC, which consequently enhances the ISC processes to produce exited triplet state of the PS, and the SOC increases with increase in atomic number. Based on this consideration, attaching heavy atom PS boosts SOC between singlets and triplets, and adding heavy atoms to AIEgens would be another strategy for AIEgens to produce ROS for PDT.

17.3.3 Aggregation of PS

The ideal PS, equipped with the features of strong absorption in visible or NIR light, low cytotoxicity, and effective ROS generation, attracts great attention in PDT. Aiming to obtain the effective PS for enhanced PDT, research have been carried out by scientists through reasonable molecular engineering, and many strategies to transfer traditional AIEgens to ROS-generated PS have been well developed. However, those strategies require precise molecular design and complex synthesis procedures. Therefore, developing new approaches to boost the ROS generation is far from satisfactory.

As described above, aggregation could result in enhanced ROS production of traditional PSs, as well as AIEgen-based PSs, which can result from the following reasons: (a) energy transfer from S_1 to T_1 would be enhanced as the energy dissipation through nonradiative channels are inhibited when AIEgens is aggregated; (2) aggregation-induced intersystem crossing [18, 42, 57]. Tian et al. [58] prepared three kinds of self-assembled nanostructured PSs based on the AIEgens of 2,3-bis(4′-(diphenylamino)-[1,1′-biphenyl]-4-yl) fumaronitrile (BDBF), as shown in Figure 17.4a. By comparing those nanostructured PSs, including BDBF nanodots, F127@BDBF nanoparticles, and BDBF@F127 nanodots, they found that all the three aggregated AIEgens showed enhanced $^1O_2$ production than that of BDBF molecules solutions. Aggregation of the binary molecule and employing the fluorescence resonance energy transfer (FRET) could also be used for enhancing ROS generation. Chang et al. [23] combined the FRET donor (BMVC, 3,6-bis-(1-methyl-4-vinylpyridinium)-carbazole diiodide) and acceptor (porphyrin or metalloporphyrin) to synthesize the binary molecule. After aggregation of the binary molecule, FRET occurred from the aggregated donor to the nonaggregated acceptor, which demonstrated the enhancement of ROS generation caused by aggregation of the binary molecule. Zou and coauthors found that the dimerization of TPE successfully transferred into a PS (Figure 17.4b) [59]. The harvested dimer of TPE, named BTPE, not only inherits the AIE characteristics from the TPE but also achieves ROS generation, boosting the PDT efficacy in HeLa tumor of the nude mice. Although Zou did not provide us with the appropriate mechanism to explain this abnormal transformation, it offered us a valuable strategy to enhance ROS generation.

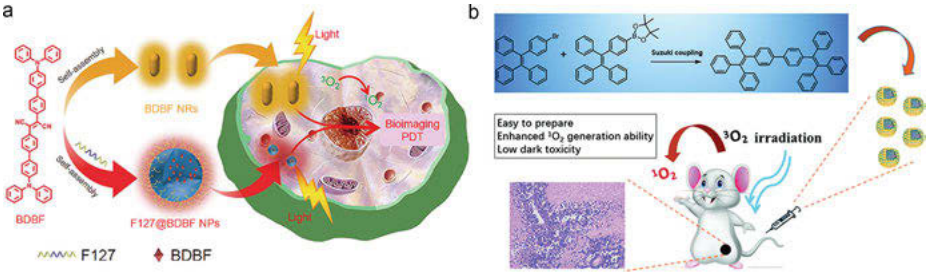

Figure 17.4: Aggregation-induced enhanced ROS generation through (a) dimerization and (b) self-assembly. Reprinted with permission from the references of [58, 59]. Copyright 2020, Royal Society of Chemistry. Copyright 2019, Springer Nature.

17.3.4 Conjugated polymers

Similar to aggregation of small molecule, conjugated polymers with backbones containing π-conjugation structure obtained from the polymerization of small molecule is the commonly used material, which endows them the ability of red-shifted absorbance and strong light-harvesting, when compared with that of their small-molecule counterparts [60–62]. For example, after polymerization, the obtained conjugated polyporphyrin exhibited an obvious red-shift in the absorption [63]; employing the light-harvesting feature, conjugated polymers can be considered as the antenna for effective photosensitization *via* energy transfer from conjugated polymers to the photosensitizer acceptors [60, 64, 65]. Based on this consideration, Liu et al. [66] synthesized four AIEgens (SM 1–4) and their analogue conjugated polymers (CP 1–4), of which CP1 exhibited the most effective ROS production under irradiation, with a 3.71-fold higher than that of the most widely used photosensitizer Ce6, and the concept of "polymerization-enhanced photosensitization" was proposed. To investigate the inherent mechanism of the concept, TD-DFT investigations (Figure 17.5a) were conducted to analyze both the singlet and triplet exited states of the small molecule of SM 1 and the conjugated polymer of CP 1 with varied repeat units. According to the calculations, the energy gap between S_1 and T_1 of CP1 is 0.23 eV, which is smaller than 0.3 eV, indicating flexibility for the ISC based on the energy gap law [67, 68]. Moreover, the transitional configurations and iso-surfaces of S_1 and T_3 were similar, which made the ISC from S_1 to T_2 or T_3 possible. Those excited channels for ISC endowed SM 1 with prefect ROS generation. As the degree of CP 1 polymerization increased, more exited triplet states could be employed for ISC transitions. Through polymerization, a 5.05-fold enhancement in ROS production was achieved. From their study, it is demonstrated that increasing the repeat units of the polymerized PS would facilitate ROS generation by employing more energy transition channels for ISC, which enhanced the ROS production, as the PSs were polymerized. Additionally, polymerization-enhanced photosensitization was also verified in the non-AIE system of SM 4 and CP 4 with a 3.42-fold higher ROS generation of CP 4 than SM 4, which expanded the scope of the concept. Based on this concept, Liu et al. [69] synthesized the polymerized PS conjugated polymer and prepared the nanoparticles by nanoprecipitation with the aid of DSPE-PEG-Mal. The obtained nanoparticles, featured with enhanced $^1O_2$ production and large two-photon absorption (2 PA) cross-sections were highly desired for tumor treatment. Further studies on the concept of "polymerization-enhanced photosensitization" were also conducted [70].

Generally, adding the donor and acceptor of the AIEgens facilitates decreased $\Delta E_{S\text{-}T}$ of S_1 and T_n. However, designing PS molecules based on the donor-acceptor pair always relies on the trial-error methods for discovering the appropriate molecular structure by tuning the electronic properties through the D-A units [45, 71]. Polymerization provides lots of ISC channels in their aggregation form *via* the energy-splitting effect to enhance ISC [18, 72–74]. Combining with polymerization,

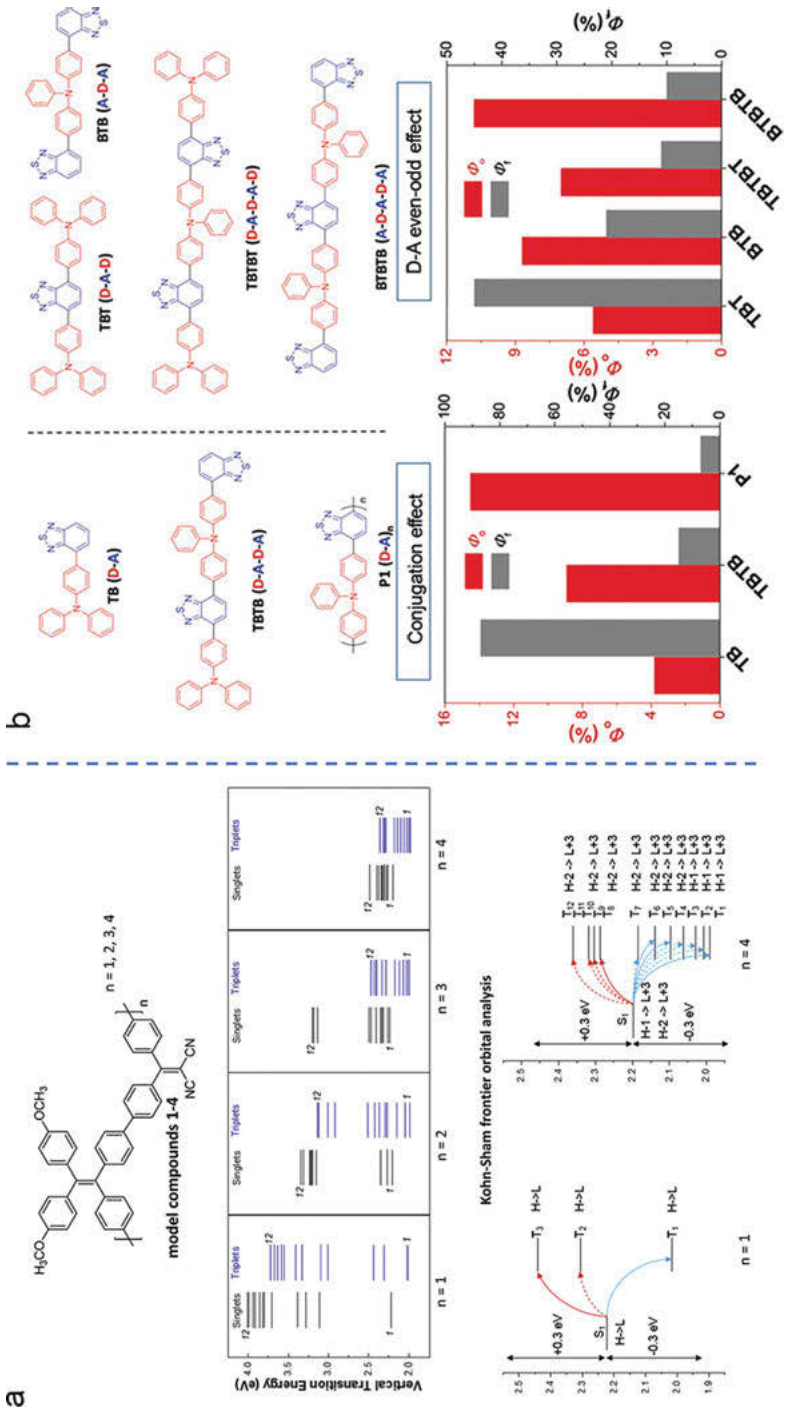

Figure 17.5: (a) Theoretical illustration of polymerization enhanced ROS generation. Reprinted with permission from the reference of [66]. Copyright 2018, Elsevier. (b) Polymerization-enhanced ROS generation with the D-A even-odd effect. Reprinted with permission from the reference of [75]. Copyright 2018, Wiley VCH.

the D-A even-odd effect would be an appropriate strategy to realize enhanced ROS generation. Therefore, employing the concept of "polymerization-enhanced photosensitization," Tang and Liu [75] developed the D-A even-odd effect based on polymerization for enhanced ROS production, as shown in Figure 17.5b. In their studies, polymerization-enhanced photosensitization was demonstrated –the donor and acceptor were polymerized together, while the even-odd effect exhibited the interesting impacts on ROS productivity. After the polymerization, as the number of accepters was more than donors, the obtained conjugated polymer showed smaller $\Delta E_{S\text{-}T}$ than that of its counterparts with higher donor fraction, which consequently lead to higher ROS production of the conjugated polymer with a high accepter fraction.

Plasmonic effect is a unique phenomenon of noble metal nanostructures to manipulate light at the nanoscale, originating from the interaction of the metal atoms and the incident light [76], and it is widely used in optical data storage [77–79], sensing [80, 81], solar cells [82, 83], photothermal therapy [84, 85], and so on. Combining AIEgen-based PSs with the noble metal nanostructure is another effective way to enhance ROS generation. Therefore, Tan and Liu et al. [86, 87] synthesized the 4-mercaptobenzoic acid-capped AgNPs and used it as the PS. Taking advantage of the plasmonic effect of Ag NPs, a 10-fold enhancement in $^1O_2$ generation was achieved by comparing with that of SiO_2 nanoparticles.

17.3.5 Aggregation microenvironment manipulation

Although many strategies based on polymerization, D-A even-odd effect, and organic-metal composite have been developed, a method to design the appropriate molecular structure used for polymerization or composition remains a challenge. The properties of AIEgens strongly depend on the aggregation of the microenvironment they are located. Thus, changing the aggregation microenvironment of AIEgens can also be employed as an alternative strategy for enhancing the ROS production. Liu and coauthors[88] found that the aggregates of BTPEAQ could not produce ROS in water. While $^1O_2$ was generated from the nanoparticles obtained from the polymeric matrix encapsulation and SiO_2 matrix encapsulation, it showed a higher ROS productivity of polymeric matrix encapsulated BTPEAQ than that of SiO_2 matrix, as shown in Figure 17.6a. The reasons for the interesting phenomenon could be assigned to the manipulation of ICT by the aggregation microenvironments. In our previous work [89], we proposed a facile approach to enhance ROS generation by manipulating the aggregation microenvironment of the AIEgens as shown in Figure 17.6b. As we all know, corannulene is a conjugated molecule with a large steric hindrance and rigid structure than that of the alkyl chain. By modifying corannulene to PEG chain (Cor-PEG) and taking this as the polymer matrix to encapsulate the AIEgens *via* nanoprecipitation, a more rigid aggregation microenvironment inside the nanoparticles

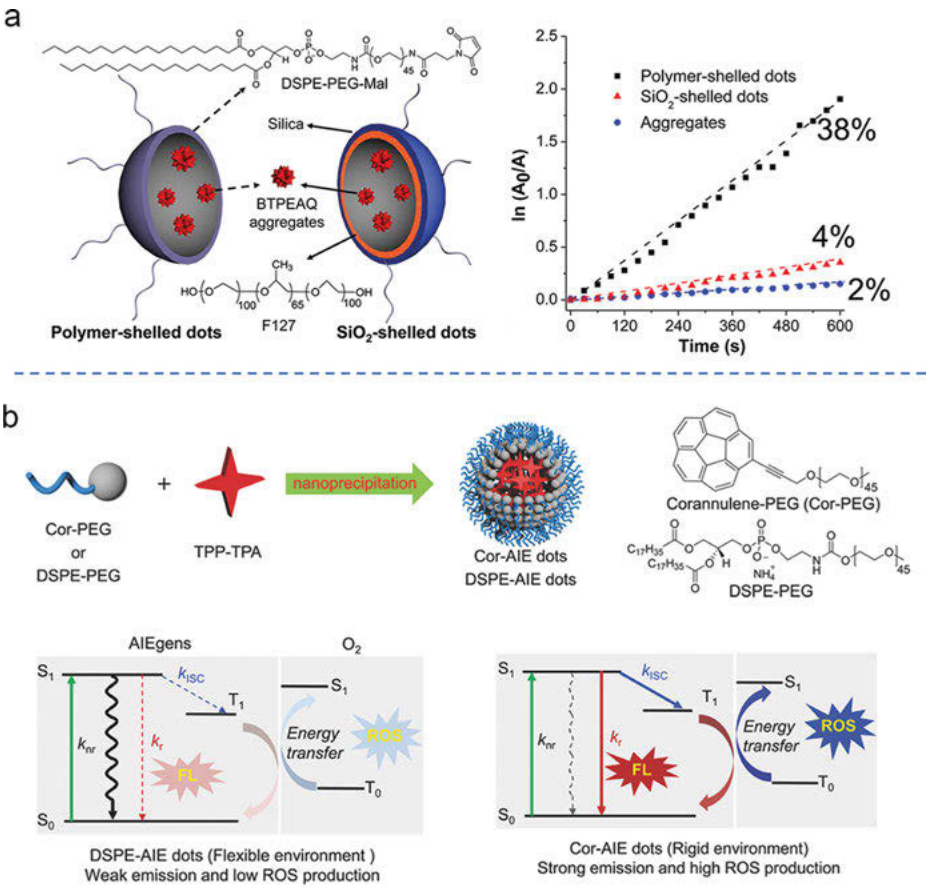

Figure 17.6: Enhanced ROS generation using aggregation microenvironment. ROS productivity manipulated by (a) polymer matrix and SiO_2 matrix, and (b) the rigidity of the polymer matrix. Modified and reprinted with permission from the references of [88, 89]. Copyright 2016 American Chemical Society and copyright 2018 Wiley VCH.

compared to the DSPE-PEG-composed nanoparticles was obtained. Through this alteration in aggregation microenvironment in Cor-PEG dots, ROS production was significantly boosted – a 5.4-fold enhancement than that of DSPE-PEG dots. This strategy relied on aggregation microenvironment, a facile way to enhance ROS production without a complicated chemical synthesis, exhibiting its potential for PDT further.

17.4 Detection of ROS

Owing to the different reactive activities of the ROS included $^1O_2$, $\cdot OH$, $O_2^{\cdot -}$, and H_2O_2 etc., detecting the species of ROS is a prerequisite for PS utilized in PDT. Many advanced approaches for ROS detection are well developed in the direct or indirect manner. The direct methods are based on the special absorption or electron spin resonance (ESR) signal collected by the UV-vis or ESR spectrometer, respectively. However, due to the short lifetimes and low concentrations of ROS in the reaction systems or physiological conditions, direct detection of the ROS should be conducted in the sub-millisecond timescale with ultrasensitive detectors, apart from the relatively stable H_2O_2. Indirect methods refer to the reaction of a specificity probe with a particular ROS, to yield a more stable, long-lived product, which has been well developed, including fluorescence reaction, chemiluminescence reaction, coloration reaction, spin trapping ESR, and so on [90]. Nevertheless, in employing indirect methods, some important aspects should be considered when choosing an ROS analysis method, which include: (1) sensitivity of the method; (2) selectivity and specificity of the method for the analyte of interest[91]. Selecting an appropriate approach for detecting a particular ROS specie is of great important for accuracy.

For detecting singlet oxygen, direct detection is possible owing to the phosphorescence of $^1O_2$ at 1270 nm in NIR region, or dimol emission occurring at 634 nm. Emission in NIR is more credible for direct detection of $^1O_2$, as its lifetime could be prolonged to 5 s [92–94]. However, the quantum yield of the emission in the steady state measurements is too low to detect, which makes it difficult for direct measurement of $^1O_2$ by emission. Direct ESR characterization could be used for measuring $^1O_2$, benefiting from its orbital angular momentum [95]. However, the more widely used approaches for detection by ESR *via* the spin trapping strategies are based on the reaction between $^1O_2$ and the spin trapping regents, with the formation of 1-oxyl radical [96]. The commonly utilized spin trapping regents include 4-hydroxy-2,2,6,6- tetramethylpiperidine (HTMP), which form the well-known stable nitroxide radical (4-hydroxy -2,2,6,6-tetramethylpiperidine 1-oxyl, TEMPOL) as it encounters $^1O_2$. Apart from spin trapping ESR measurement, indirect method of chemical reactions is most widely used, especially for the use of the indicators of singlet oxygen sensor green (SOSG) and 9,10-anthracenedipropanoic acid (ABDA). SOSG is the luminescence indicator with its emission peaks being about 528 nm with excitation at 488 nm. It shows specific sensitivity to $^1O_2$, with no appreciable response to $\cdot OH$ and $O_2^{\cdot -}$, but the photodecomposition of SOSG might affect the accuracy of the detection [97]. Resulting from the reaction between ABDA and $^1O_2$ is endoperoxide, which is commonly used as an $^1O_2$ detection agent – displayed in UV-vis absorption with the characteristic anthracene absorption bands at around 350 to 410 nm. The bleaching rate of ABDA can be employed for quantitative analysis of $^1O_2$ productivity upon light irradiation. Besides, AIEgen-based probes have also been developed for detecting $^1O_2$ [98, 99].

Direct measurement of $O_2^{\cdot -}$ generally relies on the absorption of $O_2^{\cdot -}$ at 245 nm, with the molar absorption coefficient being 2,350 $M^{-1}cm^{-1}$, but it is difficult to realize, owing to the low absorbance in UV-vis spectrum [100]. ESR is also a powerful tool to detect $O_2^{\cdot -}$. However, direct ESR cannot be used for measurement due to the same position of the unpaired electron located in the energy levels of the two orbitals, π_x^* and π_y^* [90]. By adding spin trapping regents, the feasibility of detection through ESR is increased. The commonly utilized spin trapping regents include DMPO (5,5-dimethyl-1-pyrroline N-oxide), DEPMPO (5-diethoxyphosphoryl-5-methyl -1-pyrroline N-oxide) [101], BMPO (5-tert-butoxycarbonyl-5-methyl-1-pyrroline N-oxide) [102], and CYPMPO (5-(2,2-dimethyl-1,3-propoxycyclophosphoryl)-5- methyl-1-pyrroline N-oxide) [103] etc. DMPO is the most widely used spin trapping regent for measuring $O_2^{\cdot -}$ by forming the DMPO-OOH spin adduct, and it exhibits six doublets of the DMPO-OOH EPR spectrum [104]. The other widely used detection method is based on the fluorescence reaction of probe dihydrorhodamine 123 (DHR123). As the DHR123 encounters $O_2^{\cdot -}$, it would be hydrolyzed into rhodamine 123 and emits green fluorescence at 526 nm [105, 106].

Among the various ROS, the reactivity of ·OH is considerably high and the reaction rate constants of ·OH for reacting with various substrates are near-diffusion-controlled. As ·OH is generated in the PDT processes, it would attack the cell membrane, leading to a series of successive destructions of the infringed cell, including the damage of cell membrane, destruction of sugar groups, and disorganization of DNA base sequences, eventually resulting in cell death and mutations. ESR is the often-used technology to detect ·OH, however, it is difficult to measure ·OH directly in the condensed state at room temperature because of the high reactive activities of ·OH [90]. Methods *via* spin trapping are more reliable for detecting ·OH in liquid state than that of the direct approaches. The generally used spin trapping agents include DMPO [101], BMPO [107], and CPYPMPO [103], as well as $O_2^{\cdot -}$ by the transfer of the unstable ·OH into the stable DMPO-OH, BMPO-OH, and CPYPMPO-OH, respectively. Apart from indirect ESR measurement, fluorescence reaction based on the fluorescent probe become a more convenient and quick approach to detect ·OH. While the selection of the fluorescent probe is of great significance, among the fluorescent probes, 3′-(p-hydroxyphenyl) fluorescein (HPF) and 3′-(p-aminophenyl) fluorescein (APF) have been utilized in the measurements [108–111]. HPF selectively reacts with ·OH by producing the fluorescent analyst of fluorescein, which emits at 515 nm, excited by the exciting light at 488 nm. HPF shows good specificity with ·OH, which would not react with other ROS such as $^1O_2$, $O_2^{\cdot -}$, and H_2O_2, etc. [112, 113]. APF is another fluorescent probe used for detecting ·OH, which exhibits nonfluorescence in the solution until it encounters hydroxyl radicals, leading to the production of the aminophenyl ring from the fluorescein ring system, with strong emission. However, APF can also be cleaved as they react with peroxynitrite anions (ONOO-), peroxy radicals, and the

combination of H_2O_2 and horseradish peroxidase (HRP), which would decrease its accuracy for probing ·OH [111, 114, 115].

H_2O_2 has the longest lifetime of the ROS although it relies on the environment it is located in [116, 117]. Detection of H_2O_2 can be achieved *via* directly measuring the UV-vis spectra of the concentrated solution – its special absorption peaks are around 360 nm. However, it is difficult to detect by absorption, owing to the low molar absorption coefficient of H_2O_2[90]. Besides, other measurements of coloration and fluorescent methods are also developed, making the detection of H_2O_2 a facile work [118–121]. It is worth noting that the fluorescence probe based on AIEgens is also developed for detecting H_2O_2, both *in vitro* and *in vivo* [122–124].

Additionally, 2′-7′-dichlorofluorescin diacetate (DCFH-DA) is most widely used for detecting all species of ROS, without specificity in vivo and vitro. DCFH-DA is the nonfluorescent indictor, which can be cleaved by ROS and subsequently form fluorescent dichlorofluorescein (DCF) with emission at 510–540 nm, exited by 490–520 nm.

17.5 Advanced development in PDT

As traditional PSs employed for PDT, aggregation of PSs is inevitably not important as they are delivered as nanoparticles or sent inside the infringed cell, which would result in self-quenching and lead to the failure of tumor treatment. In this regard, AIEgen-based PS overcomes the hurdles. Even since the first AIEgen-based PS for PDT was developed, it has boost PDT in tumor treatment [31, 125]. Here, some cutting-edge concerns of AIEgen-based PSs for PDT focused on far red/NIR emissions, smart PSs with targetable and activatable abilities, and PDT treatments in hypoxic environment are reviewed.

17.5.1 Far Red/NIR PSs

The penetration depth of light and the effective delivery of PSs are the main factors in PDT processes. Interactions between human tissues and light at different wavelengths are shown in Figure 17.7. It can be clearly seen that deep penetration depth would be achieved when waves of longer wavelengths are employed, and as the wavelength of light is increased to 700 nm, a depth of 10 mm is achieved. However, most of PSs exhibited the small Stokes shifts, with its absorption in the UV or the vis region. Developing an AIEgen-based PS with far red/NIR absorption for a deeper penetration is highly desirable.

Strategies to achieve far red/NIR AIEgens involve the introduction of strong electron donor and acceptor into the molecule, with the π-bridge or expansion of

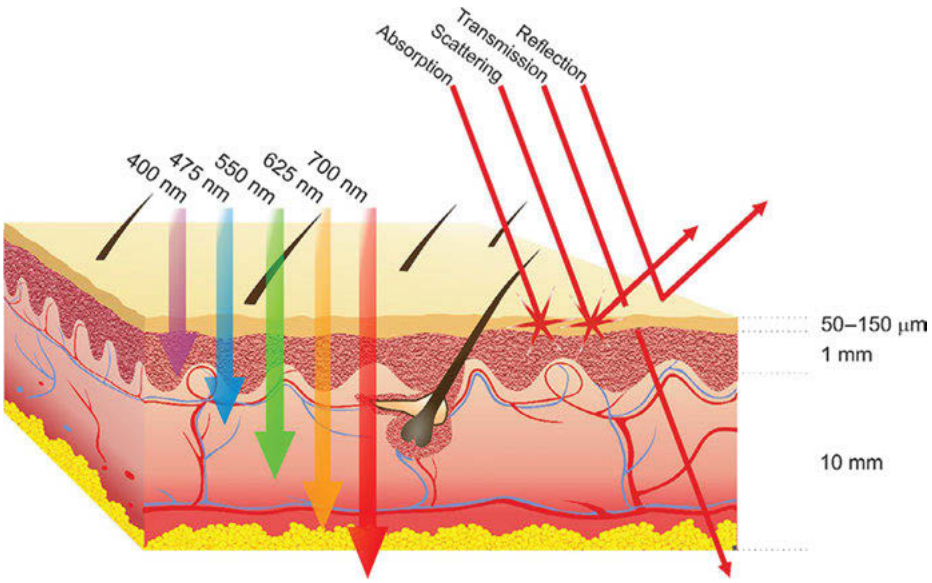

Figure 17.7: Light interactions with human tissues. Reprinted with permission from the reference of [33]. Copyright 2017 Elsevier.

π-conjugation. By introducing a strong donor and acceptor in one molecule and by the expansion of the π-conjugation, the electronic bandgaps would be decreased and the ICT would be facilitated, which consequently result in NIR absorption or emission. Based on this consideration, Liu et al. designed the NIR PSs of TTPy and MeTTPy, with a strong accepter of pyridinium moiety, and the strong donor of thiophene fragment and triphenylamine segment/two methyl groups as shown in Figure 17.8 [57]. Owing to the expanded π-conjugation of the molecule by the π-bridge of carbon–carbon double bond and thiophene fragment, AIEgens with NIR fluorescence and high ROS production were achieved, which showed a remarkable tumor-targeting PDT effect. By designing the bipolar molecule with donor-acceptor interaction, Tang and coauthors [126] synthesized a series of AIEgens by combining the donor of diphenylamine group with four different acceptors, including malononitrile, isophorone, methylpyridinium salt, and 3-cyano-4-phenyl-2 (5 H)-furanone, through an electron-rich carbazolyl ring. From their study, AIEgens with NIR emission and multiphoton absorption with varied $^1O_2$ generation were obtained, resulting from the strong donor-acceptor interaction and reduced TICT. The obtained AIEgens exhibited an excellent ability of cell imaging with lipid droplets targeting and elimination of the cancer cell by ROS production. Reduced TICT was also used in molecular engineering for constructing NIR PSs [127]. Based on the manipulation of donor and acceptor interaction and the extension of π-conjugation, Tang and coauthors constructed the three-component molecule with triphenylamine as the

donor and N-methylation as the acceptor through the conjugation of π-conjugation thiophene units. By tuning the extension of the π-conjugation of thiophene units, fluorescence imaging, photoacoustic imaging, photothermal imaging, PDT, and photothermal therapy functions of the obtained AIEgens of NIR were achieved [128].

BODIPY is commonly employed to develop NIR PS for PDT treatment. Generally, BODIPY is a special molecule with features of high molar absorption coefficients, environmental stability, photostability, and high light-dark toxicity ratios, which has been widely used in PDT treatment [129, 130]. However, BODIPYs exhibit short emission wavelengths and small Stokes shifts, which are unstratified with applications in biomedical fields. Moreover, the effect of ACQ limited its improvement of dosage in PDT as well. Hence, modifying BODIPYs with rotated additive endow BODIPYs with the features of AIE, making it possible for extended applications in PDT treatments. Yoon and his collaborators [131] put forward strategies to modify the acceptor of BODIPYs by adding twisted molecules as the donor, connected by the π-bridge of phenyl linker, through which large molar absorption coefficients in visible light region and large Stokes shift were achieved, and the ACQ hurdle was overcome through the twisted molecular structure. Additionally, $\Delta E_{S\text{-}T}$ of the modified BODIPYs was manipulated by introducing a heavy atom into the molecule as illustrated in Figure 17.9. Taking advantage of the NIR emission and ROS generation, the modified BODIPYs have been utilized in cell imaging and displayed excellent tumor elimination. Wu et al. [132] constructed the AIEgens with donor-acceptor-donor structure based on BODIPY, by conjugating triphenylamine groups to BODIPY as the donor and the 1,8-naphthalenediimide (NI) as the acceptor for enhancing the ISC processes. With these designs, the obtained BODIPY derivative of T-BDP displayed absorption in the NIR region and significant AIE characteristics. As T-BDP self-assembled into nanoparticles, T-BDP NPs exhibited strong ROS generation and photothermal conversion (50.9%) simultaneously, indicating their potential in PDT and PTT treatments.

17.5.2 Smart PSs with targeting and activatable abilities

Since the normal PSs exhibit broad-light toxicity as the PS is injected into the circulatory system in an “always on” model, a side effect is the indiscriminate elimination of the cancer and normal cells, which hinders its development in preclinical and clinical investigations. An ideal PS equipped with tumor-targeting and cancer-triggered PS is highly desirable. There are several approaches to improve the targeting of PSs, and most research works are based on the oriented targeting toward the organelle in the cancer cell by modifying the PS with a specific additive or altering the charge characteristics of the PSs [30, 133–137]. For example, Liu and coauthors [138] encapsulated the red emissive AIE PS of TTD into the amphiphilic polymer matrix of DSPE-PEG_{2000}-cRGD to form the AIE dots, and modified AIE dots with the specific targeted protein of cRGD through the fast click reaction of the maleimide

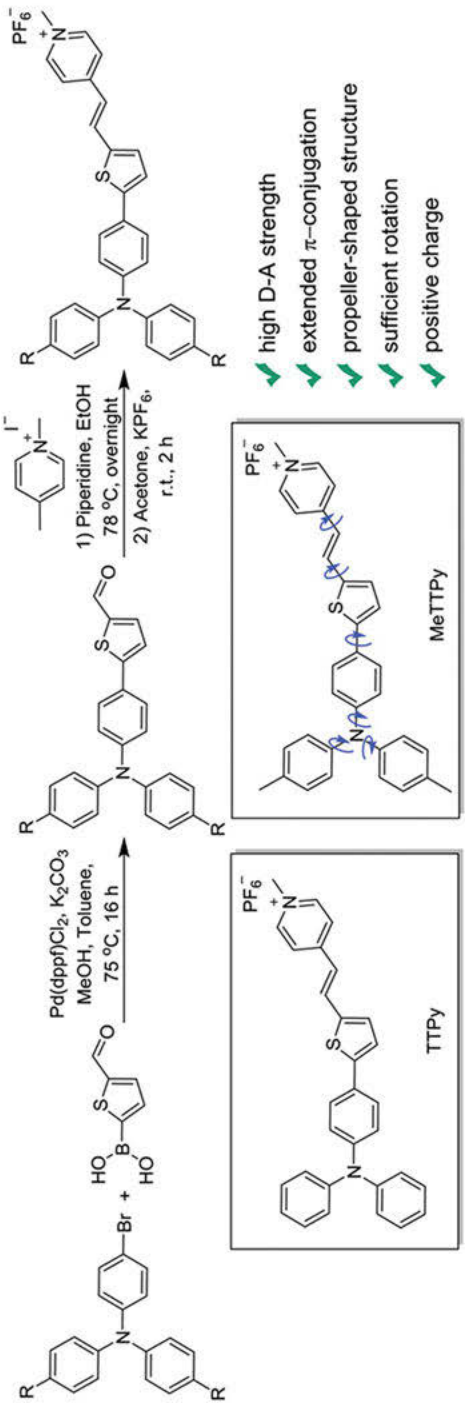

Figure 17.8: NIR PS of MeTTPy obtained from the molecule engineering of D-A interaction and extended π-conjugation. Reprinted with permission from the reference of [57]. Copyright 2018 Wiley VCH.

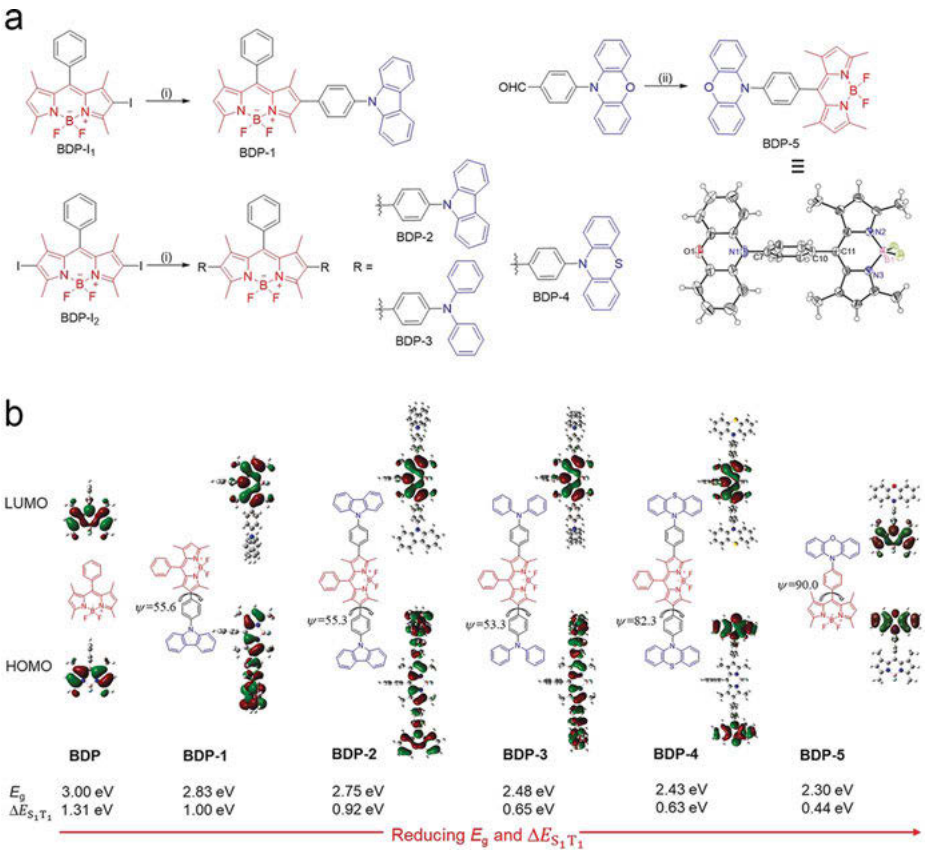

Figure 17.9: (a) Molecular engineering based on BOPIDY for designing NIR PS with AIE characteristic. (b) Frontier molecular orbitals from DFT calculations of BDP dyes in the ground state. Reprinted with permission from the reference of [131]. Copyright 2020 Wiley VCH.

group and the sulfhydryl group, enjoining the specific interaction between integrin αvβ3 and cRGD on the T-TTD dots. Targeting the PS to cholangiocarcinoma was achieved as shown in Figure 17.10.

PSs, with activable sites, that would trigger localized or activated at the target site could be one of the most promising strategies for tumor targeting [139]. Cathepsin B is a lysosomal protease overexpressed in various cancer cells, which can be used as a specific target by targeting the peptide of -Gly-Phe-Leu-Gly- (GFLG). Based on this, Liu and coauthors [140] developed a smart AIEgen with an activatable PDT, which could be cleaved by Cathepsin B, for eliminating cancer cells (Figure 17.11a). The special activatable PS is a four-component AIEgen that includes: a) an orange fluorescence emitting AIEgen of TPECM as the photosensitizer, b) the GFLG peptide as the trigger point that responds to Cathepsin B, c) a hydrophilic unit to increase the hydrophilicity, and d) the cRGD-targeting moiety. Through this strategy, the four-component activatable

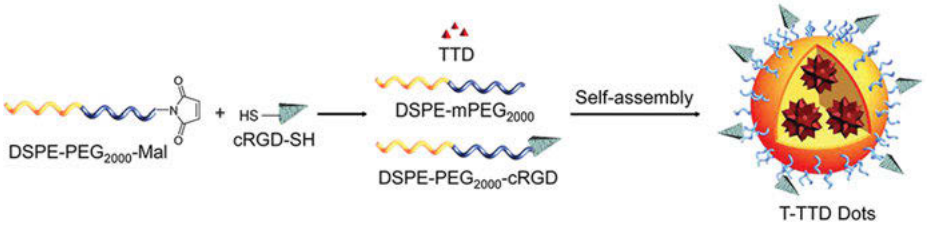

Figure 17.10: Generally employed strategies for constructing targeted AIE dots for smart PDT treatments, and the obtained result exhibited excellent targeting proprieties. Reprinted with permission from the reference of [138]. Copyright 2017 American Chemical Society.

PS displays low ROS generation in aqueous solution because the excitonic energy of the PS is dissipated *via* the free intramolecular motions. However, it can be triggered as the peptide cleaved by Cathepsin B, and the appendant to the peptide dissociated from the PS leads to express the ROS in the cancer cell. As the special molecule was introduced into the cells of MDA-MB-231, MCF-7, and 293 T cells, remarkable difference in molecular toxicity were detected, which demonstrated the potential of the strategy for developing smart PSs.

Adding quenchers or energy acceptors to the adjacent photosensitizers covalently is another method for designing activatable PSs. Mitomycin C (MMC) is an effective DNA cross-linking anticancer drug, which can also be used as the photo-induced electron transfer (PET) fluorescence quencher [141]. Conjoining MMC to the normal PSs with the tumor-responsive linker can be an effective approach to synthesize the activatable PS. Therefore, Liu and coauthors [142] (Figure 17.11b) synthesized the activatable PS of TPEPY-S-MMC by connecting the MMC with Ps *via* a disulfide bond, which could be cleaved by glutathione (GSH). In the propagation of cancer, GSH is one of the most abundant biothiols in living cells, which is overexpressed in tumor tissues than in the normal tissues, and the excess GSH generally leads to ineffective ROS for killing cancers and thus discounts the PDT performance [143]. Due to the presence of the quencher, TPEPY-S-MMC showed no ROS production and no fluoresce emission. However, TPEPY-S-MMC displayed a high level of ROS generation and bright emission in the cancer cells due to the suppression of PET from the AIEgens to MMC by breaking the disulfide linker. Taking advantage of the effective ROS production and the chemotherapeutics of MMC, a dual-prodrug combination for tumor treatment was achieved. Similar strategies were employed in Kim's studies [144]. In their studies, a tetraphenylethylene derivate (TPEPY-S-Fc) with a GSH activatable structure was used for image-guided PDT treatments. TPEPY-S-Fc comprises the well-known quencher of ferrocene and vinyl pyridinium-substituted tetraphenylethylene (TPEPY), which was linked through a GSH cleavable disulfide bond. Owing to the PET processes, ferrocene could quench the emission of TPEPY and the ROS generation. As the synthesized TPEPY-S-Fc was incubated with the cancer cells of CT-6 cells, it exhibited biocompatibility even at high concentrations.

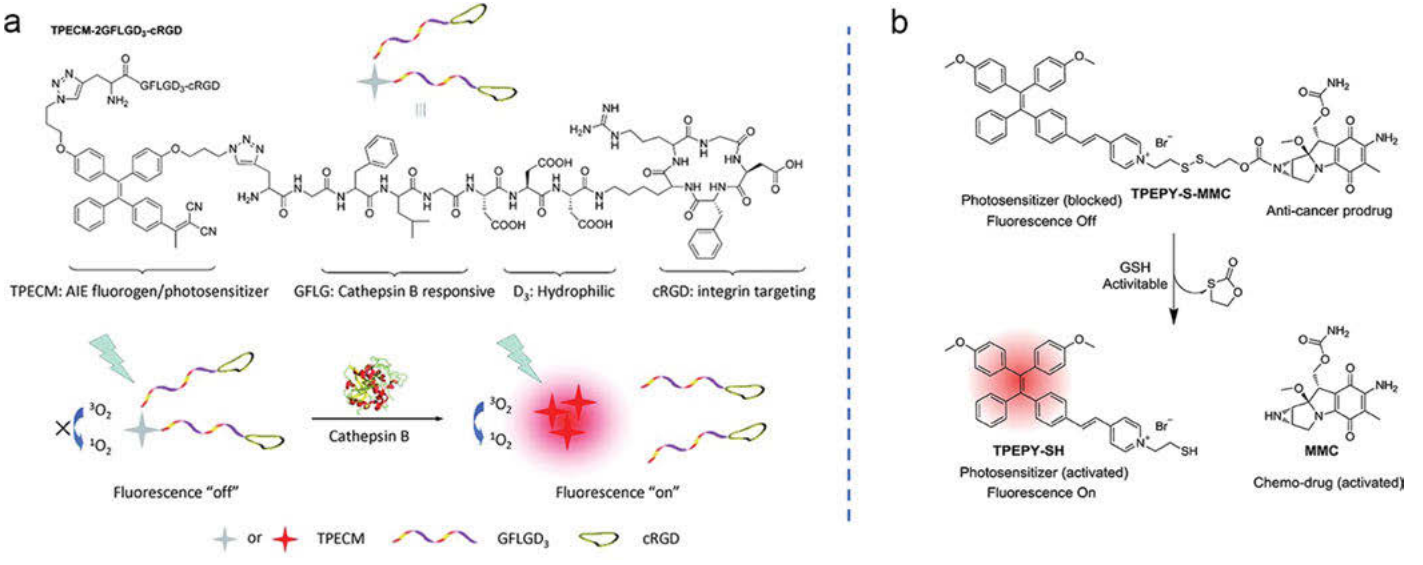

Figure 17.11: (a) Four-component functionalized AIE-PS of TPECM-2GFLGD3-cRGD and the schematic illustration of the activation by Cathepsin B. Reprinted with permission from the reference of [140]. Copyright 2015 Wiley VCH. (b) Proposed activation route for the GSH activatable AIE-PS. Reprinted with permission from the reference of [142]. Copyright 2017 Elsevier.

However, it showed aggressive toxicity toward CT-6 cells when they were irradiated under light, which can be chosen as a potential candidate for efficient photodynamic therapy in cancer treatment.

Although many strategies based on the energy transfer or electron transfer *via* covalent conjoining of quencher and normal PSs have been developed, the complicated molecule design, time-consuming synthesis, high cost, and unwanted toxicity of the normal activatable PS limit their wide implementation in practical clinic applications. Considering this, Huang and coauthors [145] (Figure 17.12) developed a novel approach to realize activatable PS *via* supramolecular host-guest interactions. The PS of molecule G was composed with the TPE core, endowing G with the AIE feature. Appending TPE with the pyridinium electron acceptor, HOMO and LUMO could be well separated and the energy gap between them was reduced to 0.2 eV, facilitating the ICT from the S_1 state to T_1 state and generating ROS. However, by modifying the molecule G with the anionic water-soluble pillar [5] arene (WP5), supramolecular construction of the host-guest interaction occurred, and fluorescence and ROS generation were suppressed due to the PET processes between the molecule G and WP5. Interestingly, WP5 exhibited pH sensitivity owing to the transformation from the hydrophilic carboxylate to the hydrophobic carboxy groups. By controlling the pH of the environment, PET interaction of molecule G and WP5 was tuned, which realized the activatable ROS generation and fluorescence. The biocompatibility of the host-guest complex WP5⊃G was demonstrated, regardless of darkness or under light irradiation, and the specific activatable WP5⊃G PS was verified by incubating with HeLa cells.

17.5.3 Hypoxic PDT treatments

Despite the clinical promise, PDT treatment suffers from a critical drawback, which is associated with its oxygen-dependent nature. Based on the mechanism of ROS generation above-mentioned, ROS is generated from PS *via* the different routes, including Type I and Type II mechanisms, and the major PSs produce ROS based on the Type II mechanism, which is dependent on the presence of oxygen. Unfortunately, oxygen concentrations vary with locations in tumors tissues, which might result from the aggressive proliferation of cancer cells and an insufficient blood supply in tumors, leading to the discounting of PDT treatments in tumors [37]. Great efforts have gone in to overcome the problem, including catalysis of the substrates in cell into oxygen and promoting the generation of ROS *via* Type I mechanism. Huang and coauthors [146] prompted the metal-organic compositing strategy to realize the oxygen generation *via* nanozyme in the hypoxic tumors for PDT treatment. In their strategy, the nanozyme was prepared from the MnO_2 nanoparticles, with ferritin nanocages (FTn) inside. Later, the nanozymes were encapsulated into the lipid bilayer with AIE-PS embedded to form the liposome (Lipo-OGzyme-AIE).

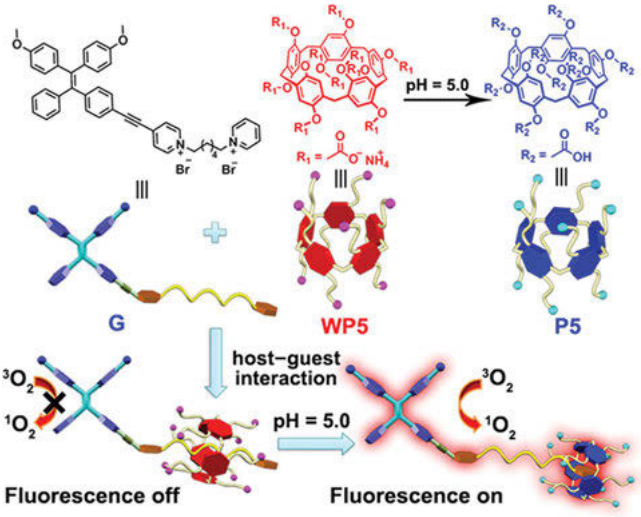

Figure 17.12: Activatable AIE-PS based on the host-guest interaction with sensitivity to pH. Reprinted with permission from the reference of [145]. Copyright 2020 Wiley VCH.

Benefiting from the presence of a lipid bilayer, Lipo-OGzyme-AIE exhibited good biocompatibility. As the nanocarriers of Lipo-OGzyme-AIE were injected into the 4T1 tumor-bearing mice, PDT treatments were conducted as the oxygen could be generated form the hydrolysis of H_2O_2 by MnO_2 nanoparticles, which realized the hypoxic PDT in the real tumor tissues. In the normal PDT treatment, both limited oxygen concentrations and the stress response from the cancer cell for the oxidative stress decrease the PDT effect. B-cell lymphoma 2 (Bcl-2) is the most common PDT resistance-related proteins of the cancer cells, which could further yield higher cellular concentration of GSH, leading to a decrease in ROS concentrations. In line with this, Liu and coauthors [147] developed the carrier-free hybrid nanosphere composed of AIE PSs, ferric ions, and the Bcl-2 inhibitor to realize PDT treatments in hypoxic tumors. Benefiting from this strategy, oxygen could be continuously generated from the cytoplasm *via* the ferric-ions-induced Fenton reaction. The ROS level in the cell could be increased by inhibiting the production of Bcl-2 protein and, eventually, the efficiency of PDT was boosted, as shown in Figure 17.13.

Compared to indirectly generating oxygen from the hypoxic environment of the tumor tissues to promote the PDT efficiency, direct transfer of the energy or electron from the excited PS to H_2O to form the radical species *via* Type I routes is more convenient. However, this process primarily relies on molecule designing. Anion-π^+ exhibits excellent subcellular targeting ability *via* charge interaction and electron-rich condition from the anionic reductant, which could be employed as the criterion to develop Type I PSs. For example, Qi et al. [36] developed a series of Type I PSs based on anion-π^+ AIEgens and proposed the concept "the more ICT effect in electron-rich anion-π^+ AIEgens,

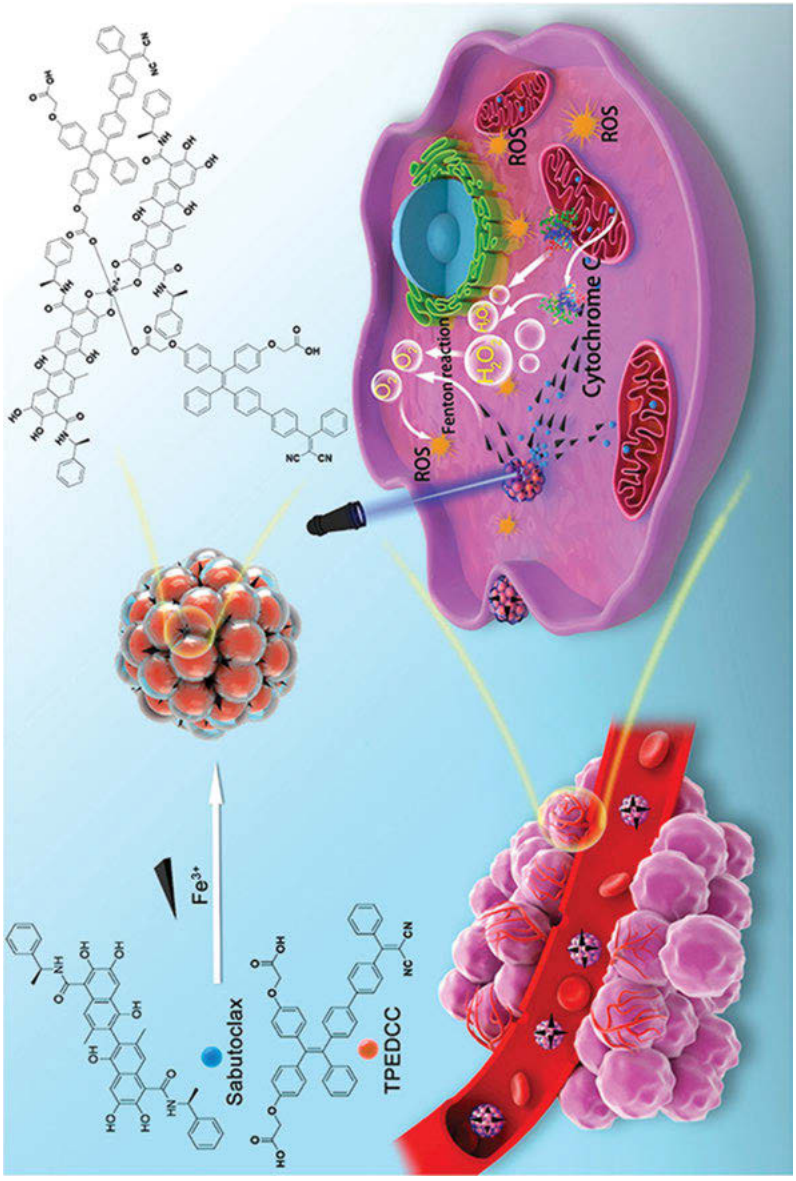

Figure 17.13: Indirect hypoxic PDT treatments of the multicomponent AIE-PS based on the oxygen generation. Reprinted with permission from the reference of [147]. Copyright 2020 American Chemical Society.

more effective is the generation of free radical ROS." Benefitting from the suppression of nonradiative internal conversion and activation of the ISC channels, the harvested AIEgens provides an electron-rich microenvironment for the electron transfer processes from AIEgens to the surrounding oxygen. Moreover, by modifying the AIEgens with electron-donating groups, the ICT processes are improved, resulting in the effective production of Type I ROS for PDT treatment, as shown in Figure 17.14a. Through electron transferred from the AIEgens to the oxygen, oxygenous radicals were obtained and exhibited a therapeutic effect on HeLa cells, providing the promise to overcome tumor hypoxia defects in PDT treatments. Similar, with that of Qi's work, Tang and coauthors realized that it is possible to eliminate HeLa and T24 cells in the hypoxic environment by designing the molecule with the electron-donating effect of anion-π^+ AIEgens using the concept of "greater ICT in electron-rich anion-π^+ AIEgens, greater is the free radical ROS generation with bright imaging" (Figure 17.14b) [35, 148]. Additionally, Type I ROS generated from the AIE-PS directly by the oxidation reaction of the substrates was also established as shown in Figure 17.14c [34].

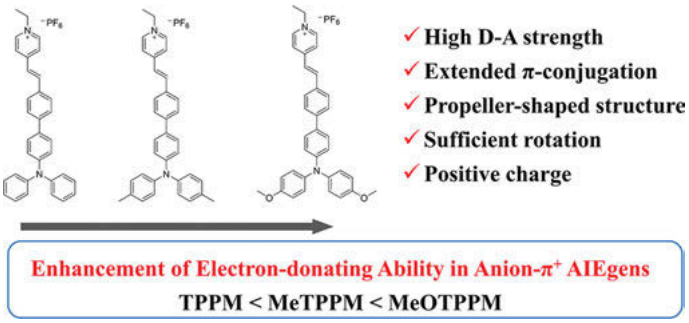

Figure 17.14: Molecular engineering of AIEgens based on the anion-π^+ strategies. Modified with permission from the reference of [34]. Published by The Royal Society of Chemistry.

17.6 Summary

As the noninvasive treatment modality, PDT has been widely used in tumor treatments for decades, and some of them have been approved by FDA for clinic treatment. Photosensitizer is the most important part in the PDT processes. However, the hurdles for the traditional photosensitizer are obvious, including the ACQ effect in the condensed solution, short wavelength of absorption, unsatisfied ROS generation, oxygen dependence, and so on. Contrary to the traditional photosensitizer, a photosensitizer based on AIE overcame some of the difficulties and endowed the photosensitizer with more flexibility for further modification. Guided by the practical application in clinic treatments, many AIEgen-based PSs are developed with

features of bright emission, effective ROS generation, large Stokes shift, far red/NIR fluorescence, and so on. In this chapter, we reviewed the development of the photosensitizer based on AIE with the scope of ROS generation mechanism, design strategies of photosensitizer, detection of ROS, and advanced developments in PDT treatments. Accordingly, an elaborate overview of the AIE-PS is presented, and provides much helpful information for guiding the molecular designing and applications in future. Prospectively, there is still a big challenge for the PSs for employing in clinic treatments. The main concerns are focused on the advanced PSs with excellent biocompatibility, deep penetration, effective ROS generation, oxygen-independent therapy, and so on. Additionally, developing smart PSs based on manipulating the antagonism of endogenous active substrate and ROS in cancer cells becomes another fascinating method for PDT treatment.

References

[1] Bonnett R, Photosensitizers of the porphyrin and phthalocyanine series for photodynamic therapy, Chem Soc Rev, 1995, 24, 19–33.
[2] Wang S, Wang X, Yu L, Sun M, Progress and trends of photodynamic therapy: From traditional photosensitizers to AIE-based photosensitizers, Photodiagn Photodyn Ther, 2021, 3, 102254.
[3] Yang L, Wei Y, Xing D, Chen Q, Increasing the efficiency of photodynamic therapy by improved light delivery and oxygen supply using an anticoagulant in a solid tumor model, Lasers Surg Med, 2010, 42, 671–679.
[4] Felsher DW, Cancer revoked: Oncogenes as therapeutic targets, Nat Rev Cancer, 2003, 3, 375–380.
[5] Josefsen LB, Boyle RW, Photodynamic therapy and the development of metal-based photosensitisers, Met-Based Drugs, 2008, 2008, 276109.
[6] Guan Q, Li Y-A, Li W-Y, Dong Y-B, Photodynamic therapy based on nanoscale metal-organic frameworks: From material design to cancer nanotherapeutics, Chem-Asian J, 2018, 13, 3122–3149.
[7] Qian CG, Chen YL, Feng PJ, Xiao XZ, Dong M, Yu JC, Hu QY, Shen QD, Gu Z, Conjugated polymer nanomaterials for theranostics, Acta Pharmacol Sin, 2017, 38, 764–781.
[8] Liu P, Yue C, Sheng Z, Gao G, Li M, Yi H, Zheng C, Wang B, Cai L, Photosensitizer-conjugated redox-responsive dextran theranostic nanoparticles for near-infrared cancer imaging and photodynamic therapy, Polym Chem, 2014, 5, 874–881.
[9] Shen X, Li S, Li L, Yao SQ, Xu QH, Highly efficient, conjugated-polymer-based nanophotosensitizers for selectively targeted two-photon photodynamic therapy and imaging of cancer cells, Chemistry, 2015, 21, 2214–2221.
[10] Yang T, Liu L, Deng Y, Guo Z, Zhang G, Ge Z, Ke H, Chen H, Ultrastable near-infrared conjugated-polymer nanoparticles for dually photoactive tumor inhibition, Adv Mater, 2017, 29, 1700487.
[11] Yoon I, Li JZ, Shim YK, Advance in photosensitizers and light delivery for photodynamic therapy, Clin Endosc, 2013, 46, 7–23.
[12] Juarranz Á, Jaén P, Sanz-Rodríguez F, Cuevas J, González S, Photodynamic therapy of cancer. Basic principles and applications, Clin Transl Oncol, 2008, 10, 148–154.

[13] Macdonald IJ, Dougherty TJ, Basic principles of photodynamic therapy, J Porphyr Phthalocyanines, 2001, 5, 105–129.
[14] Kwiatkowski S, Knap B, Przystupski D, Saczko J, Kedzierska E, Knap-Czop K, Kotlinska J, Michel O, Kotowski K, Kulbacka J, Photodynamic therapy-mechanisms, photosensitizers and combinations, Biomed Pharmacother, 2018, 106, 1098–1107.
[15] Li L, Chen Y, Chen W, Tan Y, Chen H, Yin J, Photodynamic therapy based on organic small molecular fluorescent dyes, Chin Chem Lett, 2019, 30, 1689–1703.
[16] Josefsen LB, Boyle RW, Photodynamic therapy: Novel third-generation photosensitizers one step closer? Br J Pharmacol, 2008, 154, 1–3.
[17] Hudson R, Carcenac M, Smith K, Madden L, Clarke OJ, Pelegrin A, Greenman J, Boyle RW, The development and characterisation of porphyrin isothiocyanate-monoclonal antibody conjugates for photoimmunotherapy, Br J Cancer, 2005, 92, 1442–1449.
[18] Yang L, Wang X, Zhang G, Chen X, Zhang G, Jiang J, Aggregation-induced intersystem crossing: A novel strategy for efficient molecular phosphorescence, Nanoscale, 2016, 8, 17422–17426.
[19] Ji C, Gao Q, Dong X, Yin W, Gu Z, Gan Z, Zhao Y, Yin M, A size-reducible nanodrug with an aggregation-enhanced photodynamic effect for deep chemo-photodynamic therapy, Angew Chem Int Ed, 2018, 57, 11384–11388.
[20] Zhao N, Li Y, Yin W, Zhuang J, Jia Q, Wang Z, Li N, Controllable coumarin-based NIR fluorophores: Selective subcellular imaging, cell membrane potential indication, and enhanced photodynamic therapy, ACS Appl Mater Interfaces, 2020, 12, 2076–2086.
[21] Li X, Lee D, Huang JD, Yoon J, Phthalocyanine-assembled nanodots as photosensitizers for highly efficient type I photoreactions in photodynamic therapy, Angew Chem Int Ed, 2018, 57, 9885–9890.
[22] Lee E, Li X, Oh J, Kwon N, Kim G, Kim D, Yoon J, A boronic acid-functionalized phthalocyanine with an aggregation-enhanced photodynamic effect for combating antibiotic-resistant bacteria, Chem Sci, 2020, 11, 5735–5739.
[23] Hsieh MC, Chien CH, Chang CC, Chang TC, Aggregation induced photodynamic therapy enhancement based on linear and nonlinear excited FRET of fluorescent organic nanoparticles, J Mater Chem B, 2013, 1, 2350–2357.
[24] Uchoa AF, de Oliveira KT, Baptista MS, Bortoluzzi AJ, Iamamoto Y, Serra OA, Chlorin photosensitizers sterically designed to prevent self-aggregation, J Org Chem, 2011, 76, 8824–8832.
[25] Tada DB, Baptista MS, Photosensitizing nanoparticles and the modulation of ROS generation, Front Chem, 2015, 3, 33.
[26] Luo J, Xie Z, Lam JWY, Cheng L, Chen H, Qiu C, Kwok HS, Zhan X, Liu Y, Zhu D, Tang BZ, Aggregation-induced emission of 1-methyl-1,2,3,4,5-pentaphenylsilole, Chem Commun, 2001, 1740–1741.
[27] Hong Y, Lam JWY, Tang BZ, Aggregation-induced emission, Chem Soc Rev, 2011, 40, 5361–5388.
[28] Mei J, Hong Y, Lam JWY, Qin A, Tang Y, Tang BZ, Aggregation-induced emission: The whole is more brilliant than the parts, Adv Mater, 2014, 26, 5429–5479.
[29] Mei J, Leung NLC, Kwok RTK, Lam JWY, Tang BZ, Aggregation-induced emission: Together we shine, united we soar! Chem Rev, 2015, 115, 11718–11940.
[30] Yuan Y, Feng G, Qin W, Tang BZ, Liu B, Targeted and image-guided photodynamic cancer therapy based on organic nanoparticles with aggregation-induced emission characteristics, Chem Commun, 2014, 50, 8757–8760.
[31] Hu F, Huang Y, Zhang G, Zhao R, Yang H, Zhang D, Targeted bioimaging and photodynamic therapy of cancer cells with an activatable red fluorescent bioprobe, Anal Chem, 2014, 86, 7987–7995.

[32] Kasha M, Energy transfer mechanisms and the molecular exciton model for molecular aggregates, Radiat Res, 1963, 20, 55–70.
[33] Dąbrowski JM, Chapter nine-reactive oxygen species in photodynamic therapy: Mechanisms of their generation and potentiation, Advances in Inorganic Chemistry, van Eldik R, Hubbard CD (eds.), Academic Press, Oxford, United Kingdom 2017, 343–394.
[34] Zhuang Z, Dai J, Yu M, Li J, Shen P, Hu R, Lou X, Zhao Z, Tang BZ, Type I photosensitizers based on phosphindole oxide for photodynamic therapy: Apoptosis and autophagy induced by endoplasmic reticulum stress, Chem Sci, 2020, 11, 3405–3417.
[35] Wan Q, Zhang R, Zhuang Z, Li Y, Huang Y, Wang Z, Zhang W, Hou J, Tang BZ, Molecular engineering to boost AIE-active free radical photogenerators and enable high-performance photodynamic therapy under hypoxia, Adv Funct Mater, 2020, 30, 2001057.
[36] Zhao X, Dai Y, Ma F, Misal S, Hasrat K, Zhu H, Qi Z, Molecular engineering to accelerate cancer cell discrimination and boost AIE-active type I photosensitizer for photodynamic therapy under hypoxia, Chem Eng J, 2021, 410, 128133.
[37] Li X, Kwon N, Guo T, Liu Z, Yoon J, Innovative strategies for hypoxic-tumor photodynamic therapy, Angew Chem Int Ed, 2018, 57, 11522–11531.
[38] Dempster DN, Morrow T, Quinn MF, Extinction coefficients for triplet-triplet absorption in ethanol solutions of anthracene, naphthalene, 2,5-diphenyloxazole, 7-diethylamino- 4-methyl coumarin and 4-methyl-7-amino-carbostyril, J Photochem, 1973, 2, 329–341.
[39] Cincotta L, Foley JW, Cincotta AH, Novel red absorbing benzo[a]phenoxazinium and benzo[a] phenothiazinium photosensitizers: In vitro evaluation, Photochem Photobiol, 1987, 46, 751–758.
[40] Gorman AA, Hamblett I, Lambert C, Prescott AL, Rodgers MAJ, Spence HM, Aromatic ketone-naphthalene systems as absolute standards for the triplet-sensitized formation of singlet oxygen, O2(1.DELTA.g), in organic and aqueous media. A time-resolved luminescence study, J Am Chem Soc, 1987, 109, 3091–3097.
[41] Harris F, Chatfield L, Phoenix D, Phenothiazinium based photosensitisers-photodynamic agents with a multiplicity of cellular targets and clinical applications, Curr Drug Targets, 2005, 6, 615–627.
[42] Xu S, Yuan Y, Cai X, Zhang CJ, Hu F, Liang J, Zhang G, Zhang D, Liu B, Tuning the singlet-triplet energy gap: A unique approach to efficient photosensitizers with aggregation-induced emission (AIE) characteristics, Chem Sci, 2015, 6, 5824–5830.
[43] Zhao N, Li P, Zhuang J, Liu Y, Xiao Y, Qin R, Li N, Aggregation-induced emission luminogens with the capability of wide color tuning, mitochondrial and bacterial imaging, and photodynamic anticancer and antibacterial therapy, ACS Appl Mater Interfaces, 2019, 11, 11227–11237.
[44] Guo B, Wu M, Shi Q, Dai T, Xu S, Jiang J, Liu B, All-in-one molecular aggregation-induced emission theranostics: Fluorescence image guided and mitochondria targeted chemo- and photodynamic cancer cell ablation, Chem Mater, 2020, 32, 4681–4691.
[45] Xu S, Wu W, Cai X, Zhang CJ, Yuan Y, Liang J, Feng G, Manghnani P, Liu B, Highly efficient photosensitizers with aggregation-induced emission characteristics obtained through precise molecular design, Chem Commun, 2017, 53, 8727–8730.
[46] Li W, Huang M, Li Y, Yang Z, Qu J, Novel D-π-A-D type aggregation induced emission luminogens based nanoparticles as efficient $^1O_2$ photosensitizer and bright NIR imaging agent, Dyes Pigm, 2021, 186, 109041.
[47] Sun Z, Liu Y, Guan P, Yang B, Liu B, Near-infrared dual-functional AIEgens for lipid droplets imaging in multispecies and photodynamic therapy, Dyes Pigm, 2021, 185, 108884.
[48] Cheng G, Wang H, Zhang C, Hao Y, Wang T, Zhang Y, Tian Y, Chang J, Multifunctional nano-photosensitizer: A carrier-free aggregation-induced emission nanoparticle with efficient photosensitization and pH-responsibility, Chem Eng J, 2020, 390, 124447.

[49] Tan P, Li C, Wang Y, Zhuang W, Chen M, Zhou L, Zhang J, Gong Q, Wei Q, You J, A biheteroaryl-bridged fluorescence probe enables lipid droplets-specific bioimaging and photodynamic therapy in clinical clear cell renal cell carcinoma, Dyes Pigm, 2021, 188, 109215.
[50] Deng J, Yang M, Li C, Liu G, Sun Q, Luo X, Wu F, Single molecular-based nanoparticles with aggregation-induced emission characteristics for fluorescence imaging and efficient cancer phototherapy, Dyes Pigm, 2021, 187, 109130.
[51] Zhao Q, Zhang S, Liu Y, Mei J, Chen S, Lu P, Qin A, Ma Y, Sun JZ, Tang BZ, Tetraphenylethenyl-modified perylene bisimide: Aggregation-induced red emission, electrochemical properties and ordered microstructures, J Mater Chem, 2012, 22, 7387–7394.
[52] Zhao Z, Su H, Zhang P, Cai Y, Kwok RTK, Chen Y, He Z, Gu X, He X, Sung HHY, Willimas ID, Lam JWY, Zhang Z, Tang BZ, Polyyne bridged AIE luminogens with red emission: Design, synthesis, properties and applications, J Mater Chem B, 2017, 5, 1650–1657.
[53] Wang D, Su H, Kwok RTK, Shan G, Leung ACS, Lee MMS, Sung HHY, Williams ID, Lam JWY, Tang BZ, Facile synthesis of red/NIR AIE luminogens with simple structures, bright emissions, and high photostabilities, and their applications for specific imaging of lipid droplets and image-guided photodynamic therapy, Adv Funct Mater, 2017, 27, 1704039.
[54] Chen X, Gao H, Deng Y, Jin Q, Ji J, Ding D, Supramolecular aggregation-induced emission nanodots with programmed tumor microenvironment responsiveness for image-guided orthotopic pancreatic cancer therapy, ACS Nano, 2020, 14, 5121–5134.
[55] Hu F, Xu S, Liu B, Photosensitizers with aggregation-induced emission: Materials and biomedical applications, Adv Mater, 2018, 30, e1801350.
[56] Koziar JC, Cowan DO, Photochemical heavy-atom effects, Acc Chem Res, 1978, 11, 334–341.
[57] Wang D, Lee MMS, Shan G, Kwok RTK, Lam JWY, Su H, Cai Y, Tang BZ, Highly efficient photosensitizers with far-red/near-infrared aggregation-induced emission for in vitro and in vivo cancer theranostics, Adv Mater, 2018, 30, e1802105.
[58] Han W, Zhang S, Deng R, Du Y, Qian J, Zheng X, Xu B, Xie Z, Yan F, Tian W, Self-assembled nanostructured photosensitizer with aggregation-induced emission for enhanced photodynamic anticancer therapy, Sci China Mater, 2019, 63, 136–146.
[59] Chen J, Zou Z, Ke Z, Zhang X, Feng J, Jing Y, Peng L, Yang J, Dai Y, Zou D, Dimerization of heavy atom free tetraphenylethylene with aggregation induced emission for boosting photodynamic therapy, New J Chem, 2020, 44, 7029–7034.
[60] Yuan H, Wang B, Lv F, Liu L, Wang S, Conjugated-polymer-based energy-transfer systems for antimicrobial and anticancer applications, Adv Mater, 2014, 26, 6978–6982.
[61] Wu W, Bazan GC, Liu B, Conjugated-polymer-amplified sensing, imaging, and therapy, Chem, 2017, 2, 760–790.
[62] Chan Y-H, Wu P-J, Semiconducting polymer nanoparticles as fluorescent probes for biological imaging and sensing, Part Syst Charact, 2015, 32, 11–28.
[63] Tsuda A, Osuka A, Fully conjugated porphyrin tapes with electronic absorption bands that reach into infrared, Science, 2001, 293, 79–82.
[64] Xing C, Xu Q, Tang H, Liu L, Wang S, Conjugated polymer/porphyrin complexes for efficient energy transfer and improving light-activated antibacterial activity, J Am Chem Soc, 2009, 131, 13117–13124.
[65] Xing C, Liu L, Tang H, Feng X, Yang Q, Wang S, Bazan GC, Design guidelines for conjugated polymers with light-activated anticancer activity, Adv Funct Mater, 2011, 21, 4058–4067.
[66] Wu W, Mao D, Xu S, Kenry, Hu F, Li X, Kong D, Liu B, Polymerization-enhanced photosensitization, Chem, 2018, 4, 1937–1951.
[67] Yuan J, Chen R, Tang X, Tao Y, Xu S, Jin L, Chen C, Zhou X, Zheng C, Huang W, Direct population of triplet excited states through singlet-triplet transition for visible-light excitable organic afterglow, Chem Sci, 2019, 10, 5031–5038.

[68] Uoyama H, Goushi K, Shizu K, Nomura H, Adachi C, Highly efficient organic light-emitting diodes from delayed fluorescence, Nature, 2012, 492, 234–238.
[69] Wang S, Wu W, Manghnani P, Xu S, Wang Y, Goh CC, Ng LG, Liu B, Polymerization-enhanced two-photon photosensitization for precise photodynamic therapy, ACS Nano, 2019, 13, 3095–3105.
[70] Wu W, High-performance conjugated polymer photosensitizers, Chem, 2018, 4, 1762–1764.
[71] Zhao J, Wu W, Sun J, Guo S, Triplet photosensitizers: From molecular design to applications, Chem Soc Rev, 2013, 42, 5323–5351.
[72] Wang XH, Song N, Hou W, Wang CY, Wang Y, Tang J, Yang YW, Efficient aggregation-induced emission manipulated by polymer host materials, Adv Mater, 2019, 31, e1903962.
[73] Wang Z, Wang C, Gan Q, Cao Y, Yuan H, Hua D, Donor-acceptor-type conjugated polymer-based multicolored drug carriers with tunable aggregation-induced emission behavior for self-illuminating cancer therapy, ACS Appl Mater Interfaces, 2019, 11, 41853–41861.
[74] Zhou T, Hu R, Wang L, Qiu Y, Zhang G, Deng Q, Zhang H, Yin P, Situ B, Zhan C, Qin A, Tang BZ, An AIE-active conjugated polymer with high ros-generation ability and biocompatibility for efficient photodynamic therapy of bacterial infections, Angew Chem Int Ed, 2020, 59, 9952–9956.
[75] Liu S, Zhang H, Li Y, Liu J, Du L, Chen M, Kwok RTK, Lam JWY, Phillips DL, Tang BZ, Strategies to enhance the photosensitization: Polymerization and the donor-acceptor even-odd effect, Angew Chem Int Ed, 2018, 57, 15189–15193.
[76] Odom TW, Schatz GC, Introduction to plasmonics, Chem Rev, 2011, 111, 3667–3668.
[77] Klajn R, Wesson PJ, Bishop KJM, Grzybowski BA, Writing self-erasing images using metastable nanoparticle “inks”, Angew Chem Int Ed, 2009, 48, 7035–7039.
[78] Kundu PK, Samanta D, Leizrowice R, Margulis B, Zhao H, Börner M, Udayabhaskararao T, Manna D, Klajn R, Light-controlled self-assembly of non-photoresponsive nanoparticles, Nat Chem, 2015, 7, 646–652.
[79] Ditlbacher H, Krenn JR, Lamprecht B, Leitner A, Aussenegg FR, Spectrally coded optical data storage by metal nanoparticles, Opt Lett, 2000, 25, 563–565.
[80] Yetisen AK, Butt H, da Cruz Vasconcellos F, Montelongo Y, Davidson CAB, Blyth J, Chan L, Carmody JB, Vignolini S, Steiner U, Baumberg JJ, Wilkinson TD, Lowe CR, Light-directed writing of chemically tunable narrow-band holographic sensors, Adv Opt Mater, 2014, 2, 250–254.
[81] Endo T, Ikeda R, Yanagida Y, Hatsuzawa T, Stimuli-responsive hydrogel–silver nanoparticles composite for development of localized surface plasmon resonance-based optical biosensor, Anal Chim Acta, 2008, 611, 205–211.
[82] Luo Q, Zhang C, Deng X, Zhu H, Li Z, Wang Z, Chen X, Huang S, Plasmonic effects of metallic nanoparticles on enhancing performance of perovskite solar cells, ACS Appl Mater Interfaces, 2017, 9, 34821–34832.
[83] Baek S-W, Noh J, Lee C-H, Kim B, Seo M-K, Lee J-Y, Plasmonic forward scattering effect in organic solar cells: A powerful optical engineering method, Sci Rep, 2013, 3, 1726.
[84] Lim D-K, Barhoumi A, Wylie RG, Reznor G, Langer RS, Kohane DS, Enhanced photothermal effect of plasmonic nanoparticles coated with reduced graphene oxide, Nano Lett, 2013, 13, 4075–4079.
[85] Sershen SR, Mensing GA, Ng M, Halas NJ, Beebe DJ, West JL, Independent optical control of microfluidic valves formed from optomechanically responsive nanocomposite hydrogels, Adv Mater, 2005, 17, 1366–1368.
[86] Tavakkoli Yaraki M, Pan Y, Hu F, Yu Y, Liu B, Tan YN, Nanosilver-enhanced AIE photosensitizer for simultaneous bioimaging and photodynamic therapy, Mater Chem Front, 2020, 4, 3074–3085.

[87] Tavakkoli Yaraki M, Hu F, Daqiqeh Rezaei S, Liu B, Tan YN, Metal-enhancement study of dual functional photosensitizers with aggregation-induced emission and singlet oxygen generation, Nanoscale Adv, 2020, 2, 2859–2869.
[88] Feng G, Wu W, Xu S, Liu B, Far red/near-infrared AIE dots for image-guided photodynamic cancer cell ablation, ACS Appl Mater Interfaces, 2016, 8, 21193–21200.
[89] Gu X, Zhang X, Ma H, Jia S, Zhang P, Zhao Y, Liu Q, Wang J, Zheng X, Lam JWY, Ding D, Tang BZ, Corannulene-incorporated AIE nanodots with highly suppressed nonradiative decay for boosted cancer phototheranostics in vivo, Adv Mater, 2018, 30, 1801065.
[90] Nosaka Y, Nosaka AY, Generation and detection of reactive oxygen species in photocatalysis, Chem Rev, 2017, 117, 11302–11336.
[91] Burns JM, Cooper WJ, Ferry JL, King DW, DiMento BP, McNeill K, Miller CJ, Miller WL, Peake BM, Rusak SA, Rose AL, Waite TD, Methods for reactive oxygen species (ROS) detection in aqueous environments, Aquat Sci, 2012, 74, 683–734.
[92] Schweitzer C, Schmidt R, Physical mechanisms of generation and deactivation of singlet oxygen, Chem Rev, 2003, 103, 1685–1758.
[93] Adam W, Kazakov DV, Kazakov VP, Singlet-oxygen chemiluminescence in peroxide reactions, Chem Rev, 2005, 105, 3371–3387.
[94] Gao R, Mei X, Yan D, Liang R, Wei M, Nano-photosensitizer based on layered double hydroxide and isophthalic acid for singlet oxygenation and photodynamic therapy, Nat Commun, 2018, 9, 2798.
[95] Mikio Y, Syougo T, Ryouji S, Measurement of concentration of singlet molecular oxygen in the gas phase by electron paramagnetic resonance, Chem Lett, 2004, 33, 152–153.
[96] Nakamura K, Ishiyama K, Ikai H, Kanno T, Sasaki K, Niwano Y, Kohno M, Reevaluation of analytical methods for photogenerated singlet oxygen, J Clin Biochem Nutr, 2011, 49, 87–95.
[97] Kim S, Fujitsuka M, Majima T, Photochemistry of singlet oxygen sensor green, J Phys Chem B, 2013, 117, 13985–13992.
[98] Zou F, Zhou W, Guan W, Lu C, Tang BZ, Screening of photosensitizers by chemiluminescence monitoring of formation dynamics of singlet oxygen during photodynamic therapy, Anal Chem, 2016, 88, 9707–9713.
[99] Dalapati R, Nandi S, Van Hecke K, Biswas S, Fluorescence modulation of an aggregation-induced emission active ligand via rigidification in a coordination polymer and its application in singlet oxygen sensing, Cryst Growth Des, 2019, 19, 6388–6397.
[100] Bielski BHJ, Cabelli DE, Arudi RL, Ross AB, Reactivity of HO_2/O^-_2 radicals in aqueous solution, J Phys Chem Ref Data, 1985, 14, 1041–1100.
[101] Hawkins CL, Davies MJ, Detection and characterisation of radicals in biological materials using EPR methodology, Biochim Biophys Acta, 2014, 1840, 708–721.
[102] Zhao H, Joseph J, Zhang H, Karoui H, Kalyanaraman B, Synthesis and biochemical applications of a solid cyclic nitrone spin trap: A relatively superior trap for detecting superoxide anions and glutathiyl radicals, Free Radic Biol Med, 2001, 31, 599–606.
[103] Saita M, Kobayashi K, Yoshino F, Hase H, Nonami T, Kimoto K, Lee M, ESR investigation of ROS generated by H2O2 bleaching with TiO_2 coated HAp, Dent Mater J, 2012, 31(3), 458–464.
[104] Clément J-L, Ferré N, Siri D, Karoui H, Rockenbauer A, Tordo P, Assignment of the EPR spectrum of 5,5-dimethyl-1-pyrroline N-oxide (DMPO) superoxide spin adduct, J Org Chem, 2005, 70, 1198–1203.
[105] Nam JS, Kang M-G, Kang J, Park S-Y, Lee SJC, Kim H-T, Seo JK, Kwon O-H, Lim MH, Rhee H-W, Kwon T-H, Endoplasmic reticulum-localized iridium(III) complexes as efficient photodynamic therapy agents via protein modifications, J Am Chem Soc, 2016, 138, 10968–10977.

[106] Li M, Xia J, Tian R, Wang J, Fan J, Du J, Long S, Song X, Foley JW, Peng X, Near-infrared light-initiated molecular superoxide radical generator: Rejuvenating photodynamic therapy against hypoxic tumors, J Am Chem Soc, 2018, 140, 14851–14859.
[107] Misak A, Brezova V, Grman M, Tomasova L, Chovanec M, Ondrias K, •BMPO-OOH spin-adduct as a model for study of decomposition of organic hydroperoxides and the effects of sulfide/selenite derivatives. An EPR spin-trapping approach, Antioxidants, 2020, 9, 918.
[108] Tomizawa S, Imai H, Tsukada S, Simizu T, Honda F, Nakamura M, Nagano T, Urano Y, Matsuoka Y, Fukasaku N, Saito N, The detection and quantification of highly reactive oxygen species using the novel HPF fluorescence probe in a rat model of focal cerebral ischemia, Neurosci Res, 2005, 53, 304–313.
[109] Zhuang M, Ding C, Zhu A, Tian Y, Ratiometric fluorescence probe for monitoring hydroxyl radical in live cells based on gold nanoclusters, Anal Chem, 2014, 86, 1829–1836.
[110] Schoonen MAA, Harrington AD, Laffers R, Strongin DR, Role of hydrogen peroxide and hydroxyl radical in pyrite oxidation by molecular oxygen, Geochim Cosmochim Acta, 2010, 74, 4971–4987.
[111] Cohn CA, Simon SR, Schoonen MAA, Comparison of fluorescence-based techniques for the quantification of particle-induced hydroxyl radicals, Part Fibre Toxicol, 2008, 5, 2.
[112] Naito K, Tachikawa T, Fujitsuka M, Majima T, Real-time single-molecule imaging of the spatial and temporal distribution of reactive oxygen species with fluorescent probes: Applications to TiO_2 photocatalysts, J Phys Chem C, 2008, 112, 1048–1059.
[113] Ma H, Wallis LK, Diamond S, Li S, Canas-Carrell J, Parra A, Impact of solar UV radiation on toxicity of ZnO nanoparticles through photocatalytic reactive oxygen species (ROS) generation and photo-induced dissolution, Environ Pollut, 2014, 193, 165–172.
[114] Setsukinai K-I, Urano Y, Kakinuma K, Majima HJ, Nagano T, Development of novel fluorescence probes that can reliably detect reactive oxygen species and distinguish specific species * 210, J Biol Chem, 2003, 278, 3170–3175.
[115] Heyne B, Maurel V, Scaiano JC, Mechanism of action of sensors for reactive oxygen species based on fluorescein–phenol coupling: The case of 2-[6-(4′-hydroxy)phenoxy-3H-xanthen-3-on-9-yl]benzoic acid, Org Biomol Chem, 2006, 4, 802–807.
[116] Petasne RG, Zika RG, Hydrogen peroxide lifetimes in south Florida coastal and offshore waters, Mar Chem, 1997, 56, 215–225.
[117] Moffett JW, Zajiriou OC, An investigation of hydrogen peroxide chemistry in surface waters of Vineyard Sound with $H_2{}^{18}O_2$ and $^{18}O_2$, Limnol Oceanogr, 1990, 35, 1221–1229.
[118] Diesen V, Jonsson M, Formation of H_2O_2 in TiO_2 photocatalysis of oxygenated and deoxygenated aqueous systems: A probe for photocatalytically produced hydroxyl radicals, J Phys Chem C, 2014, 118, 10083–10087.
[119] Hirakawa T, Koga C, Negishi N, Takeuchi K, Matsuzawa S, An approach to elucidating photocatalytic reaction mechanisms by monitoring dissolved oxygen: Effect of H_2O_2 on photocatalysis, Appl Catal B, 2009, 87, 46–55.
[120] Lippert AR, Van de Bittner GC, Chang CJ, Boronate oxidation as a bioorthogonal reaction approach for studying the chemistry of hydrogen peroxide in living systems, Acc Chem Res, 2011, 44, 793–804.
[121] Fu X, Tang Y, Dickinson BC, Chang CJ, Chang Z, An oxidative fluctuation hypothesis of aging generated by imaging H_2O_2 levels in live Caenorhabditis elegans with altered lifespans, Biochem Biophys Res Commun, 2015, 458, 896–900.
[122] Wu Q, Li Y, Li Y, Wang D, Tang BZ, Hydrogen peroxide-responsive AIE probe for imaging-guided organelle targeting and photodynamic cancer cell ablation, Mater Chem Front, 2021, 5, 3489–3496.

[123] Liu Y, Nie J, Niu J, Meng F, Lin W, Ratiometric fluorescent probe with AIE property for monitoring endogenous hydrogen peroxide in macrophages and cancer cells, Sci Rep, 2017, 7, 7293.
[124] Leung ACS, Zhao E, Kwok RTK, Lam JWY, Leung CWT, Deng H, Tang BZ, An AIE-based bioprobe for differentiating the early and late stages of apoptosis mediated by H_2O_2, J Mater Chem B, 2016, 4, 5510–5514.
[125] Yuan Y, Feng G, Qin W, Tang BZ, Liu B, Targeted and image-guided photodynamic cancer therapy based on organic nanoparticles with aggregation-induced emission characteristics, Cheml Commun, 2014, 50, 8757–8760.
[126] Zheng Z, Zhang T, Liu H, Chen Y, Kwok RTK, Ma C, Zhang P, Sung HHY, Williams ID, Lam JWY, Wong KS, Tang BZ, Bright near-infrared aggregation-induced emission luminogens with strong two-photon absorption, excellent organelle specificity, and efficient photodynamic therapy potential, ACS Nano, 2018, 12, 8145–8159.
[127] Wang DH, Chen LJ, Zhao X, Yan XP, Enhancing near-infrared AIE of photosensitizer with twisted intramolecular charge transfer characteristics via rotor effect for AIE imaging-guided photodynamic ablation of cancer cells, Talanta, 2021, 225, 122046.
[128] Xu W, Zhang Z, Kang M, Guo H, Li Y, Wen H, Lee MMS, Wang Z, Kwok RTK, Lam JWY, Li K, Xi L, Chen S, Wang D, Tang BZ, Making the best use of excited-state energy: Multimodality theranostic systems based on second near-infrared (NIR-II) aggregation-induced emission luminogens (AIEgens), ACS Mater Lett, 2020, 2, 1033–1040.
[129] Kamkaew A, Lim SH, Lee HB, Kiew LV, Chung LY, Burgess K, BODIPY dyes in photodynamic therapy, Chem Soc Rev, 2013, 42, 77–88.
[130] Yogo T, Urano Y, Ishitsuka Y, Maniwa F, Nagano T, Highly efficient and photostable photosensitizer based on bodipy chromophore, J Am Chem Soc, 2005, 127, 12162–12163.
[131] Nguyen VN, Yim Y, Kim S, Ryu B, Swamy KMK, Kim G, Kwon N, Kim CY, Park S, Yoon J, Molecular design of highly efficient heavy-atom-free triplet bodipy derivatives for photodynamic therapy and bioimaging, Angew Chem Int Ed, 2020, 59, 8957–8962.
[132] Yang M, Deng J, Su H, Gu S, Zhang J, Zhong A, Wu F, Small organic molecule-based nanoparticles with red/near-infrared aggregation-induced emission for bioimaging and PDT/PTT synergistic therapy, Mater Chem Front, 2021, 5, 406–417.
[133] Zhao E, Deng H, Chen S, Hong Y, Leung CW, Lam JW, Tang BZ, A dual functional AEE fluorogen as a mitochondrial-specific bioprobe and an effective photosensitizer for photodynamic therapy, Chem Commun, 2014, 50, 14451–14454.
[134] Kang M, Zhou C, Wu S, Yu B, Zhang Z, Song N, Lee MMS, Xu W, Xu FJ, Wang D, Wang L, Tang BZ, Evaluation of structure-function relationships of aggregation-induced emission luminogens for simultaneous dual applications of specific discrimination and efficient photodynamic killing of gram-positive bacteria, J Am Chem Soc, 2019, 141, 16781–16789.
[135] Chen Y, Ai W, Guo X, Li Y, Ma Y, Chen L, Zhang H, Wang T, Zhang X, Wang Z, Mitochondria-targeted polydopamine nanocomposite with AIE photosensitizer for image-guided photodynamic and photothermal tumor ablation, Small, 2019, 15, e1902352.
[136] Chang CC, Hsieh MC, Lin JC, Chang TC, Selective photodynamic therapy based on aggregation-induced emission enhancement of fluorescent organic nanoparticles, Biomaterials, 2012, 33, 897–906.
[137] Sun X, Zebibula A, Dong X, Li G, Zhang G, Zhang D, Qian J, He S, Targeted and imaging-guided in vivo photodynamic therapy for tumors using dual-function, aggregation-induced emission nanoparticles, Nano Res, 2018, 11, 2756–2770.
[138] Li M, Gao Y, Yuan Y, Wu Y, Song Z, Tang BZ, Liu B, Zheng QC, One-step formulation of targeted aggregation-induced emission dots for image-guided photodynamic therapy of cholangiocarcinoma, ACS Nano, 2017, 11, 3922–3932.

[139] Lovell JF, Liu TWB, Chen J, Zheng G, Activatable photosensitizers for imaging and therapy, Chem Rev, 2010, 110, 2839–2857.
[140] Yuan Y, Zhang CJ, Gao M, Zhang R, Tang BZ, Liu B, Specific light-up bioprobe with aggregation-induced emission and activatable photoactivity for the targeted and image-guided photodynamic ablation of cancer cells, Angew Chem Int Ed, 2015, 54, 1780–1786.
[141] Ward MD, Photo-induced electron and energy transfer in non-covalently bonded supramolecular assemblies, Chem Soc Rev, 1997, 26, 365–375.
[142] Hu F, Yuan Y, Mao D, Wu W, Liu B, Smart activatable and traceable dual-prodrug for image-guided combination photodynamic and chemo-therapy, Biomaterials, 2017, 144, 53–59.
[143] Traverso N, Ricciarelli R, Nitti M, Marengo B, Furfaro AL, Pronzato MA, Marinari UM, Domenicotti C, Role of glutathione in cancer progression and chemoresistance, Oxid Med Cell Longev, 2013, 972913.
[144] Zhang YH, Li X, Huang L, Kim HS, An J, Lan M, Cao QY, Kim JS, AIE based GSH activatable photosensitizer for imaging-guided photodynamic therapy, Chem Commun, 2020, 56, 10317–10320.
[145] Shao L, Pan Y, Hua B, Xu S, Yu G, Wang M, Liu B, Huang F, Constructing adaptive photosensitizers via supramolecular modification based on pillararene host-guest interactions, Angew Chem Int Ed, 2020, 59, 11779–11783.
[146] Gao F, Wu J, Gao H, Hu X, Liu L, Midgley AC, Liu Q, Sun Z, Liu Y, Ding D, Wang Y, Kong D, Huang X, Hypoxia-tropic nanozymes as oxygen generators for tumor-favoring theranostics, Biomaterials, 2020, 230, 119635.
[147] Shi L, Hu F, Duan Y, Wu W, Dong J, Meng X, Zhu X, Liu B, Hybrid nanospheres to overcome hypoxia and intrinsic oxidative resistance for enhanced photodynamic therapy, ACS Nano, 2020, 14, 2183–2190.
[148] Chen K, He P, Wang Z, Tang BZ, A feasible strategy of fabricating type I photosensitizer for photodynamic therapy in cancer cells and pathogens, ACS Nano, 2021, 15, 7735–7743.

Shunjie Liu, Ben Zhong Tang

Chapter 18
AIEgens for photothermal theranostics

18.1 Introduction

Photothermal therapy (PTT) is a novel therapy that converts light energy into heat to cause thermal ablation and the subsequent death of cancer cells [1–7]. PTT can precisely control the area, time, and efficacy of treatment by changing the irradiation site, duration, and power. The resultant photothermy can also be used as photoacoustic (PA) imaging (PAI) by detecting the generated ultrasound signal, surpassing the optical diffusion limit, and permits disease diagnosis in deeper tissues with higher spatial resolution. By PAI-guided cancer diagnosis, it is easy to adjust the treatment strategy in a timely manner according to the clinical needs. Therefore, exploring suitable PTT agents that can efficiently convert light energy into photothermy is of vital importance to promote further development in this field.

Compared to inorganic PTT agents, organic counterparts are promising candidates due to their excellent biocompatibility, easily tunable band gap, and accessible structural–property relationship [8–13]. To realize strong absorption in near-infrared (NIR) region, these organic materials normally possess large π-conjugated system with planar architecture. In the biologically favorable aggregated state (nanoparticles, NPs), the molecules display predominant nonradiative decay to produce heat, owing to the strong intermolecular π–π interactions. However, in most cases, the photothermal conversion efficiency (PCE) of these materials based on the mechanism of intermolecular π–π interactions remains low. Therefore, it is urgent to develop new photothermal mechanism to enhance the PTT efficiency and PA quality.

In 2001, Tang and coworkers coined the concept of aggregation-induced emission (AIE) [14–23]. In the AIE process, the fluorophores are nonfluorescent in the solution state owing to the active intramolecular motion, while they emit strongly when in the aggregated state due to the mechanism of restriction of intramolecular motion. From this concept, it is clear that the active intramolecular motion in the solution state can transform the photonic energy into thermal energy through the nonradiative relaxation of the excitons. Therefore, if we can achieve active intramolecular motion in the aggregated state to boost the nonradiative decay, enhanced PCE may be

Shunjie Liu, Key Laboratory of Polymer Ecomaterials, Changchun Institute of Applied Chemistry, Chinese Academy of Sciences, Changchun 130022; School of Applied Chemistry and Engineering, University of Science and Technology of China, Hefei 230026, e-mail: sjliu@ciac.ac.cn
Ben Zhong Tang, Shenzhen Institute of Aggregate Science and Technology, School of Science and Engineering, The Chinese University of Hong Kong, Shenzhen, Guangdong 518172, China, e-mail: tangbenz@cuhk.edu.cn

https://doi.org/10.1515/9783110673074-019

achieved. In this chapter, we summarize the recent progresses in designing highly efficient photothermal agents using AIE technologies. We hope that this chapter may inspire new principles to design advanced photothermal theranostic agents.

18.2 Molecular design of AIEgens

To design ideal AIE luminogens (AIEgens) as PTT and PA agents is a principle for molecules with low bandgaps and high PCE. According to Jablonski diagram, organic molecules absorb light energy, then transit into higher energy state (S1), followed by reverting to lower energy state (S0) through radiative (R) and nonradiative decay (NR) (Figure 18.1a) [22]. R refers to the formation of fluorescence, which has been applied as biosensing and bioimaging. NR is always accompanied by heat generation, which can be used as PAI and photothermal imaging (PTI) and PTT. However, R and NR are competitive in energy dissipation manner. To design AIEgens with high PCE, it is better to suppress R and activate NR to transform more S1 energy into heat. So how can we control this process.

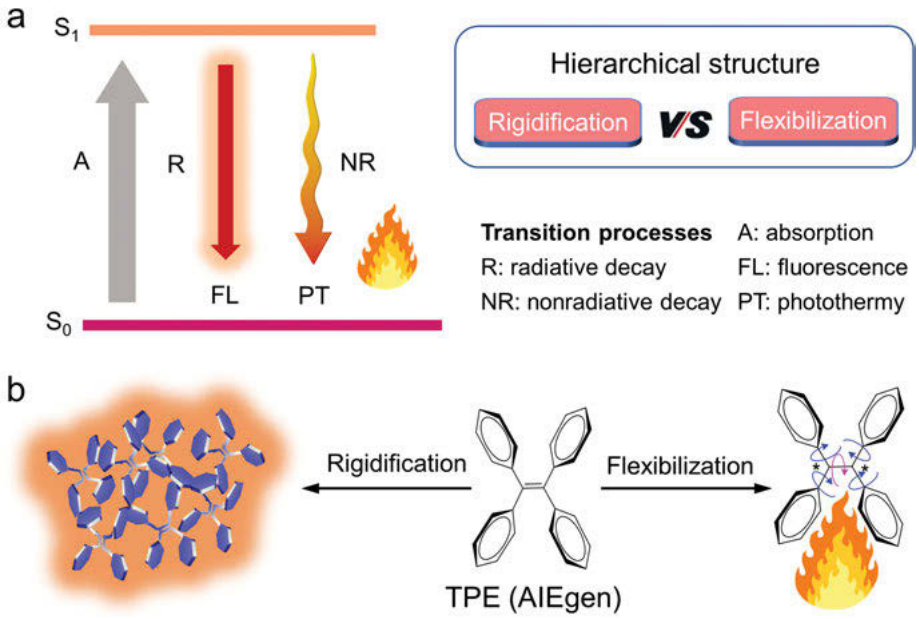

Figure 18.1: (a) Jablonski diagram. (b) Working mechanism of AIEgens. Data adapted with permission [22].

The physical energy dissipation pathway of AIEgens depends greatly on intramolecular motions, which is affected by the structure of the molecules. As shown in Figure 18.1b, AIEgens exhibited strong fluorescence through R in aggregation or rigidification state, due to the restriction of the intramolecular motions. On the contrary, AIEgens are almost nonemissive at molecular level or flexible state, owing to the dominated NR by activation of intramolecular motions. At this time, it is often accompanied by heat generation. Thus, activation of molecular motion in aggregation state is the principal strategy to design AIE-active PTT agents with high PCE.

A strategy called intramolecular motion-induced photothermy was proposed by Tang et al. to enhance PCE inside NPs [24]. As shown in Figure 18.2a-b, to provide enough space for AIEgens, keeping motion in NPs, the author integrated long alkyl chains into the structure of AIEgens. The steric hindrance of alkyl chains hampers the AIEgen forming tight stacking, consequently the molecular vibrations and rotations boosting the NR and enhancing the PCE. The temperature was higher in 2TPE-2NDTA than that of 2TPE-NDTA, and the photothermal conversion is much weaker in AIEgens that are absent in the long alkyl chains (Figure 18.2c,d). It is worth to note that the NPs remained disordered amorphous form with loose packing mode encapsulated by flexible amphiphilic polymers. The author contributes a novel platform for designing advanced PTT/PAI nanoagents.

In another work, Tang et al. proposed "molecular motion in aggregate" strategy to increase PCE, utilizing the advantages of dark twisted intramolecular charge transfer (TICT) and reversed AIE into one system [25]. The sensitivity of TICT is beneficial for producing NR processes; thus enhanced TICT character could increase heat generation (Figure 18.3a). It is worth to note that active molecular rotations are the prerequisites to form TICT state. To realize this project and lower intermolecular interaction, the central D-A core was grafted with molecular rotors and bulky alkyl chains (Figure 18.3b). The enhanced molecular motion favors the formation of a dark TICT state, whose NR will enhance the photothermal properties (Figure 18.3c). Result shows that small-molecule NIRb14 with long alkyl chains branched at the second carbon exhibits enhanced photothermal properties compared with NIRb6, with short branched chains, and much higher than NIR6, with short linear chains (Figure 18.3d).

Except involving long-branched alkyl chains and/or bulky substituents to support molecular motion in aggregate, some other strategies were also proposed to increase molecular motion in aggregate. Li et al. put forward photoinduced nonadiabatic decay by adopting molecular motor with a double bond motif to develop high PCE agents [26]. As the double bond is twisted by strong TICT upon irradiation, the excited agents can deactivate nonradiatively through the conical intersection (CI) of internal conversion (Figure 18.4a, b). The prepared C6T1 NPs showed higher temperature than commercial PTT agent Indocyanine Green (ICG) (Figure 18.4c). Tang et al. also reported a mechanism to increase PCE through a bond stretching vibration-

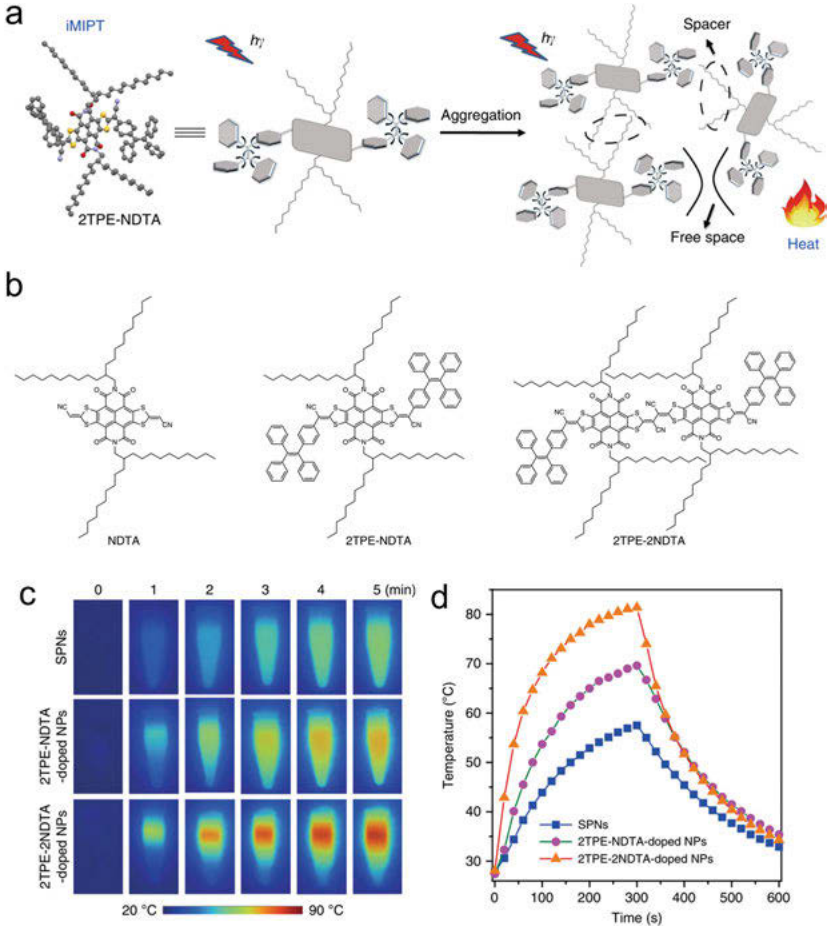

Figure 18.2: (a) Representative working mechanisms of intramolecular motion-induced photothermy for PTT/PA imaging. (b) Molecular structures of NDTA, 2TPE-NDTA, and 2TPE-2NDTA. (c) IR thermal images of various NPs in aqueous solution upon exposure to 808 nm (0.8 W cm^{-2}) laser irradiation for different times. (d) The temperature changes of solutions of various NPs as a function of time. Data adapted with permission from [24].

induced photothermy method (Figure 18.4d, e) [27]. The molecular motion was highly boosted by introducing a pyrazine-based unit into the molecule structure. At the same time, the enhanced vibration is activated by the additional phenyl ring, which promotes extra intramolecular rotation. As shown in Figure 18.4f, the DCP-PTPA NPs perform better than DCP-TPA NPs in terms of photothermal conversion (Figure 18.4f).

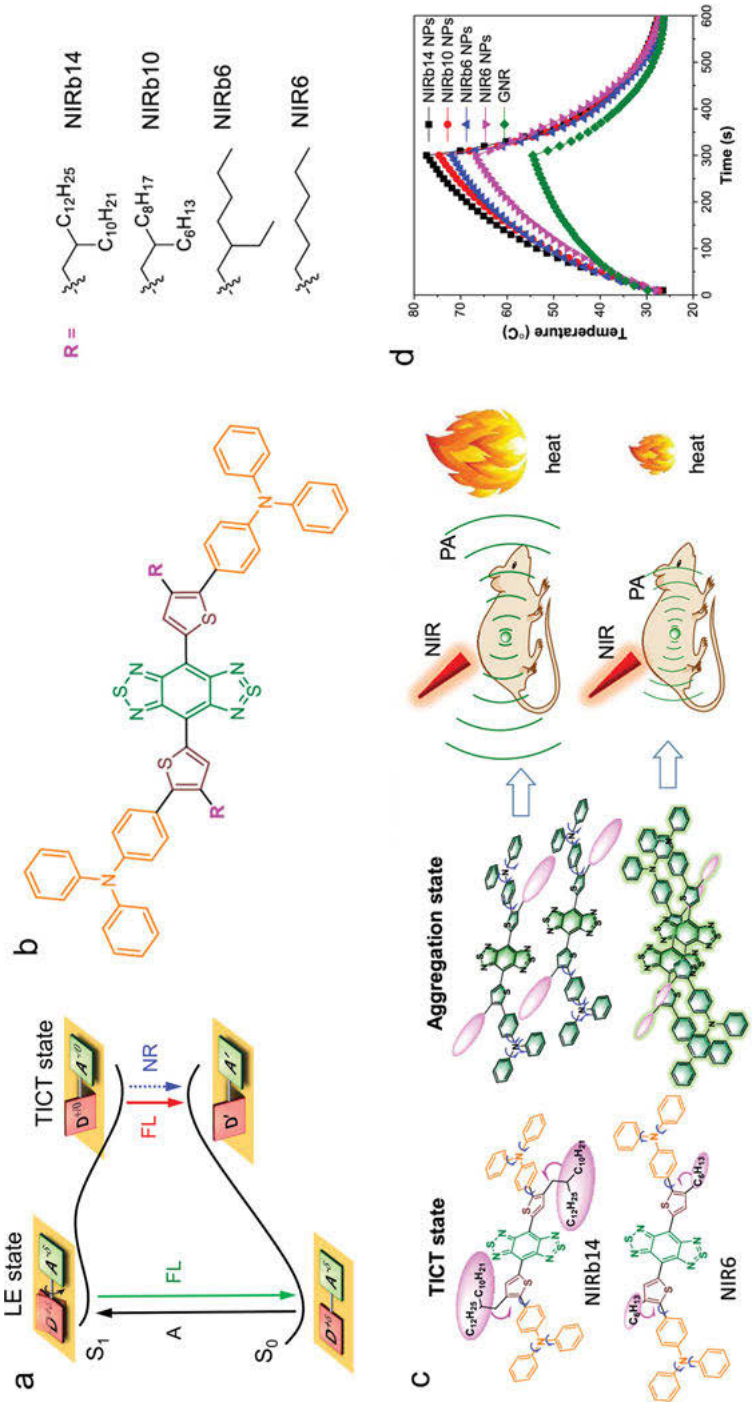

Figure 18.3: (a) Jablonski diagram illustrating the difference between AIE and TICT states. (b) Chemical structure of molecules. (c) Schematic illustration of the TICT state in solution and aggregation state. (d) The temperature changes of solutions of various NPs as a function of time. Data adapted with permission from [25].

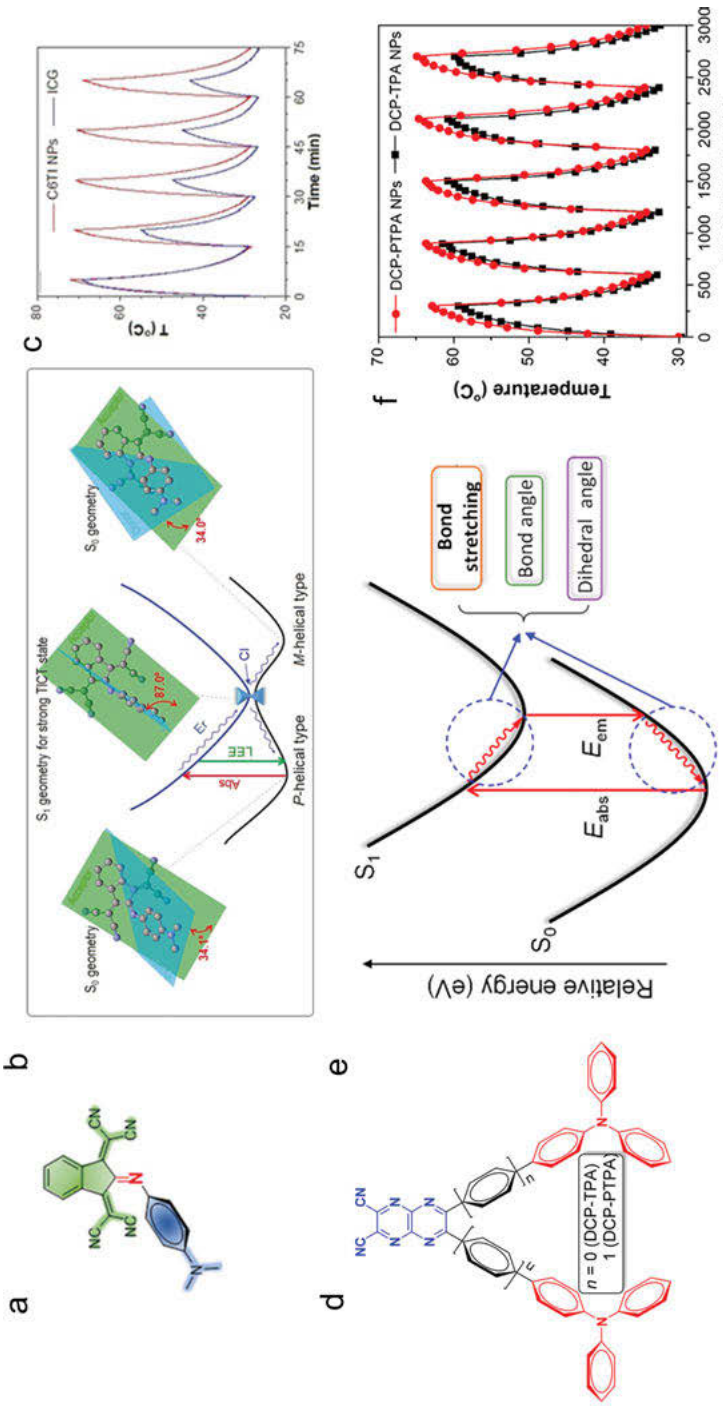

Figure 18.4: (a) Molecular structure of C1T1. (b) A proposed model of photoinduced excited-state nonadiabatic process for C1TI molecule. (c) Temperature changes of C6TI NPs and ICG (100 mg mL^{-1}) over five laser on/off cycles under 808 nm irradiation (1 W cm^{-2}). (d) Structures of DCP-TPA and DCPPTPA. (e) Schematic illustration of motion models of DCP-TPA and DCP-PTPA in the excited state. (f) Five cycles of heating–cooling process indicate the photothermal conversion stability of two NPs. Data adapted with permission from [26, 27].

18.3 Bioapplications of AIEgens in PTT theranostics

AIEgens have been widely used as efficient imaging agents for accurately guiding the PTT process due to their outstanding luminescent performance in aggregates. At the same time, the produced heat caused thermoelastic expansion, generating ultrasound waves, which can be used for PAI.

Lu et al. [28] discovered that the NIR-II (the second NIR emission window, 1,000–1,500 nm) fluorophore BPBBT with AIE + TICT property can bind to human serum albumin in high affinity through hydrogen bonds and Van der Waals interactions (Figure 18.5a–c). The specific binding prevents the intramolecular rotation and changes the planarity of the fluorophore. The temperature change and PL intensity can be tuned by the HAS/BPBBT ratio, which is applicable to intraoperative NIR-II fluorescence image-guided cancer PTT (Figure 18.5d).

Emission in the NIR wavelength takes advantage of simultaneously suppressed tissue absorption, scattering, and background interference. This results in significant improvements in image sensitivity, spatiotemporal resolution, penetration, and signal-to-noise ratio (SNR). Meanwhile, because acoustic scattering in biological tissues is substantially lower than optical scattering, NIR PAI will have a deeper penetration depth than fluorescence imaging. Liu et al. contributed TB1, an NIR-II emissive AIE molecule shown in (Figure 18.6a,b), and the formulated TB1 dots exhibited high absorptivity at 740 nm and fluorescence quantum yield of 6.2%. Thus, it is suitable for NIR-I PA imaging and NIR-II fluorescence. By decorating the TB1 dots with cRGD peptide, the TB1 dots can target the brain tumor with high signal-to-background ratio and penetration [29]. Compared with NIR-I PAI, NIR-II PAI performed better due to reduced scattering and absorption of biological tissue in this region. Thus, it is desirable to implement PAI by one NP and NIR-II fluorescence. Liu et al. constructed poly(benzodithiophene(BDT)-alt-thiadiazolobenzotriazole (TBZ)) (PBT), and the PBT NPs exhibited PA spectrum from 750 to 1,064 nm and a significant tail extended beyond 1,650 nm, with an emission peak at 1,156 nm (Figure 18.6c-d), which can be applied for NIR-II FLI and PAI at the same time [30]. The NIR-II fluorescence wide-field microscopy imaging of the brain was performed after intravenous injection of PBT NPs, and the tiny blood capillary with an apparent width of 7.1 μm was recorded. A small vessel with a diameter of even 2.2 μm was resolved with an SNR of 24.8, indicating that NIR-II fluorescence imaging had good spatial resolution (Figure 18.6e). The author uses focused ultrasound paired with microbubbles to breach the blood–brain barrier (BBB) in a safe and transitory manner, allowing NPs to diffuse from the bloodstream into the tumor location of the brain. The NIR-II PAI can detect deep microscopic brain cancers less than 2 mm at a depth of 2.4 mm underneath the dense skull and scalp (Figure 18.6f).

Through accurate diagnosis of FLI and/or PAI, the cure rate of disease can be greatly improved by using PTT. The integration of both imaging and PTT functionalities inside a single AIEgen-based nanosystem represents a straightforward and

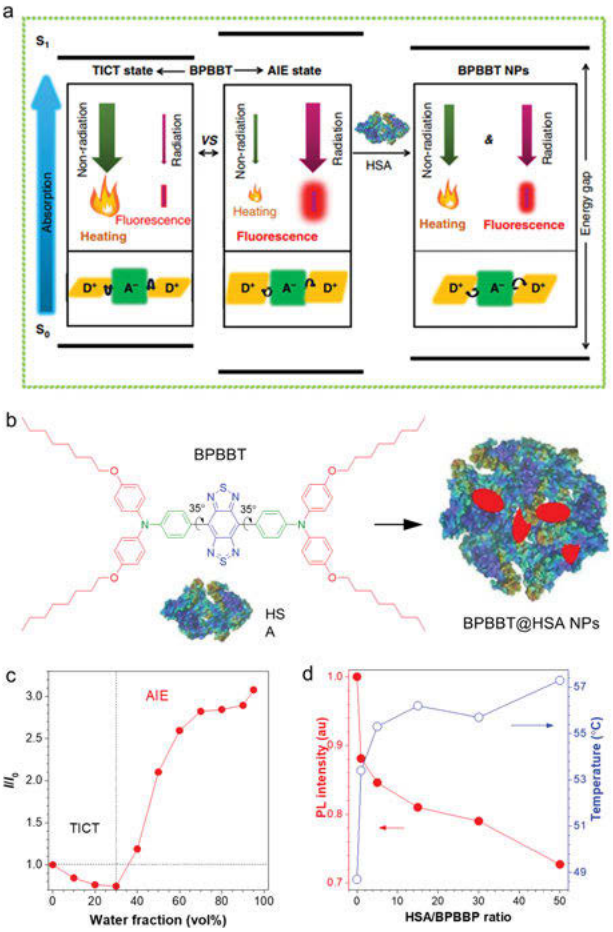

Figure 18.5: (a) Diagrammatic description of TICT and AIE states of BPBBT tailored by HAS. (b) The molecular structure of BPBBT and the assembled nanoparticle. (c) The plot of BPBBT versus water fraction in H_2O/THF mixtures. (d) The plot of I/I_0 (red curve) and temperature (blue curve) of BPBBT in THF:water (5%, v/v) versus human serum albumin/BPBBT ratio. Data adapted with permission from [28].

repeatable construction technique when compared to typical imaging-guided PTT nanoplatforms, which need multiple theranostic components. A lot of works have been reported that the tumor has been suppressed or eliminated after treatment with PTT. Recently, Tang and Cai have produced NK@AIEdots, which are natural killer cell mimic nanorobots with AIE features, by coating a natural kill cell membrane over an NIR-II AIE-active conjugated polymer (PTPTV) (Figure 18.7a, b) [31]. To undertake immune surveillance in the brain for tumor targeting, natural killer cells can penetrate the BBB by employing particular membrane proteins as tight junction modulators. The findings revealed that the NK@AIEdots can concentrate

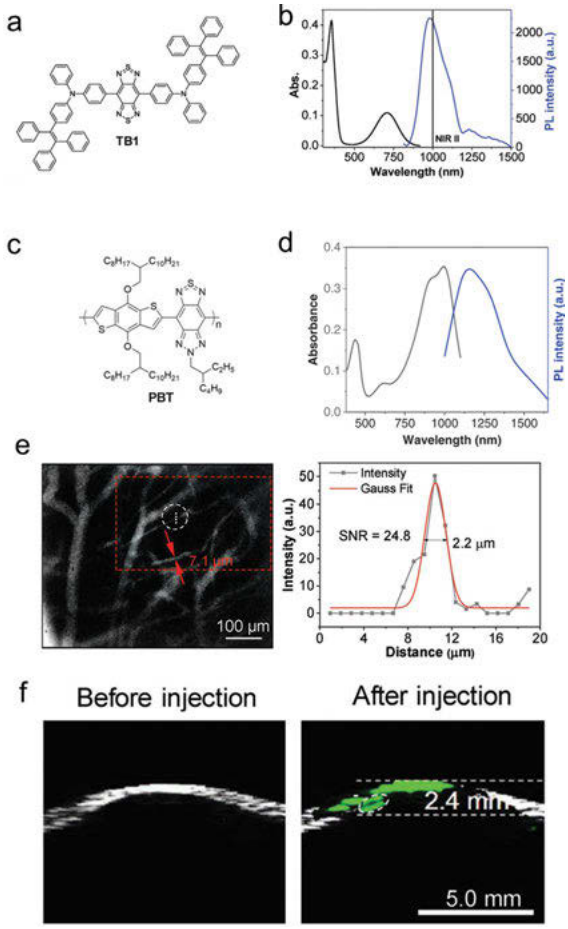

Figure 18.6: (a) The chemical structure of TB1 and (b) UV-vis and photoluminescence (PL) spectra of TB1 NP suspension in water. (c) The chemical structure of PBT and (d) UV-vis and photoluminescence (PL) spectra of PBT NP suspension in water. (e) A selected microscopic image of brain vasculature and the cross-sectional fluorescence intensity profile (black color) and the Gaussian fit profile (red color) along the white-dashed line inside the white-dashed circle. (f) B-scan PA imaging results of microscopic brain tumor before and after dual PBT NPs treatment and focused ultrasound combined with intravenous microbubbles injection. Data adapted with permission from [29].

spontaneously in glioblastoma cells in the complex brain matrix, allowing for high contrast and through-skull tumor imaging (Figure 18.7c). Under NIR light illumination, these NK@AIEdots also significantly slowed tumor development (Figure 18.7d).

Single-mode therapy is insufficient for treating intractable cancers in the clinic. Phototherapy in combination with other therapeutic treatments is a superior option

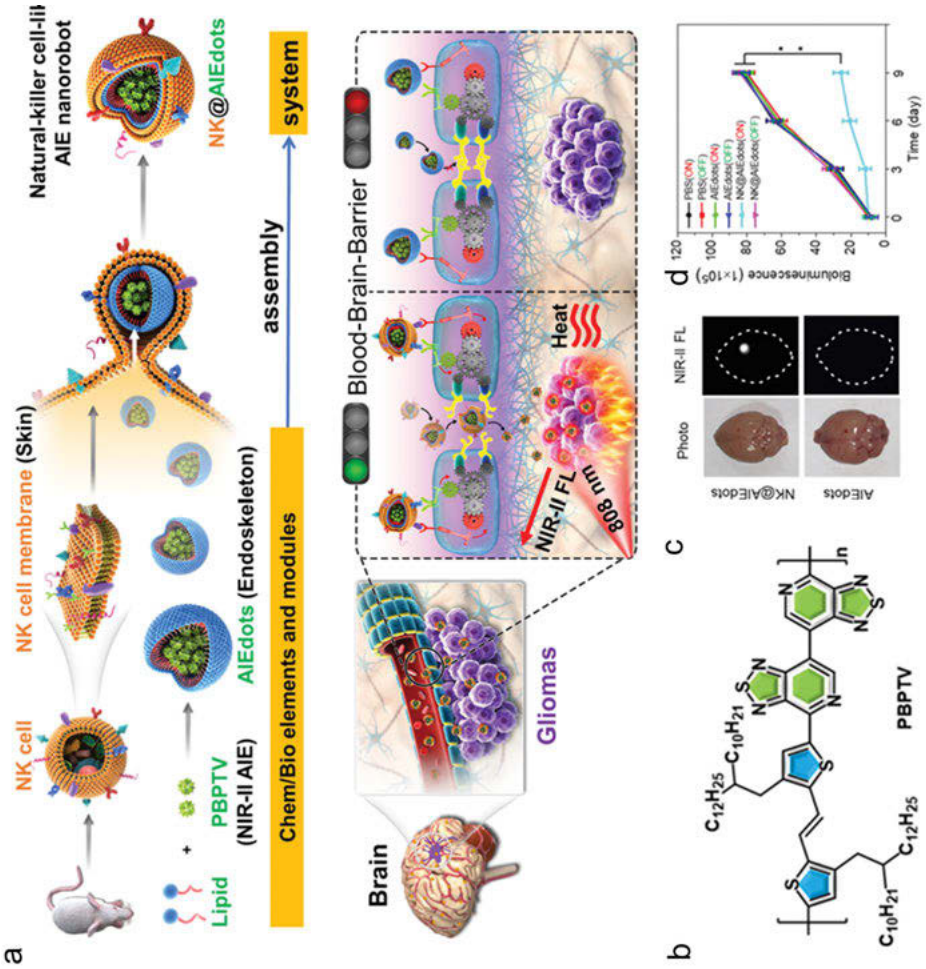

Figure 18.7: (a) Schematic illustration to show the preparation and assembly process of NK-cell-mimic AIE NPs and the "smart" tight-junction (TJ)-modulated blood–brain barrier (BBB) penetration of NK@AIEdots for brain tumor-targeted light up and inhibition. (b) Molecular structure of PBPTV. (c) In vitro NIR-II fluorescence imaging results of excised mouse brain without scalp and skull (bottom) under 808 nm illumination. (d) Quantitative analysis of in vivo bioluminescence signals at different time points in the tumor site. Data adapted with permission from [31].

for tumor treatment. Because of the lowered electronic bandgaps and promoted intersystem crossing process, AIE molecules are always equipped with a strong electron donor–acceptor (D-A) unit, which can significantly contribute to bathochromic absorption/emission and ROS formation. Thus, AIEgens can be used for imaging guided-synergetic therapy of tumor. For example, Tang's group designed TSSI (molecular structure shown in Figure 18.8b) with D-A strength and intramolecular

motion in aggregate state [32]. Upon NIR irradiation, the AIE fluorophore-based NPs emit strong NIR-II fluorescence, efficiently generate reactive oxygen species, and have a high PCE, demonstrating the realization of a balance between radiative and nonradiative energy dissipations (Figure 18.8a, b). The resultant NPs afford all phototheranostic modalities, including NIR-II FLI, PAI, PTI, PTT and PDT. Finally, the tumor was eliminated (Figure 18.8c–f).

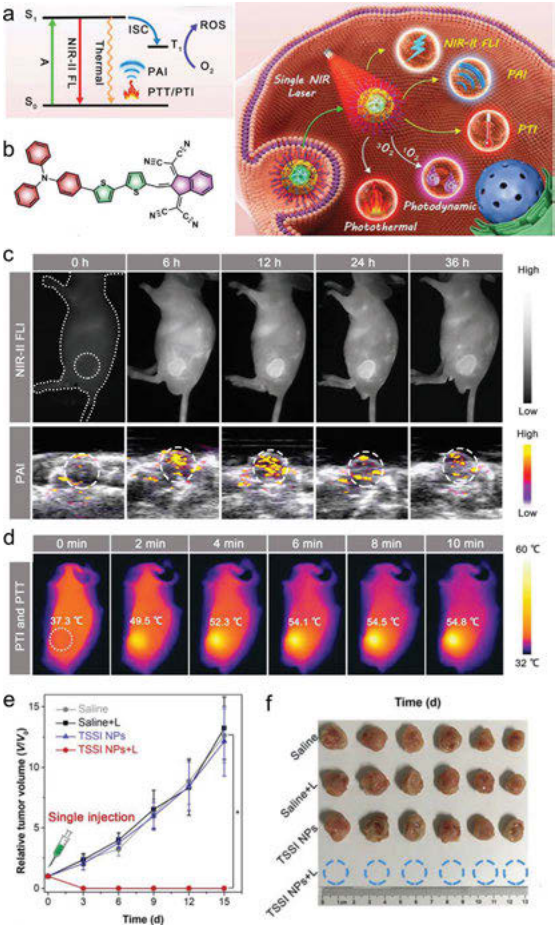

Figure 18.8: (a) Illustration of the reconciled photophysical processes and application of TSSI NPs on NIR-II FLI-PAI-PTI trimodal imaging-guided PDT–PTT synergistic cancer therapy. (b) The chemical structure of TSSI. (c) NIR-II FL images (upper row) and PA images of tumor tissues (lower row) at different monitoring times after administration of TSSI NPs. (d) Thermal images and heating temperatures (at tumor sites) of tumor-bearing mice during continuous NIR irradiation at 12 h postinjection of TSSI NPs. (e) Time-dependent tumor growth curves of tumor-bearing mice with various treatments ($n = 6$, $^*p < 0.001$). (f) Photos of the tumors harvested at day 15 after different treatments. Data adapted with permission from [32].

Sun's group also developed an AIE-based NIR-II phototheranostic agent, ZSY-TPE (Figure 18.9a), which not only inhibits tumor growth but also serves as a phototheranostic agent for bacterial infections [33]. After being intravenously injected with the ZSY-TPE dots, the NIR-II fluorescence images of the *S. aureus*-infected mice displayed significant signals corresponding to the infected areas (Figure 18.9b). The diseased skin of the mice in the ZSY-TPE dots and laser-treated group (808 nm, 10 mW cm^{-2}) gradually healed and returned to normal after 5 days of treatment, but the wounds of the mice in the control groups remained severe and even became purulent (Figure 18.9c,d).

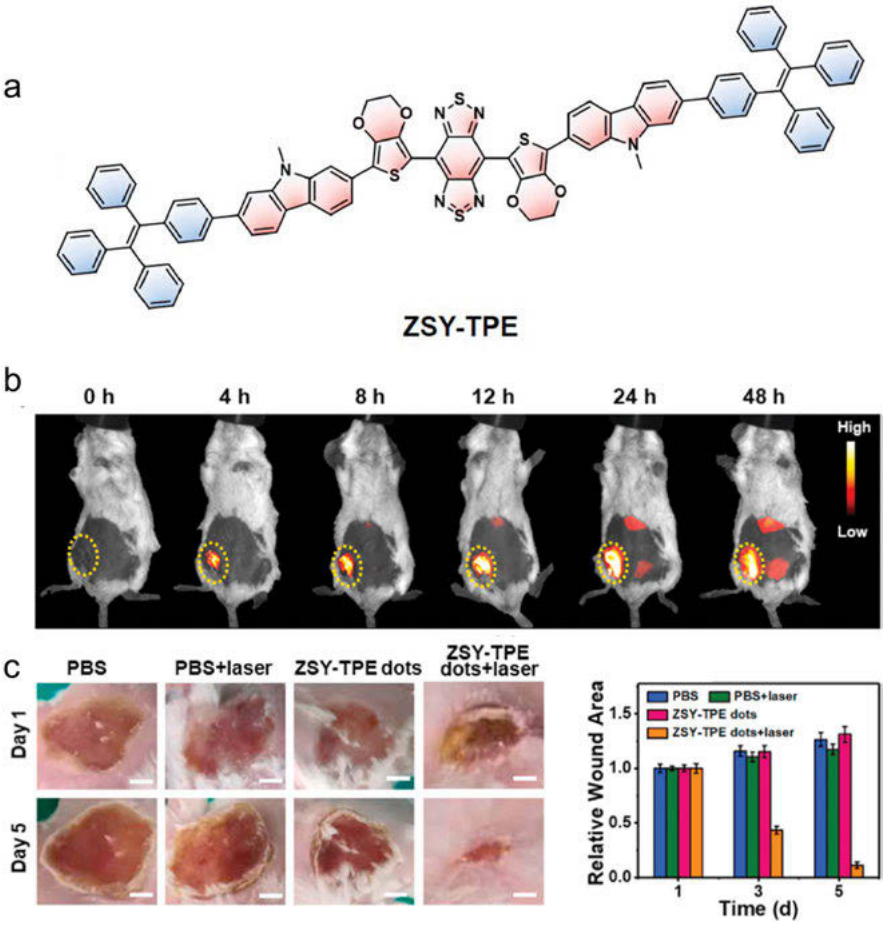

Figure 18.9: (a) The chemical structure of ZSY-TPE. (b) NIR-II fluorescence imaging (808 nm, 10 mW cm^{-2}, 1,000 LP and 50 ms) of *S. aureus*-infected mouse after tail vein injection of ZSY-TPE dots (0.2 mM, 150 μL). The yellow dotted circles indicate an abdominal subcutaneous infection area. (c) Photographs of *S. aureus*-infected wounds after different treatments; scale bar: 10 mm. (d) Changes in relative wound area with time (on days 1, 3, and 5) ($n = 3$). Data adapted with permission [33].

18.4 Current challenge and future perspectives

Despite AIE technology displays great potential in biological theranostics, several issues should be addressed for the future development. First, the overall PCE value can be further increased through other channels in addition to intramolecular motions. Second, the absorption wavelength should be further redshifted to the NIR-II region (>1,000 nm) to enhance the light penetration depth. Third, developing NIR-II theranostics agents with functional groups to target specific site or response to external stimuli are also important. Last but not least, exploring NIR-II theranostics agents with renal metabolism is of crucial importance for clinical applications.

18.5 Conclusion

In summary, a new concept of "active excited state intramolecular motion in the aggregates" based on AIE technology was proposed to enhance the photothermal properties for PTT and PA imaging of tumors in mice. The key elements in molecular design lies in introduction of specific groups such as molecular rotors, vibrators, molecular machines, and long-branched alkyl chains, to enable the intermolecular spatial isolation of dyes in the aggregated state to provide necessary rooms to promote intramolecular motions. The increased intramolecular motion in the aggregated state will then enhance the nonradiative decay to boost the photothermal properties, which provides a strategy for exploring advanced PTT or PA imaging agents with a working principle distinct from the current ones based on intermolecular π–π interactions.

References

[1] Braslavsky SE, Heibel GE, Time-resolved photothermal and photoacoustic methods applied to photoinduced processes in solution, Chem Rev, 1992, 92(6), 1381–1410.
[2] Kim C, Favazza C, Wang LV, In vivo photoacoustic tomography of chemicals: High-resolution functional and molecular optical imaging at new depths, Chem Rev, 2010, 110(5), 2756–2782.
[3] Weber J, Beard PC, Bohndiek SE, Contrast agents for molecular photoacoustic imaging, Nat Methods, 2016, 13, 639.
[4] Melancon MP, Zhou M, Li C, Cancer theranostics with near-infrared light-activatable multimodal nanoparticles, Acc Chem Res, 2011, 44(10), 947–956.
[5] Jokerst JV, Gambhir SS, Molecular imaging with theranostic nanoparticles, Acc Chem Res, 2011, 44(10), 1050–1060.
[6] Cheng L, Wang C, Feng L, Yang K, Liu Z, Functional nanomaterials for phototherapies of cancer, Chem Rev, 2014, 114(21), 10869–10939.
[7] Li J, Rao J, Pu K, Recent progress on semiconducting polymer nanoparticles for molecular imaging and cancer phototherapy, Biomaterials, 2018, 155, 217–235.

[8] Li B, Zhao M, Zhang F, Rational design of near-Infrared-II organic molecular dyes for bioimaging and biosensing, ACS Mater Lett, 2020, 2(8), 905–917.
[9] Kenry, Duan Y, Liu B, Recent advances of optical imaging in the second near-infrared window, Adv Mater, 2018, 30, 1802394.
[10] Zhu S, Tian R, Antaris AL, Chen X, Dai H, Near-infrared-ii molecular dyes for cancer imaging and surgery, Adv Mater, 2019, 31(24), 1900321.
[11] Hong G, Antaris AL, Dai H, Near-infrared fluorophores for biomedical imaging, Nat Biomed Eng, 2017, 1(1), 0010.
[12] Liu S, Li Y, Zhang H, Zhao Z, Lu X, Lam JWY, Tang BZ, Molecular motion in the solid state, ACS Mater Lett, 2019, 1(4), 425–431.
[13] Li Y, Liu S, Han T, Zhang H, Chuah C, Kwok RTK, Lam JWY, Tang BZ, Sparks fly when AIE meets with polymers, Mater Chem Front, 2019, 3(11), 2207–2220.
[14] Zhao Z, Zhang H, Lam JWY, Tang BZ, Aggregation-induced emission: New vistas at the aggregate level, Angew Chem Int Ed, 2020, 59(25), 9888–9907.
[15] Zhang H, Zhao Z, Turley AT, Wang L, McGonigal PR, Tu Y, Li Y, Wang Z, Kwok RTK, Lam JWY, Tang BZ, Aggregate science: From structures to properties, Adv Mater, 2020, 32(36), 2001457.
[16] Zhang H, Zhao Z, McGonigal PR, Ye R, Liu S, Lam JWY, Kwok RTK, Yuan WZ, Xie J, Rogach AL, Tang BZ, Clusterization-triggered emission: Uncommon luminescence from common materials, Mater Today, 2020, 32, 275–292.
[17] Li Q, Li Z, Molecular packing: Another key point for the performance of organic and polymeric optoelectronic materials, Acc Chem Res, 2020, 53, 962–973.
[18] Wang D, Lee MMS, Xu W, Kwok RTK, Lam JWY, Tang BZ, Theranostics based on AIEgens, Theranostics, 2018, 8(18), 4925–4956.
[19] Qi J, Chen C, Ding D, Tang BZ, Aggregation-induced emission luminogens: Union is strength, gathering illuminates healthcare, Adv Healthcare Mater, 2018, 7(20), 1800477.
[20] Mei J, Leung NLC, Kwok RTK, Lam JWY, Tang BZ, Aggregation-induced emission: Together we shine, united we soar!, Chem Rev, 2015, 115(21), 11718–11940.
[21] Ding D, Li K, Liu B, Tang BZ, Bioprobes Based on AIE Fluorogens, Acc Chem Res, 2013, 46(11), 2441–2453.
[22] Liu S, Li Y, Kwok RTK, Lam JWY, Tang BZ, Structural and process controls of AIEgens for NIR-II theranostics, Chem Sci, 2021, 12(10), 3427–3436.
[23] Cheng H-B, Li Y, Tang BZ, Yoon J, Assembly strategies of organic-based imaging agents for fluorescence and photoacoustic bioimaging applications, Chem Soc Rev, 2020, 49(1), 21–31.
[24] Zhao Z, Chen C, Wu W, Wang F, Du L, Zhang X, Xiong Y, He X, Cai Y, Kwok RTK, Lam JWY, Gao X, Sun P, Phillips DL, Ding D, Tang BZ, Highly efficient photothermal nanoagent achieved by harvesting energy via excited-state intramolecular motion within nanoparticles, Nat Commun, 2019, 10(1), 768.
[25] Liu S, Zhou X, Zhang H, Ou H, Lam JWY, Liu Y, Shi L, Ding D, Tang BZ, Molecular motion in aggregates: Manipulating TICT for boosting photothermal theranostics, J Am Chem Soc, 2019, 141(13), 5359–5368.
[26] Ni JS, Zhang X, Yang G, Kang T, Lin X, Zha M, Li Y, Wang L, Li K, Photoinduced Nonadiabatic A, Decay-Guided molecular motor triggers effective photothermal conversion for cancer therapy, Angew Chem Int Ed, 2020, 59(28), 11298–11302.
[27] Chen M, Zhang X, Liu J, Liu F, Zhang R, Wei P, Feng H, Tu M, Qin A, Lam JWY, Ding D, Tang BZ, Evoking photothermy by capturing intramolecular bond stretching vibration-induced dark-state energy, ACS Nano, 2020, 14(4), 4265–4275.

[28] Gao S, Wei G, Zhang S, Zheng B, Xu J, Chen G, Li M, Song S, Fu W, Xiao Z, Lu W, Albumin tailoring fluorescence and photothermal conversion effect of near-infrared-II fluorophore with aggregation-induced emission characteristics, Nat Commun, 2019, 10(1), 2206.
[29] Sheng Z, Guo B, Hu D, Xu S, Wu W, Liew WH, Yao K, Jiang J, Liu C, Zheng H, Liu B, Bright aggregation-induced-emission dots for targeted synergetic nir-ii fluorescence and nir-i photoacoustic imaging of orthotopic brain tumors, Adv Mater, 2018, e1800766.
[30] Guo B, Feng Z, Hu D, Xu S, Middha E, Pan Y, Liu C, Zheng H, Qian J, Sheng Z, Liu B, Precise deciphering of brain vasculatures and microscopic tumors with dual nir-ii fluorescence and photoacoustic imaging, Adv Mater, 2019, 31(30), e1902504.
[31] Deng G, Peng X, Sun Z, Zheng W, Yu J, Du L, Chen H, Gong P, Zhang P, Cai L, Tang BZ, Natural-Killer-Cell-inspired nanorobots with aggregation-induced emission characteristics for near-infrared-ii fluorescence-guided glioma theranostics, ACS Nano, 2020, 14(9), 11452–11462.
[32] Zhang Z, Xu W, Kang M, Wen H, Guo H, Zhang P, Xi L, Li K, Wang L, Wang D, Tang BZ, An all-round athlete on the track of phototheranostics: Subtly regulating the balance between radiative and nonradiative decays for multimodal imaging-guided synergistic therapy, Adv Mater, 2020, 32(36), e2003210.
[33] Xu Y, Zhang Y, Li J, An J, Li C, Bai S, Sharma A, Deng G, Kim JS, Sun Y, NIR-II emissive multifunctional AIEgen with single laser-activated synergistic photodynamic/photothermal therapy of cancers and pathogens, Biomaterials, 2020, 259, 120315.

Lirong Wang, Xinzhe Yang, Anjun Qin, Ben Zhong Tang

Chapter 19
AIE polymers for fluorescence imaging and therapy

19.1 Introduction

Diagnosis and treatment are very important for humans in the fight against diseases. The development of various imaging methods assures accurate diagnosis. Among the imaging methods, fluorescence imaging (FLI) is the most researched and most common method because of its high sensitivity, flexibility, simple operation, low cost, etc. Therefore, many luminescent materials have come to be used. Compared to inorganic materials with long-term side effects of heavy metals, organic luminescent materials have been researched more for biological applications. In most fluorescent materials, emission is strong in a diluted solution but weakened or becomes nonemissive in concentrated solution. This is termed aggregation-caused quenching (ACQ) effect. This phenomenon has limited further applications in biological and biomedicine fields. In 2001, Tang and coworker proposed the concept of aggregation-induced emission (AIE) based on their observation of the unique phenomenon that the silole derivatives are nonemissive when molecularly dissolved but become highly emissive upon aggregation [1]. AIE broke the bottleneck of ACQ and promoted the rapid development of luminescent materials, because AIE luminogens (AIEgens) enjoy the advantages of good biocompatibility, large stokes shift, and outstanding photostability. The restriction of intramolecular motion (RIM), which includes restriction of intramolecular rotation (RIR) and restriction of intramolecular vibration (RIV), has been rationalized as the cause of the AIE [2]. In general, organic materials with AIE property are easily constructed by introduction of AIE groups, such as tetraphenylethylene (TPE), a star molecule

Lirong Wang, Xinzhe Yang, State Key Laboratory of Luminescent Materials and Devices, Guangdong Provincial Key Laboratory of Luminescence from Molecular Aggregates, Center for Aggregation-Induced Emission, South China University of Technology, Guangzhou, 510640, China
Anjun Qin, State Key Laboratory of Luminescent Materials and Devices, Guangdong Provincial Key Laboratory of Luminescence from Molecular Aggregates, Center for Aggregation-Induced Emission, South China University of Technology, Guangzhou, 510640, China,
e-mail: msqinaj@scut.edu.cn
Ben Zhong Tang, Shenzhen Institute of Molecular Aggregate Science and Engineering, School of Science and Engineering, The Chinese University of Hong Kong (Shenzhen), 2001 Longxiang Boulevard, Longgang District, Shenzhen, Guangdong 518172, China.

https://doi.org/10.1515/9783110673074-020

in AIE field. Accordingly, various low-mass AIEgens [3–5] and AIE-active polymers [6–13] have been reported and have made great progress in biosensing, imaging, and therapy.

Compared to low mass AIEgens, AIE polymers have their unique advantages, such as various synthesis methods and structure, easy modification, multifunctionalization, and adjustable fluorescence emission. Moreover, AIE conjugated polymers also have high light-harvesting ability and enhanced ROS generation capability [12]. Based on these advantages, AIE polymers have been designed for FLI-monitoring drug delivery, tumor microenvironment response, nonconventional luminescence, photodynamic therapy (PDT), and photothermal therapy (PTT) in antibacterial and antitumor applications. Since the first AIE polymer was reported in 2003 [14], this area has developed rapidly, and several review papers have summarized the progress in the synthesis of AIE polymers [7, 15]. In this chapter, we focus on the progress of AIE polymers in FLI and therapy in the past 3 years. Finally, the conclusion and perspectives have been presented. Through this chapter, we hope that readers would grasp the advantages of AIE polymers in biological applications and would be inspired to develop more AIE polymers, with better performance in biological and biomedical fields.

19.2 Fluorescence imaging (FLI)

FLI is a common and important imaging mode, especially in in vitro imaging and surgical navigation. It enjoys many advantages such as high sensitivity, nonradiation, real time, and low cost. Compared to nonemissive polymers and low mass AIE probes, AIE polymers can be easily designed to control the fluorescent "off-on" process under H_2O_2, pH, Glutathione (GSH) or cystine, hypoxia, or pH/redox dual-responsive conditions for sensitive and specific in vitro imaging. In addition, AIE polymers can be constructed to realize the NIR and NIR-II FLI for deep penetration in tumor detection.

19.2.1 Cell imaging based on AIE biomacromolecules

Natural macromolecules (dextran, chitosan, silkworm silk, etc.) have many advantages of abundance, low cost, biocompatibility, and easy modification. By modification with AIE units, AIE macromolecules were obtained. Because of their amphiphilicity, they can self-assemble into different sizes of micelles or nanoparticles, by adjusting the molar ratio of hydrophobic AIE units and hydrophilic macromolecules, which would restrict the intramolecular motion of AIE units to enhance the emission. Fang, Li, and coworkers [16] have reported AIE dextran nanoparticles (Dex-OH-CHO) via a facile

esterification, which was composed of hydrophobic 1, 8-naphthalimide derivative, and the hydrophilic dextran (Figure 19.1A). The Dex-OH-CHO had light-blue fluorescence with quantum yield (Φ_F) of 24.4%. In addition, these nanoparticles have good photostability and cell uptake ability, which makes them useful in cell imaging applications. Besides dextran, chitosan is another frequently used macromolecule. Wang and coworkers [17] had modified the chitosan with TPE units and quaternary ammonium salt to obtain the cationic and water-soluble TPE-QCS (Figure 19.1B), which were stable over a wide range of pH values. More importantly, the positivity of TPE-QCS was beneficial for uptake by cells and adhesion to negative organelle membranes for ultra-long-term cellular tracing.

Silkworm silk is a natural fibrous protein with excellent physical properties and biodegradability. There are many primary amine groups in the lysine residues of silk proteins, which can be conjugated with AIE units to get AIEgen-silks. Bai, Tang and coworkers [18] modified the red-emissive MTPABP into hydrolyzed silk through amino-yne click reaction (Figure 19.1C). With good biocompatibility, these MTPABP-hydrolyzed silks could light up the plasma membrane of A549 cells at 2 min, and within 2 h, the silks gradually entered the cells with increased fluorescent emission, thus exhibiting the cellular uptake process (Figure 19.1D and E). In addition, these MTPABP-hydrolyzed silks could image the cells for up to 11 days, which proved their ability of long-term cell tracking.

19.2.2 Synthetic AIE polymer

The availability and structure of natural macromolecules are limited. To extend the amount and functions of materials, it is very important to synthesize novel polymers with various properties for FLI and drug tracking.

19.2.2.1 Targeted imaging

Cell or organelle imaging is the most basic and important means for studying cancers. Based on the integrity, permeability, charged property, and target groups of cell membrane, many low mass fluorescence probes have been developed, and many of them have been commercialized. However, some defects such as cytotoxicity, photobleaching, and poor specificity still exist. In contrast, AIE polymers possess the advantages of good biocompatibility, anti-photobleaching, high Φ_F, and multifunctional modification, which are beneficial in cell imaging.

Living-cell-targeted imaging is an important and challenging work because of the similar structure in the early apoptosis. Qin and coworkers [19] reported an amphiphilic AIE conjugated polymer P(TPE-2OEG), with the TPE units in the backbone and OEGs in the side chains (Figure 19.2A). This polymer had a large stokes shift

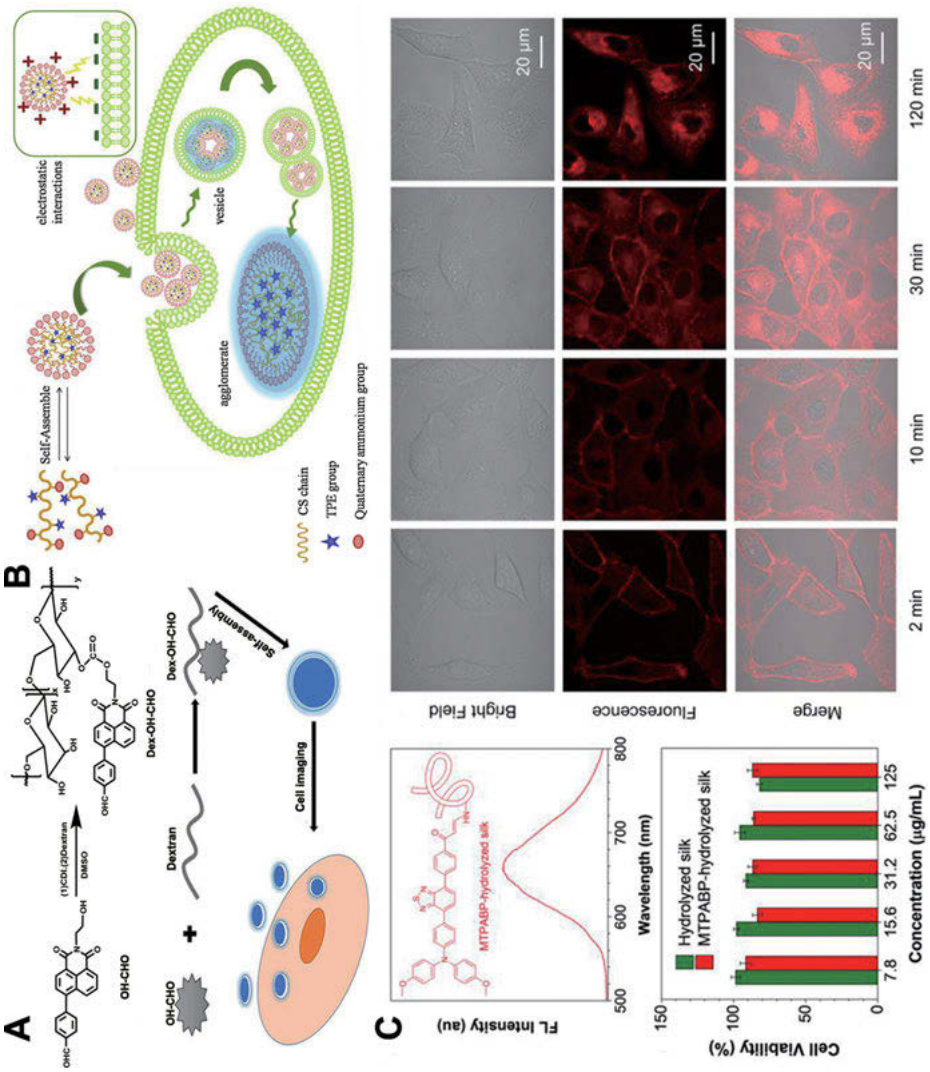

Figure 19.1: Natural macromolecules with AIE property for bioimaging. (A) Synthesis of Dex-OH-CHO polymers for cell imaging. Reproduced with permission from Ref. [16]. Copyright (Informa UK Limited.), 2019. (B) The illustration of TPE-QCS nanoparticles internalized by living HeLa cells for long-term cell imaging. Reproduced with permission from Ref. [17]. Copyright (Elsevier), 2019. (C) The structure of MTPABP-hydrolyzed silk and its Fluorescence spectrum. (D) The MTT of MTPABP-hydrolyzed silk and hydrolyzed silk, which indicated their good biocompatibility. (E) Fluorescent images of A549 cells stained by MTPABP-hydrolyzed silk with a concentration of 100 μM. Reproduced with permission from Ref. [18]. Copyright (John Wiley & Sons Inc.), 2020.

and high Φ_F of 56.2% in the solid state. Compared to Calcein AM, a commercially viable cell dye, P(TPE-2OEG) had excellent biocompatibility. It is well-known that cell apoptosis can be induced by H_2O_2, and different concentration of H_2O_2 can induce different degrees of apoptosis in cells. Annexin V-FITC and propidium iodide (PI) have been widely used to discriminate apoptotic and dead cells. As shown in Figure 19.2B, after being incubated with 0, 500, and 1,000 μM H_2O_2, apoptosis and even death of HeLa cells were generally stained by Annexin V-FITC and PI, respectively; however, P(TPE-2OEG) showed strong fluorescence in living cells, weak fluorescence in apoptotic cells, and no fluorescence in dead cells. In contrast, Calcein AM and low-mass M(TPE-2OEG) could not distinguish the viable cells from the apoptotic and dead cells. In addition, P(TPE-2OEG) could also sensitively label the viable cells from the microbes. This specificity was mainly attributed to the intensity of electrostatic repulsion and the energy-dependent endocytosis process. As we know, the phosphatidylserine (PS) would be eversion to the surface of the early apoptosis, leading to more negative surface than in living cells. The zeta potential of aggregates of P(TPE-2OEG) was also negative. Therefore, the enhanced electrostatic repulsion between apoptosis and P(TPE-2OEG) hindered the endocytosis. In addition, endocytosis process was energy dependent. The dead cells did not have enough energy to internalize P(TPE-2OEG). While low mass M(TPE-2OEG) could be easily internalized by apoptotic and dead cells via diffusion-dependent uptake. Moreover, the OEG side chain of P(TPE-2OEG) could reduce the nonspecific adsorption by cell membrane and further improve the specificity. This interaction mechanism was also applicable to the microbes because of their negatively charged surface.

Through adjusting the backbone from phenyl to benzothiadiazole units and side chains from OEGs to ethylenediaminetetraacetic acid (EDTA), Zhang, Qin and coworker [20] reported another AIE polymer of PTB-EDTA for targeting the osteoblasts and in situ monitoring of the osteogenic differentiation process (Figure 19.2C). This PTB-EDTA had good water solubility and biocompatibility. More importantly, they had high affinity towards Ca^{2+}, which ensured the specificity of osteoblasts. After chelation of Ga^{2+}, osteoblasts could uptake this polymer as the required element. In order to explore the sensitivity for the process of osteogenic differentiation, Alizarin Red S staining, the most common method, was used as the control. As shown in Figure 19.2D, at the 7th day of differentiation, the fluorescence of this polymer was detected. But for Alizarin Red S staining, the signal was only recorded at the 14th day, indicating PTB-EDTA had more sensitivity than Alizarin Red S staining for detection of osteogenic differentiation. Therefore, PTB-EDTA holds great potential as a new fluorescence probe for the rapid and real-time identification of the degree of osteogenic differentiation.

Biocompatibility is an important characteristic in biomaterials. As mentioned above, connecting hydrophilic and biocompatible groups on the side chain of a polymer is a good strategy to guarantee biocompatibility. In addition, mesoporous silica hollow nanospheres (MSHNs) are also biocompatible carriers that transport

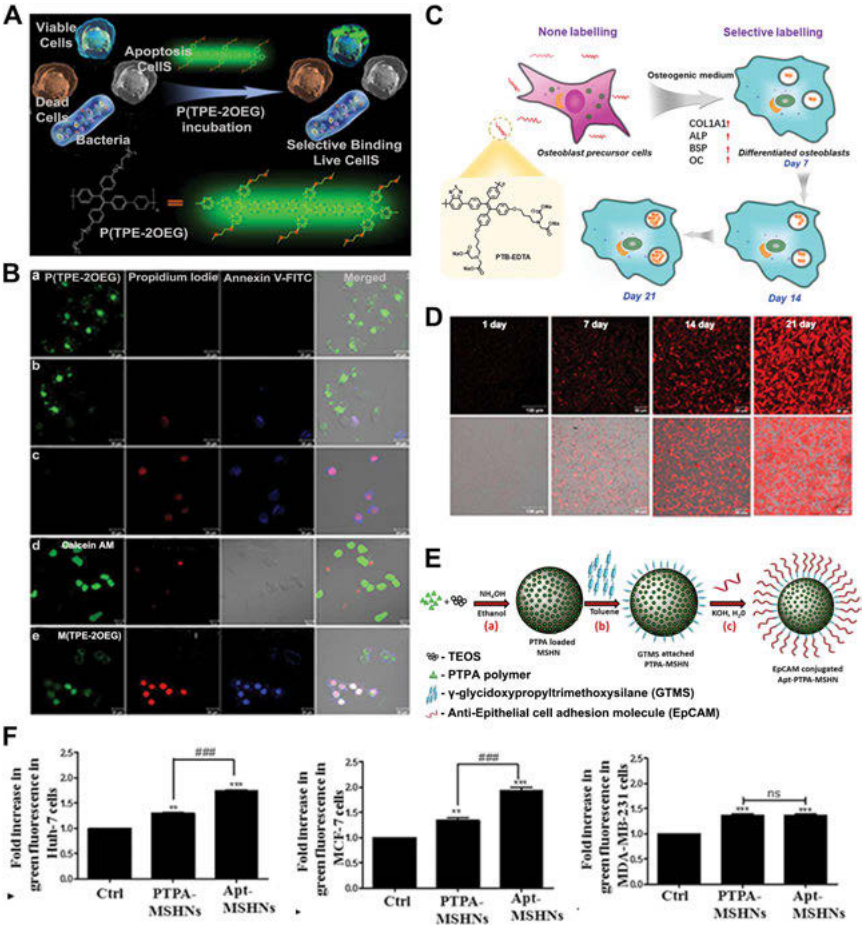

Figure 19.2: Targeting viable cell, osteoblasts, and liver cancer cell imaging. (A) Schematic illustration of selective discrimination of viable cells from apoptosis cells, dead cells, and bacteria and the molecular structure of P(TPE-2OEG). (B) CLSM of HeLa cells incubated with P(TPE-2OEG) (a-c), Calcein AM (d), and M(TPE-2OEG) (e), respectively. a–c: HeLa cells treated with 0, 500, 1,000 μM H_2O_2. d and e: HeLa cells treated with 500 μM H_2O_2. Reproduced with permission from Ref. [19]. Copyright (Elsevier), 2020. (C) The chemical structures of PTB-EDTA and cartoon illustration of its cellular internalization and high sensitivity for real-time detection of osteogenic differentiation. Reproduced with permission from Ref. [20]. Copyright (John Wiley & Sons Inc.), 2020. (D) Cell imaging of MC3T3-E1 incubated with PTB-EDTA for 12 h at indicated differentiation time. (E) (a) The synthesis of PTPA-loaded MSHNs, (b) modification of MSHNs with GTMS, and (c) conjugation of anti-EpCAM aptamer on the GTMS-attached PTPA-MSHNs. (F) Flow cytometric analysis of uptake of PTPA-MSHNs and Apt-MSHNs (100 μg/mL) in Huh7 cells, MCF-7 cells, and MDA-MB-231 cells after 24 h incubation. Reproduced with permission from Ref. [21]. Copyright (American Chemical Society), 2020.

the functional molecules. Moreover, the surface of MSHNs can modify with various functional molecules. Dineshkumar, Chowdhury, Laskar, and coworkers [21] reported a conjugated polymer PTPA with AIE property. In order to realize the good biocompatibility, they fabricated the MSHNs to load the hydrophobic PTPA (PTPA-MSHNs). Furthermore, an anti-epithelial cell adhesion molecule (anti-EpCAM) aptamer was conjugated on the surface of MSHNs through γ-glycidoxypropyltrimethoxysilane (GTMS) to obtain the Apt-PTPA-MSHNs for targeting cancer cells imaging (Figure 19.2E). To explore the cancer targeting, Huh7 cells, MCF-7 cells, and MDA-MB-231 cells were incubated with PTPA-MSHNs and Apt-PTPA-MSHNs, respectively. The results of flow cytometric analysis indicated that Apt-PTPA-MSHNs had higher specificity than PTPA-MSHNs for Huh-7 and MCF-7 cells, but not for MDA-MB-231 cells (Figure 19.2F). This was mainly because Huh-7 and MCF-7 cells could highly express EpCAM, and MDA-MB-231 cells expressed none/low levels of EpCAM. These results indicated that Apt-PTPA-MSHNs could be expected to be promising candidates for targeted cancer cell imaging.

19.2.2.2 Organelle imaging

Lysosome is an important organelle that contains a variety of hydrolases and accessory proteins. They can degrade or catabolize many biological molecules into their basic components in acidic surroundings. Lysosome dysfunction can cause various diseases including lysosomal storage diseases, cancer, neurodegenerative diseases, and others [22]. Therefore, visualizing and monitoring lysosome activity is meaningful in the detection of lysosome related diseases. Zhou, Zhao, and coworkers [23] synthesized two AIE conjugated polyelectrolytes (CPEs) P**1**$^+$ and P**2**$^+$ by Suzuki polycoupling (Figure 19.3A). Because of the introduction of hydrophilic long chain groups on the thiophene monomers, P**2** had a higher molecular weight than P**1**, which also made P**2** have a lower enhancement of fluorescence intensity and Φ_F from monodisperse state to aggregate state than P**1**. To explore the lysosome targeting, triphenyl phosphonium (PPh_3), pyridine (Pyr), and morpholine (Mor) were modified onto the side chains of P**1** and P**2**, respectively. The confocal laser scanning microscope (CLSM) results showed that P1$^+$-PPh_3 and P1$^+$-Pyr had more specificity to lysosome than P1$^+$-Mor (Figure 19.3B). The lysosome co-localization rate was high, up to 94%. This result also appeared in the CLSM result of P2$^+$-PPh_3, P2$^+$-Pyr, and P2$^+$-Mor. As we know, low mass organic molecules modified with PPh_3 and Pyr cations are typical mitochondrial-guiding agents. However, when the PPh_3 or Pyr groups were conjugated onto the P**1** or P**2**, they could target the lysosome. This result indicated that PPh_3^+ or Pyr$^+$ on the CPE chain, with strong electrostatic repulsive interactions, changed the lipophilicity of polymers and decreased the electrophoretic force, realizing the lysosome targeting ability. For Mor groups on the low mass organic molecules, they are targeted to the lysosome. However, when they were linked on the CPE chains, their lysosome targeting ability disappeared. This

was mainly because the stiff polymer chains partially block the Mor groups from effectively contacting the lysosome, leading to the loss of lysosome targeting ability.

Apart from modification of some targeting groups, novel polymers with facile preparation and targeting ability are very important. Recently, Haddleton and coworkers [24] have reported an AIE-active polyacrylate of TPE-poly(tert-butyl acrylate) (TPE-PtBA) through the Cu(0)-mediated reversible deactivation radical polymerization (RDRP). With this method, high end-group fidelity, high conversion, and low dispersity of TPE-PtBA were obtained (Figure 19.3C). TPE-PtBA could be transformed into TPE-PAA by facile deprotection. In addition, they further synthesized a range of TPE-contained block copolymers based on TPE-PtBA, with the same Cu(0)-wire-mediated RDRP protocol. Through introduction of different hydrophobic and hydrophilic groups, the luminescent properties and pH-responsibility could be tuned. Taking the TPE-PMA_{60}-b-PAA_{100} as an example, when the pH values increased from 4.0 to 7.0, the fluorescence intensity gradually decreased, but increased again, when the pH further increased to 11.0 (Figure 19.3D). This was mainly because the increased pH resulted in increased carboxylate negative ions of PAA chains, hindering the effective aggregation of TPE units. The size of aggregates decreased and fluorescence intensity also decreased, correspondingly. However, a further increase of the pH to 11 resulted in increased R_h and PL intensity. This should be attributed to the fact that the contact between the TPE core and water molecules was hindered due to the interactions between Na^+ and PAA chains. Furthermore, TPE-PMA_{60}-b-PAA_{100} with good biocompatibility could specifically stain the lysosome (Figure 19.3E). In addition, compared with Lyso Tracker Green, TPE-PMA_{60}-b-PAA_{100} exhibited excellent photobleaching resistance (Figure 19.3F). Therefore, these new AIE polymers with low cytotoxicity, high specificity, and excellent photostability hold great potential in lysosome-specific imaging.

The cell nucleus has a strong negative charge because it contains a large number of nucleic acid molecules. Ma and coworkers [25] synthesized a series of cationic AIE hyperbranched polymers by copolymerizing TPPA, DBO, and TIPA units for cell imaging (Figure 19.4A). Interestingly, these polymers could stain the cell nucleus, which was confirmed by DAPI, a cell nucleus dye (Figure 19.4B). Taking [tris(4-(pyridin-4-yl)phenyl)-amine]-[1,8-dibromooctane] ([TPPA-DBO]) as an example, strong fluorescence was observed when these polymers interacted with dsDNA and RNA with a 30-fold and 15-fold enhancement, compared to the free compound, and the corresponding Φ_F increased from 6.213 to 14.41 and 7.847, respectively. As a control, [TPPA-DBO]/PAAS exhibited negligible fluorescence enhancement after interaction with DNA and RNA, owing to the negatively charged surface of [TPPA-DBO]/PAAS. In living cells, TPPA-DBO staining A549 cells showed strong yellow fluorescence. After incubation with deoxyribonuclease (DNase), the fluorescence disappeared dramatically but was not influenced by ribonuclease (RNase) digest (Figure 19.4C), indicating the specificity and sensitivity of TPPA-DBO to DNA over RNA in living cells.

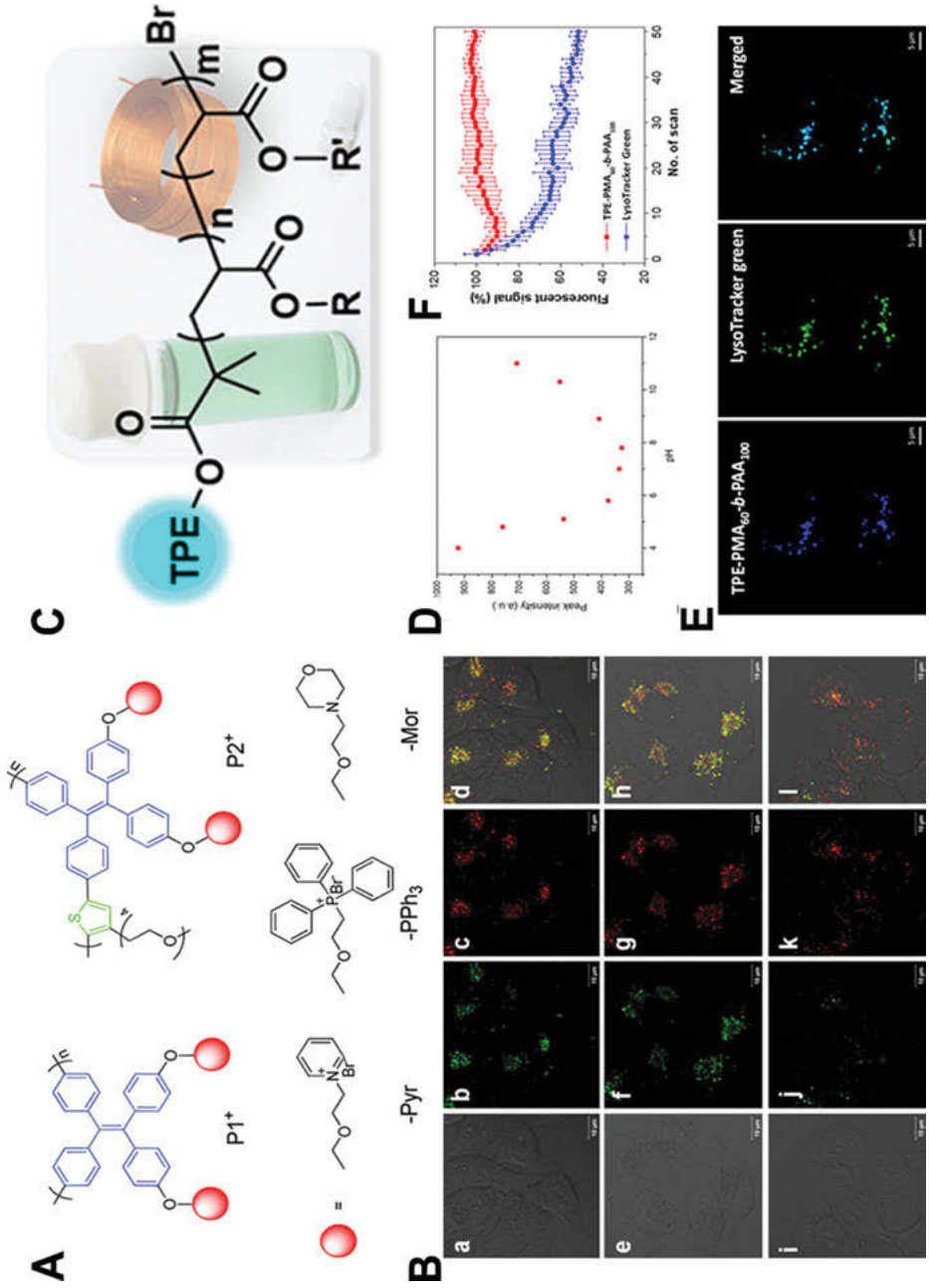

Figure 19.3: Lysosome targeted imaging. (A) Molecular structures of the AIE polymers $P1^+$ and $P2^+$. The red ball refers to PPh_3, Pyr, and Mor groups respectively. (B) CLSM images of HeLa cells (a, e and i, bright field) stained with $P2^+$–PPh_3, $P2^+$–Pyr or $P2^+$–Mor (b, f, and j), respectively for 48 h and Lyso Tracker Red (c, g and k) for 20 min, and their merged images (d, h and l). Reproduced

19.2.3 Stimuli-responsive imaging

Inspired by the multi-modification, "off-on" converted fluorescence, and good biocompatibility, various responsive bonds or groups (e.g., CO_2, pH-, temperature, redox-, hypoxia) have been conjugated onto the backbones or side chains of AIE polymers. Through the structure transformation from the monodisperse state to aggregate state, fluorescence would be turned on or enhanced.

19.2.3.1 CO_2-responsive imaging

CO_2 is one of the direct signals that helps discriminate cancer cells from normal cells. Detection of CO_2 in cells with high sensitivity is challenging. Wang and coworkers [26] reported a "breathable" triblock AIE polymer PTPE-*b*-PAD-*b*-PEO through reversible addition fragmentation chain transfer (RAFT) polymerization. The PTPE-*b*-PAD-*b*-PEO polymers consisted of an amidine-containing CO_2-responsive block and an AIE-active block. They could self-assemble into vesicles in the physiological solution with TPE moieties at the core and the hydrophilic part on the surface (Figure 19.5A). When CO_2 is bubbled into the solution, the hydrophobic PAD block could be protonated by CO_2 and changed into the hydrophilic block. Meanwhile, the increase in the hydrophilic surface area induced the aggregation of the PTPE block, and fluorescent emission enhanced (Figure 19.5B). Subsequently, when N_2 was purged into the protonated polymer solution, the PL intensity decreased (Figure 19.5C), indicating this copolymer system had good reversibility. As is well known, cancer cells have more vigorous breathing than normal cells, resulting in higher concentration of CO_2 in cancer cells than that in normal cells. Thereupon, the results of in vitro FLI (Figure 19.5D) also indicated that irrespective of whether they were cancer cells (HeLa, 5–8 F, and CNE-1) or normal cells (16HBE and GES-1), the longer the time of incubation, the stronger the fluorescence emitted. Also, the fluorescence intensity of cancer cells was brighter than that of normal cells. Therefore, these triblock AIE polymers could be used as a cell probe for cancer diagnosis.

Figure 19.3 (continued)
with permission from Ref. [23]. Copyright (The Royal Society of Chemistry), 2018. (C) AIE active polyacrylates via Cu(I)-mediated reversible deactivation radical polymerization. (D) The corresponding peak intensities ($\lambda_{max} \approx 468$ nm) of the PL spectra versus pH values for TPE-PMA_{60}-b-PAA_{100}. (E) Colocalization imaging of 4T1 cells stained with TPE-PMA_{60}-b-PAA_{100}, LysoTracker Green and their merged image. (F) Fluorescence signals of 4T1 cells incubated with TPE-PMA_{60}-b-PAA_{100} and LysoTracker Green with different scan times. Reproduced with permission from Ref. [24]. Copyright (American Chemical Society), 2020.

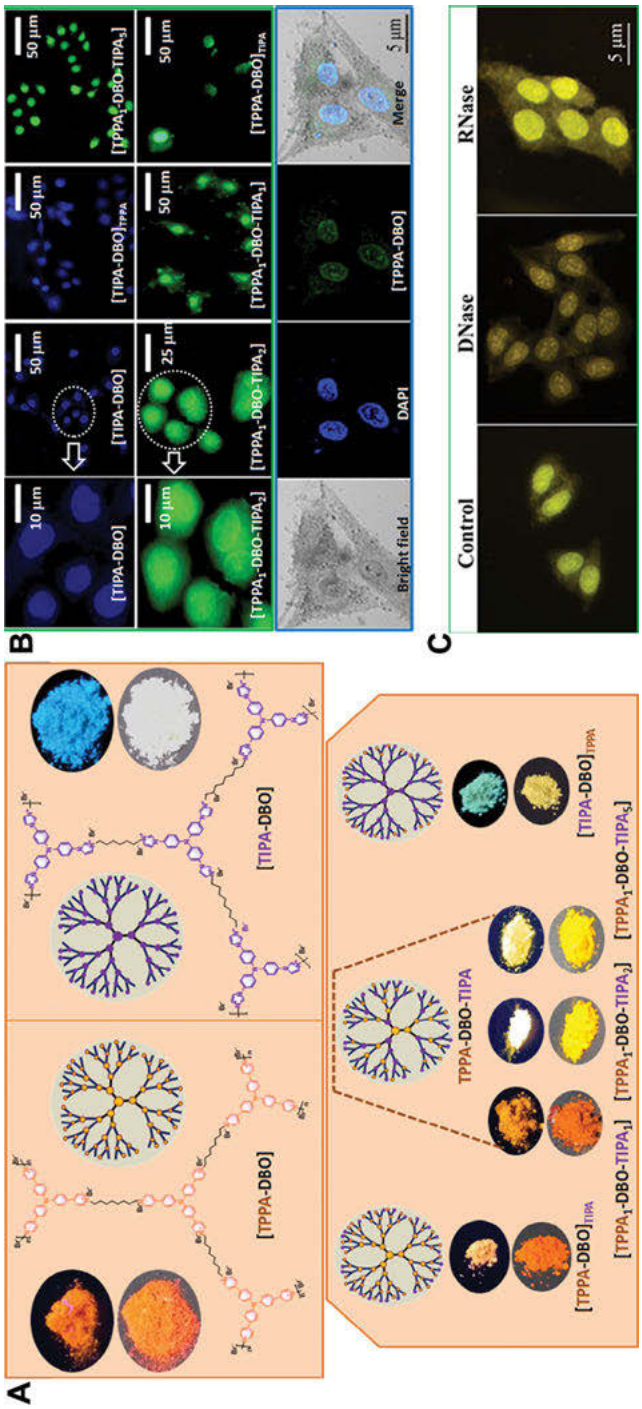

Figure 19.4: Nuclear targeted imaging. (A) Schematic illustration of the hyperbranched cationic polymers and their luminous characteristics under UV light illumination (top) and day light (bottom). (B) CLSM images of HeGP-2 cells stained with their hyperbranched polymers for 60 min in different magnifications and co-staining of nucleus-specific dye DAPI with TPPA-DBO. (C) Fluorescence images of fixed A549 cells incubated with TPPA-DBO, TPPA-DBO and DNase, and TPPA-DBO and RNase. Reproduced with permission from Ref. [25]. Copyright (American Chemical Society), 2018.

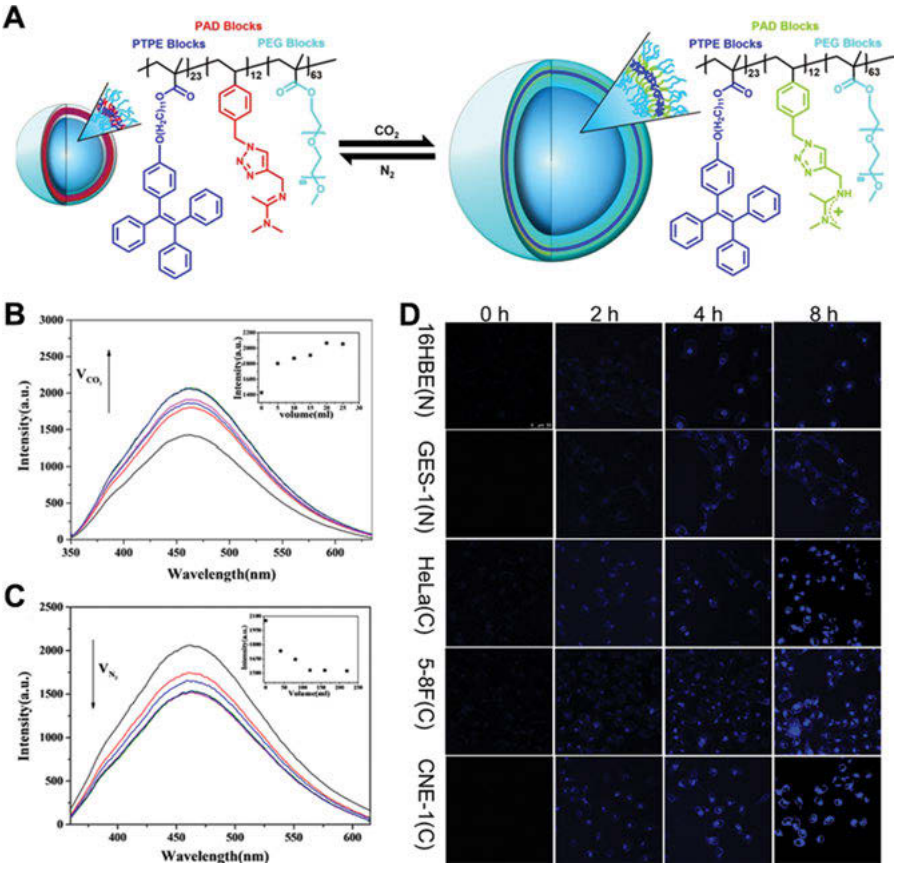

Figure 19.5: CO_2-responsive cell imaging. (A) Schematic illustration of the response process of PTPE-*b*-PAD-*b*-PEO with CO_2 and N_2 .(B) The increased PL intensity of PTPE-b-PAD-b-PEO aqueous solution with the increased volume of CO_2. (C) The decreased PL intensity of CO_2-treated PAD-*b*-PEO aqueous solution with the increased volume of N_2. (D) CLSM images of two normal cells (16HBE and GES-1) and three cancer cells (HeLa, 5–8 F, and CNE-1) after incubation with the PTPE-b-PAD-b-PEO solution at 0, 2, 4, and 8 h, respectively. Reproduced with permission from Ref. [26]. Copyright (American Chemical Society), 2019.

19.2.3.2 Temperature and pH-responsive imaging

In general, the synthesis of polymeric fluorescent thermometers is complex, and their π–π conjugation structures have a few restrictions in biological applications. Recently, a nonconjugated and AIE-active poly(*N*-vinylcaprolactam) (PNVCL) as an unconventional fluorescent thermometer has been reported by Mukhopadhyay, Bauri, De, and coworkers (Figure 19.6A) [27]. PNVCL was easily synthesized from *N*-vinylcaprolactam by free radical polymerization. Thanks to the C = O groups with

π-electrons/a lone pair of electrons and *N* atoms with a lone pair of electrons, PNVCL had the behavior of clusterization-triggered emission (CTE). In addition, PNVCL had the concentration-/excitation-dependent fluorescence phenomena, which indicated that various stable excited states with different energy levels existed in the aggregate state. Moreover, PNVCL had good water solubility and temperature-dependent phase transition behavior. At 38 °C, PNVCL emitted weakly. But when the temperature was above 38 °C, an intense blue fluorescence was observed, with 365 nm light irradiation. This could be explained as the hydrogen bonding between the C = O of lactam units and O-H of water molecules rupturing at a higher temperature, resulting in the coiled polymer chains collapsing into globular aggregates. This not only restricted intramolecular motion to realize the fluorescence enhancement, but also facilitated the cell uptake of PNVCL. MCF-7 cells were incubated with PNVCL at 25, 35, and 38 °C for 24 h (Figure 19.6B) and then were imaged under three channels, respectively. The in vitro cell imaging exhibited that blue, green, and red fluorescence with strong signal could be observed only at 38 °C (Figure 19.6C and D). All these properties enable PNVCL to serve as a next generation fluorescent thermometer that can detect minor temperature changes for the early detection of diseases.

Apart from temperature response, Deng, Zhu, and coworkers [28] reported two AIE-active reversible micelles for temperature and pH-responsive cell imaging. PNIPAM-*b*-P(DPA-*co*-TPE) and P(NIPAM-*co*-TPE)-*b*-PDPA were conveniently prepared through reversible addition-fragmentation chain-transfer (RAFT) polymerization (Figure 19.6E). Both of them had similar block length but different TPE position, and could self-assemble into reversible micelles. For PNIPAM-*b*-P(DPA-*co*-TPE) at 25 °C, with the increase of pH from 4.0 to 7.0, they aggregated to induce PL intensity enhancement (Figure 19.6F). For P(NIPAM-*co*-TPE)-*b*-PDPA at pH = 4.0, with the increase in temperature from 25 to 45 °C, the PL intensity increased due to the aggregation (Figure 19.6G). Moreover, these responses to temperature and pH were reversible. Based on these properties, the mixture of these two micelles stained MCF-7 cells and was evaluated by CLSM. As shown in Figure 19.6H, at pH 4.0 and 25 °C, bare fluorescence was observed, but strong fluorescence could be observed at pH 7.4 and 25 °C or at pH 4.0 and 40 °C, generated from the formation of aggregates of the two polymers. These results demonstrated that PNIPAM-*b*-P(DPA-*co*-TPE) and P(NIPAM-*co*-TPE)-*b*-PDPA could distinguish different pH and temperatures in vitro, simultaneously.

19.2.3.3 Biothiol-responsive imaging

Biological thiols (GSH or Cys) are of vital importance. Their abnormal levels are always related to some kinds of diseases. Chen, Wang, and coworkers [29] reported a "turn on" AIE hyperbranched poly(amido amine) with disulfide bond, named TPE-ssHPA (Figure 19.7A). This AIE polymer is different from the common "turn on" PL

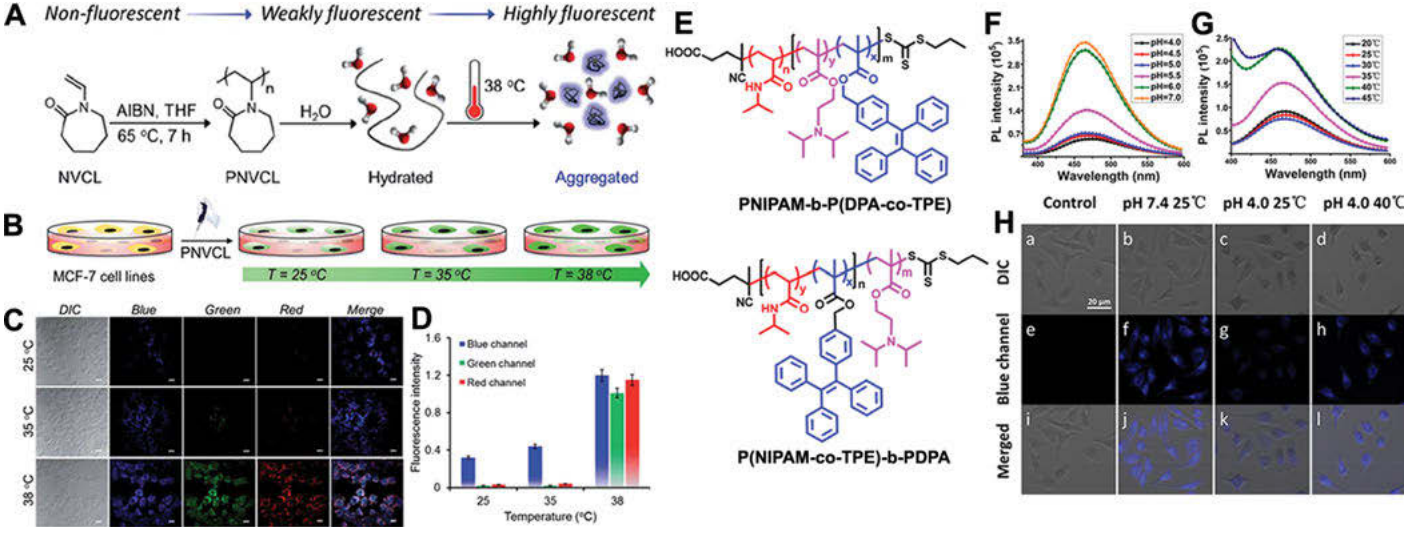

Figure 19.6: Temperature and pH responsive cell imaging. (A) Synthesis of PNVCL via FRP and its temperature-responsive conformational transformation to realize the enhancement of fluorescence. (B) Cartoon representation of MCF-7 cells incubated with PNVCL at different temperatures. (C) CLSM images of MCF-7 cells stained with PNVCL at 25, 35, and 38 °C for 24 h with blue, green, and red channel excitation. (D) A ratio of intensity of blue, green, and red fluorescence versus the blue fluorescence emitted by 4,6-diamidino-2-phenylindole (DAPI) only at 25, 35, and 38 °C, respectively. Reproduced with permission from Ref. [27]. Copyright (The Royal Society of Chemistry), 2019. (E) The structure of AIE-active reversible polymers PNIPAM-b-P(DPA-*co*-TPE) and P(NIPAM-*co*-TPE)-b-PDPA with temperature or pH stimulus response imaging. (F) PL intensity of PNIPAM-b-P(DPA-*co*-TPE) at different pH from 4.0 to 7.0 under 25 °C. (G) PL intensity of P(NIPAM-*co*-TPE)-b-PDPA at different temperatures under pH = 4.0. (H) CLSM images of MCF-7 cells incubated with the mixture of PNIPAM-b-P(DPA-*co*-TPE) and P(NIPAM-*co*-TPE)-b-PDPA at different temperature and pH. Reproduced with permission from Ref. [28]. Copyright (American Chemical Society), 2018.

probes, which are always pre-quenched with metal or organic solvent in water. TPE-ssHPA is a disulfide-functionalized hyperbranched polymer with specific topological structures. TPE units were randomly grafted onto the skeleton of the hyperbranched structure, which could prevent the aggregation of TPE units, leading to negligible emission. When in the presence of GSH or Cys, the disulfide bonds were interrupted, which led to the aggregation of TPE moieties and the enhancement of PL intensity (Figure 19.7B). Based on this detection mechanism, TPE-ssHPAs were used in biothiol-responsive imaging in yeast cells that can produce GSH. As shown in Figure 19.7C, TPE-ssHPAs could turn on the yeast cells, but could not light up the thiol-consuming NEM treated cells. Upon addition of the Cys, GSH, or HCY into the weakly emissive yeast cells, the PL of cells could be effectively enhanced, again. All of these results suggested that TPE-ssHPAs have potential as a "turn on" probe for biothiol-related living cells imaging.

19.2.3.4 Hypoxia-triggered imaging

Due to the rapid proliferation of tumor cells, the tumor microenvironment is hypoxic, low pH, and redox. As above mentioned, various AIE polymers have been designed for pH and redox-responsive imaging. Actually, being hypoxic is one of the main characteristics of tumor microenvironment, but AIE polymers based on hypoxia-triggered imaging is rarely reported. Recently, Ye and coworkers [30] reported an intelligent AIE polymer of PEG-*b*-P(DEAEAN-*co*-TPMA) by RAFT copolymerization for hypoxia-responsive imaging (Figure 19.8A). This polymer has no fluorescence due to water-solubility, but strong orange-red emission could be observed under hypoxia conditions. This could be attributed to the following processes. The azo bonds can be cleaved by the hypoxia triggering. After that, the quaternary ammonium turned into tertiary amine, with the release of 4-aminobenzyl alcohol. Subsequently, the ester bonds were cut off by a self-catalytic hydrolysis process to generate a carboxylate anion (Figure 19.8B). The negatively charged carboxylate anion could interact with the positively charged AIE moiety TPMA by electrostatic attraction to produce nanoparticles with strong fluorescent emission, due to the RIM of TPMA. This fluorescence "off-on" process was also observed in the cell imaging. As shown in Figure 19.8C, HeLa cells could be lighted up with the reduction of oxygen concentration. In addition, the three-dimensional multicellular spheroids (3D MCTS) model was applied to mimic the solid tumor microenvironment in vivo for hypoxia imaging. With the increase in incubation time, the orange-red fluorescence continued to increase (Figure 19.8D), which indicated the hypoxia-mediated in situ self-assembly process promoted the enhancement of fluorescence. This work would inspire researchers to develop the NIR or NIR-II AIE polymers for tumor hypoxia imaging.

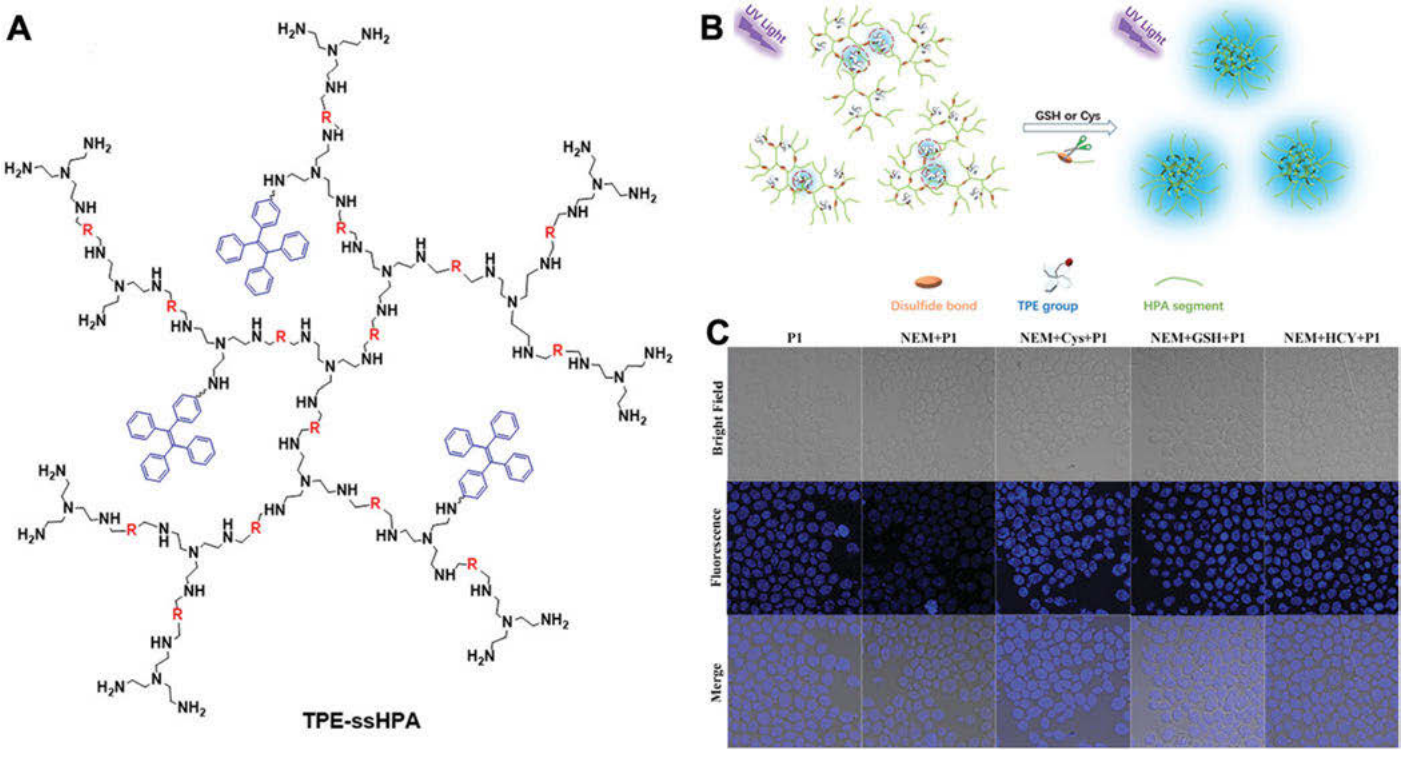

Figure 19.7: Biothiol-responsive AIE polymer TPE-$_{SS}$HPAs for cell imaging. (A) The structure of TPE-SSHPAs. (B) The mechanism of TPE-ssHPAs working as a biothiol-responsive "turn on" fluorescence probe. (C) Fluorescence inversion microscopic images of yeast cells treated with TPE-ssHPAs, TPE-ssHPAs + NEM (a thiol-consuming drug), TPE-ssHPAs + NEM + Cys, TPE-ssHPAs + NEM + GSH, and TPE-ssHPAs + NEM + HYC. Reproduced with permission from Ref. [29]. Copyright (The Royal Society of Chemistry), 2019.

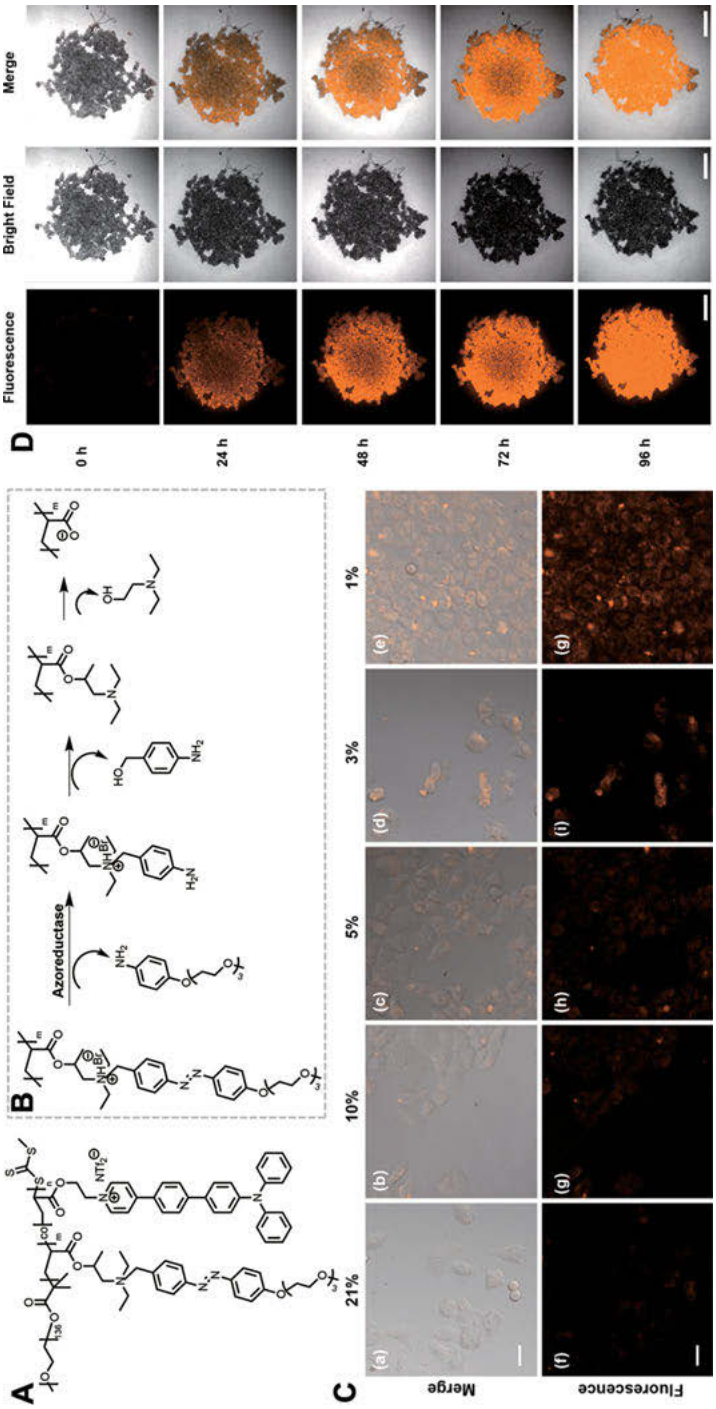

Figure 19.8: Hypoxia-responsive cell imaging. (A) The structure of PEG-*b*-P(DEAEAN-*co*-TPMA). (B) Hypoxia-triggered charge reverse process under tumor microenvironment. (C) CLSM images of HeLa cells incubated with PEG-*b*-P(DEAEAEN-*co*-TPMA) under normoxic (21% v/v O_2) and different hypoxic (10%, 5%, 3%, 1% v/v O_2) conditions. (D) Confocal images of 3D MCTS incubated with PEG-*b*-P(DEAEAEN-*co*-TPMA) at different time points. λ_{ex} = 405 nm, λ_{em} = 550–590 nm. Scale bars: 500 μm. Reproduced with permission from Ref. [30]. Copyright (American Chemical Society), 2021.

19.2.4 NIR and NIR-IIa imaging

The abovementioned AIE polymers emit white light, which are only for in vitro imaging. For in vivo imaging, the photon scattering and autofluorescence of tissues must be considered. Near-infrared (NIR) can reduce photon scattering and autofluorescence of tissues, resulting in deep penetration in vivo. Recently, Wu and coworkers [31] reported such an AIE semiconducting polymer. Phenothiazine and benzothiazole were chosen as the electron donor and acceptor to synthesize the AIE polymer PBT by Suzuki polycoupling. When the thiophene group was inserted into the main chain, the PTBT obtained was AIE-inactive (Figure 19.9A) because the enhanced planarity led to the intense ACQ effect. PBT had NIR fluorescence emission and high Φ_F. Moreover, when they were fabricated into polymer dots (Pdots), the Φ_F could be improved from 9% to 23%. Thanks to the excellent fluorescence properties and biocompatibility, PBT dots were further used in in vivo imaging. As shown in Figure 19.9B, 12 h after injection of the PBT dots, the intense fluorescence signal in the tumor and discernible margins of tumor could be clearly observed due to the enhanced permeability and retention (EPR) effect. Meanwhile, ex vivo fluorescence images after 48 h injection indicated that the PBT dots were mainly excreted through hepatobiliary pathway and feces, because of the enhanced fluorescent signals on the liver and intestine.

Compared to NIR fluorescence imaging, the second NIR window (NIR-II, 1,000 – 1,700 nm) for in vivo fluorescence imaging is more attractive, due to minimized photon scattering and autofluorescence of tissues. The semiconducting polymers with π-conjugated structure are easier to construct the NIR-II AIE polymers. Ding, Tang, and coworkers [32] have provided such a strategy for the synthesis of the NIR-II AIE polymers. In general, rigid planar π-conjugated structures have strong absorbance and emission in the isolated species. But the emission is easily quenched in the aggregate state. Twisted structures could provide high Φ_F but low absorption capacity. Therefore, combining the planarization and twisting structure into one polymer, high absorbance capability and high Φ_F could be simultaneously obtained. Based on this, pNIR-1, pNIR-2, pNIR-3, and pNIR-4 were synthesized (Figure 19.9C). pNIR-1 with planar structure was an ACQ emitter. pNIR-2 with the twisted structure was AIE-active, but its absorbance and emission were both blue-shifted. Due to the change of TPA units into TPE units, pNIR-3 had more blue-shifted absorption and emission than pNIR-2 due to the weak electron donating ability of TPE. pNIR-4, with one part of planar structure and one part of twisted structure, had both the NIR-II emission and AIE properties. Moreover, pNIR-4 NPs had an emission peak at 1,040 nm, with a tail stretching to 1,400 nm, which was suitable for the NIR-IIa imaging (1,300–1,400 nm). pNIR-3 NPs without fluorescence signal after 1,300 nm could be used as an NIR probe for subsequent in vivo imaging (Figure 19.9D). The images of the mouse brain and hind limb vasculatures exhibited that pNIR-4 NPs could provide the detailed

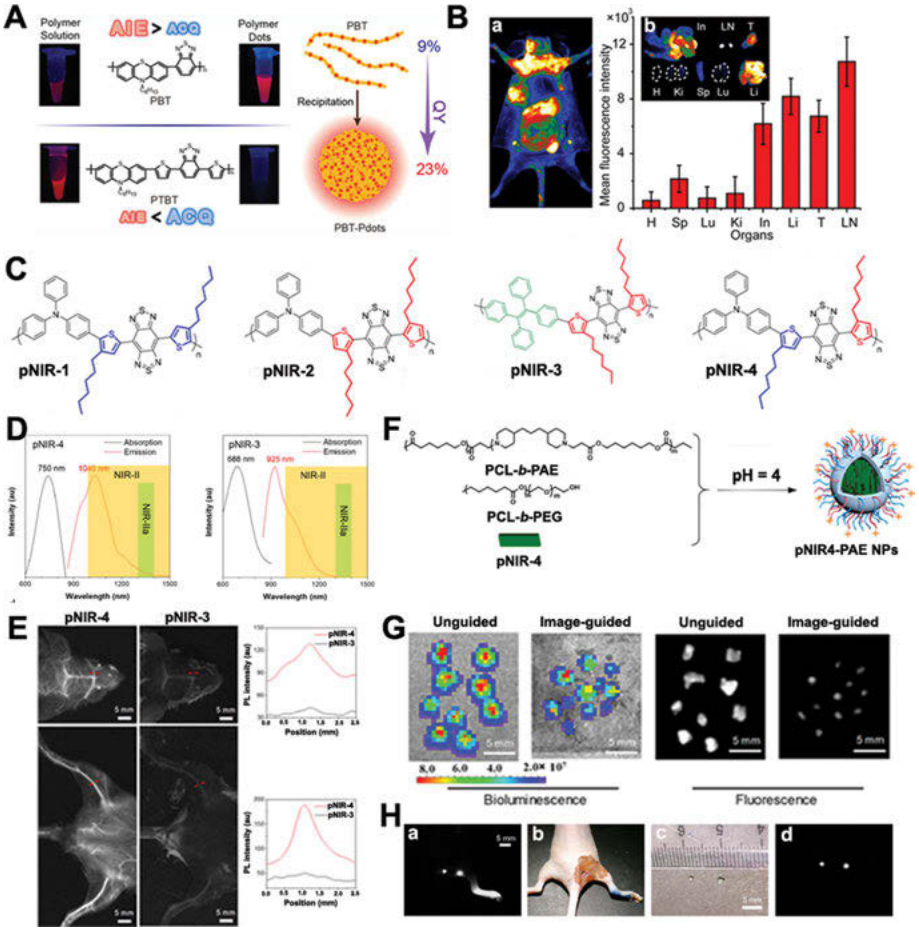

Figure 19.9: NIR and NIR-II fluorescence imaging. (A) The structure of PBT with AIE property and PTBT with ACQ effect. The Φ_F could be improved from 9% to 23% when PBT formed PBT-Pdots. (B) In vivo imaging after the opening of abdominal skin at 48 h after injection of PBT-Pdots (a). (b) Ex vivo tissue imaging of heart (H), spleen (S), lung (Lu), kidney (K), intestine (In), liver (Li), tumor (T), and lymph nodes (LN), and their mean fluorescence intensity. Reproduced with permission from Ref. [31]. Copyright (American Chemical Society), 2020. (C) The structure of pNIR-1, pNIR-2, pNIR-3, pNIR-4. (D) Absorption and emission spectra of pNIR-3, pNIR-4. (E) NIR-IIa fluorescent imaging of cerebral cortex and hind limb quality after injection of pNIR-4 and pNIR-3 nanoparticles respectively, and their corresponding cross-sectional intensity profile along the red-dashed lines. (F) The fabrication of pNIR4-PAE NPs with pH-responsive and targeting property. (G) Bioluminescence and NIR-Iia imaging of resected nodules of unguided and pNIR4-PAE NPs-guided groups. (H) NIR-IIa fluorescence images of sentinel lymph node (SLN) of pNIR-4 NPs (a), the colocalized color image of methylene blue (b), color (c) and NIR-IIa fluorescence (d) images of SLN extracted from the mouse guided by NIR-IIa fluorescence imaging of pNIR4 NPs. Reproduced with permission from Ref. [32]. Copyright (American Chemical Society), 2020.

small capillaries in the NIR-IIa region, while pNIR-3 NPs only imaged the blurry main vessels (Figure 19.9E). In order to enhance the tumor cell uptake efficiency, pNIR-4 was encapsulated by the mixed matrix of the pH-responsive PCL-*b*-PAE and PCL-*b*-PEG (Figure 19.9F). As shown in Figure 19.9G, the resected nodules under unguided surgery had large-diameter (> 1 mm). With the help of pNIR4-PAE NPs, the sub-millimeter tumor nodules could be excised under NIR-II intraoperative imaging. Furthermore, with the guidance of NIR-IIa imaging of pNIR-4 NPs, the sentinel lymph node (SLN) could be exactly detected and the smallest SLN (~1 mm) could be precisely dissected (Figure 19.9H). Overall, the pNIR-4 SPNs have great potential as an NIR-IIa probe for surgical navigation in the clinic.

19.3 Therapy

Thanks to their easy construction and modification, multifunctional AIE polymers have been synthesized and widely used in imaging-guided photodynamic therapy (PDT), photothermal therapy (PTT), chemotherapy, and so on.

19.3.1 PDT

PDT has attracted great attention among researchers in countering diseases due to the good biocompatibility, low side effects, and alleviation of patients' suffering. Light, oxygen, and photosensitizers are the main factors that influence the treatment effect [33, 34]. Considering the long-term biosafety, many organic materials have been explored for PDT. Compared to low mass molecular photosensitizers (PSs), AIE polymers, especially AIE-conjugated polymers, enjoy the advantages of high light-harvesting ability, high ROS generation ability, and easy multifunction, which ensure that AIE polymers are effective diagnostic and therapeutic PSs for antibacterial and antitumor therapy.

19.3.1.1 Antibacterial therapy

Bacterial infection is one of the biggest causes for serious damage to human health. The diseases caused by pathogenic bacteria can induce mild to severe symptoms and even death. Thanks to the excellent spatiotemporal accuracy, noninvasiveness, and anti-multidrug resistance properties, photodynamic antibacterial therapy has attracted wide attention. And the corresponding PSs based on AIE polymers have been designed and synthesized. At present, there are mainly three types of the constructive methods of AIE polymer PSs.

The first type is the directly modified, low mass molecular AIE PSs on the side chains of polymers. Liu, Wang, and coworkers [35] reported zwitterionic polyurethane nano-micelles (PU nano-micelles), which were composed of carboxybetaine as a shell and AIE PS as core in aqueous solution. These PU nano-micelles possess good biocompatibility and prolonged circulation time at neutral condition and without light irradiation. However, under white light irradiation and acidic conditions, these PU nano-micelles could image and kill all of *S. aureus*, MRSA, and *E. coli*. This was mainly because zwitterionic PU nano-micelles were positively charged under acidic condition, which enhanced the interaction between the PU nano-micelles and bacteria through electrostatic interaction, resulting in effective imaging and inhibition under white light irradiation.

As opposed to the first type of AIE polymer PSs, the second type was constructed through D-π-A conjugated polymers with AIE property. Compared to traditional low mass PSs, AIE conjugated polymers have high light-harvesting and enhanced ROS generation abilities. Qin, Tang, and coworkers [36] reported a benzothiadiazole and tetraphenylthene (TPE)-containing conjugated polymer (PTB-APFB) with D-π-A structure (Figure 19.10A). PTB-APFB had high ROS generation ability, which could be greatly enhanced when they formed the aggregates in aqueous solution. Compared to Ce 6 and low-mass MTBAPFB, the ROS generation efficiency of PTB-APFB showed 11- and 13-fold improvement, respectively (Figure 19.10B). Furthermore, PTB-APFB could not only bind with *S. aureus*, *E. coli*, and *C. albicans* efficiently, especially with *S. aureus* (Figure 19.10C), but could also selectively distinguish the microorganisms from the mammalian cells (Figure 19.10D). This ability of targeting the bacteria was mainly owing to the structure of PTB-APFB. The positively charged side chains of PTB-APFB made them readily bind with microorganisms through electrostatic interaction. And the well-balanced hydrophilicity and hydrophobicity of this polymer hindered interaction with mammalian cells. On the basis of above advantages, PTB-APFB could effectively inhibit the growth of *S. aureus* under white light irradiation or sunlight (Figure 19.10E) and exhibit quicker healing rate than the commercial Cefalotin in the inflammation model experiments (Figure 19.10F).

The third category is bacterium-templated polymer. Bacteria can selectively bind their own monomers and synthesize the corresponding polymers on their surfaces. Liu and coworkers [37] chose three specific monomers for bacterial templating – a permanent cation, AIE moiety, and a zwitterionic sulfobetaine, which could ensure their interaction with bacterial cell surface efficiently, along with AIE property and photosensitization (Figure 19.10G). Subsequently, bacterium-templated polymers could be obtained from the bacterial surfaces through copper-catalyzed atom transfer radical polymerization (ATRP). These polymers were not emissive in aqueous solution. However, when they were incubated with their exclusive bacteria, strong fluorescence signals could be detected even at a low concentration of 600 ng/mL. Furthermore, under white light irradiation, the generated ROS

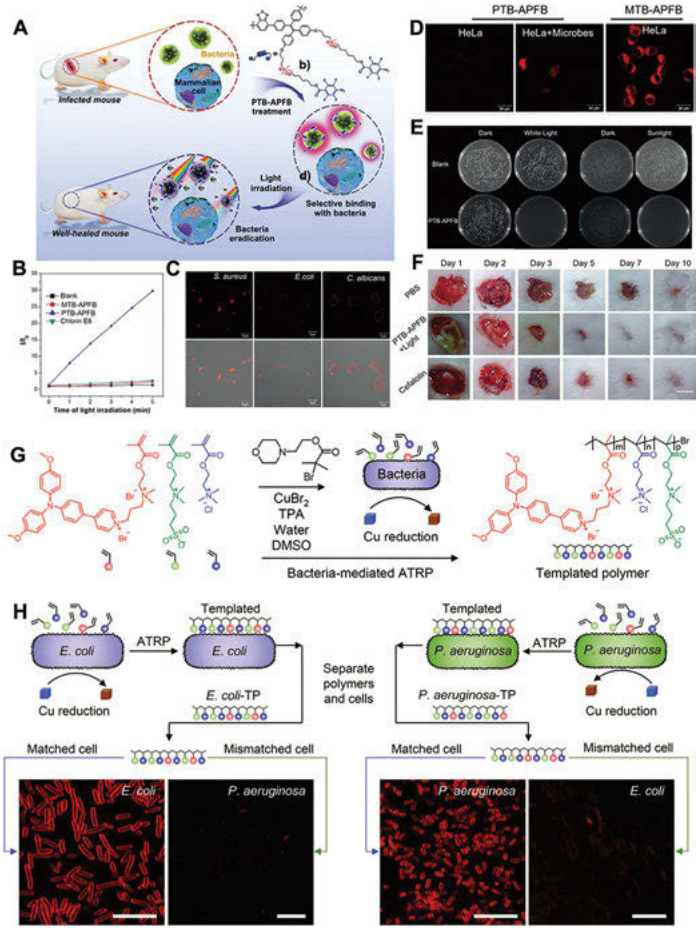

Figure 19.10: Antibacterial PDT of AIE polymers. (A) Chemical structure of PTB-APFB and its selective antibacterial application. (B) Relative fluorescence intensity of 2′,7′-dichlorofluorescein (DCFH) with addition of PTB-APFB, MTB-APFB and Ce 6, upon exposure to white light (10 mW/cm^2). (C) Fluorescent and merged CLSM images of *S. aureus*, *E. coli*, and *C. albicans*, respectively. (D) CLSM images of HeLa cells and mixed sample (HeLa cells + microorganisms) incubated with PTB-APFB or MTB-APFB, respectively. (E) Photographs of NB agar plate. (F) Photographs of the *S. aureus*-infected skin of mice treated with PBS, PTB-APFB + Light, and cefalotin, respectively. Reproduced with permission from Ref. [36]. Copyright (John Wiley & Sons Inc.), 2020. (G) Illustration of the templating process. (H) Schematic illustration of the bacteria-mediated polymer synthesis process. *E. coli* and *P. aeruginosa* were selected as templates to direct the synthesis of bacterium-templated polymers via ATRP. CLSM images of *E. coli* and *P. aeruginosa* after incubation with their templated polymers and mismatched polymers at a concentration of 600 ng/mL, respectively. Scale bars: 10 μm. Reproduced with permission from Ref. [37]. Copyright (WILEY-VCH Verlag GmbH & Co. KGaA), 2020.

could kill the bacteria. If bacteria and templated polymers were unmatched, fluorescence signal and selective ablation could not be found. In practical application, these bacterium-templated polymers not only realized the effective detection and ablation of *E. coli* and *P. aeruginosa* (Figure 19.10H), but were also suitable for the multidrug-resistant bacteria, BAK085 and SGH10. Therefore, this bacterium-templated method would be an alternative platform in developing practical materials for the specific therapeutic applications.

19.3.1.2 Antitumor therapy

Apart from chemotherapy, radiotherapy, and surgery, PDT would be an alternative treatment for cancer therapy. For in vivo tumor ablation, the light penetration depth, photosensitizing efficiency, and enrichment in the tumor site of PSs are the main key scientific issues. AIE polymers could provide a shortcut to solve these problems.

19.3.1.2.1 Polymerization-enhanced photosensitization

To improve the photosensitization efficiency of the organic photosensitizer, the strategy of "polymerization-enhanced photosensitization" has been put forward by Liu and coworkers [38, 39]. This strategy implies that conjugated polymers (CPs) can generate much higher photosensitization efficiency than their low-mass PSs. The proposed mechanism can be explained as follows. Generally, low mass molecular PSs have only one channel from the lowest singlet excited state (S_1) to the lowest triplet excited state (T_1) for intersystem crossing (ISC), while CPs contain a higher number of repeat units and relatively compact structure, which can decrease the energy levels of upper excited state (e.g., S_n and T_n) to get closer to the S_1 and T_1, offering more possible channels for ISC (Figure 19.11A). Moreover, the π-conjugated backbone structures of CPs enhance the light-harvesting ability, which can also improve the photosensitization efficiency. To verify the strategy, low mass molecular PSs SM1-SM4 and their corresponding CP1-CP4 were synthesized. As shown in Figure 19.11B, CP1-CP4 exhibited 5.06-, 5.07-, 1.73-, and 3.42-fold higher $^1O_2$ generation efficiency than SM1-SM4, respectively. Notably, SM1-SM3 and CP1-CP3 are AIE-active while SM4 and CP4 are not. These results have confirmed that the strategy of "polymerization-enhanced photosensitization" is feasible and universal. Moreover, CP1 showed a 3.71-fold higher $^1O_2$ generation than that of commercial PS Ce 6, which made CP1 a potential PS for practical applications. After encapsulation by DSPE-PEG, CP1 NPs had good biocompatibility and water solubility. Under white light irradiation, CP1 NPs could more effectively kill the 4T1 cancer cells than SM1 NPs and Ce 6 (Figure 19.11C). Thanks to the high Φ_F, CP1 had also exhibited the

ability of imaging-guided PDT in vivo (Figure 19.11D). Overall, this work has reference value for a rational photosensitizer design.

Furthermore, Tang and coworkers [40] reported that increasing the amount of electron acceptor (A) in the D-π-A CPs could further improve the photosensitization efficiency, which was named as D-A even-odd effect. The triphenylamine (T) as the electron-donor (D) and benzothiadiazole (B) as the electron-acceptor (A) were applied to synthesize four compounds, TBT (D-A-D), BTB (A-D-A), TBTBT (D-A-D-A-D), BTBTB (A-D-A-D-A) (Figure 19.11E). BTB and BTBTB with the amount of A > D exhibited an increased $^1O_2$ quantum yield (Φ_O) but a decreased Φ_F than TBT and TBTBT with the amount of D > A (Figure 19.11F). This was mainly because the A > D structure had a lower $\triangle E_{ST}$ than its D > A counterparts, which was proved by the time-dependent density functional theory (TD-DFT) calculations. Therefore, a combination of polymerization-facilitated photosensitization and D-A even-odd effect could largely improve the $^1O_2$ generation efficiency, which provides guidance for the design and synthesis of new and efficient PSs for biological application.

19.3.1.2.2 Two-photon-excited PDT

Another constraint for the efficient photodynamic tumor therapy is the light penetration depth. In solving this problem, two-photon-excited PDT (2PE-PDT) [41, 42] has attracted great attention due to their deep penetration depth and high spatiotemporal resolution for accurate cancer therapy. In general, 2 PA cross-section (σ2) and $^1O_2$ efficiency of PSs are the main influence factors for the effective 2PE-PDT [41]. For two-photon low-mass PSs, it is difficult to simultaneously enhance σ2 and $^1O_2$ efficiency. Then, Liu and coworkers [43] synthesized two AIE CPs PTPEDC1 and PTPEDC2 (Figure 19.12A). Low-mass molecular AIE PS of TPEDC was used as control. As shown in the Figure 19.12B, $^1O_2$ generation efficiency and σ2 were in the order of PTPEDC2 > PTPEDC1 > TPEDC. Moreover, all of them had higher $^1O_2$ generation efficiency than Ce 6. The TD-DFT revealed that compared with TPEDC, PTPEDC2 and PTPEDC1 had denser energy levels of both singlet and triplet states due to their π-conjugated structures, which could increase the ISC channels and facilitate more $^1O_2$ generation. In addition, owing to the flatter conjugated structure than PTPEDC1, PTPEDC2 had closer energy levels, which endowed this polymer with higher $^1O_2$ generation efficiency and σ2 than PTPEDC1. After modification of cell penetrating peptide (TAT-SH), PTPEDC2 TAT dots exhibited the strongest cancer-cell-killing effect, as compared to PTPEDC1 TAT dots and TPEDC TAT dots (Figure 19.12C). Furthermore, PTPEDC2 TAT dots realized the tumor ablation in the zebrafish liver cancer model (Figure 19.12D).

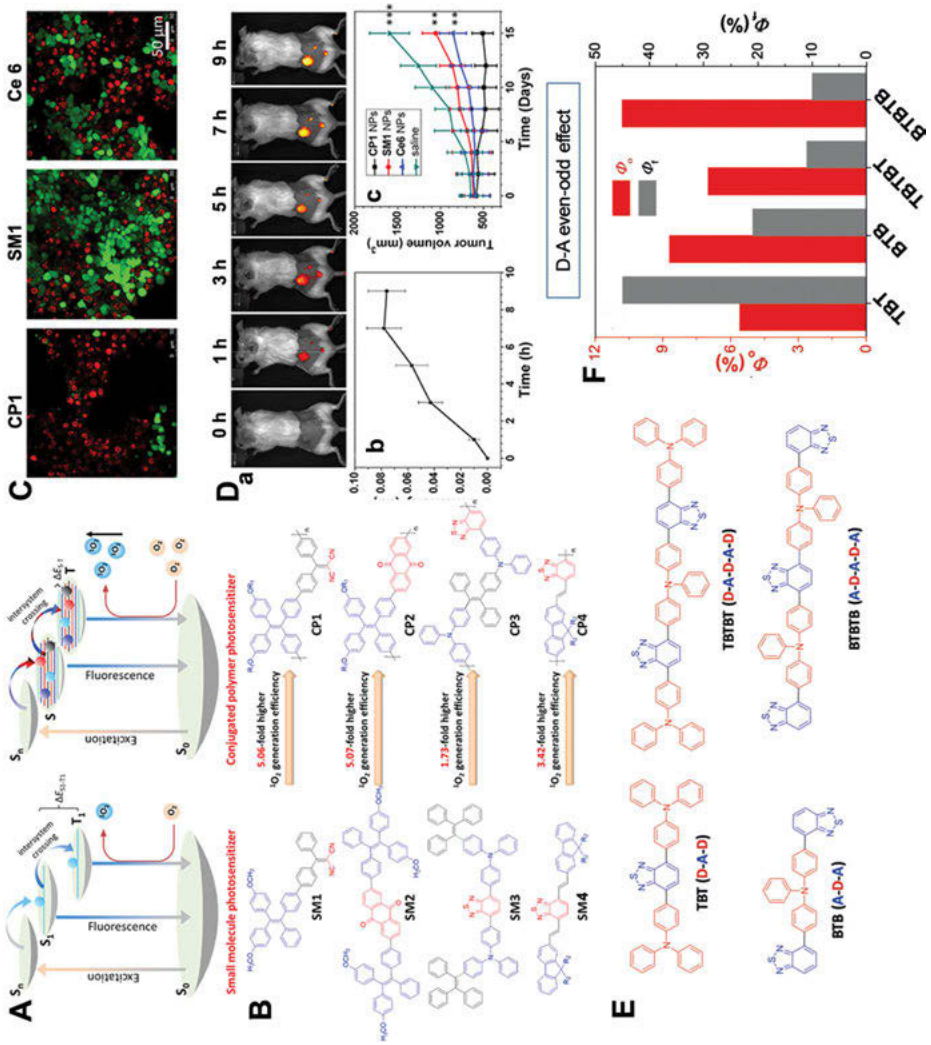

Figure 19.11: The strategy for enhancing photosensitizing efficiency. (A) The different photosensitization processes of small molecular photosensitizer and conjugated polymer photosensitizer. (B) The chemical structures of small molecules SM1-SM4 and conjugated polymers CP1-CP4. (C) Live (fluorescein diacetate, green) and dead (propidium iodide, red) staining of 4T1 cancer cells treated by CP1 NPs, SM1, and Cᴇ 6, respectively. Scale bars: 50 mm. (D) Time-dependent in vivo fluorescent images of 4T1 tumor-bearing mouse after injection with CP1 NPs (a). (b) Average fluorescence intensity of mice tumors based on (a). (c) Tumor volume measurement of different groups of mice after PDT. Reproduced with permission from Ref. [38]. Copyright (John Wiley & Sons Inc.), 2018. (E) Chemical structures of TBT (D-A-D), BTB (A-D-A), TBTBT (D-A-D-A-D), and BTBTB (A-D-A-D-A). (F) $^1O_2$ quantum yield (Φ_o) and fluorescence quantum yield (Φ_F) of TBT, BTB, TBTBT, and BTBTB. Reproduced with permission from Ref. [40]. Copyright (John Wiley & Sons Inc.), 2018.

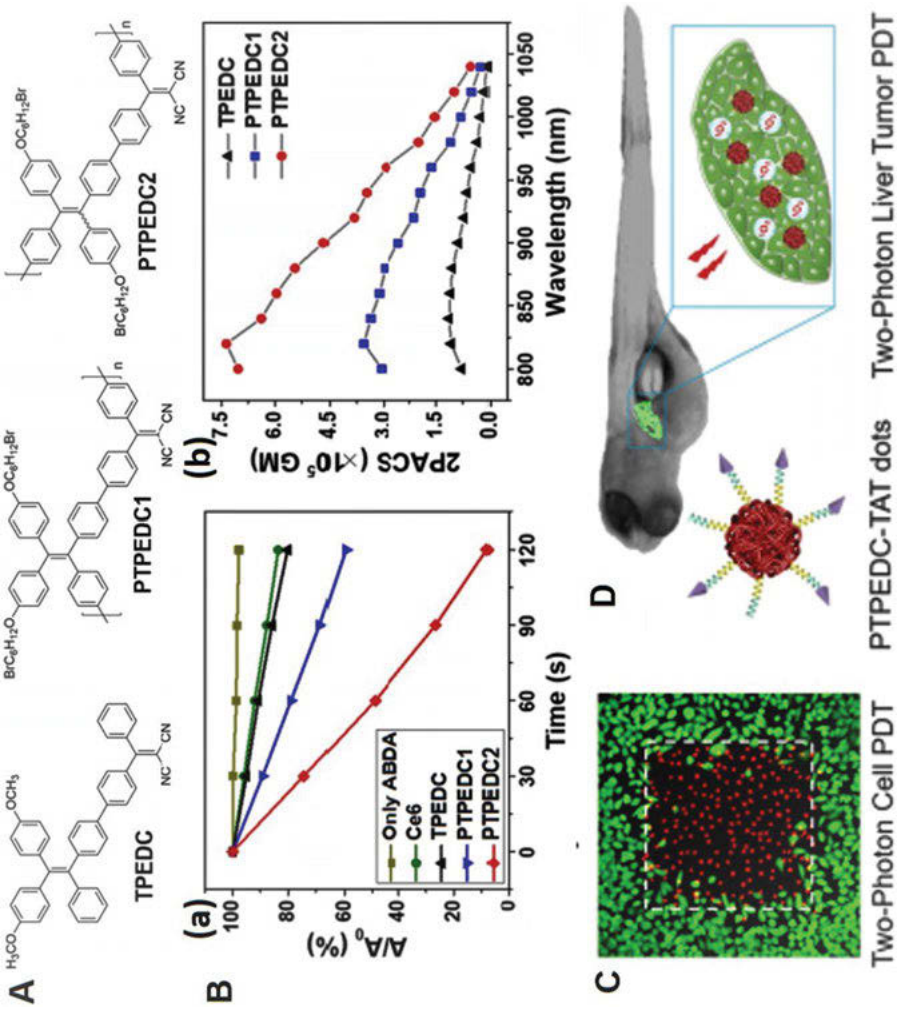

Figure 19.12: Two-photon-excited PDT. (A) Chemical structures of TPEDC, PTPEDC1, and PTPEDC2. (B) (a) Normalized degradation percentages of ABDA aqueous media in the presence of PS dots upon white light irradiation (50 mW/cm^2). (b) Two-photon absorption cross-section spectra of TPEDC, PTPEDC1, and PTPEDC2. (C) Two-photon cell PDT of PTPEDC2 dots. Excitation: 488 nm (for fluorescein diacetate) and 559 nm (for propidium iodide). (D) Schematic illustration of in vivo two-photon liver tumor PDT of zebrafish liver tumor model treated with PTPEDC2-TAT dots. Reproduced with permission from Ref. [43]. Copyright (American Chemical Society), 2019.

19.3.1.2.3 Targeting PDT

By matching the localization structure of organelles, AIE polymers with organelles targeting could be designed. Zhou, Lou, Zhao, and coworkers [44] reported three new red conjugated polyelectrolytes (CPEs) consisted of TPE and 2, 1, 3-benzothiadiazole in the main chain and triphenylphosphonium in the side chain (Figure 19.13A). The conjugated structure and triphenylphosphonium endowed these CPEs with high Φ_F and mitochondrial targeting ability, which permitted them for long-term FLI in vivo, up to 20 days (Figure 19.13B). In addition, these CPEs had good biocompatibility and strong ROS generation ability under white light irradiation, which could effectively inhibit the growth of subcutaneous tumors and prolong the survival time of liver cancer tumor-bearing mice. Therefore, the introduction of mitochondrial targeting groups to the AIE polymers would be a facile strategy to construct the AIE polymer PSs for long-term FLI-guided PDT, which could improve the utilization rate of ROS and reduce the damage to normal tissues.

Based on the hypoxia environment of tumor tissue, Li and coworkers [45] designed a hypoxia-mediated PEGylated AIE polymer PSs (PEG-azo-PS4). The AIE PS part (AAPS) was conjugated to the PEG chain through azo bond, which could be cleaved in hypoxia conditions. Under normal conditions, the hydrophilic and biocompatible PEG-azo-PS4 hardly emitted and generated $^1O_2$ due to energy dissipation through intramolecular rotation and vibration, which ensured good biosafety. When these AIE polymer PSs accumulated in the tumor, the azo bond could be cleaved by hypoxia conditions, which could lead to the aggregation of the hydrophobic AAPS to emit fluorescence for the detection of hypoxia levels in living cells (Figure 19.13C). Due to the acidic environment, the amino group of the end of AAPS could be protonated, which facilitated them to target the mitochondria for specific tumor imaging. In addition, the AAPS aggregates could generate ROS under white light irradiation to realize the tumor ablation in vitro and in vivo. This hypoxia-mediated tumor-targeting imaging and ablation could also realize the specific diagnosis and treatment of tumor.

19.3.2 NIR-II FLI-guided PTT

Apart from the PDT effect, AIE conjugated polymers can be designed with the PTT effect. Recently, Gong, Zhang, Cai, Tang, and coworkers [46] synthesized a NIR-II AIE-conjugated polymer, PBPTV, which was coated by a natural kill cell membrane to obtain the NK@AIEdots (Figure 19.14A). Due to the AIE property, NK@AIEdots had high NIR-II fluorescence intensity, with Φ_F of 7.9% and a photothermal conversion rate as high as 45.3%. Natural kill cell membrane could not only improve the blood-brain barrier (BBB) permeability of NK@AIEdots, but also could enhance the uptake of NK@AIEdots by glioma cells. The reason could be that natural kill cell membrane could be a tight-junction (TJ) modulator to cause TJ disruption and actin

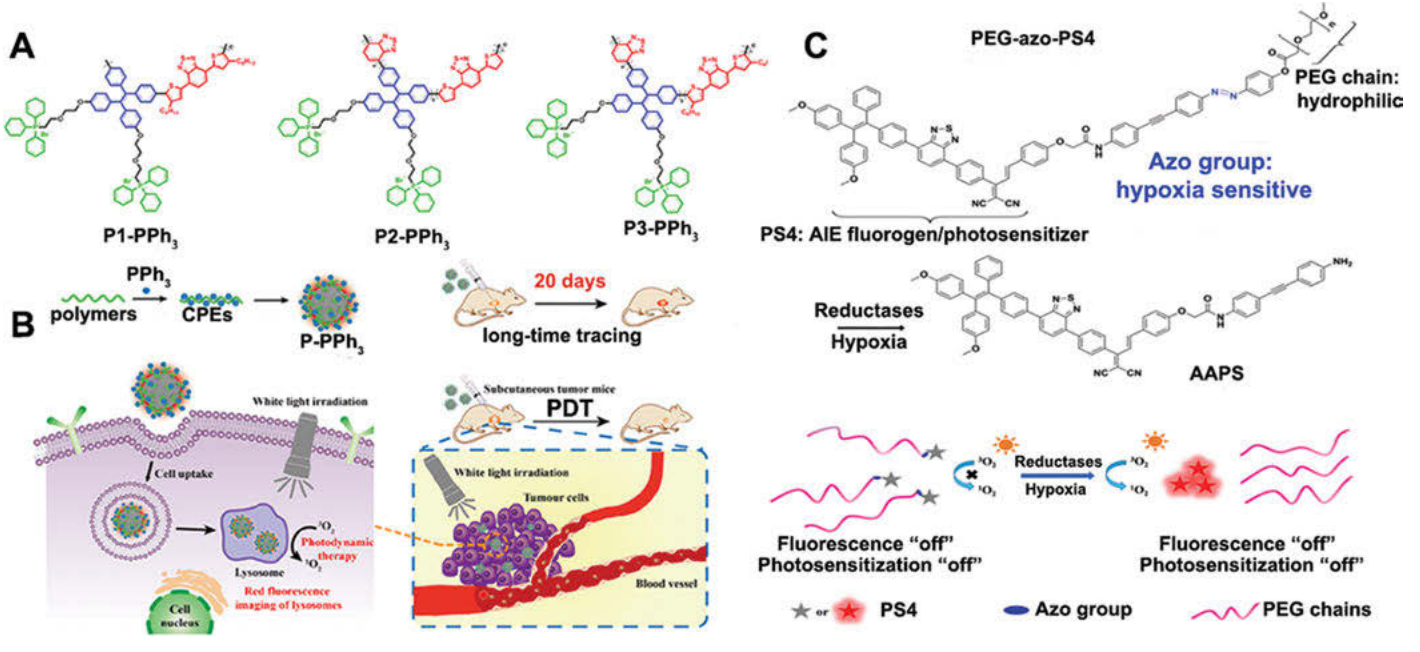

Figure 19.13: Targeting photodynamic therapy. (A) Molecular structure diagram of CPEs. (B) Schematic illustration of CPEs for in vitro fluorescence imaging, in vivo long-term tracing and photodynamic therapy of tumors (color online) [44]. Reproduced with permission from Ref. [44]. Copyright (Springer Nature), 2020. (C) Schematic illustration of the cleavage reaction and the hypoxia-mediated fluorescence emission/photosensitization of the PEG-azo-PS4 molecule [45]. Reproduced with permission from Ref. [45]. Copyright (The Royal Society of Chemistry), 2021.

cytoskeleton reorganization to form an intercellular "green channel," which helps NK@AIEdots cross BBB silently. As shown in the Figure 19.14B, at 6 h after intravenous injection of NK@AIEdots, the bright through-skull NIR-II fluorescence signal in the brain matrix was observed and approached a maximum at 24 h post-injection. However, there was no fluorescence signal found in the control AIE dots group. Under the guidance of NIR-II imaging, tumor ablation was carried out with 808 nm laser irradiation at 24 h post-injection. Compared to other control groups, NK@AIEdots, under 808 nm laser irradiation, exhibited obvious tumor inhibition (Figure 19.14C and 19.14D). Therefore, NK-cell-mimetic nanorobots showed highly efficient BBB-penetration ability, which provided the potential platform to target drug delivery for brain-related disease therapy.

19.3.3 AIE-drug polymers

Apart from PDT and PTT, chemotherapy is one of the traditional treatments applied to fight against disease, which was mainly restricted by the efficacy of the drug and the dose in reaching the target. Precise drug delivery is a scientific issue that needs to be solved. In general, amphiphilic AIE polymers easily form the micelles, which help them load drugs through noncovalent or covalent interaction. Some tumor microenvironment (TME)-responsive bonds could be introduced in the backbone or side chains of AIE polymers to release the drug at the tumor site, which could not only ensure biocompatibility but also realize the visualization and targeting of drugs. Therefore, exploring the interaction of AIE polymers and drugs is very meaningful and imperative.

19.3.3.1 Single-stimulus-responsive drug delivery

Developing "visible" drug delivery systems to target drug release has attracted great attention in the field of drug delivery polymers. AIE polymer can not only be designed for various stimuli-responsive micelles but can also realize the visualization. As we all know, TME is characterized by low pH and hypoxia and has a large content of reductase and H_2O_2 compared with normal tissues. Based on these properties of TME, a lot of TME-responsive AIE polymers have designed to deliver drugs.

One strategy of TME-responsive AIE polymers in loading the drug is through noncovalent interaction. Pan, Zhu, and coworkers [47] reported AIE polymer gels ($SeSe_y$-PAA-TPE_x) via free radical polymerization (Figure 19.15A). These gels contained the diselenide-crosslinker, which could be fragmented in the presence of H_2O_2 or dithiothreitol (DTT). The $SeSe_y$-PAA-TPE_x gels could load the DOX with a loading efficiency of 62.1%. Under conditions of H_2O_2 or redox agent, the blue fluorescence gradually enhanced with the DOX release, realizing the visualization of

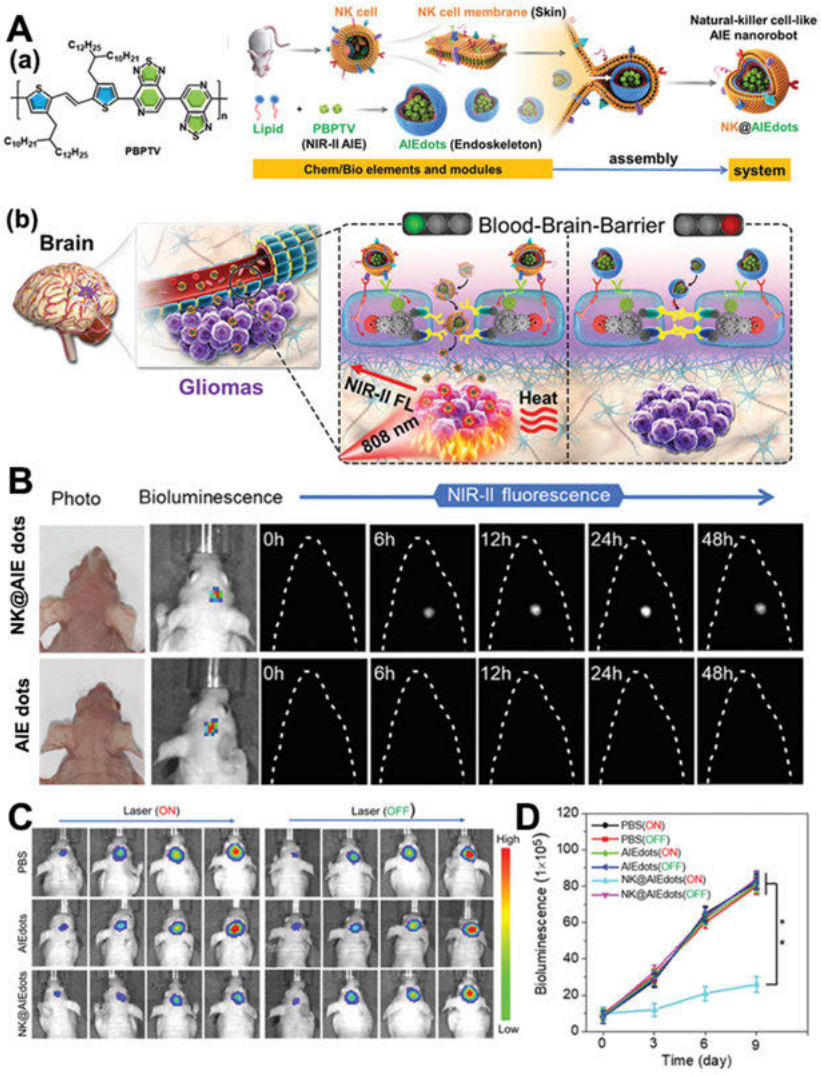

Figure 19.14: NIR-II fluorescence imaging guided PDT. (A) (a) The structure of NIR-II AIE polymer PBPTV and the preparation and assembly process of NK@AIEdots. (b) The "smart" tight-junction (TJ)-modulated BBB penetration of NK@AIEdots for brain tumor targeted imaging and inhibition. (C) Bioluminescence imaging monitored the brain tumors. And NIR-II fluorescence images of mouse brain through intact scalp and skull, under 808 nm illumination with NK@AIEdots and AIEdots administration at different time points, post-injection. (D) Representative in vivo bioluminescence images of orthotopic glioma at different time points after photothermal therapy. (E) Quantitative analysis of in vivo bioluminescence signals at different time points in the tumor site. Single asterisks indicate $p < 0.05$, and double asterisks indicate $p < 0.01$. Reproduced with permission from Ref. [46]. Copyright (American Chemical Society), 2021.

drug release. Lu, He, and coworkers [48] also reported a H_2O_2-responsive AIE polymer containing TPE unit and benzil moiety (TPG1). It has been well confirmed that the benzil groups could react with H_2O_2 through Baeyer-Villiger reaction to generate TPG2 with a benzoic acid residue, which was unstable in the presence of H_2O_2 (Figure 19.15B). This AIE polymer could self-assemble into micelles in aqueous solution, which could load DOX, with a loading capability of up to 59% by weight. The benzil moiety could be cleaved by H_2O_2, leading to the decomposition of TPG1 micelles and DOX release. Due to the disruption of the FRET process, the fluorescence of TPE enhanced, which could monitor the DOX release process. In addition to the H_2O_2 and redox-responsive AIE polymers, Zhang, Zhao, and coworkers [49] reported an amphiphilic block copolymer (CH_3O-PEG_{43}-b-P(AA-g-TPE)) (Figure 19.15C), which was modified with the TPE moieties through esterification. TPE segments as the functional hydrophobic chain could induce self-assembly of this polymer into micelles and further luminescence for DOX delivery and tracking. Meanwhile, the ester linkage endowed the polymeric micelles with enzyme responsiveness. In the presence of esterase, this polymer could collapse and release the DOX to realize the targeted treatment.

H_2S as an important signal molecule plays a key role in vasorelaxation, anti-inflammation, and anti-cancer. Lu and coworkers [50] reported a self-fluorescent polymeric H_2S-donor system, PFHMA-g-PEG/SBTHA via RAFT polymerization and post-modification (Figure 19.15D). The property of fluorescence came from the formation of salicylaldazine AIE fluorogens, which made this polymer visible in solution and living cells. Thanks to the PEG side chains, this polymer was water-soluble and biocompatible. In the presence of cysteine or glutathione, this polymer could release H_2S slowly, with a ~55 min peak time at 1 mM cysteine or ~70 min peak time at 1 mM glutathione, respectively. This result indicated that the release of H_2S required high concentration of cysteine or glutathione, which exceeded the average level of cysteine concentration (10 μM) in real human plasma.

19.3.3.2 Multiple stimuli-responsive drug delivery

Compared with single-stimulus response, multi-stimuli response has attracted more and more attention in realizing multifunction, apart from drug delivery. Han, Gao, and coworkers [51] reported such an AIE polymer, PEG-Pep-TPE. They chose the FFKY peptide as the bridge. One end was linked with PEG by disulfide bond, ensuring water-solubility and GSH response. The other end was conjugated with TPE by the imine linkage (-HC = N-) for the AIE property and pH response. This amphiphilic polymer could form the micelles that load the DOX (named as PEG-Pep-TPE/DOX NPs) (Figure 19.16A). Under UV irradiation, due to the FRET effect, red fluorescence of DOX could be detected. As is well known, cancer cells have higher concentration of GSH and lower pH compared to normal cells. When PEG-Pep-TPE/DOX NPs was

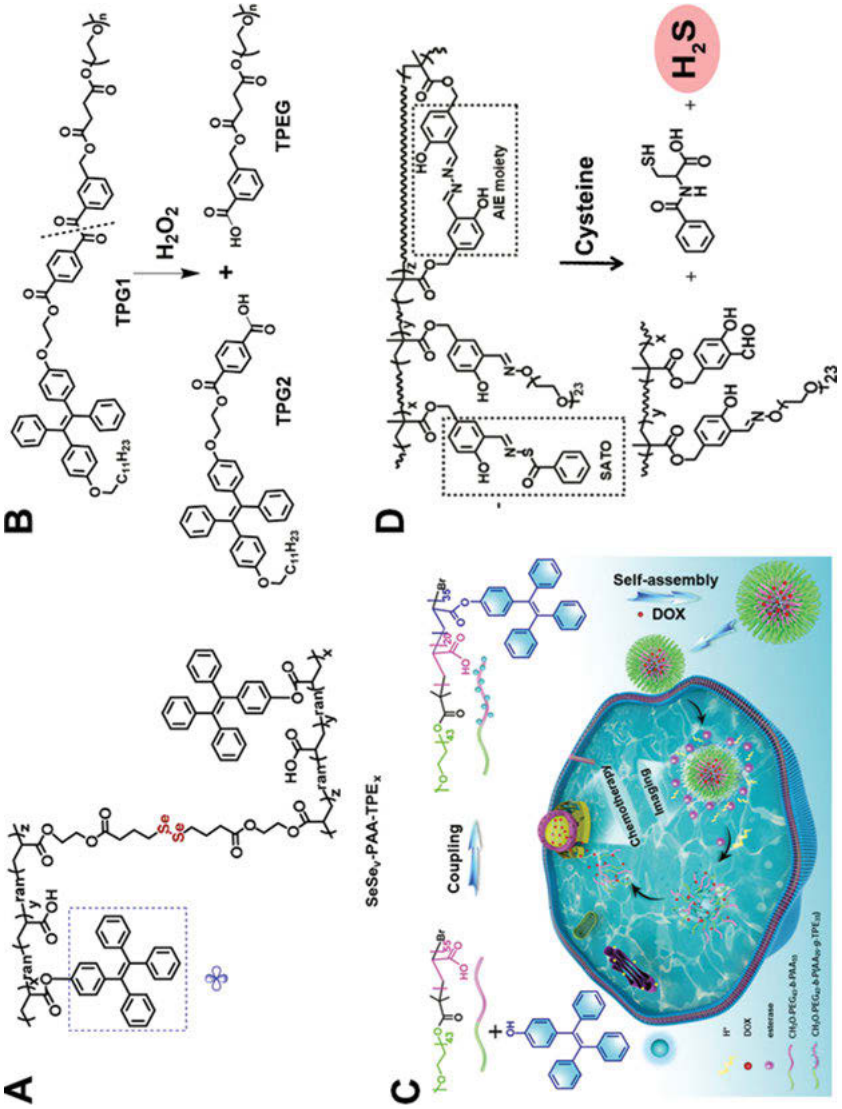

Figure 19.15: Responsive drug delivery of AIE polymers. (A) Redox-responsive AIE polymer gel $SeSe_y$-PAA-TPE_x with diselenide bonds. (B) H_2O_2-responsive AIE polymer TPG1 that could be cleaved by H_2O_2 into TPG2 and TPEG. Reproduced with permission from Ref. [48]. Copyright (The Royal Society of Chemistry), 2019. (C) The synthesis and self-assembly of block copolymer, and enzyme-responsive drug release from polymeric micelles. Reproduced with permission from Ref. [49]. Copyright (The Royal Society of Chemistry), 2020. (D) The structure of self-fluorescent polymeric H_2S-donor and the release of H_2S under cysteine triggeration. Reproduced with permission from Ref. [50]. Copyright (The Royal Society of Chemistry), 2018.

incubated with A549 cells for more than 3 h, the blue fluorescence intensity of TPE gradually became stronger, and more DOX molecules were observed in the nucleus (Figure 19.16B), indicating that the FRET effect gradually disappeared. Meanwhile, due to the crack of disulfide bond and imine bond, the FFKY peptide could self-assemble into nanofiber, which could arrest the assembly of actin in the cytoplasm and even damage the existing actin filaments in cells (Figure 19.16C). Therefore, PEG-Pep-TPE/DOX NPs may provide a potential strategy for stimuli-responsive imaging-guided combination therapy.

In addition, Li, Wang, and coworkers [52] also reported GSH redox/pH dual-responsive polymeric micelles mPEG-P(TPE-co-AEMA) through the RAFT polymerization (Figure 19.16D). TPE units were incorporated into the polymer chain by disulfide bonds for GSH redox response, which was mainly responsible for visualizing nanocarriers. The 2-azepane ethyl methacrylate (AEMA) moieties were pH-sensitive. When the pH was lower than 6.8, the hydrophobic AEMA could convert rapidly to hydrophilic groups by protonation. This was beneficial for accumulation in the tumor and uptake by cancer cells. After encapsulation of the DOX through the π–π stacking and hydrophobic interaction between TPE and DOX, this polymer could achieve the dual-color drug release and tracing (Figure 19.16E). The encapsulated DOX could be released at targeted site, which alleviated the side effects of drugs and improved survival rate.

To improve the deep penetration depth, they changed the TPE units into two-photon fluorophore with AIE property [53]. In addition, pH-responsive charge-converted units of dimethylmaleic anhydride (DA) were also conjugated into the polymer through the introduction of PEI chains, to obtain PAEEBlink-DA micelles (Figure 19.16F). These micelles could also encapsulate the DOX with a stealth property in the blood circulation. When these micelles accumulated at the tumor acidic environment through EPR effect, the DA units were triggered from negative to positive charge, which could enhance the internalization. Meanwhile, PAEMA chains were converted from hydrophobicity to hydrophilicity to accelerate the DOX release and expansion of micelle size. This tumor-responsive drug release could reduce the side effects and realize the targeting therapy. Due to the two-photon property, at 12 h after injection of these micelles without DOX, the fluorescence of liver and kidney at the depth of 150 μm could be observed under 800 nm two-photon excitation by CLSM (Figure 19.16G). Therefore, this DOX-loaded PAEEBlink-DA system holds great promise in cancer theranostic applications.

They further synthesized another AIE polymer of PMPC-*b*-P(DEMA-*co*-SS-GEM-*co*-TPMA) through RAFT polymerization (Figure 19.17A) [54]. This polymer was covalently conjugated with the gemcitabine (GEM) drugs in the side chains through GSH-redox disulfide bonds. PDEMA is a pH-responsive group, which could convert the charge and solubility from hydrophobicity to hydrophilicity under lysosome pH-triggering. Due to the amphiphilicity, this copolymer could self-assemble into micelles with the size of 53.4 nm in the physiological conditions, which facilitated

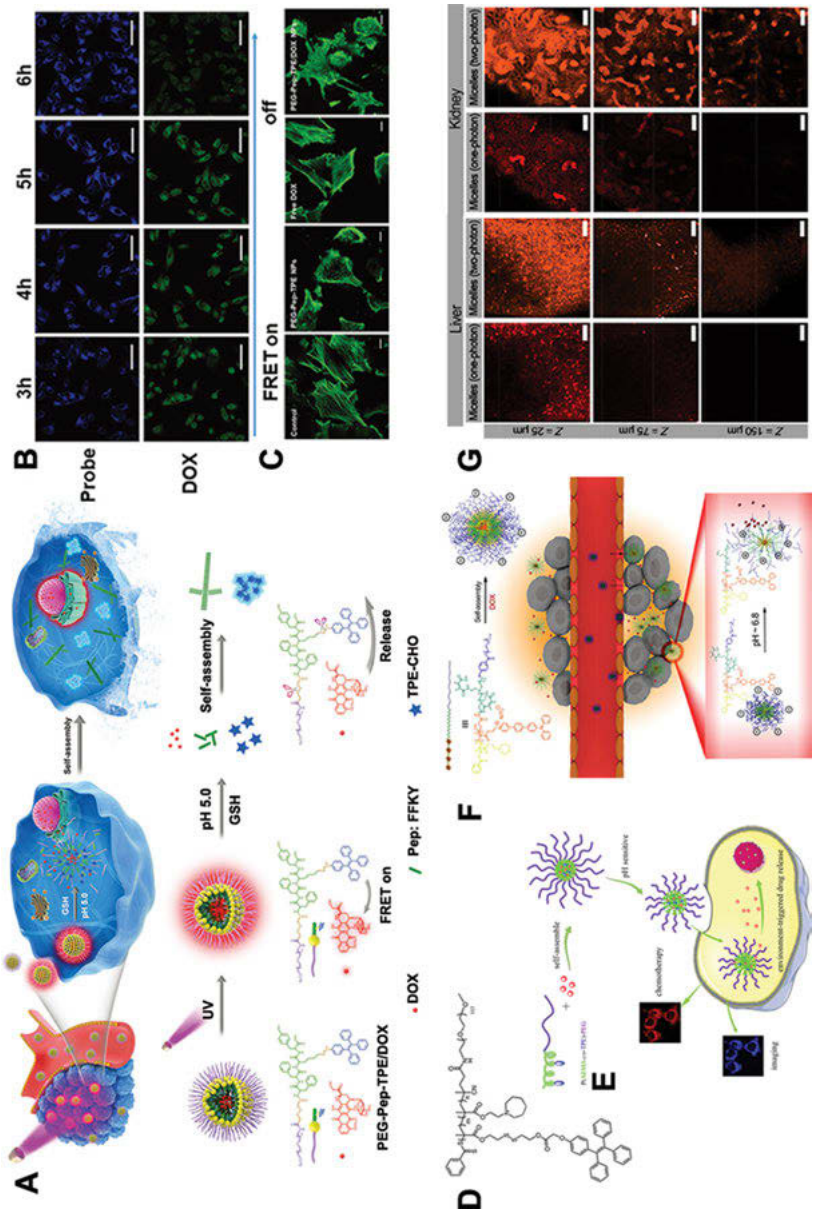

Figure 19.16: Multi-stimuli-responsive drug delivery. (A) Schematic illustration of pH/GSH-responsive drug tracking and synergistic chemotherapy. (B) CLSM images of A549 cells incubated with the PEG-Pep-TPE/DOX NPs and DOC for different time points at a dose of 10 μg/mL (DOX). Scale bars: 20 μm in all images. (C) Confocal images of cell actin filaments stained with Rhodamine Phalloidin. Scale bars: 20 μm. Reproduced with permission from Ref. [51]. Copyright (The Royal Society of Chemistry), 2020. (D) The structure of P(TPE-co-AEMA)-PEG. (E) Illustration of PEG-P(TPE-co-AEMA) micelles loading DOX for pH and redox-responsive drug release and

passive targeting to tumor by EPR effect. Subsequently, the low pH and high GSH concentration in the tumor microenvironment made these micelles more internalized by cancer cells and release the GEM drug, resulting in the two-photon-excited FLI-guided chemotherapy with high inhibition rate and reduced side effects. Overall, the TME-responsive AIE polymers loading drugs could help the visualization of drug delivery and largely improve the therapeutic effect in vitro and in vivo, which is of great significance in exploring the interaction between the drug and disease process.

19.3.4 Light-activated combination chemotherapy

Combining the abovementioned noncovalent and covalent interaction between AIE polymer and drug, Yu, Zhou, and coworkers [55] designed and synthesized a poly-prodrug polymer of PtAIECP (Figure 19.17B). Visible light-activated Pt(IV) prodrugs and TPE were embedded into the backbone of PtAIECP by copolymerization. PEG chains at both ends made this polymer water-soluble. Then, DOX could be encapsulated in nanoparticles by the π–π interaction with TPE to form the PtAIECP@DOX NPs. Due to the FRET effect between TPE and DOX and the ACQ effect of DOX, bare fluorescence could be observed. After white light irradiation, the photoactivation of the Pt(IV) prodrug induced the dissociation of PtAIECP@DOX NPs to release DOX. This readily turned on the blue fluorescence of TPE and red fluorescence of DOX, resulting in the dual-color monitoring drug delivery. Furthermore, with the visible light-activated property and combined chemotherapy of Pt(Iv) and DOX, PtAIECP@-DOX NPs realized better therapeutic effect than single-drug chemotherapy of PtAIECP in vitro and in vivo.

19.3.5 Redox-responsive combination chemo-PDT

Combination of different therapeutic modalities is also an effective strategy in fighting against cancer. However, the limitation of intracellular drug delivery system would restrict the effect of combined chemo-PDT. To overcome this obstacle, recently, Lou, Xia, Tang, and coworkers [56] reported a self-guiding combination therapy based on chemo drug PTX and PDT, with two AIE PSs (Figure 19.18). An amphiphilic block polymer,

Figure 19.16 (continued)
bioimaging. Reproduced with permission from Ref. [52]. Copyright (American Chemical Society), 2018. (F) Illustration of P(TPMA-co-AEMA)-PEI(DA)-Blink-PEG micelles loading DOX with pH-triggered charge-conversion property for drug delivery and the two-photon bioimaging. (G) Two-photon-excited CLSM images of the liver and kidney tissues with different penetration depth. Scale bars: 100 μm. Reproduced with permission from Ref. [53]. Copyright (Tsinghua University Press and Springer Nature), 2019.

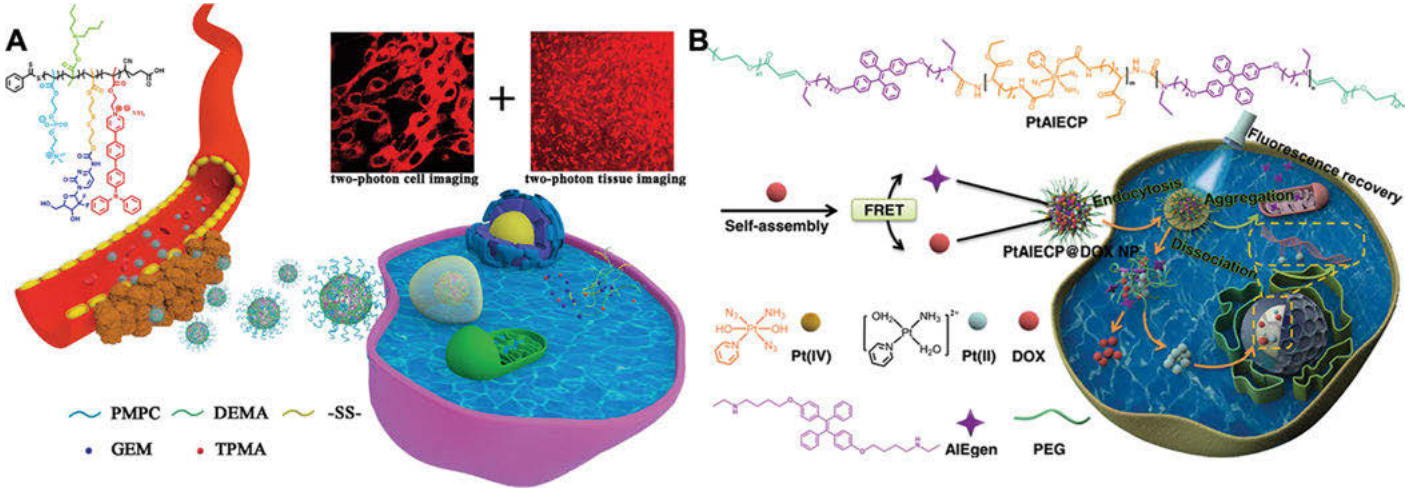

Figure 19.17: Covalent conjugation of AIE polymers and drugs. (A) Redox and pH-responsive PMPC-b-P(DEMA-co-SS-GEM-co-TPMA) copolymer micelles for AIE-active two-photon imaging and chemotherapy. Reproduced with permission from Ref. [54]. Copyright (American Chemical Society), 2019. (B) Light-activatable Pt(IV) prodrug PtAIECP with AIE property loading DOX for dual-color monitoring dual-drug release and combination therapy. Reproduced with permission from Ref. [55]. Copyright (American Chemical Society), 2019.

PEG-b-PMPMC (PM), was used as the backbones. Redox-responsive PTX (PTX-ss-N3) and AIE PSs (λ_{em} = 583 nm) were introduced into the polymer through Cu(I)-catalyzed azide-alkyne click reaction, and the polymeric prodrug PEG-b-PMPMC-g-PTX-g-PyTPE (PMPT) was eventually obtained. Owing to its amphiphilicity, this polyprodrug could self-assemble into micelles, which was used in loading another AIE PS TM (λ_{em} = 684 nm) to obtain TM@PMPT micelles. These micelles have good biocompatibility without light irradiation. When they passively targeted the tumor site, the first white light (L_1) irradiated for 6 min and the effective ROS could destroy the cell membrane, which facilitated the cell uptake of TM@PMPT micelles. Thereafter, the abundant GSH in tumor cell cytoplasm could crack the disulfide bonds to release the PTX, which reduced the hydrophobicity of these polymers, leading to the dissolution of these micelles and the release of TM. In this process, the dispersion of PyTPE promoted free rotation, which declined the AIE effect, while for TM, the fluorescence was barely affected. Based on the increase of the ratio of I_{TB}/I_{PyTPE}, the second white light (L_2) could be guided to irradiate the tumor cells for another 18 min. The cancer cells could be effectively killed but no harm was caused to normal cells. Furthermore, in vivo combined chemo-PDT results also indicated that TM@PMPT micelles ($L_1 + L_2$) had better inhibition effect than other control groups. Overall, the redox-responsive release of PTX and dual-stage light irradiation strategy of TM@PMPT exhibited enhanced chemo-PDT, which would inspire more valuable ideas to overcome the obstacles in combination therapy.

19.3.6 Killing of intracellular bacteria (ICB)

The treatment of intracellular bacteria (ICB) is another problem for the antibacterial agents that demanded drugs must be ingested by cells and should then target the ICB to destroy them. To solve these problems, Li and coworkers [57] have reported a mannose-containing AIE polymer of Man-*g*-P(EPE-*r*-TPE) to load the targeting antibiotics deferoxamine-ciprofloxacin conjugates with Fe^{3+} ($D_{Fe}C$) to obtain mPET@$D_{Fe}C$ NPs. The TPE units in the main chains made this polymer with AIE activity and hydrophobicity. The mannose moieties as the targeting groups were grafted into this polymer through the PEG chains. These groups were on the surface when this polymer self-assembled into micelles, which could encapsulate the $D_{Fe}C$ (Figure 19.19A). Due to the FRET effect, the blue fluorescence of TPE was quenched by the $D_{Fe}C$. It is well known that intracellular lipase and ALP levels would increase when cells are infected by the bacteria. Therefore, the ester and phosphoester bonds of mPET@$D_{Fe}C$ could be cleaved by these lipase and ALP to release $D_{Fe}C$ and help in recovery of the emission of TPE units. As shown in Figure 19.19B, the blue fluorescence of the bacteria-infected macrophages imaged by CLSM gradually increased with the increase of incubated time, while rare blue fluorescence of normal macrophages was observed, which indicated mPET@$D_{Fe}C$ could target the ICB by mannose-mediated endocytosis

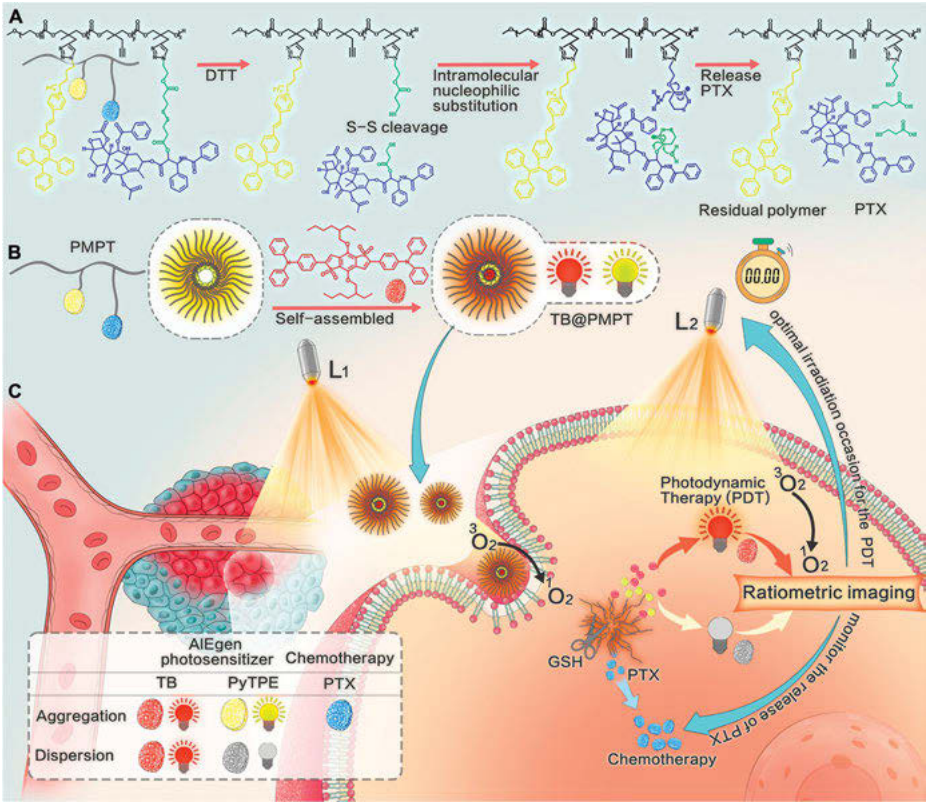

Figure 19.18: Self-guided combination of chemo-PDT. (A) The mechanism of PTX release from polymeric prodrug PMPT. (B) The encapsulation of another AIE PS TM into self-assembled PMPT micelles to obtain TM@PMPT by hydrophobic interaction. (C) Illustration of self-guided chemo-PDT for promoting cellular uptake under the first light irradiation (L_1) to combination therapy of PTX and PDT with the second light irradiation (L_2). Reproduced with permission from Ref. [56]. Copyright (American Chemical Society), 2021.

and further release the drugs. Due to the disappearance of FRET effect, the fluorescence of TPE recovered. Furthermore, mPET@D_{Fe}C showed an obvious fatality rate of *S. aureus*-infected Raw 264.7 cells, compared to other control groups (Figure 19.19C), which was owing to the effective intracellular uptake and enzyme-responsive drug delivery. Moreover, *S. aureus*-injected mice had about 100% survival rate after treatment with mPET@D_{Fe}C, while only 66% of injected mice survived with the injection of PET@D_{Fe}C, indicating mPET@D_{Fe}C could effectively eliminate the infection-caused tissue toxicities (Figure 19.19D). Moreover, mPET@D_{Fe}C had good biocompatibility and biosafety for other tissues, especially the liver and kidney. Therefore, this would be a feasible strategy for using in enzyme-responsive and traceable release of antibiotics for ICB therapy.

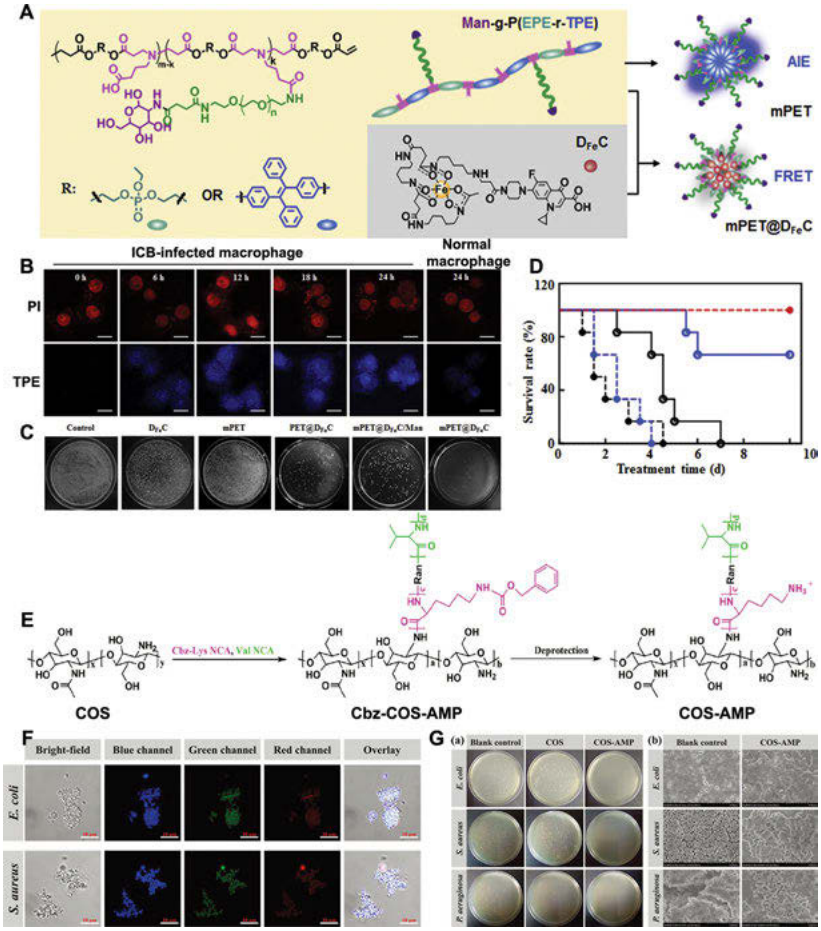

Figure 19.19: Targeting AIE polymer loading $D_{Fe}C$-antibiotics and unconventional polymer for antibacterial therapy. (A) Molecular structure of Man-g-P(EPE-r-TPE) and $D_{Fe}C$ and the assembly into mPET and mPET@$D_{Fe}C$ nanoparticles. mPET nanoparticles exhibit blue fluorescence due to the AIE of TPE segments, and the FRET effect between mPET and $D_{Fe}C$ causes the fluorescence quenching of mPET@$D_{Fe}C$ nanoparticles. (B) CLSM images of PI-stained dead ICBs (red), and blue fluorescence of TPE was gradually increased with increased incubation time of mPET@$D_{Fe}C$, while very weak blue fluorescence was found in normal macrophages even at 24 h. (C) Photographs of LB agar plates for counting bacterial colonies extracted from macrophages after different treatment for 24 h. (D) Survival rates of ICB-infected mice after treatment with PBS, free $D_{Fe}C$, mPET, PET@$D_{Fe}C$ and mPET@$D_{Fe}C$ nanoparticles. Reproduced with permission from Ref. [57]. Copyright (Elsevier), 2020. (E) Synthesis route of COS-AMP. (F) CLSM images of *E. coli* and *S. aureus* after incubation with COS-AMP (300 μg/mL) for 12 h. (G) Colony forming units of *E. coli*, *S. aureus*, and *P. aeruginosa* before and after treatment with COS and COS-AMP. Morphology of *E. coli*, *S. aureus*, and *P. aeruginosa* before and after treatment with COS-AMP. Reproduced with permission from Ref. [59]. Copyright (WILEY-VCH Verlag GmbH & Co. KGaA), 2020.

19.3.7 Antimicrobial peptide

Antimicrobial peptide (AMP) polymers have made great progress and mainly focus on the interaction of peptide and the cell membrane of bacteria [58]. However, the bacterial cell wall that contains a layer of peptidoglycan directly influences the interaction of antibacterial drugs and bacteria. Chitosan has garnered great attention due to the advantages of ease of modification, good biocompatibility, and potential anti-inflammation and antioxidation characteristics. Moreover, chitosan has the property of unconventional luminescence that is derived from the clusterization-triggered emission effect. Based on the above mentioned properties, Li, Wang, and coworkers [59] chose the low molecular weight chitosan (COS) as the skeleton to graft the copolymers of lysine and valine onto its amino group to obtain the COS-AMP (Figure 19.19E). The combination of COS and AMP endowed this cationic peptidopolysaccharide with multicolor emission and combating bacteria. As shown in Figure 19.19F, after 12 h incubation with COS-AMP, the blue, green, and red fluorescence of *E. coli* and *S. aureus* were observed under 405, 488, and 561 nm laser excitation, respectively, indicating the multicolor imaging of COS-AMP. Furthermore, the plate coating method exhibited COS-AMP had a high antibacterial efficiency over 99% on *E. coli*, *S. aureus*, and *P. aeruginosa*. And, the SEM results also showed the cell walls and membranes were dramatically destroyed (Figure 19.19G). This was mainly ascribed to two reasons: one is that the positively charged surface and unique topological structure of COS-AMP made them adsorb onto the bacterial surface and enhance the antibacterial activity; and the other is that the hydrophobic valine of COS-AMP had similar structure as peptidoglycan, which helped COS-AMP penetrate the bacterial cell walls and membranes, further leading to the destruction of bacteria. More importantly, due to the amphiphilic structure of COS-AMP, it was difficult to penetrate into mammalian cells, resulting in the good biocompatibility. This unconventional luminance imaging-guided antibacterial therapy will have good potential for practical clinical application.

19.3.8 Intracellular polymerization for killing of cancer cells

Cell is the chemical plant of human life. Tens of thousands of chemical or biological reactions are efficiently going on, all the time. Therefore, cells are natural reactors for metal-free and efficient chemical reaction to realize direct imaging and inhibition. Qin, Tang, and coworkers [60] reported a lab-in-cell strategy to synthesize the AIE polymer using their spontaneous amino-yne click polymerization, which is metal-free and efficient in aqueous solution. In this intracell polymerization, diamine-containing TPE (**1**) and carboxyl activated terminal alkynes (**2**) could spontaneously polymerize inside cells to obtain the AIE polymer, PAA with M_w of 7,300 (Figure 19.20A). Interestingly, the PAA synthesized inside cells could turn on the

cells. In contrast, cells could not be lighted up if only incubated with **1** or **2** or pre-prepared PAA (Figure 19.20B). Furthermore, the intracellularly formed PAA could kill the cells. To study the mechanism of cell death, phalloidin and alpha-tubulin antibody with Alexa Fluor-546 were used to stain the structure of actin and tubulin in cells (Figure 19.20C). Compared to the pre-prepared PAA, the lab-in-cell generated PAA could destroy the actin and tubulin in cytoplasm, leading to the cell necrosis. Therefore, the intracellular amino-yne click polymerization could be a new strategy to realize drug-free therapy through reasonable drug delivery.

The abovementioned lab-in-cell reaction is an exogenous polymerization that spontaneously occurs inside cells. As opposed to this, Lou, Xia, and coworkers [61] reported another strategy to realize the intracellular polymerization under the mediation of endogenous H_2O_2 and peroxidase. Two tyrosine (Tyr) groups-containing TPE derivatives (TT) were selected as the reaction substrate (Figure 19.20D). TPE was used as the emissive core in the middle, and tyrosine at both ends was ROS-active. After modification of the tyrosine, TT was hydrophilic with weak fluorescence in aqueous solution. When H_2O_2 and MPO are there, they would crosslink with each other by dityrosine linkages to form the AIE polymers, leading to AIE activity. Since H_2O_2 and MPO are overexpressed in inflammatory cells, inflammatory cells could be selectively lighted up and inhibited after incubation with TT, compared to normal cells. To verify the cytotoxic effects, TT was incubated with HeLa cells, RAW264.7 cells, and normal human lung fibroblast (HLF) cells. The MTT results confirmed that TT had higher cytotoxicity in HeLa and RAW264.7 cells than in HLF cells. For further exploring its inhibitory effect, RAW264.7 and HLF cells were co-cultured (Figure 19.20E). Propidium iodide (PI) with red fluorescence signal was chosen for detecting dead cells. It was easily observed that RAW264.7 cells were simultaneously stained by TT (blue), MTG (green, mitochondria staining), and PI, while no blue and red fluorescence were observed in HLF cells, excepting green fluorescence stained by MTG. This result indicated that TT could effectively inhibit RAW264.7 cells due to their H_2O_2- and MPO-overexpressing capability, but no harm was caused to normal cells. Furthermore, TEM images of RAW264.7 cells revealed that compared to PBS control groups, mitochondria had obvious damage after incubation with 20 μM and 50 μM TT (Figure 19.20F). These results confirmed that H_2O_2-responsive and MPO-mediated TT could selectively image and inhibit the inflammatory cells through mitochondria damage process. Overall, this H_2O_2-based and peroxidase-specific catalyzed TT could be broadly applied in other inflammation theranostics in the biomedical system.

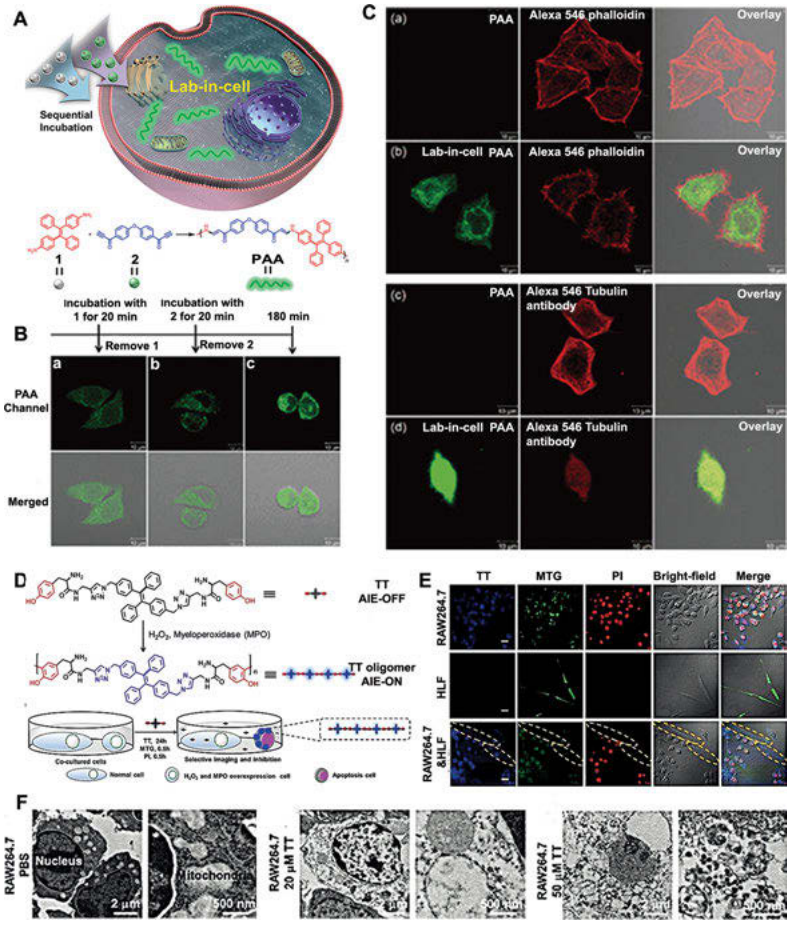

Figure 19.20: Exogenous and endogenous intracellular polymerization. (A) Illustration of the intracellular spontaneous amino-yne click polymerization, and synthetic route to poly (β-aminoacrylate) (PAA). (B) CLSM images of polymerization inside HeLa cells. CLSM images of HeLa cells incubated with 1 for 20 min (a), followed by removal of 1 and incubation with 2 for 20 min (b), and continuing incubation after the removal of 2 in the medium for additional 140 min (c). (C) Cell death mechanism. CLSM images of HeLa cells incubated with PAA (a and c) or lab-in-cell synthesized PAA (b and d), followed by Alexa 546 phalloidin (a and b) and Alexa 546 tubulin antibody (c and d) labeling. Reproduced with permission from Ref. [60]. Copyright (Springer Nature), 2019. (D) Weak fluorescence emissive TT crosslinked with each other by dityrosine linkages and became aggregates in the present of H_2O_2 and MPO, activating AIE process to realize the fluorescence "turn on." (E) CLSM images of RAW264.7 cells, HLF cells, and co-cultured RAW264.7 and HLF cells incubated with TT (24 h), MTG and PI (30 min), respectively. (F) Bio-TEM images of RAW264.7 cells treated with PBS, 20 μM TT, and 50 μM TT for 24 h. Scale bar: 20 μm. Reproduced with permission from Ref. [61]. Copyright (Wiley-VCH GmbH& Co. KGaA), 2018.

19.4 Conclusion and perspectives

This chapter reviewed the applications of AIE polymers in targeting cell or organelle imaging, TME (CO_2, H_2O_2, GSH, pH, hypoxia) responsive cell imaging, NIR, and NIR-IIa tumor and lymph nodes imaging. In addition, the AIE polymers have shown their advantages in PDT-, PTT-, TME-responsive drug delivery, and chemo-PDT. Intracellular polymerization for antibacterial and antitumor application was also introduced. Based on the characteristics of tumor microenvironment, AIE polymers could be designed by introducing the pH, H_2O_2, GSH, hypoxia-responsive bonds (-C = N-, disulfide bond, diselenide bond, azo bond, etc.) for the responsive imaging. Based on the "off-on" fluorescence, TME-responsive AIE polymers have been used in drug tracking through noncovalent or covalent bonds with drugs. Furthermore, combined chemotherapy and chemo-PDT could also be realized with these designed strategies. Notably, for AIE-conjugated polymers, ROS generation could be enhanced for efficient killing of the bacterial and tumor cells. Meanwhile, it would be a feasible strategy to obtain high Φ_F and NIR-IIa fluorescence emission through balancing twisted and planar structure.

AIE polymers for biological applications are generally amphipathic and biocompatible, which make them useful in FLI and various treatment modes. However, their degradability, especially for the conjugated polymers, needs to be further explored. For in vivo FLI and therapy, tissue penetration depth is a crucial factor. As reviewed in this chapter, many blue or white light emissive AIE polymers have been reported, but they are mainly used for in vitro imaging and therapy. NIR-II FLI has reduced photon scattering and minimized tissue autofluorescence, but AIE polymers with NIR-II fluorescence emission are rarely reported. How to reduce the difficulty of synthesis is a problem that should be solved. In addition, multimodal imaging of AIE polymers, such as NIR or NIR-II FLI with magnetic resonance imaging, photoacoustic imaging, positron emission tomography, computed tomography, and other imaging modes can provide more conclusive diagnostic information, but are rarely reported. Reasonably combining AIE polymers with other imaging probes or contrast agents into one composite material has great potential in realizing multimodal imaging-guided combination therapy. Compared to typical AIE polymers, unconventional luminescent polymers with good biocompatibility and antibacterial ability have the potential to kill multidrug-resistant bacteria, but only few kinds of related polymers have been reported, which limited their further biological applications. Overall, novel and multifunctional AIE polymers still need to be developed for biomedical applications. We hope this chapter can provide more application scenarios for the researchers, inspire them to design more fantastic AIE polymers, and pave the way for clinical transformation.

References

[1] Luo J, Xie Z, Lam JW, et al., Aggregation-induced emission of 1-methyl-1,2,3,4,5-pentaphenylsilole, Chem Commun (Camb), 2001, 18, 1740–1741.

[2] Mei J, Leung NL, Kwok RT, Lam JW, Tang BZ, Aggregation-induced emission: Together we shine, united we soar!, Chem Rev, 2015, 115, 11718–11940.

[3] Kang M, Zhang Z, Song N, et al., Aggregation-enhanced theranostics: AIE sparkles in biomedical field, Aggregate, 2020, 1, 80–106.

[4] Cai X, Liu B, Aggregation-induced emission: Recent advances in materials and biomedical applications, Angew Chem Int Ed Engl, 2020, 59, 9868–9886.

[5] Wang D, Tang BZ, Aggregation-induced emission luminogens for activity-based sensing, Acc Chem Res, 2019, 52, 2559–2570.

[6] Hu R, Leung NLC, Tang BZ, AIE macromolecules: Syntheses, structures and functionalities, Chem Soc Rev, 2014, 43, 4494–4562.

[7] Hu YB, Lam JWY, Tang BZ, Recent progress in AIE-active polymers, Chin J Polym Sci, 2019, 37, 289–301.

[8] Qiu Z, Liu X, Lam JWY, Tang BZ, The marriage of aggregation-induced emission with polymer science, Macromol Rapid Commun, 2019, 40, 1800568.

[9] Zhan R, Pan Y, Manghnani PN, Liu B, AIE polymers: Synthesis, properties, and biological applications, Macromol Biosci, 2017, 17, 1600433.

[10] Feng X, Zhang J, Hu Z, et al., Pyrene-based aggregation-induced emission luminogens (AIEgen): Structure correlated with particle size distribution and mechanochromism, J Mater Chem C, 2019, 7, 6932–6940.

[11] Hu R, Qin A, Tang BZ, AIE polymers: Synthesis and applications, Prog Polym Sci, 2020, 100, 101176.

[12] Wang L, Hu R, Qin A, Tang BZ, Conjugated polymers with aggregation-induced emission characteristics for fluorescence imaging and photodynamic therapy, Chem Med Chem, 2021, 16, 1–10.

[13] Hu R, Yang X, Qin A, Tang BZ, AIE polymers in sensing, imaging and theranostic applications, Mater Chem Front, 2021, 5, 4073–4088.

[14] Chen J, Xie Z, Lam JWY, Law CCW, Tang BZ, Silole-containing polyacetylenes. Synthesis, thermal stability, light emission, nanodimensional aggregation, and restricted intramolecular rotation, Macromolecules, 2003, 36, 1108–1117.

[15] Zhan R, Pan Y, Manghnani PN, Liu B, AIE polymers: Synthesis, properties, and biological applications, Macromol Biosci, 2017, 17, 1600433.

[16] Xu Q, Guo Y, Xu T, Fang M, Zhu W, Li C, AIE-active fluorescent polymeric nanoparticles about dextran derivative: Preparation and bioimaging application, J Biomater Sci Polym Ed, 2020, 31, 504–518.

[17] Qiao F, Ke J, Liu Y, et al., Cationic quaternized chitosan bioconjugates with aggregation-induced emission features for cell imaging, Carbohydr Polym, 2020, 230, 115614.

[18] Liu C, Bai H, He B, et al., Functionalization of silk by AIEgens through facile bioconjugation: Full-color fluorescence and long-term bioimaging, Angew Chem Int Ed Engl, 2021, 60, 12424–12430.

[19] Hu R, Zhou T, Li B, et al., Selective viable cell discrimination by a conjugated polymer featuring aggregation-induced emission characteristic, Biomaterials, 2020, 230, 119658.

[20] Zheng Z, Zhou T, Hu R, et al., A specific aggregation-induced-emission conjugated polymer enables visual monitoring of osteogenic differentiation, Bioact Mater, 2020, 5, 1018–1025.

[21] Dineshkumar S, Raj A, Srivastava A, et al., Facile incorporation of “aggregation-induced emission”-active conjugated polymer into mesoporous silica hollow nanospheres: Synthesis, characterization, photophysical studies, and application in bioimaging, ACS Appl Mater Interfaces, 2019, 11, 31270–31282.
[22] Saftig P, Sandhoff K, Killing from the inside, Nature, 2013, 502, 312–313.
[23] Wang Y, Yao H, Zhuang Z, Yao J, Zhou J, Zhao Z, Photostable and biocompatible AIE-active conjugated polyelectrolytes for efficient heparin detection and specific lysosome labelling, J Mater Chem B, 2018, 6, 6360–6364.
[24] Ma C, Han T, Kang M, et al., Aggregation-induced emission active polyacrylates via Cu-mediated reversible deactivation radical polymerization with bioimaging applications, ACS Macro Lett, 2020, 9, 769–775.
[25] Ma H, Qin Y, Yang Z, et al., Positively charged hyperbranched polymers with tunable fluorescence and cell imaging application, ACS Appl Mater Interfaces, 2018, 10, 20064–20072.
[26] Li Y, Wu X, Yang B, et al., Synergy of CO_2 response and aggregation-induced emission in a block copolymer: A facile way to “see” cancer cells, ACS Appl Mater Interfaces, 2019, 11, 37077–37083.
[27] Saha B, Ruidas B, Mete S, Mukhopadhyay CD, Bauri K, De P, AIE-active non-conjugated poly (N-vinylcaprolactam) as a fluorescent thermometer for intracellular temperature imaging, Chem Sci, 2020, 11, 141–147.
[28] Zhao Y, Wu Y, Chen S, Deng H, Zhu X, Building single-color AIE-active reversible micelles to interpret temperature and pH stimuli in both solutions and cells, Macromolecules, 2018, 51, 5234–5244.
[29] Wang B, Li C, Yang L, et al., Tetraphenylethene decorated with disulfide-functionalized hyperbranched poly(amido amine)s as metal/organic solvent-free turn-on AIE probes for biothiol determination, J Mater Chem B, 2019, 7, 3846–3855.
[30] Shen J, Shao K, Zhang W, He Y, Hypoxia-triggered in situ self-assembly of a charge switchable Azo polymer with AIEgens for tumor imaging, ACS Macro Lett, 2021, 10, 702–707.
[31] Zhang Z, Chen D, Liu Z, et al., Near-infrared polymer dots with aggregation-induced emission for tumor imaging, ACS Appl Polym Mater, 2020, 2, 74–79.
[32] Liu S, Ou H, Li Y, et al., Planar and twisted molecular structure leads to the high brightness of semiconducting polymer nanoparticles for NIR-IIa fluorescence imaging, J Am Chem Soc, 2020, 142, 15146–15156.
[33] Hu F, Xu S, Liu B, Photosensitizers with aggregation-induced emission: Materials and biomedical applications, Adv Mater, 2018, 30, e1801350.
[34] Yang B, Chen Y, Shi J, Reactive Oxygen Species (ROS)-based nanomedicine, Chem Rev, 2019, 119, 4881–4985.
[35] Ren B, Li K, Liu Z, Liu G, Wang H, White light-triggered zwitterionic polymer nanoparticles based on an AIE-active photosensitizer for photodynamic antimicrobial therapy, J Mater Chem B, 2020, 8, 10754–10763.
[36] Zhou T, Hu R, Wang L, et al., An AIE-active conjugated polymer with high ROS-generation ability and biocompatibility for efficient photodynamic therapy of bacterial infections, Angew Chem Int Ed Engl, 2020, 59, 9952–9956.
[37] Qi G, Hu F, Kenry, et al., Bacterium-templated polymer for self-selective ablation of multidrug-resistant bacteria, Adv Funct Mater, 2020, 30, 2001338.
[38] Wu W, Mao D, Xu S, et al., Polymerization-enhanced photosensitization, Chem, 2018, 4, 1937–1951.
[39] Wu W, High-performance conjugated polymer photosensitizers, Chem, 2018, 4, 1762–1764.

[40] Liu S, Zhang H, Li Y, et al., Strategies to enhance the photosensitization: Polymerization and the donor-acceptor even-odd effect, Angew Chem Int Ed Engl, 2018, 57, 15189–15193.
[41] Gu B, Wu W, Xu G, et al., Precise two-photon photodynamic therapy using an efficient photosensitizer with aggregation-induced emission characteristics, Adv Mater, 2017, 29, 1701076.
[42] Croissant JG, Zink JI, Raehm L, Durand JO, Two-photon-excited silica and organosilica nanoparticles for spatiotemporal cancer treatment, Adv Healthc Mater, 2018, 7, e1701248.
[43] Wang S, Wu W, Manghnani P, et al., Polymerization-enhanced two-photon photosensitization for precise photodynamic therapy, ACS Nano, 2019, 13, 3095–3105.
[44] Yao H, Dai J, Zhuang Z, et al., Red AIE conjugated polyelectrolytes for long-term tracing and image-guided photodynamic therapy of tumors, Sci China Chem, 2020, 63, 1815–1824.
[45] Li J, Liu W, Li Z, Hu Y, Yang J, Li J, PEGylated AIEgen molecular probe for hypoxia-mediated tumor imaging and photodynamic therapy, Chem Commun (Camb), 2021, 57, 4710–4713.
[46] Deng G, Peng X, Sun Z, et al., Natural-killer-cell-inspired nanorobots with aggregation-induced emission characteristics for near-infrared-II fluorescence-guided glioma theranostics, ACS Nano, 2020, 14, 11452–11462.
[47] Zhao J, Pan X, Zhu J, Zhu X, Novel AIEgen-functionalized diselenide-crosslinked polymer gels as fluorescent probes and drug release carriers, Polymers (Basel), 2020, 12, 551.
[48] Dai YD, Sun XY, Sun W, et al., H_2O_2-responsive polymeric micelles with a benzil moiety for efficient DOX delivery and AIE imaging, Org Biomol Chem, 2019, 17, 5570–5577.
[49] Yan K, Zhang S, Zhang K, et al., Enzyme-responsive polymeric micelles with fluorescence fabricated through aggregation-induced copolymer self-assembly for anticancer drug delivery, Polym Chem, 2020, 11, 7704–7713.
[50] Lin L, Qin H, Huang J, Liang H, Quan D, Lu J, Design and synthesis of an AIE-active polymeric H_2S-donor with capacity for self-tracking, Polym Chem, 2018, 9, 2942–2950.
[51] Wang TT, Wei QC, Zhang ZT, et al., AIE/FRET-based versatile PEG-Pep-TPE/DOX nanoparticles for cancer therapy and real-time drug release monitoring, Biomater Sci, 2020, 8, 118–124.
[52] Zhuang W, Xu Y, Li G, et al., Redox and pH dual-responsive polymeric micelles with aggregation-induced emission feature for cellular imaging and chemotherapy, ACS Appl Mater Interfaces, 2018, 10, 18489–18498.
[53] Ma B, Zhuang W, He H, et al., Two-photon AIE probe conjugated theranostic nanoparticles for tumor bioimaging and pH-sensitive drug delivery, Nano Res, 2019, 12, 1703–1712.
[54] Yu T, Zhuang W, Su X, et al., Dual-responsive micelles with aggregation-induced emission feature and two-photon absorption for accurate drug delivery and bioimaging, Bioconjug Chem, 2019, 30, 2075–2087.
[55] Wu P, Wang X, Wang Z, et al., Light-activatable prodrug and AIEgen copolymer nanoparticle for dual-drug monitoring and combination therapy, ACS Appl Mater Interfaces, 2019, 11, 18691–18700.
[56] Yi X, Hu JJ, Dai J, et al., Self-guiding polymeric prodrug micelles with two aggregation-induced emission photosensitizers for enhanced chemo-photodynamic therapy, ACS Nano, 2021, 15, 3026–3037.
[57] Chen M, He J, Xie S, et al., Intracellular bacteria destruction via traceable enzymes-responsive release and deferoxamine-mediated ingestion of antibiotics, J Control Release, 2020, 322, 326–336.
[58] Zhao J, Dong Z, Cui H, Jin H, Wang C, Nanoengineered peptide-grafted hyperbranched polymers for killing of bacteria monitored in real time via intrinsic aggregation-induced emission, ACS Appl Mater Interfaces, 2018, 10, 42058–42067.

[59] Dong Z, Wang Y, Wang C, Meng H, Li Y, Wang C, Cationic peptidopolysaccharide with an intrinsic AIE effect for combating bacteria and multicolor imaging, Adv Healthc Mater, 2020, 9, e2000419.
[60] Hu R, Chen X, Zhou T, et al., Lab-in-cell based on spontaneous amino-yne click polymerization, Sci China Chem, 2019, 62, 1198–1203.
[61] Cheng Y, Dai J, Sun C, et al., An intracellular H_2O_2-responsive AIEgen for the peroxidase-mediated selective imaging and inhibition of inflammatory cells, Angew Chem Int Ed Engl, 2018, 130, 3177–3181.

Shengnan Liu, Yu Pei, Dongxia Zhu

Chapter 20
AIE-based transition metal complexes for biological applications

20.1 Introduction

Luminescent materials with aggregation-induced emission (AIE) characteristics are becoming increasingly important for scientists due to their excellent performance [1–6]. Various AIE-active molecules, including small organic molecules, polymers, transition metal complexes and so on, have been reported and applied successfully in many fields so far [4, 7]. Among them, transition metal complexes with AIE-active have attracted more attention in various fields (such as biological applications, photoelectric fields, sensors, etc.) owing to their high luminous performance [8–11]. These transition metal complexes with d^6, d^8, and d^{10} electron configuration show strong spin-orbit coupling, leading to efficient intersystem crossing (ISC) from the singlet-excited state to the triplet-excited state and exhibiting strong phosphorescent emission [8, 12, 13]. Meanwhile, these phosphorescence-emitting transition metal complexes with large Stokes shifts, long excited-states lifetime, satisfactory photostability, and tunable photophysical properties [14, 15], have extensively used as photoluminescent probes for bioimaging [8, 16, 17]. In addition, for type II photodynamic therapy (PDT), an efficient method of improving the efficiency of singlet oxygen ($^1O_2$) generation is to accelerate the ISC by introducing heavy atoms into photosensitizer (PS) [18–20]. Hence, transition metal complexes with AIE feature have been considered as a promising PS for PDT [18, 21]. Moreover, the biological applications of transition metal complexes with AIE properties in other areas, such as antibacterial, have also been reported successively [22]. This chapter will focus on the complexes with AIE properties that are constructed by different transition metals such as Ir, Pt, Au, Ru, Cu, and Zn and discuss their applications in biological fields such as bioimaging, PDT, etc.

Shengnan Liu, Yu Pei, Key Laboratory of Nanobiosensing and Nanobioanalysis at Universities of Jilin Province, Department of Chemistry, Northeast Normal University, 5268 Renmin Street, Changchun, Jilin Province, 130024, P. R. China
Dongxia Zhu, Key Laboratory of Nanobiosensing and Nanobioanalysis at Universities of Jilin Province, Department of Chemistry, Northeast Normal University, 5268 Renmin Street, Changchun, Jilin Province, 130024, P. R. China, e-mail: zhudx047@nenu.edu.cn

https://doi.org/10.1515/9783110673074-021

20.2 Ir (III) complexes

For most organic materials, the restricted intermolecular motions (RIM) are the main mechanism of AIE [9, 23]. The RIM process can impede the radiationless decay of the excitation energy and populate the radiative decay channels through aggregation [9, 21, 24]. Several series of AIE-active cyclometalated Ir (III) complexes with the RIM of the rotatable aromatic rings have been developed, in which the nonradiative decay from the MLCT/LMCT/LLCT/IL-excited states are blocked by π–π stacking between adjacent aromatic rings, resulting in photoluminescence (PL) enhancement [9, 25–27]. In view of their ideal photophysical properties, Ir (III) complexes have been a hot topic in luminescent biological probes and anticancer agents [8, 16, 28].

The photophysical properties of AIE-active cyclometalated Ir (III) complexes could be tuned through simple ligand modification [8]. Laskar et.al tuned the emission wavelength of mono cyclometalated Ir (III) complexes by the systematic changing of the chromophoric ligands (Figure 20.1a) [8]. A mixed LC/MLCT/LLCT nature for the lowest excited states of the complexes with bright light in the solid-state was revealed by photo-physical experiments and quantum chemical calculations (Figure 20.1b, c). These Ir (III) complexes processed AIE activity (Figure 20.1d), and a simple technique has been employed, wherein the complexes were encapsulated in PEG-PLA micellar nanoparticles as a low toxicity cell-imaging probes in vitro (Figure 20.1e and f).

Besides, modified structure of Ir (III) complexes can change the luminescent signal and direct the location to various subcellular regions [9, 28]. Introducing triphenylamine (TPA) group, a propeller-like structure with electron-donating properties, into Ir (III) complexes with 1-phenyl-1H-ipidazo[4,5-*f*] [1, 10] phenanthroline derivatives, Chao et al. designed the AIE active Ir (III) complexes with excellent photostability (Figure 20.2a–c) [28]. In a short imaging time period (8 min) at a low concentration (500 nM), with no phosphorescent intensity fluctuation in the mitochondrial physiological range, **Ir1–r5** selectively and efficiently located the mitochondria and monitored mitophagy, which was induced by CCCP (Figure 20.2d–f). The problems in mitophagy tracking, like short-time dynamics change, pH fluctuation, membrane potential lost and violent morphology alteration, were tackled by this competent mitophagy probe. In 2018, AIE-active Ir (III) complex-based nucleolus-specific imaging and ribosomal RNA (rRNA)-selective probes were reported first by Khatua et al. [9] The Ir (III) complexes were synthesized with a benzimidazole-substituted 1,2,3-triazole-pyridine (BiPT) ligand (Figure 20.3a). According to the density functional theory (DFT) calculations, it is obvious that the lowest energy absorption band is mainly due to MLCT and/or LLCT (Figure 20.3b). The supramolecular π–π interactions between the benzimidazole of the BiPT ligand and the secondary structures of rRNA bring aggregation and thus enhance the PL intensity (Figure 20.3).

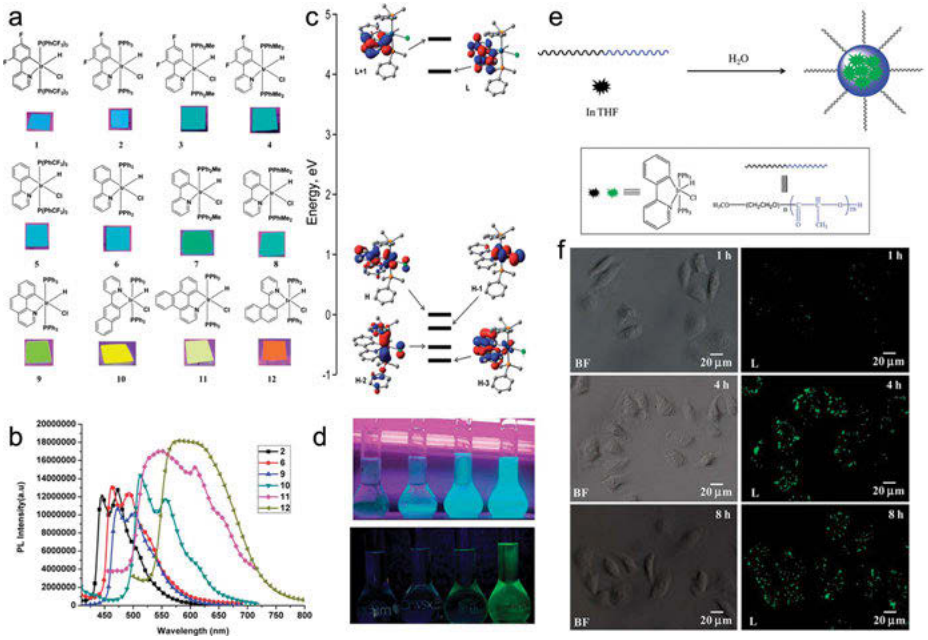

Figure 20.1: a) Tuning of emission color in solid state throughout the visible range with variation of the cyclometalated and phosphine ligands. b) Solid state photoluminescence emission spectra for complexes **2–12**, showing the tuning of emission wavelengths. c) Molecular orbital energy diagram (in eV) with respect to the HOMO energy of the frontier orbitals of 8. H and L stand for HOMO and LUMO, respectively. d) Luminescent image of complex 4 radiated with UV light at 365 nm in water-THF mixed solvents (0, 30, 60 and 90% water into THF solution) with the concentration of 1×10^{-4} mol L^{-1} (upon) and Luminescent image of complex 9 radiated with UV light at 365 nm in PEG-THF mixed solvents (0, 30, 60 and 90% PEG into THF solution) with the concentration of 1×10^{-4} mol L^{-1}. e) Schematic representation of the synthesis of luminescent Ir complex-encapsulated PEG-PLA nanoparticles. f) Photoluminescence spectra (left) and digital image (right) of Ir complex 6 in tetrahydrofuran (THF), water and in aqueous. (a–f) Copyright 2014, The Royal Society of Chemistry [8].

Due to the amelioration of ISC from the strong spin-orbit coupling, Ir (III) complexes have excellent ability for $^1O_2$ generation and are regarded as promising PSs for PDT [18]. Zhu *et al.* have first reported a series of desirable red-emitting AIE Ir (III) complexes, introducing Schiff bases as both chelate and bridging motifs, as **PS**s for efficiency PDT (Figure 20.4a, b) [18]. The diimine spacer is flexible to permit the ligands to bend and rotate freely and adopt the metal ions optimum coordination geometries. The Schiff base ligands constructed with TPA as a bridge can electronically couple one to three metal centers (Figure 20.4a). It has been discovered that the $^1O_2$ generation ability in **PS**s increases as the number of metal centers increase, leading to enhanced efficiency of PDT (Figure 20.4c and d). Furthermore, the nanoparticles (NPs) show more advantages than the corresponding pure Ir (III) complexes: (i) brighter emission; (ii) higher phosphorescence quantum yields; (iii)

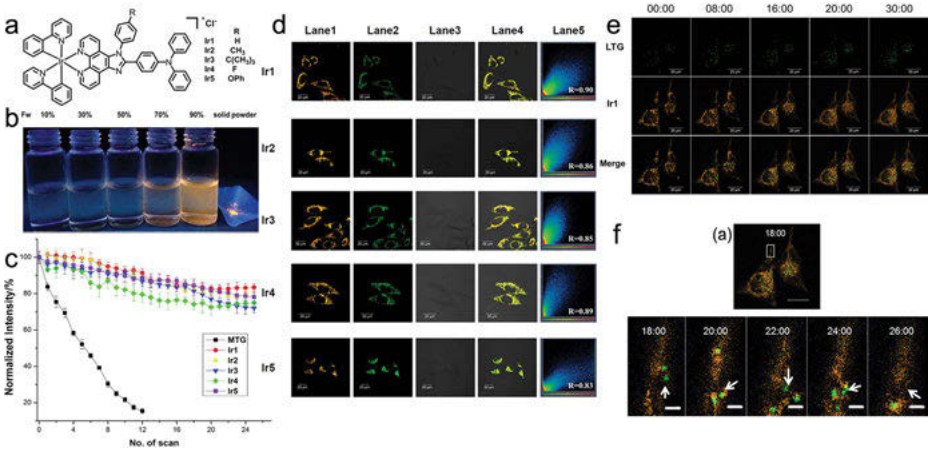

Figure 20.2: a) Chemical structures of the **Ir1–Ir5** complexes. b) Images of the room temperature luminescent emissions of **Ir1** solid powder and **Ir1** in DMSO-PBS mixtures with different water fractions (fw). c) Quantitative photobleaching results indicate that **Ir1–Ir5** exhibited robust emission intensity under continuous light irradiation. d) Confocal phosphorescence images and their images overlaid with bright-field images of living HeLa cells incubated with 500 nM of **Ir1-Ir5** in DMEM with 10% FBS (pH = 7.4) for 8 min at 37 °C followed by 100 nM of MTR**.** Lane 1, confocal phosphorescence images of **Ir1-Ir5**; Lane 2, confocal phosphorescence images of MTR; Lane 3, Bright field; Lane 4, overlay of lane 1, lane 2 and lane 3; Lane 4, the overlap coefficient of columns lane 1 and lane 2, and Pearson's colocalization coefficients are also presented. Excitation wavelength: 405 nm (for all Ir (III) complexes), 488 ns (for PTG); emission filter: 590 ± 30 ns (for all Ir (III) complexes) and 520 ± 20 ns (for MTG). e) Phosphorescence images of CCCP (10 μM) treated living HeLa cells stained with Ir1 (0.5 μM). To inhibit autophagic flux, the cells were preincubated with chloroquine (50 μM), prior to the addition of CCCP. f) Confocal images of HeLa cells stained with **Ir1** (500 nM, orange) and LTG (100 nM, green) in the presence of CCCP (10 μM). (a) Time points (min) were selected from the onset and completion of the mitophagy process. The regions (b) indicated in white boxes are enlarged from the area of this cell that is shown. Following imaging is shown in (b) until the observed mitophagy process is completed in the selected area. Scale bar: 20 μm (a) and 2 μm (b). (a-f) Copyright 2016, Springer Nature [28].

longer excited lifetime; (iv) higher $^1O_2$ generation ability; (v) better biocompatibility; and (vi) superior cellular uptake. The trinuclear **PS3** NPs with long wavelength emission, high phosphorescence quantum yields (35%), long excited-state lifetime (4.61 as), high polar absorption coefficient, excellent $^1O_2$ generation ability, and negligible dark toxicity demonstrate an especially good effect for PDT (Figure 20.4). Moreover, the PS3 NPs upon irradiation can efficiently inhibit tumor growth in mice after tail vein injection (Figure 20.4g-j).

Near-infrared (NIR) emission with weaker autofluorescence interference, little photodamage to cells and enhanced signal-to-noise ratio (SNR) of imaging is beneficial to the application of bioimaging and PDT [21, 29, 30]. Zhu *et al.* used rigid 1,3,5-triphenyl benzene to elongate the effective π- conjugation to design mono- and tri-nuclear NIR AIE cationic Ir (III) complexes (Figure 20.5a and b) [21]. Their

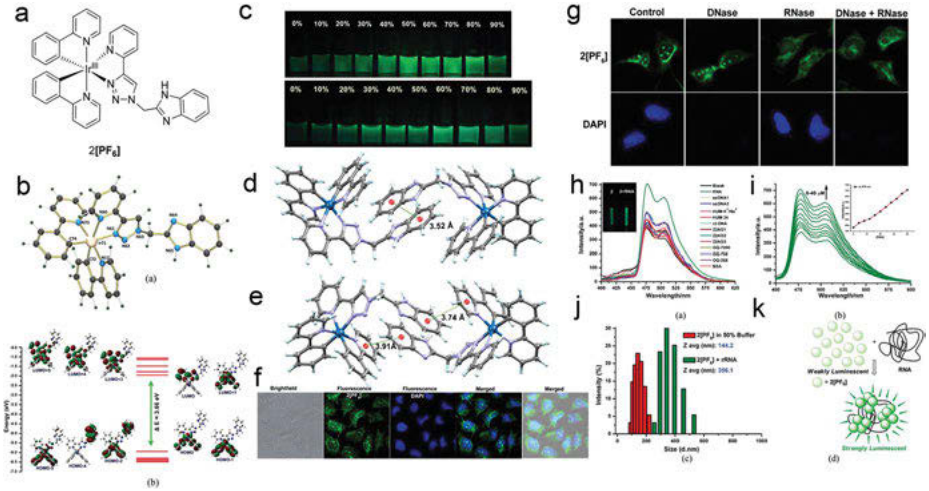

Figure 20.3: a) Chemical structures of **2[PF_6]**. b) (a) Optimized structure and (b) representations of the frontier molecular orbitals (MOs) of complex. c) Digital photograph of **2[PF_6]** in CH_3CN with increasing amount of water (0% to 90%) under 365 nm UV illumination. DFT optimized geometry of complex **2[PF_6]** showing π–π stacking between (d) two benzimidazole moieties and (e) the phenyl pyridine and benzimidazole moieties. f) Co-staining of **2[PF_6]** (green) with the DNA-specific dye DAPI (blue). g) Fluorescence images of fixed HeLa cells during DNase and RNase digest experiments with **2[PF_6]** and the nucleus staining dye DAPI (shown as comparison experiments). h) PL spectra of **2[PF_6]** (10 μM) upon addition of RNA, ctDNA, ssDNA, BSA and G-quadruplex DNA (4-fold) in CH_3CN/PBS buffer (v/v, 1: 1; pH 7.4). (Inset) Digital photograph of **2[PF_6]** (10 μM) before and after addition of RNA (40 μM) under a UV lamp. i) PL titration of **2[PF_6]** with RNA (0 to 4-fold) in CH_3CN/PBS buffer (1: 1; v/v, pH 7.4). (Inset) Plot of emission intensity as a function of [RNA]. j) DLS of **2[PF_6]** (10 μM) in 50% mixed aqueous buffer and in the presence of RNA (40 μM). k) Schematic of the interaction of **2[PF_6]** with RNA and possible AIE enhancement. (a–k) Copyright 2018, The Royal Society of Chemistry [9].

corresponding NPs were obtained through π- conjugation and symmetric structure self-assembled without any surfactants or adjuvants, avoiding structural modifications, sophisticated synthesis, potential biotoxicity, and high cost caused by the introduction of amphiphilic polymers or nanocarriers (Figure 20.5a). It is significantly important to obtain pure and efficient multinuclear Ir (III) complex NPs as PSs based on a facile self-assembly method to realize good biocompatibility for cell imaging and PDT. The trinuclear **PS3** NPs exhibited bright NIR emission at 730 ns, stronger absorption, higher $^1O_2$ generation ability and, better biocompatibility and excellent phototoxicity, which is considered as an efficient PS for bioimaging and PDT. (Figure 20.5c–f).

The prevailing chemistry-based strategies to approach mitochondria include coupling lipophilic cation scaffolds or peptides [16, 31]. As reported, cyclometalated Ir (III) complexes show a significant affinity for mitochondria, which may be similar to the underlying mechanism of lipophilic cations [16, 32]. Chao and his colleagues

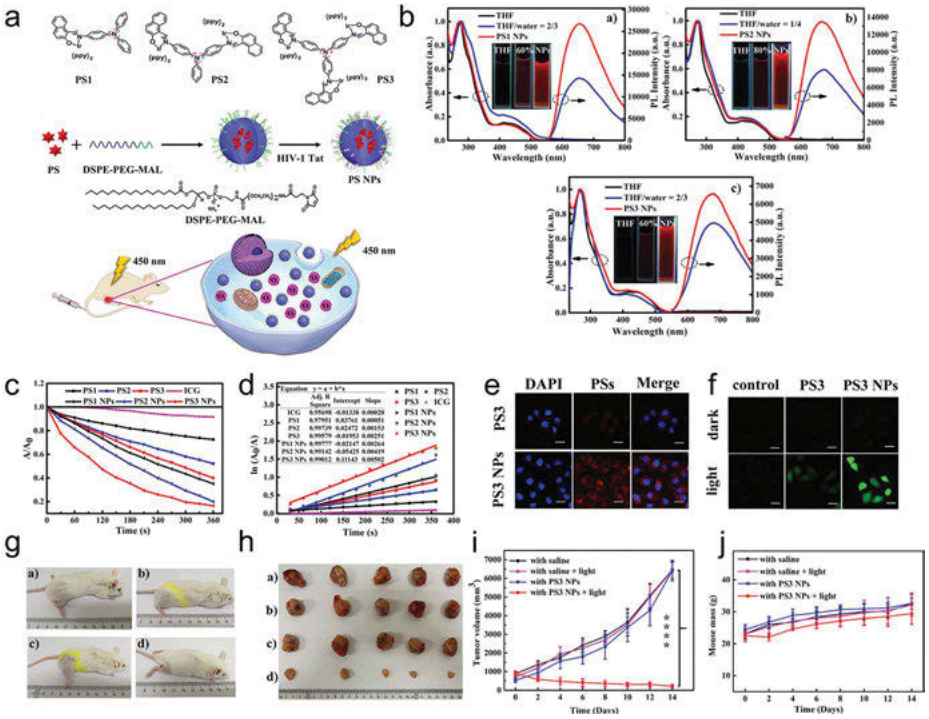

Figure 20.4: a) Chemical structures of **PS1**, **PS2**, and **PS3**; The synthesis of NPs; and schematic illustration of **PS3** NPs as PSs for PDT. b) UV-vis absorption spectra and emission spectra of **PS** in THF, and NPs in water, inset: emission images of the PS and NPs under 365 nm UV illuminations. c) Comparison of the decay rates of different **PS**s under irradiation (450 nm, 20 mW cm^{-2}), A_0 = absorption of ICG without irradiation. A = real-time absorption of ICG with different irradiation time. d) Time-dependent $^1O_2$ generation kinetics. A0 = absorption of ICG without irradiation. A = real-time absorption of ICG with different irradiation time. e) CLSM images of HeLa cells incubated with **PS3** and **PS3** NPs (20 μg mL^{-1}) for 6 h; the scale bars are 20 μm and generation of intracellular ROS mediated by **PS3** and **PS3** NPs upon irradiation (450 nm, 20 mW cm^{-2}, 20 min) as indicated by the fluorescence of DCF. g) Representative images of mice. The hair on the thigh was removed immediately before irradiation. The images were taken on day 14 after irradiation and the different hair length on the different mice is due to an inconsistent rate of hair growth. h) Harvested tumors from various groups treated (a) with saline, (b) with saline and light, (c) with **PS3** NPs, and (d) with **PS3** NPs and light (100 mg mL^{-1}, 100 mL), light irradiation (450 nm, 200 mW cm^{-2}, 20 min). i) Tumor volume measurement for different groups of mice (****, $P < 0.0001$, $n = 5$ per group, PDT vs other groups). j) Body weights of mice for different groups of mice. Copyright 2019, Wiley-VCH Verlag GpbH & Co. KGaA, Weinheim [18].

have first reported three Ir (III) complexes (**Ir1–Ir3**) with conjugated TPA as mitochondria-targeted AIE-active agents for two-photon-absorbing PDT (Figure 20.6a-c) [16]. The complexes were ingested by endocytosis, selectively accumulated in mitochondria and exert photocytotoxicity (Figure 20.6e–i). Among the complexes, **Ir1** demonstrated the most significant two-photon-absorbing cross-sections, generated

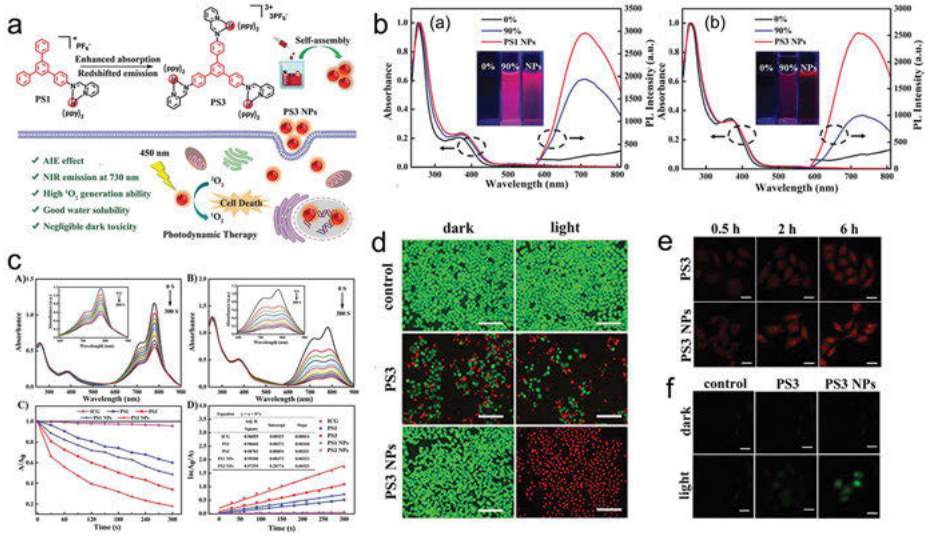

Figure 20.5: a) Structures of **PS1**/**PS3** and schematic of **PS3** NPs as a PS for PDT. b) Normalized absorption spectra and PL spectra of (left) PS1 and (right) **PS3** in DMSO, DMSO/water = 1/9, and their corresponding NPs in water. The insets are photographs of **PS1**/ **PS3**/NPs under 365 nm UV irradiation. (PS) = 10^{-5} M. c) Absorption spectra of ICG solutions containing (A) **PS1** NPs and (B) **PS3** NPs at different times upon irradiation of a 450 nm LED (0.6 J cm^{-2}). The time interval of UV recording = 30 s. (C) Decomposition of ICG at 790 nm in the presence of various **PS**s with irradiation. (D) Time-dependent $^1O_2$ generation kinetics. A_0 = the absorbance maximum before irradiation. A = the absorbance maximum after irradiation. (**PS**) = 5 × 10^{-6} M, (ICG) = 6.5 × 10^{-6} M. d) Fluorescence images of calcein-AM and PI co-stained HeLa cells in the presence of **PS3** and **PS3** NPs (8 μM). In panels A–C, all of the light groups were irradiated with 450 nm LED at 20 mW cm^{-2} for 35 min (42 J cm^{-2}). The scale bars are 40 μm. e) CLSM phosphorescence images of various **PS**-treated HeLa cells for 0.5 h, 2 h and 6 h, respectively. (**PS**) = 8 μM. f) Fluorescence images of ROS production in HeLa cells stained with **PS3** and **PS3** NPs under the light of a 450 nm LED at 20 mW cm^{-2} for 15 min (18 J cm^{-2}) using DCFH-DA as an indicator. The scale bars are 20 μm (a–f) Copyright 2020, The Royal Society of Chemistry [21].

the most ROS, and had higher lethality at low concentrations, and is believed to be a promising candidate for two-photon-absorbing PDT (Figure 20.6).

Besides, dimetal complex can be obtained based on Ir with other metals for research in the field of biology. As Tian et al. reported, the NIR-II cyclometalated Ir (III) – organotin(IV) dimetal complex (**IrSn1**) based on terpyridine carboxylate ligands can exhibit two-/three-photon phosphorescence and multiphoton AIE activity (Figure 20.7a, b) [22]. **IrSn1** specifically targeted tyrosine in both *Staphylococcus aureus* and cancer cells, reacting with tyrosine or tyrosine-containing proteins in nucleus, resulting in DNA breaking and hence leading to cell or bacterial apoptosis (Figure 20.7).

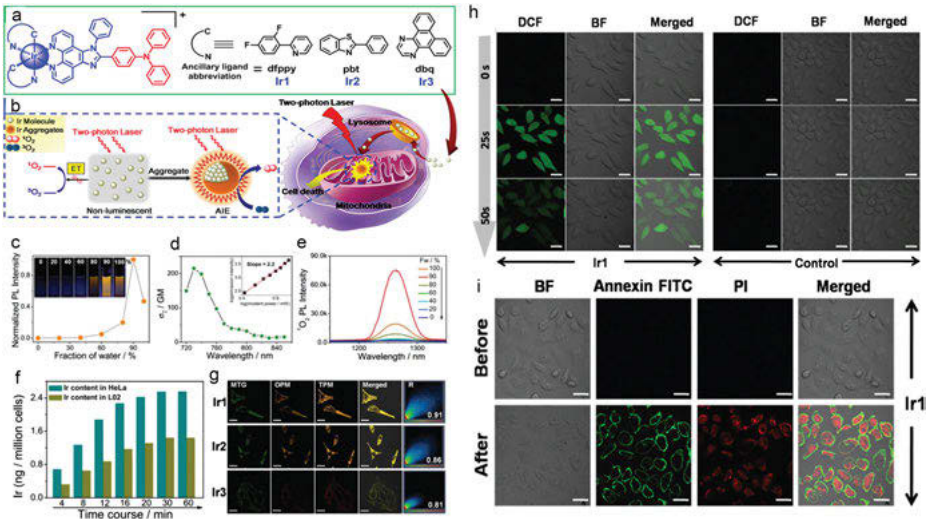

Figure 20.6: a) Chemical structures of **Ir1–Ir3**. b) Schematic illustration of lit up TPA-PDT in mitochondria of by **Ir1–Ir3**. c) Trajectory of **Ir1** emission intensity versus water fraction and visual observation of PL. d) TPA cross-sections of **Ir1**; inset: logarithmic dependence of emission intensity on incident power. e) $^1O_2$ emission spectra in the presence of **Ir1** and irradiation (lirr = 405 nm) in varying fractions of water–DMSO mixture. f) Time-dependent ICP-PS of HeLa/L02 cells pre-incubated with 0.5 pM **Ir1**. g) Confocal co-localization images of **Ir1–Ir3**. Inset scale bars: 20 mm. h) Confocal images of HeLa before and after PDT. Cells were pre-incubated with DCFH-DA. i) Annexin V-FITC/PI co-staining on HeLa cells before and after TPA-PDT. Cells were pre-incubated with Ir1. Inset scale bar: 20 mm. (a–i) Copyright 2017, The Royal Society of Chemistry [16].

20.3 Pt (II) complexes

AIE-active Pt (II) complexes with stable geometry, long excitation lifetime, low photobleaching and low light scattering have attracted excellent attention in bioimaging, in recent years [17, 33]. A cyclometalated Pt (II) complex with two-photon action cross-section was designed for bioimaging, as reported by Li et al. (Figure 20.8a–c) [17]. Benefiting from its flexible chains and abundant electronic structure, it displayed excellent AIE behavior under physiological conditions due to its self-assembly process with the proportion of water increased. Its abundant electronic structure, increased two-photon absorption cross-section and passive intermolecular hydrogen bonds enhanced two-photon activity, which is beneficial in bioimaging (Figure 20.8a–c). Another AIE-active cyclometalated Pt (II) complex [Pt(C^N) (P^P)]Cl [P^P = bis(diphenylphosphino)ethane (2)] was synthesized and used for cytotoxicity and cell imaging study from Laskar and his colleagues (Figure 20.8d–g) [33]. It can be seen that Pt (II) complex has broad application prospects in biology.

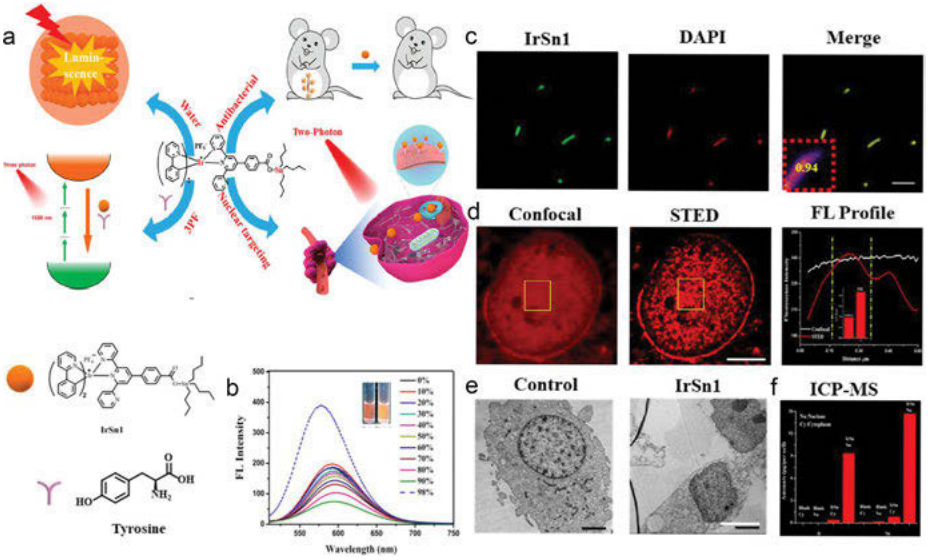

Figure 20.7: a) Graphic Scheme of **IrSn1** and Its Applications. b) Emission spectra of **IrSn1** in different H_2O fraction with concentration of 1×10^{-5} mol/L. (inset) photographs of the luminescence of **IrSn1** in water fractions (0 and 98%). c) Colocalization experiments using DAPI incubated on *Staphylococcus aureus* (inset: Pearson's coefficients Rr = 0.98), scale bar = 20 μm). d) Two-photon fluorescence confocal imaging and stipulated emission depletion (STED) microscopy of **IrSn1** staining nuclear in A549 cells (inset: S/N ratio of confocal and STED, scale bar = 5 μm). e) Transmission electron microscope (TEM) of A549 cells using osmium tetroxide (OsO_4) as membrane-localizing contrast agent, TEM microscopy of A549 cells incubated with **IrSn1** stained without osmium tetroxide (scale bar = 5 μm). f) The amount of Ir and tin in cytoplasm and nucleus fractions was measured by ICP-PS. Data were collected at least three times, independently. Copyright 2020, American Chemical Society [22].

20.4 Au (I) complexes

Recently, many Au (I) complexes have been developed for in vivo and in vitro anticancer research [2]. Among them, Au (I) N-heterocyclic carbene (Au^I-NHC) complexes are anticancer agents with high hopes due to their high cytotoxicity and good stability [2]. A series of tetraphenylethene (TPE) modified Au^I-NHC with AIE activity is reported as a bioimaging and theranostic agent for cancer (Figure 20.9a), according to the report by Tang *et al.* [2]. The introduction of TPE with AIE activity makes the system have AIE characteristics, and four different ligands directly affect the biological activity of the complex (Figure 20.9a and d). The experimental results indicate that the introduction of the bulky TPE unit not only could endow all compounds with light-upluminescence but also enhance their binding ability to thioredoxin reductase (TrxR). The systems achieve specific in situ bioimaging of cancer cells and high targeting specificity (Figure 20.9c),

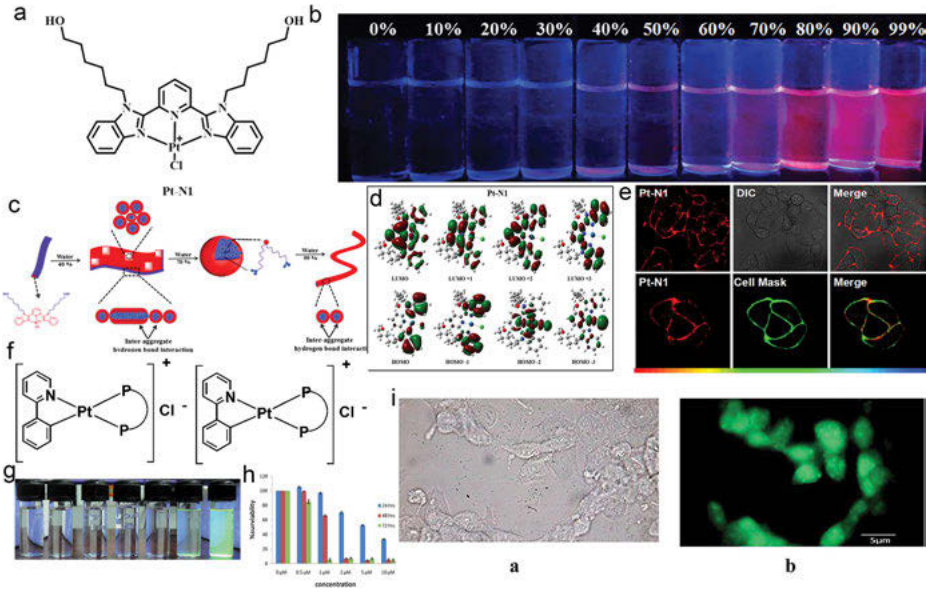

Figure 20.8: a) Diagrammatic sketch of **Pt-N1** (10^{-5} M) with increasing water content. b) (a) Two-Photon Fluorescent images of HeLa cells stained with **Pt-N1** (10 μM, excitation wavelength 860 nm) and colocalization images of HeLa cells stained with **Pt-N1** (10 μM, red channel, λ_{ex} = 860 nm, λ_{em} = 630 ± 20 nm) and CellmaskTP green (0.5 μM, green channel, λ_{ex} = 522 nm, λ_{em} = 535 ± 20 nm). c) Photographs taken under UV illumination of **Pt-N1** (10^{-5} M) with increasing PBS content. (a–c) Copyright 2020, Elsevier [17]. d) Chemical structures of the Pt (II) complex. e) Image of the complex with increasing amount of hexane. f) The time kinetic study of complex as assayed by PTT. g) Bright field image (a) and fluorescence image (b) (right, 100×) of Hep3B cells following treatment with complex 2. Fluorescence image depicts successful internalization of the complex by Hep3B cells and its AIE characteristics [Scale bar (5 pp)]. (d–g) Copyright 2014, The Royal Society of Chemistry [33].

and the Au (I) complexes can effectively inhibit highly expressed TrxR activity in cancer cells, result in a significant increase in the level of intracellular ROS, disrupt redox homeostasis in the cell, and trigger specific anticancer effects (Figure 20.9b and c).

Meanwhile, AIE-active Au (I) complexes have emerged as outstanding probes for living physiological environment monitoring owing to their excellent photophysical properties [34]. Tang et al. reported a pH-responsive stable Au (I) complex with intense AIE effects (Figure 20.9e-g) [34]. Disulfide bonds were formed to introduce pH-responsive moiety cysteine (Cys) into the Au (I)-SR complex by a radical-based mechanism (Figure 20.9e). Hydrophilic Cys at the outer layer of the NPs were stable and monodisperse in water, which resulted in spherical NPs being formed (Figure 20.9h). Owing to the change of surface charge over the acidic pH range, the aggregation extents of **Au (I)-disulfide NPs** varied and led to the obvious luminescence intensity changes at various pH values (Figure 20.9i and j). Based on the pH-responsive AIE

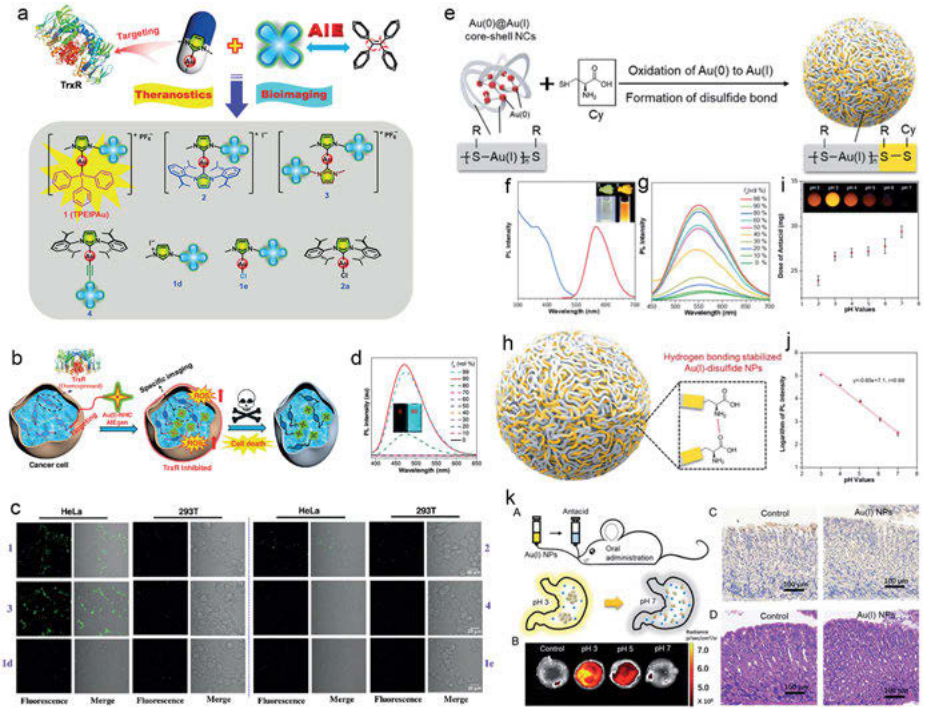

Figure 20.9: A) Molecular design and molecular structures of a series of carbene compounds. b) Illustration of AIE-active **Au-NHC** for specific cancer cell imaging and inhibition. c) Fluorescent images and merged images of HeLa cells and 293 T cells stained with of 1–4, 1d, and 1e for 2.5 h, respectively. Excitation wavelength: 405 nm; emission filter: 410–585 nm. d) PL spectra of 1 (2.0×10^{-5}M) in CH_3CN/water mixtures as a representative. (a–d) Copyright 2020, Wiley-VCH Verlag GpbH & Co. KGaA, Weinheim [2]. e) Schematic illustration of the preparation of **Au (I)-disulfide NPs**. f) Photoluminescence (red line, $\lambda_{ex} = 365$ nm) and photoexcitation (blue line, $\lambda_{em} = 565$ nm) spectra of **Au (I)-disulfide NPs**. (insets) Digital photos of **Au (I)-disulfide NPs** in the solid state (top row) and in water (bottom row) under (1) visible light and (2) UV light. g) Photoluminescence spectra of **Au (I)-disulfide NPs** in a mixture of water–ethanol with different ethanol fractions (*fe*), $\lambda_{ex} = 365$ nm and (I) variation in I/I_0 with *fe*, $\lambda_{ep} = 565$ nm. h) Schematic illustration of the structure of **Au (I)-disulfide NPs**. The hydrogen bonds between Cys existed at the outer layer of **Au (I)-disulfide NPs** and maintain the structural stability of NPs in water. In vitro monitoring acidity of the gastric fluid in an acid-suppressed therapy. (i) In vitro pH values of the gastric fluid in the presence of **Au (I)-disulfide NPs** adjusted by different doses of antacid. (j) pH-dependent logarithm of the PL intensity of the **Au (I)-disulfide NPs** in gastric fluid. k) Monitoring intragastric acidity in an acid-suppressed therapy. (A) Schematic illustration of the in vivo monitoring gastric acid process by **Au (I)-disulfide NPs**. (B) Fluorescent images of the stomach of mice cut open along the greater curvature, which was collected after 10 min post administration of **Au (I)-disulfide NPs** and antacid. The intragastric acidity was suppressed by using different doses of antacid to achieve the pH value of 3, 5, 7. Mice treated with water were used as a control. (C) Section of the mouse stomach from the mice treated with water (control) and **Au (I)-disulfide NPs** stained with the H&E assay. (D) Sections of the mouse stomach from the mice treated with water (control) and **Au (I)-disulfide NPs** stained with TUNEL assay. (e–k) Copyright 2020, The Royal Society of Chemistry [34].

characteristics, the Au (I) complex was employed as a luminescent probe to measure the intragastric acidity during the acid suppression therapy (Figure 20.9k).

20.5 Other transition metal complexes

Other transition metal complexes with AIE activity obtained through different molecular design strategy are also active in the biological field for the imaging of living cells or targeted imaging of organelles [7, 35]. Khatua et al. integrated 4,7-dichloro phenanthroline into Ru (II) complex (Figure 20.10a), and discovered the weak supramolecular interaction among the moleculars [35]. The possible reason behind the AIE property may be the weak supramolecular π. . .π, C–H. . .π, and C–Cl. . .H interactions between neighboring phen ligands as well as C–Cl. . .O halogen bonding (XB), and C–Cl. . .O XB interaction in the presence of RNA, which can form an aggregate and enhance the PL intensity (Figure 20.10b). The Ru (II) complex emitted red and exhibited AIE-active. It was constructed for RNA specific nucleolar imaging (Figure 20.10c-e). The AIE-active Zn (II) complex **DZ1** with D–A type thiophene terpyridine ligand can penetrate mitochondrial membranes passively, recognize mitochondrial RNA by charge action, and was used to label mitochondria in cells, as reported by Tian et al. (Figure 20.10f-i) [7]. AIE-active probe **DZ1** suppressed aggregation-caused quenching (ACQ) behavior due to self-aggregation under physiological conditions, but was also obtained simply and exhibited excellent photostability. Cu (I) complexes possess d^{10} electronic structure and provide a tunable phosphorescent emission at room temperature and a long luminescence lifetime of several microseconds [12]. Li and his colleagues have reported four binuclear mixed-ligand Cu (I) complexes $[Cu_2(BrphenBr)_2(Ph_2P(CH_2)_nPPh_2)_2](ClO_4)_2$ (BrphenBr = 3,8-dibropo-1,10-phenanthroline; Ph2P- $(CH_2)_nPPh_2$ = bridging diphosphine ligands, n = 1, 4, 5, or 6 (Figure 20.10j) [12]. And it is the first example of Cu (I) complexes with significant AIE-active applied for imaging in live cells (Figure 20.10j–l).

20.6 Conclusion

In this chapter, an overview on AIE-active transition metal complexes for bioimaging, cancer therapy, antibacterial, etc. is shown. Their AIE activity may resolve fluorescence quenching resulting from aggregation and permit a long-term observation without large luminescent signal loss. By introducing various cyclometallic ligands or ancillary ligands into transition metal complexes, the photophysical properties of complexes could be modified, and the intracellular localization of complexes may be targeted or the therapy effect may be improved.

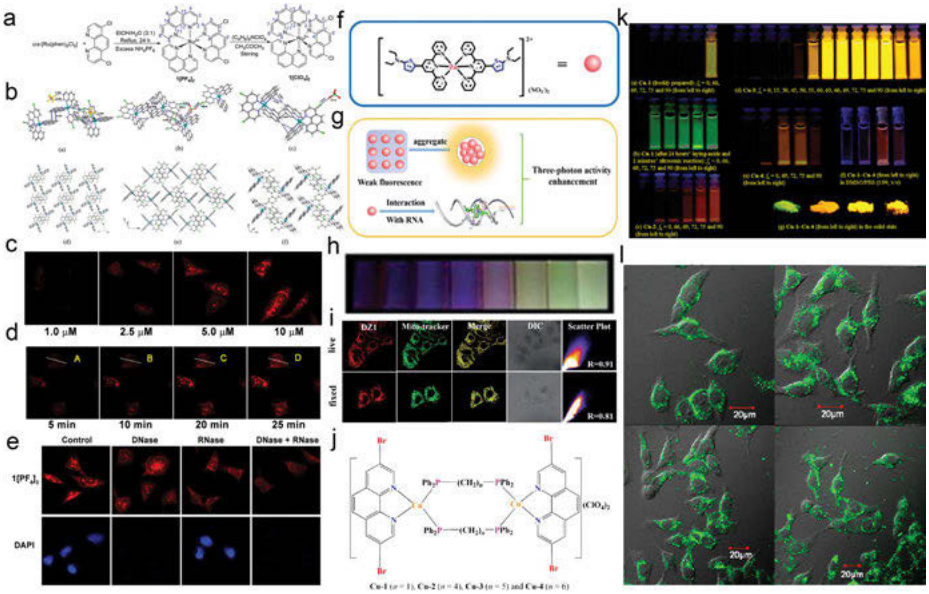

Figure 20.10: a) Synthesis of Ru (II) complex $1[PF_6]_2$ and $1[ClO_4]_2$. b) Weak supramolecular interactions (C – H ···π and π – π stacking), C – Cl ···H interaction, and C – Cl ···O XB interaction in (a) **$1[PF_6]_2$**, (b) **$1[ClO_4]_2$**, and (c) **$1[ClO_4]_2(CH_3CN)(H_2O)$**, respectively. View of the two-dimensional (2D) crystal packing in (d) compounds **$1[PF_6]_2$**, (e) **$1[ClO_4]_2$**, and (f) **$1[ClO_4]_2(CH_3CN)(H_2O)$**. Fluorescence microscopy images of HeLa cells (c) stained with different concentrations of **$1[PF_6]_2$** (1.0–10 μM) and (d) at different time points (**$1[PF_6]_2$** at 10 μM) in aqueous phosphate buffered saline (PBS) buffer. e) Fluorescence images of fixed HeLa cells during DNase and RNase digest experiments with $1[PF_6]_2$ and nucleus staining dye DAPI. (a–e) Copyright 2018, American Chemical Society [35]. f, g) Three-photon property of Zn (II) complex **DZ1** in the aggregated state or upon interaction with RNA (schematic). h) photographs of the luminescence of **DZ1** in ethyl acetate fractions (0–98%) under UV illumination at 365 nm. i) The fluorescence development of **DZ1** in fixed cells and living cells, respectively. (f–i) Copyright 2019, The Royal Society of Chemistry [7]. j) Chemical structures of complexes **Cu-1**-**Cu-4**. k) Luminescent images of **Cu-1**-**Cu-4** radiated with an ultraviolet light at 365 nm: (a–e) in hexane – DCM mixed solvents with the concentration kept at 2.5×10^{-5} mol · L^{-1}; (f) in DMSO/PBS (1:99, v:v) with concentration at 1.0×10^{-5} mol · L^{-1}; (g) in the solid state. l) Confocal luminescence imaging of complexes Cu-1-Cu-4 in HeLa cells, which were incubated with 10 μM complexes **Cu-1**-**Cu-4** in DMSO/PBS (1:99, v/v) for 15 min ((a) **Cu-1**, (b) **Cu-2**, (c) **Cu-3**, and (d) **Cu-4**). (j–l) Copyright 2014, American Chemical Society [12].

It is clear that new ideas of transition metal complexes for biological applications are reported every year. The reported works have great significance in providing insights into design and practical applications in transition metal complexes in bioimaging and anticancer.

However, the mechanisms for the changes the intracellular localization and the improvement of the therapeutic effect caused by various ligands of complexes are not clear enough. And the potential cytotoxicity induced by some transition metal complexes is nonnegligible for probes. Thus, future research need to focus on the

following aspects: i) develop more AIE activity transition metal complexes for more effective biological probes and anticancer agents, ii) explore more in-depth molecular design strategy for clinical application, iii) solve problems of the potential toxicity of complexes in application through various methods, iv) realize clearer imaging and higher therapy efficiency at low concentration.

References

[1] Luo J, Xie Z, Lam JWY, et al., Aggregation-induced emission of 1-pethyl-1,2,3,4,5-pentaphenylsilole, Chem Commun, 2001, 1740–1741.
[2] Zhang J, Zou H, Lei J, et al., Multifunctional Au (I)-based AIEgens: Manipulating molecular structures and boosting specific cancer cell imaging and theranostics, Angew Chem Int Ed, 2020, 59, 7097–7105.
[3] Hong Y, Lam JWY, Tang BZ, Aggregation-induced emission, Chem Soc Rev, 2011, 40, 5361–5388.
[4] Kwok RTK, Leung CWT, Lam JWY, Tang BZ, Biosensing by luminogens with aggregation-induced emission characteristics, Chem Soc Rev, 2015, 44, 4228–4238.
[5] Suresh VM, De A, Maji TK, High aspect ratio, processable coordination polymer gel nanotubes based on an AIE-active LMWG with tunable emission, Chem Commun, 2015, 51, 14678–14681.
[6] Zhang W, Kwok RTK, Chen Y, et al., Real-time monitoring of the mitophagy process by a photostable fluorescent mitochondrion-specific bioprobe with AIE characteristics, Chem Commun, 2015, 51, 9022–9025.
[7] Feng Z, Li D, Zhang M, et al., Enhanced three-photon activity triggered by the AIE behaviour of a novel terpyridine-based Zn (II) complex bearing a thiophene bridge, Chem Sci, 2019, 10, 7228–7232.
[8] Alap P, Das P, Clipent C, et al., Facile tuning of the aggregation-induced emission wavelength in a common framework of a cyclometalated iridium(III) complex: Micellar encapsulated probe in cellular imaging, J Mater Chem C, 2014, 2, 5615–5628.
[9] Sheet SK, Sen B, Aguan K, Khatua S, A cationic organo iridium(III) complex-based AIEgen for selective light-up detection of rRNA and nucleolar staining, Dalton Trans, 2018, 47, 11477–11490.
[10] Chowdhury A, Howlader P, Mukherjee PS, Aggregation-induced emission of platinum(II) metallacycles and their ability to detect nitroaromatics, Chem Eur J, 2016, 22, 7468–7478.
[11] Hou X-G, Wu Y, Cao H-T, et al., A cationic iridium(III) complex with aggregation-induced emission (AIE) properties for highly selective detection of explosives, Chem Commun, 2014, 50, 6031–6034.
[12] Xin X-L, Chen M, Y-b A, F-l Y, X-l L, Li F, Aggregation-induced emissive copper(I) complexes for living cell imaging, Inorg Chem, 2014, 53, 2922–2931.
[13] Chi Y, Chou P-T, Transition-metal phosphors with cyclometalating ligands: Fundamentals and applications, Chem Soc Rev, 2010, 39, 638–655.
[14] Wen -L-L, Hou X-G, Shan -G-G, et al., Rational molecular design of aggregation-induced emission cationic Ir (III) phosphors achieving supersensitive and selective detection of nitroaromatic explosives, J Mater Chem C, 2017, 5, 10847–10854.

[15] Zhao K-Y, Shan -G-G, Fu Q, Su Z-M, Tuning emission of AIE-active organometallic Ir (III) complexes by simple modulation of strength of donor/acceptor on ancillary ligands, Organometallics, 2016, 35, 3996–4001.
[16] Liu J, Jin C, Yuan B, et al., Selectively lighting up two-photon photodynamic activity in mitochondria with AIE-active iridium(III) complexes, Chem Commun, 2017, 53, 2052–2055.
[17] Yao X, Zhang W, Fang B, Li S, Tian Y, Li D, Turning on two-photon activity over N^N^N cyclometalated Pt (II) complex by introducing flexible chains, Dyes Pigm, 2021, 184, 108788.
[18] Zhang L, Li Y, Che W, et al., AIE multinuclear Ir (III) complexes for biocompatible organic nanoparticles with highly enhanced photodynamic performance, Adv Sci, 2019, 6, 1802050.
[19] Sun W, Li S, Häupler B, et al., An amphiphilic ruthenium polymetallodrug for combined photodynamic therapy and photochemotherapy in vivo, Adv Mater, 2017, 29, 1603702.
[20] Wu W, Mao D, Hu F, et al., A highly efficient and photostable photosensitizer with near-infrared aggregation-induced emission for image-guided photodynamic anticancer therapy, Adv Mater, 2017, 29, 1700548.
[21] Li L, Zhang L, Tong X, et al., Near-infrared-emitting AIE multinuclear cationic Ir (III) complex-assembled nanoparticles for photodynamic therapy, Dalton Trans, 2020, 49, 15332–15338.
[22] Zhang Q, Lu X, Cao H, et al., Multiphoton absorption iridium(III)–organotin(IV) dimetal complex with AIE behavior for both sensitive detection of tyrosine and antibacterial activity, ACS Appl Bio Mater, 2020, 3, 8105–8112.
[23] Zhang L, Che W, Yang Z, et al., Bright red aggregation-induced emission nanoparticles for multifunctional applications in cancer therapy, Chem Sci, 2020, 11, 2369–2374.
[24] Cheng Y, Dai J, Sun C, et al., An intracellular H_2O_2-responsive AIEgen for the peroxidase-mediated selective imaging and inhibition of inflammatory cells, Angew Chep Int Ed, 2018, 57, 3123–3127.
[25] Huang K, Wu H, Shi P, Li F, Yi T, Huang C, Reply to comment on 'aggregation-induced phosphorescent emission (AIPE) of iridium(III) complexes': Origin of the enhanced phosphorescence, Chem Commun, 2009, 1243–1245.
[26] You Y, Huh HS, Kip KS, Lee SW, Kip D, Park SY, Comment on 'aggregation-induced phosphorescent emission (AIPE) of iridium(III) complexes': Origin of the enhanced phosphorescence, Chem Commun, 2008, 3998–4000.
[27] Zhao Q, Li L, Li F, et al., Aggregation-induced phosphorescent emission (AIPE) of iridium(III) complexes, Chem Commun, 2008, 685–687.
[28] Jin C, Liu J, Chen Y, et al., Cyclometalated iridium(iii) complexes as AIE phosphorescent probes for real-time monitoring of mitophagy in living cells, Sci Rep, 2016, 6, 22039.
[29] Dai J, Li Y, Long Z, et al., Efficient near-infrared photosensitizer with aggregation-induced emission for imaging-guided photodynamic therapy in multiple xenograft tumor models, ACS Nano, 2020, 14, 854–866.
[30] Wang D, Su H, Kwok RTK, et al., Facile synthesis of Red/NIR AIE luminogens with simple structures, bright emissions, and high photostabilities, and their applications for specific imaging of lipid droplets and image-guided photodynamic therapy, Adv Funct Mater, 2017, 27, 1704039.
[31] Smith RAJ, Hartley RC, Cochepé HM, Murphy MP, Mitochondrial pharmacology, Trends Pharmacol Sci, 2012, 33, 341–352.
[32] McKenzie LK, Sazanovich IV, Baggaley E, et al., Metal complexes for two-photon photodynamic therapy: A cyclometallated iridium complex induces two-photon photosensitization of cancer cells under near-IR light, Chem Eur J, 2017, 23, 234–238.

[33] Pasha SS, Alap P, Dash S, et al., Rare observation of 'aggregation induced emission' in cyclometalated platinum(II) complexes and their biological activities, RSC Adv, 2014, 4, 50549–50553.
[34] Wang J, Li J, Li Y, et al., pH-Responsive Au (I)-disulfide nanoparticles with tunable aggregation-induced emission for monitoring intragastric acidity, Chem Sci, 2020, 11, 6472–6478.
[35] Sheet SK, Sen B, Patra SK, Rabha P, Aguan K, Khatua S, Aggregation-induced emission-active ruthenium(II) complex of 4,7-dichloro phenanthroline for selective luminescent detection and ribosomal RNA imaging, ACS Appl Mater Interfaces, 2018, 10, 14356–14366.

Dan Wu, Zhixuan Zhou, Xuzhou Yan, and Guocan Yu

Chapter 21
The marriage of aggregation-induced emission with discrete supramolecular coordination complexes: brighter AIEgens for biomedical applications

21.1 Introduction

To understand the molecular and cellular mechanisms involved in physiology and disease, biomedical research increasingly aims for noninvasive imaging with cellular resolution *in vivo* [1–4]. In order to create the most accurate representation of biological objects and/or processes, many cutting-edge imaging technologies have emerged with the objective of increasing the resolution. Fluorescent imaging, in particular, has become a promising technique in preclinical studies of human diseases because of its high sensitivity, lower cost, avoidance of ionizing radiation, and multiplex detection capabilities [5–8]. The high sensitivity of fluorescent imaging allows the study of rapid biological processes in greater detail than the currently available imaging modalities such as magnetic resonance imaging, ultrasound, and computed tomography [9–12]. Fluorescent probes that can provide useful information from biological responses through specific interactions are of paramount importance for medicine, molecular and cellular biology, chemistry, chemical biology, and other interdisciplinary sciences [13–16]. However, light emission from conventional fluorescent materials is often quenched at high concentrations and in the aggregated state, and this phenomenon is often referred to as aggregation-caused quenching (ACQ)

Acknowledgements: We are very grateful to Professors Ben Zhong Tang and Xinggui Gu for their kind invitation and guidance. We are also very thankful to Prof. Peter J. Stang, Prof. Feihe Huang, Prof. Xiaoyuan (Shawn) Chen, and Prof. Xi Zhang for their enormous help, support, and encouragement. G.Y. is thankful for the startup funds from the Tsinghua University.

Dan Wu, Key Lab of Organic Optoelectronics & Molecular Engineering, Department of Chemistry, Tsinghua University, Beijing, 100084, P. R. China; College of Materials Science and Engineering, Zhejiang University of Technology, Hangzhou, 310014, P. R. China
Zhixuan Zhou, Max Planck Institute for Polymer Research, Mainz, 55128, Germany, e-mail: zhixuan.zhou@mpip-mainz.mpg.de
Xuzhou Yan, School of Chemistry and Chemical Engineering, Frontiers Science Center for Transformative Molecules, Shanghai Jiao Tong University, Shanghai, 200240, P. R. China
Guocan Yu, Key Lab of Organic Optoelectronics & Molecular Engineering, Department of Chemistry, Tsinghua University, Beijing, 100084, P. R. China, e-mail: guocanyu@mail.tsinghua.edu.cn

https://doi.org/10.1515/9783110673074-022

effect. The ACQ effect forces researchers to employ low concentrations of fluorophores for biomedical applications, thus greatly compromising their photostability [17]. To overcome the ACQ effect, various physical, chemical, and engineering methods have been explored. However, rare successes have been realized because it remains challenging to fight against the natural tendency of aggregate formation of fluorescent dyes [18–20].

In 2001, a novel phenomenon, defined as aggregation-induced emission (AIE), was discovered by Tang and coworkers [21, 22]. The AIE effect is just the opposite of the ACQ effect and can offer the ultimate solution to the ACQ issue. AIE fluorogens (AIEgens) are weakly emissive in dilute solution or in the molecular state, but emit bright fluorescence in the aggregate or solid state [23]. In dilute solution, the active intramolecular motions (including vibration and rotation) of AIEgens boost the nonradiative decay channels to quench the emission. However, in the aggregate state, the intramolecular motions are severely restricted and the nonradiative decay channels are blocked, thus leading to the stable and intensive fluorescence [24]. In the meantime, owing to the nonplanar molecular structure of AIEgens, the π–π stacking interactions during aggregation are also significantly avoided, further lighting up the fluorescence of AIEgens [25]. The preeminent photophysical and photochemical properties, as well as the excellent biocompatibility of AIEgens, have promoted their application in various fields [26–32].

Although AIEgens can emit intensive fluorescence in the aggregate state, their fluorescence can be hardly detected in the mono-dispersed state, meaning, the sensitivity of AIEgens in the mono-dispersed state is likely to be low. Hence, in the pursuit for more efficient AIEgens, improving the sensitivity of molecular AIEgens is the priority. Over the last few decades, coordination-driven self-assembly has developed into an efficient strategy to construct discrete supramolecular coordination complexes (SCCs), in which functional building blocks (Lewis acidic acceptors and Lewis basic donors) can be integrated and their unique characteristics can be maintained [33–37]. Attributing to the directionality and moderate bond energy of metal-ligand bonds, the structure of SCCs can be highly tuned. To date, a wide variety of SCCs with different topological structures, such as two-dimensional (2D) metallacycles, and three-dimensional (3D) metallacages, have been ingeniously constructed [38–41]. Owing to the excellent optical property of AIEgens and the directionality of the metal-ligand bond, AIE-active donors have been integrated into SCCs and the intramolecular rotations of AIEgens are effectively restricted, thus generating AIE-active SCCs, which can emit strong fluorescence, both in the dilute solution and in the aggregate state [42–45]. AIE-active SCCs usually have high sensitivity and outstanding photostability; so, they are excellent candidates for fluorescent imaging. As archetypical AIE-active donors, tetraphenylethylene (TPE) derivatives are widely used in the construction of AIE-active SCCs [46–50]. Meanwhile, metal acceptors, such as Pd, Pt, Rh, Ru, Ir, Co, Zn, and Cd, have been used as metal acceptors to construct SCCs for various purposes. For example, Ir-, Zn- or Rh-containing SCCs are

mainly used in drug delivery systems [51, 52], while the Ru- and Pt-containing metallacycles and metallacages are used as drug carriers or anticancer drugs [53–55]. Upon the formation of SCCs, the selectivity of metal chemotherapeutics towards target cells can be significantly improved, thus reducing their side effects and enhancing their therapeutic index. Furthermore, their drawbacks, including rapid clearance and poor solubility, can be efficiently optimized. Based on the AIE effect and therapeutic effects, these AIE-active SCCs have great potential in the development of high-efficiency theranostic platforms for various diseases.

With the rapid development of AIE-active SCCs, they have been endowed with multiple biological functions. For example, they can serve as biomolecular sensors, cell imaging agents, anti-cancer drugs, and antimicrobial agents. In this chapter, the design of AIE-active SCCs and the influence factors on their photophysical characteristics are fully described. Moreover, the biomedical applications of AIE-active SCCs are also discussed. Attributing to the flexibility and diversity of supramolecular coordination reactions, smarter AIE-active SCCs can be constructed and applied in biomedical studies, even in clinical transformation stages.

21.2 Strategies for introducing AIE behaviors in SCC-based systems

Coordination-driven self-assembly of SCCs allows the introduction of functionalities in their structure *via* molecular precursor building blocks, containing specific functional groups. The continuous development in the structural and synthetic chemistry of SCCs offers scaffolds for incorporating various functionalities where the stoichiometry and position of the individual functional groups can be precisely controlled, and novel multicomponent self-assemblies provide even more approaches towards novel SCCs, with increased structural and functional complexities [33, 56]. Upon self-assembly, the functionalities can further interact, giving rise to a higher level of functionality. These advances facilitate the rational design of novel, multifunctional SCC-based systems with AIE behavior. AIE-active SCCs can be generally classified into two types: small molecules and polymers (Figure 21.1). In the small molecular AIE-active SCCs, AIEgens usually act as the main building blocks (Figure 21.1a) or the pendants (Figure 21.1b) of SCCs. In the AIE-active SCC-based polymers, AIE-active SCCs act as the core or the monomer of polymers (Figure 21.1c), achieving win-win results for AIE-active SCCs and polymers.

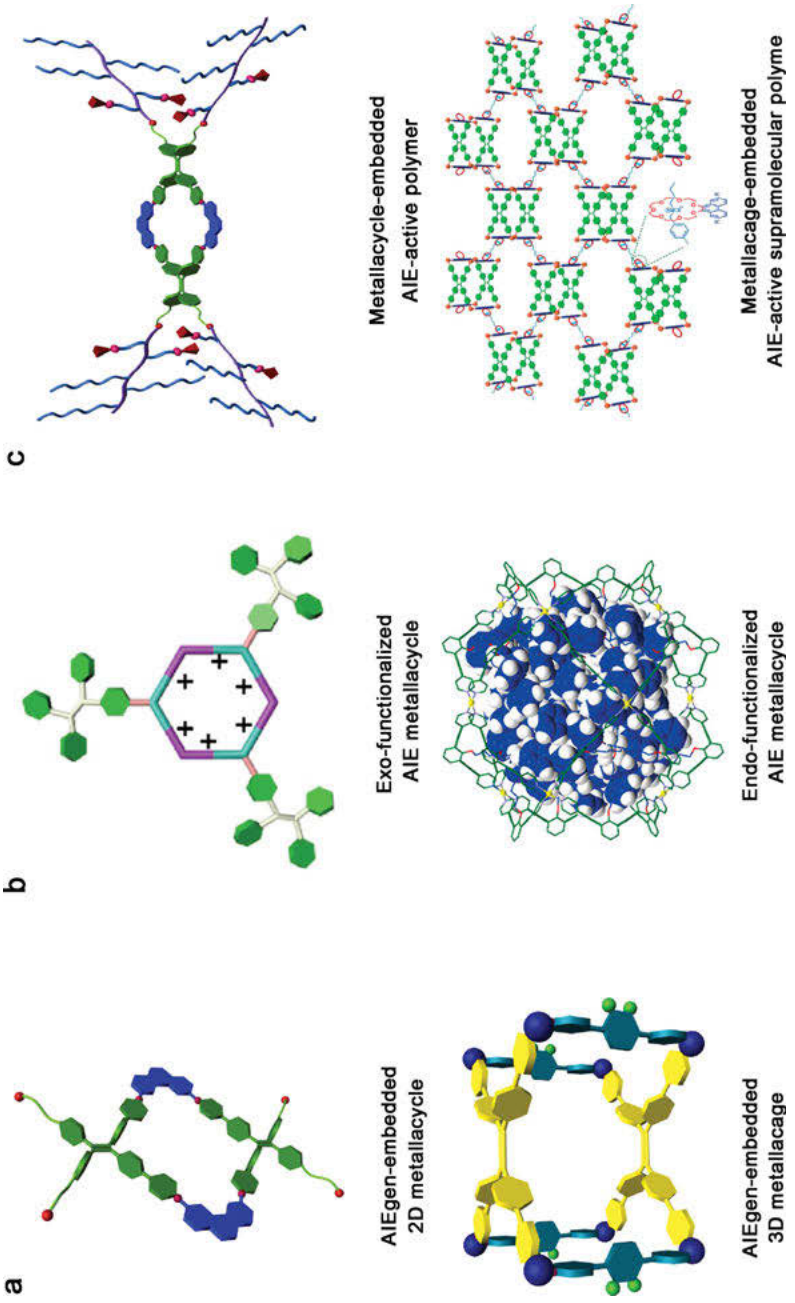

Figure 21.1: a) Schematic illustration of AIEgen-embedded metallacycle and metallacage. b) Schematic illustration of AIEgen-functionalized metallacycle and metallacage. c) Schematic illustration of AIE-active metallacycle-embedded polymer or metallacage-embedded supramolecular polymer.

21.2.1 AIEgens as structural building blocks

As a consequence of their straightforward nature, modification of known AIEgens with functional groups that serve as the impetus for coordination driven self-assembly is widely exploited for the construction of AIE-active SCCs. These functional groups are often electron-rich "donor" units for coordination interaction, such as pyridyl, carboxylate, and *N*-heterocyclic carbene (NHC) groups. In comparison, modifying AIEgens with electron-poor "acceptor" units, including phosphine-based Pd(II) and Pt(II) moiety, is less explored due to the challenges associated with their synthesis and the potential of competitive nonradiative processes such as intramolecular charge transfer (ICT) and intersystem crossing (ISC), which result in a low luminescence quantum yield and short excited-state lifetime, relative to the free AIEgens [57]. Since high rigidity is often required for the structural building block to ensure the exclusive formation of a single, discrete SCC under thermodynamic control, TPE is extensively employed as a structural building block for the construction of AIE-active SCCs. In addition, TPE possesses advantageous properties such as good chemical stability under general conditions, ease of modification, and a reliable AIE effect, which tolerates a great variety of functional groups.

The first systematic investigation on AIE-active SCCs was reported in 2015 by Yan and coworkers [50]. They coupled pyridyl groups on each phenyl ring of the TPE, and mixed the resulting tetrapyridyl ligand (**1**) with benzene dicarboxylate (**3**) and platinum phosphine complex (**2**) with two open coordination sites at 90-degree bite angles in a 1:2:4 molar ratio to create an AIE-active discrete tetragonal metallacage (**5**) (Figure 21.2a). In addition to the simple benzene dicarboxylate, metallacage decorated with pendant poly(ethylene glycol) (PEG) (**6**) was self-assembled in the same manner using PEG-functionalized dicarboxylate ligand (**4**). The charge separation of the pyridyl and carboxylate ligands ensured the quantitative three-component coordination-driven self-assembly in one pot. While the TPE ligand showed almost no fluorescence emission when dissolved in CH_2Cl_2 solutions, both assemblies displayed bright-yellow fluorescence in CH_2Cl_2 solutions, and their emission spectra were centered at 555 nm, with luminescence quantum yield (Φ_F) values of 23.2 and 10.8%, respectively. The significant increase in the fluorescence efficiency was attributed to the attenuated phenyl-ring rotation and the ethylenic C=C bond twisting when the TPE moiety was immobilized within the rigid 3D scaffold. In addition, the Φ_F for both **5** and **6** further increased upon raising the content of hexane (60.6% and 51.3% when hexane content in the mixed solution reached 90% for **5** and **6**, respectively), a poor solvent for the metallacages, in the solution, which lead to aggregation. The aggregation of the assemblies entirely forbade the decay of excitation energy through the limitation of intramolecular motion, resulting in further enhancement in the fluorescence efficiency. The high fluorescence efficiencies of the metallacages, both in the dilute solution and in the aggregate state, represent a novel photophysical behavior that bridge the gap between conventional fluorophores,

which are highly light-emitting in the dilute solution, but oftentimes show quenched emission due to ACQ. In contrast, AIE-based fluorophores were highly emissive when their intramolecular motions were restricted in the aggregate state (Figure 21.2b and c). It should be noted that the metallacages not only showed aggregation-induced light-emitting behavior in the mixture solution, but also displayed color-tunable fluorescence by simply varying the volume ratio of the two solvents used (Figure 21.2d and e). More interestingly, the absorption intensity and the shift of the obtained tetragonal metallacages were dependent on the polarity of the solvents – **5** and **6** exhibited variable-wavelength visible light emission, including rare white-light emission in tetrahydrofuran (Figure 21.2f and g).

In a following study, a series of 2D metallacycles were prepared by combining a TPE-based dipyridyl ligand and appropriately designed organoplatinum(II) acceptors *via* two-component coordination-driven self-assembly [53]. The metallacycles displayed high molar absorption coefficients but lower Φ_F in dilute solutions, than metallacages constructed by tetrapyridyl TPE because of the existence of freely rotating phenyl rings in the TPE moiety. Nonetheless, these species exhibited clear AIE-activity, as supported by fluorescence enhancements and markedly increased quantum yields, upon aggregation caused by poor solvents and in the solid state. The synthetic strategy enabled the precise control over the size, shape, as well as the distribution and the total number of TPE moieties incorporated within the SCCs. Such modularity and versatility make the SCCs excellent candidates as highly sensitive fluorescence chemosensors for detecting explosive nitroaromatic molecules *via* steady-state interactions that are consistent with a static quenching mechanism due to the formation of nonemissive ground-state complexes.

The coordination between AIEgen-containing "donor" building blocks and the metal-containing "acceptor" building blocks facilitates their interactions that may significantly influence the optical properties of the SCCs. As a result, the metal ion or metal complex used for self-assembly is an important concern for building AIE-active SCCs. While Pt(II) species are widely adopted due to their simple coordination geometries and low quenching effect over the fluorescence emission from the AIEgens, other metals such as Ag(I), Au(I), Zn(II), Cd(II), Zr(IV), *etc.* [58–62] are also possible candidates for the preparation of AIE-active SCCs. Hahn, Han, and coworkers synthesized AIE-active dinuclear Ag(I) and Au(I) complexes using coordination interactions between the metal ions and NHC-modified TPE ligands. These metallacycles displayed significant Φ_F enhancement (Φ_F value up to 55%) compared to the weakly emissive free ligand ($\Phi_F < 1\%$) in dilute solutions, as a result of immobilization of the TPE moiety by metalation. AIE behavior was observed for these SCCs, which was reflected by fluorescence enhancements in the presence of poor solvents.

Yang and Li collaborated the synthesis of three generations of AIE-active ligands (**7, 9** and **11**) with full conjugation of TPE with 2,2′,6′,2″-terpyridine (TPY). Rosette-like SCCs, ranging from generation 1 to generation 3 (**8**, **10** and **12**), were assembled *via* the coordination interactions between the TPY groups and Cd(II) ions (Figure 21.3) [58].

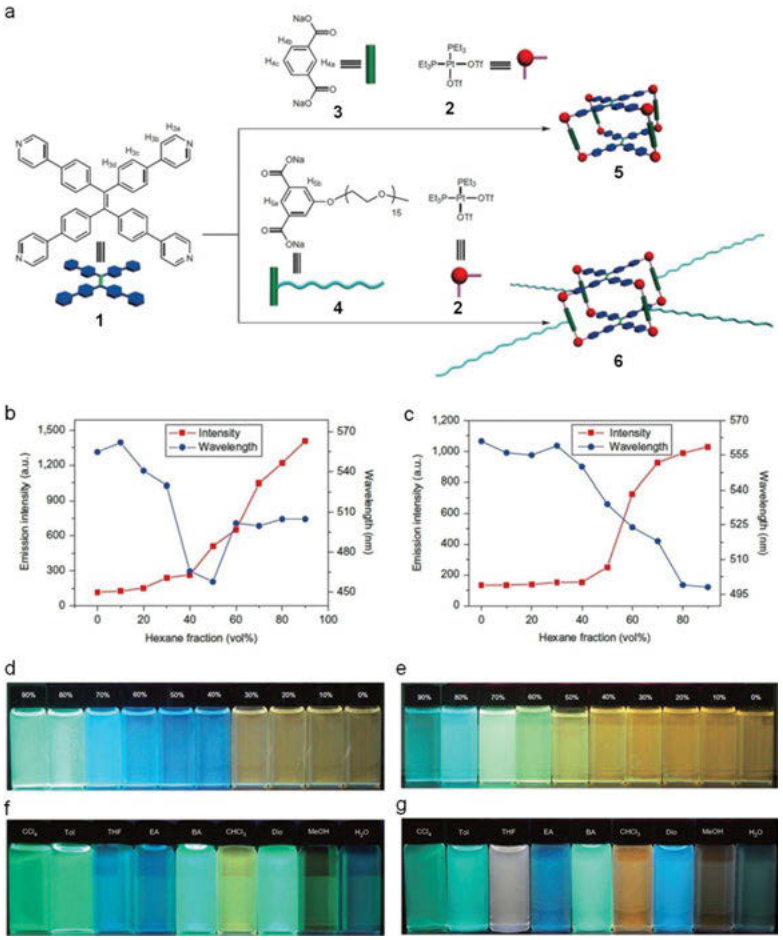

Figure 21.2: a) Self-assembly of **1**, **2** and **3** to furnish **5** and of **1**, **2** and **4** to furnish **6** *via* the heteroligation-directed self-assembly of 90° Pt(II) acceptors with pyridyl and carboxylate ligands. b) Plots of maximum emission intensity and wavelength of metallacages **5** (b) and **6** (c) versus hexane fraction in CH_2Cl_2/hexane mixtures. The photographs are of metallacages **5** (d) and **6** (e) in CH_2Cl_2/hexane mixtures with different fractions of hexane on excitation at 365 nm using an ultraviolet lamp. Photographs of metallacages **5** (f) and **6** (g) in different solvents. Copyright 2015 Nature Publishing Group.

8 showed weak fluorescence due to the free rotation of two phenyl groups in the TPE motif and a typical AIE behavior upon aggregation in poor solvents. In contrast, **10** and **12** displayed 2- and 6-fold enhancements in emission, relative to the corresponding ligands in dilute solutions, but remained at a moderate Φ_F when aggregated. This difference was ascribed to a higher number of TPY groups in the second and third generation ligands than the first generation ligand, which restricted the intramolecular motions of the TPE units upon coordination with Cd(II) and activated the TPE-based

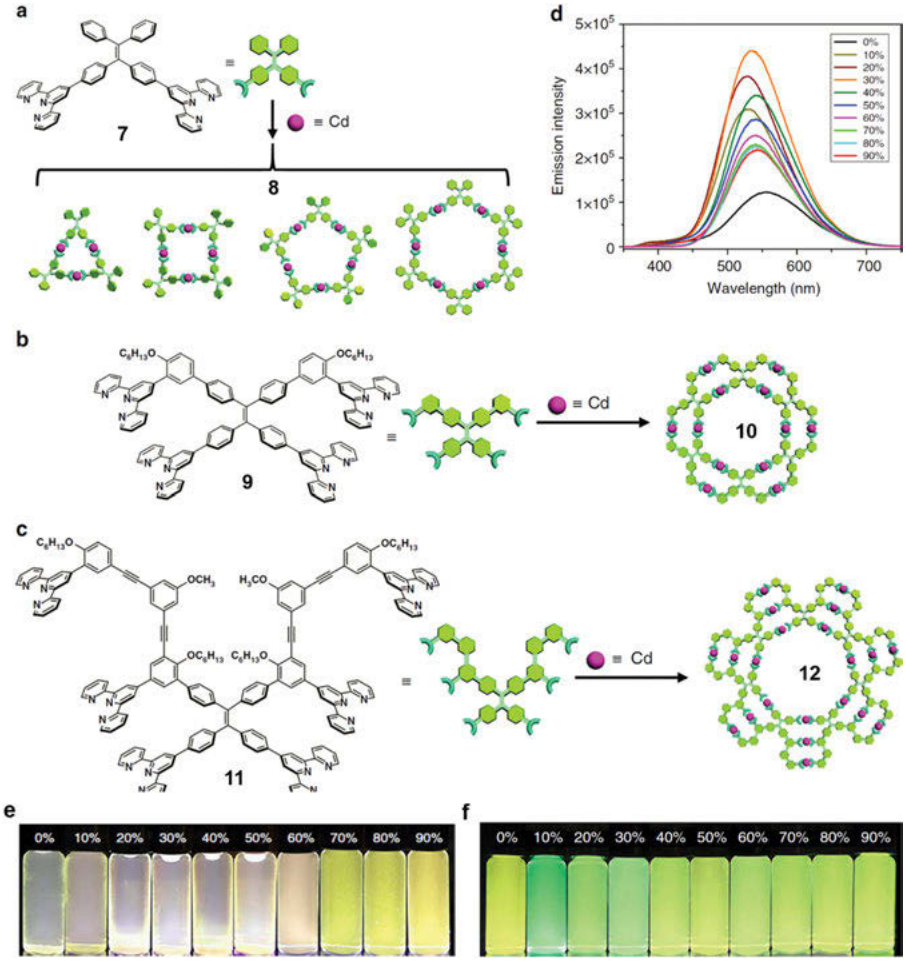

Figure 21.3: a) **7** assembled with Cd^{2+} to form a mixture of trimer, tetramer, pentamer and hexamer macrocycles (**8**). b) **9** assembled with Cd^{2+} to form a discrete hexamer (**10**). c) **11** assembled with Cd^{2+} to form a discrete heptamer (**12**). d) Fluorescence spectra of **12** in CH_3CN/water with various water fractions. e) Photographs of **10** in CH_3CN/water with various water fractions. f) Photographs of **12** in CH_3CN/water with various water fractions. Copyright 2018 Nature Publishing Group.

fluorescence emission in the dilute solution (Figure 21.3d). In poor solvents, however, the AIE phenomenon of **10** and **12** was partially offset due to their face-to-face staking, facilitated by their large planar structure, which led to ACQ. The spectra of **12** showed that the intramolecular charge transfer emission peaks centered at around 550 nm, with green-yellow color (Figure 21.3f). Intriguingly, **10** emitted pure white light when the water fraction was 60% and emitted yellow fluorescence when the water fraction was 90% (Figure 21.3e), suggesting that this SCC could be a brilliant candidate for the fabrication of color-tunable optoelectronic materials.

The ability of SCCs to encapsulate functional guest molecules provides approaches toward unique AIE behavior. The motivation of this strategy arises from the increased awareness of the opportunities available for catalysis, sensing, light-emitting materials, and drug delivery when the well-defined cavity-based microenvironment can be utilized. Sun and coworkers prepared a lantern-type SCC *via* the coordination-driven self-assembly between TPE-based bipyridyl ligand and Pd(II) ion [63]. Similar to other TPE-containing SCCs, the metallacage displayed AIE characteristic. In a poor solvent (toluene/DMSO = 99/1, *v*/*v*), a 10-fold enhancement in fluorescence intensity was observed for the assembly when compared with that in a suitable solvent (pure DMSO). Notably, the authors found that the addition of tetrabutylammonium (TBA) salts of HCO_3^-, F^-, Cl^-, and Br^- to the assembly solutions (with OTf^- as the counterion for reference) led to significant enhancement in the fluorescence intensities. Among these anions, HCO_3^- was found to be most effective, with a 2.7-fold enhancement. Given the large size of OTf^- ion that forbade its encapsulation within the cavity of the SCC, the enhancement in emission was attributed to the strong hydrogen bonds between the encapsulated anions and the inner surface of the SCC, which led to the twisting TPE motif and the inhibition of intramolecular motions.

21.2.2 AIEgens as pendant functional groups

Introducing AIEgens into SCC-based systems through conjugation to the rigid structural precursor building blocks further expands the possible range of AIE-active SCCs, because good structural rigidity is no longer required for the AIEgens. This strategy also avoids the potential interference on the photophysical properties of AIEgens by modification with the recognizing group for coordination or the subsequent self-assembly process responsible for the SCCs formation.

Yang and coworkers constructed an AIE-active hexagonal metallacycle *via* the coordination-driven self-assembly between TPE-decorated 120° bipyridyl donor and 120° diplatinum(II) acceptor in a 3:3 molar ratio [64]. As a result, three TPE units were presented in the exterior of the final supramolecular assembly. The assembly showed weak luminescence when dissolved in CH_2Cl_2, and a gradual increase in the hexane ratio in the mixed solvents led to the enhancement in fluorescence, supporting the AIE characteristic of the metallacycle.

The use of TPY-containing ligand decorated with Pt(II) 2,6-bis(benzimidazole-2′-yl) pyridine motifs (**13**) for coordination-driven self-assembly with Cd(II) ions in a 6:12 molar ratio led to the formation of a giant, discrete concentric metallahexagon **14** (Figure 21.4a) [65]. The large supramolecular architecture (>10 nm and molecular weight > 26,000 Da) exhibited room-temperature phosphorescence emission, which originated from the metal-perturbed [3] π,π* emission of the 2,6-bis(benzimidazole-2′-yl) pyridine. In the CH_3CN solution containing 5% CH_2Cl_2, both the TPY-

containing ligand and the assembly **14** were weakly emissive, and **14** showed emission bands with a maximum at 567 nm and a shoulder at 607 nm. The phosphorescence nature of the emission was supported by its partial quenching by oxygen and the long excited-state lifetime of 218 ns, which was significantly longer than the supramolecular assembly without the Pt(II) moiety (excited-state lifetime less than 5 ns). Increasing the fraction of the poor solvent, H_2O, for **14** led to a stronger phosphorescence emission (Figure 21.4b), which was attributed to molecular aggregation, induced by the combined effect of the Pt(II) motif and the TPY-Cd(II) units. An approximately 5.5-fold increase in the luminescence intensity was observed for **14**, upon aggregation, higher than what was observed in the TPY-containing ligand (1.8-fold enhancement). Transmission electron microscopy (TEM) investigation provided further insights into the origin of the AIE behavior (Figure 21.4f–i). The TPY-containing ligand assembled into a layered nanosheet-like structure in CH_3CN/H_2O, whereas **14** aggregated into a worm-like structure.

The increase of H_2O fraction in the mixed solvent extended the length of the worm-like structure, and finally yielded a crosslinked structure (Figure 21.4e). The difference in the aggregation morphology between the precursor and the assembly was attributed to the large size of the SCC, which effectively prohibited the $\pi - \pi$ stacking and Pt – Pt interaction in a face-to-face orientation but in a head-to-tail manner (Figure 21.4c and d). This study suggested that the aggregation behavior of the pendant AIEgens can be modulated through the formation of bulky SCCs, inducing photophysical features that are not accessible to individual AIEgens. Interestingly, the solution deoxygenated by N_2 resulted in a 3.1-fold enhancement in the emission of **14** (Figure 21.4j and k), an indicator of potential applications in gas sensing.

21.2.3 SCC-based AIE active supramolecular polymers

The ease of introducing multiple functional groups and the unique structural versatility of SCCs scaffold lead them to being heavily considered for the construction of functional supramolecular polymers, especially those with crosslinked network structures. When AIE behavior and supramolecular polymerization are combined in SCC-based systems, soft materials that unify interesting photophysical properties and advantages originated from supramolecular polymerization, such as responsiveness and self-healing, and favorable mechanical properties can be obtained.

Metal-ligand coordination, hydrogen bonding, and crown ether-based host-guest interaction were unified in a hierarchical system designed by Stang and coworkers [66]. Coordination-driven self-assembly of SCCs, decorated with pendant 2-ureido-4-pyrimidinone (UPy) group and benzo-21-crown-7 (B21C7) groups, represented the first level of complexity. The second level of organization took advantage of the simultaneous dimerization of the UPy groups, which furnished supramolecular polymer networks with rigid SCCs as crosslinkers. The complexity was further amplified based on

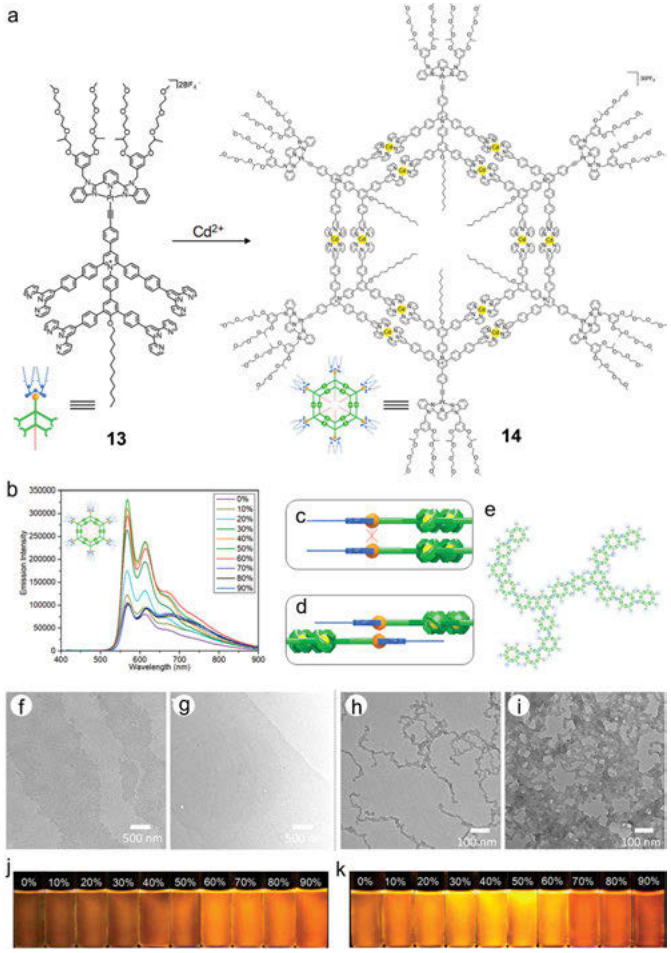

Figure 21.4: a) Preparation of discrete concentric metallahexagon **14**. b) Phosphorescent emission spectra of **14** in N_2 deoxygenated CH_3CN/H_2O solvent. c) Unfavorable face-to-face stacking. d) Proposed head-to-tail Pt – Pt interaction bridging supramolecules without ring stacking. e) Worm-like aggregates of **14**. TEM images of the aggregates of **14** formed in CH_3CN/H_2O mixtures containing f) 20%, g) 40%, h) 60%, and i) 80% water. j) Emission photographs of **14** in nondeoxygenated CH_3CN/H_2O with various water fractions. k) Emission photographs of **14** in N_2 deoxygenated CH_3CN/H_2O with various water fractions. Copyright 2020 American Chemical Society.

B21C7-based host-guest interactions, which led to the generation of supramolecular networks, with designed functionalities based on the guest molecule. The addition of a TPE-containing dialkylammonium salt endowed supramolecular system with AIE characteristic. The light-emitting feature of the supramolecular polymer was retained in the solid state. When swelled in an appropriate solvent, the crosslinks resulted in light-emitting gel-like soft materials. The supramolecular polymer showed a blue-shift

in fluorescence, relative to the free AIEgen in the solid state and in the gel form, as a consequence of the decrease in the planarization of the TPE motif within the polymeric network.

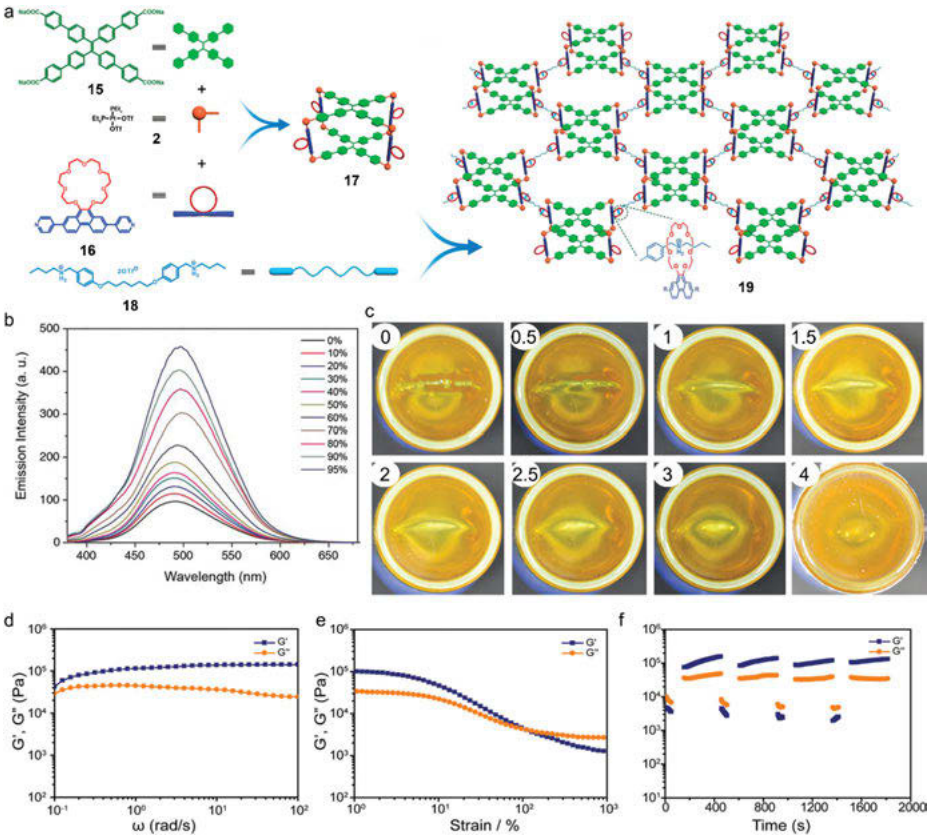

Figure 21.5: a) Self-assembly of B21C7-functionalized metallacage **17** and formation of cross-linked supramolecular polymer network **19** from **17** and bisammonium salt **18**. b) Fluorescence emission spectra of **17** versus hexane fraction in acetone/hexane mixtures. c) Photographs of the self-healing process of the supramolecular gel **19**. The gel was cut and left standing for 0, 0.5, 1.0, 1.5, 2.0, 2.5, 3.0, and 4.0 min. Storage modulus (G′) and loss modulus (G″) values of gel **19** versus d) frequency (ω); e) strain sweep; and f) continuous step strain. Copyright 2016 American Chemical Society.

A self-assembled metallacage **17** containing pendant B21C7 moieties was used to form an extended supramolecular network **19**, upon introduction of a bisammonium salt **18** that acted as crosslinkers, based on the host-guest interactions (Figure 21.5a) [67]. The AIE feature of the metallacage was introduced by using a TPE-based sodium benzoate as a building block for the self-assembly (Figure 21.5b). The formation of a supramolecular gel in acetone was supported by rheological experiments, which showed a

larger storage modulus than loss modulus, and the storage modulus was independent of the angular frequency (Figure 21.5d–f). The supramolecular gel also showed enhanced stiffness compared to a model gel without metallacages, due to the rigidity and the high branch functionality of the metallacage. Further rheological investigations showed that the storage modulus and loss modulus of the gel rapidly recovered after the gel was broken under both large (300%) and small (0.1%) strains, indicating that the supramolecular gels possessed good self-healing properties (Figure 21.5c). The supramolecular gel exhibited a fluorescence emission band centered at 497 nm and a Φ_F value of 4.55%, higher than that of the discrete counterpart (Φ_F = 2.65%), as a result of a higher degree of restriction over the motions of the TPE motifs in the networks.

21.3 Factors influencing the photophysical behaviors of AIE-active SCCs

Many AIEgens change their photophysical properties in response to external stimuli or environmental variations due to their unique working mechanism that involves the motion of chemical groups. These variations include mechanical force, pH, fuming (vapor), photonic irradiation (light), solvent polarity, electric field, and so on [23]. A majority of AIE-active SCCs preserve the responsiveness originated from their AIEgen precursor building blocks. In some cases, the unique topologies of SCCs can give rise to novel characteristics. Apart from the external factors, factors internal to the SCCs, such as geometries and counterions may also play a crucial role in determining the photophysical properties, providing an alternative approach for exploring the working mechanism of AIEgens, and for the construction of novel light-emitting materials.

21.3.1 Factors internal to the SCCs

As mentioned in the previous sections, using AIEgens as the structural motifs of SCCs often enhance the Φ_F *via* activating the irradiative decay of excitation energy through the limitation of molecular motions. As a result, the degree of constraint imposed on the molecular motions, which highly correlates to the geometries of the SCCs, shows marked influence over the photophysical feature. Zhou and coworkers synthesized discrete-fused metallarhomboid **23** and a triangle **24**, wherein a TPE-based tetrapyridyl donor was anchored within the SCCs as the bridging ligand (Figure 21.6) [43]. Both the fused polygons were innately emissive in dilute solution due to restriction of the intramolecular motion by SCC formation, and aggregation by addition of poor solvent led to a further increase in the Φ_F (Figure 21.6b and c).

Interestingly, under the same conditions, fused rhomboid **23** showed a lower Φ_F in dilute solutions, relative to that of the fused triangle **24** (Φ_F = 0.24% and 0.88% for **23** and **24**, respectively), while a reversal of emission intensities was observed in the aggregated state (Φ_F = 14.6% and 2.5% for **23** and **24**, respectively). These differences in solution were attributed to the differences in the strength and rigidity of the assemblies, as supported by a lower (4.3 kJ/mol) calculated activation barrier for **23**, compared to that of **24**. In the aggregated state, however, the higher Φ_F detected for **23** was attributed to the higher flexibility of the rhomboidal skeletons, which allows them to aggregate much more tightly than the rigid triangular structures, as well as the higher number of Pt centers in **24** than that in **23**, which might increase the intersystem crossing and thus lower the emission of **24**.

The cavity of SCCs provides a unique environment for tuning the properties of AIEgens. Inspired by the light-emitting characteristic of green fluorescent protein, Stang and coworkers constructed two TPE-based $M_{12}L_{24}$ nanospheres, with the TPE moieties either confined within (*endo*-functionalized) or positioned outside (*exo*-functionalized) of the nanospheres through covalent linkers [68]. In dilute solutions, the *endo*-functionalized sphere showed a higher Φ_F as a consequence of a higher local concentration and more restrained motion of the enclosed 24 TPE units, compared to the *exo*-functionalized counterpart, in which the 24 TPE units could undergo free motions. Both nanospheres displayed typical AIE behavior upon the addition of poor solvents and showed comparable fluorescence features in the aggregate state.

The interactions between the building blocks of SCCs and the AIEgens may also alter the photophysical feature, and such changes can be utilized for fluorescence tracking of complex supramolecular transformation processes [69]. Yan and coworkers prepared a molecular trigonal prism *via* the self-assembly between a TPE-based tetrapyridyl donor and *cis*-$Pt(PEt_3)_2(OTf)_2$. The addition of a molecular square consisting 4,4′-bipyridine and *cis*-$Pt(PEt_3)_2(OTf)_2$ to the solution of the trigonal prism in a 3:2 molar ratio led to a supramolecular fusion of the two assemblies that resulted in the formation of a three-component molecular cage. The molecular cage showed lower fluorescence intensities when compared with the trigonal prism under the same condition (Φ_F = 28.8% and 0.80% for the trigonal prism and the molecular cage, respectively), along with a minor red-shift in the maximum emission wavelength (490 nm to 505 nm). Based on theoretical computations, the observed decrease in fluorescence efficiency was the consequence of the photo-induced electron transfer process between the TPE and 4,4′-bipyridine motifs, because the LUMO of the molecular cage was located on the bipyridine rings. The distinctive fluorescence features of the ligands and the supramolecular assemblies allowed for facile tracking of the supramolecular assembly and the fusion process, utilizing the changes in fluorescence profiles as output signals.

Counterions are another critical factor that influence the photophysical characteristics of AIE-active SCCs. AIE-active SCCs (**27** and **29**), constructed by using TPE-

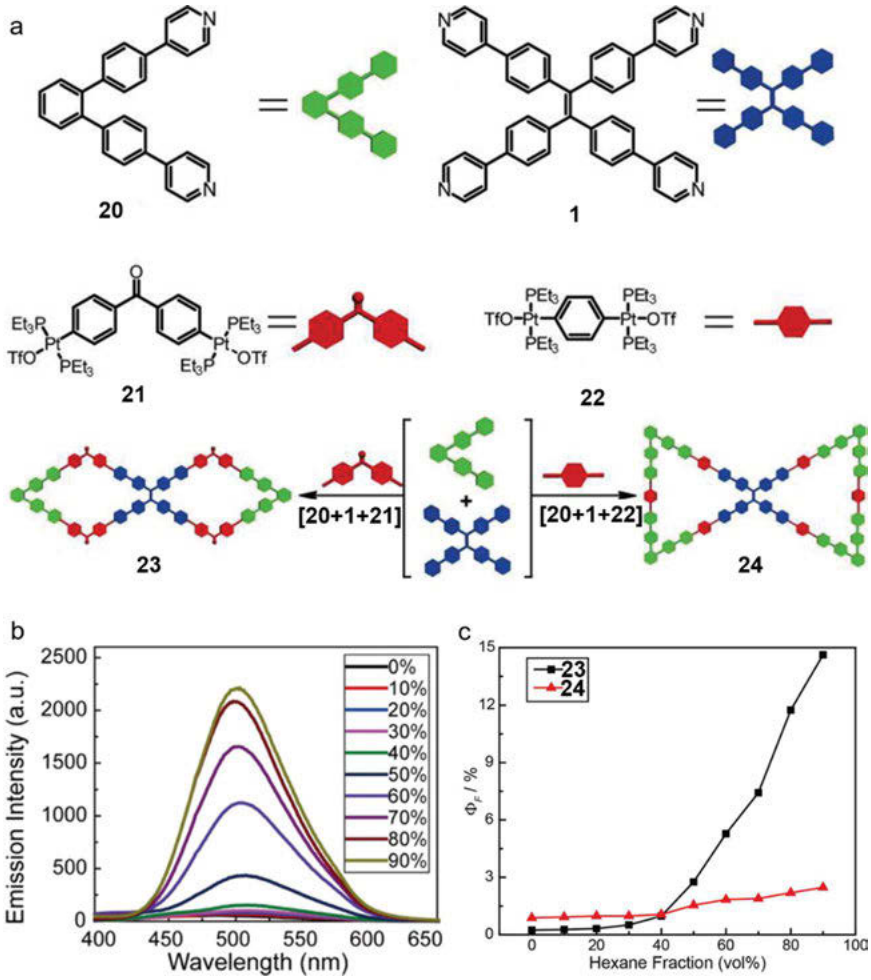

Figure 21.6: a) Preparation of double rhomboid **23** and double triangle **24** *via* multicomponent coordination-driven self-assembly. b) Fluorescence emission spectra of **23** versus hexane fraction in CH_2Cl_2/hexane mixtures. c) Quantum yields of **23** and **24** versus hexane fraction in CH_2Cl_2/hexane mixtures. Copyright 2016 American Chemical Society.

containing donor and acceptors, were found to exhibit different fluorescence emission intensities and Φ_F values, following the order of $PF_6^- > OTf^- > NO_3^-$ in the aggregate state (Figure 21.7) [45]. It was hypothesized that the counterions played a vital role in the solubility of the SCCs and the packing mode of the SCCs in the aggregate state, which led to differences in the properties of the AIE-active SCCs.

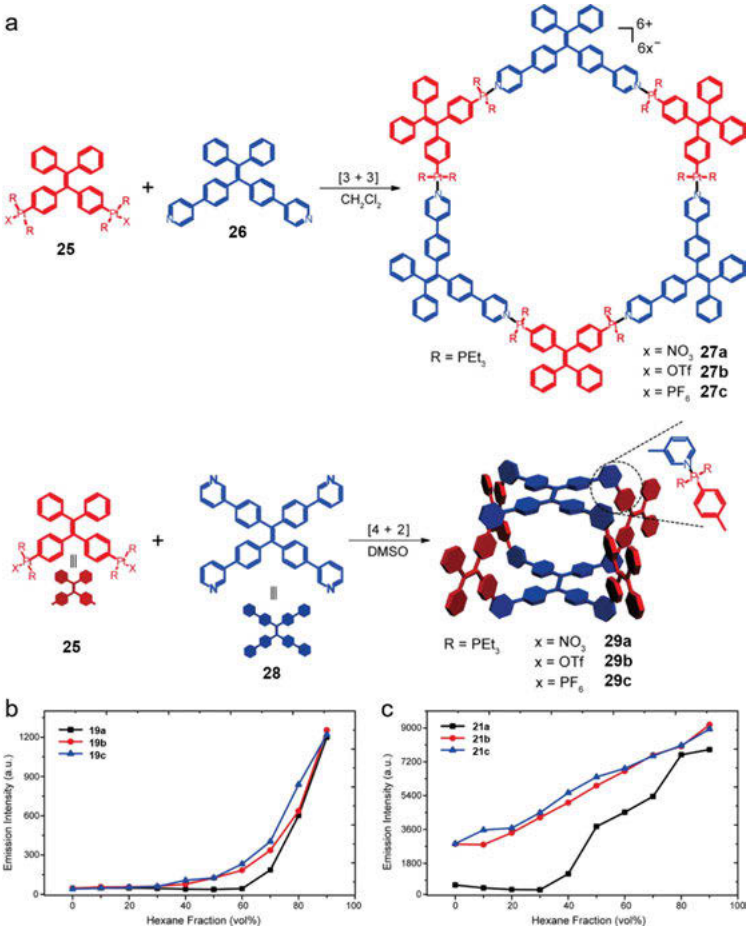

Figure 21.7: a) Self-assembly of **27** and **29** with different counterions. Plots of maximum emission intensity of b) **27** and c) **29** versus hexane fraction in CH_2Cl_2/hexane mixtures. Copyright 2016 American Chemical Society.

21.3.2 External factors

The discrete nature of SCCs endows them with good solubility in common organic solvents, making it possible to study the influence of solvent on the photophysical properties of SCCs. One major factor is the polarity of the solvent, which influences the charge-transfer state of the excited-state AIEgens, resulting in a red-shift in the maximum fluorescence emission. Another major factor is the solubility of the SCCs. Poor solvents often induce the aggregation of SCCs and hence increase the luminescence emission efficiency. Additional functional groups, especially those that can promote the hierarchical self-assembly of SCCs, may significantly affect the aggregation

process (in terms of time, assembly morphology, responsiveness, etc.) [70–73], and thus the luminescence properties. Generally, all AIE-active SCCs displayed responsiveness to changes in solvents due to the combined effect of solvent polarity and solvent induced-aggregation.

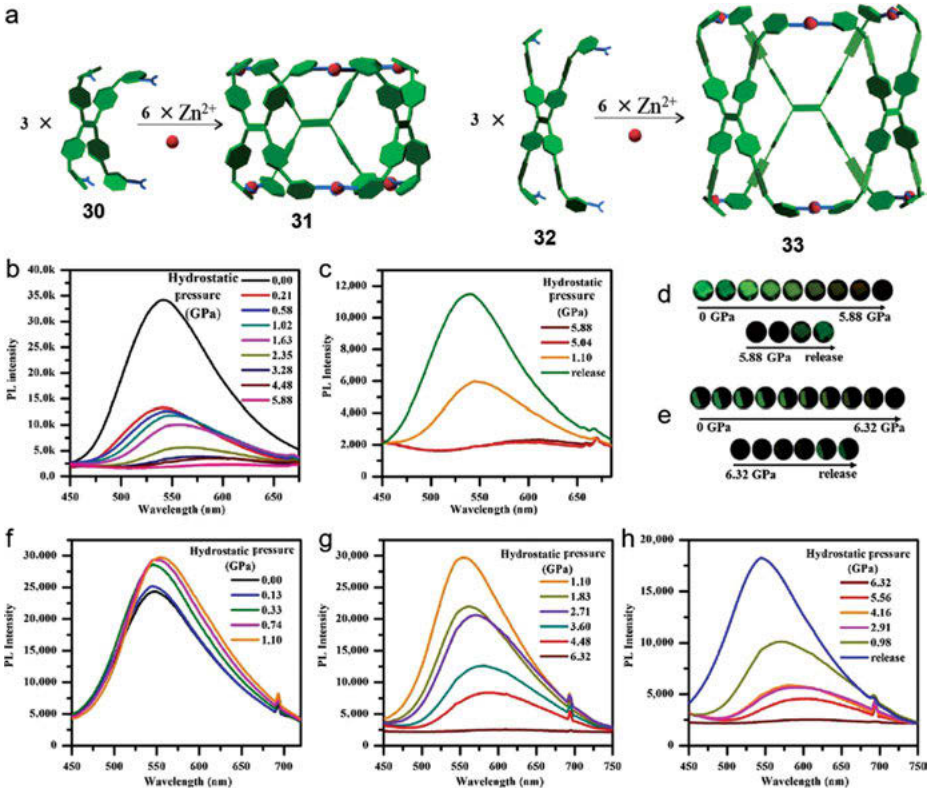

Figure 21.8: a) Self-assembly of the complexes **31** and **33**. Effects of applied pressure on AIE-based ligand and their supramolecular derivatives. Fluorescence emission responses for b) **32**, at varying applied pressures, c) **32**, gradual pressure withdrawal. Photomicrographs of d) **32** (solid) and e) **33** (solid). Fluorescence emission responses upon for f) **33**, at varying applied pressures, g) **33**, at varying applied pressures, and h) **33**, gradual pressure withdrawal. Copyright 2020 Chinese Chemical Society.

Temperature is another widely observed factor that influences the properties of AIE-active SCCs. It is well known that elevated temperatures facilitate intramolecular motions and thus decrease the luminescence efficiency of the AIEgens [50, 74]. Similar to solvents, temperature may exert a more significant effect on the properties when SCCs undergo hierarchical self-assembly that leads to more complex supramolecular architectures that are more sensitive to temperature changes [75].

Recently, external pressure was identified as another factor that influences the photophysical properties of AIE-active SCCs in the solid state, likely because most studies focused on the solution phase. Wang and coworkers prepared two metallacages, **31** and **33**, *via* the self-assembly between the TPE-based tert-TPY donors (**30** and **32**) and Zn(II) ions (Figure 21.8) [74]. For both the donor building blocks and assembly **31**, increasing the hydrostatic pressure led to a decrease in the emission intensity, which was ascribed to tight molecular packing that promoted π–π and dipole–dipole interactions under high pressure (Figure 21.8b–d). In contrast, the fluorescence intensity of **33** showed a marked increase under the low hydrostatic pressure from 0 to 1.10 GPa, likely due to a further limitation on the rotation of TPE moieties. Further increase in the pressure led to gradual quenching as a consequence of excessive molecular packing (Figure 21.8e–h).

21.4 AIE-active SCCs for sensing biomolecules

Although TPE derivatives can emit strong fluorescence in the aggregate state owing to the restriction of intramolecular motions, their fluorescence can hardly be detected in dilute solution or in the molecular state. However, the metal-coordination can suppress the partial intramolecular rotation of TPE units in SCCs; hence, these AIE cages are highly emissive in dilute solution. Based on this strategy, Stang et al. prepared three AIE-active tetragonal prismatic metallacages (**35a**–**35c**), in which 90° Pt(II) acceptors, dipyridyl ligands and benzoate-decorated TPE units, respectively, served as the corners, pillars, and faces of AIE-active SCCs (Figure 21.9a, I) [76]. The fluorescence emission of three metallacages can be smartly tuned by the different dipyridyl ligands and solvents. For instance, **35a** and **35b** had good emission at around 490 nm in the different solvents, due to the presence of TPE group. In contrast, **35c** showed two distinct emissions at around 470 nm and 540 nm, which were the characteristic emission peaks of TPE unit and BODIPY fluorophore. Interestingly, **35b** was nonemissive in the mixture of methanol and water (1:1), but emitted strong fluorescence upon addition of thiol-containing amino acids such as glutathione and cysteine, suggesting **35b** could serve as a delicate fluorescence sensor of thiol-containing amino acids (Figure 21.9a, II). After a series of studies, it was demonstrated that the sensing process obeyed a self-destructive mechanism. In detail, thiol-containing amino acids had a better complexing capability with Pt(II) ions, resulting in the collapse of the metallacages and the formation of Pt(II)-amino acid complexes. Meanwhile, the AIE-active ligand **7** was released, thus acting as the fluorescent indicator of amino acid sensing (Figure 21.9a, III). Of note, the metallacages could be regenerated post-addition of $Pt(PEt_3)_2(OTf)_2$, suggesting the thermodynamic stability of the Pt-amino acids complexes is higher than that of the cages. Hence, these metallacages not only act as new AIE-active materials that emit strong

fluorescence in dilute solutions but also provide an excellent possibility of serving as chemo-sensors for thiol-containing amino acids.

For covalent fluorescent chemosensors, inherent low selectivity or high fluorescence background derived from the multiple interfering substances makes it difficult for them to be widely applied in biological systems [77, 78]. Lately, indicator-displacement assays (IDAs) on the basis of supramolecular self-assembly provide an alternative strategy to overcome the limits of organic fluorescent chemosensors. Through proper design, indicators in the system can be freely introduced or displaced with the help of different supramolecular reactions, resulting in distinct intensity changes of fluorescence or UV absorption. Being able to avoid tedious synthetic steps, improve selectivity, and decrease background interference, IDAs are receiving increased attention. Zhu et al. designed two metalla-supramolecular assemblies (***Z*/*E*-37**) in which pyrocatechol violet (**PV**) and TPE-based dinuclear Zn^{2+}–cyclen complex served as building blocks (Figure 21.9b, I) [79]. Attributing to the energy transfer, the fluorescence of the TPE unit was completely quenched in ***Z*/*E*-37**. However, owing to the hydrogen bonding and strong coordination interactions between the DNA macromolecule and the Zn^{2+}–cyclen group, **PV** molecules were displaced by the DNA, and the energy transfer process from TPE and **PV** was also interrupted, eventually leading to the fluorescence recovery of TPE. After a systematic study, it was found that both ***Z*/*E*-37** had high selectivity for T-rich DNA sequence, and ***Z*-37** had a relatively higher selectivity than ***E*-37**, owing to the participation of the neighboring group (Figure 21.9b, II). In living cells, ***Z*/*E*-37** groups showed the lowest background interference and relatively high fluorescence signals, compared to control groups (Figure 21.9b, III), suggesting IDAs strategy based on these two metalla-supramolecular assemblies can be efficiently realized in living cells, and will provide deep insights into the future development direction of DNA probes.

Of late, the strategy of utilizing hierarchical self-assembly to construct artificial functional materials is receiving considerable attention. Since metal-ligand bonds are well compatible with other noncovalent interactions, SCCs are good participants for hierarchical self-assembly. Inspired by the vast complicated supramolecular architectures constructed by electrostatic interactions, Yang et al. envisioned that the interactions between negatively charged polymers and positively charged metallacycles might lead to the formation of novel and smart supramolecular aggregates [64]. An AIE-active tris-TPE hexagonal metallacycle **38** and the widely used clinical anticoagulant heparin were selected as the positively charged metallacycles and the negatively charged polymers, respectively, to study their hierarchical self-assembly. Upon addition of heparin into the solution of **38**, the fluorescence at 486 nm was significantly enhanced (Figure 21.9c, I), suggesting that electrostatic interactions occurred between **38** and the heparin chain. In the following, a series of theoretical and experimental investigations demonstrated that electrostatic interactions triggered the generation of bead-like aggregates (Figure 21.9c, II). The aggregation was ascribed to the electrostatic interactions between the positively charged

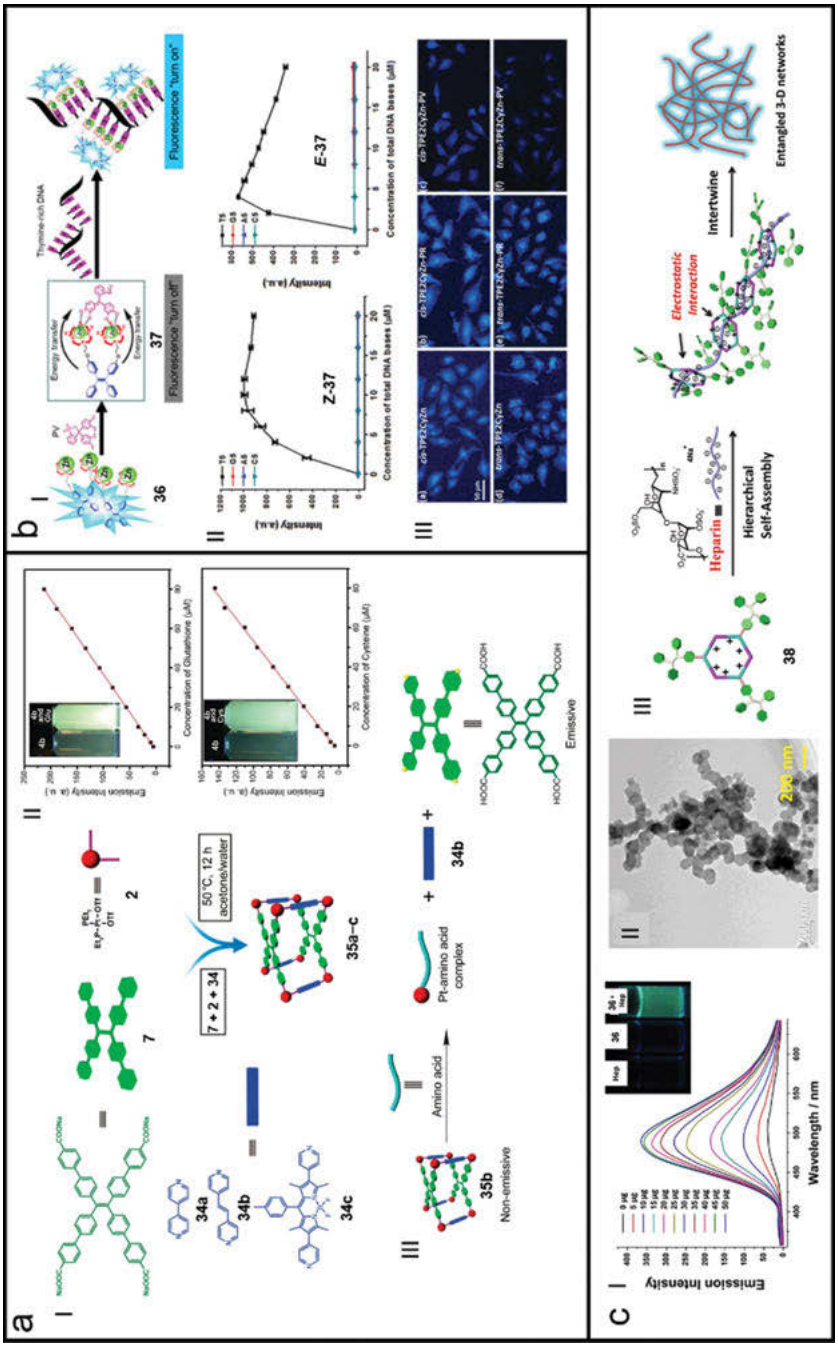

Figure 21.9: a) AIE-active platinum(II) cages for amino acid sensing. I) Cartoon representations and synthetic routes of **35a** – **35c**. II) The plots of emission intensities at 500 nm *vs* the glutathione or

skeleton of **38** and the negatively charged -OSO_3^- and -COO^- groups of heparin, which induced the organization of the metallacycles along the heparin chain. Subsequently, the positive charge on **38** further interacted with another flexible polysaccharide chain, thus leading to the intertwining of chains. At high concentration, these networks cross-linked with each other, eventually forming bulky bead-like microstructures (Figure 21.9c, III). Since there was a noticeable fluorescence change in aggregation, it was hypothesized that **38** could serve as a fluorescent probe for quantifying heparin. Through a fluorescence titration experiment, it was demonstrated that the detection range of heparin was 0–28 μM, which covered the clinical dosage, indicating **38** had a great potential to quantificationally detect heparin, which is very important for surgery and anticoagulant therapy. Compared to other control biomolecules and negatively charged artificial polymers, the fluorescence increase in **38** + heparin group was the highest, suggesting that the selectivity of **38** toward heparin was good. This study not only accurately reveals the mechanism of electrostatic interaction-triggered hierarchical self-assembly between discrete metallacycles and clinically used heparin, but also offers a promising strategy for quantificationally detecting biological macromolecules.

21.5 AIE-active SCCs for cell imaging

Although AIE-active SCCs have presented excellent optical properties and have been used in various fields, their unsatisfactory solubility is severely limiting their further application in biological studies. Therefore, AIE-active SCCs with good biocompatibility are urgently needed. Inspired by the biological application of supra-amphiphiles, Yang et al. constructed a TPE-based supra-amphiphilic metallacycle with good biocompatibility [71]. In the system, 120° dipyridyl donors, decorated with TPE unit, coordinated with 120° di-Pt(II) acceptors, anchored with chain transfer agents (CTAs), forming a hexagonal AIE-active metallacycle **39**. Attributing to the anchored CTAs, three *N*-isopropylacrylamide-based polymeric arms could be conjugated onto the periphery of metallacycle *via* radical polymerization, forming a metallacycles-cored supra-amphiphile (Figure 21.10a, I). The obtained metallacycles-cored supra-amphiphile not only self-assembled into fluorescent and high-

Figure 21.9 (continued)
cysteine concentration. III) The proposed self-destructive mechanism of metallacages. Copyright 2017 American Chemical Society. b) An AIE-active metalla-supramolecular assembly for DNA sensing. I) Schematic illustration of IDA strategy for probing T-rich DNA. II) Fluorescence spectra of ***Z***/***E*-37** under different DNA concentrations. III) Fluorescence images of B16-F10 cells under different conditions. Copyright 2018 Royal Society of Chemistry. c) AIE-active metallacycles **38** for detecting heparin. I) Changes of fluorescence spectra of **38** upon addition of heparin. II) TEM image of **38**. III) The proposed mechanism of detecting heparin. Copyright 2015 American Chemical Society.

ordered nanoparticles in water, but also possessed good biocompatibility, which provided a possibility for serving as a new type of DNA probe. Because *N*-isopropylacrylamide is a thermosensitive polymer that can undergo morphological change at its lower critical solution temperature (LCST) (about 32 °C), the hydrodynamic radius (R_h) and optical properties of supramolecular polymer **40** were greatly influenced by the temperature. For instance, in the low temperature range (20 to 30 °C), the R_h value (Figure 21.10a, II) and fluorescence intensity (Figure 21.10a, III) of **40** changed slightly, but showed a sharp change in the range of 30–70 °C, suggesting that the thermosensitivity of *N*-isopropylacrylamide was maintained. *In vitro*, **40** showed no obvious cytotoxicity even at high concentration, indicating it was safe for biological study. After incubation with bone mesenchymal stem cells (BMSCs), **40** mainly gathered in the nucleus (Figure 21.10a, IV), suggesting that the supramolecular polymer tightly interacted with the DNA, showing great potential as a DNA probe. This AIE-active supra-amphiphilic metallacycle provides a new strategy for constructing functional amphipathic SCCs that are good at imaging DNA molecules.

Although various methods have been developed to construct supramolecular polymers and complexes, the strategy of covalently linking metallacycles to synthesize target polymers is rarely reported, owing to the dynamic structure of metallacycle. Two metallacycle-cored polymers (**46** and **47**) were successfully synthesized based on mild amidation reactions by Stang et al. (Figure 21.10b, I) [80]. In MeOH solution, tetraamino-functionalized rhomboidal TPE-based metallacycle **43** efficiently reacted with the activated linker **44** or **45**, generating cross-linked polymers (**46** and **47**). Because the polymerization of monomers enhanced the aggregation of TPE units, the fluorescence of **46** and **47** was greatly improved. At high concentrations, **46** and **47** also spontaneously aggregated into the network structure, thus further enhancing fluorescence emission. Based on these excellent optical properties, **46** and **47** demonstrate great potential as cell imaging agents. As expected, there was a bright green signal derived from **47** in the cytoplasm after 6 h incubation *in vitro* (Figure 21.10b, II), indicating **47** could be efficiently phagocytized by cells. *In vivo*, after intra-tumoral injection of **47**, a distinct fluorescence was observed at the tumor site and this signal could still be recognized even after 24 h (Figure 21.10b, III), suggesting that **47** was both photostable and chemostable *in vivo*, which was a prerequisite for imaging agents. After intravenous injection of **47**, **47** mainly gathered in the lung of mice (Figure 21.10b, IV). As Pt(II), with anticancer activity, was involved in the structure of metallacycles, the lung-targeted **47** may serve as an alternative anti-carcinogen for lung cancer therapy. With great potential in bioimaging and lung cancer therapy, these metallacycle-cored polymers offer another development direction for theranostic reagents.

Although SCCs have advantages in forming host-guest complexes *via* their tunable cavities and serving as nanocarriers, there remain enormous hurdles in biological applications. For example, living cell imaging is hard to realize owing to some inherent limitations of SCCs: (1) the hydrophobicity of SCCs; (2) the weak fluorescence signal of

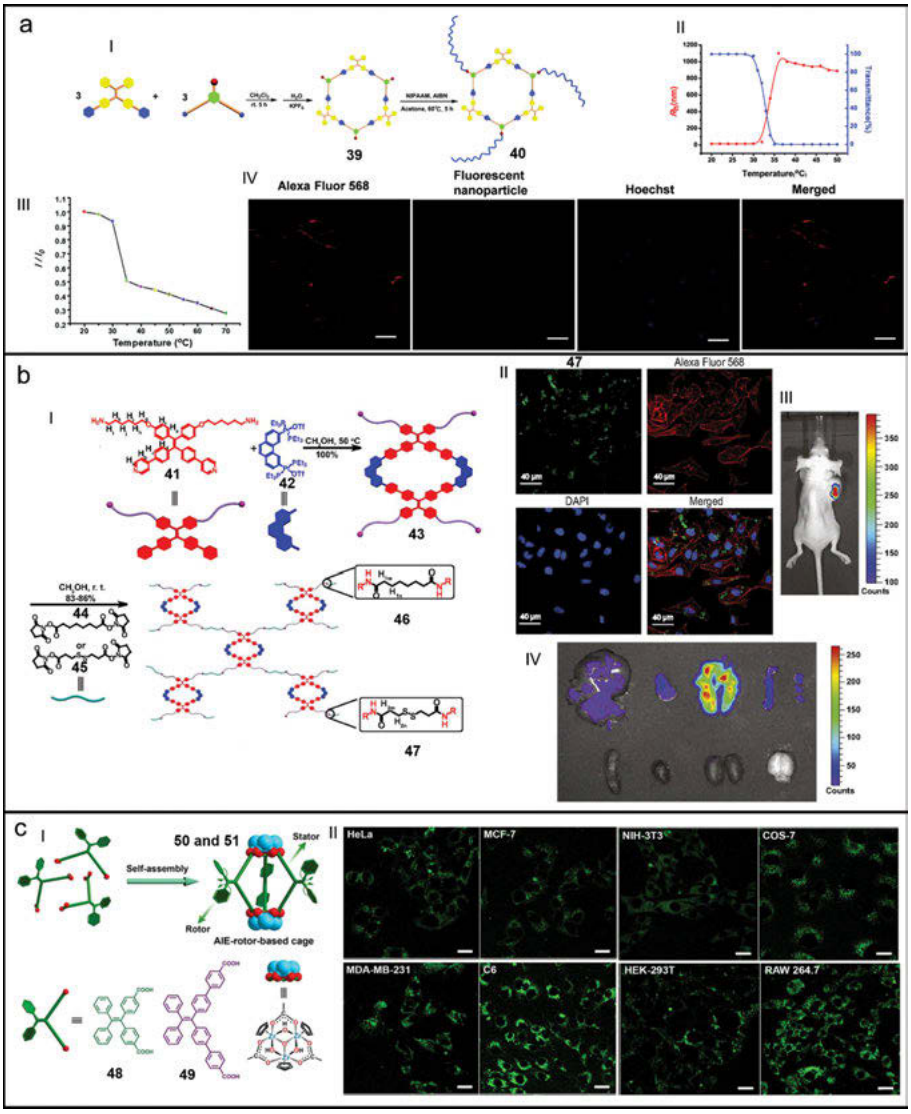

Figure 21.10: a) An AIE-active supra-amphiphilic metallacycle with good biocompatibility for cell imaging. I) Synthetic route of **40**. II) The plots of transmittance or R_h value *vs* temperature. III) The relative fluorescence intensity of **40** at different temperature. IV) Confocal laser scanning microscopy (CLSM) images of BMSCs stained with different dyes. Copyright 2017 Royal Society of Chemistry. b) AIE-active metallacycle-cored polymers for cell imaging. I) Cartoon representations and synthetic routes of **46** and **47**. II) CLSM images of A549R cells incubated with **47**. III) *In vivo* fluorescence image of mice injected with **47**. IV) Fluorescence images of different *ex vivo* organs. Copyright 2016 National Academy of Sciences. c) AIE-active zirconium(IV) coordination cages for live-cell imaging. I) Cartoon representations and synthetic routes of **50** and **51**. II) CLSM images of four noncancerous cells and cancerous cells incubated with **50**. Copyright 2020 John Wiley & Sons, Inc.

SCCs in living system (induced by ACQ effect or short ligand-to-metal charge transfer (LMCT)); (3) relatively high cytotoxicity of SCCs. To overcome these problems, Zhao et al. constructed the first zirconium(IV)-based coordination cages (**50**, **48** ligand; **51**, **49** ligand) (Figure 21.10c, I) [81]. In the structure of TPE ligands, the carboxyl-decorated phenyl rings and free phenyl rings, respectively, served as the molecular rotors and stators. The dynamic molecular rotors assuredly exist in the structure of coordination cages, as indicated by the tunable AIE characteristic of the cages, induced by various external stimuli, such as temperature, viscosity, and guest size. Attributing to the strong structural stability and preeminent AIE property, **50** and **51** were stable in neutral, acidic, and weak basic solutions. These SCCs had high quantum yields and low cytotoxicity in the aqueous solution, suggesting that they were suitable for living cell imaging. *In vitro*, **50** was efficiently internalized *via* an endocytic pathway and aggregated in the lysosomes of cancerous or noncancerous cells (Figure 21.10c, II), suggesting that these AIE-active cages could act as an effective fluorescent probe to label various cell lines. Furthermore, the fluorescent signal from the control group, without TPE molecular rotors, was much weaker than that in the SCCs groups, further confirming that AIE rotors in coordination cages were vital for living cell imaging. These AIE-active and highly stable zirconium(IV)-based coordination cages pave the way for more biological applications such as drug delivery and cancer theranostics.

21.6 AIE-active SCCs for cancer therapy

Although SCCs are receiving increased attention because of their aesthetic architecture and wide application, there are burning questions about SCCs that need to be solved, such as their poor stability in the physiological environment, and insufficient tumor accumulation and limited solubility. Because supramolecular amphiphile can not only enhance the stability and solubility of SCCs but can also load other anticarcinogen to obtain a synergistic effect, SCCs-based supramolecular amphiphile is an excellent answer to the above questions. Stang et al. developed an SCCs-based amphiphilic polymer **54**, in which AIE-active metallacycle **53** acted as the core and glutathione (GSH)-responsive amphiphilic copolymers served as the four arms (Figure 21.11a, I) [82]. This amphiphilic polymer self-assembled into nanoparticles (NP) or vesicles (**VC**) with various sizes through different preparation techniques. For instance, 50 nm (**NP1**) and 500 nm (**NP2**) nanoparticles were acquired by reprecipitation or dialysis method, while 0.8–3.0 μm **VC** were obtained by a double emulsion technique. Possessing different sizes and morphologies, these assemblies had different internalization rates and endocytic pathways. For **NP1** and **NP2**, they were mainly phagocytized by clathrin-mediated endocytic pathway. In the case of **VC**, the internalization was dependent on the micropinocytosis-mediated pathway. Of note, the hydrophobic core of nanoparticles and the hydrophilic cavity

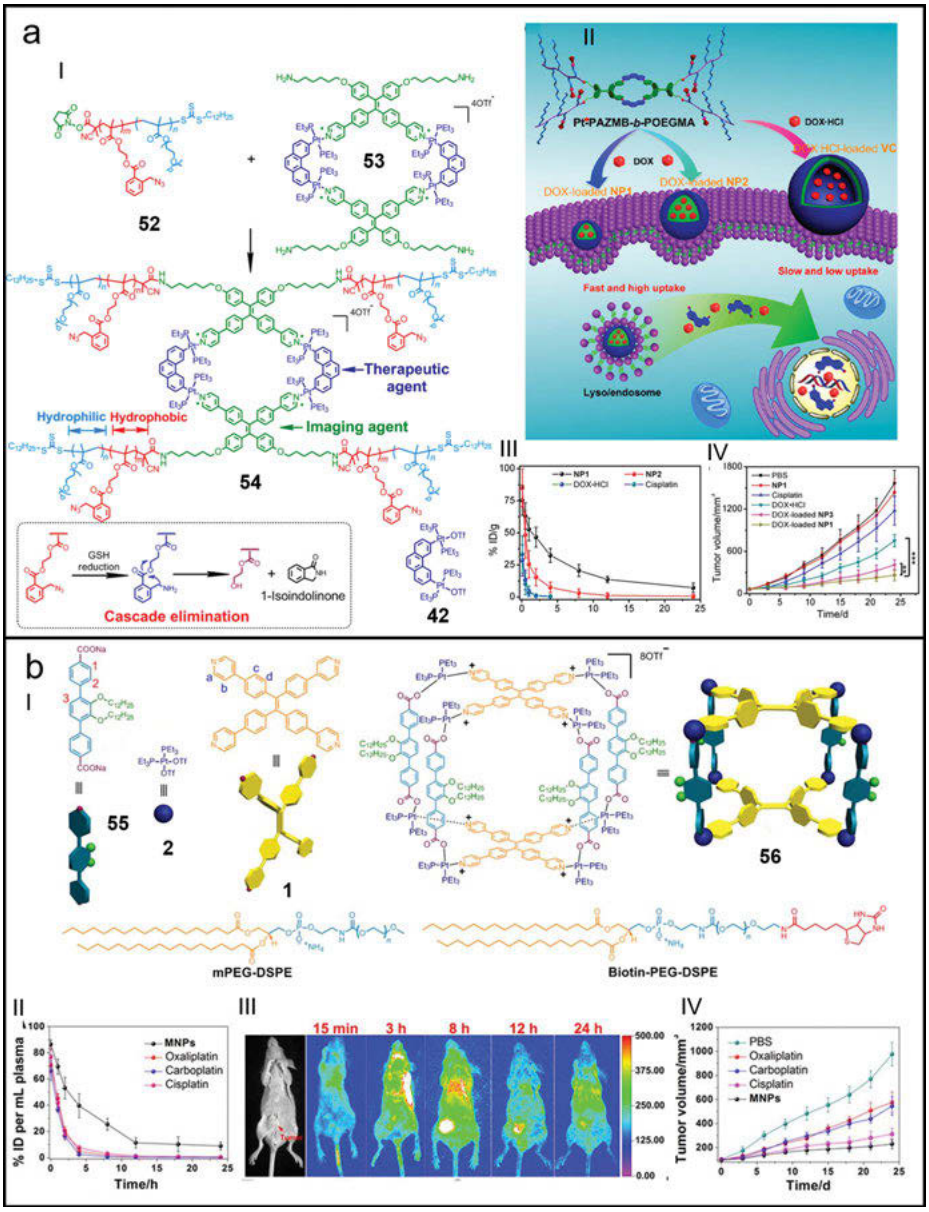

Figure 21.11: a) An AIE-active self-assembled metallacycle with anti-tumor activity. I) Synthetic route of **52**. II) Illustration of cellular uptake of DOX-loaded self-assemblies. III) Blood circulation time of different formulations. IV) Tumor growth curves of mice after different treatments. Copyright 2017 American Chemical Society. b) An AIE-active metallacycle **54** as a theranostic platform. I) Cartoon representations and chemical structures of **54**, **biotin-PEG-DSPE** and **PEG-DSPE**. II) Blood elimination kinetics of different anticarcinogens. III) *In vivo* fluorescence imaging of mice injected with **MNPs**. IV) Tumor growth curves of mice after different treatment. Copyright 2016 National Academy of Sciences.

of **VC** can be used to encapsulate neutral doxorubicin (DOX) or doxorubicin hydrochloride (DOX · HCl), achieving a dual-drug delivery system (Figure 21.11a, II). Due to the presence of the GSH-triggered self-eliminating group, the nanostructures disassembled inside cancer cells expressing abundant GSH, and the loaded chemotherapeutic agents such as **PhenPt** and DOX (DOX · HCl) were subsequently released, realizing the synergistic treatment. *In vitro* studies indicated that the IC_{50} values of assemblies loaded with DOX or DOX · HCl were relatively low. The combination index (CI) of DOX-loaded **NP1** was 0.79, suggesting that the synergistic anticancer effect of the nanomedicines was good. As the size of **NP1** was beneficial for cell uptake and the peripheral PEG chain could protect them from being cleared by the reticuloendothelial system (RES), **NP1** showed the best drug delivery efficiency (Figure 21.3a, III). Compared to other control groups, the anti-tumor effect of DOX-loaded **NP1** was the best (Figure 21.11a, IV), likely owing to the synergistic anticancer effect of **PhenPt** and DOX. Moreover, there were no apparent changes in body weight and blood biochemistry for the mice treated with DOX-loaded **NP1**, indicating the systemic toxicity of this SCCs-based supramolecular amphiphile was negligible. Based on these satisfying results, this study offers valuable methodology and strategy for the design of alternative drug delivery systems, based on supramolecular amphiphilic structures.

Except for chemical modification of SCCs, physical encapsulation by suitable copolymers is another effective method to solve the inherent drawbacks of SCCs such as low selectivity, rapid clearance, poor solubility, and lack of targeting ability. Stang et al. utilized two kinds of 1,2-distearoyl-phosphatidylethanolamine-polyethylene glycol-based amphiphilic copolymers (**biotin-PEG-DSPE** and **PEG-DSPE**) to modify an AIE-active metallacage **56** (Figure 21.11b, I) [53]. Attributing to the directional metal coordination bonds, the TPE core was tightly fixed in the structure of **56** and the AIE effect was then introduced. Attributing to the PEG and biotin decoration, **56** showed remarkable stability and targeting capability. *In vitro* investigations demonstrated that the metallacage-loaded nanoparticles (**MNPs**) could be selectively internalized by biotin receptor-overexpressing cancer cells arising from the receptor-mediated internalization. In addition, **MNPs** showed enhanced cytotoxicity against biotin receptor-overexpressing cancer cells, compared to normal cells. Under the protection of PEG shell, **MNPs** owned a longer circulation time (Figure 21.11b, II) and provided a strong motivation to improve the efficiency of chemotherapy. Because of the optimal size, targeting ability, and longer circulation time, **MNPs** were prone to accumulate in the solid tumor aided by the enhanced permeability and retention (EPR) effect and the active targeting effect. For imaging purpose, intensive fluorescence signals could be observed at tumor sites, and the fluorescence maintained as long as 24 h (Figure 21.11b, III), confirming that the targeting ability and the longer circulation time of **MNPs** played important roles in *in vivo* imaging. In anti-tumor studies, **MNPs** were most efficient in inhibiting tumor growth (Figure 21.11b, IV), demonstrating that **MNPs** were an effective platinum-based anticancer drug. Furthermore, minor changes in body weight, undetectable tissue damage, and prolonged survival rate were observed in

the **MNPs**-treated group, indicating the low systemic toxicity of this novel theranostic nanomedicine. This newly developed SCCs-based theranostic nanoplatform can provide valuable information for the development of next-generation metal-based targeted nanomedicine.

21.7 AIE-active SCCs for bacterial imaging and ablation

Due to their attractive properties and moderate stabilities, SCCs have been used for the construction of metallacage or metallacycle-cored hierarchical self-assemblies. Utilizing the machinability of polymers and the stimuli-responsiveness of SCCs, various metallacage-crosslinked networks have been developed. Because these networks consist of multiple components, there is a great demand to figure out how the components' individual properties transfer to the entire supramolecular system, and then influence their functions and applications. Zhang et al. treated AIE-active hexagonal metallacycles anchored with poly(*N*-isopropylacrylamide) (PNIPAAM) polymers as joints to prepare three supramolecular networks (**61a**–**61c**) (Figure 21.12a) [83]. Because the cross-linking degree in these supramolecular networks is different, it is necessary to study the structure-property relationship of networks for further biological applications. In the system of supramolecular networks, NIPAAM polymers endowed the networks with feasible processability and good hydrophilicity, while the Pt-based metallacycles brought antibacterial activity and excellent imaging capability. Hence, these networks were ideal theranostic platforms for simultaneously imaging and killing bacteria. As the intramolecular rotation of TPE unit was restricted by the metal-coordination bonds, **61a**–**61c** emitted strong fluorescence even in low concentrations. After the measurement of temperature-dependent UV/Vis spectra, the clouding points (T_{cloud}) of **61a**–**61c** were 42 °C, 38 °C, and 34.5 °C, respectively, indicating that the introduction of PNIPAAM polymer not only introduced the thermoresponsiveness into supramolecular networks but also increased their water solubility, both of which were beneficial for further biomedical applications. Attributing to the presence of trimethylamine groups and platinum(II) in metallacycles, the supramolecular networks could kill both *E. coli* and *S. aureus*, suggesting their broad-spectrum antibacterial ability (Figure 21.12b). Of note, the antibacterial activity of **61a**–**61c** followed the same order of densities of metallacycles in networks, confirming that the platinum (II) metallacycles played crucial roles in fighting against bacteria. Furthermore, the bacteria could be lit up by **61a** (Figure 21.12c), indicating that **61a** may act as a potential imaging agent. This study provides new methods to construct SCCs-based supramolecular networks and extends their applications in imaging and killing bacteria, which will attract more efforts for the development of metallacycle-cored supramolecular networks.

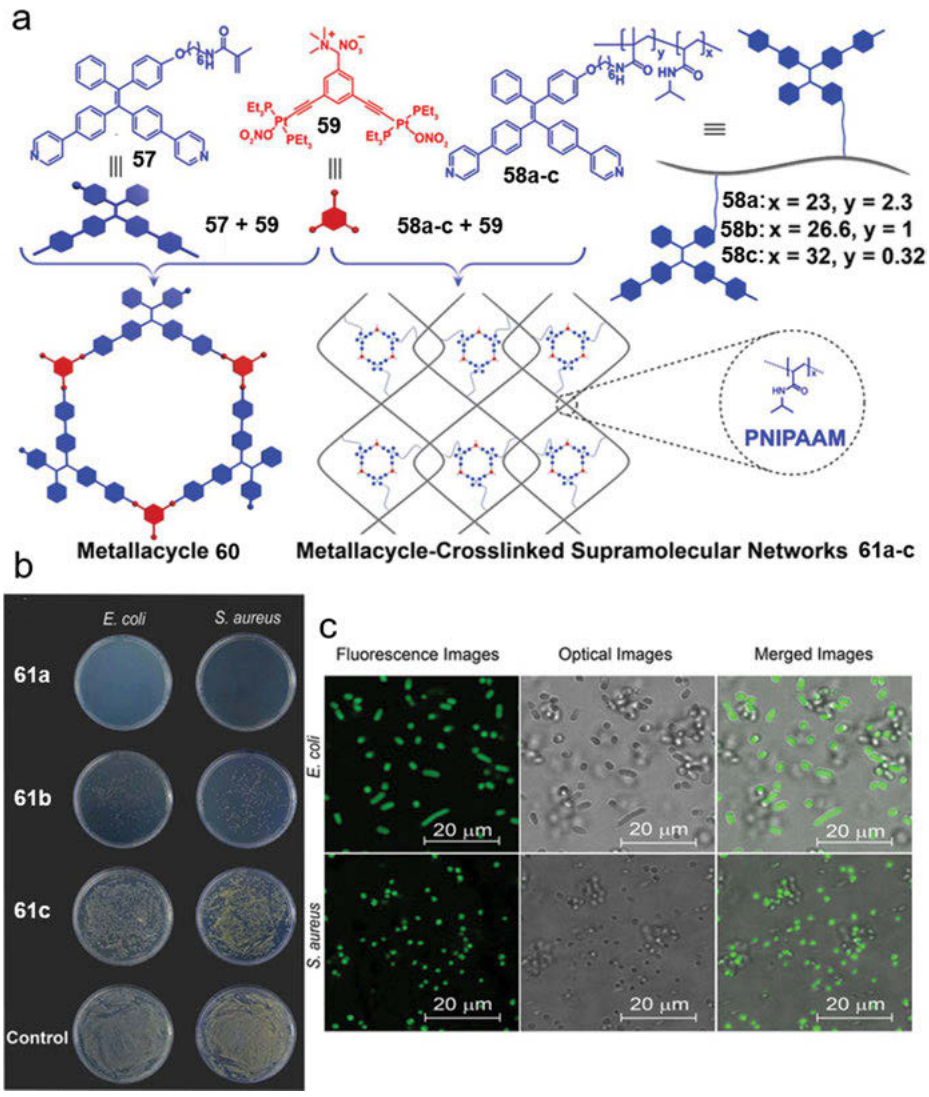

Figure 21.12: AIE-active metallacycle-crosslinked supramolecular networks for bacterial imaging and killing. a) Synthetic routes of **61a** – **61c**. b) Colony-forming of *E. coli* and *S. aureus* incubated with **61a** – **61c**. c) Fluorescence images of *E. coli* and *S. aureus* incubated with **61a**. Copyright 2020 John Wiley & Sons, Inc.

Because of the increasing antibiotic resistance, bacterial infection has become a major threat to global health. Search for novel antibacterial agents that can catch up with the evolution of antibiotic resistance is urgently needed. Attributing to the minimal invasiveness and spatiotemporal selectivity, photodynamic inactivation (PDI) strategy is attracting increasing attention. Upon light irradiation,

photosensitizers can transform O_2 into reactive oxygen species (ROS) such as hydroxyl radical (•OH) and singlet oxygen ($^1O_2$), which can destroy DNA, proteins, or membrane lipids and eventually result in irreversible bacterial death. However, owing to the ACQ effect, the fluorescence and ROS generation of traditional photosensitizers are significantly reduced. AIE-active photosensitizers, with the ability to maintain ROS production even in the aggregated state, are good candidates as PDI agents. To enhance the PDI efficiency of the photosensitizers, membrane-intercalating moieties have been introduced into the structure of photosensitizers. Niu et al. reported a novel PDI system for anti-bacteria. Benefiting from the electrostatic interactions, positively charged TPE-based metallacycle (**62**) was covered with negatively charged tobacco mosaic virus coat protein, which was prematurely conjugated with a trans-acting activator of transduction (TAT) peptide (**63**) (Figure 21.13a) [84]. The TAT peptide provided a strong membrane-intercalating ability for **63**, thus remarkably enhancing their antibacterial properties. Owing to the heavy atom effect of platinum, the ability of ROS generation of **62** was also significantly improved. Hence, the assembled **64** could not only tightly stick to the cell membrane of *E. coli*, but could also destroy cell membrane (Figure 21.13b and c). Compared to the control groups, the survival rate of *E. coli* in the assembled **64** group was the lowest and reached nearly 0% at 40 μM (Figure 21.13d), suggesting that the enhanced bacterial accumulation contributed to the high bacterial inhibition. It is worth noting that the cytotoxicity of **64** against mammalian cells in the dark or under light irradiation was low, which confirmed **64** had good biocompatibility. After careful observation of the bacteria morphology, the antibacterial mechanism was revealed. Under light irradiation, membrane lysis was induced by the generated ROS and the cell contents then leaked out, which eventually led to the death of bacteria. Although **64** showed broad-spectrum antibacterial property, the bacterial inhibition rate of Gram-negative bacteria was markedly higher than that of the Gram-positive bacteria. The reason may be that the TAT peptide on **64** had a strong affinity to the cell-wall structure of Gram-negative, thus achieving a higher bacterial inhibition rate. Based on the low cytotoxicity and broad-spectrum antibacterial property, **64** presents as a candidate with excellent potential for control of wound infection at superficial locations.

Owing to the prevalence of bacterial biofilms, bacterial infectious diseases cannot be treated effectively. Although diverse biofilm inhibitors have been developed, the one that can support an efficient and straightforward antibiotic therapy is urgently desired. Because the polysaccharides layer on the surface of bacteria plays a vital role in bacteria communication, the polysaccharides-decorated antibacterial agent may be able to greatly facilitate the communication between material and bacteria, thus significantly improving their antiseptic property. Chen et al. developed a new strategy in which saccharide-coated assemblies could closely contact with bacteria to achieve an effective biofilm inhibition [85]. To improve the biocompatibility and enhance the communication between materials and bacteria,

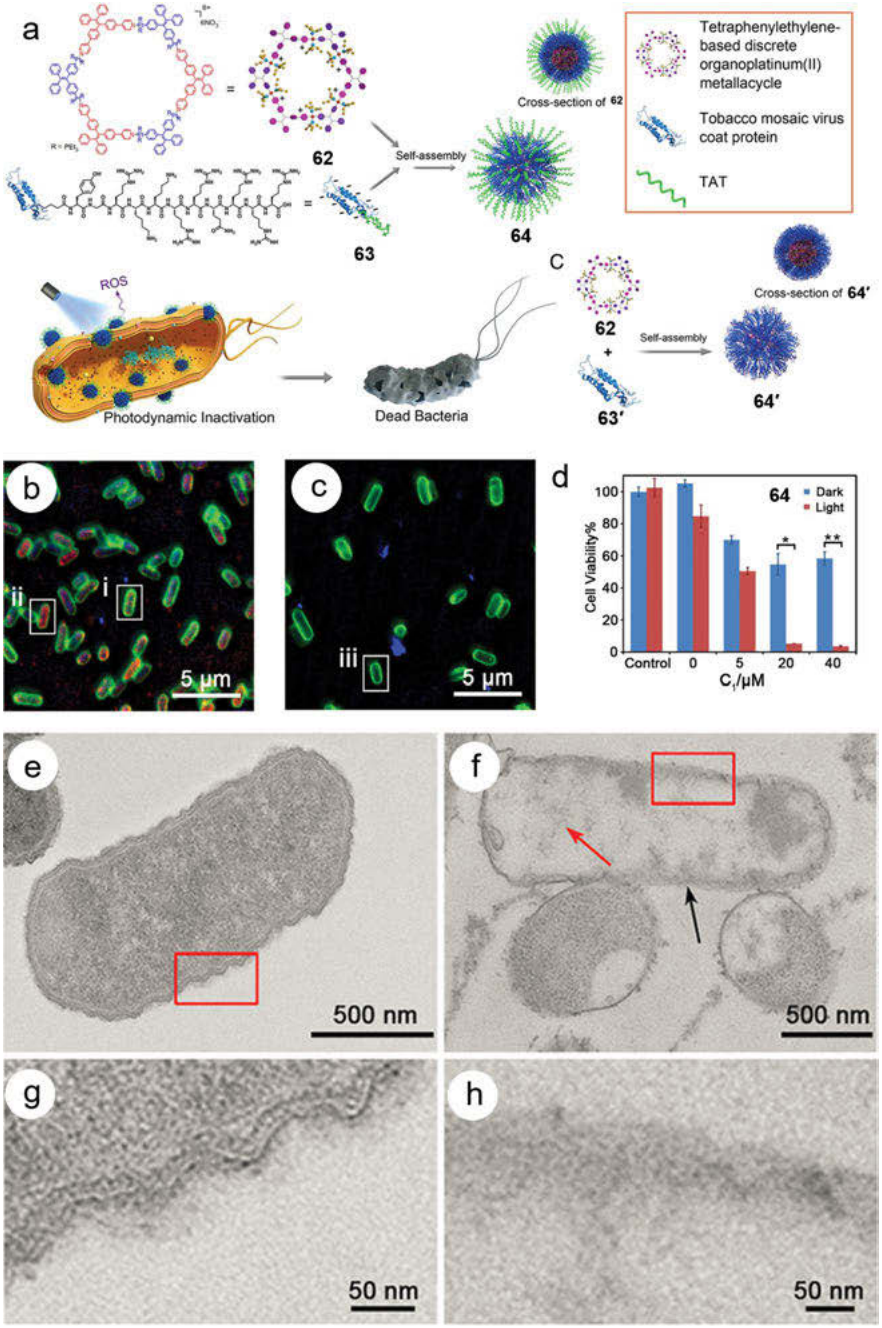

Figure 21.13: An AIE-active metallacycle decorated with TAT-targeted virus coat protein for PDI of bacteria. a) Scheme illustration of the supramolecular assembly and its antibacterial capability. SIM images of *E. coli* incubated with b) **62** and c) **64**. d) *E. coli* viability after treatment with **64**

hydrophilic moieties, such as pentaethylene glycol ($\mathbf{EG_5}$) or galactoside (**Gal**) were introduced into the structures of **donor 1** and **donor 2**, thus generating four glyco-metallacycles (**[2 + 2]-Gal**, **[3 + 3]-Gal**, **[3 + 3]-$\mathbf{EG_5}$** and **[6 + 6]-Gal**) with outstanding self-assembly behaviors (Figure 21.14a). Due to the presence of multiple positive charges, these metallacycles effectively inhibited the growth of biofilms and bacteria *in vitro* and *in vivo*, providing the first example of metallacycles-cored hierarchical self-assembly for inhibition of bacteria and biofilms. *In vitro* evaluations suggested that four glyco-metallacycles exhibited antibacterial activity and their antibacterial efficiency followed the order: **[6 + 6]-Gal** > **[3 + 3]-Gal** > **[2 + 2]-Gal** > **[3 + 3]-$\mathbf{EG_5}$** (Figure 21.14b–e), suggesting that galactosides moiety contributed to better antibacterial activity. The results from biofilms experiments matched well with that in antibacterial experiments, further demonstrating that these assemblies could also effectively inhibit biofilms formation. A pneumonia animal model induced by *S. aureus* was constructed to assess the *in vivo* efficacy. Compared with the *S. aureus* group, the expression of cytokines (IL-6 and TNF-α) in **[6 + 6]-Gal**-treated group decreased (Figure 21.14g and h), which verified that **[6 + 6]-Gal** assemblies efficiently alleviated pneumonia. Based on the satisfactory *in vitro* and *in vivo* results, this study provides a new avenue for the design of biofilm inhibitors based on the "sweet-talking" between polysaccharides-decorated metallacycles and bacteria.

21.8 Summary and outlook

Benefiting from the excellent optical properties, good tunable shape and size, as well as multi-functionalities, AIEgens-based SCCs have been employed in various biomedical applications. In sharp contrast to traditional light-emitting materials that usually need tedious and complicated synthetic processes, AIEgens-based SCCs can be intelligently constructed by simply tuning the structure of the individual building blocks. Attributing to the excellent compatibility and the diversity of supramolecular chemistry, functional building blocks equipped with other non-covalent interactions can be introduced into AIE-active SCCs to form hierarchical self-assemblies that possess not only the perfect topological structure but also have promising potential in biological applications. Although many AIEgens-based SCCs have been constructed to solve biomedical problems, such as living cell imaging, cancer theranostics, bacteria imaging, and antibacterial treatments, the biomedical exploration of these AIEgens-based SCCs is just at the beginning,

Figure 21.13 (continued)
under different conditions. TEM section images of *E. coli* without any treatment in the dark e) or incubated with **64** under 420 nm light irradiation for 15 min f). g) and h) are enlarged images of the red squares in e) and f), respectively. Copyright 2019 National Academy of Sciences.

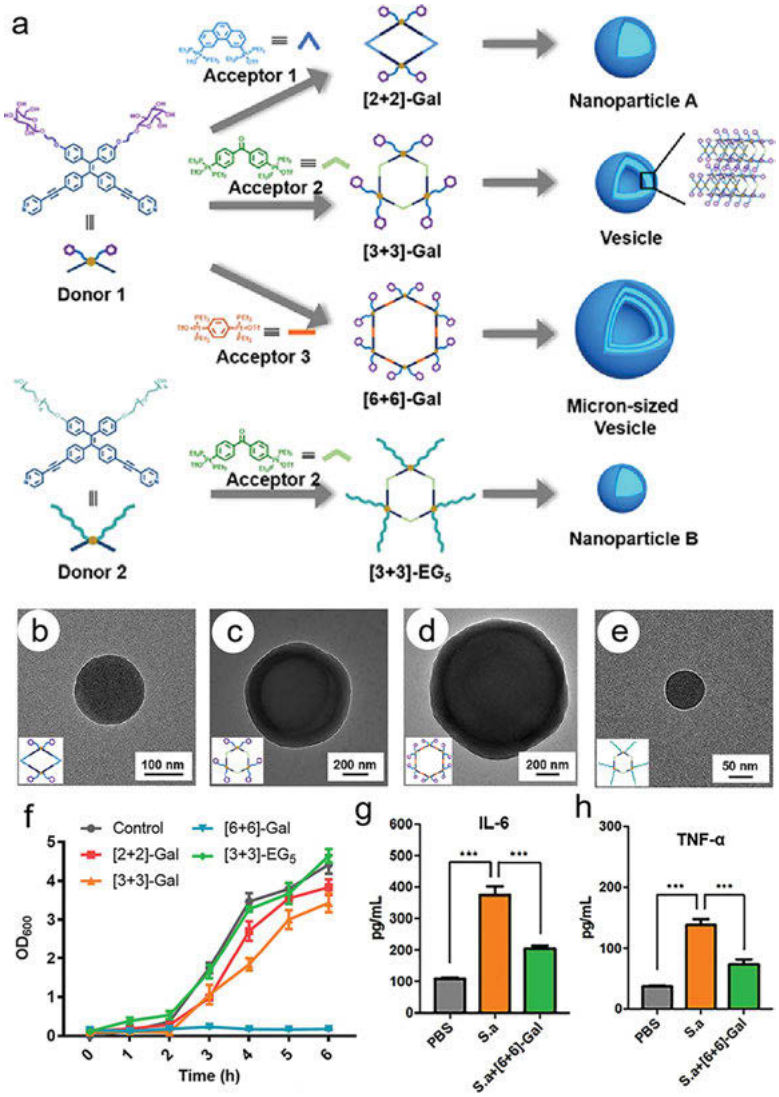

Figure 21.14: Saccharide-decorated amphiphilic metallacycles for inhibiting biofilms. a) Schematic illustration of chemical structures, synthetic process and self-assembly morphologies of amphiphilic metallacycles. TEM images of b) **[2 + 2]-Gal**, c) **[3 + 3]-Gal**, d) **[6 + 6]-Gal**, and e) **[3 + 3]-EG_5** self-assemblies. f) Growth curves of *S. aureus* treated with different amphiphilic metallacycles. The ELISA results of g) IL-6 and h) TNF-α cytokines after different treatments. Copyright 2020 American Chemical Society.

and there is huge possibility to broaden their applications. (1) Until now, almost all of the reported AIE-active SCCs are built on the TPE-based AIEgens. Novel AIE-active building blocks with unique optical properties are urgently needed to develop sophisticated SCCs, with more interesting properties. (2) The light used to activate AIEgens is often UV or visible light. Hence, the present AIE-active SCCs are not very suitable for living organisms. In the near future, NIR I or NIR II AIEgens, with low autofluorescence background, good biocompatibility, and deep tissue penetration should be preferentially selected to seek biomedical applications. (3) Owing to the hydrophobicity of common AIE-active SCCs, the limited water solubility and poor cell uptake are major hurdles for their bio-application. Furthermore, the harsh physiological environment can induce the disassembly of SCCs, causing severe side effects and wrong diagnostic results; thus, further chemical post-modification and physical encapsulation by amphiphilic copolymers are required. After physical or chemical modification, metallacycle/metallacage-cored AIE-active supramolecular assemblies are formed, in which metallacycles/metallacages are protected by copolymer shells, consequently increasing their stability and phagocytosis efficiency. In addition, multiple stimuli-responsiveness and targeting ability can simultaneously be brought in these assemblies to improve therapeutic efficiency and efficiently reduce the potential side effects. (4) The intrinsic cavity of the SCCs is underutilized in the current biomedical applications. Since various functional guests can be introduced into the hydrophobic cavity of SCCs *via* host-guest interactions, the functionality of AIE-active SCCs can be further modulated through extrinsic guest molecules. (5) Considering the future development of AIE-active SCCs, the synergistic therapy that relies on the unification of multiple functional molecular building blocks should also be prioritized to overcome the potential of resistance that is commonly encountered in the single treatment strategy.

Recent advances of AIE-active SCCs in the biomedical field have been summarized in this chapter, according to their various applications. Based on these inspiring methods and strategies, this chapter will undoubtedly provide meaningful information to the future development of SCCs. However, it is clear that smarter SCCs platforms need to be exploited, while systematic studies and evaluations need to be accomplished before these supramolecular self-assemblies, integrating diagnostic and therapeutic functions become clinically available. Considering the enormous contributions made by scientists from chemistry, materials, and biology, we are confident that the AIE-active SCCs can find diverse applications in the near future.

References

[1] Weissleder R, Scaling down imaging: Molecular mapping of cancer in mice, Nat Rev Cancer, 2002, 2, 11–18.
[2] Iagaru A, Chen XY, Gambhir SS, Molecular imaging can accelerate anti-angiogenic drug development and testing, Nat Rev Clin Oncol, 2007, 4, 556–557.
[3] Lee S, Xie J, Chen XY, Peptides and peptide hormones for molecular imaging and disease diagnosis, Chem Rev, 2010, 110, 3087–3111.
[4] Jokerst JV, Gambhir SS, Molecular imaging with theranostic nanoparticles, Acc Chem Res, 2011, 44, 1050–1060.
[5] Hong GS, Antaris AL, Dai HJ, Near-infrared fluorophores for biomedical imaging, Nat Biomed Eng, 2017, 1, 1–22.
[6] Koch M, Symvoulidis P, Ntziachristos V, Tackling standardization in fluorescence molecular imaging, Nat Photon, 2018, 12, 505–515.
[7] Ranjit S, Lanzanò L, Libby AE, Gratton E, Levi M, Advances in fluorescence microscopy techniques to study kidney function, Nat Rev Nephrol, 2021, 17, 128–144.
[8] Yao J, Yang M, Duan YX, Chemistry, biology, and medicine of fluorescent nanomaterials and related systems: New insights into biosensing, bioimaging, genomics, diagnostics, and therapy, Chem Rev, 2014, 114, 6130–6178.
[9] Kolanowski JL, Liu F, New EJ, Fluorescent probes for the simultaneous detection of multiple analytes in biology, Chem Soc Rev, 2018, 47, 195–208.
[10] Vahrmeijer AL, Hutteman M, van der Vorst JR, van de Velde CJH, Frangioni JV, Image-guided cancer surgery using near-infrared fluorescence, Nat Rev Clin Oncol, 2013, 10, 507–518.
[11] Nguyen QT, Tsien RY, Fluorescence-guided surgery with live molecular navigation-a new cutting edge, Nat Rev Cancer, 2013, 13, 653–662.
[12] He SQ, Song J, Qu JL, Cheng Z, Crucial breakthrough of second near-infrared biological window fluorophores: Design and synthesis toward multimodal imaging and theranostics, Chem Soc Rev, 2018, 47, 4258–4278.
[13] Wolfbeis OS, An overview of nanoparticles commonly used in fluorescent bioimaging, Chem Soc Rev, 2015, 44, 4743–4768.
[14] Guo ZQ, Park S, Yoon J, Shin I, Recent progress in the development of near-infrared fluorescent probes for bioimaging applications, Chem Soc Rev, 2014, 43, 16–29.
[15] Hu RR, Leung NLC, Tang BZ, AIE macromolecules: Syntheses, structures and functionalities, Chem Soc Rev, 2014, 43, 4494–4562.
[16] Fernández-Suárez M, Ting AY, Fluorescent probes for super-resolution imaging in living cells, Nat Rev Mol Cell Biol, 2008, 9, 929–943.
[17] Hong YN, Lam JWY, Tang BZ, Aggregation-induced emission, Chem Soc Rev, 2011, 40, 5361–5388.
[18] Algar WR, Hildebrandt N, Vogel SS, Medintz IL, FRET as a biomolecular research tool-understanding its potential while avoiding pitfalls, Nat Methods, 2019, 16, 815–829.
[19] Hong YN, Lam JWY, Tang BZ, Aggregation-induced emission: Phenomenon, mechanism and applications, Chem Commun, 2009, 7, 4332–4353.
[20] Gao M, Tang BZ, Fluorescent sensors based on aggregation-induced emission: Recent advances and perspectives, ACS Sens, 2017, 2, 1382–1399.
[21] Luo JD, Xie ZL, Lam JWY, et al., Aggregation-induced emission of 1-methyl-1,2,3,4,5-pentaphenylsilole, Chem Commun, 2001, 18, 1740–1741.
[22] Peng Q, Yi YP, Shuai ZG, Shao JS, Toward quantitative prediction of molecular fluorescence quantum efficiency: Role of duschinsky rotation, J Am Chem Soc, 2007, 129, 9333–9339.

[23] Mei J, Leung NLC, Kwok RTK, Lam JWY, Tang BZ, Aggregation-induced emission: Together we shine united we soar! Chem Rev, 2015, 115, 11718–11940.
[24] Ding D, Li K, Liu B, Tang BZ, Bioprobes based on AIE fluorogens, Acc Chem Res, 2013, 46, 2441–2453.
[25] Cai XL, Liu B, Aggregation-induced emission: Recent advances in materials and biomedical applications, Angew Chem Int Ed, 2020, 59, 9868–9886.
[26] Liang J, Tang BZ, Liu B, Specific light-up bioprobes based on AIEgen conjugates, Chem Soc Rev, 2015, 44, 2798–2811.
[27] Li K, Liu B, Polymer-encapsulated organic nanoparticles for fluorescence and photoacoustic imaging, Chem Soc Rev, 2014, 43, 6570–6597.
[28] Wang Y-F, Zhang TB, Liang X-J, Aggregation-induced emission: Lighting up cells revealing life!, Small, 2016, 12, 6451–6477.
[29] Yan LL, Zhang Y, Xu B, Tian WJ, Fluorescent nanoparticles based on AIE fluorogens for bioimaging, Nanoscale, 2016, 8, 2471–2487.
[30] La DD, Bhosale SV, Jones LA, Bhosale SV, Tetraphenylethylene-based AIE-active probes for sensing applications, ACS Appl Mater Interfaces, 2018, 10, 12189–12216.
[31] Feng GX, Liu B, Aggregation-induced emission (AIE) dots: Emerging theranostic nanolights, Acc Chem Res, 2018, 51, 1404–1414.
[32] Hu F, Xu SD, Liu B, Photosensitizers with aggregation-induced emission: Materials and biomedical applications, Adv Mater, 2018, 30, 1801350.
[33] Cook TR, Stang PJ, Recent developments in the preparation and chemistry of metallacycles and metallacages via coordination, Chem Rev, 2015, 115, 7001–7045.
[34] Han MX, Engelhard DM, Clever GH, Self-assembled coordination cages based on banana-shaped ligands, Chem Soc Rev, 2014, 43, 1848–1860.
[35] Clever GH, Shionoya M, Metal-base pairing in DNA, Coord Chem Rev, 2010, 254, 2391–2402.
[36] Wang W, Wang Y-X, Yang H-B, Supramolecular transformations within discrete coordination-driven supramolecular architectures, Chem Soc Rev, 2016, 45, 2656–2693.
[37] Yu GC, Jiang MJ, Huang FH, Chen XY, Supramolecular coordination complexes as diagnostic and therapeutic agents, Curr Opin Chem Biol, 2020, 61, 19–31.
[38] Yamashina M, Sartin MM, Sei Y, et al., Preparation of highly fluorescent host–guest complexes with tunable color upon encapsulation, J Am Chem Soc, 2015, 137, 9266–9269.
[39] Han MX, Michel R, He B, et al., Light-triggered guest uptake and release by a photochromic coordination cage, Angew Chem Int Ed, 2013, 52, 1319–1323.
[40] Ramsay WJ, Rizzuto FJ, Ronson TK, Caprice and K, Nitschke JR, Subtle ligand modification inverts guest binding hierarchy in $M^{II}_8L_6$ supramolecular cubes, J Am Chem Soc, 2016, 138, 7264–7267.
[41] Fujita D, Ueda Y, Sato S, et al., Self-assembly of $M_{30}L_{60}$ icosidodecahedron, Chem, 2016, 1, 91–101.
[42] Tian Y, Yan XZ, Saha ML, Niu ZW, Stang PJ, Hierarchical self-assembly of responsive organoplatinum(II) metallacycle–TMV complexes with turn-on fluorescence, J Am Chem Soc, 2016, 138, 12033–12036.
[43] Zhou ZX, Yan XZ, Saha ML, et al., Immobilizing tetraphenylethylene into fused metallacycles: Shape effects on fluorescence emission, J Am Chem Soc, 2016, 138, 13131–13134.
[44] Yan XZ, Wang HZ, Hauke CE, et al., A suite of tetraphenylethylene-based discrete organoplatinum(II) metallacycles: Controllable structure and stoichiometry, aggregation-induced emission, and nitroaromatics sensing, J Am Chem Soc, 2015, 137, 15276–15286.
[45] Yan XZ, Wang M, Cook TR, et al., Light-emitting superstructures with anion effect: Coordination-driven self-assembly of pure tetraphenylethylene metallacycles and metallacages, J Am Chem Soc, 2016, 138, 4580–4588.

[46] Zhao ZJ, Lam JWY, Tang BZ, Tetraphenylethene: A versatile AIE building block for the construction of efficient luminescent materials for organic light-emitting diodes, J Mater Chem, 2012, 22, 23726–23740.
[47] Yu Y, Qin AJ, Feng C, et al., An amine-reactive tetraphenylethylene derivative for protein detection in SDS-PAGE, Analyst, 2012, 137, 5592–5596.
[48] Zhao E, Hong YN, Chen SJ, et al., Highly fluorescent and photostable probe for long-term bacterial viability assay based on aggregation-induced emission, Adv Healthcare Mater, 2014, 3, 88–96.
[49] Yuan WZ, Tan YQ, Gong YY, et al., Synergy between twisted conformation and effective intermolecular interactions: Strategy for efficient mechanochromic luminogens with high contrast, Adv Mater, 2013, 25, 2837–2843.
[50] Yan XZ, Cook TR, Wang P, Huang FH, Stang PJ, Highly emissive platinum(II) metallacages, Nat Chem, 2015, 7, 342–348.
[51] Schmitt F, Freudenreich J, Barry NPE, Juillerat-Jeanneret L, Süss-Fink G, Therrien B, Organometallic cages as vehicles for intracellular release of photosensitizers, J Am Chem Soc, 2012, 134, 754–757.
[52] Gupta G, Denoyelle-Di-Muro E, Mbakidi J-P, Leroy-Lhez S, Sol V, Therrien B, Delivery of porphin to cancer cells by organometallic Rh(III) and Ir(III) metalla-cages, J Organomet Chem, 2015, 787, 44–50.
[53] Yu GC, Cook TR, Li Y, et al., Tetraphenylethene-based highly emissive metallacage as a component of theranostic supramolecular nanoparticles, Proc Natl Acad Sci USA, 2016, 113, 13720–13725.
[54] Yu GC, Yu S, Saha ML, et al., A discrete organoplatinum(II) metallacage as a multimodality theranostic platform for cancer photochemotherapy, Nat Commun, 2018, 9, 4335.
[55] Yu GC, Zhu BY, Shao L, et al., Host–guest complexation-mediated codelivery of anticancer drug and photosensitizer for cancer photochemotherapy, Proc Natl Acad Sci USA, 2019, 116, 6618–6623.
[56] Chakrabarty R, Mukherjee PS, Stang PJ, Supramolecular coordination: Self-assembly of finite two- and three-dimensional ensembles, Chem Rev, 2011, 111, 6810–6918.
[57] Saha ML, Yan X, Stang PJ, Photophysical properties of organoplatinum(II) compounds and derived self-assembled metallacycles and metallacages: Fluorescence and its applications, Acc Chem Res, 2016, 49, 2527–2539.
[58] Yin G-Q, Wang H, Wang X-Q, et al., Self-assembly of emissive supramolecular rosettes with increasing complexity using multitopic terpyridine ligands, Nat Commun, 2018, 9, 567.
[59] Sinha N, Stegemann L, Tan TTY, Doltsinis NL, Strassert CA, Hahn FE, Turn-on fluorescence in tetra-NHC ligands by rigidification through metal complexation: An alternative to aggregation-induced emission, Angew Chem Int Ed, 2017, 56, 2785–2789.
[60] Sun L-Y, Feng T, Das R, Hahn FE, Han Y-F, Synthesis, characterization, and properties of tetraphenylethylene-based tetrakis-NHC ligands and their metal complexes, Chem Eur J, 2019, 25, 9764–9770.
[61] Yan Y, Yin G-Q, Khalife S, He Z-H, Xu C, Li XP, Self-assembly of emissive metallocycles with tetraphenylethylene, BODIPY and terpyridine in one system, Supramol Chem, 2019, 31, 597–605.
[62] Yang LL, Jing X, He C, Chang ZD, Duan CY, Redox-active M_8L_6 cubic hosts with tetraphenylethylene faces encapsulate organic dyes for light-driven H_2 production, Chem Eur J, 2016, 22, 18107–18114.
[63] Zhang T, Zhang G-L, Yan -Q-Q, et al., Self-assembly of a tetraphenylethylene-based capsule showing both aggregation- and encapsulation-induced emission properties, Inorg Chem, 2017, 57, 3596–3601.

[64] Chen L-J, Ren -Y-Y, Wu N-W, et al., Hierarchical self-assembly of discrete organoplatinum(II) metallacycles with polysaccharide via electrostatic interactions and their application for heparin detection, J Am Chem Soc, 2015, 137, 11725–11735.
[65] Li ZK, Li YM, Zhao YM, et al., Synthesis of metallopolymers and direct visualization of the single polymer chain, J Am Chem Soc, 2020, 142, 6196–6205.
[66] Zhou ZX, Yan X, Cook TR, Saha ML, Stang PJ, Engineering functionalization in a supramolecular polymer: Hierarchical self-organization of triply orthogonal non-covalent interactions on a supramolecular coordination complex platform, J Am Chem Soc, 2016, 138, 806–809.
[67] Lu CJ, Zhang M, Tang DT, et al., Fluorescent metallacage-core supramolecular polymer gel formed by orthogonal metal coordination and host–guest interactions, J Am Chem Soc, 2018, 140, 7674–7680.
[68] Yan XZ, Wei PF, Liu YH, et al., Endo- and exo-functionalized tetraphenylethylene $M_{12}L_{24}$ nanospheres: Fluorescence emission inside a confined space, J Am Chem Soc, 2019, 141, 9673–9679.
[69] Li GF, Zhou ZX, Yuan C, et al., Trackable supramolecular fusion: Cage to cage transformation of tetraphenylethylene-based metalloassemblies, Angew Chem Int Ed, 2020, 59, 10013–10017.
[70] Zhang C-W, Ou B, Jiang S-T, et al., Cross-linked AIE supramolecular polymer gels with multiple stimuli-responsive behaviours constructed by hierarchical self-assembly, Polym Chem, 2018, 9, 2021–2030.
[71] Zheng W, Yang G, Jiang S-T, et al., A tetraphenylethylene (TPE)-based supra-amphiphilic organoplatinum(ii) metallacycle and its self-assembly behavior, Mater Chem Front, 2017, 1, 1823–1828.
[72] Chen L-J, Jiang B, Yang H-B, Transformable nanostructures of cholesteryl-containing rhomboidal metallacycles through hierarchical self-assembly, Org Chem Front, 2016, 3, 579–587.
[73] Zhang C-W, Jiang S-T, Yin G-Q, Li XP, Zhao X-L, Yang H-B, Dual stimuli-responsive cross-linked AIE supramolecular polymer constructed through hierarchical self-assembly, Isr J Chem, 2018, 58, 1265–1272.
[74] Li M, Jiang S, Zhang Z, et al., Tetraphenylethylene-based emissive supramolecular metallacages assembled by terpyridine ligands, CCS Chem, 2020, 2, 337–348.
[75] Hu Y-X, Hao XT, Xu L, et al., Construction of supramolecular liquid-crystalline metallacycles for holographic storage of colored images, J Am Chem Soc, 2020, 142, 6285–6294.
[76] Zhang MM, Saha ML, Wang M, et al., Multicomponent platinum(II) cages with tunable emission and amino acid sensing, J Am Chem Soc, 2017, 139, 5067–5074.
[77] Liu XJ, Smith DG, Jolliffe KA, Are two better than one? Comparing intermolecular and intramolecular indicator displacement assays in pyrophosphate sensors, Chem Commun, 2016, 52, 8463–8466.
[78] Han ZX, Dong LH, Sun F, et al., A novel fluorescent probe with extremely low background fluorescence for sensing hypochlorite in zebrafish, Anal Biochem, 2020, 602, 113795.
[79] Tian D, Li F, Zhu ZC, Zhang LB, Zhu JT, An AIE-based metallo-supramolecular assembly enabling an indicator displacement assay inside living cells, Chem Commun, 2018, 54, 8921–8924.
[80] Zhang MM, Li SY, Yan XZ, et al., Fluorescent metallacycle-cored polymers via covalent linkage and their use as contrast agents for cell imaging, Proc Natl Acad Sci USA, 2016, 113, 11100–11105.

[81] Dong JQ, Pan YT, Wang H, et al., Self-assembly of highly stable zirconium(IV) coordination cages with aggregation induced emission molecular rotors for live-cell imaging, Angew Chem Int Ed, 2020, 59, 10151–10159.
[82] Yu GC, Zhang MM, Saha ML, et al., Antitumor activity of a unique polymer that incorporates a fluorescent self-assembled metallacycle, J Am Chem Soc, 2017, 139, 15940–15949.
[83] Jeyakkumar P, Liang YP, Guo MY, et al., Emissive metallacycle-crosslinked supramolecular networks with tunable crosslinking densities for bacterial imaging and killing, Angew Chem Int Ed, 2020, 59, 15199–15203.
[84] Gao SJ, Yan XZ, Xie GC, et al., Membrane intercalation-enhanced photodynamic inactivation of bacteria by a metallacycle and TAT-decorated virus coat protein, Proc Natl Acad Sci USA, 2019, 116, 23437–23443.
[85] Tao GQ, Ji T, Wang N, et al., Self-assembled saccharide-functionalized amphiphilic metallacycles as biofilms inhibitor via “Sweet Talking”, ACS Macro Lett, 2020, 9, 61–69.

Index

https://doi.org/10.1515/9783110673074-023